第七届“空间信息网络”学术论坛

The 7th Space Information Networks Symposium

会议论文集

湖北 · 武汉
2023年10月

目　录

A System-Level Entity-in-the-Loop Simulation Platform for Space-Terrestrial Integrated Network

Houze Liang[1], Xinhua Zheng[1], Junrong Li[1],Tianyu Lu[1], Xiang Chen[1*]

[1]Sun Yat-sen University, Guangzhou, China
Corresponding author: Xiang Chen, chenxiang@mail.sysu.edu.cn.

***Abstract*—As terrestrial mobile networks continue to converge with Low-Earth-Orbit (LEO) satellite systems to augment connectivity and facilitate low-latency services, the imperative for exhaustive validation mechanisms grows increasingly salient. This paper introduces a flexible space-terrestrial integrated testbed designed to address this gap. The testbed enables the flexible validation of diverse network architectures, focusing on systemic challenges in satellite networks. The paper further analyzes the exacerbating impact of high mobility and handovers on long-haul signaling procedures in space-terrestrial integrated networks. Utilizing systemic simulation and a satellite-based edge core network deployment strategy facilitated by the testbed, we achieve improvements in access robustness. Lastly, the testbed's adaptability and potential as a tool for future network design and optimization are also highlighted.**

***Keywords* — Space-Terrestrial Integrated Communication, LEO Satellites, Entity-in-the-Loop(EIL) Testbed**

I. INTRODUCTION

Over the past few decades, mobile communication networks have improved a lot, moving from 2G to 5G systems. These improvements have increased speed and bandwidth and have also made services available to billions of people around the world. However, there are still challenges like high costs and limited coverage, especially in remote and sea areas.

To mitigate the coverage gaps inherent in conventional mobile networks in these specialized settings, Low Earth Orbit (LEO) satellite systems have become a popular solution. Initiatives like Iridium and Globalstar pioneered the use of LEO satellites for global communications as early as the 1990s. These early efforts faced problems with cost and technology. With the advent of the 21st century, advances in technology and better business plans have made LEO satellite systems more promising. Notably, projects such as SpaceX's Starlink [1] and OneWeb [2] have improved these systems by offering faster data speeds and lower delays while achieving near-global coverage via extensive satellite constellations.

As work on Beyond 5G (B5G) and 6G technologies continues, there's a growing effort to combine these new mobile technologies with LEO satellite networks [3]. The goal is to provide high-quality, everywhere access to meet the changing communication needs of the future. However, this integration introduces complexities, including costly capital expenditures (CapEx) and challenges in comprehensive validation.

Current simulation tools for validation, such as OPNET for satellite network [5-7] and UERANSIM/free5GC [8] for mobile networks, each offer unique advantages but also limitations. The former excels in managing complex network topologies but is not as good at simulating detailed behaviors of individual network node behaviors. Conversely, node-wise protocol simulations tools that focus on these details struggle with bigger, system-level challenges.

A prominent issue is that relying solely on any single tool makes it difficult to capture various complex factors in space-terrestrial integrated systems, such as congestion, signaling storms, and other special scenarios like high-speed satellite moving and dense access caused by urban tides. Study [9] employs system-level simulation modeling at the PHY and MAC layers, providing a detailed description of high mobility and high downlink interference switching scenarios in LEO satellite networking, thereby analyzing the performance of switching algorithms. This method allows for customized analysis and optimization of the handover process but is limited in its applicability to large-scale issues such as network architecture improvements. Study [10] addresses the issue of signaling storms generated by state migration during high-speed satellite transits and uses business dataset [11] to model this situation, analyzing and validating the architectural improvements proposed in the article. However, due to the general shortage of business datasets for space-terrestrial integrated networks, it is difficult to validate updated procedures when the network architecture is updated. This makes traditional simulation approaches inadequate for comprehensively and accurately describing and optimizing specific scenarios.

In order to tackle the aforementioned problem, this paper integrates the aforementioned large-scale network simulation with detailed protocol stack simulation tools, while putting forward a system-level simulation method based on the Entity-in-the-Loop(EIL) paradigm. The aim is to provide a more comprehensive and accurate simulation of the performance of LEO satellite systems. Employing this methodology enables us to leverage actual node-generated business datasets while facilitating nuanced analyses of specialized scenarios, including control plane signaling congestion and extended latencies.

The remainder of this paper is organized as follows:

Section 2 discuss the features and architecture of the space-terrestrial integrated EIL Simulation platform, presents the deployment of satellite edge AMF/SMF/UPF network topology based on its systematic feature.

Section 3 conducts experiments on the aforementioned network topology, analyzes the system latency to user access both in normal and congestion scenarios. This section demonstrates the system's capability to analyze metrics in specific architecture workflows in space-terrestrial integrated networks.

Section 4 concludes the paper and outlines avenues for future research.

II. AIR-GROUND INTEGRATED SYSTEM-LEVEL PLATFORM

The space-terrestrial integrated EIL topology is composed of two main components: the EIL simulation platform and the customized deployment utilizing this platform. To accurately depict specific scenarios and workflows in space-terrestrial integrated networking, such as signaling storms during handovers and hotspot area access, we introduce the EIL simulation platform. This platform employs a nearly complete protocol stack to simulate real interactions within the network and replicating dedicated scenarios. Based on this simulation platform, diverse B5G satellite core network topologies can be constructed to simulate the aforementioned customized scenarios.

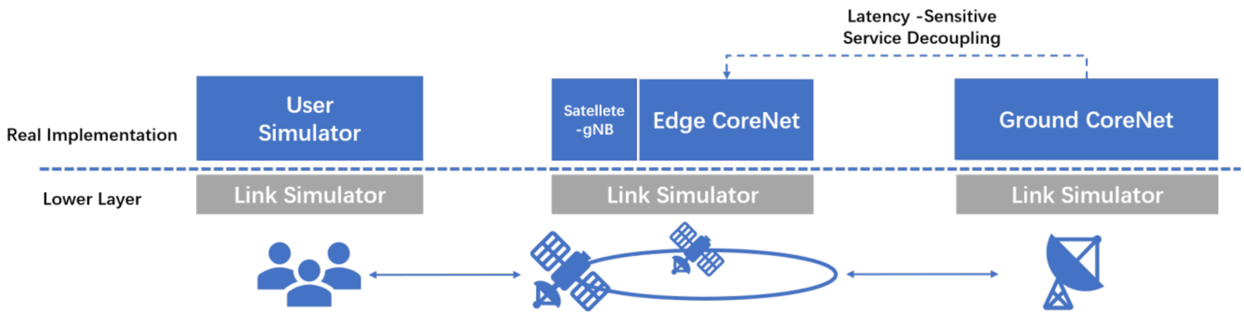

Figure 1 Lower and Upper Layer Modeling of Nodes

A. Space-terrestrial integrated EIL Simulation Platform

The EIL simulation platform consists of EIL nodes and a simulation medium environment. The former includes EIL modeling of satellites, ground stations, and users, while the latter describes the interaction or medium between EIL nodes, including their positional and visibility relationships, and the status of connected channels.

a) EIL Modeling of Integrated Nodes

EIL simulation is employed to precisely emulate procedures or workflows within specified architectures, activated by targeted signaling behaviors. The key to this approach is the EIL modeling of satellites, ground stations, and users, which we call integrated nodes. Each node's EIL model is split into two main parts: the basic infrastructure and lower-layer communication layer, and the higher-level protocols that connect to the real nodes. This two-part model gives us a detailed look at how each node actually behaves.

The core infrastructure mainly uses statistical models to simplify real network connections. Our simulation platform leverages OPNET's packet mechanisms to manage the complexities of lower layers, ensuring reliable point-to-point data transfer. For aspects like retransmission requests, we've employed statistical models, such as bit error rate and packet loss rate. This approach is sufficient for our goal: to simulate specific behavior in given architecture like control and user-plane congestion across various network setups, without adding unnecessary complexity.

The upper protocol layer defines the capabilities and responses of simulated nodes. We've customized open-source 5G core network software free5GC [12] and 5G access network software UERANSIM [13] to fit the interaction logic in our integrated EIL simulation platform. These customizations are integrated into the core infrastructure, allowing for consistent interactions within the simulated network. To enable flexible setup of base stations and core network components, we've modularized the protocol stack software. This modularity allows for the distributed deployment of latency-sensitive functions in AMF/SMF/UPF, either on satellites or other edge locations, thereby enhancing the platform's adaptability for testing various network architectures.

b) EIL Node Interaction Simulation

In the construction of the EIL simulation platform, EIL modeling of node interactions occupies a central position. Based on the aforementioned modeling, the

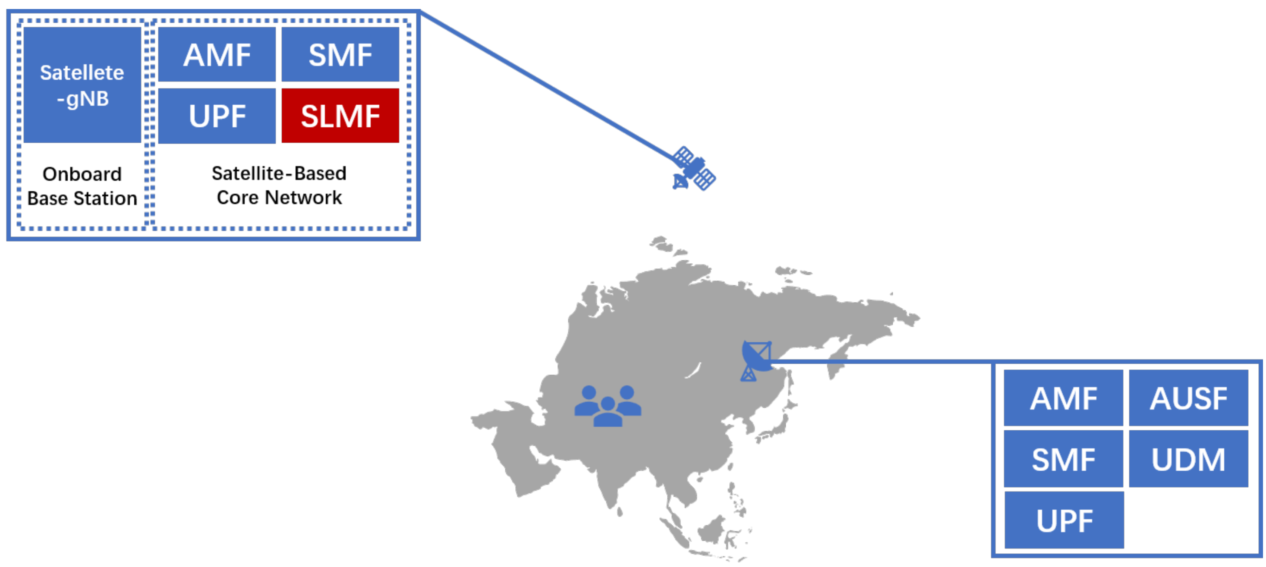

Figure 2 Deployment Topology of Satellite Core Network

system provides detailed depictions of the interactions and intermediate steps between these basic units, simulating complex dynamic topologies and describing these nodes' interactions within the topology. These basic interactions include connection, tracking, and movement. Changes in topology affect basic interactions like connection, communication, and tracking, which in turn influence different strategies composed of these basic interactions.

B. Deployment and Verification of Satellite Core Network Topology

Unlike standard 5G mobile networks, space-ground integrated networks face unique challenges like on-board routing and managing ground user access. We've adapted the AMF/SMF/UPF functions from 5G to work on satellite nodes and introduced new algorithms tailored for the fast-changing conditions in LEO satellite networks.

As Figure 2 shows, LEO satellites serve as base stations, allowing direct links with ground users. Other core network functions, like UDM/AUSF and less time-sensitive AMF/SMF/UPF tasks, are handled at ground stations. Ground users connect directly to these on-board base stations, and both satellite and ground networks work together to manage user data and control signals.

We've also added a Satellite Link Management Function (SLMF) to the system, which is unique to space-based networks. SLMF helps collect and store global link data and operates under various strategies. Specifically, it monitors and manages:

a) The connectivity between adjacent satellites

b) The quality of these inter-satellite links

c) Global inter-satellite link information of the entire LEO network

.

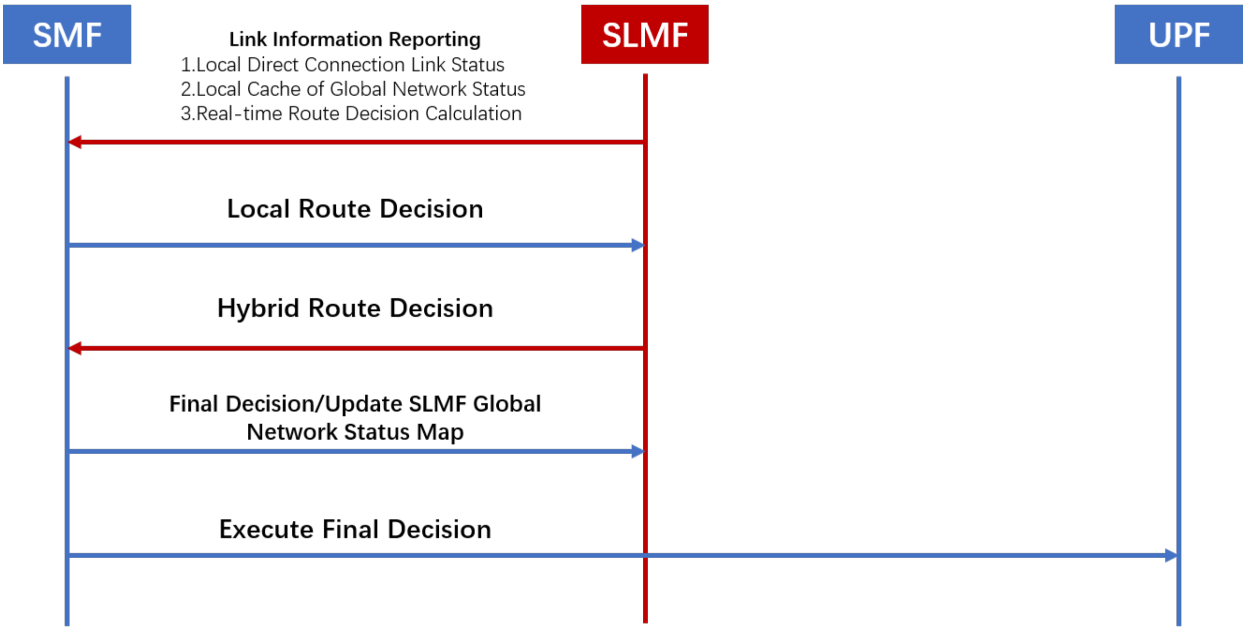

Figure 3 SLMF Decision Procedure

SLMF with the previously mentioned state data plays an active role in network routing. It alleviates the routing complexity arising from the fast-changing and periodic nature of LEO satellites by utilizing comprehensive inter-satellite link data. For routing decisions, SLMF relies on its local topology data and periodically sends key information to SMF, allowing for more informed routing choices.

The configuration of the LEO constellation consists of 12*18 satellites forming a rose constellation, with its constellation parameters shown in Table I and Figure 4. There are a total of seven ground stations, mainly located in mainland China, and users are deployed globally according to a configured distribution.

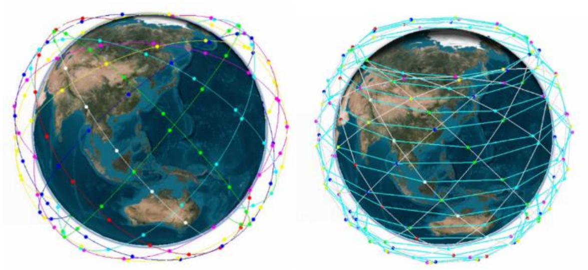

Figure 4 216 Rose Constellation and Inter-Satellite Link Connectivity

Control of direct satellite-to-Earth links and on-orbit routing is implemented at upper-layer signaling procedure handling functions. The SLMF component operates as a strategic plugin within the on-board protocol stack, linked to a specialized inter-satellite link management module. By aggregating link data for routing decisions, it contributes to control-plane routing led by SMF/UPF.

Table II Parameters of the 216-Satellite Inclined Orbit Rose Constellation

Parameter	Orbital Altitude	Orbital Inclination	Total Number of Satellites	Number of Orbital Planes	Number of Satellites per Orbital Plane	Phase Factor
	1150 km	50°	216	12	18	1

III. EXPERIMENTAL RESULTS

Based on the topology delineated in the preceding section, we executed a series of experiments to evaluate critical performance metrics, including latency and congestion, throughout the access procedure. Beyond the topology and parameters outlined in Section Ⅱ.B, we exploited the discrete-event simulation capabilities of our system to configure the processing delay to be substantially lower than the associated transmission delay. The ensuing results and their comprehensive analysis are detailed in the subsequent subsections.

A. Satellite Access Latency

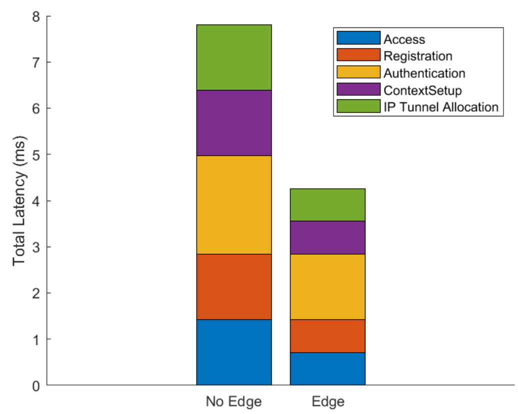

Figure 5 Comparative Latency Analysis Across Various Procedures in Edge-Deployed AMF/SMF/UPF Architecture

Figure 5 contrasts the latency during the access registration procedure between the architecture proposed herein and the "No Edge" topology, where the satellite serves only as an access base station and forwarding relay interacting with users and the ground core network without edge NFs. The edge-integrated terrestrial-satellite framework demonstrates a marked reduction in latency during onboard satellite access. This design leverages the locational advantages of edge deployment, significantly diminishing transmission time over N2 interfaces and curtailing the latency induced by multi-hop satellite links. In scenarios involving extended multi-hop transmissions, both round-trip times and computational delays adversely affect satellite mobility. During simulations, there is a likelihood that the authentication procedure remains incomplete; this, coupled with satellite mobility, necessitates intra-satellite beam switching, thereby triggering an expedited reconnection or even necessitating a re-initiation of the authentication procedure.

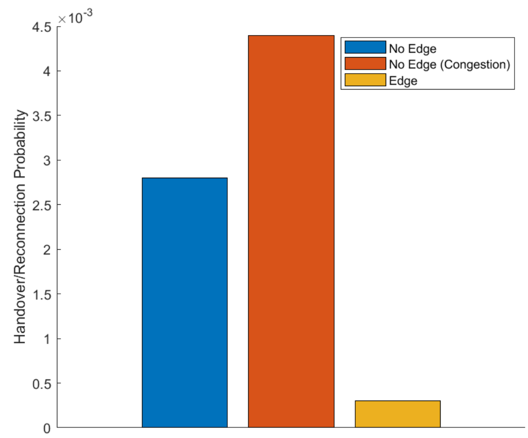

Figure 6 Probability of Reconnection/Intra-Satellite Beam Switching During Extended Procedures Across Different Deployment Strategies, Averaging 500 Users per Satellite

Figure 6 illustrates the probability of either reconnection or intra-satellite beam switching during protracted procedures for both traditional and proposed topologies. Owing to the inherent multi-hop nature of these extended procedures, the latency incurred frequently surpasses that of terrestrial mobile communication systems. This results in an increased likelihood of enforced reconnections or switching, exacerbated by the high-velocity moving of satellites and on-orbit congestion. The strategic placement of latency-sensitive network service at the access satellite can mitigate these challenges by eliminating superfluous inter-satellite link relay steps, thereby not only reducing transmission latency but also alleviating the uncertainties introduced by prolonged congestion.

IV. CONCLUSION

This research presents the formulation of a EIL simulation platform tailored for space-terrestrial integrated systems. In light of the complexities associated with extended deployment cycles and CapEx in next-generation integrated space-terrestrial mobile communication ecosystems, our methodology leverages the software-defined attributes intrinsic to various networks. By employing system-level EIL simulations, we furnish a versatile framework that serves dual purposes: the design and validation of network architectures. As an illustrative case, we scrutinize the congestion risks inherent in satellite access and handover/reconnection procedures within our proposed network configuration. Future endeavors will concentrate on the meticulous design and optimization of diverse network architectures and topologies.

References

[1] SpaceX Starlink. https://www.starlink.com/, 2021.

[2] OneWeb constellation. https://www.oneweb.world/, 2021.

[3] Chen S, Sun S, Kang S. System integration of terrestrial mobile communication and satellite communication—the trends, challenges and key technologies in B5G and 6G[J]. China communications, 2020, 17(12): 156-171.

[4] Jia Y, Peng Z. The analysis and simulation of communication network in Iridium system based on OPNET[C]//2010 2nd IEEE International Conference on Information Management and Engineering. IEEE, 2010: 68-72.

[5] Jia Y, Peng Z. The analysis and simulation of communication network in Iridium system based on OPNET[C]//2010 2nd IEEE International Conference on Information Management and Engineering. IEEE, 2010: 68-72.

[6] Wang P, Zhang J, Zhang X, et al. Performance evaluation of double-edge satellite terrestrial networks on OPNET platform[C]//2018 IEEE/CIC International Conference on Communications in China (ICCC Workshops). IEEE, 2018: 37-42.

[7] Wang P, Zhang J, Zhang X, et al. Performance evaluation of double-edge satellite terrestrial networks on OPNET platform[C]//2018 IEEE/CIC International Conference on Communications in China (ICCC Workshops). IEEE, 2018: 37-42.

[8] Kim J, Lee J, Ko H, et al. Space mobile networks: Satellite as core and access networks for B5G[J]. IEEE Communications Magazine, 2022, 60(4): 58-64.

[9] Li Y, Li H, Liu W, et al. A case for stateless mobile core network functions in space[C]//Proceedings of the ACM SIGCOMM 2022 Conference. 2022: 298-313.

[10] Juan E, Lauridsen M, Wigard J, et al. 5G new radio mobility performance in LEO-based non-terrestrial networks[C]//2020 IEEE Globecom Workshops (GC Wkshps. IEEE, 2020: 1-6.

[11] https://github.com/yuanjieli/SpaceCore-SIGCOMM22

[12] https://github.com/free5gc/free5gc

[13] https://github.com/aligungr/UERANSIM

About the authors

Houze Liang is currently pursuing the Master's degree in Communication Engineering at Sun Yat-sen University, Guangzhou. His research interests include Space-Terrestrial Integrated Communication.
(Email: lianghz3@mail2.sysu.edu.cn)

Xinhua Zheng is currently pursuing the Master's degree in Information and Communication Engineering at Sun Yat-sen University, Guangzhou. Her research interests include Orthogonal Time Frequency Space, Satellite Communication.
(Email: zhengxh56@mail2.sysu.edu.cn)

Junrong Li is currently pursuing the Master's degree in Communication Engineering at Sun Yat-sen University, Guangzhou. Her research interests include Satellite Communication, Resource Allocation.
(Email: lijr75@mail2.sysu.edu.cn)

Xiang Chen (Member, IEEE) received the B.E. and Ph.D. degrees from the Department of Electronic Engineering, Tsinghua University, Beijing, China, in 2002 and 2008, His research interests mainly include 5G wireless and mobile communication networks, the Internet of Things (IoT). Corresponding author.
(Email: chenxiang@mail.sysu.edu.cn)

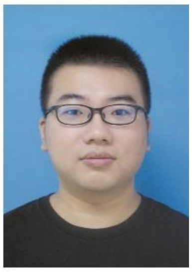

Tianyu Lu is currently pursuing the PhD in electronic information at Sun Yat-sen University, Guangzhou. His research interests include 6G AI-Native Air Interface.
(Email: luty25@mail2.sysu.edu.cn)

A Content-Based Generator Method for Vessel Detection

Yang Yang[1], Zhenzhen Xu[1], Xingyu Liu[1], Jun Pan[1*], Likun Liu[2]
1 State Key Laboratory of Information Engineering in Surveying, Mapping and Remote Sensing, Wuhan University, 129 Luoyu Road, Wuhan 430079, China;
2 China Ship Development and Design Center, 268 Zhangzhidong Road, Wuhan 430064, China;
* Correspondence: panjun1215@whu.edu.cn

Abstract—With the advancement of satellite imaging technology, the interpretation of remote sensing(RS)images has become an important subject. Especially in the object recognition field, accurate acquisition of vessel location and classification information is crucial to develop strategic plans. However, the lack of ship samples in RS images has been hindering the research of ship fine categorization. In this paper, a vessel generation method based on generative adversarial network is proposed to solve the insufficient samples in RS images. Dealing with sample insufficiency by prior global-local segmentation, category image generation and domain translation composition. Experiments on the HRSC2016 dataset show that the generated pseudo-images are highly similar to the real vessel, which verifies the effectiveness of the method. Besides, we constructed a ship dataset containing 10,000 images, which have great significance in vessel classification and localization.

Keywords—Data expansion, deep learning, Vessel detection, Contextual separation

I. INTRODUCTION

Remote sensing (RS) image analysis has always been a significant research focus in the fields of computer vision and machine learning. It finds crucial applications in various domains such as maritime traffic surveillance, environmental monitoring, and marine management[1- 3]. In recent years, with advancements in satellite imaging technology and the availability of high-resolution RS data, efficient interpretation of RS images has become increasingly important.

Particularly in the safety and civil domain[4-6], obtaining precise vessel location and classification information is crucial for detecting the movement trajectories of vessels, enabling strategic planning, and ultimately achieving accurate targeting of ships. An excellent ship classification and recognition algorithm must be capable of correctly detecting instances belonging to the ship category, identifying the specific subcategory of the object, and accurately locating the detected ship[7-8]. However, most previous research has primarily focused on distinguishing between ships and backgrounds or a few broad categories such as commercial and military vessels. There has been limited research on fine-grained ship classification in RS images. Due to the limited availability of annotated ship datasets and the small inter-class differences in terms of shape, color, and texture among ships, conventional object detection and recognition methods struggle to achieve precise and fine-grained ship classification and localization[9-10].

For fine-grained image classification and localization tasks, there exist well-known large-scale natural datasets such as CUB-200-2011[11], Stanford Cars, and Aircraft datasets that have significantly contributed to the advancement of fine-grained image classification and localization tasks in natural scenes. Although features learned from natural images through deep convolutional networks can be fine-tuned to transfer to RS images[12], the differences in data distribution between natural and RS images cannot be eliminated. This causes models fine-tuned for natural images to perform poorly on fine-grained ship classification and location tasks for RS images. Despite the progress made using deep learning methods in object detection and recognition in RS images, the lack of a publicly available large-scale fine-grained ship classification dataset in RS images continues to pose a challenge for fine-grained ship classification and localization.

To accelerate research in fine-grained ship classification and localization in optical RS images, this paper proposes a ship dataset augmentation method based on Generative Adversarial Networks (GANs)[13] and utilizes this method to create a subclass-rich ship classification and localization dataset. We collected RS images from Google Earth and popular RS image datasets like HRSC2016[14], covering various class scales of ships. The dataset comprises 10,000 images across four categories, encompassing different types of ships, various lighting conditions, and background environments. Additionally, compared to the ship data in the HRSC2016 dataset previously used for ship classification, the number of instances for each ship category has significantly increased. This greatly enhances the task of fine-grained ship classification and localization in RS images. Our primary contributions in this work are as follows:

1.We propose a novel ship data augmentation method that can expand ship samples to approximate real images, even with limited samples. This method can provide a good data base for ship detection.

2. We create a diverse RS image fine-grained ship classification and localization dataset (HRSC-warcraft10k), which consisting 10,000 images.

II. THE PROPOSED METHOD

A. PRIOR GLOBAL-LOCALSEGMENTATION

In ship training background images, objects resembling ship features, such as bridges, dams, buildings, and containers, often appear. Unfortunately, this presence can be detrimental to the learning and training of deep convolutional neural networks. To address this issue, it is essential to implement prior global-local segmentation, aiming to eliminate the disruptive influence of complex background information. The primary processes involved in achieving this goal encompass mask extraction, straightforward data enhancement, data augmentation-based domain transfer[15], and pseudo-image generation.

By effectively distinguishing between the foreground and background, we can significantly reduce the noise impact in ship images[16]. This segmentation process yields cleaner images, leading to improved accuracy and performance when undertaking downstream tasks such as image analysis, feature extraction, target detection, and image classification.

B. CATEGORY IMAGE GENERATION

The ships conform to a standardized design, characterized by sleek and linear aesthetics. Therefore, by implementing style normalization based on these consistent attributes, a broader spectrum of ship samples can be generated.

The generator in StyleGAN2 is a layered network, wherein each layer is responsible for generating distinct details within the image. Initially, a Mapping network transforms the input random noise vector into an intermediate representation vector. Subsequently, a style modulator integrates style information with the intermediate representation vector to govern the appearance and characteristics of the generated image at every level of generation. Finally, these features undergo convolution to produce specific details and textures.

The discriminator part of StyleGAN2 adopts a progressive growing strategy, commencing with the generation and evaluation of images at lower resolutions and gradually advancing to generate higher-resolution images. This process incorporates normalization layers as well as instance normalization layers. Moreover, StyleGAN2 employs equalized learning rates to ensure equitable updates for each layer's weights. Lastly, it estimates the standard deviation for each mini-batch in order to evaluate the quality of the generated image.

C. DOMAINTRANSLATION COMPOSITION

In the context of training a Generative Adversarial Network (GAN) specifically tailored for object detection tasks, we have meticulously devised a sequential approach to generate images that encompass background information while ensuring precise annotation of ship objects in terms of their position and size. The following section outlines the methodology employed:

1) Local sample instance generation

The primary objective of our study was to eliminate any potential interference from the background and concentrate solely on generating high-quality images of the ship. This approach enables Gans to effectively learn and capture the visual features as well as morphology of ships, resulting in a consistent and diverse set of samples that style and type.

2) Global synthesis based on color consistency

To generate a ship-free background image, we employed a mask to accurately delineate the boundary between water and land areas in the raw data. Subsequently, we assigned a specific pixel value to represent the water region and uniformly applied it to all pixels within this area. This processing step yields an image processed ship-free water region. By employing pixel-level background replacement, we successfully obtain a pristine and impurity-free sea surface background image, which serves as an ideal backdrop for synthesizing pseudo-samples.

3) Overall scene details composition

Ultimately, the ship objects generated were randomly placed within the water body regions of the pure background images. This randomization process was introduced to replicate the diversity observed in real-world scenarios, thereby avoiding the imposition of excessive regularity on the data that could potentially compromise the generalization performance of the object detection model.

Through this sequence of steps, composite RS images that incorporate background information were successfully created. These images provide additional contextual information and diversify object detection tasks. This methodology significantly contributes to enhancing robustness, facilitating adaptation to various backgrounds and scenes, and ultimately resulting in exceptional performance in practical applications.

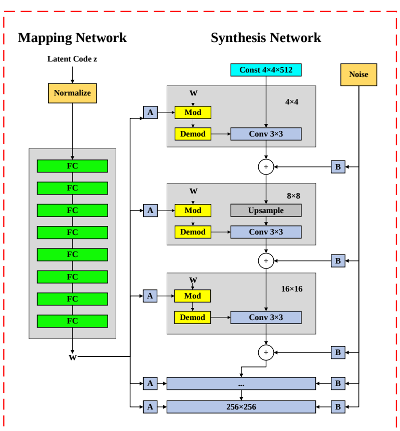

Fig. 1 StyleGANv2 framework

Ⅲ. EXPERIMENTAL EVALUATION

A. DATASET DESCRIPTION

The data used in this experiment is from the HRSC2016 dataset, which was released by Northwestern Polytechnical University in 2016. It includes images from two scenarios: open-sea vessels and near shore vessels. All the images were collected from six well-known ports, encompassing default imagery from Google Earth as well as corresponding historical data. The images in this dataset are annotated in the Oriented Bounding Box (OBB) format, with resolutions ranging from 2 meters to 0.4 meters and image sizes varying from 300×300 to 1500×900, with most exceeding 1000×600. In total, there are 1061 images with valid annotations distributed across training, validation, and test sets, consisting of 436, 181, and 444 images, respectively.

However, the dataset also has the following problems: the docking ships are densely distributed, and the coincidence of the label frames is high, making it difficult to separate a single vessel; The background of the RS image is complex, and the similarity between the texture of the ship to be measured and the nearshore is large. The number of ships of each class is small, and the small sample size leads to insufficient learning and training, and poor robustness; Some images have cloud occlusion issues, and data quality is uneven. Therefore, we chose ships with relatively difficult data acquisition and a low number as the research object.

Furthermore, to enhance sample diversity, prevent overfitting during the training process, and improve robustness, data augmentation is applied to the original data, including operations such as image flipping, image rotation, adding noise, changing brightness, altering contrast, modifying saturation, and performing histogram equalization, among others. The choice of augmentation techniques is made based on specific circumstances.

B. EVALUATION INDEXES

The IOU is used to evaluate the degree of overlap between two bounding boxes[17]. It requires a ground truth bounding box(Bgt) and predicted bounding box(Bp)[18]. As shown in Eq. 1, by applying the IOUs, we can tell whether the prediction is true positive or false positive.

$$IOU = \frac{\text{area}(B_p \cap B_{gt})}{\text{area}(B_p \cup B_{gt})} \tag{1}$$

Commonly used quantitative evaluation indicators for object detection include precision P, recall R[19], mean average accuracy mAP, etc. As shown in Eq. 2, precision refers to the proportion of correctly classified samples in all samples, reflecting the model's ability to identify relevant targets. As shown in Eq. 3, recall reflects the model's ability to find the true regression box (i.e., the box labeled by the label).

$$Precision = \frac{TP}{TP+FP} \tag{2}$$

$$Recall = \frac{TP}{TP+FN} \tag{3}$$

where TP refers to the number of positive cases correctly classified by the classifier as positive cases when the iou is greater than or equal to the threshold, FP refers to the number of positive cases that the classifier misclassifies - predicts as positive cases, and FN refers to the number of positive cases that the classifier mistakenly classifies positive cases as negative cases when the iou is less than the threshold.

AP (Average Percision) is the average accuracy, R is the horizontal axis, P is the vertical axis to draw the PR curve, AP is the area under the PR curve of a specific type of all pictures, which can measure the quality of a category of target detection[20]. mAP refers to the average of all categories of APs in all images, and the higher the map, the higher the prediction accuracy of the model. mAP@0.5 refers to the mAP when the iou threshold is taken as 0.5, and mAP@0.5:0.95 refers to the average of the model under each iou threshold.

C. EXPERIMENTAL ANALYSIS

As shown in Fig. 2, a total of 10,000 pseudo-ship RS images were generated. It is obvious that our generated vessel samples are well shaped and unified style, which can better satisfy the requirement of model training. In addition, we also put the generated pseudo-ship images into the target detection model trained with real ship RS images, and obtained high accuracy and recall rate, indicating that the pseudo-ship images generated by us are highly similar to the real ship images. The test results are shown in Table 1.

Table 1 Verification accuracy of the sample image

Image	P	R	mAP50	mAP50-95
1	1.000	0.769	0.865	0.828
2	0.990	1.000	0.995	0.977
3	1.000	0.788	0.879	0.788
4	0.997	1.000	0.995	0.897
5	1.000	0.924	0.995	0.826
6	0.833	0.833	0.903	0.763
7	1.000	0.590	0.749	0.528
8	0.833	1.000	0.995	0.857
9	1.000	1.000	0.995	0.924
10	`0.778	0.875	0.892	0.758

Figure 2 The generated pseudo-ship images

VI. CONCLUSION AND FUTURE WORK

In this paper, we propose a novel ship data augmentation method that can augment ship samples with a small number of samples. Additionally, based on this method, a high-resolution remote sensing image dataset for fine-grained ship detection (HRSC-warcraft10k) was created, which comprising 10,000 images. We employ the mask to separate the ship from the background, and Style GAN was used to learn the characteristics of the ship and expand the ship data. Finally, the generated data was randomly fused with the background to obtain a large number of pseudo-RS images. Experiments show that the ship generated by our method is closed to the real acquired ship target. Besides, It can be well identified by the ship target detection model.

References

[1] Ball, John E., Derek T. Anderson, and Chee Seng Chan. "Comprehensive survey of deep learning in remote sensing: theories, tools, and challenges for the community." Journal of applied remote sensing 11.4 (2017): 042609-042609.

[2] Ma, Lei, et al. "Deep learning in remote sensing applications: A meta-analysis and review." ISPRS journal of photogrammetry and remote sensing 152 (2019): 166-177.

[3] Signoroni, Alberto, et al. "Deep learning meets hyperspectral image analysis: A multidisciplinary review." Journal of Imaging 5.5 (2019): 52.

[4] Kanjir, Urška, Harm Greidanus, and Krištof Oštir. "Vessel detection and classification from spaceborne optical images: A literature survey." Remote sensing of environment 207 (2018): 1-26.

[5] Arnesen, Tonje Nanette, and Richard Olsen. "Literature review on vessel detection." (2004).

[6] Al-Rawi, Mohammed, Munib Qutaishat, and Mohammed Arrar. "An improved matched filter for blood vessel detection of digital retinal images." Computers in biology and medicine 37.2 (2007): 262-267.

[7] Sheng, Kai, et al. "Research on ship classification based on trajectory features." The Journal of Navigation 71.1 (2018): 100-116.

[8] Huang, Longhui, et al. "Multiple features learning for ship classification in optical imagery." Multimedia Tools and Applications 77 (2018): 13363-13389.

[9] Zhang, Tianwen, et al. "SAR ship detection dataset (SSDD): Official release and comprehensive data analysis." Remote Sensing 13.18 (2021): 3690.

[10] Wang, Yuanyuan, et al. "A SAR dataset of ship detection for deep learning under complex backgrounds." remote sensing 11.7 (2019): 765.

[11] C. Wah, S. Branson, P. Welinder, P. Perona, and S. Belongie. The caltech-ucsd birds-200-2011 dataset. Technical Report CNS-TR-2011-001, California Institute of Technology, 2011

[12] Mallat, Stéphane. "Understanding deep convolutional networks." Philosophical Transactions of the Royal Society A: Mathematical, Physical and Engineering Sciences 374.2065 (2016): 20150203..

[13] Creswell, Antonia, et al. "Generative adversarial networks: An overview." IEEE signal processing magazine 35.1 (2018): 53-65.

[14] Liu, Z.; Wang, H.; Weng, L.; Yang, Y. Ship rotated bounding box space for ship extraction from high-resolution optical satellite images with complex backgrounds. IEEE Geosci. Remote. Sens. Lett. 2016, 13, 1074–1078.

[15] Karras, Tero, Samuli Laine, and Timo Aila. "A style-based generator architecture for generative adversarial networks." Proceedings of the IEEE/CVF conference on computer vision and pattern recognition. 2019.

[16] Porter, Thomas, and Tom Duff. "Compositing digital images." Proceedings of the 11th annual conference on Computer graphics and interactive techniques. 1984.

[17] Everingham, Mark, et al. "The pascal visual object classes (voc) challenge." International journal of computer vision 88 (2010): 303-338.

[18] Papageorgiou, Constantine, and Tomaso Poggio. "A trainable system for object detection." International journal of computer vision 38 (2000): 15-33.

[19] Davis, Jesse, and Mark Goadrich. "The relationship between Precision-Recall and ROC curves." Proceedings of the 23rd international conference on Machine learning. 2006.

[20] YANG, Gao, and Bin CHEN. "Application of improved YOLOv5 object detection model in urban street scenes." Journal of Computer Applications (2023): 0.

Yang Yang received the M.S. degree in China University of Geosciences, Wuhan. 2023. He is currently pursuing the Pn. D. inthe State Key Laboratory of Surveying, Mapping and Remote Sensing Information Engineering, Wuhan University. His major research includesobject detection. (Email: yangyang1@whu.edu.cn)

Jun Pan. [corresponding author]is a professor at the State Key Laboratory of Information Engineering in Surveying, Mapping, and Remote Sensing, Wuhan University. He received the PhD degree from Wuhan University in 2008. His research interests include remote-sensing data intelligent processing and image quality improvement.(Email: panjun1215@whu.edu.cn)

基于卫星互联网环境的深度强化学习任务调度算法

JIANG Yunke[1], SUN Xiaojuan[2], ZHENG Bingbing[3]

摘　要：卫星互联网环境的动态性、高时延使得卫星移动边缘计算（Satellite Mobile Edge Computing， S-MEC）场景中具有依赖的任务调度变得尤为复杂。针对卫星动态接收任务在轨计算场景，设计了一种具有资源感知能力的深度强化学习调度系统（RA-DRL）。本文首先对 S-MEC 任务调度问题进行建模，然后使用图嵌入和注意力机制来提取 DAG 子任务的特征。同时，为了使调度方法能够适应卫星互联网拓扑的变化，使用了一种动态任务优先级机制反映计算节点之间的链路带宽。最后，使用基于 Advantage Actor–Critic 结构的深度强化学习算法对调度代理进行训练，在降低任务执行时延的同时避免了资源负载不均和网络动态拓扑的干扰。通过仿真实验以及模拟遥感视频目标检测实验表明，该算法能够适应高度动态的卫星网络条件，在进行不同的任务拓扑时都具有良好的表现。

关键词：卫星边缘计算；A2C 算法；图卷积网络；动态任务调度

Deep reinforcement learning task scheduling algorithm based on satellite Internet environment

JIANG Yunke[1], SUN Xiaojuan[2], ZHENG Bingbing[3]

Abstract: The dynamic nature and high latency of the satellite Internet environment make the scheduling of dependent tasks in the Satellite Mobile Edge Computing (S-MEC) scenario particularly complex. Aiming at the on-orbit computing scenario of satellite dynamic reception tasks, a resource-aware deep reinforcement learning scheduling system (RA-DRL) is designed. This paper first models the S-MEC task scheduling problem, and then uses graph embedding and attention mechanisms to extract the features of DAG subtasks. At the same time, in order to enable the scheduling method to adapt to changes in satellite Internet topology, a dynamic task priority mechanism is used to reflect the link bandwidth between computing nodes. Finally, a deep reinforcement learning algorithm based on the Advantage Actor–Critic structure is used to train the scheduling agent, which reduces task execution delays while avoiding interference from uneven resource loads and dynamic network topology. Through simulation experiments and simulated remote sensing video target detection experiments, it is shown that the algorithm can adapt to highly dynamic satellite network conditions and has good performance in different mission topologies.

Key words: Satellite edge computing, Advantage Actor–Critic, graph convolutional network, dynamic task scheduling

1　引言

近年来，卫星技术在制造、点波束天线、激光传输等方面取得了长足进步，使得卫星特别是低轨卫星更加经济、小型化、高通量，极大地促进了空天地一体化网络（SAGIN）的发展[1]，作为支持移动通信的重要替代方案，SAGIN 也受益于移动边缘计算(MEC)的优势，这种针对卫星互联网的边缘计算技术称为卫星移动边缘计算（SMEC）[2]。它使得边缘计算的范式从地面边缘计算转向空中/轨道边缘计算，将地面边缘计算设施推向天空（例如卫星、无人机），从而实现无处不在的连接和全球范围覆盖的可靠云计算服务。此外，SMEC 还具有低成本、组网灵活、实时数据传感和处理的优势，在偏远、复杂地形地区以及天气监测、对地观测、救灾等场景下具有广泛的应用[3]。

然而，将边缘计算集成到 SAGIN 中仍然面临着众多挑战。首先，卫星拓扑呈现高度动态的特点[4]，星间链路（ISL）带宽和连通性时变性强。同时每个卫星节点难以实现负载均衡，任务负载的变化使得其计算和通信资源快速变化。并且计算节点之间没有明确的协同策略来确保高效的任务调度，同时充分利用计算资源。

为了解决以上问题，Zhang[2]提出了动态网络虚

拟化技术来整合网络资源，并进一步设计了协作计算卸载（CCO）模型以实现 STN 中的并行计算。Tang[5]提出了一种提出了一种具有三层计算架构的混合云和边缘计算 LEO 卫星（CECLS）网络，并使用基于 ADMM 的低计算复杂度的分布式计算卸载方案解决计算卸载问题。以上方案将边缘计算任务卸载与卫星互联网结合，但是算法没有充分考虑计算节点资源的异构性，并且对动态网络拓扑的适应性较低。

为了适应高度动态的卫星网络条件，缩短任务响应延迟，实现卫星集群计算资源的高效利用，Han[6]提出一种基于动态优先级队列（SDPLS）的卫星任务时间优化调度算法，Hu[4] 提出了一种基于 A3C 算法的动态调度算法，将任务卸载到多颗卫星上的协同执行。Chai[7] 提出了一种结合注意力机制和近端策略优化协作（A-PPO）算法的训练方法，以最低的成本实现多任务系统的联合卸载。但是上述算法没有充分考虑计算节点集群中的负载均衡以及 DAG 中子任务特征和它们之间的关联。

在高度动态性的网络拓扑方面，车联网系统网络拓扑不稳定的特点[8]与卫星移动边缘计算系统具有高度的相似性，Liu[9]提出了一种基于深度强化学习的动态车辆云上的 DAG 任务调度系统。

综上所述，本文提出一种具有资源感知能力的深度强化学习调度系统（RA-DRL），能够准确的提取任务工作流中子任务的特征和它们之间的关联，减少链路中断和节点宕机对任务调度的影响，同时平衡节点负载和减少任务完成时延。综上所述，本文的贡献总结如下：

（1）提出一种基于图嵌入和深度强化学习的算法，解决动态卫星互联网环境任务调度问题。

（2）优化了动态任务优先级队列算法，反映计算节点网络拓扑的变化，将其应用于多层卫星移动边缘计算系统。

（3）将动态任务调度问题转化为马尔可夫决策过程，提出了针对卫星计算节点负载均衡和是时延优化的 DDQN 组件，仿真结果验证了所提出的算法优于其他算法。

本文其余组织部分：

下一节介绍系统模型。第 3 节介绍具有注意力机制的图编码器和解码器模型。第 4 节介绍了 MDP 任务调度模型和基于 A3C 的负载平衡与时延优化算法。第 5 节介绍实验结果，第 6 节介绍了结论性意见和未来工作。

2 系统模型：

本节介绍了卫星动态互联网环境下的移动边缘计算场景，包括系统整体结构，任务模型与动态资源模型、计算卸载模型、任务优先级以及优化模型。

2.1 卫星移动边缘计算系统结构：

在空天地一体化网络（SAGIN）中，如图 1 所示，多任务 MEC 系统由三层设备组成，即地面终端、低轨卫星群和高轨卫星群。其中，地面终端由地面网段连接，低轨卫星集群位于距离地球表面较近的轨道上，通信时延较低，但同时具有移动性高，网络连接不稳定，计算资源有限的特点，在卫星移动边缘计算系统结构中构成边缘层，高轨卫星集群位置相对于地球是固定的，覆盖范围广，计算资源较为充足，但同时由于距离地面终端较远，通信时延较长，在卫星移动边缘计算系统结构中构成云计算层。

综上，卫星移动边缘计算系统任务调度流程如下：用户生成任务以及任务信息，发送至调度器，调度器根据调度算法以及任务信息进行任务卸载决策并将决策返回用户，用户终端执行卸载决策，将任务在本地执行或上传到边缘设备或云计算层，并将执行结果返回用户。

2.2 任务模型与动态资源集群模型：

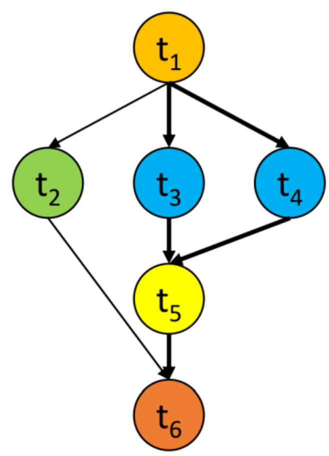

Figure 1 Example of DAG

应用程序通常可以使用有向无环图（directed acyclic graph，DAG） $G_{task}=(V_{task},E_{task})$ 来描述，如图 2 所示。 V_{task} 中有 n 个节点，每个节点代表一个子任务。每个任务 $v_i \in V_{task}$ 是放置在资源节点上的最小单元，由两个参数来表示特征： $v_{i.cpu}$ （所

需的 CPU 时钟周期数）和 $v_{i.mem}$（所占用的内存）。任务 v_j 的前驱任务集表示为 $pred(v_j)$，后继任务集表示为 $succ(v_j)$，连接任务 (v_i, v_j) 的边 $e_{ij} \in E_{task}$ 表示两个子任务之间传输的数据量，将所有入度为零的节点称为入口任务，记为 v_{entry}，将所有出度为零的节点称为出口任务，记为 v_{exit}。

资源集群模型由完全连接的无向图 $G_{res} = (V_{res}, E_{res})$ 表示，节点 $u_m \in V_{res}$ 代表卫星移动边缘计算系统中的每一个计算节点，其中，u_m 有两个特征：$u_{m.cpu}$ 代表节点 CPU 计算能力，即节点的计算能力，$u_{m.mem}$ 代表节点内存资源。边 $d_{mn} \in E_{res}$ 代表节点 (u_m, u_n) 之间的通信带宽。

2.3　卸载模型

任务所在计算节点的最早就绪时间：

$$Avaliable(n) = \max_{v_i \in pred(v_j)} (AFT_i), v_j \in V_{task} \qquad 公式\ 2\text{-}1$$

任务 v_j 的最早就绪时间时计算节点 u_n 获取到所有前序任务的输出的时间，其中，AFT 表示 v_j 的所有前驱子任务 $v_i \in pred(v_j)$ 的实际完成时间。

任务传输时间：

$$TT_{i,m;j,n} = \begin{cases} c_{ij}(t), m \neq n \\ 0, m = n \end{cases}, \qquad 公式\ 2\text{-}2$$

$$c_{ij}(t) = hop(m,n,t) \times \frac{e_{ij}}{d_{mn}(t)} \qquad 公式\ 2\text{-}3$$

其中，$TT_{i,m;j,n}$ 代表当子任务 v_i 和其后继任务 v_j 分别分配给设备 u_m, u_n 时，相关数据的传输时间，当 $m = n$ 时，传输时间为 0。$hop(m,n,t)$ 为 t 时刻从设备 u_m 到 u_n 的路由跳数，$d_{mn}(t)$ 表示 t 时刻设备之间的传输带宽。

任务最早可执行时间：

$$EST(v_j, u_n) = \max\{Avaliable(n), \max_{v_i \in pred(v_j)} (AFT_i + TT_{i,m;j,n})\} \qquad 公式\ 2\text{-}4$$

子任务 v_j 在节点 u_n 的最早可执行时间为计算节点 u_n 的就绪时间 $Avaliable(n)$ 和任务依赖的所有数据到达节点 u_n 的时间中的较大值。

任务的最早完成时间：

$$EFT(v_j, u_n) = EST(v_j, u_n) + \frac{v_{j.cpu}}{u_{n.cpu}} \qquad 公式\ 2\text{-}5$$

其中，$v_{j.cpu}$ 表示任务 v_i 的计算资源需求，$u_{m.cpu}$ 表示执行该任务的设备的计算能力。

2.4　优化约束：

为了确保卫星节点计算资源的有效利用，我们以保持设备负载均衡和最小化任务整体完成时间为目标，定义了卫星移动边缘计算任务调度的优化成本函数：

$$COST = \alpha Makespan + (1-\alpha) Load \qquad 公式\ 2\text{-}6$$

$$Makespan = \xi_{j,n} \max_{v_j \in V_{task}, u_n \in V_{res}} \{EFT_{j,n}\} \qquad 公式\ 2\text{-}7$$

$$Load = \sqrt{\frac{1}{|V_{res}|} \sum_{n=1}^{|V_{res}|} \left(A_{n,t+1}^{cpu} - \frac{\sum_{m=1}^{|V_{res}|} A_{m,t+1}^{cpu}}{|V_{res}|}\right)^2} \qquad 公式\ 2\text{-}8$$

$$A_{n,t+1}^{cpu} = \begin{cases} \dfrac{A_{n,t}^{cpu} - v_{j.cpu}}{u_{n.cpu}}, if A_{n,t}^{cpu} - v_{j.cpu} \geq 0, \\ 0, otherwise, \end{cases} \qquad 公式\ 2\text{-}9$$

约束条件：

（1）$\sum_{u_n \in V} \xi_{j,n} = 1$

（2）$\xi_{j,n} \in \{0,1\}$

（3）$EST_{i,m} \geq EFT_{j,n}$

其中 $A_{n,t}^{cpu}$ 和 $v_{j.cpu}$ 分别表示当前计算节点 u_n 的可用 CPU 资源和执行当前任务 v_j 所需的 CPU 资源。$u_{n.cpu}$ 表示计算节点的 CPU 算力。$A_{n,t+1}^{cpu}$ 表示 $t+1$ 时刻计算节点 u_n 的资源利用率，当 $A_{n,t}^{cpu} - v_{j.cpu} \geq 0$ 时，计算节点 u_n 的可用 CPU 资源大于或等于执行当前任务 v_j 所需的资源，任务调度后 CPU 和内存资源没有过载。对于导致资源过载的动作，将 u_n 上的 CPU 和内存资源的标准差设置为 0，并对资源过载成本函数中的行为进行惩罚。

$\dfrac{\sum_{m=1}^{|V_{res}|} A_{m,t+1}^{cpu}}{|V_{res}|}$ 表示所有计算节点在 $t+1$ 时刻的平均资源利用率，$\left(A_{n,t+1}^{cpu} - \dfrac{\sum_{m=1}^{|V_{res}|} A_{m,t+1}^{cpu}}{|V_{res}|}\right)^2$ 表示资源利用率与平均利用率的差值的平方和，将其取平均数并开方，得到资源利用率的标准差，即 CPU 负载均衡的成本。

约束条件分别表示：

（1）每个子任务只分配给一个计算节点

（2）将分配变量 $\xi_{j,n}$ 限制为二进制变量

（3）每个任务的执行必须在子任务都执行完成之后才能开始

3　具有注意力机制的图编码器和解码器模型

本节提出了一种解决任务调度问题的编码器-解码器模型来生成调度方案，使用图嵌入和注意力机制提取子任务的特征和关联。图 2 显示了编码器-解码器模型的整体架构。

A. Encoder-Decoder Model：

首先将 G_{task} 和 G_{res} 分别编码为节点嵌入。然后基于 RNN 的解码器使用注意力机制依次生成每个任务的位置，该算法借鉴了 Huang[10]等提出的编码器-解码器任务放置模型。

3.1　图编码器：

对于结构不同的任务 DAG，使用图卷积网络（GCN）将图中的信息编码为一组嵌入向量来表明节点自身的特征和它们之间的关联，。

首先，将 v_{task} 的前序和后继邻居节点的信息分别聚合，前序邻居节点表示为 $N_u(v)$，后继邻居节点表示为 $N_d(v)$，对于每个节点 $v \in N_u(v)$，它在第 k 步的嵌入是 e_u^k。计算前序邻居节点信息的嵌入：

$$e_u^{(up)} = \tanh(\boldsymbol{W}_1^{(\boldsymbol{up})} e_u^k) \qquad \text{公式 3-1}$$

使用平均值作为聚合函数更新节点 v 包含前序邻居节点信息的嵌入：

$$e_v^{(up)} = \tanh(\boldsymbol{W}_2^{(\boldsymbol{up})} \left[e_v^k : \frac{\sum_{u \in N_u(v)} e_u^{(up)}}{|\mathrm{N}_u(v)|} \right]) \qquad \text{公式 3-2}$$

同理，计算 v_{task} 在加入后继邻居节点信息的第 k 步嵌入 $e_v^{(down)}$。并在下一轮迭代中将两个嵌入进行拼接：

$$e_v^{k+1} = \left[e_v^{(up)} : e_v^{(down)} \right] \qquad \text{公式 3-3}$$

G_{res} 是一个完全连接的无向图，节点之间的连接表示节点之间 t 时刻的通信带宽，具有边缘特征，将边缘特征与邻居节点特征拼接，更新具有边权重的邻居节点嵌入：

$$e_u^{(neighbor)} = \mathrm{ReLU}(\boldsymbol{W}_1^{(\boldsymbol{res})} \left[e_u^k : d_{(u_m, v_n)} \right]) \qquad \text{公式 3-4}$$

聚合函数：

$$e_v^{k+1} = \mathrm{ReLU}(\boldsymbol{W}_2^{(\boldsymbol{res})} \left[e_v^k : \frac{\sum_{u \neq v} e_u^{(neighbor)}}{|V_{task}| - 1} \right]) \qquad \text{公式 3-5}$$

经过 k 次迭代后，计算所有节点的嵌入，任务图信息可以通过将每个任务的嵌入提供给全连接层计算。

3.2　图解码器：

在图解码器的结构设计中，与原算法[10]中单一针对任务执行顺序的拓扑排序算法不同，采用了一种基于动态优先级队列的任务排序算法，使得任务排序不只考虑任务的执行先后顺序，同时考虑节点的网络连接以及执行时长。

1）基于动态优先级队列的任务排序算法

在空天地一体化网络（SAGIN）中，节点拓扑具有高度动态性，为了减少节点网络连接中断带来的任务重调度，使用基于网络装款确定优先级的排序方法保证任务卸载的顺序，从而在网络状况影响下获取优先级最高的任务，并选择合适的处理器或卫星节点进行处理，排名值 R_j 由平均执行成本（$\overline{AEC_j}$）、数据传输成本 $\overline{c_{ij}(t)}$ 和前置任务的等级 R_i 决定：

$$R_j = \max_{v_i \in pred(v_j)} \{R_i + \overline{AEC_j} + \overline{c_{ij}}\} \qquad \text{公式 3-6}$$

$$\overline{AEC_j} = \frac{\sum_{n=1}^{|V_{res}|} \frac{v_{j.cpu}}{u_{n.cpu}}}{|V_{res}|}, \qquad \text{公式 3-7}$$

$$\overline{c_{ij}(t)} = \overline{hop} \times \frac{e_{ij}}{d_{mn}(t)} \qquad \text{公式 3-8}$$

R_j 综合考虑了任务的依赖，任务的计算成本和基于当前网络连接带宽的传输成本，其中 $\overline{AEC_j}$ 为 v_j 在每个计算节点的计算成本的平均值，$\overline{c_{ij}(t)}$ 为 t 时刻子任务 v_i 的数据从设备 u_m 传输到 u_n 的传输时延。

2）图解码器：

首先，根据 R_j 任务优先级对任务进行排序，图解码器将按任务优先级顺序生成每个任务的调度动作，其中 G_{task} 上任务 v_i 的嵌入为 e_{v_i}，G_{res} 上计算节点的嵌入为 e_{u_m}，算法的目标是将 $v_i \in V_{task}$ 放置在计算节点 $u_m \in V_{res}$ 上，将解码器生成的最终放置方案表示为 P：

$$p(\mathcal{P} \mid G_{task}, G_{res}) = \prod_i p(s_{v_i} \mid \mathcal{S}^{(up)}(v_i), G_{task}, G_{res}) \qquad \text{公式 3-5}$$

其中，$\mathcal{S}^{(up)}(v_i)$ 表示 v_i 所有前序任务调度的目标设备的集合。

通过循环神经网络 *RNN* 采用 *GRU* 门控制通

过学习状态表示 h_{v_i} 来记忆依赖关系，对 $\mathcal{S}^{(up)}(v_i)$ 和 G_{task} 任务节点相关的信息进行编码：

$$h_{v_i} = \text{GRU\_Cell}(e_{v_{i-1}}, h_{v_{i-1}}, \mathcal{S}^{(up)}(v_i)) \quad \text{公式 3-5}$$

其中，$e_{v_{i-1}}$ 表示在任务排序中上一个任务的嵌入，通过时间注意力机制获取上下文向量 c_i，从而实现对执行任务 v_i 的计算节点 u_m 的预测：首先，获取 h_{v_i} 与任务 e_{v_j} 的点积 $e_{ij} = h_{v_i} e_{v_j}$，e_{ij} 为 e_{v_j} 在第 i 步的注意力分数，将 e_{ij} 输入 $soft\max$ 层转换为分布概率 α_{ij}，则上下文向量:

$$c_i = [h_{v_i} : \sum_j \alpha_{ij} e_{v_j}] \quad \text{公式 3-5}$$

c_i 同时包含当前环境信息和任务信息。

计算在上下文环境 c_i 的条件下任务 v_i 被调度到特定计算节点的概率 $p(s_{v_i} | c_i)$，根据自注意力机制：

$$q_{c_i} = \boldsymbol{W}^{\boldsymbol{Q}} c_i, k_j = \boldsymbol{W}^{\boldsymbol{K}} e_{u_j}, v_j = \boldsymbol{W}^{\boldsymbol{V}} e_{u_j} \quad \text{公式 3-5}$$

则注意力得分：

$$u_{(c_i)j} = C \cdot \tanh\left(\frac{q_{c_i}^T k_j}{\sqrt{d_k}}\right), \quad \text{公式 3-5}$$

其中，$q_{c_i}^T k_j$ 代表当前上下文环境与计算节点的相关性，d_k 表示计算节点嵌入的维度。将 $u_{(c_i)j}$ 经过 $\text{soft}\max$ 变换，得到 $p(s_{v_i} | c_i)$：

$$p_k = p_\theta(s_{v_i} = s_k | c_i) = \frac{e^{u_{(c_i)k}}}{\sum_j e^{u_{(c_i)j}}} \quad \text{公式 3-5}$$

表示任务 v_i 被调度到计算节点 s_k 的概率。通过顺序预测每个任务的位置，模型将生成最终的调度方案 $\mathcal{P}$。

4　A2C 的负载平衡与时延优化算法

在本节中，我们使用 A2C(Advantage Actor–Critic)算法训练注意力机制获得的参数。通过 A2C 算法、注意力机制和环境之间的交互来最小化任务调度系统的总成本。

A.MDP 模型:

MDP 可以表示为 $M = (S, A, P, R, \gamma)$，其中 S 表示问题的状态空间，A 表示动作空间，P 表示状态转移概率，R 表示奖励函数，γ 表示折扣因子。

4.1　状态

$$s^{(t)} = \left\{ e_{v_i}(t), e_{u_m}(t) \right\}, \quad \text{公式 4-1}$$

其中，$e_{v_i}(t)$ 为经过编码器编码之后形成的子任务嵌入向量，$e_{u_m}(t)$ 为计算节点资源编码后形成的嵌入向量。

4.2　动作

在每个时间步中，我们需要根据系统状态 $s^{(t)}$ 确定子任务放置的计算节点。对于当前子任务 v_t，动作 $a^{(t)}$ 被定义为 $a^{(t)} \in \{1, 2, \cdots, |V_{res}|\}$。

其中 $a^{(t)} = 1$ 时当前子任务在本地处理，$a^{(t)} \in \{2, \cdots, |V_{res}|\}$ 时当前子任务 v_t 被分配到其他计算节点。

4.3　奖励函数

奖励函数表示在状态 $s^{(t)}$ 下执行动作 $a^{(t)}$ 后的效果。在任务调度过程中，任务到达或网络拓扑的改变可能导致操作选择和状态转换的更新。

$$R(s_t, a_t, s_{t+1}) = -(\alpha \sum_{n=1}^{|V_{res}|} \xi_{j,n} Makespan + (1-\alpha) Load_t) \quad \text{公式 4-2}$$

而累计奖励奖励为 $COST$。

4.4　A2C 算法

A2C 是 Actor-Critic 算法的改进，使用优势函数代替 Critic 网络中的原始回报。

（1）状态价值函数

状态价值函数定义为:

$$v(s_{t+1}; \theta_t) = \sum_{a_t} \pi(a_t | s_t)(r_{t+1} + \gamma v(s_{t+1}; \theta_t))$$

用于评价调度动作的价值。并使用时间差分（TD）算法计算损失函数,对于状态价值函数，TD 误差可以定义为:

$$\delta_t = r_{t+1} + \gamma v(s_{t+1}; \theta) - v(s_t; \theta)$$

则损失函数为:

$$L(\theta) = \delta_t^2 = \left(r_{t+1} + \gamma v(s_{t+1}; \theta) - v(s_t; \theta)\right)^2$$

（2）策略函数

策略函数使用训练期间观察到的奖励，对神经网络参数执行梯度下降来更新，该模型的目标是最大化以下值:

$$J(\theta) = \sum_{\mathcal{P}} \pi_\theta(\mathcal{P}) r(\mathcal{P})$$

其中，$\pi_\theta(\mathcal{P})$ 表示所有可能的任务调度方案的分布。

并使用 *REINFORCE* 算法计算策略梯度并学习网络参数 θ：

$$\nabla_\theta J(\theta)=\frac{1}{N}\sum_{n=1}^{N}\nabla_\theta \log\pi_\theta(\mathcal{P}_n)\left[r(\mathcal{P}_n)-b\right]$$

其中，N 是固定批量大小，B 是 N 个样本的平均奖励，用于减少策略梯度的方差。

其中，$\nabla_\theta \log\pi_\theta(\mathcal{P}_n)$ 表示策略的对数关于策略参数的梯度。通过梯度上升更新参数 θ 来增加那些带来更高奖励的动作的概率：$\theta \leftarrow \theta+\alpha\nabla_\theta J(\theta)$。其中，$\alpha$ 为学习率。

4.5 训练过程

Algorithm 1 *Training GAT - A2C*

初始化 $actor$ 网络参数 $\boldsymbol{\theta}$ 和 $Critic$ 网络参数 $\boldsymbol{\omega}$

$for\ each\ episode\ do:$

初始化状态 $\mathbf{s}$

$perform\ action\ according\ to\ policy\ \pi(a\mid s;\theta)$

$get\ reward\ s'\ from\ eromenvirinment$

$\delta = reward+\gamma V_\omega(s')-V_\omega(s)$

$\theta=\theta+\alpha\nabla_\theta \log\pi_\theta(s,a)\delta$

$\omega=\omega+\beta\delta\nabla V_\omega(s)$

$s\leftarrow s'$

$\mathbf{until}\ num\ of\ \ step\ reaches\ \lim it;$ **5 实验**

RA-DRL 基于 Pytorch 构建，其中任务图和资源图的图嵌入中的迭代次数为 2，任务嵌入和节点嵌入的长度设置为 128，批量大小 N 设置为 20。任务负载与完成时间的平衡参数 λ 设置为 0.5。学习率 α 设置为为 0.0001，采用 Adam 优化器进行梯度下降，训练轮数为 1500。

训练数据集：

采用 python 模拟器创建包含 1000 个任务执行流程图和 500 个资源拓扑图的数据集。任务图和资源图的特征根据第三章中 G_{task} 和 G_{res} 的特征创建，每个图顶点的初始特征随机分配。资源图集包含同构和异构设备，每个训练样本由任务流程和资源拓扑组成。并在谷歌云平台（GCP）上建立了一个边缘集群，集群中设置 33 个节点，其中，终端节点 20 个，边缘节点 10 个，云服务中心 3 个。云服务中心节点配置为 8 vCPU、32 GB 内存，边缘节点配置为 4 vCPU、16 GB 内存，终端节点配置多个 1 vCPU、4 GB 内存，卫星计算节点之间的通信带宽设置为[50,500] *Mbps*。

实验结果分析

为了验证 RA-DRL 方法，将 RA-DRL 算法与两种基线算法，即贪婪算法、HEFT 算法进行了比较，根据 Pegasus 工作流程管理工具中的 Montage_100 和任务进行测试，结果如下。

本文中的算法使用相同的数据集。

1）贪心算法：所有任务都卸载到 S-MEC 服务器进行处理。

2）HEFT 算法：该算法首先根据优先级对任务进行排序，然后以最低的卸载成本来调度每个任务。

3）SDPLS 算法[6]：该算法以根据优先级会任务队列进行排序，选择完成时间最小的计算节点作为子任务的映射节点

根据图 5，RA_DRL 在完成 Montage_workflow 的性能显著优于其他四种算法，在执行 Montage_workflow_1000 任务中，RA_DRL 分别比贪心算法、HEFT 算法、SDPLS 算法在完成时间上提升了 47.37%、35.79%、24.53%。根据图 6，RA_DRL 在完成 CyberShake 的性能同样显著优于其他四种算法，在执行 CyberShake_100 任务中，RA_DRL 分别比贪心算法、HEFT 算法、SDPLS 算法在完成时间上提升了 49.70%、30.42%、24.77%。

根据图 7，10 个边缘节点的负载进行叠加，结果表明 10 个节点在 1000 个时间步内均未发生过载。

6 CONCLUSION AND FUTURE WORK

本文提出了一种通用的基于 DRL 的资源感知框架来解决卫星互联网环境下的任务调度问题。使用图卷积网络来提取 DSP 任务图和资源图中的信息。重点对于动态网络环境下的任务与计算资源匹配机制进行了改进。并针对一种工作流处理进行了任务完成时间和设备负载均衡测试。未来我们将进一步将调度算法与流式计算平台进行集成，更好的处理流式数据。

参考文献：

[1] YU S, GONG X, SHI Q, 等. EC-SAGINs: Edge Computing-enhanced Space-Air-Ground Integrated Networks for Internet of Vehicles[M/OL]. arXiv, 2021[2023-09-12]. http://arxiv.org/abs/2101.06056.

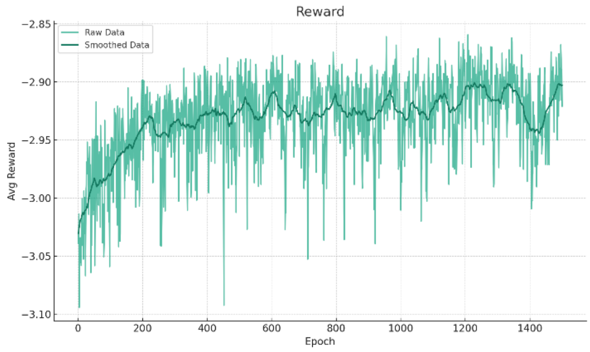

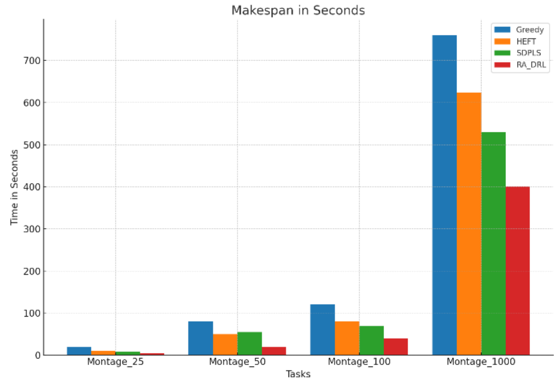

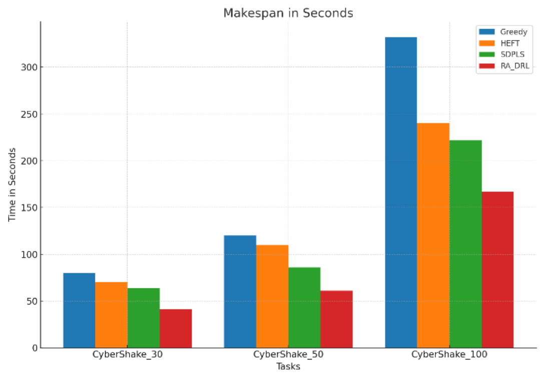

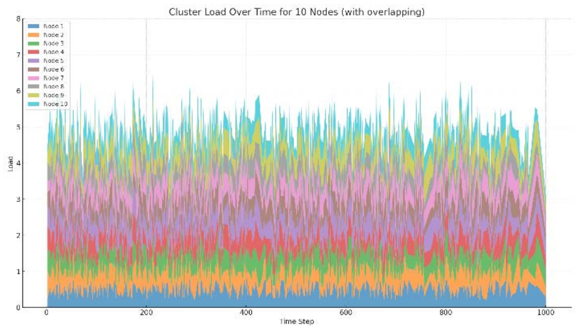

[2] ZHANG Z, ZHANG W, TSENG F H. Satellite Mobile Edge Computing: Improving QoS of High-Speed Satellite-Terrestrial Networks Using Edge Computing Techniques[J]. IEEE Network, 2019.

[3] WANG Y, YANG J, GUO X, 等. Satellite Edge Computing for the Internet of Things in Aerospace[J/OL]. Sensors, 2019, 19(20): 4375. https://doi.org/10.3390/s19204375.

[4] HU Y, LI G, GONG W. An A3C-based dynamic task scheduling algorithm for satellite edge computing[R/OL]. In Review, 2023[2023-09-11]. https://www.researchsquare.com/article/rs-3029663/v1.

[5] TANG Q, FEI Z, LI B, 等. Computation Offloading in LEO Satellite Networks With Hybrid Cloud and Edge Computing[J/OL]. IEEE Internet of Things Journal, 2021, 8(11): 9164-9176. https://doi.org/10.1109/JIOT.2021.3056569.

[6] HAN J, WANG H, WU S, 等. Task Scheduling of High Dynamic Edge Cluster in Satellite Edge Computing[C/OL]//2020 IEEE World Congress on Services (SERVICES). Beijing, China: IEEE, 2020: 287-293[2023-08-26]. https://ieeexplore.ieee.org/document/9284173/.

[7] CHAI F, ZHANG Q, YAO H, 等. Joint Multi-Task Offloading and Resource Allocation for Mobile Edge Computing Systems in Satellite IoT[J/OL]. IEEE Transactions on Vehicular Technology, 2023, 72(6): 7783-7795. https://doi.org/10.1109/TVT.2023.3238771.

[8] SHI J, DU J, WANG J, 等. Priority-Aware Task Offloading in Vehicular Fog Computing Based on Deep Reinforcement Learning[J/OL]. IEEE Transactions on Vehicular Technology, 2020, 69(12): 16067-16081. https://doi.org/10.1109/TVT.2020.3041929.

[9] LIU Z, HUANG L, GAO Z, 等. GA-DRL: Graph Neural Network-Augmented Deep Reinforcement Learning for DAG Task Scheduling over Dynamic Vehicular Clouds[M/OL]. arXiv, 2023[2023-08-26]. http://arxiv.org/abs/2307.00777.

[10] HUANG X, JIANG Y, FAN H, 等. TATA: Throughput-Aware TAsk Placement in Heterogeneous Stream Processing with Deep Reinforcement Learning[C/OL]//2021 IEEE Intl Conf on Parallel & Distributed Processing with Applications, Big Data & Cloud Computing, Sustainable Computing & Communications, Social Computing & Networking (ISPA/BDCloud/SocialCom/SustainCom). New York City, NY, USA: IEEE, 2021: 44-54[2022-11-22]. https://ieeexplore.ieee.org/document/9644756/.

[作者简介]

ZHANG San was born in ... . He received the B.E. degree in electronic engineering from China University of Mining and Technology. He is now a Ph.D. candidate of ... . His research interests include ... and ... . (Email: ...@ ...)

SMITH Peter M. [corresponding author] was born in ... . He received the Ph.D. degree in electronic engineering from Cambridge University, UK. He is now a doctor candidate of ... . His research interests include ... and ... . (Email: ...@ ...)

基于 DQN 的低轨巨型星座切换策略研究

尹政龙，陈全，杨磊，杨华果
国防科技大学空天科学学院，湖南长沙 410073

摘　要：低轨巨型星座系统由于其广覆盖性和低延迟的特点，在应对不断增长的通信需求方面具有巨大潜力。然而，低轨卫星的高速运动和不断变化的通信环境使得星座切换决策变得复杂而具有挑战性。本论文致力于研究一种基于深度强化学习中的深度 Q 网络（Deep Q-Network, DQN）的低轨巨型星座切换策略。在本研究中，我们提出了一种基于 DQN 的卫星切换策略，从网络整体性能考虑，增加了最小跳数估算作为多属性切换指标，进行智能决策。实验结果表明，基于 DQN 的星座切换策略在低轨巨型星座中表现良好，与传统切换方法相比，在保证较低切换次数的同时具有更低的网络延迟。

关键词：低轨巨型星座；卫星切换；深度强化学习；深度 Q 网络；最小跳数估算

Research on DQN-Based Constellation Switching Strategy in Low Earth Orbit Mega-Constellations

Yin zhenglong, Chen quan, Yang lei, Yang huaguo
(College of Aerospace Science and Engineering, National University of Defense Technology, Changsha, Hunan 410073)

Abstract: Low Earth Orbit (LEO) mega-constellation systems exhibit significant potential in addressing the escalating demands of communication due to their extensive coverage and low-latency characteristics. However, the high-speed movement of LEO satellites and the ever-changing communication environment introduce complexity and challenges in making constellation handover decisions. This paper is dedicated to the investigation of a constellation handover strategy for LEO mega-constellations, leveraging the Deep Q-Network (DQN) framework within the realm of deep reinforcement learning. In this study, we introduce a satellite handover strategy based on DQN, which incorporates the estimation of minimum hop counts as a multi-attribute handover metric for intelligent decision-making, taking into account the overall network performance. Experimental results demonstrate that the DQN-based constellation switching strategy performs admirably in LEO mega-constellations, offering lower network latency compared to traditional switching methods while ensuring a reduced number of handovers.

Key words: LEO mega-constellation; satellite switching; deep reinforcement learning; Deep Q-Network; minimum hop estimation

1　引言

由于低轨卫星星座的密集覆盖性和高动态性，同一时刻覆盖用户的卫星数目有很多，但是覆盖时间却很短，为保证用户与卫星之间的连续通信，用户与卫星之间的星地链路需要不断地在用户的可视卫星中进行切换[1]。随着低轨卫星星座的发展，大量的星地链路切换策略被相继提出，传统方法中卫星切换主要考虑以下三个指标作为切换因子：剩余服务时间、卫星仰角和可用空闲信道资源，以及它们的相关推导指标。其中剩余服务时间即用户与卫星的可视时间，主要影响卫星的切换次数和信令开销；卫星仰角主要影响用户与卫星的通信质量；可用信道资源主要影响卫星的网络负载。

文献[2]将可用卫星信道容量作为切换依据，将多媒体业务区分为两种类型，然后根据每种业务类型的队列状态来评估两种不同的切换策略，旨在将强制终止概率保持在最小，同时将阻塞概率保持在可接受水平。在文献[3]中，作者以可用信道数量作为评价指标，提出了基于动态多普勒的切换优先级方案，该方案利用多普勒频移监测来估计实际的切换请求数量和实际发生的时间，以克服资源预约时

间过长的问题，最小化强制终止概率和阻塞率。在文献[4]中，作者提出了一种双门限硬切换方案，该方案使用两个不同的高度角阈值来选择最高和次高卫星以减少信令开销。文献[5]提出了一种混合信道自适应算法，可以在硬切换和软切换中运行。Hu 等[6]提出了一种运动用户动态更新的速度感知切换管理算法，基于之前的状态来动态寻找时间扩展图的最短路径，所提方法能够有效避免切换预测失败，减少静态更新算法带来的冗余计算。Duan 等[7]提出了一种考虑路由影响的分布式切换方法，所提策略能够在保证切换次数可接受的同时降低传播时延，并保持较低的复杂度。Wu 等[8]提出了一种基于图论的星间切换策略，采用最短路径算法得到最优的切换方案。此外，该切换模型还可以通过改变路径权重实现其他单属性切换准则。由于上述研究仅考虑了候选卫星单一属性的影响，无法在切换次数、系统负载和切换成功率之间取得较好的折中。

Wu 等[9]提出了一种基于潜在博弈的切换算法，该策略考虑了剩余服务时间和卫星高度角，可用于最小化平均卫星切换次数和降低掉话概率。他们还提出了一种旨在平衡网络负载的终端随机接入算法。Miao 等[10]提出了一种基于多属性决策的 LEO 卫星切换策略。该策略采用逼近理想解排序(TOPSIS)评价方法计算信号强度、剩余服务时间和剩余空闲信道 3 个属性的加权值。然后，该策略选择出综合性能最优的候选卫星。Zhang 等[11]考虑了信道质量、剩余服务时间和服务用户数对切换策略的影响，并利用熵值法对各因素进行加权，将其转化为单目标优化问题。随着人工智能技术的逐渐发展，研究人员开始采用人工智能方法解决星地链路切换问题。He 等[12]提出了一种基于多智能体强化学习的负载感知卫星切换策略，可以均衡卫星负载避免网络拥塞，同时保持较低的信令开销。Xu 等[13]提出了一种 QoE 驱动的 LEO 卫星网络切换策略，该策略考虑了路由延迟、剩余服务时间和高速移动用户的空闲信道，使用基于 Q-learning 的强化学习方法进行链路切换。由于星上缓存资源有限，Leng 等[14]具有缓存感知策略的 LEO 卫星系统的星间切换策略，采用基于 DQN 的深度强化学习方法对多属性的智能切换策略进行训练。Jia 等[15]设计一种基于强化学习的面向大规模星座多属性星地切换策略，该策略首先以位置、速度和带宽需求属性对用户进行聚类，再根据接收信号强度(Received Signal Strength，RSS)、速度、网络带宽利用率和切换代价等属性，基于提出的强化学习方法进行切换决策。

之前所述的卫星切换主要针对卫星星座中卫星数目较少的情况，当研究低轨巨型星座问题时，必然会导致计算代价的急剧上升，现有方法则不够适用，因此需要研究专门面向巨型星座的星地切换算法。本文考虑在巨型星座场景下，采用基于 DQN 的强化学习方法，从整体网络考虑，将最小跳数估计作为切换因子，在保证较低的切换次数同时保持较低的整体网络时延。

2　系统模型和问题建模

2.1　系统模型

在低轨巨型星座网络中，主要采用天网地网的架构，如图 1 所示，用户终端（User Terminal，UT）通过低轨卫星及星间链路将数据传输至信关站（Gateway，GW），再通过信关站接入地面骨干网完成宽带通信。其中，与地面用户建立连接的卫星称为接入卫星（Access Satellite，AS），用户与接入卫星之间建立的星地链路称为用户链路；与信关站建立连接的卫星称为网关卫星，信关站与网关卫星之间建立的星地链路称为馈电链路；卫星与同轨道相邻两颗卫星建立同轨星间链路，与相邻轨道面两颗卫星建立异轨星间链路，中继卫星与网关卫星之间通过星间链路建立连接。在采用 Walker-Delta 构型的倾斜低轨巨型星座中，卫星的网络拓扑构型不变，星间链路可以保持稳定的连接，按照卫星在某一时刻的运行方向，分别将飞行过程中星下点纬度递增和递减的卫星分别称之为升轨道（Ascending，A）卫星和降轨道（Descending，D）卫星，如图 1 中的蓝色和绿色轨道上的卫星。

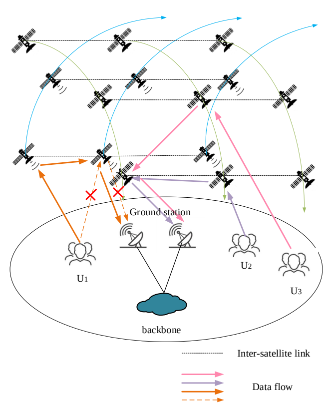

图 1　低轨巨型星座通信示意图

假设低轨巨型星座中一共有 N 颗卫星，用 S_n 表示第 n 颗卫星，其中 $n\in[1,N]$，同理，假设地面用户终端的个数为 M，用 UT_m 表示第 m 个用户终端，其中 $m\in[1,M]$，假设分布在地面的信关站个数为 K，用 G_k 表示第 k 个信关站，其中 $k\in[1,K]$，假设每个信关站最多可同时连接 P 颗网关卫星，记为 $G_{k,p}$，其中 $p\in[1,P]$。在某一时刻，用户终端通常被多颗低轨卫星同时覆盖，由于用户通信时间往往大于卫星的覆盖时间，因此用户必须在有限时间内移交给下一颗可见卫星来维持通信，假设用户终端在每个时隙 t 进行切换决策，根据切换策略选择接入卫星，接入卫星通过星间链路将数据包传输至网关卫星，最后通过信关站与地面骨干网进行通信。如何选择最优的接入卫星来保持无缝连接并且保证低切换次数条件下的高吞吐量和负载均衡，是本文旨在解决的主要问题。

2.2 问题建模

假设用户终端 UT 可以通过全球卫星定位系统（GPS）知道其当前的准确位置，并且能够获取可见卫星的星历信息，由于卫星的运动轨迹可以预测，因此计算出未来一段时间内卫星与用户之间的通信质量变化。针对不同的 QoS 需求，可以采用上述切换准则的一个或者几个来选择最优的接入卫星。本文采用虚拟拓扑法，将优化问题建模在一个特定的时间段 T，并将 T 划分为多个相等的时隙，假设每个时隙内星间链路保持固定不变，在每个时隙的起始时刻 t，根据获得的实时信息决定是否进行切换。

（1）星地链路信道模型

信道模型表达式可以简单建模为传输路径损耗、小尺度衰落和大气衰减三部分组成。t 时刻用户 UT_m 与卫星 S_n 之传输路径损耗 $L(t)$ 表达式为

$$L(t)=\left(\frac{c}{4\pi d_{m,m}(t)\,f_c}\right)^2 \tag{1}$$

式中，$d_{m,n}(t)$ 是 t 时刻用户 UT_m 与卫星 S_n 之间的距离，c 和 f_c 分别代表光速和载波频率。

大气衰减 $A(t)$ 表达式为

$$A(t)=10^{\frac{3\chi d_{m,n}(t)}{10h}} \tag{2}$$

式中，χ 是穿过云和雨的衰减，单位为 dB / km；h 为卫星的轨道高度。

信道增益表达式为

$$G_{m,n}(t)=L(t)A(t)\varphi \tag{3}$$

其中，φ 代表小尺度衰落。

信号接收功率 P_r 表示为

$$P_r=P_tG_tG_{m,n}(t)G_r \tag{4}$$

其中，P_t 代表发射功率，G_t 和 G_r 分别代表发射端和接收端的天线增益。

UT_m 与卫星 S_n 之间的信干噪比（Signal-to-Interference-plus-Noise Ratio, SINR）可以表示为

$$\gamma_{m,n}(t)=\frac{P_tG_tG_{m,n}(t)G_r}{P_tG_t\sum_{k\neq m}^{M}G_{k,n}(t)G_r+\sigma^2} \tag{5}$$

其中 $P_tG_t\sum_{k\neq m}^{M}G_{k,n}(t)G_r$ 表示其他用户与卫星 S_n 相连时对用户 UT_m 信道造成的影响，σ^2 表示高斯噪声功率。假设每个信道只能连接一颗卫星，则根据香农定理，可用信道容量为

$$C_{m,n}(t)=B\log_2(1+\gamma_{m,n}(t)) \tag{6}$$

其中 B 是频谱的带宽。

（2）剩余服务时间

由于低轨卫星具有较高的机动性，一般在用户可见范围内停留约 5-10 min，在此期间卫星可以与用户进行通信，这段时间称为最大服务时间。剩余服务时间是指在接入卫星移出用户可视范围之前，用户选择某一接入卫星建立通信链路，该通信链路所能维持的时间。由于用户的速度远小于卫星的速度，我们假设用户终端相对于卫星是静止的。剩余服务时间决定用户切换的频率。由于已知卫星的星历信息，因此剩余服务时间可以利用轨道外推模型进行计算，剩余服务时间可表示为：

$$T_{rem}=T_{\max}-(T-T_0) \tag{7}$$

其中，$T_{\max}$ 代表最大服务时间，T 代表当前时刻，T_0 代表卫星刚进入可视范围的时刻。

（3）最小跳数估计模型

为保证用户通信的端到端时延较低，还应该考虑接入卫星到信关站的通信时延，由于在大多数情

况下最短距离路径属于最小跳数路径集合，最小跳数路径也可保证较小的路径传播时延，且由于不同网关卫星与信关站之间的链路时延差异不大，因此可以通过估算接入卫星与网关卫星的最小跳数来估算时延。另外，尽管在卫星运动过程中地面用户可能选择切换其他接入卫星，但是由于星座中卫星均匀分布，网络的拓扑动态性具有规则性和可预测性，且巨型星座卫星分布密集，因此连接两端用户的星间转发跳数相对稳定。

本文采用文献[16]提出的跳数估计算法，根据星下点运行规律和星座构型，根据接入卫星和网关卫星的升（A）/降（D）轨类型将路径划分为 A2A、A2D、D2A、D2D 共 4 种类型，分别为各个路径类型确定计算模型的具体表达式，最终取四种路径类型中的最小值为连接用户两端的最小跳数。

不同星间传输路径模式下的具体表达式如表 1，详细公式推导间参考文献[16]：

其中 u_1、u_2 分别为两个卫星的相位，$\xi(u)$ 为卫星当前位置相对于升交点的经度差，φ 为卫星纬度，α 为轨道倾角。将用户可见卫星的升/降轨状态记为 S_n^A 和 S_n^D，网关卫星的升/降轨状态记为 $G_{k,p}^A$ 和 $G_{k,p}^D$，接入卫星到网关卫星的四种路径跳数可表示为 $H_{n,k}^{A2A}$，$H_{n,k}^{A2D}$，$H_{n,k}^{D2A}$ 和 $H_{n,k}^{D2A}$。当用户做切换决策时，接入卫星的升/降轨类型已经确定，则接入卫星到信关站的最短跳数可以计算得到：

$$H_n=\begin{cases}\min(H_{n,k}^{A2A},H_{n,k}^{A2D}), & S_n\text{为升轨卫星}\\ \min(H_{n,k}^{D2A},H_{n,k}^{D2D}), & S_n\text{为降轨卫星}\end{cases} \tag{8}$$

将上述切换因子进行归一化，得到效用函数，具体表达式为：

$$U_{m,n}(t)=\omega_1 N(C_{m,n}(t))+\omega_2 N(T_{rem})+\omega_3 N(H_n)+\omega_4 N(R_n) \tag{9}$$

其中 $N(\cdot)$ 代表归一化函数，其目的是消除切换因子数量级上的差异，避免切换决策倾向于数量级大的切换因子。其中，

$$N(C_{m,n}(t))=\frac{C_{m,n}(t)}{C_{\max}(t)},C_{m,n}(t)\le C_{\max}(t) \tag{10}$$

$C_{\max}(t)$ 代表最大可用容量。

$$N(T_{rem})=\frac{T_{rem}}{T_{\max}},T_{rem}\le T_{\max} \tag{11}$$

$T_{\max}$ 为最大服务时间。

$$N(H_{n,k})=\frac{H_{\max}-H_n}{H_{\max}},H_n\le H_{\max} \tag{12}$$

$H_{\max}$ 为最大跳数。另外，考虑到候选卫星和接入卫星具有非常接近的切换因子时，容易引起乒乓切换，增加切换次数，因此定义了切换代价因子 R_n，定义为：

$$R_n=\begin{cases}-C, & \text{切换}\\ 0, & \text{不切换}\end{cases} \tag{13}$$

其中 C 为一个正常数。ω_1，ω_2，ω_3 和 ω_4 为权重，且 $\omega_1+\omega_2+\omega_3+\omega_4=1$。还需定义连接函数 $x_{m,n}(t)$，用于指示

$$x_{m,n}(t)=\begin{cases}0, & \text{用户}m\text{在}t\text{时刻不接入卫星}n\\ 1, & \text{用户}m\text{在}t\text{时刻选择接入卫星}n\end{cases} \tag{14}$$

因此，我们可以在满足切换决策约束以及跳数需求的情况下，建立以最大化整体网络长期效用为目标的优化问题。具体表达式如下：

$$\max\sum_{t=0}^{T}\sum_{m\in M}\sum_{n\in N}x_{m,n}(t)U_{m,n}(t) \tag{15}$$

表 1　不同星间传输路径模式跳数估算公式

	A2A	A2D	D2A	D2D
u_1	$\arcsin\frac{\sin\varphi_1}{\sin\alpha}$	$\arcsin\frac{\sin\varphi_1}{\sin\alpha}$	$\frac{\varphi_1}{\lvert\varphi_1\rvert}\pi-\arcsin\frac{\sin\varphi_1}{\sin\alpha}$	$\frac{\varphi_1}{\lvert\varphi_1\rvert}\pi-\arcsin\frac{\sin\varphi_1}{\sin\alpha}$
u_2	$\arcsin\frac{\sin\varphi_2}{\sin\alpha}$	$\frac{\varphi_2}{\lvert\varphi_2\rvert}\pi-\arcsin\frac{\sin\varphi_2}{\sin\alpha}$	$\arcsin\frac{\sin\varphi_2}{\sin\alpha}$	$\frac{\varphi_2}{\lvert\varphi_2\rvert}\pi-\arcsin\frac{\sin\varphi_2}{\sin\alpha}$
$\zeta(u_1)$	$\arctan(\cos\alpha\tan u_1)$	$\arctan(\cos\alpha\tan u_1)$	$\pi+\arctan(\cos\alpha\tan u_1)$	$\pi+\arctan(\cos\alpha\tan u_1)$
$\zeta(u_2)$	$\arctan(\cos\alpha\tan u_2)$	$\pi+\arctan(\cos\alpha\tan u_2)$	$\arctan(\cos\alpha\tan u_2)$	$\pi+\arctan(\cos\alpha\tan u_2)$

$$s.t.\quad x_{m,n}(t)\in\{0,1\},\qquad \forall t,\forall m\in M,\forall n\in N \tag{16}$$

$$\sum_{n\in N} x_{m,n}(t)=1,\qquad \forall m\in M \tag{17}$$

公式（17）代表用户在时刻 t 可以接入至多一颗卫星。

3　基于 DQN 的卫星切换策略

多目标优化问题(15)的目标是基于每个 UE 的局部信息最大化长期性能。强化学习中的智能体可以利用简单的局部信息，通过不断地与环境交互来学习隐藏的变化模式，从而得到最优的长期切换策略。因此，本文针对多目标优化问题，采用了一种基于 DQN 的切换方案。

3.1　强化学习场景构建

强化学习的流程图如 2 所示，智能体（Agent）一直与环境（Environment）进行互动，在不同时刻下，智能体根据环境的状态（State）选择某一动作（Action）之后，得到奖励（Reward），智能体能够在不同的环境下不断尝试动作，使获得的累积奖励最大，最终获得完成任务的最优动作。结合卫星切换问题场景，智能体就是用户终端 UT，环境就是 UT 和巨型星座网络，将状态空间、动作空间和奖励函数定义如下：

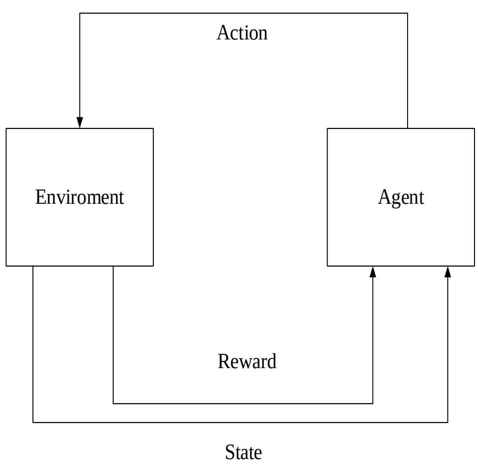

图 2　强化学习流程图

（1）状态空间

用 $State(t)$ 表示系统在 t 时刻的状态 s 的集合，包括用户与卫星之间的可用容量 C、剩余服务时间 T_{rem}、最小跳数 H，具体可描述如下：

$$State(t)=\left\{\left\{C^1,T_{rem}{}^1,H^1\right\},\left\{C^2,T_{rem}{}^2,H^2\right\},\ldots,\left\{C^N,T_{rem}{}^N,H^N\right\}\right\} \tag{18}$$

（2）动作空间

智能体的动作为 UT 选择接入卫星进行切换，因此动作空间定义为所有动作 a 的集合，即所有卫星集合，动作空间 $Action(t)$ 定义为：

$$Action(t)=\{1,2,\ldots,N\} \tag{19}$$

（3）奖励函数

可以将效用函数 $U_{m,n}(t)$ 直接作为选择接入卫星时的奖励函数，该函数能够将各个切换指标进行均衡，还可以根据 QoS 需求，调整权重参数的大小来优化奖励函数。奖励函数 $Reward(t)$ 表示如下：

$$Reward(t)=U_{m,n}(t) \tag{20}$$

3.2　基于 DQN 的卫星切换策略

深度 Q 网络（DQN）使用神经网络来近似 Q 函数，即神经网络的输入是当前状态，输出是选择的接入卫星。通过神经网络计算出 Q 函数后，DQN 使用 ϵ−greedy 策略来输出动作。此时根据奖励函数去更新 Q 函数网络的参数，接着进入下一个状态，如此循环下去，直到训练出一个好的 Q 函数网络为止。值得注意的是，为了加速收敛，DQN 有两个 Q 网络参与训练，分别是主 Q 网络和目标 Q 网络，根据状态、动作和奖励的定义，可以计算出目标 Q 网络值：

$$y=R(s,a)+\gamma\max_{a'}Q_t(s,a';\theta^-) \tag{21}$$

其中，$R(s,a)$ 是在某个状态 s 下采取动作 a 后智能体获得的即使奖励值，$\max_{a'}Q_t(s,a';\theta^-)$ 是智能体通过不断训练之后通过累积的经验获得的最大受益，θ^- 是目标 Q 网络参数，γ 是折扣因子，用于将未来的汇报折现的当前的汇报计算中。然后，计算均方误差损失函数为：

$$L(\theta)=E[(R(s,a)+\gamma\max_{a'}Q_t(s,a';\theta^-)-Q(s,a;\theta))^2] \tag{22}$$

其中 θ 是主 Q 网络的网络参数。在计算损失函数后，使用梯度下降策略来更新主网络参数。为了打破序列之间的时间相关性，使用记忆池存储经验，并使用小批量数据的随机样本进行学习。具体算法描述如算法 1 所示。

算法 1：基于 DQN 的卫星切换策略

1-初始化：记忆池 ，学习率 α，折扣因子 γ，Q 网络并使用随机参数 θ，目标 Q 网络，$\theta^{-}=\theta$

2-For $episode=1$，K do：

3-重置环境

4-　While $t<T$　do:

5-生成一个随机数 $\tau \in (0,1)$

6-If　$\tau<\varepsilon$:

7-随机选一个动作 $a(t)$

8-　　Else：

9- $a=\arg\max_{a} Q(s,a;\theta)$

10-执行动作 a，并且获得奖励 $R(s,a)$，下一状态 s'

11-存储 (s,a,r,s') 到记忆池

12-当记忆池满时，从中随机抽取小批量数据 (s,a,r,s')

13-根据公式(22)中定义的损失函数，使用梯度下降法更新主 Q 网络参数 θ

14-每间隔 q 次 *episode* 更新目标 Q 网络参数，$\theta^{-}=\theta$

15-Endfor

4　仿真分析

为了验证所提出的方法的可行性及切换性能，利用 STK 仿真工具，模拟星链（Starlink）建立一个包含 1584 颗卫星的低轨巨型星座模型，并在地面设立北京、三亚、酒泉三个信关站，星座具体参数如表 2 所示：

表 2　　　　星座仿真参数

参数	值
轨道高度（km）	550
轨道倾角（°）	53
轨道数	72
每个轨道卫星数	22
相位因子	0
用户链路最小仰角（°）	10
仿真时间（min）	10
仿真时隙长度（s）	10

采用 5 层全连接神经网络来模拟 Q 函数，中间的隐藏层分别为 128、48、64，折扣因子 0.7，采用学习率 10^{-4}，从图 3 中可以看到平均奖励和平均损失变化情况，证明 DQN 算法的有效性和收敛性。

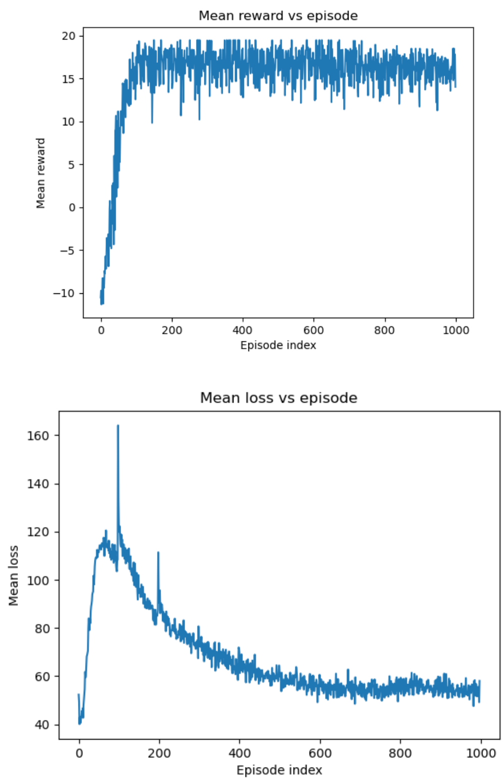

图 3　算法平均奖励和平均损失

对比传统的卫星切换算法，选择基于最大剩余服务时间的切换算法（MS）、基于最大仰角的切换算法（ME）和基于最低链路损耗的切换算法（MP）与本文方法（DQN）进行比较，从图可以看出，在切换次数比较上，MP 方法的切换次数最高，因为用户总是选择链路损耗最低的卫星，而随着卫星的运动，链路损耗变化较大，切换就会较为频繁，ME 算法能够保证最大的服务时长，因此切换次数较低，DQN 算法介于 ME 算法和 MP 算法之间，切换次数相对较低。

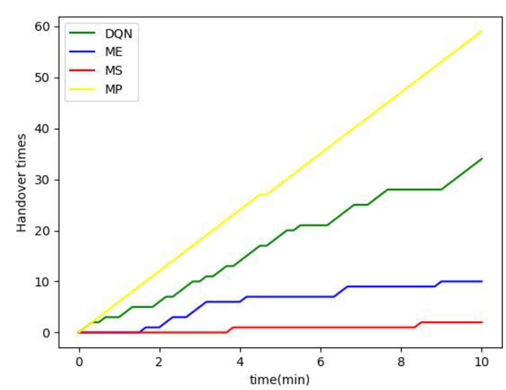

图 4　切换次数比较

另外，对比了几种算法的最小跳数，从表 3 中可以看出，因 DQN 算法加入了最小跳数评估作为切换指标，因此平均跳数最低，其他算法对接入卫星的选择上并不区分升轨或者降轨，因此平均跳数接近且相对较高，因为最短距离路径属于最小跳数路径集合，时延也会相应较低，因此可以认为 DQN 算法可以降低系统整体的网络时延。

表 3　平均跳数比较

算法	ME	MS	MP	DQN
平均跳数	32	35	34	28

5　结论

本章采用深度强化学习方法，研究了基于 DQN 的低轨巨型星座切换策略。利用最小跳数评估参与多属性切换决策，注重提高网络整体性能。通过仿真并与传统方法结果比较表明，所提方法能够在保证较低的切换次数同时能够显著降低星间链路跳数水平，保持较低的网络时延。

参考文献：

[1] 陈全, 杨磊, 郭剑鸣, 等. 低轨巨型星座网络：组网技术与研究现状[J]. 通信学报,2022, 43(5) : 177–189.

[2] KARAPANTAZIS S, PAVLIDOU F-N. QoS handover management for multimedia LEO satellite networks [J]. Telecommunication Systems, 2006, 32(4) : 225–245.

[3] PAPAPETROU E, PAVLIDOU F. Analytic study of doppler-based handover management in LEO satellite systems [J]. IEEE Transactions on Aerospace and Electronic Systems, 2005, 41(3) : 830–839.

[4] GKIZELI M, TAFAZOLLI R, EVANS B. Modeling handover in mobile satellite diversity based systems[C]//IEEE 54th Vehicular Technology Conference. VTC Fall 2001. Proceedings (Cat. No.01CH37211).Atlantic City, NJ, USA:, IEEE, 2001, 1 : 131–135.

[5] GKIZELI M, TAFAZOLLI R, EVANS B G. Hybrid channel adaptive handover scheme for non-GEO satellite diversity based systems[J]. IEEE Communications Letters,2001, 5(7) : 284–286.

[6] HU X, SONG H, LIU S, et al. Velocity-aware handover prediction in LEO satellite communication networks [J]. International Journal of Satellite Communications and Networking, 2018, 36(6) : 451–459.

[7] DUAN C, FENG J, CHANG H, et al. A Novel Handover Control Strategy Combined with Multi-hop Routing in LEO Satellite Networks [C]//2018 IEEE International Parallel and Distributed Processing Symposium Workshops (IPDPSW). Vancouver, BC:, IEEE, 2018 : 845–851.

[8] WU Z, JIN F, LUO J, et al. A Graph-Based Satellite Handover Framework for LEO Satellite Communication Networks [J]. IEEE Communications Letters, 2016, 20(8) : 1547–1550.

[9] WU Y, HU G, JIN F, et al. A satellite handover strategy based on the potential game in LEO satellite networks (September 2019) [J]. IEEE Access, 2019, PP(99) : 1–1.

[10] MIAO J, WANG P, YIN H, et al. A Multi-attribute Decision Handover Scheme for LEO Mobile Satellite Networks [C]//2019 IEEE 5th International Conference on Computer and Communications (ICCC). 2019.

[11] ZHANG S, LIU A, LIANG X. A Multi-objective Satellite Handover Strategy Based on Entropy in LEO Satellite Communications [C]//2020 IEEE 6th International Conference on Computer and Communications (ICCC). Chengdu, China:, IEEE, 2020 : 723–728.

[12] HE S, WANG T, WANG S. Load-Aware Satellite Handover Strategy Based on Multi-Agent Reinforcement Learning [C]//GLOBECOM 2020 - 2020 IEEE Global Communications Conference. Taipei, Taiwan:, IEEE, 2020 : 1–6.

[13] XU H, LI D, LIU M, et al. QoE-Driven Intelligent Handover for User-Centric Mobile Satellite Networks [J]. IEEE Transactions on Vehicular Technology, 2020, 69(9) : 10127–10139.

[14] LENG T, XU Y, CUI G, et al. Caching-Aware Intelligent Handover Strategy for LEO Satellite Networks [J]. Remote Sensing, 2021, 13(11) : 2230.

[15] JIA X, ZHOU D, SHENG M, et al. Reinforcement Learning-Based Handover Strategy for Space-Ground Integration Network with Large-Scale Constellations [J]. Journal of Communications and Information Networks, 2022, 7(4) : 421–432.

[16] CHEN Q, GIAMBENE G, YANG L, et al. Analysis of Inter-Satellite Link Paths for LEO Mega-Constellation Networks [J]. IEEE Transactions on Vehicular Technology, 2021, 70(3) : 2743–2755.

[作者简介]

尹政龙（1988− ），男，辽宁沈阳人，国防科技大学博士研究生，主要研究方向卫星切换、低轨卫星网络。

陈全（1992− ），男，安徽宿州人，博士，国防科技大学讲师，主要研究方向为低轨卫星网络、无人机通信网络、微纳卫星技术等。[本文通信作者]

杨磊（1979− ），男，河南洛阳人，博士，国防科技大学研究员，主要研究方向为空间信息网络、卫星集群网络等。

杨华果（2000− ），女，四川成都人，国防科技大学硕士研究生，主要研究方向为低轨卫星网络。

Applications of Deep Learning in Satellite Communication: A Survey

YuanzhiHe[1,2,*], BiaoSheng[1,2], Yuan Li[2], Changxu Wang[2],XiangChen[1],Jinchao Liu[3]

[1]School of systems science and engineering, Sun Yat-Sen University, Guangzhou100876, China

[2]Institute of Systems Engineering, AMS, PLA, Beijing 100000, China

[3]China Coast Guard, Beijing 100000, China

[*]The corresponding author, email: he_yuanzhi@126.com

Abstract—Satellite communication is an important part of the future 6G communication networks, and the promotion effect of AI technology based on deep learning on satellite communications has attracted much attention. This paper summarizes the application research status of deep learning in satellite communication from the perspective of the physical layer, datalink layer, and network layer, analyzes the shortcomings of deep learning in the application of satellite communication, and looks forward to the possible application research directions in the future.

Keywords—satellite communication, deep learning, physical layer, data link layer, network layer

I. INTRODUCTION

In recent years, the construction of satellite communication system has been greatly developed, and related new concepts, technologies and projects have emerged one after another. The low-earth orbit (LEO) constellations represented by StarLink[1] and Hongyan[2]

are under construction, which promote the development of a series of satellite communication networks with different focuses, such as Internet of satellite (IoS)[3],space-ground integration network (SGIN)[4,5], Integrated Satellite-Terrestrial Networks (ISTN)[6], and mobile phone direct connection satellite[7]. Figure 1 shows a typical space-air-ground-sea integrated satellite communication network, including satellites, aircraft, unmanned aerial vehicles, pseudo satellite, vehicles, ships, etc.

In June 2023, the International Telecommunication Union (ITU) approved the IMT-2030 (6G) Vision Framework[8]. Among them, AI-related capabilities and full coverage are the important communication capabilities proposed in IMT-2030, as shown in Figure 2. Satellite communication is an important way to connect remote areas, ocean and the air. The integration of artificial intelligence and satellite communication is inevitable under the vision of ITU. These emerging technologies have been widely concerned by researchers, and the role and status of satellite communication are becoming more and more important.

With the construction of new satellite communication networks such as SGIN, many new problems and difficulties related to satellite communication have also emerged. For example, wireless resource allocation and routing become more difficult in the SGIN than that in single satellite. How to solve the various problems better is the key to improve the quality of satellite communication service.

Deep learning (DL) is a representative technology in the field of artificial intelligence, which can effectively train a deep neural network (DNN) bylarge amount of data, the DNN can extract the features contained in the data, and solve many classification and decision optimization problems. Deep learning has a wide range of applications such as image classification, speech recognition, Go, games and other fields. Deep learning has the ability to solve classification problems and sequential decision problems with high quality, which provides the possibility for it to solve the related problems in satellite communication.

In this paper, the applications of deep learning in satellite communications will be studied in different communication levels, and the main contributions of this paper include:

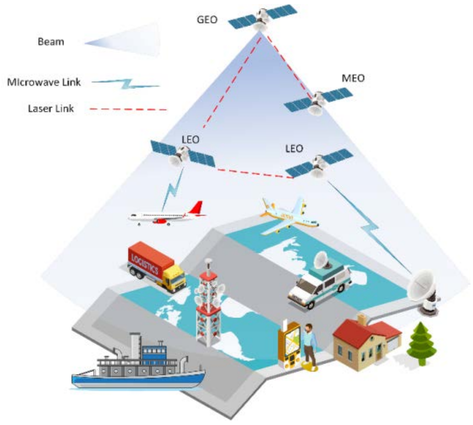

Figure 1 Architecture of space-air-ground-sea integrated information network.

- Both satellite communication and deep learning are developing rapidly, and this paper tracks the latest development of deep learning in satellite communications.
- This paper analyzes the applications of deep learning in satellite communications from the perspective of physical layer, link layer and network layer, which is helpful to understand the role of deep learning at different levels. Most of the existing reviews on satellite communication are aimed at a specific application or method. For example, reviews on access[9], or reviews on the application of deep reinforcement learning in satellite communication, or the focus is not on the relationship between deep learning and satellite communication[10], and these literatures rarely consider the relationship between deep learning and satellite communication from a hierarchical perspective[11].
- This paper focuses on the network model, hardware computing power, and training data that are very important in deep learning. Butthere's very little literature focus on this. The neural network applied to satellite communication is usually a classical network structure, the training data is mainly simulation data, and the hardware computing power is not given in detail.

In order to better understand the research progress of the application of deep learning in satellite communication, this paper firstly classifies it from the perspective of physical layer, data link layer and network layer, and expounds the category of deep learning technology used in different communication layers, as shown in Figure 3. Then, the related status of satellite network types, deep learning methods, neural network models, datasets, and hardware information-inthesatellitecommunication are summarized. Finally, some problems and possible development directions of deep learning in enabling satellite communication are pointed out.

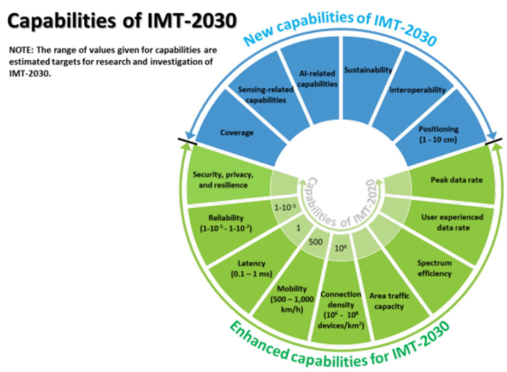

Figure 2 Schematic diagram of the communication capabilities in IMT-2030

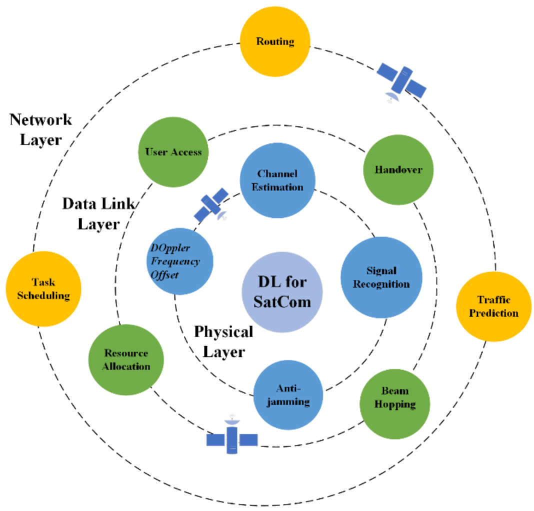

Figure 3TypicalApplications of deep learning in satellite communications

II. PHYSICAL LAYER

The role of the physical layer is to enable the signal to obtain reliable transmission on the physical channel. Signal processing at the transmitter includes source coding, channel coding, modulation, etc., and signal recovery, channel estimation and other processing at the receiver. Deep learning has been applied to channel estimation[12], signal identification[13], interference suppression[14], Doppler shift[15] and other problems at the physical layer.

A. CHANNEL ESTIMATION

In satellite communication, information is transmitted in space by electromagnetic waves. The space environment is complex and changeable, and the electromagnetic wave will produce path loss, rain attenuation, fog attenuation and other damages in the transmission process, which leads to the difference between the transmitted signal and the received signal. Therefore, channel estimation for satellite communication has important value.

In LEO satellite communication systems, obtaining accurate channel state information (CSI) is crucial to achieve high performance. Least Squares (LS) channel estimation is a simple traditional channel estimation scheme, but it does not consider the compensation of channel estimation error. Kang et al. [16] proposed a denoising convolutional neural network (DnCNN) based on deep learning for channel estimation of massive multiple-input single-output LEO satellite communication system. Numerical results show that the proposed DnCNN based on deep learning can effectively improve the accuracy of the LS channel estimator in estimating the channel.

ZHANG et al.[17] proposed a CSI prediction scheme based on deep learning to solve the channel aging problem of massive multiple-Input multiple-Output (mMIMO) LEO satellite communication system by exploiting the correlation of varying channels. In this paper, a satellite channel predictor composed of Long Short-Term Memory (LSTM) units is designed. The predictor is first trained by offline learning, and then the corresponding output results are fed back online according to the input data to realize the channel feature extraction and future CSI prediction in LEO satellite scenarios. Numerical results show that the proposed deep learning-based predictor can effectively alleviate the channel aging problem in LEO satellite mMIMO systems.

Aiming at the problem that the channel of the high altitude platform satellite communication network will be affected by time-varying conditions, GUVEN et al.[18] introduced a method based on deep learning to solve the channel estimation problem. Firstly, the channel equalization and carrier frequency offset with residual Doppler effect were minimized by using the proposed Convolutional Neural Network (CNN) -based estimator. Then, the data rate is increased by improving the spectral efficiency using the non-orthogonal multiple access method. The proposed AI-driven HAPS-LEO network provides not only high data throughput per second but also higher quality of service.

B. SIGNAL RECOGNITION

Compared with terrestrial communication, satellite communication has lower power and poorer signal quality. More excellent and reliable signal detection and identification technology can improve the quality of satellite communication, which is an important technology in satellite communication.

Zha et al.[19] proposed a signal recognition and demodulation model based on recurrent neural network. The Recurrent Neural Unit (RNN) was used to directly extract the deep features of the signal timing, and the Fully Connected Neural Network (FCNN) was used to map the dimensions of the features, and finally the modulation recognition and demodulation of the target signal were completed. The method does not need to estimate the carrier to noise ratio of the target signal, overcomes the defect of artificially determining the threshold, and has a strong tolerance for signal frequency offset error and timing error. Simulation results show that when the network training reaches the steady state, the target signal recognition rate is close to 98%, and the demodulation error rate is close to the theoretical threshold under the condition of Signal-to-noise ratio (SNR) of 6dB.

Ren et al.[20] proposed a Recurrent Neural Network (RNN) algorithm for satellite modulation signal recognition, which takes the IQ data of the signal as the input of the model, extracts time-sharing features through LSTM, classifies the fully connected layer, and finally completes the recognition. When the sampling length is 512 and SNR is greater than 4dB, the recognition rate approaches 100%. Compared with KNN classifier, LSTM network has better recognition performance, especially in the case of low SNR, it can recognize multiple modulation modes efficiently activity.

C.ANTI-JAMMING

Signal to Noise ratio (SNR) is a key factor affecting the quality of communication, satellite communication because the signal power is small, anti-jamming capability is very important for satellite communication.

For the anti-jamming problem of Heterogeneous Internet of Satellite (IoS), HAN et al.[21] studied a spatial anti-jamming scheme, aiming to minimize the anti-jamming routing cost through Stackelberg game and deep reinforcement learning. Firstly, the routing anti-jamming problem is formulated as a hierarchical anti-jamming Stackelberg game. Secondly, the IoS spatial anti-jamming scheme consists of two phases: available route selection and fast anti-jamming decision. A deep reinforcement learning based routing algorithm (DRLR) was proposed to obtain the available route subset. In addition, in order to make a fast anti-jamming decision, a fast response anti-jamming algorithm (FRA) based on available route subset was proposed. Users empirically analyze the jammer's strategy using DRLR and FRA algorithms, and adaptively make anti-jamming decisions according to the jamming environment. Finally, simulation results show that the proposed algorithm has lower routing cost and better anti-interference performance than the existing methods.

D.DOPPLER FREQUENCY OFFSET

The Doppler frequency offset caused by the high dynamic characteristics of LEO satellite increases the difficulty of signal recovery at the receiver.

Aiming at the problem of Doppler frequency offset in LEO satellite communication system, Li et al.[22] proposed a Doppler frequency offset pre-compensation algorithm based on Multi-modal Long Short-Term Memory (MLSTM-DPC). By judging the difference between the current ephemeris data and the current time, single or multiple LSTM models are selected to predict the orbit parameters. The predicted orbit parameters are used to infer orbits. Finally, the Doppler frequency offset pre-compensation value was predicted. Simulation results show that the effective frequency offset of MLSTM-DPC algorithm is improved by 36.39%, and the calculation time is significantly reduced.

E. SUMMARY

Deep learning algorithms help to acquire channel knowledge and predict time-varying channels at the physical layer. The algorithm mainly focuses on the relationship between input and output in wireless channels, and generally uses supervised learning methods. Deep learning algorithms perform better in classification problems and are more robust to unpredictable errors because they can learn it if the dataset is complete. It has more advantages than traditional methods in signal recognition.

Deep learning has high requirements for computing power, algorithm and data. Table 1 gives a brief statistics of the literature from the perspective of satellite network types, deep learning methods, neural network models, datasets and hardware information. It can be found that the types of satellite networks are relatively rich. The deep learning method used mainly focuses on supervised learning, the neural network model is mainly based on the classical CNN and LSTM model, and the data set is all obtained from simulation, which is relatively lack of authority, reusability and standard. And most papers do not disclose the CPU or GPU used for training.

III. DATA LINK LAYER

The role of the link layer is to provide access, error detection, multiplexed data streams for user data, and provide reliable data connection services for users. Deep learning has been applied in data link layer resource allocation [23], user access [24], link switching[25], beam hopping[26] and other problems.

A. RESOURCE ALLOCATION

Limited by its platform, satellite communication can use limited bandwidth and power resources, so resource allocation algorithm is very important to the quality of satellite communication. Deep learning, especially deep reinforcement learning, is relatively widely used in the field of resource allocation.

Table 1 Typical applications of deep learning in the physical layer

Applications	satellite networks	Deep Learning Methods	Neural Network model	Open Source Datasets	Hardware information	Ref.
Channel Estimation	LEO	SL	DnCNN	No	/	[16]
	LEO	SL	LSTM	No	/	[17]
	HAPS-LEO	SL	CNN	No	/	[18]
Signal Recognition	DVB-S2Satellite network	SL	LSTM	No	/	[19]
	non-specific	SL	LSTM	No	/	[20]
Anti-Jamming	IoS	DRL	LSTM	No	/	[21]
Doppler Frequency Offset	LEO	SL	LSTM	No	CPU	[22]

Due to the limited resources of space-ground integrated satellite network, how to effectively allocate the resources of space-ground integrated satellite network has become a big challenge. Li et al.[27] proposed a NOMA-based resource allocation framework for terrestrial satellite networks. In the proposed framework, Multi-agent Deep Deterministic Policy Gradient (MADDPG) method was used to achieve maximum energy efficiency through user association, power control and cache design. Finally, the simulation results show that the proposed method has better optimization performance than the traditional single-agent deep reinforcement learning algorithm, and can effectively solve the problem of resource allocation and cache design in the space-ground integrated network.

With the expansion of multi-beam satellite MBS network scale, how to efficiently and dynamically allocate scarce bandwidth and spectrum resources while ensuring user Quality of Service (QoS) has become a huge challenge. MA et al.[28] designed a dynamic bandwidth allocation framework using Proximal Policy Optimization (DBA-PPO) to meet time-varying traffic demand, maximize utilization and guarantee QoS of users in the MBS system. Experimental results show that the proposed bandwidth allocation algorithm can flexibly achieve the desired effect with lower complexity and is more cost-effective for large-scale MBS communication scenarios.

B. USER ACCESS

In the field of satellite access, at present, NOMA[29,30] related schemes have attracted more attention from researchers and are considered as possible access schemes for 6G. However, the access enabled by deep learning has also been studied accordingly.

Zhang et al.[31] studied the user pairing problem in the power domain non-orthogonal multiple access scheme in satellite networks. It is assumed that different satellite applications have different delay quality of service (QoS) requirements, and the concept of effective capacity is adopted to characterize the impact of delay constraints on the achieved performance. The goal is to select users to form NOMA user pairs and make efficient use of resources. To this end, the power allocation factor is first obtained by ensuring that the capacity achieved by the delay-sensitive users is not less than that achieved by the Orthogonal Multiple Access (OMA) scheme. Then, considering the non-convex user selection in the delay-constrained NOMA satellite network, the DRL algorithm was used for dynamic user selection. The channel conditions and delay requirements of the users are considered as states, and the DRL algorithm is used to search for the best user that can achieve the maximum performance under the power allocation factor, which is paired with the dely-sensitive user to form a NOMA user pair. Simulation results show that the proposed DRL-based user selection scheme can output the optimal action in each time slot, thus providing superior access performance than the random selection strategy and OMA scheme.

Leo satellite networks exhibit extremely long link distances for many users under time-varying network topologies. This makes existing multiple access protocols unsuitable. To overcome this problem, LEE et al.[32] proposed a contention-based random access solution called Emergency Random Access Channel Protocol (eRACH). It emerges by interacting with a non-stationary network environment using multi-agent deep reinforcement learning. By exploiting known satellite orbit patterns, eRACH does not require central coordination or additional communication between users. Simulation results show that the average network throughput of the proposed eRACH is 54.6% higher, and the average access delay is reduced by about two times.

C. HANDOVER

Since the large-scale construction of Leo constellation communication by Starlink, more and more Leo satellite communication systems have been proposed and are under steady construction. In the process of satellite communication, a single communication link is difficult to maintain for a long time, and users need to switch in different beams.

Yang et al.[33] proposed a switching method of DQN framework with momentum adaptive learning rate (DQN-ALRM), which can not only improve the decision-making accuracy, but also improve the learning efficiency. The customized DQN framework can solve the problem of large-size state space, and the proposed ALRM method can adjust the learning rate at any time according to the training error situation. Simulation results show that the proposed method has advantages in convergence speed, handoff rate, call failure rate and multi-index quality of Service (QoS).

WANG et al. [34] proposed a new handoff scheme based on deep reinforcement learning (DRL) by simultaneously considering multiple handoff factors such as handoff signaling overhead, remaining visible time, received signal strength, shortest distance, and satellite load balance. Simulation results show that the proposed DRL-based handoff scheme can reduce the number of handoffs by more than 21% compared to the comparison baseline in the case of no handoff failure.

LENG et al. [35] proposed a multi-attribute decision making handover strategy that jointly considered three factors of satellite buffer capacity, remaining service time and remaining idle channel. In addition, a cache-aware intelligent switching strategy based on Deep Reinforcement Learning (DRL) was given to maximize the long-term benefit of the system. Compared with the traditional strategy, the proposed strategy can reduce the handoff failure rate up to 81% when the system buffer occupancy rate reaches 90%, and has a lower call blocking probability in the multi-user arrival scenario. Simulation results show that the proposed strategy can effectively reduce the handoff failure rate caused by buffer resource occupation, and flexibly allocate channel resources to reduce call blocking.

XU et al.[36] proposed a user-centric intelligent handover mechanism for mobile satellite networks, which selects the access satellite by predicting the service time and communication channel resources. Deep reinforcement learning is used to maximize the quality of experience of the user terminal through the predicted switching factors. Simulation results show that the proposed handover mechanism has good performance in terms of handover time, handover success rate and end-to-end delay.

D. BEAM HOPPING

Beam-hopping is a flexible beam scheduling method envisaged by multi-beam satellites to improve system throughput.

LEI et al.[37] developed a deep learning-assisted approach to facilitate efficient beam hopping (BH) in multi-beam satellite systems. Adopting BH can provide a high degree of flexibility to manage irregular and time-varying traffic requests within the satellite coverage area. This paper proposes a method combining learning and optimization to provide fast, feasible and near-optimal solutions for BH scheduling. Numerical studies show that the learning component is able to greatly accelerate the process of BH mode selection and allocation, while the optimization component can guarantee the feasibility of the solution and improve the overall performance.

E. SUMMARY

Because deep reinforcement learning has a good effect in serialization decision, it has been applied to many satellite communication tasks that require decision optimization, such as resource allocation, user access, handover and beam hopping. Deep reinforcement learning technology can learn the relationship between input and output on a large amount of data, and use the reward to find the best optimization scheme.

Similar to Table 1, Table 2 presents statistics of the literature from the perspective of satellite network types, deep learning methods, neural network models, datasets, and hardware. It can be found that the types of satellite networks are relatively rich, and the methods are mainly focused on deep reinforcement learning. The datasets used are all obtained by simulation, and the CPU or GPU used for training is not disclosed in the literature. Compared with Table 1, the neural network model will use a fully connected layer, and the dataset also has the problems of no standard, not authority, and difficult reuse.

IV. NETWORK LAYER

The network layer has the role of connecting different networks, deciding the best route, and managing network traffic. The role of deep learning in the network layer includes routing optimization[38], traffic prediction[39], task scheduling[40], etc.

A. ROUTING

Routing is a key function of network layer. Bad routing algorithm will lead to network congestion and many other problems, which must be treated carefully.

LIU et al.[41] conceive SAGIN supporting maritime communications, in which LEO satellite constellations, passenger aircraft, ground base stations, and ships serve as space, air, ground, and sea layers, respectively. In order to meet the heterogeneous service requirements and adapt to the time-varying and self-organizing nature of SAGIN, a deep learning assisted multi-objective routing algorithm was proposed, which utilized the quasi-predictive network topology and operated in a distributed manner. Simulation results based on real satellite, flight and shipping data in the North Atlantic region show that the proposed deep learning-assisted multi-objective routing algorithm can achieve near-Pareto optimal performance.

WANG et al.[42] combined SDN, AI technology and fuzzy logic to optimize the multi-task routing strategy in the ISTN. The GEO controller collects the load information of ISTN at different moments, and the ground computing center collects historical traffic data from the GEO controller for CNN model training and updating. The GEO satellite utilizes the trained CNN model to make routing decisions. Considering

Table 2　　Application status of deep learning in link layer

Application	satellite networks	Deep Learning Methods	Neural Network model	Open Source Datasets	Hardware information	Ref.
Resource Allocation	Terrestrial-Satellite Networks	MADDPG	/	NO	/	[27]
	Multi-Beam Satellite	DBA-PPO	FCNN	NO	/	[28]
User Access	NOMA-Based Satellite Networks	DRL	/	NO	/	[31]
	LEO	MADRL	FCNN	NO	/	[32]
Handover	SGIN	DRL	/	NO	/	[33]
	LEO	DRL	Conv2D	NO	/	[34]
	LEO	DRL、DQN	/	NO	/	[35]
	Mobile Satellite Networks	DRL	/	NO	/	[36]
Beam Hopping	LEO	DL	/	NO	/	[37]

that the judgment of CNN may contradict the user requirements, fuzzy logic is used to evaluate the task requirements to improve the output of CNN to obtain the best routing policy. Simulation results show that the multi-task routing method based on fuzzy CNN has better performance under different conditions.

B. TRAFFIC PREDICTION

Traffic prediction is important in many satellite applications such as congestion control, dynamic routing, dynamic channel assignment, network planning, and network security.

Wan et al.[43] proposed a traffic classification method based on deep Packet Inspection (DPI) and CNN and verified it with open datasets. Experimental results show the effectiveness of the proposed method.

ZHU et al.[44] proposed a LSTM model with attention mechanism for traffic prediction. Considering that the input and output of traffic prediction are a sequence, the proposed model can balance the influence of different parts of the input on the output. Simulation results show that compared with ARIMA, random forest and traditional RNN the prediction accuracy of the proposed model is highly improved.

C. TASK SCHEDULING

Task scheduling is a common task in the network layer, especially the scheduling of computing tasks is the focus of research.

Zhang et al.[45] studied the scheduling problem of computing tasks in SAGIN for remote IoT. The optimization objective is to design an offloading strategy for each UAV that maximizes the number of tasks and reduces the UAV energy consumption. In order to adapt to the dynamic and complex environment, a task offloading method based on the Actor-Critic framework was proposed. The actor observes the environment and outputs the current offloading decision, and the critic evaluates the behavior of the actor and coordinates the behavior of all UAVS to increase the reward of the system. Simulation results show that the proposed offloading strategy has fast convergence speed, increases the number of tasks, and improves the energy utilization of the UAV.

Lan et al.[46] proposed anISTN to achieve satellite-assisted mission unloading under dynamic condition. A privacy protection algorithm based on deep reinforcement learning is introduced to achieve the optimal unloading strategy. Experimental results show that the proposed algorithm is superior to other benchmark algorithms in completion time, energy consumption, privacy protection and communication reliability.

Zhang et al.[47] studied the problem of computing task offloading and resource allocation in multi-layer LEO satellite networks assisted by UAVS. In order to minimize the weighted sum of energy consumption and delay in the system, the problem was formulated as a constrained optimization problem, and then it was transformed into a Markov decision problem (MDP), and a task offloading and resource allocation algorithm based on deep deterministic policy gradient and Long Short-Term Memory (DDPG-LSTM) was proposed. Simulation results show that the proposed solution outperforms baseline methods, and the proposed framework and algorithm have the potential to provide reliable communication services in emergency situations.

Han et al.[48] proposed an ISTN architecture to support delay-sensitive task offloading in remote Internet of Things (IoT). In order to minimize the overall task offloading delay, a hierarchical Markov Decision process (H-MDP) framework was established, and an algorithm based on Hybrid Proximal Policy Optimization (H-PPO) was further developed. The proposed algorithm designs a hybrid actor-critic architecture to deal with mixed discrete and continuous actions, and designs an action mask layer and an action shaping function. Simulation results verify the superiority of the proposed ISTN architecture and the H-PPO-based algorithm.

D. SUMMARY

The routing optimization and task offloading tasks of the network layer are mainly performed by deep reinforcement learning, while the traffic prediction related tasks are solved by supervised learning.

From Table 3, it can be found that the types of satellite networks in the network layer are also relatively rich, but the focus is on the space-ground integrated network, because the space-ground integrated network has a large number of nodes, complex topology, and large user traffic, which poses great challenges to routing optimization. Deep Learning methods are mainly focused on supervised learning and deep reinforcement learning, and there are many types of neural network models, such as CNN, LSTM, FCNN, etc. They are also not as complex as neural networks used in the ground or computer field. Some researches use open source data sets to conduct their experiments，however，these datasets have been modified for use in satellite communications. Most papers do not disclose the CPU or GPU used for training.

V. CONCLUSION

Deep learning and satellite communication technology are developing rapidly, and satellite communication technology powered by deep learning brings a better experience for space-ground integrated networks. The application of deep reinforcement learning in resource allocation, handover, and routing control has been widely studied. Meanwhile, supervised learning plays an important role in signal recognition, and traffic prediction.

However, deep learning still faces some problems to be solved in satellite communication:

1. The dataset problem. Using simulation data to verify the effect of communication system is the mainstream solution, perhaps because the network structure is always different, and makes it difficult to establish a general dataset. There is no standard open source dataset related to satellite communication, and the lack of datasets restricts the research progress of deep learning for satellite communication. It is of great significance to increase the construction of open datasets for satellite communication.

2. The problem of neural network fragmentation. When solving different problems, different types of deep learning algorithms and neural network models need to be used, which will form a large number of neural network fragments and take up a lot of storage space.

3. Computing power problem. Deep learning requires a lot of computing power, and the larger the model, the more the power. On handheld terminals or satellites, it is difficult to meet such computing power. At present, many studies do not consider the impact of neural network scale in the specific practice of satellite communication, especially the competition between satellite computing power and communication power consumption.

4. Practical application problems. Compared with the practice of deep learning in Go, automatic driving and UAV flight, there is no practice of deep learning in satellite communication at present, and it is often verified by simulation. Deep learning-based satellite communication needs more practical implementation.

Solving the above problems can effectively promote the application research of deep learning in satellite communication. In addition, strengthen the inte-

Table 3 Application status of deep learning in network layer

Application	satellite networks	Deep Learning Methods	Neural Network model	Open Source Datasets	Hardware information	Ref.
Routing	SAGINs	DL	DNN	Yes	/	[41]
	ISN	SL	CNN	Yes	/	[42]
Traffic Prediction	non-specific	SL	CNN	Yes	CPU	[43]
	LEO	SL	LSTM+Attention	Yes	/	[44]
Task Scheduling	SAGIN for IoRT	DRL	FCNN	No	GPU	[45]
	ISN	DRL	/	No	GPU	[46]
	UAV-Assisted LEO Satellite	DRL	LSTM	No	/	[47]
	ISTN for IoT	DRL	FCNN	No	/	[48]

gration of deep learning and satellite communication at the hardware level, for example, carrying out the end-to-end physical layer design of satellite communication[49,50]from the perspective of system theory, may promote the development of intelligent endogenous network. At the same time, based on the idea of AI for science, it is very valuable to conduct basic theory research based on deep learning in satellite communication, rather than limited it to the engineering application level.

References

[1] DUAN T, DINAVAHI V. Starlink Space Network-Enhanced Cyber–Physical Power System[J/OL]. IEEE Transactions on Smart Grid, 2021, 12(4): 3673-3675. DOI:10.1109/TSG.2021.3068046.

[2] Wang Zijian , Du Xinjun , Yin Jiawei, et al . Development and prospect of LEO satellite Internet[J]. Application of Electronic Technique ， 2020 ， 46(7) ：49-52.

[3] WANG Peng, ZHU Siting, LI Chen, et al. Analysis on Development of Satellite Internet Standardization[J].Radio Communications Technology, 2023,49(5): 1-7.

[4] WANG Chunting, ZHAI Lijun, XU Xiaofan. Development and Prospects of Space-Terrestrial Integrated Information Network[J]. Radio Communications Technology，2020，46(5) : 493－504.

[5] FANG X, FENG W, WEI T, et al. 5G Embraces Satellites for 6G Ubiquitous IoT: Basic Models for Integrated Satellite Terrestrial Networks[J/OL]. IEEE Internet of Things Journal, 2021, 8(18): 14399-14417.

[6] ZHANG Shijie, ZHAO Xiangtian, ZHAO Yafei, et al. Integration of Satellite Internet and Terrestrial Networks: Integrated Mode, Frequency Usage and Application Prospects [J].Radio Communications Technology, 2023,49(5).

[7] SUN Yaohua, PENG Mugen. Low earth orbit satellite communication supporting direct connection with mobile phones: key technologies, recent progress and future directions [J]. Telecommunications Science, 2023, 39(02): 25-36.

[8] ITU-R, Workshop on "IMT for 2030 and beyond", https://www.itu.int/en/ITU-R/study-groups/rsg5/rwp5d/imt-2030/Pages/default.aspx

[9] XIAO Z, YANG J, MAO T, et al. LEO Satellite Access Network (LEO-SAN) Towards 6G: Challenges and Approaches[M/OL]. arXiv, 2022[2023-09-05]. http://arxiv.org/abs/2207.11896.

[10] AZARI M M, SOLANKI S, CHATZINOTAS S, 等. Evolution of Non-Terrestrial Networks From 5G to 6G: A Survey[J/OL]. IEEE Communications Surveys & Tutorials, 2022, 24(4): 2633-2672.

[11] FOURATI F, ALOUINI M S. Artificial intelligence for satellite communication: A review[J/OL]. Intelligent and Converged Networks, 2021, 2(3): 213-243.

[12] WANG X, SHEN W, XING C, et al. Joint Bayesian Channel Estimation and Data Detection for OTFS Systems in LEO Satellite Communications[J/OL]. IEEE Transactions on Communications, 2022, 70(7): 4386-4399.

[13] YAN Wenkang, YAN Yi, FAN Yanan, YAO Xiujuan, GAO Xiang, SUN Wen. A modulation recognition algorithm based on wavelet transform entropy and high-order cumulant for satellite signal modulation （in Chinese）。Chin.J. Space Sci.，2021，41（6）：968-975.

[14] LI J, TANG X, GAO L, et al. Satellite communication anti-jamming based on artificial bee colony blind source separation[C/OL]//2021 6th International Conference on Communication, Image and Signal Processing (CCISP). 2021: 240-244.

[15] SUBRAMANIAN V, KARUNAMURTHY J V, RAMACHANDRAN B. Hardware doppler shift emulation and compensation for LoRa LEO satellite communication[C/OL]//2023 International Conference on IT Innovation and Knowledge Discovery (ITIKD). 2023: 1-6.

[16] KANG M J, LEE J H, CHAE S H. Channel Estimation with DnCNN in Massive MISO LEO Satellite Systems[C/OL]//2023 Fourteenth International Conference on Ubiquitous and Future Networks (ICUFN). 2023: 825-827. DOI:10.1109/ICUFN57995.2023.10200015.

[17] ZHANG Y, WU Y, LIU A, et al. Deep Learning-Based Channel Prediction for LEO Satellite Massive MIMO Communication System[J/OL]. IEEE Wireless Communications Letters, 2021, 10(8): 1835-1839. DOI:10.1109/LWC.2021.3083267.

[18] GUVEN E, KURT G K. CNN-aided Channel and Carrier Frequency Offset Estimation for HAPS-LEO Links[C/OL]//2022 IEEE Symposium on Computers and Communications (ISCC). Rhodes, Greece: IEEE, 2022: 1-6[2023-09-05].

[19] ZHA Xiong，PENG Hua，QIN Xin，LI Tian-yun，LI Guang; Satellite Amplitude-Phase Signals Modulation Identification and Demodulation Algorithm Based on the Cyclic Neural Network [J]. ACTA ELECTＲONICA SINICA, 2019(11 vo 47): 2443-2448.

[20] REN Jin，JI Libin，DANG Liu．Satellite Signal Modulation Recognition Algorithm Based on Deep Learning［J］．Radio Engineering，2022，52 (4) : 529－535.

[21] HAN C, HUO L, TONG X, et al. Spatial Anti-Jamming Scheme for Internet of Satellites Based on the Deep Reinforcement Learning and Stackelberg Game[J/OL]. IEEE Transactions on Vehicular Technology, 2020, 69(5): 5331-5342. DOI:10.1109/TVT.2020.2982672.

[22] LI H, LIU Y, SHI J, et al. Multimodal LSTM forecasting for LEO Satellite Communication Terminal access[C/OL]//2023 IEEE 97th Vehicular Technology Conference (VTC2023-Spring). 2023: 1-5. DOI:10.1109/VTC2023-Spring57618.2023.10199836.

[23] LIAO X, HU X, LIU Z, et al. Distributed Intelligence: A Verification for Multi-Agent DRL Based Multibeam Satellite Resource Allocation[J/OL]. IEEE Communications Letters, 2020, PP(99):1-1. DOI:10.1109/LCOMM.2020.3019437.

[24] WU Xiaowen, LING Xiang , ZHU Lidong. Access and mobility management technologies for 6G satellite communications network [J]. Telecommunication science, 2021(78-90).

[25] JIANG Z, LI W, WANG X, et al. A LEO Satellite Handover Strategy Based on Graph and Multiobjective Multiagent Path Finding[J/OL]. International Journal of Aerospace Engineering, 2023, 2023: 1-16. DOI:10.1155/2023/1111557.

[26] HU X, ZHANG Y, LIAO X, et al. Dynamic Beam Hopping Method Based on Multi-Objective Deep Reinforcement Learning for Next Generation Satellite Broadband Systems[J]. IEEE Transactions on Broadcasting, 2020, PP(99): 1-17.

[27] LI X, ZHANG H, ZHOU H, et al. Multi-Agent DRL for Resource Allocation and Cache Design in Terrestrial-Satellite Networks[J/OL].

IEEE Transactions on Wireless Communications, 2023, 22(8): 5031-5042. DOI:10.1109/TWC.2022.3231379.

[28] MA S, HU X, LIAO X, et al. Deep Reinforcement Learning for Dynamic Bandwidth Allocation in Multi-Beam Satellite Systems[C/OL]//2021 IEEE 6th International Conference on Computer and Communication Systems (ICCCS). Chengdu, China: IEEE, 2021: 955-959[2023-09-04]. https://ieeexplore.ieee.org/document/9449160/. DOI:10.1109/ICCCS52626.2021.9449160.

[29] MAKKI B, CHITTI K, BEHRAVAN A, et al. A Survey of NOMA: Current Status and Open Research Challenges[M/OL]. arXiv, 2019[2022-11-08]. http://arxiv.org/abs/1912.10561.

[30] ZHU X, JIANG C, KUANG L, et al. Non-Orthogonal Multiple Access Based Integrated Terrestrial-Satellite Networks[J/OL]. IEEE Journal on Selected Areas in Communications, 2017, 35(10): 2253-2267. DOI:10.1109/JSAC.2017.2724478.

[31] ZHANG Q, AN K, YAN X, et al. User Pairing for Delay-Limited NOMA-Based Satellite Networks with Deep Reinforcement Learning[J/OL]. Sensors, 2023, 23(16): 7062. DOI:10.3390/s23167062.

[32] LEE J H, SEO H, PARK J, et al. Learning Emergent Random Access Protocol for LEO Satellite Networks[J/OL]. IEEE Transactions on Wireless Communications, 2023, 22(1): 257-269. DOI:10.1109/TWC.2022.3192365.

[33] YANG J, XIAO Z, CUI H, 等. DQN-ALrM-Based Intelligent Handover Method for Satellite-Ground Integrated Network[J/OL]. IEEE Transactions on Cognitive Communications and Networking, 2023, 9(4): 977-990. DOI:10.1109/TCCN.2023.3262239.

[34] WANG J, MU W, LIU Y, et al. Deep Reinforcement Learning-based Satellite Handover Scheme for Satellite Communications[C/OL]//2021 13th International Conference on Wireless Communications and Signal Processing (WCSP). Changsha, China: IEEE, 2021: 1-6.

[35] LENG T, XU Y, CUI G, et al. Caching-Aware Intelligent Handover Strategy for LEO Satellite Networks[J/OL]. Remote Sensing, 2021, 13(11): 2230.

[36] XU H, LI D, LIU M, et al. QoE-Driven Intelligent Handover for User-Centric Mobile Satellite Networks[J/OL]. IEEE Transactions on Vehicular Technology, 2020, 69(9): 10127-10139. DOI:10.1109/TVT.2020.3000908.

[37] LEI L, LAGUNAS E, YUAN Y, et al. Deep Learning for Beam Hopping in Multibeam Satellite Systems[C/OL]//2020 IEEE 91st Vehicular Technology Conference (VTC2020-Spring). Antwerp, Belgium: IEEE, 2020: 1-5[2022-11-08].

[38] CAO X, LI Y, XIONG X, et al. Dynamic Routings in Satellite Networks: An Overview[J/OL]. Sensors, 2022, 22(12): 4552. DOI:10.3390/s22124552.

[39] LIU Y, YU J J Q, KANG J, et al. Privacy-Preserving Traffic Flow Prediction: A Federated Learning Approach[J/OL]. IEEE Internet of Things Journal, 2020, 7(8): 7751-7763. DOI:10.1109/JIOT.2020.2991401.

[40] WU G, LUO Q, ZHU Y, et al. Flexible Task Scheduling in Data Relay Satellite Networks[J/OL]. IEEE Transactions on Aerospace and Electronic Systems, 2022, 58(2): 1055-1068. DOI:10.1109/TAES.2021.3115587.

[41] LIU D, ZHANG J, CUI J, et al. Deep Learning Aided Routing for Space-Air-Ground Integrated Networks Relying on Real Satellite, Flight, and Shipping Data[M/OL]. arXiv, 2021[2022-09-25]. http://arxiv.org/abs/2110.15138.

[42] WANG F, JIANG D, WANG Z, et al. Fuzzy-CNN Based Multi-Task Routing for Integrated Satellite-Terrestrial Networks[J/OL]. IEEE Transactions on Vehicular Technology, 2022, 71(2): 1913-1926. DOI:10.1109/TVT.2021.3131975.

[43] WAN X, FU X, LI J, et al. Research on Satellite Traffic Classification based on Deep packet recognition and convolution Neural Network[C/OL]//2023 8th International Conference on Computer and Communication Systems (ICCCS). 2023: 494-498. DOI:10.1109/ICCCS57501.2023.10151173.

[44] ZHU F, LIU L, LIN T. An LSTM-based Traffic Prediction Algorithm with Attention Mechanism for Satellite Network[J].

[45] ZHANG S, LIU A, HAN C, et al. Multi-agent Reinforcement Learning-Based Orbital Edge Offloading in SAGIN Supporting Internet of Remote Things[J/OL]. IEEE Internet of Things Journal, 2023: 1-1. DOI:10.1109/JIOT.2023.3287737.

[46] LAN W, CHEN K, LI Y, et al. Deep Reinforcement Learning for Privacy-Preserving Task Offloading in Integrated Satellite-Terrestrial Networks[M/OL]. arXiv, 2023[2023-09-12]. http://arxiv.org/abs/2306.17183.

[47] ZHANG H, XI S, JIANG H, et al. Resource Allocation and Offloading Strategy for UAV-Assisted LEO Satellite Edge Computing[J/OL]. Drones, 2023, 7(6). https://www.mdpi.com/2504-446X/7/6/383. DOI:10.3390/drones7060383.

[48] HAN D, YE Q, PENG H, et al. Two-Timescale Learning-Based Task Offloading for Remote IoT in Integrated Satellite–Terrestrial Networks[J/OL]. IEEE Internet of Things Journal, 2023, 10(12): 10131-10145. DOI:10.1109/JIOT.2023.3237209.

[49] LUO X, CHEN H H, GUO Q. Semantic Communications: Overview, Open Issues, and Future Research Directions[J/OL]. IEEE Wireless Communications, 2022, 29(1): 210-219. DOI:10.1109/MWC.101.2100269.

[50] DAI J, ZHANG P, NIU K, et al. Communication Beyond Transmitting Bits: Semantics-Guided Source and Channel Coding[J/OL]. IEEE Wireless Communications, 2022: 1-8. DOI:10.1109/MWC.017.2100705.

基于可参考图像重采样方法的卫星遥感影像高倍率压缩方法

张真，肖晶*，蔺骁翼

摘　要：随着遥感成像技术的不断发展带来的星上数据量逐渐，如何实现高分辨率遥感图像高倍压缩是卫星遥感实时应用面临的一个重要挑战。图像重采样技术能够将高分辨率图像降采样以方便数据的存储和传输，随后将降采样后的图像上采样以保证视觉质量，是辅助遥感图像高倍压缩的关键技术。然而，现有的重采样方法更关注重建质量，而不是降采样图像的可压缩性，这不利于遥感影像的压缩传输。在遥感场景中，周期性观测带来的历史图像为减轻重建质量与可压缩性之间的冲突提供了契机，即作为参考的历史图像指导在降采样阶段可以丢弃哪些信息以降低降采样图像中的信息量，并在上采样阶段提供丢弃的信息从而提高图像重建质量。基于这个想法，我们提出了一种新的基于参考图像重采样方法的压缩框架。具体来说，我们提出了一个参考网络来计算相似图以提供参考条件，然后将其注入到可逆神经网络中，以指导降尺度阶段的信息丢弃和上采样阶段的图像恢复。此外，我们还提出了一种新的损失函数，以进一步约束降采样图像的数据量。实验表明，在卫星周期观测场景下我们的方法优于最先进的方法。

关键词：深度学习；图像重采样；可逆神经网络

Reference-based Image Resampling for High-ratio Compression of Remote Sensing Images

Zhen Zhang, Jing Xiao*, Xiaoyi Lin

Abstract: With the continuous development of remote sensing imaging technology and the gradual expansion of on-board data, how to achieve high compression efficiency of remote sensing images is a challenge problem. Image resampling aims to downsample images to facilitate data transmission and storage before encoding, and reconstructs the quality through upsampling after decoding, which is a key technology to assist in high-ratio compression. However, existing studies seek to high reconstruction quality, neglecting the high information content conveyed in the downsampled images. In remote sensing periodic observation scenarios, historical images provide an opportunity to alleviate the conflict between reconstruction quality and compressibility, that is, the historical images as reference indicates what information can be dropped at downsampling to reduce the information content and provides the dropped information to improve the reconstruction quality at upsampling. Based on this consideration, we propose a novel reference-based image resampling framework for high-ratio compression. Specifically, a referencing network is proposed to calculate the similarity map to provide the referencing condition, which is then introduced into the conditional invertible neural network to guide the information drop at downsampling and image restoration at upsampling. Additionally, a novel loss is proposed to further constrain the data amount of the downsampled image. Experiments show the superior performance of our approach over the state-of-the-art methods.

Key words: Deep Learning, Image Resampling, Invertible Neural Networks

1　引言

随着成像技术的快速发展，遥感卫星图像的空间分辨率不断提高，单张图像占据的存储空间越来越大，巨大的数据量给图像的存储和传输带来了巨大的挑战，高倍率的图像压缩算法对于图像的存储、传输、管理甚至遥感实时服务的发展至关重要。近几十年来，为了实现低比特率下的图像传输，产生了许多诸如稀疏表示的高倍率压缩方法。其中，基于重采样的编码框架可以在低码率下减少量化引入的误差，从众多方法中脱颖而出。在基于重采样的编码框架中，图像重采样是一项必不可少的技术，它包含了图像降采样与图像上采样两个过程。降采样产生的低分辨率（Low-resolution，LR）图像可以显著减少传输所需数据量，而当需要查看图像内容时，上采样技术能够将图像恢复到原始分辨率或使其适应不同分辨率的屏幕，以保证重建后图像的视觉质量。然而，降采样过程中不可逆转地丢失了图像的高频细节信息，这对后续的图像上采样重建带来了极大的挑战，使其成为不适定问题或病态问题[1,2,3,4]。

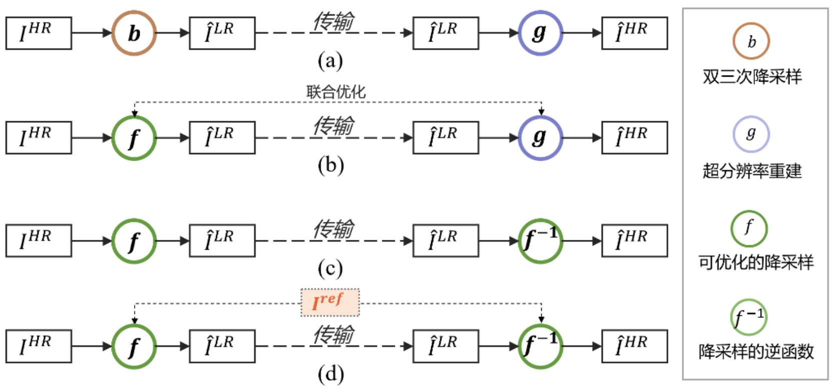

图 1　4 种图像重采样框架示意图

为了解决图像降采样与上采样这一组问题，目前对图像重采样的研究主要分为三类[5]。第一类方法使用固定的降采样核对图像进行降采样处理，同时利用图像超分辨率重建（Super-resolution，SR）技术对 LR 图像进行上采样处理[3,6,7]（图 1（a））。虽然先进的 SR 方法可以恢复视觉上合理的高频纹理，但它生成的纹理真实性难以保证。在认识到合适的降采样过程有利于保留 LR 图像中有助于上采样重建的信息之后，第二类方法尝试在统一的框架内优化这两个过程来保留利于反向恢复的关键信息[8,9,10]（图 1（b））。这些方法通过联合优化定义了自己的 LR 图像空间，在降采样图像中留下比简单的降采样方法（如双三次降采样）更多的线索，因而重建图像具有更好的视觉质量且更加真实可靠。为了满足可信图像重建的要求，一些研究使用了可逆神经网络（Invertible Neural Network，INN）[11,12,13]。这些方法将降采样和上采样构建为一个可逆过程[14,15]（图 1（c））。总而言之，上述的重采样方法极大地提高了重建后 HR 图像的质量，但却很少有研究去关注 LR 图像的数据量，而这正是可能导致存储和传输的信息量过大的关键。

本项研究旨在同时解决两个问题，即最小化降采样图像中的信息量，同时最大化重建图像的质量。受最近基于参考的 SR 方法的启发[16,17,18,19,20]，我们希望基于遥感卫星的周期性观测特性引入历史参考图像来实现这一目标。具体来说，历史参考图像可以在降采样过程中引导去除图像中与其相似的冗余信息，并

在上采样过程中提供这些信息从而弥补细节的损失。基于此想法，我们提出了一个基于参考的图像重采样方法（图 1（d）），通过利用 HR 图像与其相应的历史参考图像之间的相关性来缓解 LR 图像的低信息量与重建 HR 图像的高视觉质量之间的矛盾。一方面，在降采样过程中，我们希望尽可能多地减少 HR 图像与参考图像相似的互信息，同时保留无法从参考图像中恢复的特征信息；另一方面，参考图像提供的互信息可以为 HR 图像的重建提供指导。为了利用参考图像辅助重采样过程，我们构建了一个参考网络（Referencing Network，Ref-Net）来提取 HR 和参考图像之间的相关信息，并提出了一个新的条件可逆神经网络（conditional INN，c-INN），该可逆神经网络将互信息嵌入到遵循指定分布的潜变量中，同时保留 LR 图像中与参考图像无关的信息。在上采样阶段，重采样框架基于 LR 图像、参考图像和随机采样的潜在变量重建 HR 图像。在训练阶段，采用新提出的基于相似度的 LR 损失函数来指导训练过程中的图像间冗余消除。

综上所述，本文的主要贡献有：

- 我们在遥感场景中引入参考图像进行图像重采样，实现有利于降采样和上采样的联合优化。消除参考图像与当前图像之间的互信息有助于减少降采样图像中的信息量，同时参考图像可以在上采样阶段提供被丢弃的信息用于图像重建。
- 我们提出了一种新的重采样方法，通过参考图像生成的参考条件特征来表示参考图像与当前图像的相关性，并且通过条件可逆神经网络在降采样和上采样过程中有条件地丢弃和恢复互信息，从而将参考图像整合到一个可逆的重采样网络中。
- 我们将所提出的重采样方法应用与基于重采样的压缩框架中，实验结果表明，我们的方法在低码率的场景下能够实现更高的重建质量。

2 相关工作

2.1 图像重采样

图像重采样的目标是将 HR 图像降采样至更低空间分辨率的 LR 图像，然后从 LR 图像中恢复出原始分辨率的图像，它包含了图像降采样与上采样两个过程。先前的工作通常将这两个过程单独处理，它们使用固定的高频滤波器进行降采样，如双线性和双三次插值。之后的一些方法试图在降采样后的图像中保留更多的结构和细节，以获得更高的视觉质量。Kopf 等人[21]提出了一种内容自适应的方法来优化降采样核的形状和位置，以提升降采样图像的视觉质量。Oeztireli 等人[22]利用结构相似度（SSIM）优化降采样图像，使其保留感知上重要的特征和细节，从而获得与输入空间一致的表示。Weber 等人[23]设计了一种基于卷积滤波器的算法，通过强调颜色偏离其局部邻域的像素来保留视觉上重要的细节。Liu 等人[24]提出了梯度比先验与降采样先验，以保留显著边缘与原始图像的视觉感知。另一方面，上采样过程通常是通过图像超分辨率重建技术实现的。自第一个基于卷积神经网络的单幅图像超分（Single Image Super-resolution, SISR）方法[2]问世以来，人们提出了各式各样的 SR 模型以提升图像的重建质量[25,26,27]。其中，一些有效的结构被提出以获得更深层次的模型和更高的精度，如残差连接[24,25]，密集连接[27,28]等。由于重建图像的纹理依旧

存在模糊和扭曲，之后的一些方法[29,30]采用生成对抗网络（GANs）来产生视觉上更为合理的结果。最近，标准化流[31,32]和扩散模型[33]也被用于 SISR 中，并取得了优异的效果。

在认识到图像降采样和上采样之间的潜在相关性之后，最近的研究中出现了针对这两个过程共同优化的重采样模型，实现了更高质量的图像重建。Kim 等人[29]首先提出了一种基于自编码器的方法，编码器和解码器分别模拟降采样和上采样过程。Li 等人[9]提出学习一种紧凑分辨率图像，它拥有与高分辨率图像相当的视觉质量和信息量。Sun 等人[10]提出了一种无监督的内容自适应降采样核来保持输入图像的结构。近来，基于可逆神经网络的方法在图像重采样领域中被提出。IRN[15]率先提出使用双射变换的可逆神经网络对整个重采样过程进行建模，通过在降采样过程中明确建模丢失了哪些信息，使得重建质量得到了飞跃式的提高。HCFlow[14]进一步以生成的低频分量为条件对高频分量进行建模，取得了更优的重建质量。这些方法虽然取得了出色的重建效果，但对 LR 信息含量要求大，这增加了数据存储和传输的负担。

2.2　基于重采样的编码

基于重采样的编码框架对输入信号进行降采样，在相同比特率下每个变换系数保留更多的比特，从而能够减少量化引起的误差，而在解码阶段则通过上采样恢复至原始分辨率。最初，Ilgin 等人[34]和 Nguyen 等人[35]在 DCT 域中进行降采样，减少变换系数的数量，从而为低频系数分配更多的位。Barreto 等人[36]提出在编码前对 HR 图像进行降采样，然后使用超分辨率技术作为解码器中的后处理模块来恢复图像。至此，基于重采样的编码框架渐具雏形。Shen 等人[37]构建了一个包含大量 HR 图像及其降采样图像对的训练集，采用基于示例的超分辨率方法并在集合中进行最近邻搜索，以获取高频细节并添加到重建图像中。

最近，随着卷积神经网络在图像超分辨率技术中的广泛应用，基于深度学习的超分辨率方法也被用于基于重采样的编码框架中。Li 等人[38]提出一种基于卷积神经网络的帧内视频压缩上采样方法。Lin 等人[39]将基于卷积神经网络的上采样从帧内编码扩展到帧间编码，即利用相邻帧之间的时域相关性来提高重建质量。为了解决由于压缩伪影引起的超分辨率退化问题，Ho 等人[40]提出了一种退化感知的方法，共同完成恢复和重建。这些方法对基于重采样的编码框架中的上采样过程优化进行了深入的研究，但是并未将降采样与上采样综合地考虑，而对降采样过程的认识与建模毫无疑问能够对上采样过程产生正向作用。

3　研究方法

3.1　总体框架

我们提出的基于可参考图像重采样方法的压缩框架如图 2 所示，包括图像的降采样、编码、解码与上采样过程。记$I^{HR} \in R^{3\times W\times H}$为 HR 图像，$I^{ref} \in R^{3\times W\times H}$为相应的历史参考图像，其中$W$和$H$分别表示图像的宽度和高度，与压缩框架的流程可以表示为：

$$I^{LR} = Down\left(I^{HR}, I^{ref}; \theta\right) \tag{1}$$

$$b = encode(I^{LR}; \phi) \tag{2}$$

$$\hat{I}^{LR} = decode\left(\hat{b}; \varphi\right) \tag{3}$$

$$I^{HR} = Up\left(\hat{I}^{LR}, I^{ref}; \theta\right) \tag{4}$$

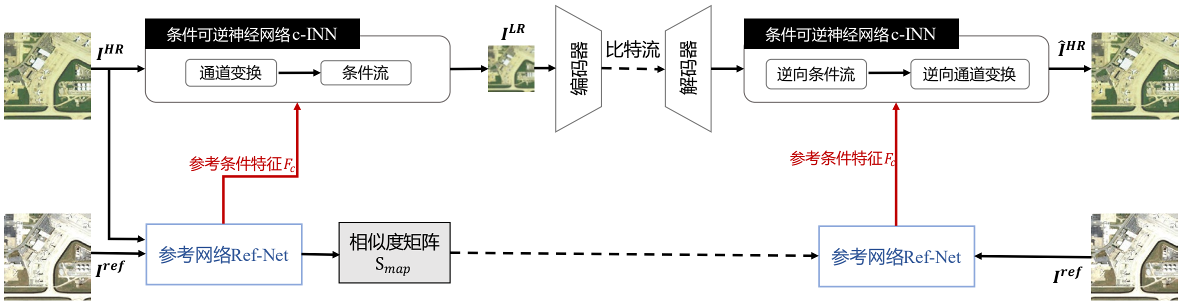

图 2　基于可参考图像重采样方法的压缩框架

其中，I^{LR}和$\hat{I}^{LR}$分别表示降采样后的I^{HR}和解码后的I^{LR}，b是编码后的码流，ϕ与φ分别为编码器与解码器的参数，θ为重采样网络的参数。值得注意的是，由于我们使用了双向映射的可逆神经网络来实现重采样，因此降采样过程与上采样共用相同的参数。

在基于参考的重采样过程中，我们设计了两个子网络分别进行参考条件特征的生成和使用：一是参考网络（Ref-Net），利用高分辨率图像I^{HR}和相应的参考图像I^{ref}间的相关性信息生成参考条件特征，这些特征将用于后续的降采样和重构；二是条件可逆神经网络（c-INN），利用参考条件特征指导图像的降采样和上采样。在降采样阶段，Ref-Net 计算I^{HR}和I^{ref}之间的相似度矩阵S_{map}，并生成参考条件特征F_c。S_{map}还用于 LR 相关的损失函数$\mathcal{L}_{LR}$的计算，从而在图像间相似的区域去除更多细节并在图像间不同的区域保留更多信息。在F_c的指导下，c-INN 对I^{HR}进行处理，生成信息量较少的 LR 图像I^{LR}。在上采样阶段，Ref-Net 以I^{ref}和S_{map}作为输入来生成参考条件特征F_c。c-INN 使用F_c从 LR 图像$\hat{I}^{LR}$反向重建 HR 图像。由于I^{HR}在上采样端不可见，S_{map}需要和$\hat{I}^{LR}$一起从降采样端存储和传输到上采样端，因此我们设计了一系列方法减少它的尺寸。

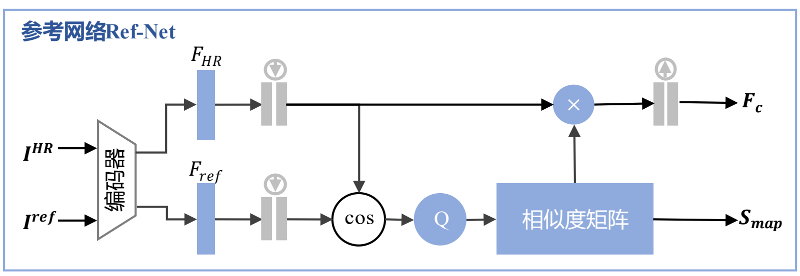

图 3　参考网络 Ref-Net 的结构

3.2　参考网络 Ref-Net

参考网络 Ref-Net 捕获I^{HR}和I^{ref}之间的相关性，并生成用于LR损失函数的相似度矩阵S_{map}和用于 c-INN 的参考条件特征F_c。相似度矩阵S_{map}和条件特征F_c的提取过程如图 3 所示，I^{HR}和I^{ref}经由同一个编码器处理并输出特征F_{HR}和F_{ref}，随后在像素级进行余弦相关性计算得到S_{map}：

$$S_{map}^{i,j}=\left\langle \frac{F_{HR}^{i,j}}{\left|F_{HR}^{i,j}\right|},\frac{F_{ref}^{i,j}}{\left|F_{ref}^{i,j}\right|}\right\rangle \tag{5}$$

其中，(i,j)为空间位置索引。参考条件特征F_c由F_{ref}与S_{map}通过逐元素相乘得到。

由于I^{HR}在上采样时不可见，因此需要保留S_{map}并将其传输到上采样端，以生成与降采样阶段相同的

参考条件特征。为了实现这一点，我们采用瓶颈结构和量化模块来减小S_{map}的大小。首先，通过降采样层对F_{HR}和F_{ref}进行处理，获得较低分辨率的图像特征用于计算S_{map}。其次在计算F_c时，通过上采样层对S_{map}进行处理，使空间大小与F_c匹配。最后，在传输过程中，使用量化模块将S_{map}从浮点数转换为整数，进一步减小数据大小。

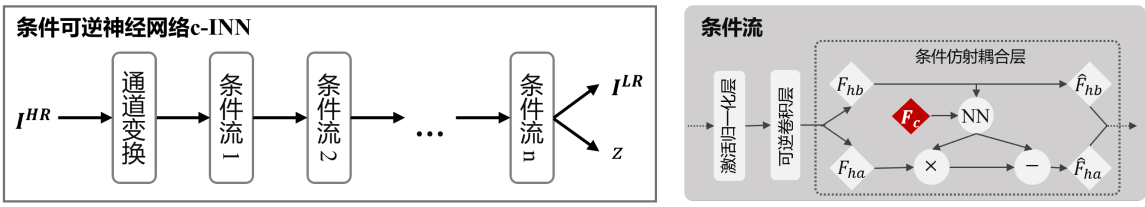

图 4　条件可逆神经网络 c-INN 及条件流模块的结构

3.3　条件可逆神经网络 c-INN

为了利用图像间的互信息指导图像的重采样，我们提出了一个条件可逆变换$f(\cdot): I^{HR} \overset{c}{\leftrightarrow} [I^{LR}, z]$，其中$c$是 HR 和参考图像之间的互信息，$z$是潜变量。在实际应用中，我们使用预定义的降采样图像为$\tilde{I}^{LR}$，参考条件特征F_c为c。具体来说，我们设计了一个带有条件注入的仿射耦合变换的条件 INN，如图 4 所示。该子网络由一个通道变换模块和一组条件流模块（Conditional Flow Block，CFB）组成。通道变换模块通过重组空间与通道的维度使输入的空间维度与 LR 图像对齐。CFB 则包括一个激活归一化层、一个可逆卷积层和一个条件仿射耦合层，这样的结构基于参考条件特征F_c逐步地将图像间冗余从$\hat{I}^{LR}$分离开来。整个降采样和反向重构过程可表示为：

$$\left[\hat{I}^{LR}, z\right] = f(I^{HR} \mid F_c) \tag{6}$$

$$\hat{I}^{HR} = f^{-1}\left(\hat{I}^{LR}, \hat{z} \mid F_c\right) \tag{7}$$

条件注入：将F_c注入到 CFB 的条件仿射耦合层中用于辅助相似信息的丢弃。基于F_c中可以获得的信息，c-INN 将从数据流中逐步丢弃图像间的互信息。具体来说，在条件仿射耦合层中，输入特征流F_h沿着通道维度被分割成两个子特征F_{ha}和F_{hb}，然后在F_c的辅助下进行仿射变换来决定哪些信息应该被丢弃，这个过程可以表示为：

$$\hat{F}_{ha} = F_{ha} \odot exp\left(\psi(F_{hb}, F_c)\right) - \phi(F_{hb}, F_c) \tag{8}$$

$$\hat{F}_{hb} = F_{hb} \tag{9}$$

其中，$\psi(\cdot)$和$\phi(\cdot)$为可学习的变换函数，$\left[\hat{F}_{ha}, \hat{F}_{hb}\right]$为输出特征。通过$\psi(\cdot)$和$\phi(\cdot)$将$F_{hb}$和$F_c$融合以生成仿射变换参数，最后将仿射变换参数应用于$F_{ha}$以丢弃可从参考中恢复的信息。

3.4　损失函数

与 IRN[14]类似，我们约束了I^{HR}的重建质量和潜变量z的分布。此外，我们在I^{LR}上使用基于相似度矩阵的 LR 损失函数，以确保降采样过程中丢弃的信息可以从参考中恢复。

HR 图像重建：我们使用$\mathcal{L}_1$损失来度量重建的 HR 图像与真值之间的差值，具体表示如下：

$$\mathcal{L}_{HR} = \left\| I^{HR} - \hat{I}^{HR} \right\| \tag{10}$$

分布匹配：该项的目的是促使生成的潜在变量 z 服从一个特定的分布：

$$\mathcal{L}_{distr} = CE(p(z), f^z[q(I^{HR})]) \tag{11}$$

其中，$q(I^{HR})$和$p(z)$分别为 HR 图像I^{HR}和潜变量z的分布，$f^z(\cdot)$为图像到潜变量的变换，$CE(\cdot)$为交叉熵函数。我们假设$p(z)$服从标准高斯分布，因此可以很容易地通过对潜变量z进行$\mathcal{L}_2$正则化来计算分布匹配损失。

LR 损失：Ref-Net 将提取的图像间相关性传递给 c-INN，c-INN 从中得知哪些信息可以在降采样阶段丢弃和并在之后的上采样阶段得到恢复。为此我们给出了一个基于相似度矩阵的 LR 图像损失函数，指导 c-INN 进行降采样和上采样。不同于直接利用基于双三次降采样的图像来指导 LR 图像生成的方法，我们将双三次降采样图像作为图像间不相似区域的详细信息指导。此外，因为图像之间的相似信息主要涉及结构和边缘信息，所以我们使用信息量较少但仍具有视觉可识别性的高斯模糊降采样图像来指导图像间相似区域的降采样。高斯模糊降采样图像由一个降采样-高斯模糊-上采样的流水线处理得到，这样可以丢弃大量的细节从而减少图像的信息量。基于相似度矩阵S_{map}对 LR 的不同区域进行区分，分别约束其视觉质量，其公式化表达为：

$$\mathcal{L}_{LR} = \left\|(I_{bic}^{LR} - \hat{I}^{LR}) \odot S_{map}\right\| + \left\|(I_{blur}^{LR} - \hat{I}^{LR}) \odot (1 - S_{map})\right\| \tag{12}$$

其中，I_{bic}^{LR}和I_{blur}^{LR}分别是基于双三次降采样的和基于高斯模糊降采样得到的降采样图像。该损失函数将促使I^{LR}丢弃更多的 HR 图像与参考图像相似的信息，而保留在I^{LR}中不可恢复的细节。

总损失：我们通过最小化由 HR 重建损失$\mathcal{L}_{HR}$、基于相似度矩阵的 LR 损失$\mathcal{L}_{LR}$和分布匹配损失$\mathcal{L}_{distr}$组成的总损失来优化我们的模型：

$$\mathcal{L}_{total} = \lambda_{HR}\mathcal{L}_{HR} + \lambda_{LR}\mathcal{L}_{LR} + \lambda_{distr}\mathcal{L}_{distr} \tag{13}$$

其中，λ_{HR}，λ_{LR}和λ_{distr}为相应的权重。

4 实验

4.1 实验设置

数据集：为了验证所提出的重采样方法与压缩框架的有效性，我们使用了带历史参考图像的自建遥感数据集。我们从 SPOT-5 卫星上收集了各个城市的遥感影像，它们的原始分辨率范围从 1878×1400 到 6264×3456。为了构建训练集，我们将它们裁剪成 512×512 大小的无重叠的小块，得到 6690 个带参考的图像对。我们使用 58 张图像构建测试集，其中每张图像都有 5 张在不同时间拍摄的历史图像作为参考图像。

对比方法：在重采样方面，我们对比了三种图像重采样方法：1）双三次降采样与 SR 方法，包括六种 SISR 方法（双三次上采样，EDSR[41]，RCAN[6]，NLSN[42]，LDL[43]，LTE[44]），以及两种 RefSR 方法（TTSR[17]，C^2 Matching[45]）；2）联合优化的重采样方法（TAD&TAU[7]）；3）基于 INN 的重采样方法（IRN[14]，HCFlow[13]）。其次，在压缩方面，我们对比了在传统的图像压缩方法 JPEG 上使用不同重采样方法的差异。

评价指标：在重采样方面，我们采用 PSNR 和 SSIM 来衡量图像重建质量。我们还采用空间信息（Spacial Information，SI）[46]作为度量 LR 图像的图像复杂性的指标。SI 已被证明与基于 JPEG 的图像复杂度度量

呈正相关，具体可以通过下式进行计算：

$$SI = \sqrt{s_h^2 + s_v^2} \tag{14}$$

其中，s_h和s_v分别表示用水平和垂直两个方向的 Sobel 算子滤波后的Y通道数据。此外，我们使用 JPEG 算法来压缩 LR 图像，并将其像素深度（bits per pixel，bpp）作为 SI 的辅助度量。在压缩方面，我们使用率失真（rate-distortion，R-D）曲线来衡量压缩效率。

类别	方法	2 倍				4 倍			
		PSNR ↑	SSIM ↑	SI ↓	bpp ↓	PSNR ↑	SSIM ↑	SI ↓	bpp ↓
双三次降采样与 SISR	Bicubic & Bicubic	28.82	0.878	0.454	2.55	23.21	0.658	0.561	3.12
	Bicubic & EDSR	30.9	0.903	0.454	2.55	25.04	0.727	0.561	3.12
	Bicubic & RCAN	32.48	0.908	0.454	2.55	26.41	0.719	0.561	3.12
	Bicubic & NLSN	31.07	0.906	0.454	2.55	25.17	0.722	0.561	3.12
	Bicubic & LDL	31.77	0.872	0.454	2.55	26.24	0.694	0.561	3.12
	Bicubic & LTE	31.18	0.908	0.454	2.55	26.54	0.719	0.561	3.12
双三次降采样与 RefSR	Bicubic & TTSR	–	–	–	–	26.74	0.737	0.561	3.12
	Bicubic & C^2 Matching	–	–	–	–	27.62	0.773	0.561	3.12
联合优化	TAD & TAU	31.62	0.897	0.442	2.46	26.13	0.709	0.557	3.10
可逆神经网络	IRN	38.22	0.983	0.487	2.59	30.66	0.876	0.569	3.13
	HCFlow	–	–	–	–	30.92	0.881	0.573	3.14
历史参考	**Ours**	**43.3**	**0.994**	**0.358**	**2.03**	**31.31**	**0.879**	**0.451**	**2.37**

表 1　在遥感数据集上不同重采样方法的定量对比

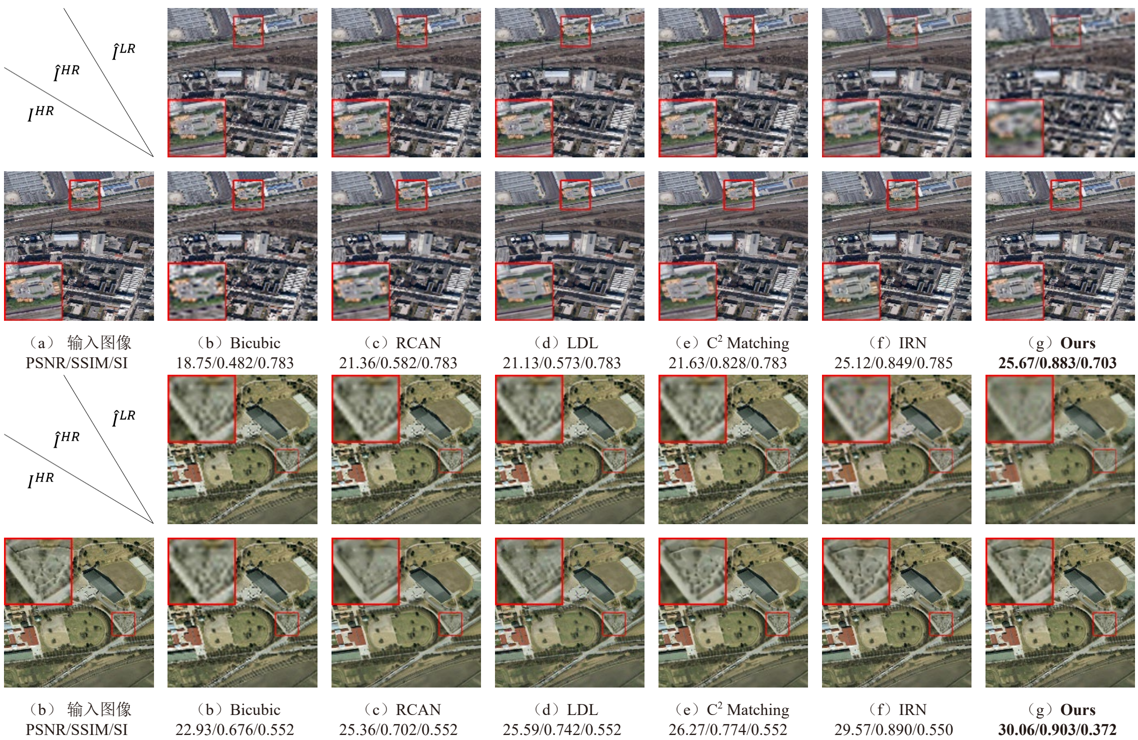

图 5　在遥感数据集上不同重采样方法的定性对比

4.2　实验结果

定量结果：为了确保公平的比较，我们对遥感数据集上的所有对比方法进行了微调。重采样性能对比的结果如表 1 所示，我们的方法具有优异的性能，具体表现为更高的 PSNR 和 SSIM 和更低的 SI 与 bpp。尽管使用联合优化和基于 INN 的重采样方法得到的图像质量优于一般的 SR 方法，但这也会导致 RS 数据集上 SI 的增加。相比之下，我们的方法可以更好地恢复图像细节，生成更平滑的 LR 图像并且显著降低 SI，

有利于存储和传输。

压缩框架整体的性能比较如图 6 所示，我们对比了原生的 JPEG 压缩算法和不同重采样框架下的 JPEG 算法。从图中可以看到，重采样框架下的 JPEG 算法在低码率的情况下取得了较原生 JPEG 算法更高的重建质量，这得益于重采样方法对低频信息的显式去除，而我们的方法进一步地去除了与参考图像间的信息冗余，因此我们的方法表现最佳。

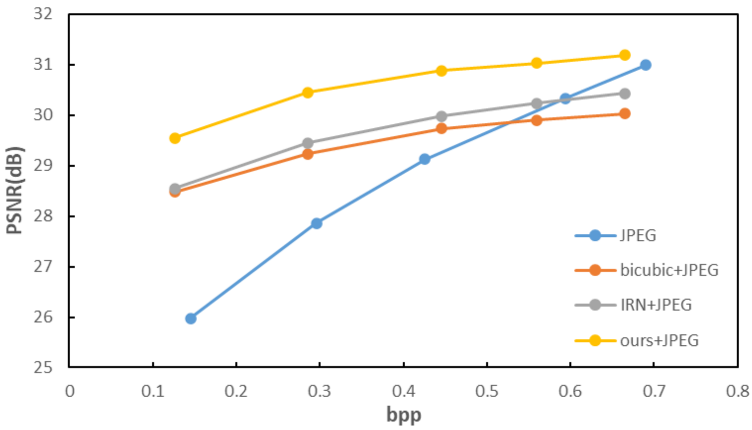

图 6　在 JPEG 上不同重采样方法的压缩性能对比

定性结果：为了展示降采样图像和重建 HR 图像的视觉对比，我们将遥感数据集中的样本在 4 倍的重采样尺度进行了可视化。如图 3 所示，我们的方法生成了更清晰、更真实的 HR 图像。这些 HR 图像与通过对比方法重建的 HR 图像相比包含更多细节，更加接近真值。这样的结果得益于参考图像提供了丰富的辅助信息。此外，我们的模型利用参考图像来指导降采样过程丢弃互信息，这使得降采样图像比其他方法更平滑，包含更少的细节信息。

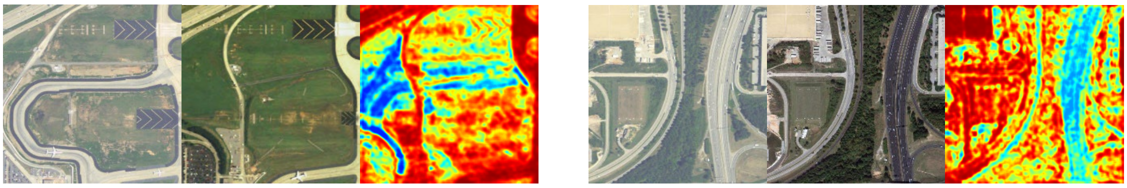

图 7 相似性矩阵的可视化

4.3　消融实验

相似性矩阵的可视化：为了展示 Ref-Net 如何获取相似度矩阵，我们在图 4 中给出了相似度的可视化表示。该图表明我们的方法可以从与 HR 图像具有相似纹理或结构的参考图像中捕获相似的信息。图 4 中的暖色区域表明参考图像和 HR 图像之间存在丰富的相似性。可以看出，本文提出的方法可以有效地检测不同相似度的区域，例如新建的机场跑道。在这种情况下，我们的方法可以保留 LR 图像中的特征信息以便更好地恢复原始图像。

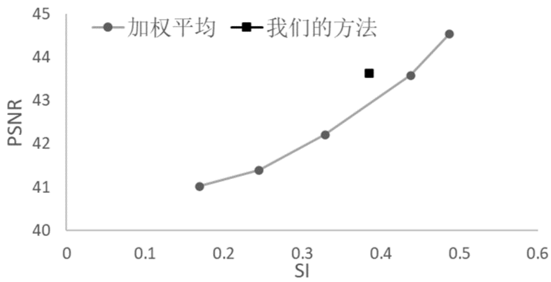

图 8　所提出的 LR 损失与加权方案的对比

LR 损失函数分析：为了评估基于相似度矩阵的 LR 损失函数的有效性，我们使用不同类型的降采样图像约束 LR 进行了对比实验，该降采样图像由双三次降采样图像和高斯模糊降采样图像加权平均生成，即：

$$\tilde{I}^{LR} = \omega \times I_{\mathrm{bic}}^{LR} + (1-\omega) \times I_{\mathrm{blur}}^{LR}, (\omega = 0,0.25,0.5,0.75,1) \tag{16}$$

结果如图 5 所示，基于相似度矩阵的结果在曲线的左上角，表明我们的方案可以同时达到更高的 PSNR 和更低的 SI。

5　结论

在本文中，我们提出了一种基于参考图像的重采样方法用于基于重采样方法的压缩框架中，生成较低信息量的降采样图像和高视觉质量的重建图像。它包含一个参考网络，利用待传输图像和参考图像之间的相关性来生成相似度矩阵并生成参考条件，该参考条件指导降采样图像的生成。我们还提出了一种将互信息映射至潜变量的条件可逆神经网络，同时保留参考条件下降采样图像中的独特信息。实验表明，我们的方法在图像重建质量和数据量方面都优于目前最先进的方法，在遥感周期观测的场景下具有潜在应用价值。

融合红外卫星云图和再分析数据的热带气旋风半径估计

金永军[1]，任开军[2]，刘佳[1,*]，汪祥[2]，邓科峰[2]，邓重九[1]

1 中国地质大学（武汉）计算机学院，湖北 武汉，430000

2 国防科技大学气象海洋学院，湖南 长沙，410073

摘　要：作为一种复杂的天气系统，热带气旋受多方面因素影响，单一卫星云图难以全面刻画风结构特征。针对此问题，本文提出一种融合红外卫星云图和再分析数据的热带气旋风半径估计方法。首先，基于并行的双分支特征提取网络分别提取红外云图和再分析数据的高层语义特征；然后，设计一种基于注意力机制的多源数据特征融合模块，实现红外云图和再分析数据的特征级融合；另外，融入最大持续风速作为辅助物理信息，进一步约束解空间；最后，通过回归网络得到风半径估计值。实验验证了该方法在全球范围和热带气旋高发区域北大西洋的性能。结果表明，相比现有方法，本文方法具有优越的风半径估计能力，且再分析数据、辅助最大持续风速信息的融合策略，以及设计的融合模块均有效提升了模型性能。

关键词：卫星云图，再分析数据，热带气旋，风半径估计，多源数据融合，注意力机制

Estimation of Tropical Cyclone Wind Radii by Fusion of Infrared Satellite Cloud Image and Reanalysis Data

Yongjun Jin[1]，Kaijun Ren[2]，Jia Liu[1,*]，Xiang Wang[2]，Kefeng Deng[2]，Chongjiu Deng[1]

1 School of Computer Science, China University of Geosciences, Wuhan 430074, China

2 College of Meteorology and Oceanography, National University of Defense Technology, Changsha 410073, China

Abstract: As a complex weather system, tropical cyclones are affected by many factors, and it is difficult to fully depict wind structures with satellite cloud images. To address this issue, a tropical cyclone wind radii estimation method that combines infrared satellite cloud images and reanalysis data has been proposed in this paper. First, the high-level semantic features of infrared cloud images and reanalysis data are extracted through a dual-branch feature extraction network, and then fed into a designed multi-source data feature fusion module based on the attention mechanism. In addition, the implicit relationship between auxiliary physical information maximum sustained surface wind and wind radii is embedded into the network to further reduce the solution space. Finally, the wind radii estimate is obtained through the regression network. The performance of this method was validated on a global scale and in the North Atlantic region through experiments, and compared with existing methods. The results indicate that the proposed method exhibits high performance.

Key words: satellite cloud image, reanalysis data, tropical cyclone, wind radii estimation, multi-source data fusion, attention mechanism

1　引言

TC（Tropical Cyclone，热带气旋）是一种强大且深厚的热带天气系统，起源于热带及亚热带洋面[1]。TC 往往伴随着暴雨、大风、风暴潮等极端天气灾害，对沿海地区人民生命财产安全造成巨大威胁。我国是世界上受 TC 影响最严重的国家之一。风半径主要用于提供 TC 风结构特征的定量估计[2]，能够反映 TC 的影响范围[3]，是多种数值预报模型的初始化条件[4]，准确的 TC 表面风结构有助于改善 TC 强度和轨迹预报的性能[5]。常用的风半径参数包括：R34（Radius of Gale Wind，大风风半径）、R50（Radius of Destructive Wind，破坏力风半径）、R64（Radius of Hurricane Wind，飓风风半径）和 RMW（Radius of Maximum Wind，最大风速半径）等[6, 7]。本文关注最广泛使用的风半径参数 R34 和 RMW。其中，R34 反映 TC 的潜在影响范围，常用于表示 TC 尺寸，RMW 反映 TC 的内核结构[8]。

地面站、船只、浮标等实地观测手段能够提供最准确的数据，但 TC 起源于海洋深处，这些实地观测手段通常不可用。飞机侦察能够提供低层风场或表面风场的详细描绘，但成本高昂，通常只在 NA（North Atlantic，北大西洋）区域可用[2]。因此，风半径估计严重依赖卫星遥感数据。星载测风仪器能够直接获得 TC 风场结构（如微波散射计、SAR（Synthetic Aperture Radar，合成孔径雷达）等），但这些仪器通常搭载在极轨卫星上，重访周期长，且观测条带可能无法完整覆盖 TC[9]。相比而言，星载红外仪器通常搭载在静止卫星上，重访周期短（我国的 FY-4 能够每 15min 提供一次观测数据），观测区域广，大部分情况下能够完整覆盖 TC。并且，与可见光云图相比，红外谱段不受昼夜交替的影响，能够全天候、全天时的提供观测数据[10, 11]，适用场景更广。

风半径估计的传统方法可以分为两类，风场分析法和统计学方法。风场分析法是从表面风产品中按一定规则提取风半径的方法，表面风产品包括散射计产品、辐射计产品、合成孔径雷达产品和红外云导风产品等[6, 12-15]。统计学方法是从数据中提取特征，并利用传统统计学方法建立特征与风半径之间关系方程的一类方法，采用 PCA（Principal Component Analysis，主成分分析）等经典方法提取特征，利用多元线性回归等统计方法建立回归方程[16-18]。

传统方法的特征提取能力有限且实现繁琐，深度学习能够自动地从海量数据中提取特征，在计算机视觉、自然语言处理等领域中表现出了强大的能力。目前，深度学习已经被应用到风半径估计中。例如，Zhuo 等人[19]在 VGG 的基础上设计了一个多任务风半径估计模型，模型性能优于 MTCSWA（Multiplatform Tropical Cyclone Surface Wind Analysis，多平台热带气旋表面风分析）[20]。Chen 等人[21]利用深度学习模型生成风廓线曲线，进而从风廓线曲线中提取风半径、强度等。Wang 等[22]在 VGG 的基础上设计了一个非对称风半径估计模型，他们将方位角象限的图像切片放入一个分支网络，以引导模型注意正确的区域。Tian 等人[21]也设计了一个多任务模型，使用 IR（Infrared Radiation，红外）、WV（Water Vapor，水汽）和 PMW（Passive Micro-wave Rainrate，被动微波降雨量）作为输入数据，采用双注意力机制整合不同波段数据特征。Yuan 等人[9]根据 TC 的旋转不变性质，引入群等变卷积，并添加 SHIPS（Statistical Hurricane Intensity

Prediction Scheme）预测因子提供额外信息。

TC 是一种复杂的系统，受到多方面因素影响，单一的卫星云图数据难以全面刻画 TC。再分析数据集是利用物理定律将模型数据与来自世界各地的观测数据结合形成的全球完整且一致的数据集[23]，具有时空连续性。已有研究尝试从再分析风场按照一定规则直接提取风半径（例如：Bian 等[24]、Schenke 等[25]、Gori 等[26]），但是受限于再分析场粗糙的网格分辨率和保守的物理参数化方案，这些工作关注于外层风半径（R2-12，方位角平均风速等于 2-12m/s 的半径），且误差较高。融合再分析资料与红外云图多源数据，能够提供额外的信息和约束，有助于提高风半径估计模型性能。此外，有多种物理参数用于描绘 TC，在深度学习模型中嵌入这些参数与风半径的隐含关系，也将进一步约束解空间。

在上述背景下，本文开展融合红外卫星云图和再分析数据的热带气旋风半径估计方法研究，主要贡献包括：首先，提出了一个融合红外卫星云图、再分析数据和辅助物理信息 MSW（Maximum Sustained Wind Speed，最大持续风速）的热带气旋风半径估计网络；其次，为加强所提网络中多源数据特征交互，以提升风半径估计性能，设计了一个基于注意力机制的多源数据特征融合模块；最后，通过详实的实验和分析表明了本文提出的热带气旋风半径估计网络框架、多源数据利用及特征融合模块的有效性。

2 研究方法

2.1 融合红外卫星云图和再分析数据的风半径估计网络概述

本文风半径估计模型整体结构如图 1 所示，主要包括多源数据特征提取子网络、基于注意力机制的多源数据融合模块，以及风半径回归子网络。首先，基于并行的两个特征提取分支，分别输入红外云图和再分析数据，提取高层语义特征；然后，利用设计的基于注意力机制的融合模块，实现卫星云图和再分析数据的特征级融合，并与辅助物理信息（MSW）拼接；最后，通过 MLP（Multilayer Perceptron，多层感知机）得到风半径估计值。后续章节将具体介绍网络模型的每一部分。

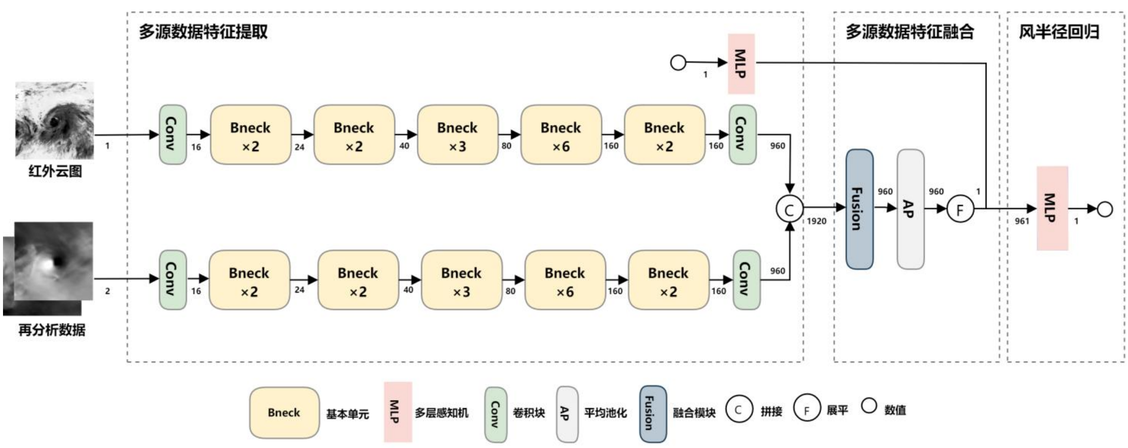

图 1 风半径估计模型总体结构示意图

2.2 多源数据特征提取

本文综合考虑精度和效率性能，采用经典轻量化 CNN 模型 MobileNetV3[27]作为特征提取主干网络。

MobileNetV3 是 Google 在 2019 年提出的一个轻量化 CNN 模型，特征提取部分由多个 Bneck 块堆叠而成。每个 Bneck 块由深度可分离卷积、SE 注意力机制和残差连接组成，如图 2 所示。特征图进入 Bneck 块后首先通过 1×1 卷积扩展通道，然后通过深度可分离卷积提取特征，最后设置了一个残差连接。深度可分离卷积是 MobileNetV3 实现轻量化的关键，其将标准卷积拆分为逐通道卷积和逐点卷积（等价于 1×1 卷积），有效地降低了参数量和计算量。MobileNetV3 在逐通道卷积和逐点卷积之间加入了一个 SE 注意力机制，在保持轻量级性能的同时，增强模型表达能力。

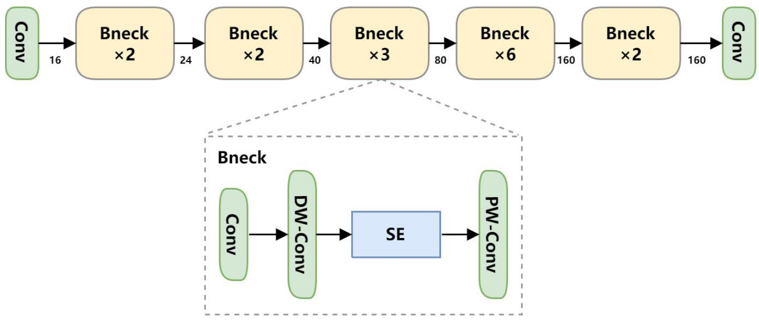

图 2 MobilNetv3 特征提取主干网络结构示意图

本文使用 ERA5[23]再分析资料中的 10m 海面风场（10m-wind）作为辅助数据。相比上一代再分析资料，ERA5 在模式物理、核心动力学和数据同化技术等方面进行改进，并显著提升了空间分辨率（79km-31km）。已有研究证明 ERA5 再分析风场在描绘 TC 外层风场结构方面的有效性[24, 25]。10m-wind 以东向分量（U）和北向分量（V）的形式给出（U、V 与风速和风向的关系如下所示）。式中，W 为风速，θ 为风向。

$$\begin{aligned} U &= W\cos\theta \\ V &= W\sin\theta \end{aligned} \quad (1)$$

ERA5 再分析数据以常规经纬度网格形式存储，形式上与图像相似。并且，在数据预处理阶段已经将空间分辨率通过插值与红外云图对齐。因此，再分析资料特征提取分支与卫星云图特征提取分支网络结构相同。由于再分析风场以 U、V 分量形式给出，该分支第一层卷积输入通道更改为 2。

已有研究表明，TC 强度与 R34 和具有较强的线性相关度[28-31]。MSW 是常用于表示 TC 强度的参数，该参数的定义为 TC 底层中心附近最大平均风速（平均风速指在给定的某一时段内风速的平均值[32]）。需要注意的是，不同机构的风速平均周期不完全相同。例如，中国机构为 2 分钟，而美国机构为 1 分钟。因此，本文将 MSW 也作为辅助信息输入风半径估计网络。MSW 是单独的数值，本文采用三层 MLP 对其进行非线性变换以提取特征。

2.3 基于注意力机制的多源数据特征融合模块

为进一步加强多源数据特征交互，提高风半径估计模型的性能，本文设计了一个基于注意力机制的多源数据特征融合模块。该模块的总体结构如图 3 所示，主要由两部分构成，特征过滤模块和跨模态特征交互模块。首先通过特征过滤模块过滤多源数据特征，去除冗余信息，减少噪声干扰，然后通过跨模态特征交互模块捕捉多源数据特征之间的相关关系，深度融合多源数据特征。

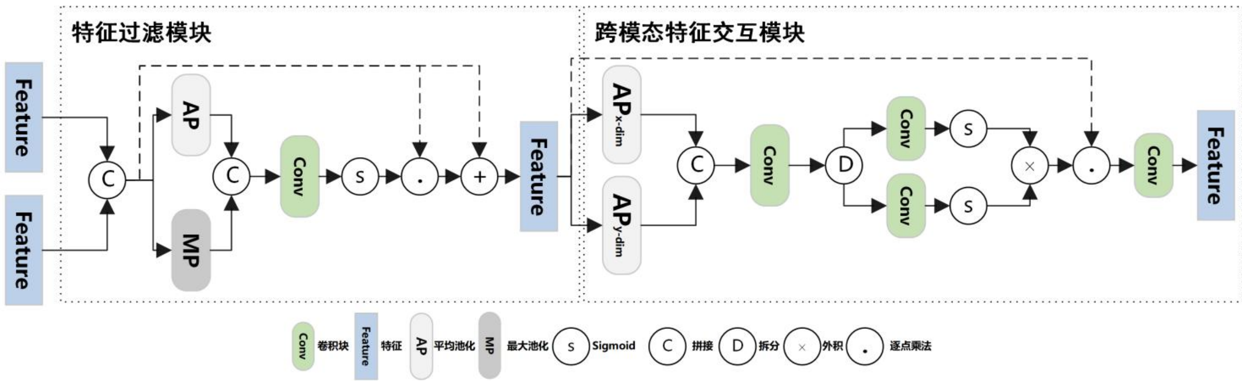

图 3 多源数据特征融合模块示意图

特征过滤模块的作用是过滤模态冗余特征。本文采用了一个空间注意力机制。设 $X_{IR} \in R^{C\times H\times W}$，$X_{SW} \in R^{C\times H\times W}$ 分别为红外云图和再分析资料特征提取分支输出的特征矩阵。首先，将 X_{IR} 和 X_{SW} 在通道维度上拼接，得到 $X_C \in R^{2C\times H\times W}$。随后，分别计算最大值矩阵 $X_{\max} \in R^{1\times H\times W}$ 和平均值矩阵 $X_{\text{avg}} \in R^{1\times H\times W}$，将 $X_{\max}$ 和 X_{avg} 在通道维度上拼接，通过一个 1×1 卷积压缩通道，经过 Sigmoid 得到权重矩阵 $W_{Filter} \in R^{1\times H\times W}$。最后，将 W_{Filter} 和 X_c 逐点相乘。另外，为降低原始信息损失，设置了一个残差连接。

跨模态特征交互模块的作用是进行跨模态的信息交互，捕捉模态间的相关关系。本文采用了一种新颖的通道注意力机制 CoordAttention[33]。设 $X_{Filter} \in R^{2C\times H\times W}$ 为特征过滤模块的输出。首先，在 x 轴方向和 y 轴方向通过平均池化聚合信息，获得两个特征向量 $X_{x-\dim} \in R^{2C\times H}$ 和 $X_{y-\dim} \in R^{2C\times W}$，以嵌入坐标信息。将 $X_{x-\dim}$ 和 $X_{y-\dim}$ 在空间维度拼接，通过一个 1×1 卷积压缩通道，再在空间维度上拆分为两个压缩后的特征向量，通过两个 1×1 卷积还原通道，这一步骤使模型进行了跨模态信息交互，捕获了模态间的相关关系。通过 Sigmoid 得到两个权重向量 $W_{x-\dim} \in R^{2C\times H\times 1}$ 和 $W_{y-\dim} \in R^{2C\times 1\times W}$，将 $W_{x-\dim}$ 与 $W_{y-\dim}$ 相乘，得到权重矩阵 $W_{cross} \in R^{2C\times H\times W}$。将 W_{cross} 与 X_{Filter} 逐点相乘，嵌入跨模态信息。最后，通过一个 1×1 卷积压缩通道，得到融合特征 $Y_{fusion} \in R^{C\times H\times W}$。

2.4 损失函数

回归任务中，使用最广泛的损失函数是 MSE（Mean Square Error，均方误差）和 MAE（Mean Absolute Error，平均绝对误差）。HuberLoss 结合了 MSE 和 MAE 的优点。相比于 MSE，HuberLoss 对异常值具有更强的鲁棒性；相比于 MAE，HuberLoss 具有更快的下降速率。HuberLoss 的计算公式如下所示。式中，$\hat{y}$ 为模型估计值，y 为真实值，δ是一个常数。

$$HurberLoss(\hat{y}, y) = \begin{cases} \frac{1}{2}(\hat{y} - y)^2, if\ |\hat{y} - y| < \delta \\ \delta(|\hat{y} - y| - 0.5\delta), otherwise \end{cases} \tag{2}$$

3 实验与分析

3.1 实验数据

本文使用的红外云图来自 HURSAT-B1[34]数据集。HURSAT-B1 包含 1979-2016 年间约 380000 张全球 TC 图像，图像尺寸为 301×301，空间分辨率约为 0.7°，时间分辨率为 3 小时。这些图像由 FY-2、GOES、Meteosat、GMS 等静止气象卫星拍摄。光谱覆盖范围包括可见光（约 0.6μm）、红外窗口（约 11μm）、水汽（约 6.7μm）、近红外（约 3.9μm）和红外分窗（约 12μm）。本文使用 2001-2016 年的红外窗口波段图像。

本文使用的再分析数据来自 ERA5[23]数据集。ERA5 是 ECMWF 发布的第五代全球气候和天气再分析数据集。ERA5 自 1940 年以来长期可用，空间分辨率为 0.25°，时间分辨率为 1 小时。本文中，为与红外云图数据对齐，使用了 2001-2016 年以 3 小时为间隔采样的再分析资料。

本文使用的风半径标签和辅助物理信息来自 IBTrACS[35]（International Best Track Archive for Climate Stewardship，国际最佳气候管理档案）。IBTrACS 聚合了全球多个机构提供的 TC 最佳轨迹记录，原始时间分辨率为 6 小时，通过插值获得了 3 小时分辨率。

3.2 数据预处理

气象数据具有自回归的特点，为避免数据泄露的发生，本文将 2001 年-2016 年的 TC 数据按时间划为两部分，数据集的详细信息如表 1 所示。其中，2001-2014 年的数据用于训练，2015-2016 年的数据用于测试。另外，根据 Zhuo 等人[19]的做法，本文仅考虑生命周期最大强度至少为 34kt 的 TC，样本中的温带系统和热带波被移除，防止造成干扰。

表 1 数据集划分详细情况

标签	训练集（2001-2014）	测试集（2015-2016）
R34	63114	8206
RMW	56592	8206

数据增强能够有效提升样本量，提高模型泛化能力。TC 具有旋转不变性，因此，本文采用了在线随机旋转数据增强，旋转角度在 0-270°中随机选取。

从 HURSAT-B1 中获取的红外图像中，部分样本存在缺失条带，本文采用双三次插值对缺失条带进行插补。为提高模型训练速度和稳定性，对输入数据进行 Z-Score 标准化处理，计算公式如下所示。式中，x 为原始数据，μ为平均值，σ为标准差。

$$x_{norm} = \frac{x - \mu}{\sigma} \tag{3}$$

IBTrACS 中提供的 R34 记录以四象限给出，本文将其进行非零方位角平均，作为风半径标签。以 R34 记录为基准，RMW 记录有一定缺失，本文将缺失值置为 0。

3.3 实验设置与评价指标

本文实验硬件环境为高性能服务器，CPU 为 Intel Xeon E5-2680 v4，内存 64G，配备 NVIDIA RTX 3090 GPU。软件环境为 Ubuntu 20.04，安装 CUDA 11.7、Python 3.7.1、Pytorch 1.13.1，使用优化器 Adam。

本文采用 R（Pearson correlation coefficient，皮尔逊相关系数）、RMSE（Root Mean Squared Error，均方根误差）和 MAE 评估模型性能。R 用于衡量模型估计值与真实值之间的线性关系程度，RMSE 用于衡量模型估计值与真实值之间的标准偏差，MAE 用于衡量模型估计值与真实值值之间的绝对误差。R、RMSE 和 MAE 的计算公式分别如式（4）-（6）所示。其中，$\hat{y}$ 为模型估计值，y 为真实值，$\bar{\hat{y}}$ 和 $\bar{y}$ 分别为模型估计值和真实值的平均值，N 为样本数量。

$$R = \frac{\sum_{i=1}^{N}(y_i - \bar{y}_i)(\hat{y}_i - \bar{\hat{y}}_i)}{\sqrt{\sum_{i}^{N}(y - \bar{y}_i)^2}\sqrt{\sum_{i}^{N}(\hat{y} - \bar{\hat{y}}_i)^2}} \tag{4}$$

$$RMSE = \sqrt{\frac{1}{N}\sum_{i=1}^{N}(\hat{y}_i - y_i)^2} \tag{5}$$

$$MAE = \frac{1}{N}\sum_{i=1}^{N}|\hat{y}_i - y_i| \tag{6}$$

3.4 实验结果与分析

3.4.1 风半径估计性能与分析

本文提出的风半径估计模型记为 MS-TCNet。图 3 给出了 MS-TCNet 的估计值与最佳轨迹数据的散点图，以直观展示 MS-TCNet 在全球 TC 样本上的性能。其中，横轴为 MS-TCNet 估计值，纵轴为真值（最佳轨迹数据）。图 4 左侧展示 MS-TCNet 对参数 R34 估计的性能，右侧展示 MS-TCNet 对参数 RMW 估计的性能。可以看到，在 R34 估计中，估计值与真实值具有很高的线性相关程度，仅存在少量离群点，R 为 0.844。在 RMW 估计中，RMW 值较小时散点聚集在轴线周围，RMW 值较大时模型呈现出明显的低估趋势，估计值与真实值之间的线性相关程度相对较低，R 为 0.738。

这一现象的出现与不平衡的数据分布有关，风半径数据呈现典型的长尾分布。另外，研究表明最佳轨迹风半径误差可高达 25%-40%，这取决于可用观测的质量和数量[8, 19]。并且，最佳轨迹数据中 RMW 记录和早期 R34 记录没有经过仔细的季后再分析，质量有待仔细检查，这可能也是引起上述现象的原因。此外，需要注意的是，图 4 中存在一个真实值对应多个估计值的情况。这是由于 TC 可能受多个卫星同时观测，观测角度的差异导致云图有一定差异，进一步导致模型给出不同估计值。

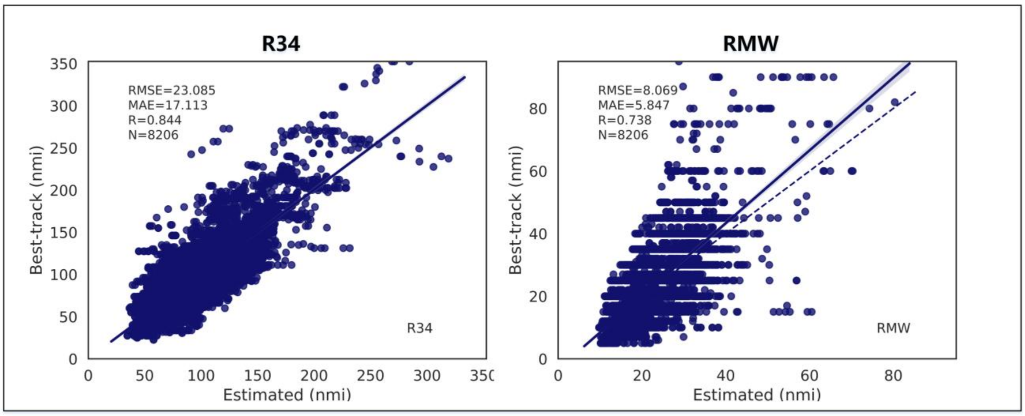

图 4 MS-TCNet 在全球 TC 样本上的性能表现（散点图）

北大西洋（NA）区域是 TC 高发区域，且具有飞机侦察任务，相比全球其他地区，NA 区域的最佳轨迹数据具有更高质量。因此，本文在 NA 区域评估了所提出的 MS-TCNet，散点图如图 5 所示。可以看到，在 NA 区域，MS-TCNet 具有更高的性能。在 R34 估计中，除少数离群点外 MS-TCNet 拟合很好，R 值为 0.936。在 RMW 估计中，MS-TCNet 估计值与真值的相关性比全球范围更好，R 值为 0.812，但 RMSE 和 MAE 相比全球更高，分别为 9.753nmi（海里）和 6.503nmi。可以看到，NA 区域 MS-TCNet 对 RMW 的低估同样显著。

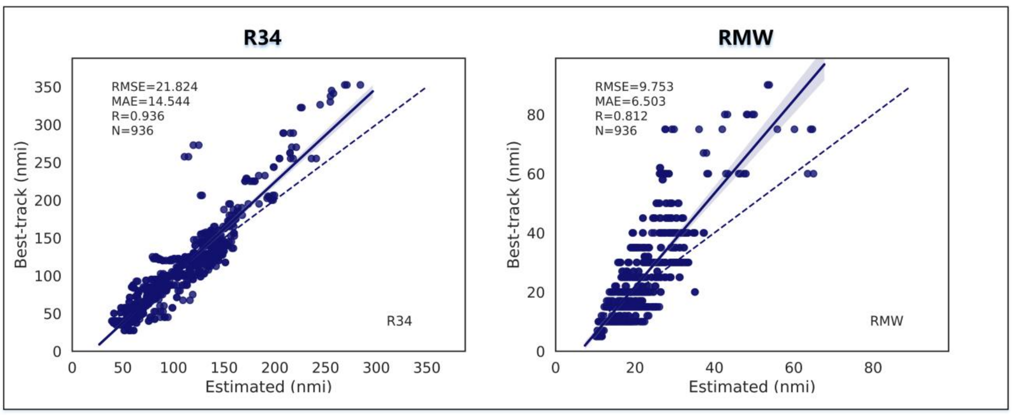

图 5 MS-TCNet 在 NA 区域 TC 样本上的性能表现（散点图）

为评估所提风半径估计方法的有效性，本文将 MS-TCNet 与现有方法进行对比，对比结果如表 2 所示。值得注意的是，各项研究工作的研究区域和时间范围均有所不同，难以进行完全一致的对比。WP（Northwest Pacific，西北太平洋）、EP（Northeast Pacific，东北太平洋）和 AL（Atlantic Ocean，大西洋）覆盖全球大部分海洋，故本文将研究区域为 WP、EP 和 AL 的方法与研究区域为全球的方法进行对比。表 2 中，Dolling 等[36]、Kossin 等[16]和 Knaff 等[20]为传统方法，其他均为深度学习方法。可以看到，传统方法与深度学习方法性能有较大差距。在全球范围，Chen 等[21]在深度学习方法中性能最低，但仍显著优于传统方法[18]（R34 估计 MAE 分别为 27.31nmi 和 36.5nmi）。本文方法在 R34 估计中，RMSE 略弱于 Tian 等[3]（分别为 23.08nmi 和 23.01nmi），而 MAE 显著更优（分别为 17.11nmi 和 21.84nmi）；在 RMW 估计中最优（MAE 为 5.85nmi）。在 NA 区域中，本文方法在 R34 估计中，RMSE 与 Zhuo 等[19]基本持平（分别为 21.82nmi 和 21.80nmi），

而 MAE 显著更优（分别为 14.55nmi 和 17.00nmi），且相关性更好（R 分别为 0.93 和 0.87）；在 RMW 估计中，本文方法 RMSE 和 MAE 均优于 Zhuo 等[19]（RMSE 分别为 9.75nmi 和 11.35nmi，MAE 分别为 6.50nmi 和 7.55nmi），但相关性稍弱（R 分别为 0.81 和 0.83）。总的来看，本文方法适用的研究区域最广，且具有优越的性能。

表 2 本文所提 MS-TCNet 与现有方法的对比

区域	方法	数据	RMSE（nmi）		MAE（nmi）		R	
			R34	RMW	R34	RMW	R34	RMW
NA	Baseline	IR	29.82	11.84	21.60	8.20	0.84	0.60
NA	Dolling 等[36]	IR	25.49	-	20.79	-	0.85	-
NA	Kossin 等[16]	IR	-	-	24.19	11.39	0.73	0.58
NA	Zhuo 等[19]	IR	**21.80**	11.35	17.00	7.55	0.87	**0.83**
NA	**MS-TCNet（ours）**	**IR 10m-wind**	21.82	**9.75**	**14.55**	**6.50**	**0.93**	0.81
GLOBAL	Baseline	IR	26.311	9.546	19.204	7.052	0.800	0.605
GLOBAL	Knaff 等[20]	IR AMSU Scatter	-	-	36.50	-	0.57	-
WP EP AL	Meng 等[37]	IR	36.49	-	24.4	-	-	-
WP EP AL	Chen 等[21]	IR PMW	37.62	-	27.31	-	-	-
WP EP AL	Tian 等[3]	IR PMW WV	**23.01**	-	20.89	-	-	-
GLOBAL	Yuan 等[38]	IR WV	-	-	21.54	6.37	-	-
GLOBAL	**MS-TCNet（ours）**	**IR 10m-wind**	23.08	**8.07**	**17.11**	**5.85**	**0.84**	**0.74**

此外，本文以 2016 年大西洋飓风季第十三场风暴 Matthew 为例，绘制风半径的标签和估计值，以直观展示 MS-TCNet 的性能，如图 6 所示。

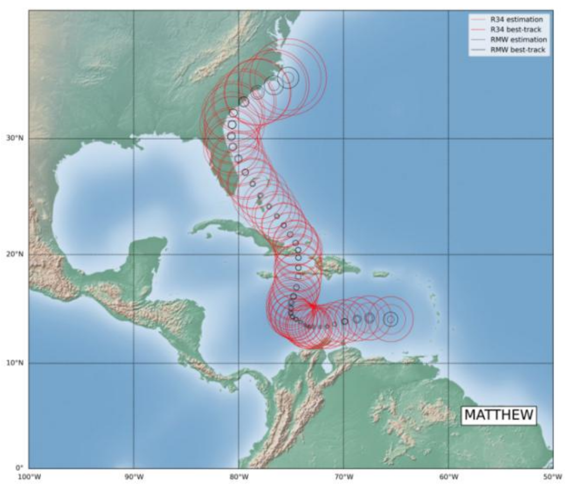

图 6 MS-TCNet 在 Matthew 上的性能表现

3.3.2 消融实验与分析

本节开展消融实验验证所提方法关键组成部分的有效性。基线模型是仅使用红外云图作为输入数据的 MobileNetV3。本文首先在基线模型的基础上，添加辅助信息 MSW，实验结果如表 3 表 3 所示。加入 MSW 后，在 R34 估计中，模型的 RMSE 为 25.153 nmi，MAE 为 18.871 nmi，R 为 0.813。相比于基线模型，RMSE 降低了 4.40%，MAE 降低了 1.73%，R 提升了 0.013。在 RMW 估计中，模型的 RMSE 为 8.439，MAE 为 6.099，R 值为 0.714。相比于基线模型，RMSE 降低了 11.59%，MAE 降低了 13.51%，R 提升了 0.109。可以看到，MSW 辅助信息大幅提升了风半径估计模型在 RMW 估计中的表现，并较好地提升了模型在 R34 估计中的表现。实验表明，MSW 与 RMW 具有更密切的关系。

表 3 加入辅助物理信息前后模型性能的对比

模型	RMSE（nmi）		MAE（nmi）		R	
	R34	RMW	R34	RMW	R34	RMW
Baseline	26.311	9.546	19.204	7.052	0.800	0.605
+MSW	**25.153**	**8.439**	**18.871**	**6.099**	**0.813**	**0.714**

在上述基础上，本文进一步融合再分析资料，采用简单拼接融合的方式，实验结果如表 4 表 4 所示。加入再分析资料后，在 R34 估计中，模型的 RMSE 为 23.952nmi，MAE 为 17.296nmi，R 为 0.813，相比于基线模型，RMSE 降低了 4.77%，MAE 降低了 8.35%，R 提升了 0.021。在 RMW 估计中，模型的 RMSE 为 8.278nmi，MAE 为 5.899nmi，R 为 0.717，相比于基线模型，RMSE 降低了 1.91%，MAE 稍有升高，但幅度较小，R 略有提升。RMSE 降低而 MAE 基本不变，说明模型估计值中异常值减少。可以看到，再分析资料有效地提升了模型在 R34 估计中的性能，在 RMW 估计中则提升幅度相对较小。这可能源于再分析资料粗糙的空间分辨率（0.25°）和保守的物理参数化方案使其难以很好地反映 TC 内核风场结构[26]。另外，本文将再分析风场和红外云图空间分辨率对齐时采用了双三次插值，这可能无法准确还原 TC 内核风场结构。

表 4 加入再分析资料前后模型性能的对比

模型	RMSE（nmi）		MAE（nmi）		R	
	R34	RMW	R34	RMW	R34	RMW
Baseline	25.153	8.439	18.871	**5.892**	0.813	0.714
+10m-wind	**23.952**	**8.278**	**17.296**	5.899	**0.834**	**0.717**

在前述加入多源数据的基础上，本文进一步验证所提融合模块的有效性，实验结果如表 5 表 5 所示。使用融合模块后，在 R34 估计中，模型的 RMSE 为 23.085nmi，MAE 为 17.113nmi，R 值为 0.844，相比于基线模型，RMSE 降低了 3.62%，MAE 降低了 1.06%，R 值提高了 0.01。在 RMW 估计中，模型的 RMSE 为 8.069nmi，MAE 为 5.850nmi，R 值为 0.738，相比于基线，RMSE 降低了 2.52%，MAE 基本不变，R 值

提高了 0.021。可以看到，融合模块进一步提升了风半径估计模型的性能。相比于简单拼接融合，本文提出的基于注意力机制的多源数据融合模块能够更好利用多源数据，捕捉多源数据之间的交互关系。

表 5 使用融合模块前后模型性能的对比

模型	RMSE（nmi）		MAE（nmi）		R	
	R34	RMW	R34	RMW	R34	RMW
Baseline	23.952	8.278	17.296	5.899	0.834	0.717
+Fusion Block	**23.085**	**8.069**	**17.113**	**5.850**	**0.844**	**0.738**

4 结束语

作为一种复杂的天气系统，TC 受到多方面因素影响，单一的卫星云图难以全面描绘。本文提出了一种融合红外云图和再分析资料的风半径估计方法。该方法通过并行的双分支特征提取网络分别提取红外云图和再分析数据特征，设计基于注意力机制的多源数据特征融合模块进行特征融合。为进一步缩小解空间，向模型中融入辅助物理信息 MSW。本文分别在全球范围和 TC 高发区域北大西洋评估了所提模型的性能，通过消融实验验证了再分析数据、辅助物理信息和融合模块的有效性。结果表明，相比现有方法，本文方法具有优秀的性能，且再分析数据、辅助物理信息和融合模块均有效提升了模型性能。

致谢

本文工作由国家自然科学基金 62372460、41901376 资助。

参考文献

[1] Tropical cyclone - Glossary of Meteorology[EB/OL]. [2023/9/5]. https://glossary.ametsoc.org/wiki/Tropical_cyclone.

[2] KNAFF J A, SLOCUM C J, MUSGRAVE K D, et al. Using Routinely Available Information to Estimate Tropical Cyclone Wind Structure[J]. Monthly Weather Review, 2016,144(4): 1233-1247.

[3] TIAN W, ZHOU X, NIU X, et al. A Lightweight Multitask Learning Model With Adaptive Loss Balance for Tropical Cyclone Intensity and Size Estimation[J]. IEEE Journal of Selected Topics in Applied Earth Observations and Remote Sensing, 2023,16: 1057-1071.

[4] BENDER M A, MARCHOK T P, SAMPSON C R, et al. Impact of Storm Size on Prediction of Storm Track and Intensity Using the 2016 Operational GFDL Hurricane Model[J]. Weather and Forecasting, 2017,32(4): 1491-1508.

[5] BENDER M A, MORIN M, MARCHOK T, et al. Upgrades to the GFDL/GFDN Operational Hurricane Models Planned for 2015, 2015.

[6] REUL N, CHAPRON B, ZABOLOTSKIKH E, et al. A New Generation of Tropical Cyclone Size Measurements from Space[J]. Bulletin of the American Meteorological Society, 2017,98(11): 2367-2385.

[7] P E REZ-ALARC O N A, SOR I R, FERN A NDEZ-ALVAREZ J E C, et al. Comparative climatology of outer tropical cyclone size using radial wind profiles[J]. Weather and Climate Extremes, 2021,33: 100366.

[8] KNAFF J A, SAMPSON C R. After a Decade Are Atlantic Tropical Cyclone Gale Force Wind Radii Forecasts Now Skillful?[J]. Weather and Forecasting, 2015,30(3): 702-709.

[9] YUAN S, YOU Q, MU B, et al. Estimating the tropical cyclone wind structure using physics-incorporated networks[J]. Frontiers in Earth Science, 2023,10.

[10] RAJAKUMAR C, SATHEESKUMARAN S. Singular value decomposition and saliency - map based image fusion for visible and infrared images[J]. International Journal of Image and Data Fusion, 2022,13(1): 21-43.

[11] FAN Q, HOU F, SHI F. A fusion method for infrared and visible images based on iterative guided filtering and two channel adaptive pulse coupled neural network[J]. International Journal of Image and Data Fusion, 2021,12(1): 23-47.

[12] SOISUVARN S, OUDOMYING S. Characterization of the Tropical Cyclones Wind Radii in the North Western Pacific Basin Using the ASCAT Winds Data Products[Z]. 20181428-1433.

[13] LIU S, LIN W, PORTABELLA M, et al. Characterization of Tropical Cyclone Intensity Using the HY-2B Scatterometer Wind Data[J]. Remote Sensing, 2022,14(4).

[14] COMBOT C, MOUCHE A, KNAFF J, et al. Extensive high-resolution synthetic aperture radar (SAR) data analysis of tropical cyclones: Comparisons with SFMR flights and best track[J]. Monthly Weather Review, 2020,148(11): 4545-4563.

[15] MUELLER K J, DEMARIA M, KNAFF J, et al. Objective estimation of tropical cyclone wind structure from infrared satellite data[J]. Weather and forecasting, 2006,21(6): 990-1005.

[16] KOSSIN J P, KNAFF J A, BERGER H I, et al. Estimating hurricane wind structure in the absence of aircraft reconnaissance[J]. Weather and Forecasting, 2007,22(1): 89-101.

[17] LU X, YU H, YANG X, et al. Estimating tropical cyclone size in the Northwestern Pacific from geostationary satellite infrared images[J]. Remote Sensing, 2017,9(7): 728.

[18] DEMUTH J L, DEMARIA M, KNAFF J A. Improvement of Advanced Microwave Sounding Unit tropical cyclone intensity and size estimation algorithms[J]. Journal of applied meteorology and climatology, 2006,45(11): 1573-1581.

[19] ZHUO J, TAN Z. Physics-Augmented Deep Learning to Improve Tropical Cyclone Intensity and Size Estimation from Satellite Imagery[J]. Monthly Weather Review, 2021,149(7): 2097-2113.

[20] KNAFF J A, DEMARIA M, MOLENAR D A, et al. An Automated, Objective, Multiple-Satellite-Platform Tropical Cyclone Surface Wind Analysis[J]. Journal of Applied Meteorology and Climatology, 2011,50(10): 2149-2166.

[21] CHEN B, CHEN B, HSIAO C M. CNN Profiler on Polar Coordinate Images for Tropical Cyclone Structure Analysis[J]. Proceedings of the AAAI Conference on Artificial Intelligence, 2021,35(2): 991-998.

[22] WANG C, LI X. A Deep Learning Model for Estimating Tropical Cyclone Wind Radius from Geostationary Satellite Infrared Imagery[J]. Monthly Weather Review, 2022.

[23] HERSBACH H, BELL B, BERRISFORD P, et al. ERA5 hourly data on single levels from 1979 to present[J]. Copernicus climate change service (c3s) climate data store (cds), 2018,10(10.24381).

[24] BIAN G, NIE G, QIU X. How well is outer tropical cyclone size represented in the ERA5 reanalysis dataset?[J]. Atmospheric Research, 2021,249: 105339.

[25] SCHENKEL B A, LIN N, CHAVAS D, et al. Evaluating Outer Tropical Cyclone Size in Reanalysis Datasets Using QuikSCAT Data[J]. Journal of Climate, 2017,30(21): 8745-8762.

[26] GORI A, LIN N, SCHENKEL B, et al. North Atlantic Tropical Cyclone Size and Storm Surge Reconstructions From 1950-Present[J]. Journal of Geophysical Research: Atmospheres, 2023,128(5): e2022J-e37312J.

[27] HOWARD A, SANDLER M, CHU G, et al. Searching for MobileNetV3, 2019.October.

[28] SHEA D J, GRAY W M. The Hurricane's Inner Core Region. I. Symmetric and Asymmetric Structure[J]. Journal of Atmospheric Sciences, 1973,30(8): 1544-1564.

[29] RUAN Z, WU Q. Relationship Between Size and Intensity in North Atlantic Tropical Cyclones With Steady Radii of Maximum Wind[J]. Geophysical Research Letters, 2022,49(3): e2021G-e95632G.

[30] QUIRING S, SCHUMACHER A, LABOSIER C, et al. Variations in mean annual tropical cyclone size in the Atlantic[J]. Journal of Geophysical Research: Atmospheres, 2011,116(D9).

[31] MUELLER K J, DEMARIA M, KNAFF J, et al. Objective Estimation of Tropical Cyclone Wind Structure from Infrared Satellite Data[J]. Weather and Forecasting, 2006,21(6): 990-1005.

[32] 中国气象局国家气象中心. GB/T 19201-2006 热带气旋等级[S]. 北京：中国标准出版社, 2006.

[33] HOU Q, ZHOU D, FENG J. Coordinate Attention for Efficient Mobile Network Design, 2021.

[34] KENNETH R K, JAMES P K. New global tropical cyclone data set from ISCCP B1 geostationary satellite observations[J]. Journal of Applied Remote Sensing, 2007,1(1): 13505.

[35] KNAPP K R, KRUK M C, LEVINSON D H, et al. The International Best Track Archive for Climate Stewardship (IBTrACS): Unifying Tropical Cyclone Data[J]. Bulletin of the American Meteorological Society, 2010,91(3): 363-376.

[36] DOLLING K, RITCHIE E A, TYO J S. The Use of the Deviation Angle Variance Technique on Geostationary Satellite Imagery to Estimate Tropical Cyclone Size Parameters[J]. Weather and Forecasting, 2016,31(5): 1625-1642.

[37] MENG F, XIE P, LI Y, et al. Tropical Cyclone Size Estimation Using Deep Convolutional Neural Network, 2021.

[38] YUAN S, YOU Q, MU B, et al. Estimating the tropical cyclone wind structure using physics-incorporated networks[J]. Frontiers in Earth Science, 2023,10.

[作者简介]

金永军（1999 年-），男，目前于中国地质大学（武汉）计算机学院攻读硕士学位，主要研究方向为多源数据融合、多任务学习，及其在台风监测中的应用。

任开军（1975 年-），男，博士，国防科技大学气象海洋学院研究员，主要研究方向为高性能计算、云计算、大数据，及其在气象海洋领域的应用。

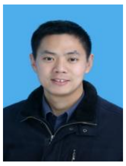

刘佳（1988 年-），女，博士，中国地质大学（武汉）计算机学院副教授，主要研究方向为高性能计算、边缘智能，及其在遥感图像解译、气象灾害监测中的应用。

汪祥（1989 年-），男，博士，国防科技大学气象海洋学院副研究员，主要研究方向为气象海洋智能分析预报。

邓科峰（1985 年-），男，博士，国防科技大学气象海洋学院副研究员，主要研究方向为大数据、机器学习，及其在气象海洋领域的应用。

邓重九（1999 年-），男，目前于中国地质大学（武汉）计算机学院攻读硕士学位，主要研究方向为基于深度学习的降雨临近预报。

空间信息网络中的时间基准同步技术

薛林山 [1]，康成斌 [1*]，邢雷 [2]，张建军 [1]

1. 中国空间技术研究院
2. 中国航天员中心

摘　要：随着星座系统规模逐渐增加，如何维持空间信息网络的各卫星时频基准的稳定，高效的传递通信导航数据是空间网络信息传输理论研究的重点。通过星间链路进行时间基准的同步是当前在 GNSS 系统重广泛使用的技术，但其基于时分体制的伪码测量精度为 ns 级别，无法满足未来逐步提升的时间同步需求。本文在传统的星间时间同步技术基础上，采用伪码辅助加双频时分的方式来解算载波的解算整周模糊度，将传统的星间链路时间同步中的受伪随机码速率限制的测量精度进行提升。最终在 40dB-Hz 的载噪比上，X 频段测距误差优于 1mm，Ka 频段测距误差优于 0.17mm。随着载噪比的提升，测量精度会进一步提升。

关键词：时间基准，卫星网络，时间同步

Abstract: As the scale of the constellation system gradually increases, maintaining the stability of the time and frequency reference for space navigation information networks and efficiently transmitting communication measurement data are key technology of space network information transmission. Synchronizing time references through inter-satellite links is a widely used technique in current GNSS systems. However, its pseudocode measurement accuracy, which based on a time-division scheme, is at the nanosecond level and cannot meet the increasing time synchronization demands in the future. This paper introduces a algorithm based on dual one way ranging and utilizes pseudocode-aided dual-frequency to resolve carrier phase ambiguities. Therefore, the method improves the measurement accuracy constrained by the pseudo-random code rate in traditional inter-satellite link time synchronization. Ultimately, with a carrier-to-noise ratio of 40 dB-Hz, the ranging error in the X-band is better than 1 mm, and in the Ka-band, the accuracy is better than 0.17 mm. With the carrier-to-noise ratio increases, measurement accuracy will further improve.

Key words: Time Reference，Satellite Network，Time Synchronization

1　引言

随着星座系统规模逐渐增加，如何在整个系统内部实现通信、测量信息的高效传输，是空间网络的信息传输理论研究的重点。对于未来的空间导航信息网络来说，卫星需要形成覆盖所有成员的全网通信体系，该体系需要满足全网实时共享需求。该网络由异步双工链路构成，在一定程度上支持多跳通信和路由业务，从而服务地面站信息的指令信息上注及遥测信息下传；并在整个网络中实现时间基准的同步，将整网的时间基准同步至单个卫星。

因此，星间通信测量信息的交互是空间网络信息传输的重点，该项需求导致了星间链路（Inter-satellite link）技术在空间网络中的大规模使用。星间链路技术指通过卫星与卫星之间建立通信、测量链路，有效扩大地面站的测控通信范围[1-2]。一方面，通过星间链路进行测量，可有效提升 GNSS 系统中的轨道确定及时间同步，另一方面，地面站可通过星间链路控制无法与地面站直接建链的卫星，进行遥控数据的上注，提升星座性能[4]。

基于无线电的星间链路测量可通过伪随机码测量、载波相位测量和方波测量。伪随机码的测量原理与 GNSS 伪距测量相似，载波相位测量通过发射和接收的相位延迟来进行距离的测量，方波测量通过收发双方方波的时间延迟来对距离进行[5-6]。当前，在美国的 GRACE 项目中的 K 波段星间测距系统（K Band Ranging System，KBR）中可对低轨卫星进行定轨和距离变化率。在星间距离为 200 km 的情况下，测速精度为 1 μm/s，测距方差精度为 1~2 mm[7]。除此之外，黄飞等人（2010）提出了一种卫星动态双向时间同步算法，该算法利用星间伪距离拟合多项式和时差拟合多项式联合求解星间相对时差，可以将时间同步误差控制在 5ns 以内[8]。Wang H.Y.等人讨论了一种基于单点伪距转换的时间同步算法，该算法可应用于高动态环境下的星地/星间双向时间同步[9]。潘军洋结合北斗试验星星地 L 双

向时频传递设备采集的星地钟差和星间链路获得的星间相对钟差，实现了对星间链路通道传输时延的在轨标定，时延解算精度优于 0.3ns[10]。

可以看到，采用微波扩频码进行测距的方式收到扩频码速率的限制，测距精度约为码长的百分之一，约为厘米级。若采用激光双向测距，虽然测距精度可提升至 fs 级别，但收到激光指向的限制，服务用户的相对位置较为固定，无法灵活的为接入用户提供服务。因此，采用微波载波相位进行测量是一种星间链路测量的有效手段。当前，星地载波相位测量多采用精密单点定位及多频载波相位测量，前者通过卫星的轨道、电文等先验信息，通过测量载波相位可获得高精度的定位结果，当前在理论和工程上都已较为完善。多频载波相位测量通过卫星同时发射多个频点的信号， Cocard 等针对 GPS 双频进行了研究分析，而后又将该表达式扩展到三频，并通过严谨的数学推导，分析了 GPS 三频整数线性组合[11]。Zhang 等基于 Cocard 等人的研究，对 BDS 三频载波相位组合进行了详细分析[12]。除了线性组合法，学者也会通过搜索的方式对整周模糊度进行确定，典型算法如 Lambda 算法，在提升计算复杂度的情况下，提升了结算的性能。

因此，本文针对星间链路应用环境，在原 DOWR 同步方法的基础上提出了一种改进时间同步方法，通过伪随机码与 Ka 频段载波相位测量相结合的方式，提升测量精度，不考虑通道等系统误差的情况下，测量精度约为 100μm 量级。

2　星间链路中双向非相干测量算法

星间链路之间需要双向的信息传输链路，来实时的传输测量信息和通信数据，当前多采用双向非相干测量的方式进行。

2.1　双向非相干测距

星间双向非相干测量的原理如图 1。

两颗卫星各安装扩频发射机和接收机，通过本地伪码再生测距的方法各自测量本地伪距，通过双向异步传输帧伪距交换本地伪距测量结果计算出本地钟面时误差，实现两星之间几何距离测量、时间同步和数据交互。其中每个卫星能够独立完成数据的调制发射和接收解调，且能够通过发射的扩频码实现单通道伪距测量功能。其中星 A 测量得到的信号时延 T_{A} 和星 B 测量得到的信号时延 T_{B} 如式（1）：

$$\begin{cases} T_{\mathrm{A}} = \tau_{\mathrm{AB}} + \tau_{\mathrm{clock}} + \tau_{\mathrm{Bt}} + \tau_{\mathrm{Ar}} \\ T_{\mathrm{B}} = \tau_{\mathrm{AB}} - \tau_{\mathrm{clock}} + \tau_{\mathrm{At}} + \tau_{\mathrm{Br}} \end{cases} \tag{1}$$

其中， τ_{AB} 是真实的信号传输时延， τ_{clock} 星 A、B 的钟差， τ_{At}、 τ_{Bt} 为星 A、B 的发射通道延迟， τ_{Ar}、 τ_{Br} 为星 A、B 的接收通道延迟。经过式（2）的变换，可得到无钟差的真距 D 和两设备 $\Delta t_{\mathrm{clock}}$ 的钟差。

$$\begin{cases} D = \dfrac{1}{2}\left[\left(T_{\mathrm{A}} + T_{\mathrm{B}}\right) - \left(\tau_{\mathrm{Ar}} + \tau_{\mathrm{At}} + \tau_{\mathrm{Br}} + \tau_{\mathrm{Bt}}\right)\right] \bullet c \\ \Delta t_{\mathrm{clock}} = \dfrac{1}{2}\left[\left(T_{\mathrm{A}} - T_{\mathrm{B}}\right) + \left(\tau_{\mathrm{Ar}} - \tau_{\mathrm{At}} + \tau_{\mathrm{Bt}} - \tau_{\mathrm{Br}}\right)\right] \end{cases} \tag{2}$$

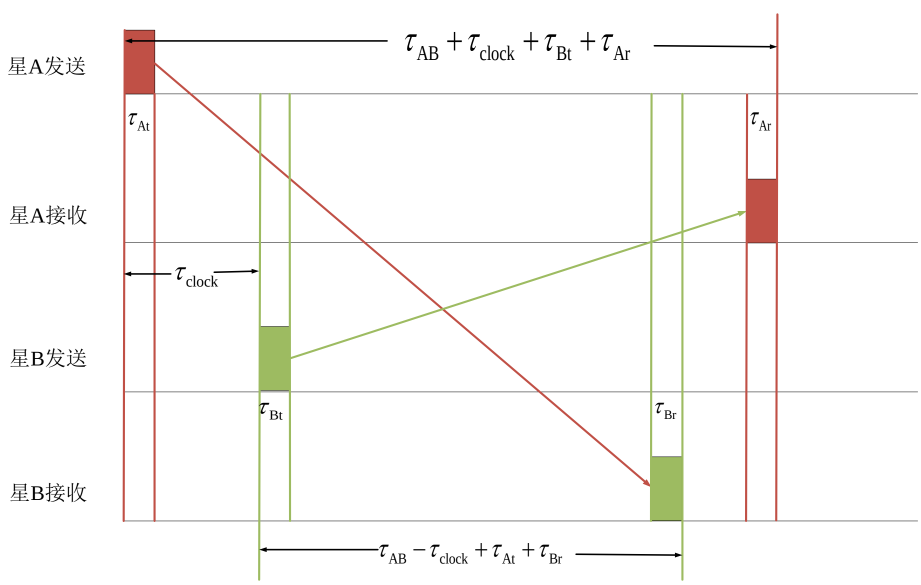

图 1　双向非相干测距

而 τ_{At}、τ_{Bt}、τ_{Ar}、τ_{Br} 都可在事先通过通道标校得到，在此看作已知量。

2.2　多频载波相位测距

载波相位的测量精度虽然相比较于伪随机码的测量精度高出多个量级，但其自身的携带的整周模糊度解算难度较大。当前多采用多频载波相位测量及载波平滑伪距的方式进行载波相位测距的实现。

假设通过同一个发射机同时发射两个频点的信号，则解模糊算法的模型如下

$$\rho_{PRN}+c\Delta t+\varepsilon_{PRN}=\frac{\Delta\varphi_1}{2\pi}\bullet\frac{c}{f_1}+\frac{c}{f_1}N_1+c\Delta t+\varepsilon_{f_1} \quad (3)$$

$$\rho_{PRN}+c\Delta t+\varepsilon_{PRN}=\frac{\Delta\varphi_2}{2\pi}\bullet\frac{c}{f_2}+\frac{c}{f_2}N_2+c\Delta t+\varepsilon_{f_2} \quad (4)$$

式中，ρ_{PRN} 为扩频码测量测量结果，$\Delta\varphi_i\,(i=1,2)$ 是频率为 f_1 和 f_2 的信号的载波相位小数周数测量值，该测量值可由跟踪环路直接得到。$N_i\,(i=1,2)$ 是频率为 f_1 和 f_2 的信号的载波相位整数周数测量值，该测量值为未知量。c 为光速，Δt 为收发卫星间钟差，ε_{PRN} 为伪码测距误差。$\varepsilon_{f_i}\,(i=1,2)$ 是频率为 f_1 和 f_2 的信号的载波相位测量误差。将（3）与（4）相加得到（5），相减得到（6）

$$N_1+N_2=\rho_{PRN}\left(\frac{f_1}{c}+\frac{f_2}{c}\right)+\sqrt{\left(\frac{f_1}{c}\varepsilon_{PRN}\right)^2+\left(\frac{f_2}{c}\varepsilon_{PRN}\right)^2+\varepsilon_{f_1}^2+\varepsilon_{f_2}^2}-\frac{\Delta\varphi_1}{2\pi}-\frac{\Delta\varphi_2}{2\pi} \quad (5)$$

$$N_1-N_2=\rho_{PRN}\left(\frac{f_1}{c}-\frac{f_2}{c}\right)+\sqrt{\left(\frac{f_1}{c}\varepsilon_{PRN}\right)^2+\left(\frac{f_2}{c}\varepsilon_{PRN}\right)^2+\varepsilon_{f_1}^2+\varepsilon_{f_2}^2}-\left(\frac{\Delta\varphi_1}{2\pi}-\frac{\Delta\varphi_2}{2\pi}\right) \quad (6)$$

通过式（5）和（6）的结果，可解算得到载波相位整周模糊度度。

但该方法的问题，整周模糊度的结算误差由公式左边第二项决定，该项误差中，包含伪随机码的测量误差及载波相位的测量误差，该项误差在未经处理的情况下，在分米甚至米级。若载波的频率较高，由于该项误差影响，无法获得正确的整周模糊度解算结果。

3　新体制星间载波相位测量

3.1　信号模型

基于当前伪码测距精度不足及载波相位整周模糊度解算误差较大的问题，本问提出基于双向非相干体制的星间载波相位测量技术。如果两个卫星同时收发双拼信号，收发段的频率切换方式如图所示。每个频率的传输时间为T_{swit}。在这段时间内，接收机可以完成捕获和粗跟踪。每颗卫星提供两个频率 f_1 & f_2 的信号用于发射接收。

发射信号数学表达如式

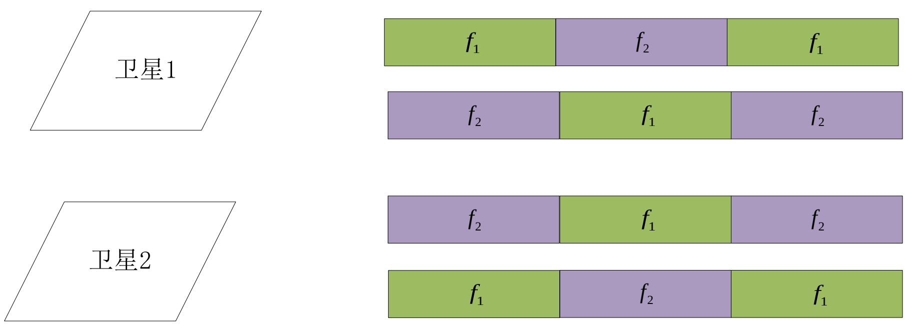

(a)

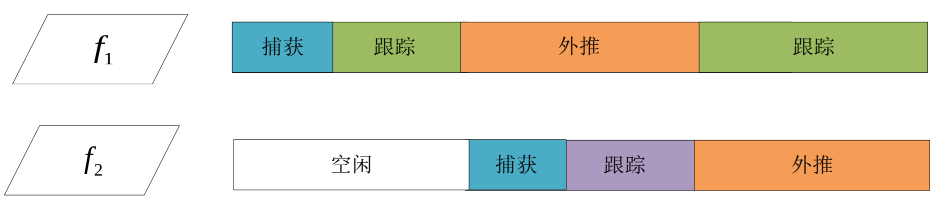

(b)

图 2　收发双工体制下的双向载波相位测量时隙(a)收发时隙（b）接收链路

$$s(t)=\begin{cases}C(t)*D(t)*\cos(2\pi f_1 t) & (n-1)T_{swit}<t<nT_{swit}\\ C(t)*D(t)*\cos(2\pi f_2 t) & nT_{swit}<t<(n+1)T_{swit}\end{cases} \tag{7}$$

式中，$s(t)$为卫星发射信号，$C(t)$为扩频码序列，此处采用码长为1023，速率为5.115MHz从接收到的信号。$D(t)$为链路数据。$f_i(i=1,2)$为两个频点的射频频率，T_{swit}为信号切换时间，考虑导捕获时间和外推误差，此处取2 s。

3.2　星间双向非相干载波相位测距技术

在载波相位观测中，需要实时的从载波跟踪环路中提取载波相位，除此之外，由于星间链路采用时分双向测量体制，需将包含接收和发射时刻两个时间变量的单向测量数据归算为等效的瞬发观测值，即修正传播时延对测量的影响的过程，然后是通过历元归算将已进行光行时修正的前向链路和后向链路归算到同一时刻t 。由于每个卫星都需要时分的发送多个频点的信号，因此卫星段对多个频点的跟踪环路会频繁失锁和重连，导致载波相位的跟踪不稳定，最终导致整周模糊度解算的错误。因此需要相应的载波和伪码环路外推算法来保证载波相位跟踪的稳定性，并基于环路外推算法对单向载波相位测量数据进行历元归算。如图3所示。

本文通过轨道外推，在没有匹配信号输入的情况下模拟输入信号。因此，跟踪环路可以实现对信号的稳定跟踪。

外推过程包括以下五个步骤，其中t_1被视为测距/速度测量的参考时间：

Step1：根据卫星轨道根数（或卫星惯性导航系统）计算加速度，并沿来波方向方向进行矢量投影，计算出卫星与来波方向之间的径向加速度值$a(t)$；

Step2：根据径向加速度$a(t)$和式（8）计算卫星与卫星的径向速度$v(t_2)$

$$v(t_2)=v(t_1)+\int_{t_1}^{t_2}a(t)dt \tag{8}$$

Step3：多普勒频移可通过速度进行推算，将该值引入载波跟踪环以修正外推环路信号载波相位；

Step4：根据径向速度$v(t_2)$和式（9）计算卫星与卫星的径向距离$\rho(t_2)$变化。

$$\rho(t_2)=\rho(t_1)+\int_{t_1}^{t_2}\left[v(t_1)+\int_{t_1}^{t_2}a(t)dt\right]dt \tag{9}$$

公式右侧第二项为距离修正量；

Step5：修正后的距离测量值可用于实现伪码相位的外推，并将其发送到码跟踪环路进行伪码相位的修正。

在此过程中，星间链路的切换时间为T_{SW}，通过INS和轨道根数得到的径向加速度误差为Δa，通过INS和轨道根数得到的径向速度误差为Δv。则通过式（8）积分得到的径向速度修正误差为$\Delta a\times T_{\mathrm{SW}}$，通过式（9）积分得到的径向测距值修正误差为$(\Delta v+\Delta a\times T_{\mathrm{SW}}/2)\times T_{\mathrm{SW}}$。假设$T_{\mathrm{SW}}=2\mathrm{s}$，$\Delta v\le 0.1\mathrm{m/s}$，$\Delta a\le 1\times10^{-5}\mathrm{g}$，则速度修正误差小于$1.96\times10^{-4}\mathrm{m/s}$，X频段的多普勒修正误差小于$0.0052\mathrm{Hz}$，Ka频段多普勒修正误差小于$0.02\mathrm{Hz}$，对应至载波相位测量上，仅会造成百分之一个整周模糊度的测量误差，与测量环路造成的载波相位整周模糊度误差近似，因此可将其结果用于

当外推误差过大时，系统也会进行重捕获，其阈值如0所示，其中σ_{ce}为测距误差，$\sigma_{\mathrm{Doppler}}$为多普勒估计误差，$T_{\mathrm{chip}}$为单个码片长度，$T_{\mathrm{coh}}$为积分累积时间。

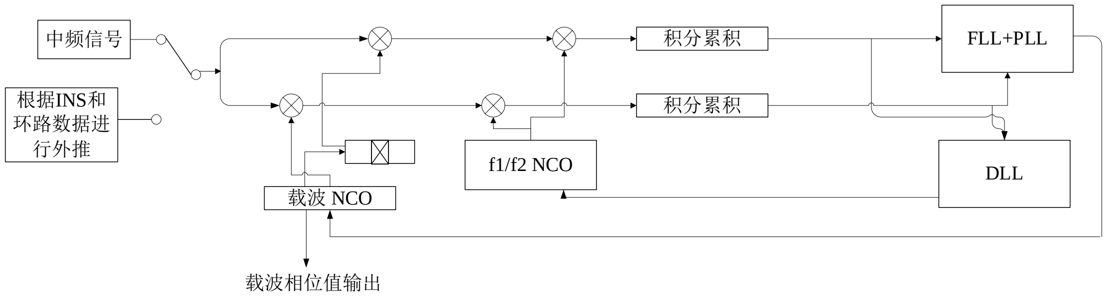

图3　载波相位提取

表 1　　修正误差与跟踪过程是否需要重新捕获之间的关系。

阈值	跟踪过程是否需要重捕获
$\sigma_{\text{ce}} \le \pm 0.25T_{\text{chip}} \cdot c$ 并且 $\sigma_{\text{Doppler}} \le \pm \dfrac{1}{4T_{\text{coh}}}$	否
$\sigma_{\text{ce}} > 0.25T_{\text{chip}} \cdot c$ 或 $\sigma_{\text{Doppler}} > \pm \dfrac{1}{4T_{\text{coh}}}$	是

3.3　星间双向非相干载波相位整周模糊度解算

由于载波相位中包含了未知的整周模糊度，因此需要通过一定方式对载波的整周模糊度进行解算。

首先在星间链路载波相位中，由于载波相位的整周数较大，因此需要通过伪距取整来约束载波相位整周模糊度的范围。通过星间链路的伪码距离测量值 ρ_k，可获得整周模糊度粗略估值 $\tilde{N}_i$ 如式

$$\tilde{N}_i = \left\lfloor \frac{\rho_k}{\lambda_i} \right\rfloor \tag{10}$$

其中，k 为星间链路标志，i 为频率标志，$\lfloor \bullet \rfloor$ 为向下取整符号。在星间链路测量中，未经后处理的伪码测距精度约为 1~5 m。因此，对于 8 GHz 的 X 频段，残余整周模糊度在[-67,67]范围内；对于 31 GHz 的 Ka 频段，残余整周模糊度在 $[-267, 267]$ 范围内。通过以下方式估算残余整周模糊。

Step1：获得星间链路的时延差，并将其转换为距离差。使用载波相位测量的距离差应大致等于伪码测量的距离加上伪码测量误差，如式（11）所示

$$\rho_{21}^* - \Delta\rho \le N_1\lambda_1 + \varphi_{21f1}\lambda_1/2\pi \approx N_2\lambda_2 + \varphi_{21f2}\lambda_2/2\pi \le \rho_{21} + \Delta\rho \tag{11}$$

此处，ρ_{21}^* 为 PN 码测距结果，$\Delta\rho$ 为 PN 码测距误差，N_1 为 f_1 频点信号的整周模糊度，λ_1 为 f_1 信号的波长，φ_{21f1} 为星间链路在 f_1 频点的相位差分结果，该值小于一个整周数。同理，N_2，λ_2 和 φ_{21f2} 为 f_2 频点的对应参数；

Step2：式（11）可转化为式（12）

$$N_1\lambda_1 - N_2\lambda_2 \approx \varphi_{21f2} * \lambda_2/2\pi - \varphi_{21f1}\lambda_1/2\pi \tag{12}$$

该式中，等式右侧信号的未知数可通过 f_1 和 f_2 频点的载波跟踪环来确定，并且测量误差小于四分之一波长；

Step3：在 $\left[\rho_{21}^* - \Delta\rho, \rho_{21}^* + \Delta\rho\right]$ 范围内搜索 N_1 和 N_2，获得当式（13）最小时的 N_1，记为 $\min(N_1)$。

$$e_{f12} = \left[N_1\lambda_1 + \varphi_{21f1}\lambda_1/2\pi\right] - \left[N_2\lambda_2 + \varphi_{21f2} * \lambda_2/2\pi\right] \tag{13}$$

式中，$\min(\bullet)$ 为求最小值算子。

Step4：计算距离差分值如式（14）

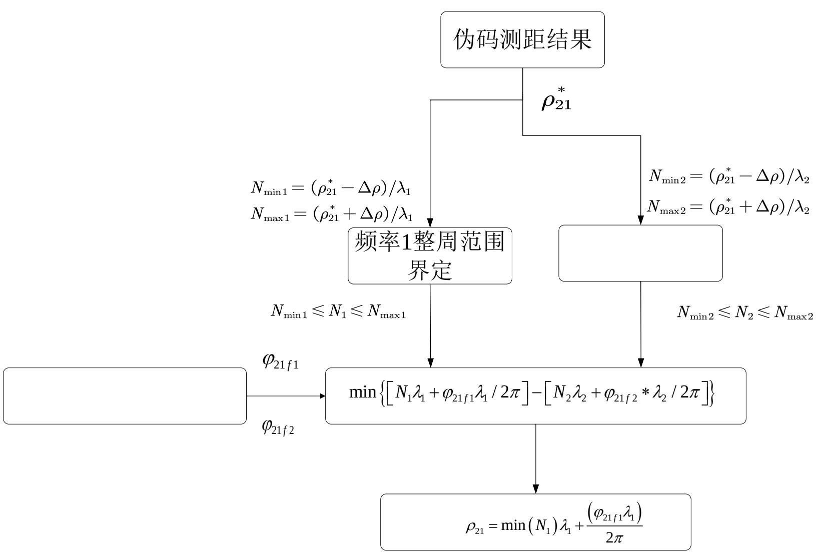

图 4　双频解模糊算法

$$\rho_{21}=\min\left(N_{1}\right)\lambda_{1}+\frac{\left(\varphi_{21f1}\lambda_{1}\right)}{2\pi} \tag{14}$$

4. 误差分析及仿真结果

4.1 信号捕获时间

对于传统 TDD 模式下的卫星，切换过程会伴随着信号的重捕获和冲跟踪。根据文献，信号捕获各流程所耗费时间如图所示。在单次捕获过程中所需要的全部时钟周期如式

$$T_{\mathrm{acq}}=T_{\mathrm{code}}+T_{\mathrm{FFT}}+T_{\mathrm{IFFT}}+T_{\mathrm{mul}}+T_{\mathrm{Max}}+\Delta t_{\mathrm{acq}} \tag{15}$$

式中，T_{code} 为 PN 码周期，T_{FFT} 和 T_{IFFT} 为 4096 个点的 FFT 和 IFFT 所耗费的时间，T_{mul} 为本地 FFT 结果和接收信号 FFT 结果相乘所耗费的时间，T_{Max} 为搜索 IFFT 最大值所耗费的时间，Δt_{acq} 为其他运算过程所耗费的时钟，大约为 100 个时钟周期。本系统采用 80 MHz 的系统采样率，因此，对单个频点的捕获时间为 0.6 ms。

因为单次捕获会导致虚警概率和漏警概率的增加，因此本系统采用多次检测来增加捕获概率。对于星间链路，一般采用检测次数为 6 的唐检测器，星间残余多普勒频率搜索范围为-12 kHz~12 kHz，而多普勒频率搜索间隔为 500 Hz。基于以上参数，可以给出传统星间链路系统中 TDD 信号实现重捕获的总时间为

$$T_{\mathrm{acq\_total}}=\frac{12000\mathrm{Hz}*2}{500\mathrm{Hz}}*6*T_{\mathrm{acq}}=172.8\mathrm{ms} \tag{16}$$

因此，切换时间 2s 的情况下，足够卫星完成初始捕获

4.2 误差分析

1. 接收机测量环路噪声

接收机的距离测量精度主要由伪码跟踪环路的热噪声误差和相对运动引起的动态应力误差造成。前者的体现在伪码跟踪环路的随机抖动，后者是体现在码多普勒变化。而码多普勒变化与载波多普勒有严格的耦合关系，可通过载波环提供的多普勒偏移抑制误差。因此，动态应力误差可以忽略不计，仅考虑热噪声引起的测距误差。伪码相位测距误差为：

$$\sigma_{\mathrm{BOC}}=T_{\mathrm{chip}}\sqrt{\frac{4F_{1}d^{2}B_{n}}{C/N_{0}}\left[2\left(1-d\right)+\frac{4F_{1}d}{T\bullet C/N_{0}}\right]} \tag{17}$$

上式中：T_{chip} 为伪码码片宽度（ns）。d 为伪码延迟锁定环超前/即时/滞后之间的码元间距。B_n 为码跟踪环路滤波器等效带宽（Hz）。T 为跟踪环路进行单次估计所需的时间；F_1 为码环相关器因子，本处取 0.5；F_2 为码环鉴别器因子，本处取 1。

可以看到，调整 B_n、T、C/N_0 都可以提升测量精度。但其皆有一定限制：B_n 的降低将会导致跟踪性能变差，T 的增加将会导致估计时间变长，C/N_0 收到信道和发射机的限制，有一定约束。

在本文中，假设选取对于扩频码长 1023、扩频码速率 5.115 MHz 的伪码测距系统，则码片长度 $T_{\mathrm{chip}}=200ns$，d=1/4，$F_1=0.5$，$F_2=1$，$B_n=2\mathrm{Hz}$，$T=2\mathrm{ms}$，得到热噪声引起的伪距测量误差：在 $C/N_0=53$dB-Hz 时，为 30mm。

2.载波相位测量误差

本文采用二阶锁频辅助三阶锁相环的方式，因此，环路热噪声相位误差为

$$\sigma_{PLL}=[\frac{B_{PF}}{C/N_{0}}(1+\frac{1}{2T\cdot C/N_{0}})]^{0.5} \tag{18}$$

跟踪环路对应的多普勒频率误差为

$$\sigma_{Doppler}=\frac{\sqrt{2}\sigma_{PLL}}{2\pi\bullet\Delta t_{\mathrm{doppler}}} \tag{19}$$

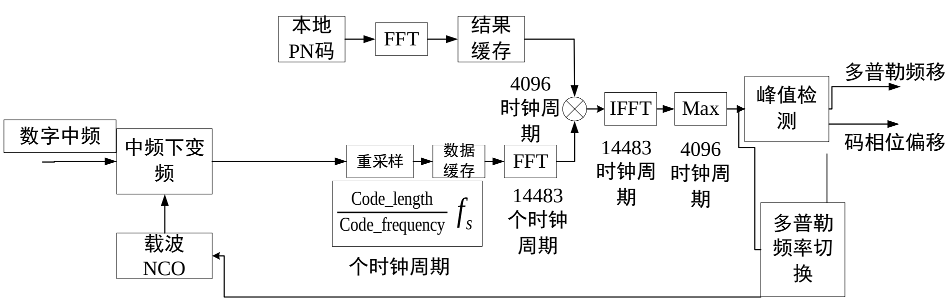

图 5　信号捕获过程

式中，B_{PF} 为锁相环带宽，此处取 10 Hz，积分累积时间 T 为 2 ms，$\Delta t_{\mathrm{doppler}}$ 为多普勒频率测量时间，取 0.1 s，在 C/N$_0$=53 dB-Hz 的情况下，$\sigma_{\mathrm{PLL}} = 7.07\times10^{-3}\mathrm{rad}$，$\sigma_{\mathrm{doppler}} = 1.55\times10^{-4}\mathrm{Hz}$。

4.3　仿真分析

当跟踪环路稳定时，载波相位的跟踪精度如式（18）和式（19）。在环路不需重捕获的前提下，对环路进行蒙特卡罗仿真。为了模拟星间链路动态变化中的复杂环境，假设固定多普勒偏移为 5 kHz，并加入 250 Hz 的正弦多普勒频率变化。该多普勒频移中包含多普勒加速度和多普勒加加速度的变化，适用于模拟轨道约束下的多普勒加速度变化。CNR=50 dB-Hz 时的跟踪环路结果如图 4-1 所示。可以看出，在此情况下，使用跟踪回路可以稳定跟踪信号。环路以每 2s 的频率进行射频频点切换，切换频点选择 $f_1 = 8\mathrm{GHz}$，$f_2 = 8.1\mathrm{GHz}$ 。

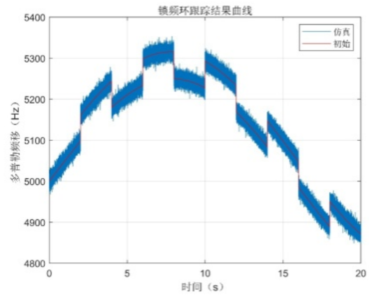

(a)

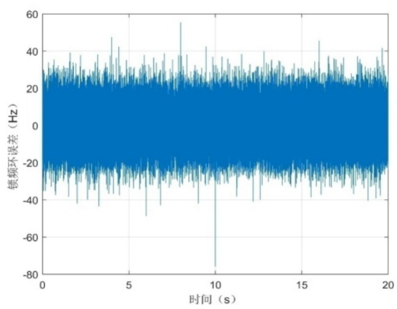

(b)

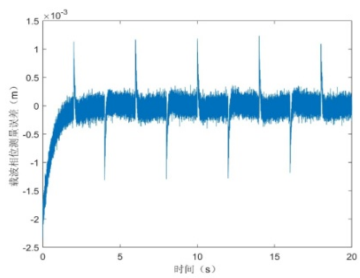

(c)

图 6 载噪比 40dB-Hz 情况下的跟踪环路结果。

在距离解模糊算法仿真中，参数设计如下：$\Delta\rho < 1\mathrm{m}$，X 频段，$f_1 = 8\mathrm{GHz}$，$f_2 = 8.1\mathrm{GHz}$；Ka 频段，$f_1 = 32\mathrm{GHz}$，$f_2 = 32.1\mathrm{GHz}$。不同 SNR 值下的精度如 2 所示。

根据图中所示的模拟结果。当相位和码外推误差较小时，环路能够稳定跟踪。当轨道外推误差发生时，即载波相位和码相位在每次频率切换时（切换时间为 0.2s）偏移，环路可在每次切换时再次锁定。

表 2　不同载噪比不同频段下角度测量误差

载噪比（dB-Hz）	载波相位测量误差（RMSE）/m	
	X 波段 （8 GHz）	Ka 波段（31GHz）
50	6.3159e-4	6.5062e-05
40	8.3123e-4	1.6614e-04
30	2.9623e-3	5.2322e-04

X 频段不同伪距测量误差情况下的载波相位测距的结果如表 3 所示。可以看出，在 $\Delta\rho < 1m$ 的范围内，模糊度解算的结果是正确的，误差不超过一个周期。但当伪距测量误差范围扩大时，多频解模糊的误差也会随之增加，这种情况在载噪比较低时更加明显。载波相位差分测量误差主要由载噪比决定，当载噪比小于 40 dB-Hz 时，可能会产生整周模糊度结算错误。

表 3　不同信噪比不同伪距测量误差情况下的角度测量误差

载 噪 比（dB-Hz）	载波相位测量误差（RMSE） /m		
	$\Delta\rho = 3\mathrm{m}$	$\Delta\rho = 5\mathrm{m}$	$\Delta\rho = 2\mathrm{m}$
50	2.7362e-04	4.4832e-04	1.8302e-04
40	3.6143e-04	3.7435e-04	2.5640e-04
30	0.0136	0.0166	0.0154

5.　结论

本文对基于载波相位的星间双向测量技术进行了研究，首先通过基于伪随机码的测距结果提供了粗测距结果，并剥离了较大的载波相位整周模糊度，其次通过搜索法进行解模糊，提出较小的载波相位整周模糊度。最终在 40dB-Hz 的载噪比上，X 频段测距误差优于 1mm，Ka 频段测距误差优于 0.17mm。随着载噪比的提升，测量精度会进一步提升。但载噪比低于 30dB-Hz 的情况下，由于整周模糊度错误解算概率

的增加，测量精度会劣化至厘米量级，

参考文献

[1] LI Xingxing, ZHANG Wei, YUAN Yongqiang, et al. Review of GNSS precise orbit determination: status, challenges, and opportunities[J]. Acta Geodaetica et Cartographica Sinica, 2022, 51(7): 1271-1293.

[2] Huabin W.，Yonghui H． Design and implementation of precise ranging and time synchronization system based on DOWR ［C］． Proceedings of 2012 International Conference on Measurement，Information and Control．Harbin，China: IEEE，2012．

[3] Xie Xin, Geng Tao, Zhao, etc. Precise orbit determination for BDS-3 satellites using satellite-ground and inter-satellite link observations[J].GPS Solutions, 2019, 23(2).

[4] Qile Zhao. Research on precise orbit determination theory and software of both GPS navigation constellation and LEO satellite[D]. Wuhan:Wuhan universit

[5] 王天枢，林鹏，董芳，刘显著，马万卓，付强.空间激光通信技术发展现状及展望[J].中国工程科学,2020,22(3):92-99

[6] Shen, Q., Guan, J. -Y., Ren, J. -G., etc. Free-space dissemination of time and frequency with 10−19 instability over 113 km. Nature（2022）.

[7] 蒙艳松,钟兴旺,杨珊珊.GRACE KBR 的测量新体制及其精度分析[J].空间电子技术, 2008, 5(3):6.

[8] F. Wang, D. Liu and Z. Nie, "A Pseudo-Code-Aided Carrier Synchronization Method for THz Communication System," 2018 10th International Conference on Communication Software and Networks (ICCSN), Chengdu, 2018, pp. 140-145.

[9] Wang H Y , Juang J C. An Improved Precise Point Positioning Method Based on Between-Satellite Single-Difference and Carrier Smoothing[J].Journal of Aeronautics, Astronautics and Aviation, A, 2020(4):52.

[10] 潘军洋, 胡小工, 唐成盼, 等. 北斗新一代卫星时分体制星间链路测量的系统误差标定[J]. 科学通报, 2017, 62(23): 2671-2679.

[11] Cocard M, Bourgon S, Kamali O, Collins P. A systematic investigation of optimal carrier-phase combination for modernized triple-frequency GPS[J]. J. Geod. 2008, 82: 555-564.

[12] Li B, Feng Y, Shen Y. Three carrier ambiguity resolution: distance-independent performance demonstrated using semi-generated triple frequency GPS signals [J]. GPS Solut. 2010,14(2):177–184.

Energy-constrained model pruning for efficient in-orbit object detection in optical remote sensing images

QIU Shaohua[1], CHEN Du[2], XU Xinghua[1], LIU Jia[2*]

Abstract — **Efficient object detection from optical remote sensing (RS) images has always been an important interpretation task for in-orbit RS applications. In recent years, convolutional neural networks have been widely used for object detection with significantly improved detection accuracy. However, the large detection models pose great challenges for the computing, memory and energy supply of resource-constrained in-orbit platforms. In this paper, we propose an efficient in-orbit object detection method with low memory, computation and energy requirements. The proposed method first integrates the compact modules of GhostNet into the detector and further performs L1-norm based filter pruning to significantly reduce model size and computational complexity. Besides, we propose to use energy as a key metric in filter pruning, and present a novel energy-guided layer-wise pruning rate estimation method so as to achieve energy-efficient object detection. Comprehensive experiments have shown the effectiveness of the proposed method in terms of model size, computational complexity, latency and energy consumption, while maintaining comparable detection accuracy.**

Keywords—**in-orbit object detection, optical remote sensing images, constrained resources, lightweight CNN, filter pruning**

[1]National Key Laboratory of Electromagnetic Energy, Naval University of Engineering, Wuhan 430033, China;

[2]School of Computer Science, China University of Geosciences, Wuhan 430074, China.

[*]Corresponding author.

This work is supported by National Natural Science Foundation of China under Grant 41901376, Hubei Provincial Natural Science Foundation of China under Grant 2022CFB989, Foundation for the National Key Laboratory of Science and Technology under Grant 6142217210503.

I. INTRODUCTION

Object detection from optical remote sensing imagery tries to localize geospatial objects of interest, e.g. airplanes, ships, etc., with their corresponding categories. It is a crucial task of image interpretation, and has been widely applied in a variety of applications such as environmental monitoring, disaster reduction, etc. In recent years, object detectors with deep learning, especially convolutional neural networks (CNN), have achieved success in RS community. Methods are developed considering the specific issues of RS scenes, e.g. rotation, multi-scale, complex background, tiny objects [1-3]. They generally design large models to enhance feature extraction capacity, thereby improving accuracy. It results in an increase in model size, computational complexity and energy consumption, which poses huge challenges for their implementations on resource-constrained platforms[4].

The traditional RS data application flow of "acquisition - delivery - processing" is sometimes too long, which easily delays the response time of time-sensitive object detection tasks. In recent years, with the development of the sensor technology, the number of RS terminal and edge infrastructures (satellite constellation, etc.) keeps increasing. In last year, several intelligent RS satellites, like LuoJia3[5], have been launched. These platforms are generally equipped with expandable real-time edge computing architecture, which provides in-orbit RS data processing and distributed spaceborne intelligent inference. The RS image object detection model based on deep learning deployed in the above edge platform closer to the data source and providing computing services nearby, can effectively reduce redundant data flow, relieve the pressure of communication, reduce response latency, and provide important support for intelligent time-sensitive tasks. However, these edge platforms are with limited capacity, and the resources such as computing, storage, and power supply are limited.

On the other side, studies have found that redundant information exist in large models, and not all parameters and structures contribute to the high discriminability [6, 7]. Therefore, compact networks are designed, such as MobileNetV1[8], MobileNetV2[9] and ShuffleNet[10], which rely on hand-crafted features and need domain experts to obtain a design solution with tradeoff of model size, efficiency and accuracy. Recently, there are several works, e.g. MobileNetV3[11] and FBNet[12], deriving compact networks through neural architecture search (NAS) which is an automating architecture engineering process rather than manually designing networks[13]. NAS is also a sub-domain of auto machine learning that requires extensive computing resources[14].

In addition, a great deal of researches try to compress and accelerate large models while maintaining high accuracy. The common ways can be divided into model pruning, low-rank factorization, parameter quantization, and knowledge distillation[4]. Low-rank factorization attempts to factorize large weight matrix/tensor into smaller ones layer by layer, which normally involves in convolutional layer and fully-connected layer, while its decomposition operation is computationally expensive [6]. Parameter quantization performs the low-bit representation for weights which are generally 32-bit floating-point numbers, normally leading to an accuracy decrease[15]. Knowledge distillation is to train a lightweight “student” network with less parameters and computational complexity from a larger “teacher” network while maintaining its generalization ability[7]. Generally, model performances are sensitive to the network structure and application, and require training from scratch. Parameter pruning tries to reduce redundant parameters that contribute little to the performance, and has been widely used to reduce network complexity and address the over-fitting issue[6]. In parameter pruning, different ways of granularities are performed, for instance, the neuron-level pruning, filter-level pruning and layer-level pruning.

To meet the demands of resource-constrained RS scenarios, e.g. onboard satellites platforms, there are works towards compact object detectors from RS images. Miao et al. replaced the shallow convolutional layers in ResNet-50 with Ghost modules to achieve lightweight ship detector for SAR images[16]. To adopt to satellite computing configuration, Pang et al. proposed a lightweight in-orbit fine-grained object recognition network SOCNet with flat multi-branch feature extraction and depthwise separable convolutions to speedup inference[17]. Some researches attempt at achieving near real-time RS object detection with lightweight CNN as feature extraction backbone in one-stage detectors, such as SSD with MobileNet[18], R2-CNN with its backbone Tiny-Net[19], RetinaNet with Ghost module[16], and YOLO with MobileNet[20].

In addition to limited computing and memory resources, edge devices aboard satellites are generally small in size and rely on batteries or green energy, and its constrained energy supply will limit the operation time and shorten the service time, thus limiting the intelligent development[21]. The previous research and practice elaborate on the insights and potentials of deploying lightweight RS object detection methods based on deep learning on resources-constrained in-orbit platforms. However, more attempts for efficient pipelines to significantly compress and accelerate deep detectors via combining multiple steps are desired. Besides, most existing works focus on the metrics of computational complexity, model size and runtime, and ignore their energy consumption which is important for end and edge devices with constrained energy supply onboard satellites.

To solve this problem, this paper introduced the energy consumption limit of edge-side satellite platform into model pruning, so as to reduce the number of model parameters, computational complexity and inference energy consumption of in-orbit object detection model.

The major contributions are as follows:

(1) We first achieve efficient object detection from RSI by a combination of compact CNN and network pruning. Taking the classical and high-performance one-stage detector YOLOv5 as the basis, we integrate compact modules of GhostNet to obtain a lightweight detection model, and further compress it with a L1-norm based filter pruning. This pipeline significantly reduces the model size, computational complexity and latency.

(2) We present an energy guided filter pruning method for the above detection model, thereby achieving energy-efficient detection. In this process, layer-wise pruning rates of detector are estimated with the presented automatic search algorithm given an overall energy consumption constraint, and then the L1-norm based filter pruning with the corresponding pruning rate is performed.

(3) Comprehensive experiments on the benchmark dataset DOTA-v2.0 have been conducted. In addition to accuracy, the efficiency metrics in terms of model size, computational complexity, latency, as well as energy consumption have been evaluated and show the effectiveness and superiority of the proposed method.

II. THE PROPOSED METHOD

A. OVERVIEW

The flowchart overview of this method is shown in Fig. 1.

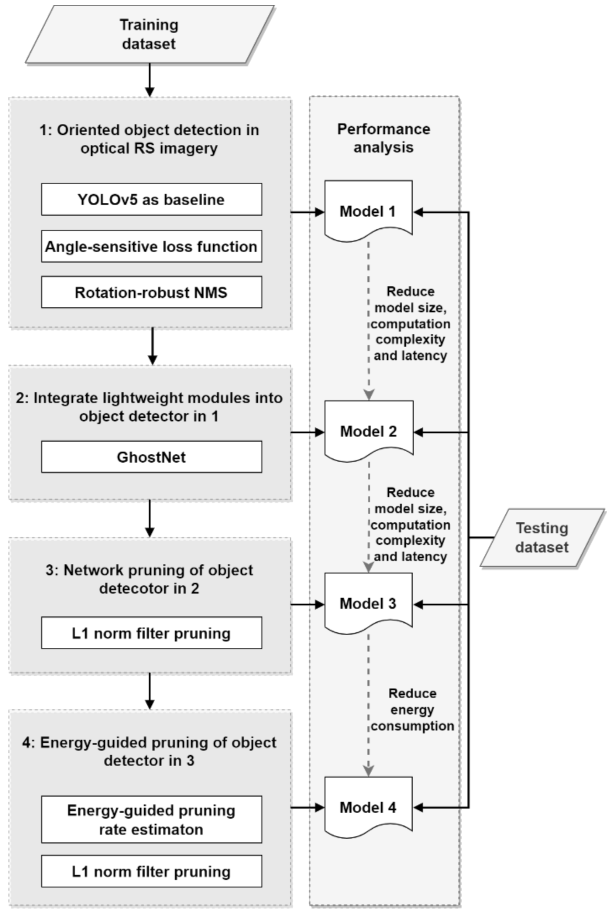

Figure 1 The flowchart of the proposed method.

Given the fact that the in-plane directions of objects in RS images are arbitrary, an oriented object detection method is implemented firstly by using the rotated bounding box representation, rotation-robust Intersection-over-Union (IoU) and an angle-sensitive loss function. It is used as the baseline for the subsequent object detection network. After that, lightweight Ghost convolution is introduced to greatly reduce the number of parameters and computational complexity in backbone network. Then, for the above lightweight detection network, we adopt the classical convolutional filter selection criterion of "smaller norm - less importance" to carry out the structured filter pruning based on L1 norm and remove the redundant filters. The model is fine-tuned to further increase the sparsity of the object detection model in RS images. On this basis, considering the energy supply limit of satellite platform, the energy consumption of object detection model inference is used as the basis of filter pruning, and an energy-guided layer-wise pruning rate estimation method is proposed to achieve lightweight detection that meets the energy constraint of in-orbit platform. The flowchart of the proposed method shown in Fig. 1 will be described in details in the following subsections.

B. LIGHTWEIHT ORIENTED OBJECT DETECTION NETWORK

In this paper, the classical one-stage object detection network, specifically the standard version YOLOv5l, is used as the baseline for object detection in optical RS images. It consists of backbone, neck and head. Backbone extracts features from input images, and plays a crucial role in the detection performance. It adopts a new CSPDarknet as backbone, which is based on cross stage partial networks (CSP) and Focus structure. Compared with its previous version, Focus module is designed for computational complexity reduction and speed increase. Neck mainly fuses the extracted features. A new CSP path aggregation network structure (CSP-PAN) have been employed as the neck network. Head is where the final detection is performed. It is mainly responsible for applying anchors on features, generating outputs with associated class confidence, objectness score, and bounding boxes. The head is consistent with the previous YOLOv3 and YOLOv4.

Since the complex backbone CSPDarknet53 takes up over 50% parameters and computations of the detection model, we first simplify the heavy backbone by integrating lightweight modules from the state-of-the-art GhostNet. The improved lightweight YOLOv5l is shown in Fig. 2. Considering that the output feature maps calculated by ordinary convolution filters are with much redundancy, it is unnecessary to be generated with a large number of FLOPs and parameters, GhostNet[22] uses a novel plug-and-play Ghost module, i.e. GhostConv to generate informative ghosts features from a series of linear transformations. In Fig. 2, C3Ghost is composed of three GhostBottleNeck modules stacked in a sequential order, where Ghost bottleneck consists of two stacked Ghost modules and shortcuts similar to the basic residual block in ResNet. Note that the compact modules are also integrated into Neck.

Subsequently, the detector output, loss function and non-maximum suppression (NMS) of YOLOv5 are adapted to the oriented objects widely existed in RS imagery. An additional rotation angle parameter is added to the definition of bounding box, which better reflects the size and aspect ratio of objects. Accordingly, a classification loss for angle is added in Eq. 1. The rotation-robust intersection over union (RIoU)[23] is used for NMS to filter out duplicate detection bounding boxes.

$$L_{total} = \lambda_{box} L_{box} + \lambda_{obj} L_{obj} + \lambda_{cls} L_{cls} + \lambda_{\theta} L_{\theta} \tag{1}$$

In Eq. 1, L_{box} is the localization loss for bounding box regression and uses complete intersection over union (CIoU) loss L_{box}=1-CIoU in [24]; L_{cls} and L_{obj} are the classification loss and confidence loss respectively, both adopt binary cross entropy (BCE) loss; L_{θ} is the added angle classification loss shown in Eq. 2 where y is the ground truth and $\hat{y}$ is the predicted value, and we take it as a classification task with 180 values, i.e. $\theta \in [-90, 90)$ and is an integer. λ_{box}, λ_{cls}, λ_{obj} and λ_{θ} represent the proportion of L_{box}, L_{cls}, L_{obj} and L_{θ} in L_{total}.

$$L_{\theta} = -\sum_{i=1}^{N} y^{(i)} \log \hat{y}^{(i)} + (1 - y^{(i)}) \log(1 - \hat{y}^{(i)}) \tag{2}$$

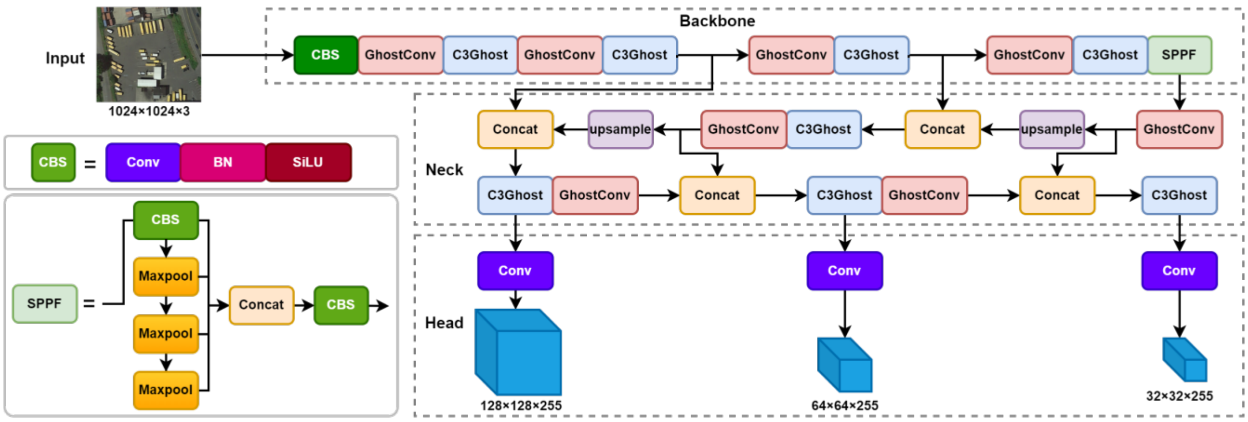

Figure 2 The baseline network architecture with lightweight module.

C. FILTER PRUNING OF RS OBJECT DETECTOR WITH L1-NORM

After integrating the lightweight feature extraction network into the detector, the parameters and computations have been reduced significantly, but still contain much redundancy, which can be compressed further. Model pruning removes redundant parameters according to the designed evaluation criteria for network parameters based on pre-trained large models. It can be divided into unstructured pruning and structured pruning, in terms of the granularity of pruned components. The fine-grained unstructured pruning such as weight pruning, can greatly reduce the model size and computation by removing redundant weights while maintaining accuracy, however requires special hardware and runtime libraries to accelerate the resulting unstructured sparsity[25]. In contrast, the coarse-grained structured pruning is preferred to compress and accelerate models under the existing architectures, where filter pruning is a widely adopted strategy[26, 27].

Following a classical criterion "smaller-norm-less-important", this work applies a filter pruning process with smaller L1-norm values in the overall detection network derived from the previous subsections. The corresponding pseudo-code is given in Algorithm 1. Specifically, the L1-norm values, i.e. the sum of its absolute kernel weights of all filters in each convolution layer in the model, are calculated respectively. Hence, the filters with smaller L1-norm values than a threshold value are identified as unimportant and are then pruned. The threshold is determined by a given pruning rate p. The L1-norm values of all filters are sorted in ascending order, and the threshold is then the L1-norm value of the $round(N \times p)$ filters, where N is the filter numbers of a layer. In this work, the pruning rate p can vary across layers and is set as 0.5, namely 50% filters will be pruned for all layers. The pruned model are then fine-tuned for performance recovery.

Algorithm 1 Detector filter pruning with L1-Norm

Input: Filter of each layer x, Number of layers n, Pruning rate p

Output: Pruned detector

```
for i = 0 to n−1 do
    filter ← x[i];
    N = filter.shape[0];
    for j = 0 to N−1 do
        array[j] = L1(filter[j]);
    end
    copyArray = copy(array);
    sortByL1(array);
    threshold = array[Round(p × N ) − 1];
    for j = 0 to N − 1 do
        if copyArray[j] <threshold then
            pruning(x[i], copyArray, j);
        end
    end
end
```

D. ENERGY-GUIDED LAYER-WISE PRUNING RATE ESTIMATION

Energy consumption is an indicator that does not simply linearly decrease along with the model size and computations. It is important but usually ignored by current research of lightweight RS object detection. Therefore, this subsection presents a simple but practical energy-guided layer-wise pruning rate estimation method to achieve energy-efficient object detection in RS images.

The energy consumption are first measured and calculated for the inference of the resulting models from the subsection II.B and subsection II.C. With a fixed size (3×1024×1024) inputs, we record the start time T_0 and end time T_n. The time (e.g. T_i) and corresponding instantaneous power of graphics processing unit (GPU) P_i at regular intervals are measured using the command *nvidia-smi* provided by the official NVIDIA plug-in. The energy consumption are measured and approximated for the inference stage as Equation 3. In this work, and the energy consumption of each model is measured 10 times to obtain the average value.

$$W = \sum_{i=1}^{n} (T_i - T_{i-1}) \times P_i \tag{3}$$

In subsection II.B, we apply the pruning rate 50%. However, different layers actually contribute different energy consumption to the model. Therefore, the sparsity of each layer is randomly generated, and the corresponding energy consumption of the model is measured respectively. As a result, a dataset with 5000 records which is related to the parameter sizes and the computations in FLOPs with the energy consumption respectively is obtained. It can be observed from the dataset that the energy consumption maintains an approximate linear correlation with FLOPs for the detection model derived from the previous subsections. This relationship does not hold for energy consumption and parameter sizes. It provides the foundation for the following key step, the automatic rate search for pruning with energy constraint.

The pseudo-code for pruning rate estimation is in Algorithm 2. To reduce the inference energy consumption of model, we disperse it to each layer, which can be defined by Equation 4. W_t is the given target energy consumption, W_o is the original energy consumption, and the energy consumption reduced by pruning is $W_s = W_o - W_t$.

$$W_i = W_s \times FLOPs_i \Big/ \sum_{i=1}^{n} FLOPs_i \tag{4}$$

Algorithm 2 Energy-guided pruning rate estimation

Input: Model x, reduced energy consumption W_s, number of layer n, computations $FLOPs$, tolerance $error$

Output: Estimated pruning rate arr

```
for i = 0 to n − 1 do
    W[i] = Ws × FLOPs[i]/sum(FLOPs);
end
sortByFlops(W);
for i = 0 to n−1 do
    for j = 0.25 to 0.75 do
        w = getEnergy(x, j);
        k = getLayerIndex(W);
        if |w − W[i]| < error then
            arr[k] = j;
            break;
        end
    end
end
```

III. EXPERIMENTAL RESULTS AND ANALYSIS

A. DATASET, EXPERIMENTAL SETTINGS AND EVALUATION METRICS

A large-scale aerial RS image dataset for object detection, DOTA-v2.0, is adopted for the performance evaluation. Its images are collected from Google Earth, GF-2 Satellite and aerial images. Image sizes range from 800×800 to 20,000×20,000 pixels and each image contains objects exhibiting a wide variety of scales, orientations, and shapes. There are 18 common categories with 11,268 images and 1,793,658 instances.

The categories in DOTA-v2.0 include plane (PL), ship (SP), storage tank (ST), baseball diamond (BD), tennis court (TC), basketball court (BC), ground track field (GTF), harbor (HB), bridge (BG), large vehicle (LV), small vehicle (SV), helicopter (HC), roundabout (RA), soccer ball field (SBF), swimming pool (SWP), container crane (CC), airport (AP) and helipad (HP).

Considering the limited GPU memory, we crop the images into a fixed size of 1024×1024 with an overlapping width of 200 pixels. Moreover, we augment the categories with too few samples through rotating, mirroring, and adding noise etc. to avoid the imbalance issue. For the rotated annotations, we convert the original 8-d.o.f.-parameter label into 5-parameter one with rotating angle.

Experiments are performed on a server with an Intel Xeon E5-2680v4 CPU, 64GB random access memory (RAM) and an NVIDIA RTX 3090 GPU. The system runs Ubuntu 20.04 LTS with CUDA 11.1, cuDNN 8.0.5, Pytorch 1.8.0, and torchvision 0.9.0. Models are trained with a batch size of 16 by stochastic gradient descent (SGD) with an initial learning rate of 0.01 and momentum of 0.937 for 250 epochs. The learning rate is adjusted using the cosine annealing algorithm.

The detection accuracy are evaluated according to the mAP. The model sizes (MB), computational complexity (FLOPs), frame per second (FPS), and energy consumption (J) are used for efficiency. FLOPs refers to the number of floating point operations performed for model inference, and is a common metric to measure the computational complexity of a model. FPS refers to the number of images that can be inferred per second, and the time of each image inferred is $Latency$. The energy consumption can be obtained by Equation 3.

B. DETECTION RESULTS AND ACCURACY

The experimental results of detection accuracy including AP for each category and mAP (%) are presented in Table 1. YOLOv5l, YOLOv5l-G, YOLOv5l-GP and YOLOv5l-GPE stand for the adapted YOLOv5 for oriented object detection, the lightweight YOLOv5 with compact modules, the model using filter pruning with L1-norm (fixed pruning rate of 0.5), and the energy-guided model (energy constraints ratio of 0.5).

Table 1 Detection accuracy (%) on DOTA-v2.0 dataset.

Class	Model			
	YOLOv5l	YOLOv5l-G	YOLOv5l-GP	YOLOv5l-GPE
PL	**97.2**	96.9	95.9	96
BD	78.2	**79.0**	76.3	76.8
BG	**57.0**	56.6	49.9	51.1
GTF	71.2	72.1	72.4	**73.1**
SV	**73.8**	71.2	67.6	67.6
LV	**84.9**	83.7	82.7	82.5
SP	**95.1**	93.8	92.4	92.5
TC	**96.7**	96.3	95.7	95.9
BC	**79.2**	77.9	75.0	76.9
ST	**73.2**	69.3	66.6	70.1
SBF	**54.3**	49.6	52.2	50.7
RA	60.9	58.1	63.9	**66.6**
HB	**82.5**	81.8	80.7	81.3
SWP	70.9	**72.5**	65.8	68.7
HC	74.6	71.8	62.5	**74.9**
CC	**3.5**	0.9	1.4	1.0
AP	28.0	64.7	**66.8**	51.4
HP	**50.9**	50.6	33.5	50.0
mAP	68.4	**69.3**	66.7	68.2

Table 1 shows that generally all models perform well for the categories with more training data and distinct geometric features, e.g. plane, ship and tennis court, while the accuracy performance varies for the categories with less training data, e.g. helipad, container crane and airport. Specifically, the baseline YOLOv5l achieves a mAP of 68.4%, with the highest accuracy in AP for the majority of categories. The YOLOv5l-G without pruning has a slightly higher mAP of 69.3%, and the YOLOv5l-GP that prunes the YOLOv5l-G using a fixed pruning rate of 0.5 achieves an accuracy of 66.7%. The mAP of the final energy-efficient YOLOv5l-GPE is 68.2%, only with a slight accuracy loss of 1.1% and 0.2% compared with the unpruned YOLOv5l-G and baseline YOLOv5l. Some detection results of the final energy-efficient detection model from DOTA-v2.0 dataset are shown in Fig. 2.

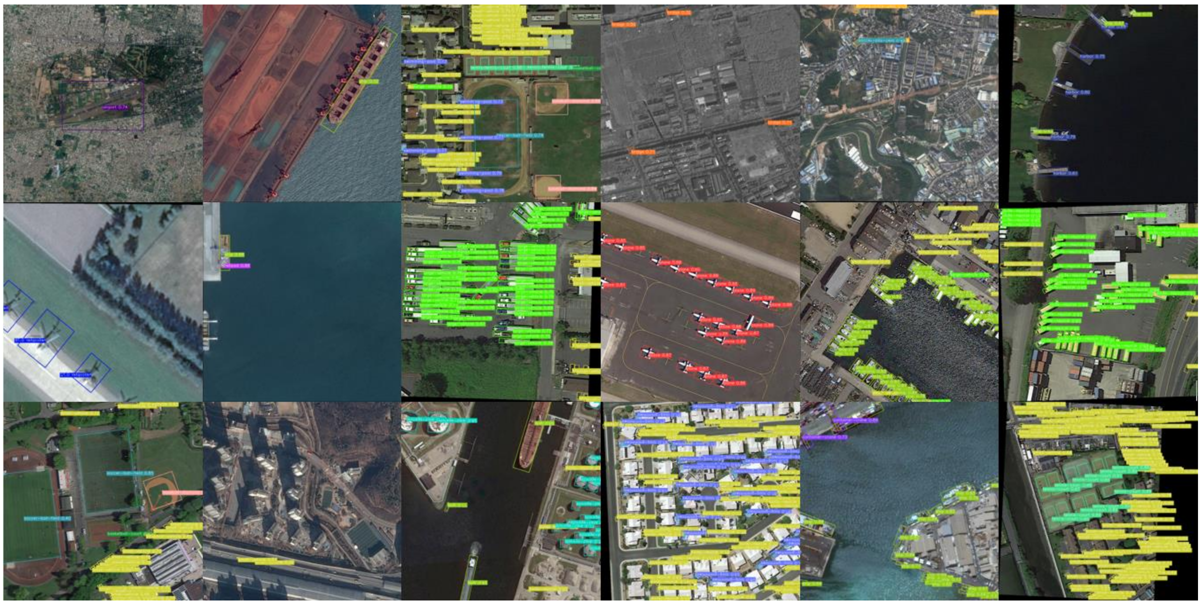

Figure 2 The sample detection results of the energy-efficient detection model from the DOTA-v2.0 dataset.

C. MODEL SIZE AND COMPUTATIONAL COMPLEXITY ANALYSIS

In addition to the detection accuracy, the parameter numbers, model size (MB) and computational complexity (GFLOPs) are presented to evaluate the efficiency performance in Table 2. It can be observed that the model size of YOLOv5l-G decreases from 71.7 MB to 32.8 MB when using float16, the YOLOv5l-GP exploits the redundancy of detection models, and further significantly reduces the model size to 9.61 MB, which account for only 13.40% of the baseline YOLOv5l, and 29.30% of the YOLOv5l-G with lightweight modules. With an energy consumption constraint ratio of 0.5, the final YOLOv5l-GPE reduces to 12.4 MB with a compression ratio of 5.78× to the YOLOv5l and 2.65× to the YOLOv5l-G. Its model size compression efficiency decrease, but the accuracy increases compared with the YOLOv5l-GP.

Computational complexity is measured in GFLOPs, which does not directly corresponds to parameters. Generally, convolution operations contain small number of parameters, however are computationally intensive, while the full connection layers are on the contrary. The computation complexities decrease to 93.1 GFLOPs, 27.0 GFLOPs and 29.6 GFLOPs respectively, accounting for 42.73%, 12.39% and 13.58% of the baseline YOLOv5l. The compression ratio of FLOPs is slightly significant than that of the model size.

Table 2 Experimental results of model size, computational complexity, latency, FPS and energy consumption

Metric	Model			
	YOLOv5l	YOLOv5l-G	YOLOv5l-GP	YOLOv5l-GPE
mAP(%)	68.4	69.3	66.7	68.2
Model size (MB)	71.7	32.8	9.61	12.4
Computational Complexity (GFLOPs)	217.9	93.1	27.0	29.6
Latency (ms)	24.5	22.3	20.4	20.3
FPS	40.8	44.8	49.0	49.3
Energy Consumption (J)	1158.3	1097.4	590.5	580.2

As shown in Table 2, the detection latency and FPS have only a slight improvement, and the highest speedup is 1.21×. It can be observed that FLOPs cannot be used directly as an indicator of inference speed, i.e. low FLOPs does not correspond to high FPS, since it does not take factors, e.g. memory access cost, parallelism and platforms that influence speed into account. It should be noted that the efficiency improvement due to the parallelism on the corresponding accelerators is not the focus of this paper, so the latency and FPS have not be tuned.

D. ENERGY CONSUMPTION ANALYSIS

In this subsection, we further explore the energy consumption for detection, which is another crucial metric to be considered for resource-constraint platforms. Table 2 shows the energy consumption results for the YOLOv5l, YOLOv5l-G, YOLOv5l-GP (fix pruning rate of 0.5), and YOLOv5l-GPE (energy constraints ratio of 0.5). The energy consumption results (J) in Table 2 refer to the model inference with an image of 3×1024×1024 for 100 times, and the measurements are performed 10 times for the average. It can be seen that, although the energy-guided YOLOv5l-GPE has slightly higher model size and computational complexity, it consumes less energy of 580.2J than YOLOv5l-GP.

Specifically, the energy constraint settings of 0.4, 0.5 and 0.6 are configured to show the performance of YOLOv5l-GPE. The setting of 0.4 represents that a decline by 40% in energy consumption is desired. Since for a model, the same pruning sparsity on different layers may lead to different influences on the total energy consumption, the layer-wise pruning rates are first estimated according to subsection II.D. The corresponding results are given in Fig. 3. Note that the layers with a searched pruning rate of 0 involve no convolution operations. Under different settings, the estimated pruning rates vary, and range from 0.25-0.69 (setting of 0.4), 0.25-0.74 (setting of 0.4), and 0.32-0.74 (setting of 0.6) respectively. The maximum pruning rate for each layer is 0.75 for accuracy.

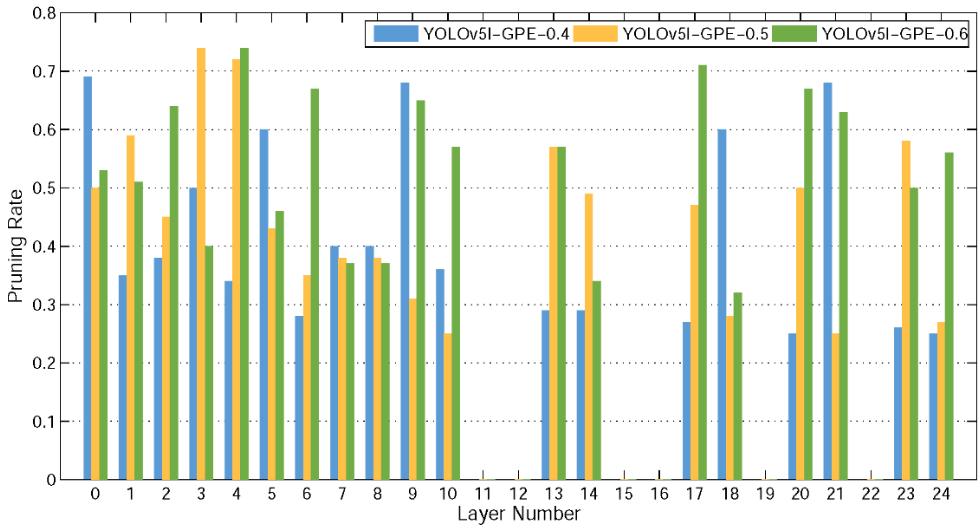

Figure 3 The layer-wise pruning rates under different settings.

In addition, we also present the consumption constraint variations with the pruning rate adjustment in Fig. 4. With the continuous adjustment of sparsity along the iterations, the energy consumption of model decreases in general, and the final result approaches the desired constraint. The fluctuations in the energy consumption mainly appear in the process of pruning rate search within a certain layer, and the iteration number with the final searched results are marked with the layer number. The slight fluctuations across layers are mainly due to that the pruning rates to meet the requirements are unavailable, as well as deviations exist in the energy consumption measurements. Fig. 4 also shows the layer order of pruning rate search process, i.e. from the layer with the highest proportion of FLOPs to that with the lowest as depicted in subsection II.D. The orders are consistent with different energy consumption constraint.

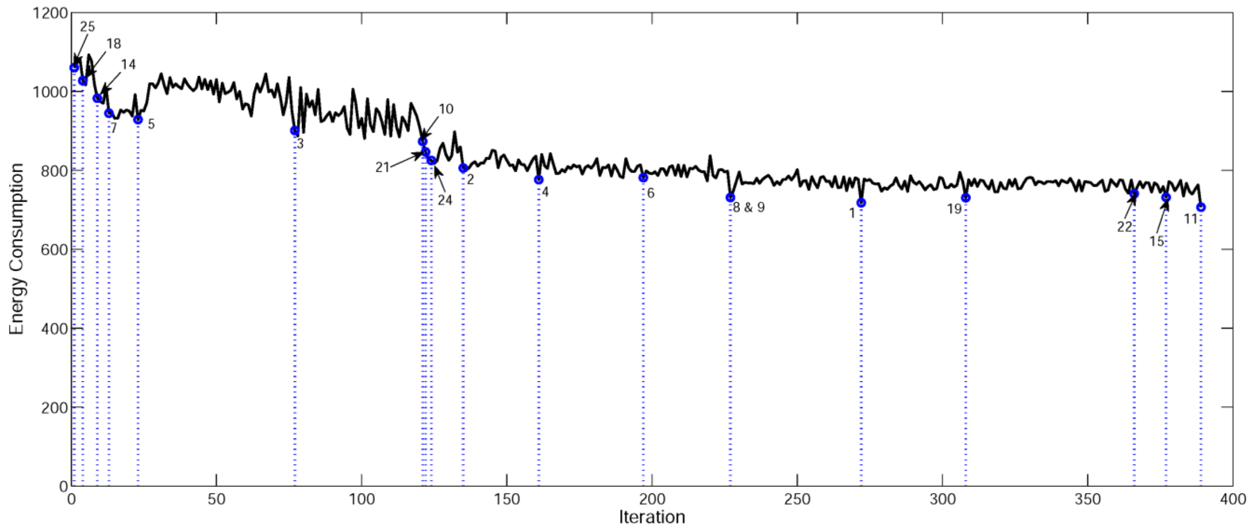

(a) Energy consumption constraint settings of 0.4

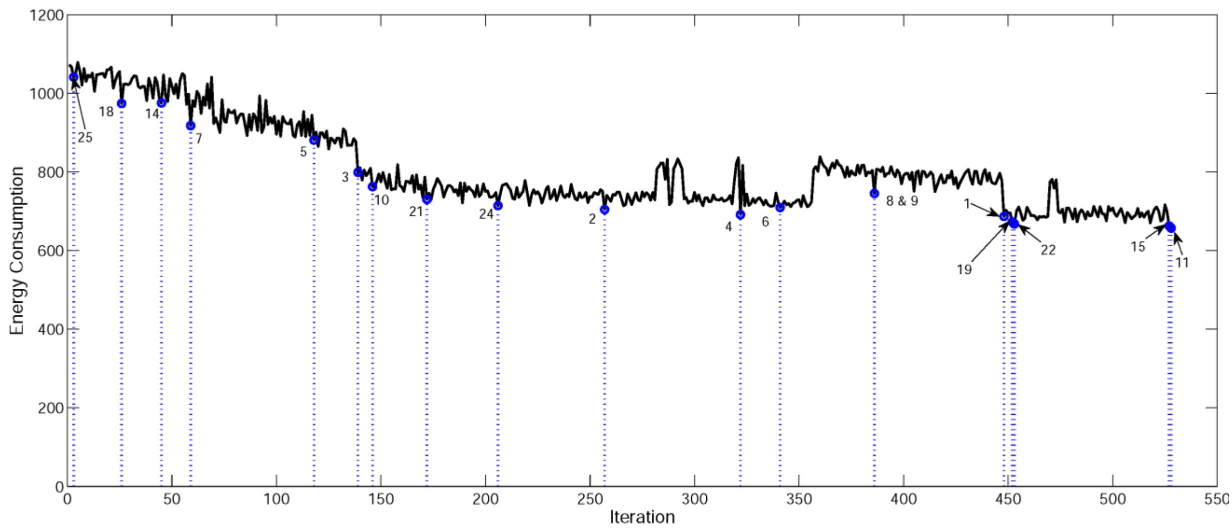

(b) Energy consumption constraint settings of 0.5

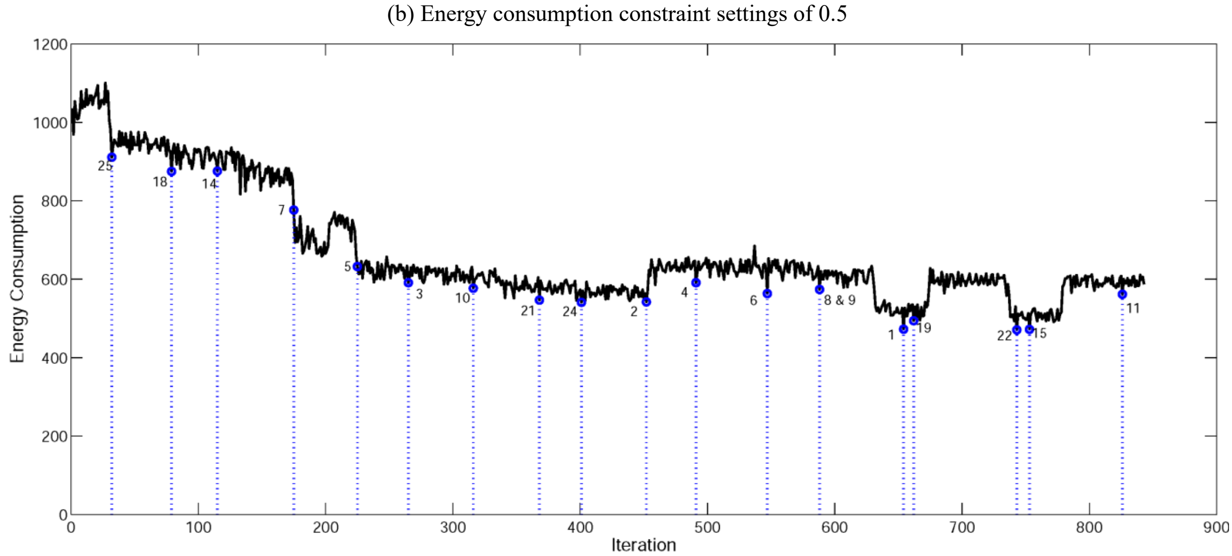

(c) Energy consumption constraint settings of 0.6

Figure 4 The consumption constraint variations during the pruning rate adjustment.

The energy consumption results under different constraint settings are also presented in Table 2. Note that YOLOv5l-G is the baseline for the settings of Energy-0.4, Energy-0.5 and Energy-0.6. The proposed energy-guided YOLOv5l-GPE with a higher energy constraint achieves a lower model size, computational complexity and energy consumption. There is a decline in detection accuracy. With the corresponding energy consumption constraint, the actual energy consumption reduction is 448.4J, 517.2J and 548.7J, which corresponds to 40.86%, 47.13% and 50% of the YOLOv5l-G. It indicates that the actual energy consumption decline is approaching the target constraint 40%, 50% and 60%. However, higher energy consumption constraint setting makes this process more difficult.

IV. CONCLUSIONS

In this paper, we propose a novel energy-constrained model pruning method for efficient in-orbit object detection in optical remote sensing images to reduce the memory, computation and energy supply requirements for resource-constrained satellite in-orbit platforms, while preserving comparable detection accuracy. It is achieved by lightweight CNN and filter pruning supported by a novel energy-guided layer-wise pruning rate estimation method. Comprehensive experiments show that compact modules and a simple L1-norm based filter pruning can achieve a minimal model size of 9.61MB (7.46×), computational complexity of 27.0 GFLOPs (8.07×) compared with the baseline YOLOv5l, with an accuracy loss of 1.7% in mAP. Considering the energy consumption further, the layer-wise pruning rates are estimated, and the energy-guided YOLOv5l-GPE leads to a lower energy consumption (40.86%-50%) approaching to the constraint.

References

[1] DONG Z, WANG M, WANG Y, ZHU Y, ZHANG Z. Object detection in high resolution remote sensing imagery based on convolutional neural networks with suitable object scale features[J]. IEEE Transactions on Geoscience and Remote Sensing, 2020, 58(3): 2104-2114.

[2] YU D, JI S. A new spatial-oriented object detection framework for remote sensing images[J]. IEEE Transactions on Geoscience and Remote Sensing, 2022, 60: 1-16.

[3] XU Z, RAO M. Multiscale information fusion-based deep learning framework for campus vehicle detection[J]. International Journal of Image and Data Fusion, 2021, 12(1): 83 - 97.

[4] LIU J, XIANG J, JIN Y, LIU R, YAN J, WANG L. Boost precision agriculture with unmanned aerial vehicle remote sensing and edge intelligence: A survey[J]. Remote Sensing, 2021, 13(21).

[5] ZHANG Z, QU Z, LIU S, LI D, CAO J, XIE G. Expandable on-board real-time edge computing architecture for luojia3 intelligent remote sensing satellite[J]. Remote Sensing, 2022, 14(15): 3596.

[6] CHENG Y, WANG D, ZHOU P, ZHANG T. Model compression and acceleration for deep neural networks: The principles, progress, and challenges[J]. IEEE Signal Processing Magazine, 2018, 35(1): 126-136.

[7] CHOUDHARY T, MISHRA V, GOSWAMI A, SARANGAPANI J. A comprehensive survey on model compression and acceleration[J]. Artificial Intelligence Review, 2020, 53(7): 5113-5155.

[8] HOWARD A G, ZHU M, CHEN B, KALENICHENKO D, WANG W, WEYAND T, ANDREETTO M, ADAM H. Mobilenets: Efficient convolutional neural networks for mobile vision applications[J]. arxiv 1704.04861, 2017.

[9] SANDLER M, HOWARD A, ZHU M L, ZHMOGINOV A, CHEN L C. Mobilenetv2: Inverted residuals and linear bottlenecks[M]. 2018.

[10] ZHANG X, ZHOU X Y, LIN M X, SUN R. Shufflenet: An extremely efficient convolutional neural network for mobile devices[M]. 2018.

[11] HOWARD A, SANDLER M, CHU G, CHEN L C, CHEN B, TAN M X, WANG W J, ZHU Y K, PANG R M, VASUDEVAN V, LE Q V, ADAM H, IEEE. Searching for mobilenetv3. 2019: 1314-1324.

[12] WU B, DAI X, ZHANG P, WANG Y, SUN F, WU Y, TIAN Y, VAJDA P, JIA Y, KEUTZER K. Fbnet: Hardware-aware

efficient convnet design via differentiable neural architecture search[J], 2019.
[13] ELSKEN T, METZEN J H, HUTTER F. Neural architecture search: A survey[J]. Journal Of Machine Learning Research, 2019, 20.
[14] HE X, ZHAO K Y, CHU X W. Automl: A survey of the state-of-the-art[J]. Knowledge-based Systems, 2021, 212.
[15] LI Z S, SUN Y R, TIAN G Z, XIE L, LIU Y, SU H Y, HE Y F. A compression pipeline for one-stage object detection model[J]. Journal of Real-Time Image Processing, 2021, 18(6): 1949-1962.
[16] MIAO T, ZENG H, YANG W, CHU B, ZOU F, REN W, CHEN J. An improved lightweight retinanet for ship detection in sar images[J]. IEEE Journal of Selected Topics in Applied Earth Observations and Remote Sensing, 2022, 15: 4667-4679.
[17] PANG Y, ZHANG Y, WANG Y, WEI X, CHEN B. Socnet: A lightweight and fine-grained object recognition network for satellite on-orbit computing[J]. IEEE Transactions on Geoscience and Remote Sensing, 2022, 60: 1-13.
[18] LI L, ZHANG S, WU J. Efficient object detection framework and hardware architecture for remote sensing images[J]. Remote Sensing, 2019, 11(20): 2376.
[19] PANG J, LI C, SHI J, XU Z, FENG H. R2-cnn: Fast tiny object detection in large-scale remote sensing images[J]. IEEE Transactions on Geoscience and Remote Sensing, 2019, 57(8): 5512-5524.
[20] HONG Q, JIANG L, ZHANG Z, JI S, GU C, MAO W, LI W, LIU T, LI B, TAN C. A lightweight model for wheat ear fusarium head blight detection based on rgb images[J]. Remote Sensing, 2022, 14(14): 3481.
[21] GUO C, WANG X, ZHONG Z, SONG J. Research advance on neural network lightweight for energy optimization[J]. Chinese Journal of Computers, 2023, 46(1): 85-102.
[22] HAN K, WANG Y, TIAN Q, GUO J, XU C, XU C. Ghostnet: More features from cheap operations[C]. Proceedings of the IEEE/CVF Conference on Computer Vision and Pattern Recognition (CVPR), 2020: 1580-1589.
[23] ZHENG Y, ZHANG D, XIE S, LU J, ZHOU J. Rotation-robust intersection over union for 3d object detection[C]. European Conference on Computer Vision, 2020: 464-480.
[24] ZHENG Z, WANG P, LIU W, LI J, YE R, REN D. Distance-iou loss: Faster and better learning for bounding box regression[C]. AAAI Conference on Artificial Intelligence, 2020: 12993-13000.
[25] XIE X, LIN J, WANG Z, WEI J. An efficient and flexible accelerator design for sparse convolutional neural networks[J]. IEEE Transactions on Circuits and Systems I-Regular Papers, 2021, 68(7): 2936-2949.
[26] LUO J-H, WU J, LIN W. Thinet: A filter level pruning method for deep neural network compression[C]. 2017 IEEE International Conference on Computer Vision(ICCV), 2017: 5068-5076.
[27] HE Y, LIU P, WANG Z, HU Z, YANG Y. Filter pruning via geometric median for deep convolutional neural networks acceleration[C]. 2019 IEEE/CVF Conference on Computer Vision and Pattern Recognition (CVPR 2019), 2019: 4335-4344.

About the authors

QIU Shaohua received the B.E. degree in remote sensing science and technology from Wuhan University, Wuhan, China, in 2011, and the M.S. and Ph.D. degree in information and communication engineering from National University of Defense Technology, Changsha, China, in 2013 and 2018, respectively. He is currently an Assistant Professor with the National Key Laboratory of Electromagnetic Energy, Naval University of Engineering, Wuhan, China. His research interests include deep learning and image analysis. (Email: qiush125@163.com)

Coverage in Cooperative LEO Satellite Networks

SHANG Bodong[1], Li Xiangyu[1], Li Caiguo[1], and Li Zhuhang[1]

Abstract—Low-earth orbit (LEO) satellite networks ignite global wireless connectivity. However, signal outages and co-channel interference limit the coverage in traditional LEO satellite networks where a single satellite provides service for a user. This paper explores the possibility of satellite cooperation in the downlink transmissions. Using tools from stochastic geometry, we model and analyze the downlink coverage of a typical user with satellite cooperation under Nakagami-m fading channels. Our model incorporates fading channels, cooperation among several satellites, satellites' density and altitude, and co-channel interference. Extensive Monte Carlo simulations are performed to validate analytical results. Simulation and numerical results suggest that coverage with LEO satellite cooperation considerably exceeds coverage without cooperation. Moreover, there are optimal satellite density and satellite altitude that maximize the coverage probability, which gives valuable network design insights.

Keywords—low earth orbit satellite, cooperative communications, coverage probability, satellite-terrestrial networks, non-terrestrial networks

.

I. INTRODUCTION

One of the fundamental goals for sixth generation (6G) networks is a radical increase in global coverage [1]. Low-earth orbit (LEO) satellites, which establish a (Corresponding author: Bodong Shang. Email: bdshang@eias.ac.cn)

B. Shang, X. Li, C. Li, and Z. Li are with Eastern Institute for Advanced Study, Eastern Institute of Technology, Ningbo 315200, China.

constellation, are expected to be densely deployed. Such non-terrestrial network (NTN) technology makes a paradigm shift in wireless connectivity where users on the earth's surface could directly access the Internet through LEO satellites [2].

NTN has attracted a lot of attention in academia and industry. In the Release 14 stage, 3GPP proposes satellite communication requirements and application prospects as a fifth generation (5G) access method. Technical discussions on NTN were held in Release 15 [3] and Release 16 [4], and standard protocol modifications began in Release 17 [5], [6]. The development of global LEO satellites continues to be hot, and many parties have participated in the wave of satellite networking, including SpaceX Starlink, Amazon Kuiper, One Web, Telesat, and other companies that have successively planned satellite launch plans for various applications in NTN.

Satellite systems have been studied in the past. In [7], the authors investigated downlink coverage and rate in the LEO satellite constellation based on the binomial point process (BPP). However, the Rayleigh fading channels were assumed in satellite-terrestrial links, which are not applicable in practical systems but tractable in analysis. In [8], a Poisson point process (PPP) model was introduced to analyze the coverage of the LEO satellite networks. However, the authors did not consider satellite cooperation by assuming that users on the earth have access to their nearest satellite, which facilitates the Laplace transform in coverage analysis. In [9], cooperation between satellite and aerial relaying links was considered, where a satellite and an unmanned aerial vehicle (UAV) assist a group of other UAVs to forward their data to a remote destination. However, [9] only considered a single satellite, and the interference

from other satellites was not incorporated. Such a single satellite model was also used in [10], where the authors derived outage probability/coverage probability and symbol error rate over satellite communication downlink channels when the users are randomly located in single beam and multibeam areas. In [11], the authors analyzed the satellite-to-airplane communication in the Terahertz band by assuming that the airplane connects to its nearest satellite. It is worth noting that the above works did not model and analyze cooperative LEO satellites in downlink joint transmissions.

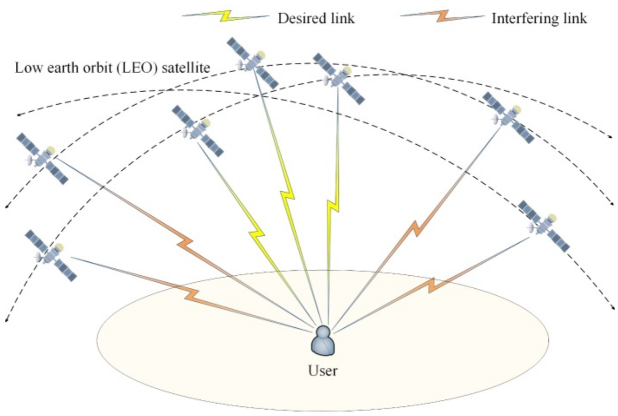

Fig. 1An illustration of cooperative LEO satellite networks

Satellite cooperation is one of the ways to increase coverage by enhancing the desired signal strength and reducing co-channel interference. The densification of LEO satellites facilitates satellite cooperation, especially for a user in remote areas with many visible satellites. In situations marked by extraordinary conditions, especially in remote regions characterized by a sparse user population but abundant satellite availability, the imperative to optimize the efficient utilization of satellite communication resources becomes evident. In pursuit of this objective, this paper introduces an innovative model that harnesses multiple satellites for transmitting identical data while employing a single-user signal reception methodology, as shown in Fig. 1. Simultaneously, it is noteworthy that typical users contend with interference from interfering satellites. Consequently, we comprehensively analyze the coverage probability within the model mentioned above. The contributions of this paper are summarized as follows.

- *Cooperative satellites modeling:* We introduce a satellite cooperation system where several nearest satellites jointly transmit data to the typical user. Moreover, we consider the large-scale distance-dependent path-loss and small-scale Nakagami-m fading in each serving and interfering link.
- *Coverage probability analysis:* We derive the coverage probability under Nakagami-m fading channels by analyzing the Laplace transform of interference and the desired signal distribution. An approximated but tractable expression of coverage probability is derived. Furthermore, the joint distance distribution of the serving satellite and the expectation of interference power are given. In addition, the coverage of two and three cooperative satellites are given, respectively.
- *Network design insights:* Simulation results demonstrate that coverage probability with satellite cooperation is significantly improved compared to that without satellite cooperation. Specifically, coverage can be enhanced by more than 100 percent when only two satellites work cooperatively.Moreover, there is an optimal combination of satellite altitude and the number of satellites that maximize the coverage probability.

II. SYSTEM MODEL

In this section, we introduce system model in cooperative LEO satellite networks.

A. NETWORK MODEL

In our analysis, we begin with the foundational assumption that both serving and interfering satellites are positioned on the surface of a sphere, characterized by a radius denoted as R_S, shown in Fig. 2. The spatial distribution of serving satellites is rigorously modeled using a homogeneous Spatial Poisson Point Process (SPPP), wherein the density parameter λ_S governs the distribution. Consequently, the set $\Phi_S = \{X_1,...,X_N\}$ represents the discrete locations of serving satellites. Here, each X_i for $i \in N$ is considered as an independent and uniformly distributed point on the surface of the sphere. The variable N signifies the number of serving satellites allocated to the typical user k, following a Poisson distribution. As a result, $|\Phi_S| = N$ .Similarly, the quantity $|\Phi_I|$ denotes the number of interfering satellites that affect the typical user k. This parameter also adheres to a Poisson distribution. Each satellite in the system operates with a transmit power represented as P_T , while the satellite transmit antenna gain is denoted by G_T . Additionally, it is essential to consider the geographical placement of a typical user on the Earth's surface, which is characterized by a radius R_E . Our model assumes that wireless transmissions to the user exclusively originate from satellites positioned above its local horizon.

We consider a typical user positioned at coordinates $(0,0,R_E)$. As illustrated in Fig.2, we define a typical spherical cap $\mathcal{A}$ that lies within the field of view at the location of the typical user. For clarity, this spherical cap signifies the section of the surface of the sphere with radius R_S that intersects with a tangent plane to the Earth. The center of this tangent plane is located at coordinates $(0,0,R_E)$. The surface area of this typical spherical cap can be written as

$$|\mathcal{A}| = 2\pi\left(R_S - R_E\right)R_S . \tag{1}$$

Moreover, we define a spherical cap $\mathcal{A}_{r_i}$ with a distance r_i from the typical receiver's location. This cap encompasses all points located within a distance less than r_i from the typical receiver's position, the surface area of $\mathcal{A}_{r_i}$ can be written as

$$\left|\mathcal{A}_{r_i}\right| = 2\pi\left(R_S - R_E - \frac{\left(R_S{}^2 - R_E{}^2\right) - r_i^2}{2R_E}\right)R_S . \tag{2}$$

We note that only the satellites on the typical spherical cap $\mathcal{A}$ are visible to the typical user.

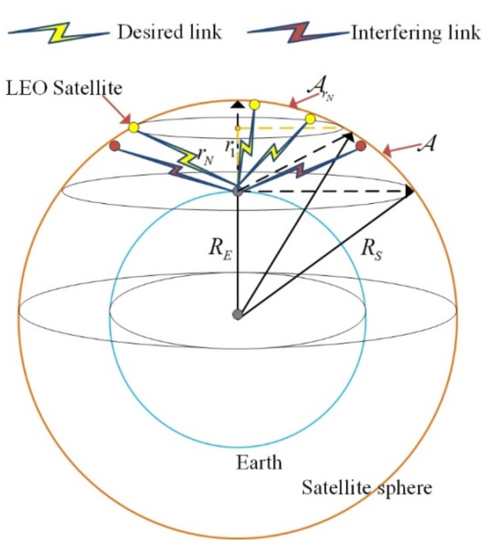

Fig.2Geometry of cooperative LEO satellites.

B. CHANNEL MODEL

The wireless channel propagation is characterized by a composite model encompassing path-loss attenuation and small-scale fading. We employ the free-space path-loss model to account for large-scale fading effects, defined as

$$\beta(r_i) = \beta_0 r_i^{-\alpha} . \tag{3}$$

In this equation, β_0 represents the path loss at a reference distance, r_i signifies the distance between the i−th nearest satellite and the typical user, and α denotes the path loss exponent. We adopt the Nakagami-m distribution to introduce the element of randomness associated with small-scale channel fading. Let h_i denote the fading coefficient between i-th nearest satellite and the typical user. We model h_i as $h_i \sim \mathrm{Nakagami}(m,\Omega)$, where $|h_i|^2 \sim \mathrm{Gamma}(k,\theta)$, with $k = m, \theta = \Omega / m$. Under the assumption of $E[|h_i|^2] = 1$, the probability density function (PDF) of h_i takes the following form,

$$f(h_i) = \frac{2m^m \cdot h_i^{2m-1}}{\Gamma(m)\cdot\Omega} \cdot e^{-\frac{mh_i^2}{\Omega}} \tag{4}$$

where $\Gamma(m)$ represents the gamma function defined as $\Gamma(m) = \int_0^\infty t^{m-1}e^{-t}dt$. The $Nakagami-m$ distribution offers versatility in modeling a wide range of small-scale fading phenomena. Notably, it converges to the Rayleigh distribution for $m=1$ and to the Rician-K distributions for $m = (K+1)^2 / (2K+1)$. The general expression for channel coefficients linking satellites and the typical user can be succinctly written as

$$g(X_i) = \sqrt{\beta_0 r_i^{-\alpha}} \cdot h_i . \tag{5}$$

C. SIGNAL MODEL AND SINR

We consider that a typical user is being served by N nearest satellites while simultaneously experiencing interference from Φ_I satellites. Accordingly, the received signal at the typical user located at $(0,0,R_E)$ is expressed as follows

$$y = \sum_{i=1}^{N} \sqrt{P_T G_T \beta_0 r_i^{-\alpha}} h_i \cdot x + I + n_0 . \tag{6}$$

Let x represent the transmitted signal originating from the serving satellites to the typical user and let I denote the interfering signal emanating from interfering satellites to the typical user. The power of the interfering signal is designated as

$$P_I = \sum_{i=1}^{|\Phi_I|} P_T G_T \beta_0 {r_{I,i}}^{-\alpha} \left|h_{I,i}\right|^2 . \tag{7}$$

where $r_{I,i}$ signifies the distance between the i-th interfering satellite and the typical user, and $h_{I,i}$ represents the small-scale fading coefficient between the i-th interfering satellite and the typical user.

The Signal-to-Interference-plus-Noise Ratio (SINR) at the typical user equipped with a single antenna is

$$\mathrm{SINR} = \frac{\left|\sum_{i=1}^{N} \sqrt{P_T G_T \beta_0 r_i^{-\alpha}}\, h_i\right|^2}{\sum_{i=1}^{|\Phi_I|} P_T G_T \beta_0 {r_{I,i}}^{-\alpha} \left|h_{I,i}\right|^2 + {\sigma_{n_0}}^2} . \tag{8}$$

where ${\sigma_{n_0}}^2$ denotes the variance of the noise.

D. COVERAGE PROBABILITY

The performance metric, in this paper, known as coverage probability, is formally defined as follows

$$\mathbb{P}_{\mathrm{cov}} = \mathbb{P}\left\{\mathrm{SINR} \geq \gamma_{th}\right\} \tag{9}$$

where γ_{th} represents the minimum SINR required for successful data transmission. In simpler terms, when the SINR of the typical user, considering both its N serving satellites and $|\Phi_I|$ interfering satellites , exceeds the threshold value γ_{th}, it is considered to be within the coverage area of the satellite communication network.

III. INTERMEDIATE RESULTS

In this section, we derive some intermediate technical results that will be used in the calculation of coverage probability in the sequel.

Lemma 1:The joint distance distribution of N nearest serving LEO satellites is shown as follows.

$$f_R(\mathbf{r}) = \prod_{i=1}^{N} 2\pi\lambda_S \frac{R_S}{R_E} \frac{e^{\pi\lambda_S \frac{R_S}{R_E}\left({R_S}^2 - {R_E}^2\right)} e^{\lambda_S\left|\mathcal{A}_{r_{i-1}}\right|}}{e^{2\pi\lambda_S R_S (R_S - R_E)} - e^{\lambda_S\left|\mathcal{A}_{r_{i-1}}\right|}} r_i e^{-\pi\lambda_S \frac{R_S}{R_E} {r_i}^2} \tag{10}$$

where $e^{\lambda_S\left|\mathcal{A}_{r_{i-1}}\right|} = e^{2\pi\lambda_S R_S (R_S - R_E)} e^{\pi\lambda_S \frac{R_S}{R_E}\left[\left({R_S}^2 - {R_E}^2\right) - {r_{i-1}}^2\right]}$.

Proof: We first derive the distribution of the two nearest satellites, then derive the distribution of the N closest satellites. The distribution of the closest satellites is given by

$$f_{R_1}(r_1) = \begin{cases} \nu(\lambda_S, R_S)\, r e^{-\lambda_S \pi \frac{R_S}{R_E} r^2}, & \text{for } R_{\min} \leq r_1 \leq R_{\max} \\ 0, & \text{otherwise} \end{cases} \tag{11}$$

where

$$\nu(\lambda_S, R_S) = 2\pi\lambda_S \frac{R_S}{R_E} \frac{\exp\left(\lambda_S \pi \frac{R_S}{R_E}\left({R_S}^2 - {R_E}^2\right)\right)}{\exp\left(2\lambda_S \pi R_S (R_S - R_E)\right) - 1},$$

$$R_{\min} = R_S - R_E, R_{\max} = \sqrt{{R_S}^2 - {R_E}^2}$$

The joint distance distribution of two nearest satellites to the typical user is expressed as

$$f_R(r_1, r_2) = f_{R_2|R_1}(r_2|r_1)\, f_{R_1}(r_1) \tag{12}$$

where $f_{R_2|R_1}(r_2|r_1)$ is the conditional distance distribution of the second nearest satellite. The complementary cumulative distribution function (CCDF) of the conditional r_2 conditioned on r_1 is given by

$$\begin{aligned}
&\mathbb{P}\left\{R > r_2 \middle| \Phi\left(\mathcal{A}/\mathcal{A}_{r_1}\right) > 0\right\} \\
&= \mathbb{P}\left\{\Phi\left(\mathcal{A}_{r_2}/\mathcal{A}_{r_1}\right) = 0 \middle| \Phi\left(\mathcal{A}/\mathcal{A}_{r_1}\right) > 0\right\} \\
&= \frac{\mathbb{P}\left\{\Phi\left(\mathcal{A}_{r_2}/\mathcal{A}_{r_1}\right) = 0, \Phi\left(\mathcal{A}/\mathcal{A}_{r_1}\right) > 0\right\}}{\mathbb{P}\left\{\Phi\left(\mathcal{A}/\mathcal{A}_{r_1}\right) > 0\right\}} \\
&= \frac{\mathbb{P}\left\{\Phi\left(\mathcal{A}_{r_2}/\mathcal{A}_{r_1}\right) = 0\right\} \mathbb{P}\left\{\Phi\left(\mathcal{A}/\mathcal{A}_{r_2}\right) > 0\right\}}{\mathbb{P}\left\{\Phi\left(\mathcal{A}/\mathcal{A}_{r_1}\right) > 0\right\}} \\
&= \frac{\mathbb{P}\left\{\Phi\left(\mathcal{A}_{r_2}/\mathcal{A}_{r_1}\right) = 0\right\}\left(1 - \mathbb{P}\left\{\Phi\left(\mathcal{A}/\mathcal{A}_{r_2}\right) = 0\right\}\right)}{\mathbb{P}\left\{\Phi\left(\mathcal{A}/\mathcal{A}_{r_1}\right) = 0\right\}} \\
&= \frac{\exp\left(-\lambda_S\left|\mathcal{A}_{r_2}/\mathcal{A}_{r_1}\right|\right) - \left(1 - \exp\left(-\lambda_S\left|\mathcal{A}/\mathcal{A}_{r_2}\right|\right)\right)}{1 - \exp\left(-\lambda_S\left|\mathcal{A}/\mathcal{A}_{r_1}\right|\right)} \\
&= \frac{\exp\left(-\lambda_S\left|\mathcal{A}_{r_2}/\mathcal{A}_{r_1}\right|\right) - \exp\left(-\lambda_S\left|\mathcal{A}/\mathcal{A}_{r_1}\right|\right)}{1 - \exp\left(-\lambda_S\left|\mathcal{A}/\mathcal{A}_{r_1}\right|\right)}
\end{aligned} \tag{13}$$

where A/B represents the area that A excludes B. The cumulative distribution function (CDF) of r_2 conditioned on r_1 is given by

$$
\begin{aligned}
&F_{R_2|\Phi(\mathcal{A}/\mathcal{A}_{r_1})>0}\left(r_2|r_1\right)\\
&=1-\mathbb{P}\left\{R>r_2\middle|\Phi\left(\mathcal{A}/\mathcal{A}_{r_1}\right)>0\right\}\\
&=\frac{1-\exp\left(-\lambda_S\left|\mathcal{A}_{r_2}/\mathcal{A}_{r_1}\right|\right)}{1-\exp\left(-\lambda_S\left|\mathcal{A}/\mathcal{A}_{r_1}\right|\right)}\\
&=\frac{1-\exp\left(-\lambda_S\left|\mathcal{A}_{r_2}\right|\right)\exp\left(\lambda_S\left|\mathcal{A}_{r_1}\right|\right)}{1-\exp\left(-\lambda_S\left|\mathcal{A}\right|\right)\exp\left(\lambda_S\left|\mathcal{A}_{r_1}\right|\right)}\\
&=\frac{e^{4\pi\lambda_S R_S\left(R_S-R_E\right)}-e^{-\pi\lambda_S\frac{R_S}{R_E}\left[r_2^2-\left(R_S^2-R_E^2\right)\right]}e^{-\pi\lambda_S\frac{R_S}{R_E}\left[r_1^2-\left(R_S^2-R_E^2\right)\right]}}{e^{4\pi\lambda_S R_S\left(R_S-R_E\right)}-e^{-\pi\lambda_S\frac{R_S}{R_E}\left[r_1^2-\left(R_S^2-R_E^2\right)\right]}}
\end{aligned}
\tag{14}
$$

and we have

$$\left|\mathcal{A}_{r_i}\right|=2\pi\left(R_S-R_E-h_{r_i}\right)R_S \tag{15}$$

where $h_{r_i}=\dfrac{\left(R_S^{\,2}-R_E^{\,2}\right)-r_i^2}{2R_E}$.

Then, the probability density function (PDF) of r_2 conditioned on r_1 is obtained by calculating the derivation of its CDF, as follows:

$$
\begin{aligned}
&f_{R_2|\Phi(\mathcal{A}/\mathcal{A}_{r_1})>0}\left(r_2|r_1\right)\\
&=\frac{\partial F_{R|\Phi(\mathcal{A}/\mathcal{A}_{r_1})>0}\left(r_2|r_1\right)}{\partial r}\\
&=\frac{\partial}{\partial r_2}\frac{1-e^{-2\pi\lambda_S R_S\left(R_S-R_E\right)}e^{-\pi\lambda_S\frac{R_S}{R_E}\left[r_2^2-\left(R_S^2-R_E^2\right)\right]}e^{\lambda_S\left|\mathcal{A}_{r_1}\right|}}{1-e^{-2\pi\lambda_S R_S\left(R_S-R_E\right)}e^{\lambda_S\left|\mathcal{A}_{r_1}\right|}}\\
&=2\pi\lambda_S\frac{R_S}{R_E}\frac{e^{\pi\lambda_S\frac{R_S}{R_E}\left(R_S^2-R_E^2\right)}}{e^{2\pi\lambda_S R_S\left(R_S-R_E\right)}-e^{\lambda_S\left|\mathcal{A}_{r_1}\right|}}e^{\lambda_S\left|\mathcal{A}_{r_1}\right|}r_2e^{-\pi\lambda_S\frac{R_S}{R_E}r_2^2}
\end{aligned}
\tag{16}
$$

Finally, the joint distribution of r_1 and r_2 is obtained as follows:

$$
\begin{aligned}
&f_R\left(r_1,r_2\right)\\
&=2\pi\lambda_S\frac{R_S}{R_E}\frac{e^{\pi\lambda_S\frac{R_S}{R_E}\left(R_S^2-R_E^2\right)}}{e^{2\pi\lambda_S R_S\left(R_S-R_E\right)}-e^{\lambda_S\left|\mathcal{A}_{r_1}\right|}}e^{\lambda_S\left|\mathcal{A}_{r_1}\right|}r_2e^{-\pi\lambda_S\frac{R_S}{R_E}r_2^2}\\
&\quad\cdot 2\pi\lambda_S\frac{R_S}{R_E}\frac{e^{\pi\lambda_S\frac{R_S}{R_E}\left(R_S^2-R_E^2\right)}}{e^{2\pi\lambda_S R_S\left(R_S-R_E\right)}-1}r_1e^{-\lambda_S\pi\frac{R_S}{R_E}r_1^2}
\end{aligned}
\tag{17}
$$

Based on the above result, we can generalize to any number N of cooperating LEO satellites. The joint distance distribution of N nearest LEO satellites is

$$f_R\left(\mathbf{r}\right)=\prod_{i=1}^{N}2\pi\lambda_S\frac{R_S}{R_E}\frac{e^{\pi\lambda_S\frac{R_S}{R_E}\left(R_S^2-R_E^2\right)}}{e^{2\pi\lambda_S R_S\left(R_S-R_E\right)}-e^{\lambda_S\left|\mathcal{A}_{r_{i-1}}\right|}}e^{\lambda_S\left|\mathcal{A}_{r_{i-1}}\right|}r_ie^{-\pi\lambda_S\frac{R_S}{R_E}r_i^2} \tag{18}$$

which completes the proof.

When the LEO satellites are densely deployed, the typical user has a high probability to observe its serving satellites. Therefore, we have a simplified expression of the joint distance distribution of N nearest LEO satellites, as shown in Lemma 2.

Lemma 2:In dense LEO satellite networks, the joint distance distribution of N nearest serving LEO satellites is approximated by

$$
\begin{aligned}
f_R\left(\mathbf{r}\right)\approx&\left(2\pi\lambda_S\frac{R_S}{R_E}\right)^N e^{-2\pi\lambda_S R_S\left(R_S-R_E\right)}e^{\pi\lambda_S\frac{R_S}{R_E}\left(R_S^2-R_E^2\right)}\\
&\cdot e^{-\pi\lambda_S\frac{R_S}{R_E}r_N^2}\prod_{i=1}^{N}r_i
\end{aligned}
\tag{19}
$$

Proof: When the LEO satellites become dense, the denominator in Lemma 1 approaches to one, and thus we have

$$
\begin{aligned}
&f_R\left(\mathbf{r}\right)\\
&\approx\left(2\pi\lambda_S\frac{R_S}{R_E}e^{-2\pi\lambda_S R_S\left(R_S-R_E\right)}e^{\pi\lambda_S\frac{R_S}{R_E}\left(R_S^2-R_E^2\right)}\right)^N\\
&\quad\cdot\prod_{i=1}^{N}e^{\lambda_S\left|\mathcal{A}_{r_{i-1}}\right|}r_ie^{-\pi\lambda_S\frac{R_S}{R_E}r_i^2}
\end{aligned}
\tag{20}
$$

Lemma 2 is obtained from (20) with some mathematical manipulations.

IV. COVERAGE PROBABILITY

Now we are in the position of deriving coverage probability of cooperative LEO satellite networks.

A. MAIN RESULTS

The coverage probability of a typical user is derived in the following.

$$
\begin{aligned}
&\mathbb{P}_{\mathrm{cov}}\left(\gamma_{th};\lambda_S,R_S,P_T,G_T,m,N\right)\\
&=\mathbb{P}\left\{\mathrm{SINR}\geq\gamma_{th}\right\}\\
&=\mathbb{P}\left\{\frac{\left|\sum_{i=1}^{N}\sqrt{P_TG_T\beta_0r_i^{-\alpha}}h_i\right|^2}{\sum_{i=1}^{|\Phi_I|}P_TG_T\beta_0r_{I,i}^{\;-\alpha}\left|h_{I,i}\right|^2+\sigma_{n_0}^{\;2}}\geq\gamma_{th}\right\}
\end{aligned}
$$

$$= \mathbb{P}\left\{\left|\sum_{i=1}^{N}\sqrt{r_i^{-\alpha}}h_i\right|^2 \geq \gamma_{th}\sum_{i=1}^{|\Phi_I|} r_{I,i}{}^{-\alpha}\left|h_{I,i}\right|^2 + \frac{\gamma_{th}\sigma_{n_0}{}^2}{P_T G_T \beta_0}\right\} \tag{21}$$

We derive the distribution of $P_S = \left|\sum_{i=1}^{N} r_i^{-\frac{\alpha}{2}} h_i\right|^2$ which is the left-hand side term of the last step of the above inequality. Since $h_i \sim \text{Nakagami}(m,\Omega)$, we obtain an upper bound of P_S shown as follows:

$$P_S = \left|\sum_{i=1}^{N} r_i^{-\frac{\alpha}{2}} h_i\right|^2 \leq \sum_{i=1}^{N} r_i^{-\alpha} \sum_{i=1}^{N} \left|h_i\right|^2 = P_S^{UP} \tag{22}$$

where $\sum_{i=1}^{N}\left|h_i\right|^2 \sim \Gamma\left(Nm, \frac{1}{m}\right)$, P_S^{UP} denotes an upper bound of P_S, and $\Gamma(a,b)$ indicates the Gamma distribution with parameters a and b.

Theorem1: The coverage probability for the typical user in a downlink cooperative LEO satellite network where N LEO satellites jointly transmit to it is given in (23) at the bottom of the page.

Proof: The coverage probability can be reformulated as

$$\begin{aligned}&\mathbb{P}\left\{P_{S,Nak}^{UP} \geq \gamma_{th}\left(\sum_{i=1}^{|\Phi_I|} r_{I,i}{}^{-\alpha}\left|h_{I,i}\right|^2 + \frac{\sigma_{n_0}{}^2}{P_T G_T \beta_0}\right)\right\} \\ &= \mathbb{P}\left\{\sum_{i=1}^{N}\left|h_i\right|^2 \geq \frac{\gamma_{th}}{\sum_{i=1}^{N} r_i^{-\alpha}}\left(\sum_{i=1}^{|\Phi_I|} r_{I,i}{}^{-\alpha}\left|h_{I,i}\right|^2 + \frac{\sigma_{n_0}{}^2}{P_T G_T \beta_0}\right)\right\}\end{aligned} \tag{24}$$

Then, we derive the Laplace transform of the summation of small-scale fading channel power gain, the Laplace transform of interference and noise power.

$$\begin{aligned}&\mathbb{P}\left\{P_{S,Nak}^{UP} \geq \gamma_{th}\left(I_{Nak}+N\right)\right\} \\ &= \int_{r_{\min}<r_1<\cdots<r_N<r_{\max}} f_R(\mathbf{r}) \int_{-\infty}^{+\infty} \mathcal{L}_{I_{Nak}}\left(2j\pi\frac{\gamma_{th}}{\sum_{i=1}^{N} r_i^{-\alpha}}s\right)\mathcal{L}_N\left(2j\pi\frac{\gamma_{th}}{\sum_{i=1}^{N} r_i^{-\alpha}}s\right)\frac{\mathcal{L}_{\sum_{i=1}^{N}|h_i|^2}(-2j\pi s)-1}{2j\pi s}ds d\mathbf{r} \\ &= \int_{r_{\min}<r_1<\cdots<r_N<r_{\max}} f_R(\mathbf{r}) \int_{-\infty}^{+\infty} \mathcal{L}_{I_{Nak}}\left(2j\pi\frac{\gamma_{th}}{\sum_{i=1}^{N} r_i^{-\alpha}}s\right)\exp\left(-2j\pi\frac{\gamma_{th}}{\sum_{i=1}^{N} r_i^{-\alpha}}s\frac{\sigma_{n_0}{}^2}{P_T G_T \beta_0}\right)\frac{1}{2j\pi s}\left(\frac{1}{\left(1+\frac{-2j\pi s}{m}\right)^{Nm}}-1\right)ds d\mathbf{r}\end{aligned} \tag{25}$$

$$\text{where } I_{Nak} = \sum_{i=1}^{|\Phi_I|} r_{I,i}{}^{-\alpha}\left|h_{I,i}\right|^2, N = \frac{\sigma_{n_0}{}^2}{P_T G_T \beta_0}, \mathcal{L}_N(s) = \mathbb{E}\left\{e^{-s\frac{\sigma_{n_0}{}^2}{P_T G_T \beta_0}}\right\} = e^{-s\frac{\sigma_{n_0}{}^2}{P_T G_T \beta_0}}, \mathcal{L}_{\sum_{i=1}^{N}|h_i|^2}(s) = \frac{1}{\left(1+\frac{s}{m}\right)^{Nm}}$$

By utilizing the Laplace transform, the coverage probability is given in (25) at the top of this page. In the following, we derive the Laplace transform of the interference power in (26).

$$\begin{aligned}&\mathcal{L}_{I_{Nak}}(s) \\ &= \mathbb{E}_{\Phi_I,h}\left\{\exp\left(-sI_{Nak}\right)\right\} \\ &= \mathbb{E}_{\Phi_I}\left\{\prod_{i=1}^{|\Phi_I|}\mathbb{E}_h\left\{\exp\left(-sr_{I,i}{}^{-\alpha}\left|h_{I,i}\right|^2\right)\right\}\right\} \\ &= \mathbb{E}_{\Phi_I}\left\{\prod_{i=1}^{|\Phi_I|}\frac{1}{\left(1+\frac{sr_{I,i}{}^{-\alpha}}{m}\right)^m}\right\} \\ &= \exp\left(-\lambda_S\int_{r\in\mathcal{A}_I} 1-\frac{1}{\left(1+\frac{sr^{-\alpha}}{m}\right)^m}dr\right) \\ &= \exp\left(-2\pi\lambda_S\frac{R_S}{R_E}\int_{r_{\min}}^{r_{\max}}\left[1-\frac{1}{\left(1+\frac{sr^{-\alpha}}{m}\right)^m}\right]rdr\right) \\ &= \exp\left(-2\pi\lambda_S\frac{R_S}{R_E}m^{-\frac{2}{\alpha}}s^{\frac{2}{\alpha}}\int_{\left(\frac{s}{m}\right)^{-\frac{2}{\alpha}}r_{\min}{}^2}^{\left(\frac{s}{m}\right)^{-\frac{2}{\alpha}}r_{\max}{}^2} 1-\frac{1}{\left(1+u^{-\frac{2}{\alpha}}\right)^m}du\right)\end{aligned} \tag{26}$$

where $r_{\min} = R_S - R_E, r_{\max} = \sqrt{R_S^2 - R_E^2}$.

By substituting (26) to (25), we obtain the desired results, which completes the proof.

In Theorem 1, we give an analytical expression of coverage probability for the typical user based on Laplace transform. However, Theorem 1 involves multiple integrals which reduces the analytical tractability. In the following Theorem, we give an approximated coverage probability based on the fading distribution which is simple and concise.

Theorem2:An approximated coverage probability for the typical user in a downlink cooperative LEO satellite network where N LEO satellites jointly transmit to it is given by

$$\mathbb{P}_{\text{cov}} \approx 1-\frac{\left(2\pi\lambda_S \frac{R_S}{R_E}\right)^N}{\Gamma(Nm)} \cdot \exp\left(\pi\lambda_S \frac{R_S}{R_E}\left(R_S{}^2-R_E{}^2\right)-2\pi\lambda_S R_S\left(R_S-R_E\right)\right) \cdot \int\limits_{r_{\min}<r_1<\cdots<r_N<r_{\max}} \gamma\left(Nm, \frac{\gamma_{th} m\left(\tilde{I}_{Nak}+\frac{\sigma_{n_0}{}^2}{P_T G_T \beta_0}\right)}{\sum_{i=1}^{N} r_i^{-\alpha}}\right) \frac{\prod_{i=1}^{N} r_i}{e^{\pi\lambda_S \frac{R_S}{R_E} r_N{}^2}} d\mathbf{r} \tag{27}$$

where $\tilde{I}_{Nak}=\Omega 2\pi\lambda_S \frac{R_S}{R_E}\int_{r_{\min}}^{r_{\max}}\int_{r_N}^{r_{\max}} r^{1-\alpha} f_{R_N}\left(r_N\right) dr dr_N$ is the average interference power received at the typical user, $f_{R_N}\left(r_N\right)$ is the marginal PDF of r_N which is given by

$$f_{R_N}\left(r_N\right)=\int\limits_{r_{\min}<r_1<\cdots<r_{N-1}<r_{\max}} f_R(\mathbf{r}) d\mathbf{r} = \int\limits_{r_{\min}<r_1<\cdots<r_{N-1}<r_{\max}} \prod_{i=1}^{N} 2\pi\lambda_S \frac{R_S}{R_E} \frac{e^{\pi\lambda_S \frac{R_S}{R_E}\left(R_S{}^2-R_E{}^2\right)} e^{\lambda_S\left|\mathcal{A}_{i-1}\right|}}{e^{2\pi\lambda_S R_S\left(R_S-R_E\right)}-e^{\lambda_S\left|\mathcal{A}_{i-1}\right|}} r_i e^{-\pi\lambda_S \frac{R_S}{R_E} r_i{}^2} d\mathbf{r} \tag{28}$$

Proof: The coverage probability for a typical user is derived in (29) at the top of this page. In the first step of (29), we use the upper bound of the desired signal power under Nakagami-m fading channel, where, in (a), we use the incomplete Gamma function to represent the distribution of sum of small-scale channel power gain, in (b), we use the joint distance distribution function which is obtain in Lemma 1 and Lemma 2 to average the distance between serving satellites and the typical user, in (c), we calculate the average interference directly to achieve an approximated coverage probability.

$$\begin{aligned}
&\mathbb{P}_{\text{cov}}\left(\gamma_{th};\lambda_S, R_S, P_T, G_T, m, N\right) \\
&\le \mathbb{P}\left\{\sum_{i=1}^{N} r_i^{-\alpha}\sum_{i=1}^{N}\left|h_i\right|^2 \ge \gamma_{th}\sum_{i=1}^{\left|\Phi_I\right|} r_{I,i}{}^{-\alpha}\left|h_{I,i}\right|^2+\frac{\gamma_{th}\sigma_{n_0}{}^2}{P_T G_T \beta_0}\right\} \\
&=\mathbb{P}\left\{\sum_{i=1}^{N}\left|h_i\right|^2 \ge \frac{\gamma_{th}}{\sum_{i=1}^{N} r_i^{-\alpha}}\left(\sum_{i=1}^{\left|\Phi_I\right|} r_{I,i}{}^{-\alpha}\left|h_{I,i}\right|^2+\frac{\sigma_{n_0}{}^2}{P_T G_T \beta_0}\right)\right\} \\
&\overset{(a)}{=}1-\mathbb{E}_{N,I}\left\{\frac{1}{\Gamma(Nm)}\gamma\left(Nm, \gamma_{th} m \frac{1}{\sum_{i=1}^{N} r_i^{-\alpha}}\left(\sum_{i=1}^{\left|\Phi_I\right|} r_{I,i}{}^{-\alpha}\left|h_{I,i}\right|^2+\frac{\sigma_{n_0}{}^2}{P_T G_T \beta_0}\right)\right)\right\} \\
&\overset{(b)}{=}1-\frac{1}{\Gamma(Nm)}\int\limits_{r_{\min}<r_1<\cdots<r_N<r_{\max}} \mathbb{E}_I\left\{\gamma\left(Nm, \gamma_{th} m \frac{1}{\sum_{i=1}^{N} r_i^{-\alpha}}\left(\sum_{i=1}^{\left|\Phi_I\right|} r_{I,i}{}^{-\alpha}\left|h_{I,i}\right|^2+\frac{\sigma_{n_0}{}^2}{P_T G_T \beta_0}\right)\right)\right\} f_R(\mathbf{r}) d\mathbf{r} \\
&\overset{(c)}{\approx}1-\frac{1}{\Gamma(Nm)}\int\limits_{r_{\min}<r_1<\cdots<r_N<r_{\max}} \gamma\left(Nm, \gamma_{th} m \frac{1}{\sum_{i=1}^{N} r_i^{-\alpha}}\left(\tilde{I}_{Nak}+\frac{\sigma_{n_0}{}^2}{P_T G_T \beta_0}\right)\right) f_R(\mathbf{r}) d\mathbf{r}
\end{aligned} \tag{29}$$

Note that the average interference power is obtained by using Campell theorem and averaging on r_N , which is shown as follows:

$$
\begin{aligned}
\tilde{I}_{Nak} &= \mathbb{E}\left\{\sum_{i=1}^{|\Phi_I|} r_{I,i}{}^{-\alpha}\left|h_{I,i}\right|^2\right\} \\
&= \mathbb{E}\left\{\left|h_{I,i}\right|^2\right\}\mathbb{E}\left\{\sum_{i=1}^{|\Phi_I|} r_{I,i}{}^{-\alpha}\right\} \\
&= \Omega\mathbb{E}_{r_N}\left\{\lambda_S\frac{\partial|\mathcal{A}_r|}{\partial r}\int_{r_N}^{r_{\max}} r^{-\alpha}dr\right\} \\
&= \Omega 2\pi\lambda_S\frac{R_S}{R_E}\int_{r_{\min}}^{r_{\max}}\int_{r_N}^{r_{\max}} r^{1-\alpha} f_{R_N}\left(r_N\right)dr dr_N
\end{aligned}
\tag{30}
$$

where $f_{R_N}\left(r_N\right)$ is given in (28) which is obtained from the joint distance distribution. After some mathematical manipulations, we obtain the desired results in (27), which completes the proof.

B. PARTICULAR CASES

In this subsection, we derive some valid but closed-form technical results in particular cases.

Corollary1:If $N=2$, the coverage probability for the typical user in a downlink cooperative LEO satellite network where two LEO satellites jointly transmit to it is expressed as

$$
\begin{aligned}
\tilde{I}_{Nak} &= 2\pi\lambda_S\frac{R_S}{R_E}2\left(\pi\lambda_S\frac{R_S}{R_E}\right)^2 e^{-2\pi\lambda_S R_S\left(R_S-R_E\right)}e^{\pi\lambda_S\frac{R_S}{R_E}\left(R_S{}^2-R_E{}^2\right)}\int_{r_{\min}}^{r_{\max}} r_2 e^{-\pi\lambda_S\frac{R_S}{R_E}r_2{}^2}\left(r_2{}^2-\left(R_S-R_E\right)^2\right)\int_{r_2}^{r_{\max}} r^{1-\alpha}dr dr_2 \\
&= \frac{4}{\alpha-2}\left(\pi\lambda_S\frac{R_S}{R_E}\right)^3 e^{-2\pi\lambda_S R_S\left(R_S-R_E\right)}e^{\pi\lambda_S\frac{R_S}{R_E}\left(R_S{}^2-R_E{}^2\right)}\int_{r_{\min}}^{r_{\max}} r_2 e^{-\pi\lambda_S\frac{R_S}{R_E}r_2{}^2}\left(r_2{}^2-\left(R_S-R_E\right)^2\right)\left(r_2{}^{2-\alpha}-r_{\max}{}^{2-\alpha}\right)dr_2 \\
&= \frac{4}{\alpha-2}\left(\pi\lambda_S\frac{R_S}{R_E}\right)^3 e^{-2\pi\lambda_S R_S\left(R_S-R_E\right)}e^{\pi\lambda_S\frac{R_S}{R_E}\left(R_S{}^2-R_E{}^2\right)}\left[\int_{r_{\min}}^{r_{\max}} r_2 e^{-\pi\lambda_S\frac{R_S}{R_E}r_2{}^2}\left(r_2{}^{4-\alpha}-r_2{}^{2-\alpha}\left(R_S-R_E\right)^2-r_{\max}{}^{2-\alpha}r_2{}^2+r_{\max}{}^{2-\alpha}\left(R_S-R_E\right)^2\right)dr_2\right] \\
&= \frac{4}{\alpha-2}\left(\pi\lambda_S\frac{R_S}{R_E}\right)^3 e^{-2\pi\lambda_S R_S\left(R_S-R_E\right)}e^{\pi\lambda_S\frac{R_S}{R_E}\left(R_S{}^2-R_E{}^2\right)}
\left[\begin{array}{l}
\dfrac{\gamma\left(3-\frac{\alpha}{2},\pi\lambda_S\frac{R_S}{R_E}r_{\max}{}^2\right)-\gamma\left(3-\frac{\alpha}{2},\pi\lambda_S\frac{R_S}{R_E}r_{\min}{}^2\right)}{2\left(\pi\lambda_S\frac{R_S}{R_E}\right)^{3-\frac{\alpha}{2}}} \\
-\dfrac{\left(R_S-R_E\right)^2}{2\left(\pi\lambda_S\frac{R_S}{R_E}\right)^{2-\frac{\alpha}{2}}}\left(\gamma\left(2-\frac{\alpha}{2},\pi\lambda_S\frac{R_S}{R_E}r_{\max}{}^2\right)-\gamma\left(2-\frac{\alpha}{2},\pi\lambda_S\frac{R_S}{R_E}r_{\min}{}^2\right)\right) \\
-\dfrac{r_{\max}{}^{2-\alpha}}{2\left(\pi\lambda_S\frac{R_S}{R_E}\right)^2}\left(\gamma\left(2,\pi\lambda_S\frac{R_S}{R_E}r_{\max}{}^2\right)-\gamma\left(2,\pi\lambda_S\frac{R_S}{R_E}r_{\min}{}^2\right)\right) \\
+\dfrac{r_{\max}{}^{2-\alpha}\left(R_S-R_E\right)^2}{2\pi\lambda_S\frac{R_S}{R_E}}\left(\gamma\left(1,\pi\lambda_S\frac{R_S}{R_E}r_{\max}{}^2\right)-\gamma\left(1,\pi\lambda_S\frac{R_S}{R_E}r_{\min}{}^2\right)\right)
\end{array}\right]
\end{aligned}
\tag{34}
$$

$$
\begin{aligned}
&\mathbb{P}_{\mathrm{cov}}\left(\gamma_{th};\lambda_S,R_S,P_T,G_T,m,N=2\right) \\
&\approx 1-\frac{\left(2\pi\lambda_S\frac{R_S}{R_E}\right)^2}{\Gamma\left(2m\right)} \\
&\cdot\exp\left(\pi\lambda_S\frac{R_S}{R_E}\left(R_S{}^2-R_E{}^2\right)-2\pi\lambda_S R_S\left(R_S-R_E\right)\right) \\
&\cdot\int_{r_{\min}}^{r_{\max}}\int_{r_{\min}}^{r_2} r_1 r_2 e^{-\pi\lambda_S\frac{R_S}{R_E}r_2{}^2} \\
&\gamma\left(2m,\frac{\gamma_{th}m\left(\tilde{I}_{Nak}+\frac{\sigma_{n_0}{}^2}{P_T G_T\beta_0}\right)}{\left(r_1{}^{-\alpha}+r_2{}^{-\alpha}\right)}\right)dr_1 dr_2
\end{aligned}
\tag{31}
$$

Proof: When $N=2$, the joint distance distribution is

$$
f_R\left(r_1,r_2\right)=
\left(2\pi\lambda_S\frac{R_S}{R_E}\right)^2 e^{-2\pi\lambda_S R_S\left(R_S-R_E\right)}e^{\pi\lambda_S\frac{R_S}{R_E}\left(R_S{}^2-R_E{}^2\right)}r_1 r_2 e^{-\pi\lambda_S\frac{R_S}{R_E}r_2{}^2}
\tag{32}
$$

Thus, the PDF of r_2 is derived as follows:

$$
\begin{aligned}
f_{R_2}\left(r_2\right) &= \int_{r_{\min}}^{r_2} f_R\left(r_1,r_2\right)dr_1 \\
&= \left(2\pi\lambda_S\frac{R_S}{R_E}e^{-2\pi\lambda_S R_S\left(R_S-R_E\right)}e^{\pi\lambda_S\frac{R_S}{R_E}\left(R_S{}^2-R_E{}^2\right)}\right)^2 \\
&\quad\cdot r_2 e^{-\pi\lambda_S\frac{R_S}{R_E}r_2{}^2}\int_{r_{\min}}^{r_2} e^{\lambda_S|\mathcal{A}_1|}r_1 e^{-\pi\lambda_S\frac{R_S}{R_E}r_1{}^2}dr_1
\end{aligned}
$$

$$
\begin{aligned}
&= 2\left(\pi\lambda_S \frac{R_S}{R_E}\right)^2 r_2 e^{-\pi\lambda_S \frac{R_S}{R_E} r_2^2} e^{-2\pi\lambda_S R_S (R_S - R_E)} \\
&\quad \cdot e^{\pi\lambda_S \frac{R_S}{R_E}\left(R_S^2 - R_E^2\right)} \left(r_2^2 - \left(R_S - R_E\right)^2\right)
\end{aligned}
\tag{33}
$$

where $e^{\lambda_S |\mathcal{A}_{r_1}|} = e^{2\pi\lambda_S R_S (R_S - R_E)} e^{-\pi\lambda_S \frac{R_S}{R_E}\left(R_S^2 - R_E^2\right)} e^{\pi\lambda_S \frac{R_S}{R_E} r_1^2}$

By substituting the PDF of r_2 to the expression of average interference power, we obtain the closed-form interference power for $N = 2$, shown in (34) at the top of this page. It is worth noting that the average interference power incorporating lower incomplete Gamma functions which can be calculated efficiently.

Substituting (33) and (34) into (29), we can express (31), which completes the proof.

Corollary2: If $N = 3$, the coverage probability for the typical user in a downlink cooperative LEO satellite network where three LEO satellites jointly transmit to it is expressed as

$$
\begin{aligned}
&\mathbb{P}_{\mathrm{cov}}\left(\gamma_{th}; \lambda_S, R_S, P_T, G_T, m, N = 3\right) \\
&\approx 1 - \frac{\left(2\pi\lambda_S \frac{R_S}{R_E}\right)^3}{\Gamma(3m)} \\
&\quad \cdot \exp\left(\pi\lambda_S \frac{R_S}{R_E}\left(R_S^2 - R_E^2\right) - 2\pi\lambda_S R_S \left(R_S - R_E\right)\right) \\
&\quad \cdot \int_{r_{\min}}^{r_{\max}} \int_{r_{\min}}^{r_3} \int_{r_{\min}}^{r_2} r_1 r_2 r_3 e^{-\pi\lambda_S \frac{R_S}{R_E} r_3^2} \\
&\quad \cdot \gamma\left(3m, \frac{\gamma_{th} m \left(\tilde{I}_{Nak} + \frac{\sigma_{n_0}^2}{P_T G_T \beta_0}\right)}{\left(r_1^{-\alpha} + r_2^{-\alpha} + r_3^{-\alpha}\right)}\right) dr_1 dr_2 dr_3
\end{aligned}
\tag{35}
$$

Proof: When $N = 3$, the joint distance distribution is

$$
\begin{aligned}
&f_R\left(r_1, r_2, r_3\right) \\
&= \left(2\pi\lambda_S \frac{R_S}{R_E}\right)^3 e^{-2\pi\lambda_S R_S (R_S - R_E)} e^{\pi\lambda_S \frac{R_S}{R_E}\left(R_S^2 - R_E^2\right)} r_1 r_2 r_3 e^{-\pi\lambda_S \frac{R_S}{R_E} r_3^2}
\end{aligned}
\tag{36}
$$

Thus, the PDF of r_3 is derived as follows:

$$
f_{R_3}\left(r_3\right) = \int_{r_{\min}}^{r_3} \int_{r_{\min}}^{r_2} f_R\left(r_1, r_2, r_3\right) dr_1 dr_2
$$

$$
\begin{aligned}
&= \left(2\pi\lambda_S \frac{R_S}{R_E}\right)^3 e^{-2\pi\lambda_S R_S (R_S - R_E)} e^{\pi\lambda_S \frac{R_S}{R_E}\left(R_S^2 - R_E^2\right)} \\
&\quad \cdot r_3 e^{-\pi\lambda_S \frac{R_S}{R_E} r_3^2} \int_{r_{\min}}^{r_3} \int_{r_{\min}}^{r_2} r_1 r_2 dr_1 dr_2 \\
&= \left(\pi\lambda_S \frac{R_S}{R_E}\right)^3 e^{-2\pi\lambda_S R_S (R_S - R_E)} e^{\pi\lambda_S \frac{R_S}{R_E}\left(R_S^2 - R_E^2\right)} \\
&\quad \cdot r_3 e^{-\pi\lambda_S \frac{R_S}{R_E} r_3^2} \left(r_3^4 - 2r_{\min}^2 r_3^2 + r_{\min}^4\right)
\end{aligned}
\tag{37}
$$

The average interference power at the typical user is

$$
\begin{aligned}
\tilde{I}_{Nak} &= \frac{2\left(\pi\lambda_S \frac{R_S}{R_E}\right)^4}{\alpha - 2} e^{-2\pi\lambda_S R_S (R_S - R_E)} e^{\pi\lambda_S \frac{R_S}{R_E}\left(R_S^2 - R_E^2\right)} \\
&\quad \cdot \int_{r_{\min}}^{r_{\max}} r_3 e^{-\pi\lambda_S \frac{R_S}{R_E} r_3^2} \\
&\quad \cdot \left(r_3^4 - 2r_{\min}^2 r_3^2 + r_{\min}^4\right)\left(r_3^{2-\alpha} - r_{\max}^{2-\alpha}\right) dr_3
\end{aligned}
\tag{38}
$$

Substituting (37) and (38) into (29), we can express (35), which completes the proof.

We have completed main results of this paper, i.e., the derivation of coverage probability for a typical user with LEO satellites cooperation under Nakagami-m fading channels. By setting different m values such as $m = 1$ and $m = \infty$ in the expressions, we can obtain the coverage probabilities for Rayleigh and no-fading cases, respectively.

IV.SIMULATION AND NUMERICAL RESUTLS

In this section, we numerically evaluate and validate the coverage probability against important parameters for the typical user in cooperative LEO satellites, including altitude, Nakagami fading parameter m, number of cooperative satellites and total number of satellites. In addition, we also illuminate a trade-off between the desired signal power and the interference signal power under the impacts of the number of satellites and the altitude of satellites.

We do Monte Carlo simulations in MATLAB for the comparison of the simulation and analysis results. As is shown in Fig. 3, we first depict a 3D diagram for LEO satellite networks. The users and LEO satellites are respectively distributed on the earth surface sphere and satellite orbit sphere independently, according to homogeneous SPPP with different densities.

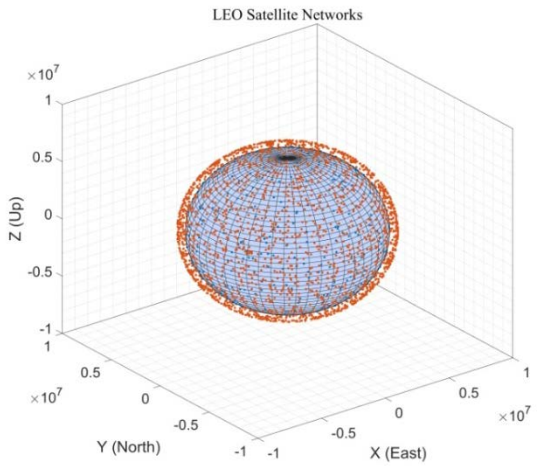

Fig. 3An illustration of simulation scenario.

In simulations, we set R_E =6372 km, the path loss exponent α =2.1, the density of LEO satellites λ_S =1e-12 $/m^2$, the Nakagami-m fading parameters Ω =1, m =2, transmit power at the LEO satellite P_T =1 Watt, transmit antenna gain G_T =30 dBi, unless specified otherwise.

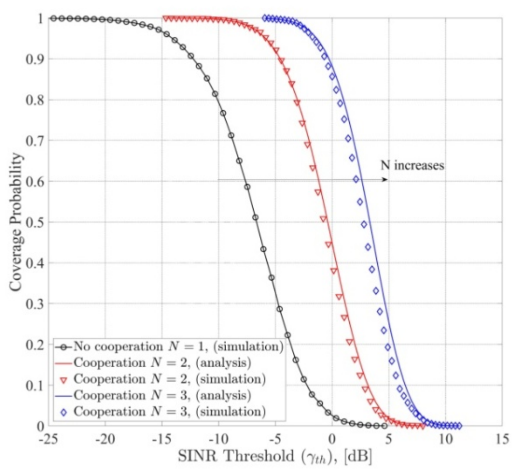

Fig. 4 Coverage probability versus the SINR threshold under different numbers of serving satellites, where $m = 2$.

Taking into account the impact of the serving satellite number, Fig. 4 shows the coverage probability under different numbers of serving satellites, compared with traditional no-cooperation scenario. It is found that with the increase of serving satellite number, the coverage probability of cooperate LEO satellite networks becomes higher under the given SINR threshold.

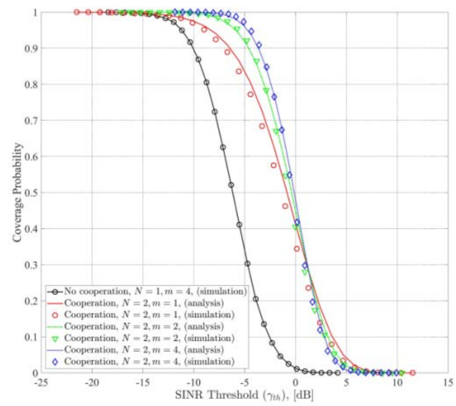

Fig. 5 Coverage probability versus the SINR threshold under different Nakagami fading parameters m .

Fig. 5 compares the coverage probability under different Nakagami fading parameter m. It is clear that the case of m=4 outperforms other cooperation counterparts when the SINR threshold is lower than 1 dB; however, its coverage probability drops fastest as SINR threshold increases, thus it is surpassed by that of other cases. Note that no-operation case falls far behind the cooperation cases.

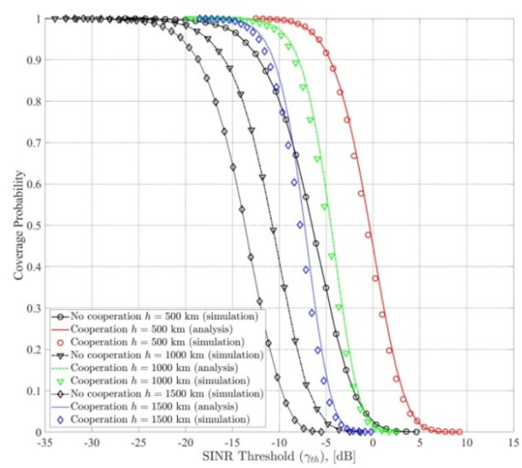

Fig. 6 Coverage probability versus the SINR threshold under different altitudes of satellites, where $N = 2$, $m = 2$.

The impact of satellite altitudes on the coverage probability of cooperative LEO satellite networks is compared in Fig. 6. It is revealed that for both cooperative and non-cooperative scenarios, the coverage probability increases with the altitude; however, for the same altitude, the cooperative case enjoy apparently higher coverage probability than it opposite non-cooperative case. This is because with a lower altitude, the increase of desired signal power dominates the increase of interference power, resulting in the improvement of SINR and coverage probability.

In the case of serving satellite quantity is $N = 2$, Nakagami fading parameter is $m = 2$, and the SINR threshold being -3dB, we conducted a comparative analysis of coverage probability concerning satellite altitude across varying satellite quantities, both with and without satellite cooperation. This analysis aimed to substantiate that the implementation of LEO satellite cooperation significantly enhances downlink coverage, surpassing the coverage achievable in the absence of cooperation.

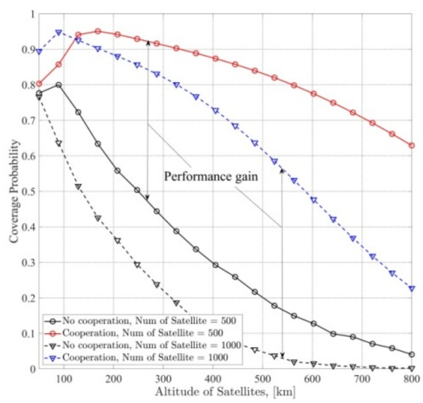

Fig. 7 Coverage probability versus the altitude of satellites with different SINR thresholds, where $N = 2$, $m = 2$, $\gamma_{th} = -3$ dB.

Fig. 7 provides a comparative assessment, elucidating the coverage probability in situations involving satellite cooperation (indicated by colored lines) versus non-cooperation (depicted by black lines) with respect to satellite quantities of 500 (represented by lines with circles) and 1000 (indicated by lines with triangles). The visual evidence gleaned from the figure unequivocally highlights that the collaborative transmission of data among serving satellites leads to a substantial enhancement in coverage probability for ground user, as opposed to scenarios where such cooperation is lacking. This performance improvement is conspicuously discernible within the graphical representation.

Furthermore, upon examining the scenario of non-cooperation among satellites in Fig. 7, denoted by the black line with circles as opposed to the black line with triangles, we can deduce that a smaller satellite number exhibits a higher coverage probability. This observation also holds true in the context of cooperation among serving satellites. This is because the network with a smaller satellite number has a lower co-channel interference power than the network with a high satellite number, and thus it is beneficial to the coverage.

Moreover, in instances where satellites do not engage in cooperative behavior, there is a noticeable decline in coverage probability with increasing satellite altitude. Upon closer examination of the blue and red lines depicted in Fig. 7, it becomes evident that even when satellites cooperate, the coverage probability experiences a decline as satellite altitude rises. However, it is noteworthy that slight increments are observed when satellite altitude remains below 150 km. This is because that when the satellite altitude is very low, the typical user could not always see the sufficient serving satellites for cooperation. When the satellite altitude is very high, the desired signal power decreases due to the increased distance-dependent large-scale fading. Therefore, there is an optimal satellite altitude given the number of satellite.

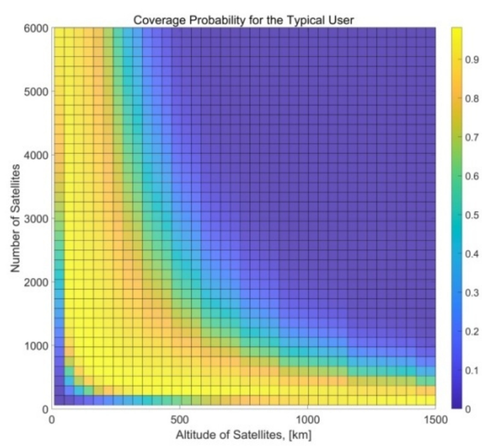

Fig. 8 Coverage probability versus the altitude of satellites and the number of satellites, where $N = 2$, $m = 2$, $\gamma_{th} = -5$ dB.

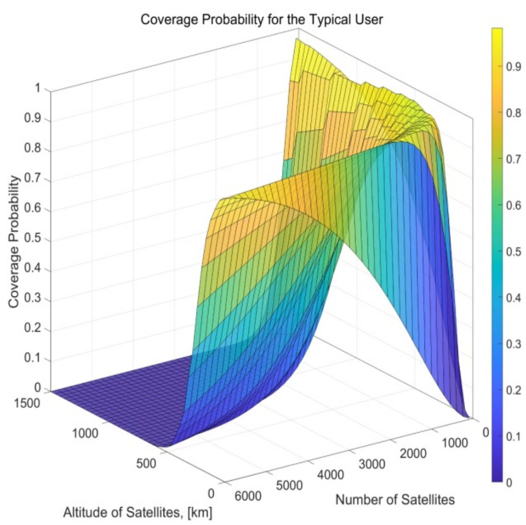

Fig. 9 Coverage probability versus the altitude of satellites and the number of satellites in a 3D plot, where $N=2$, $m=2$, $\gamma_{th}=-5$ dB.

In Fig. 8 and Fig. 9, we exam the coverage probability versus the number of satellites and the altitude of satellites in 2D and 3D views, respectively. We observe that there is an optimal combination of the number of satellites and satellite altitude, which gives system design insights. The reasons behind this are as follows.Regardingsatellite altitude, there is a trade-off between the probability of seeing sufficient serving satellites in cooperation and the desired signal power at the typical user. Regarding the number of satellites, there is a trade-off between the distance-dependent path loss (or the desired signal power) and the interference power from other satellites.

Moreover, we observe from Fig. 8 and Fig. 9 that when deploying dense LEO satellites for satellite-terrestrial communications, it is better to reduce the satellite altitude. This is because for densification of satellites, reducing satellite altitude deceases the number of interfering satellites for the typical user and increases the desired signal power. This guided us to seize the low-earth orbit.

V. CONCLUSIONS

In this paper, we proposed and modelled a novel satellite cooperation system which incorporates several nearest satellites to provide services to the typical user. Considering the satellite altitude, Nakagami fading channels, the number of serving satellites and all visible satellites, and other related parameters, we derived approximated but tractable and closed-form expressions for the coverage probability of the satellite cooperation system. It was shown that in the satellite cooperation system, the increase of cooperative satellite number significantly brought about larger coverage for the typical user, significantly surpassing that in non-cooperative satellite downlink transmission system. Specifically, there is a trade-off between the desired signal power and the interference signal power brought by the total number and the altitude of satellites.

References

[1] D. Zhou, M. Sheng, J. Li and Z. Han, “Aerospace Integrated Networks Innovation for Empowering 6G: A Survey and Future Challenges,” in IEEE Communications Surveys & Tutorials, Feb. 2023.

[2] B. Shang, Y. Yi, and L. Liu, “Computing over space-air-ground integrated networks: Challenges and opportunities,” IEEE Network, vol. 35, no. 4, pp. 302–309, 2021.

[3] Technical Specification Group Radio Access Network; Study on New Radio (NR) to support non-terrestrial networks (Release 15), document 3GPP TR 38.811 V15.4.0, 3rd Generation Partnership Project, Sep. 2020.

[4] Technical Specification Group Radio Access Network; Solutions for NR to support non-terrestrial networks (NTN) (Release 16), document 3GPP TR 38.821 V16.1.0, 3rd Generation Partnership Project, May. 2021.

[5] Technical Specification Group Radio Access Network; Study on Narrow-Band Internet of Things (NB-IoT) / enhanced Machine Type Communication (eMTC) support for Non-Terrestrial Networks (NTN) (Release 17), document 3GPP TR 36.763 V17.0.0, 3rd Generation Partnership Project, Jun. 2021.

[6] Technical Specification Group Radio Access Network; Solutions for NR to support non-terrestrial networks (NTN): Non-terrestrial networks (NTN) related RF and co-existence aspects (Release 17), document 3GPP TR 38.863 V17.0.0, 3rd Generation Partnership Project, Mar. 2022.

[7] N. Okati, T. Riihonen, D. Korpi, I. Angervuori and R. Wichman, "Downlink Coverage and Rate Analysis of Low Earth Orbit Satellite Constellations Using Stochastic Geometry," in IEEE Transactions on Communications, vol. 68, no. 8, pp. 5120-5134, Aug. 2020.

[8] J. Park, J. Choi and N. Lee, "A Tractable Approach to Coverage

Analysis in Downlink Satellite Networks," in IEEE Transactions on Wireless Communications, vol. 22, no. 2, pp. 793-807, Feb. 2023.

[9] D. -H. Na, K. -H. Park, Y. -C. Ko and M. -S. Alouini, "Performance Analysis of Satellite Communication Systems with Randomly Located Ground Users," in IEEE Transactions on Wireless Communications, vol. 21, no. 1, pp. 621-634, Jan. 2022.

[10] X. Wang, N. Deng, and H. Wei, "Coverage and Rate Analysis of LEO Satellite-to-Airplane Communication Networks in Terahertz Band," in IEEE Transactions on Wireless Communications.

About the author

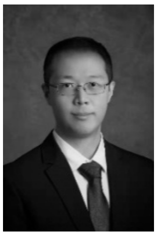

SHANG Bodong [corresponding author]received his B.Eng. degree in the School of Information Science and Technology at Northwest University, Xi’an, China, his M.S. degree in the School of Telecommunications Engineering at Xidian University, Xi’an, China, and his Ph.D. degree from the Department of Electrical and Computer Engineering at Virginia Tech, Blacksburg, USA. He was a postdoctoral research associate at Carnegie Mellon University, Pittsburgh, USA. He is an assistant professor at Eastern Institute for Advanced Study (EIAS), Eastern Institute of Technology (EIT), Ningbo, China. He received the Chinese government award for outstanding self-financed students abroad and held a summer research internship at Nokia Bell Labs, USA. His current research areas are wireless communications and networking, including 6G, non-terrestrial networks, internet of vehicles, integrated sensing and communications, edge computing, and reconfigurable intelligent surfaces. (Email: bdshang@eitech.edu.cn)

LI Xiangyu received the B.Eng. degree in Electronic Information Engineering from Nantong University, Nantong, China, in June 2021 and the M.S. degree in Electrical and Computer Engineering from Georgia Institute of Technology, Atlanta, United States, in May 2023. He is currently working toward the Ph.D. degree with Shanghai Jiao Tong University, Shanghai, China, in the EIT-SJTU Joint PhD Program. His research interests include space-air-ground integrated networks, massive MIMO, and performance analysis of wireless systems.(Email: xyli@eias.ac.cn)

LI Caiguo received her B.S. degree in the College of Computer and Information Engineering from Henan University, China, in 2020, and her M.S. degree in Computer Science and Technology from Shenzhen University, China, in 2023. She is a research assistant at the Eastern Institute for Advanced Study (EIAS), Ningbo, Chian. Her research interests include edge computing, wireless communication, and information security. (Email: licaiguo2023@163. com)

LI Zhuhang received the B.S. degree from the University of Electronic Science and Technology of China (UESTC), Chengdu, China, in 2022, and the M.S. degree from the Nanyang Technological University in 2023. She is a research assistant at the Eastern Institute for Advanced Study (EIAS), Ningbo, China. Her research interests include space-air-ground-sea integrated networks, and Internet-of-Things.(Email: jdhdyxj@163.com)

Dual Decoding Convolutional Attention Network for Sea-Land Segmentation with Remote Sensing Image

Batu Xie[1], **Jun Pan** [1,*]

1 State Key Laboratory of Information Engineering in Surveying, Mapping and Remote Sensing, Wuhan University, 129 Luoyu Road, Wuhan 430079, China;

* Correspondence: panjun1215@whu.edu.cn

Abstract: As an important preprocessing step for acquiring information about the ocean, remote sensing image sea-land segmentation technology is of great significance for extracting coastlines and automating the detection of targets in nearby waters. However, the sea-land fine segmentation is still a difficult problem in remote sensing image processing due to the influence of coastal objects and terrain. This article proposes a dual decoding convolutional attention network (DDCANet) based on the improvement of SegNeXt network. It abandons redundant features in the original network and associates shallow features with deep features. It improves the spatial attention mechanism based on the multi-scale convolutional structure to enhance the ability to focus on land and sea. It builds a dual decoding header structure based on the sea-land structure for constructing large-sized features and obtains sea-land features with multi-scale deep learning using a combination of deep separable dilated convolution and "Hamburger" decoding header. It also constructs a structure for selecting difficult cases for deep training in complex scenes. This paper obtains publicly available remote sensing images of sea-land intersections and ports from around the world and annotates them to construct a sea-land segmentation dataset. Comparative experiments on this dataset show that compared with other semantic segmentation methods and the SegNeXt method, this paper has advantages in sea-land segmentation.

Keywords: sea-land segmentation; deep learning; convolutional neural network; attention mechanism;

1 Introduction

As the number of satellites in orbit from various satellite constellations around the world continues to increase, the volume of remote sensing image data is growing rapidly. It has become increasingly important to effectively utilize this remote sensing data and extract valuable information from it. Approximately 70% of the Earth's surface is covered by water bodies, and distinguishing and extracting the oceanic regions is a crucial preprocessing step for further obtaining information from remote sensing images. Remote sensing image-based sea-land segmentation refers to the method of using remote sensing image technology to segment land and sea areas. Remote sensing image technology involves remote measurement of the Earth's surface using sensors such as optical, microwave, and infrared sensors to obtain image data of the Earth's surface. On these data, image processing techniques can be employed to effectively differentiate between the oceanic and land regions based on pixel characteristics such as grayscale and texture.

Common traditional remote sensing image-based sea-land segmentation methods include threshold segmentation, active contour modeling, region growing, and Markov random field-based methods. These methods primarily rely on differences in grayscale, texture, and other aspects between land and sea in the images and can achieve good segmentation results when there is a clear grayscale difference at the water-land boundary and a simple shoreline shape. However, these methods are susceptible to noise interference, require manual parameter tuning, and have poor robustness. In recent years, remote sensing image sea-land segmentation methods based on deep learning techniques have gradually gained popularity. Mohammad A et al.[1] made improvements to the U-Net network, using different loss functions and two fusion methods to combine RGB and NIR images. Subsequently, based on morphological operations and pixel connectivity analysis, the segmentation results are passed to a subsequent automatic shoreline extraction network. Cui et al.[2] designed SANet, which introduced two innovations on top of the classical encoder-decoder structure. First, to integrate spectral, textural, and semantic features of objects at different scales, an Adaptive Multi-scale Feature Learning Module (AML) was designed to replace traditional serial convolution operations. The AML module consists of multiple multi-scale feature extraction units and an adaptive feature fusion unit. The former captures multi-scale details and contextual semantic information of objects in the early stages, while the latter adaptively fuses features from different scales. Second, a compression and excitation module was used to bridge corresponding layers of the encoder and decoder, allowing SANet to selectively emphasize weak features at the sea-land boundary.

Currently, there are still limitations in sea-land segmentation methods. Shallow water areas at the boundaries between land and sea often contain numerous interfering objects, such as floating man-made structures, waves, large rocks, or islands. Semantic segmentation using deep learning methods typically relies on convolution or attention mechanisms to learn semantic features of objects for segmentation. However, objects on the sea surface exhibit diverse semantic features, and some of these features may be similar to those found on land. Their presence can impact the results of sea-land segmentation. Furthermore, with the rapid advancement of remote sensing technology and the widespread use of super-resolution techniques, research on sea-land segmentation methods for high-resolution remote sensing images is an inevitable trend. In this context, challenges arise when dealing with low-resolution images where certain features are difficult for the human eye to discern, such as elongated levees extending into the sea or vessels near the shoreline. This presents new challenges for semantic segmentation methods based on high-resolution image data.

Currently, semantic segmentation methods in the field of image analysis can be broadly categorized into two types. The first type is represented by fully convolutional neural networks with an "encoder-decoder" structure, such as UNet, PSPNet, and Deeplab series[4-11]. These networks combine multiscale features and expand the receptive field to aggregate contextual information from different regions. However, they may still face issues when it comes to feature extraction for large-scale objects in sea-land segmentation, where target sizes exceed the receptive field, resulting in inconspicuous Classes. The second type is based on attention mechanism networks[12-14], such as the Vision Transformer. These networks focus on the target to be segmented by introducing attention mechanisms, which can effectively differentiate between targets and backgrounds in complex sea-land scenes. However, the computational complexity of these networks can lead to an increase in the number of parameters, and attention mechanisms may overly concentrate on certain regions while neglecting the overall context.

This paper is based on the SegNeXt network model, which utilizes convolutional attention mechanisms. The designers of the SegNeXt model have reimagined the structure of traditional convolutional blocks to implement spatial attention mechanisms for multiscale features through convolution, which proves more effective compared to standard convolution and self-attention in encoding spatial information. In the decoder part, the "Hamburger" structure is designed to gather features from different stages, further extracting context features from local to global scales.

2 Dual Decoding Convolutional Attention Network

The overall structure of the DDCANet model based on SegNeXt improvement in this article is as follows, proposed in this paper, is as follows: designing an "encoder-decoder" structure deep learning network, mimicking attention mechanisms to construct the fine-grained convolutional attention feature extraction block in Stage (i)，i ϵ {0， 1， 2， 3}， the results of some stages are concatenated and input into two decoding ends, which are optimized using dual loss functions. The resulting optimized features are input into a multilayer perceptron to obtain feature extraction results.

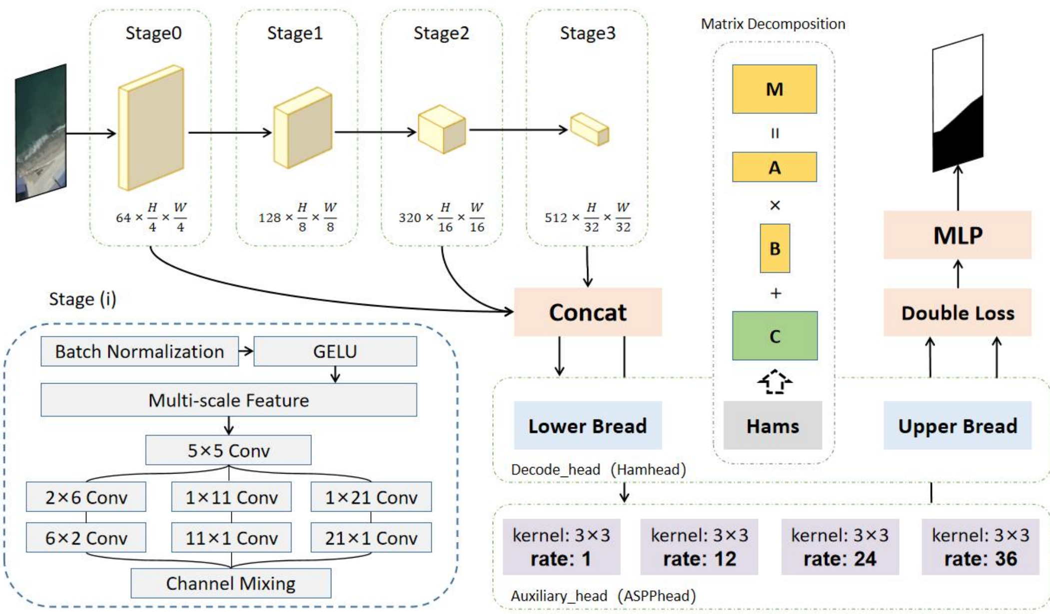

Figure 1. Network architecture diagram

2.1 Multilevel feature fusion

As a dense prediction task, semantic segmentation requires excellent context information interaction to obtain features. For convolutional neural networks, deep-level features are extracted by continuously performing convolutions and pooling, but the shallow features and transition features extracted through convolution and pooling are not well utilized. Gao Hui et al.[15] designed a novel network based on Res2Net and applied it to sea-land segmentation by using five different feature levels extracted by the model's encoder as input for the decoder to fuse features. However, excessive features can cause an increase in parameters during network training. Guo et al.[16] designed the SegNeXt model for sea-land segmentation, in which the last three stages of the features extracted by the encoder were chosen as the input of the decoder. The shallow features obtained in Stage 1 were abandoned, which can increase the number of parameters during network training due to their larger size.

However, for high-resolution remote sensing image sea-land segmentation, the semantic features of the ocean and land are continuously distributed over large areas in the image, so the shallow features obtained in Stage 1 can roughly obtain the ocean boundary. Stage 2 obtains deeper-level information based on Stage 1 and extract features of objects floating on the sea surface. These features can affect an ordinary sea-land segmentation. Stages 3 and 4 perform refined feature extraction for sea-land semantic features to obtain accurate sea-land boundaries. High and others designed a novel network, based on Res2Net, and applied it to sea-land segmentation by using five features, extracted from different levels of the model's encoder, as inputs for the decoder for feature fusion. However, the excessive number of features can lead to an increase in the number of parameters during network training.

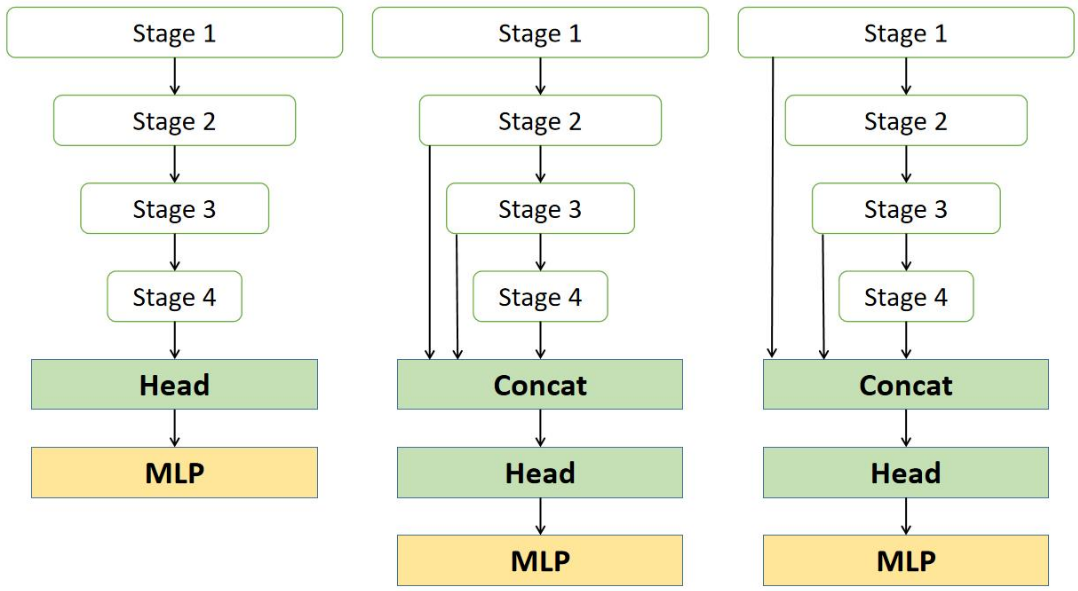

(a) CNN (b) SegNeXt (c) Ours

Figure 2. Comparison of Decoder Structure Differences.

2.2 Encoder based on sea-land segmentation

Inspired by the multi-scale contextual awareness structure in the SegNeXt model, 1k and k1 strip convolutions were used to extract semantic features of elongated objects. The 1k and k1 strip convolutions form k*k convolution blocks to achieve large kernel convolution. Different k values were used to create a multi-scale convolution feature extraction module, which then utilizes spatial attention mechanisms to learn global and local feature information. By stacking multi-scale convolutions at each level, local contextual knowledge can be captured effectively.

Based on the task of sea-land segmentation, it is necessary to extract the characteristics of large-sized objects with a more square shape. The existence of strip convolutions increases spatial attention to elongated objects, thereby affecting the extraction of sea-land features. However, large kernel convolutional blocks composed of strip convolutions can achieve a larger receptive field with fewer parameters, which is suitable for sea-land segmentation and should be retained. Therefore, DDCANet optimizes this structure by replacing 1*k and k*1 strip convolutions with 2*k and k*2 rectangular convolutional blocks to form k*k wide receptive field convolutional blocks. This method expands the range of the receptive field while using fewer parameters.

2.3 Global information optimization and channel fusion

For the "Encoder-Decoder" structure semantic segmentation model, the decoder is crucial as it needs to project the low-resolution discriminative features learned by the encoder into the high-resolution pixel space. SegNeXt references the role played by the Visual Attention Network (VAN)[17] model in image classification and adopts the lightweight "Hamburger"[18] structure to combine the aggregated features as input to the encoding side and to combine global contextual information with multi-level information.

Based on this, DDCANet employs deep separable dilated convolution for the decoder. Deep separable dilated convolution combines depthwise separable convolution and dilated convolution. It performs different convolution operations using different convolution kernels for each feature map channel in the input and then concatenates the resulting feature maps to output a new feature map. Deep separable convolution associates features extracted from different channels of the feature map to achieve channel fusion and introduces dilated convolution kernels to replace ordinary convolution kernels, allowing for multi-scale feature fusion through different dilation scales.

2.4 Multiple loss function

For semantic segmentation tasks, the calculation of the loss function is of paramount importance, and the commonly used approach is to compute the Cross-Entropy Loss. The formula for calculating the Cross-Entropy Loss is as follows:

$$\mathrm{loss}(\mathrm{x},\mathrm{class}) = \mathrm{weight}[\mathrm{class}]\left(-\mathrm{x}[\mathrm{class}] + \log\left(\sum_{\mathrm{j}} \exp(\mathrm{x}[\mathrm{j}])\right)\right)$$

The Cross-Entropy Loss function is effective in balancing the segmentation classes of multiple targets for classification problems, but for sea-land segmentation tasks, only one class (ocean) needs to be distinguished. Therefore, other loss functions need to be introduced for targeted processing.

DDCANet introduces the Dice Loss function, which is commonly used for binary semantic segmentation problems where the pixel values of the true image labels are composed of only 0 and 1, and the problem is transformed into True or False. For predicted labels where the True value is false in the true label, it is considered an incorrect response, and vice versa is considered a correct response. Based on this, confidence calculations are conducted, where high confidence is associated with a high Dice coefficient. The Dice coefficient formula calculates the similarity level of a sample, where samples with a higher similarity level have a higher Dice coefficient.

$$Dice = \frac{2|X \cap Y|}{|X| + |Y|}$$

Where $|\mathrm{X} \cap \mathrm{Y}|$ s the number of intersecting elements between X and Y, and $|\mathrm{X}|$ and $|\mathrm{Y}|$ represent the number of elements in X and Y, respectively. The expression for the Dice Loss function is as follows:

$$DiceLoss = 1 - Dice = \frac{2|X \cap Y|}{|X| + |Y|}$$

The Dice Loss function is primarily applied to mitigate the segmentation tasks with imbalanced distribution between foreground and background in the samples. For sea-land segmentation problems, land and sea regions usually exhibit a large-scale distribution where some areas are the sea surface and others are land, leading to certain image regions not containing the target while others are entirely composed of the target. By using the Dice Loss function, the focus is increased on the foreground region, but there may be an issue of loss saturation. To address this, the Cross-Entropy Loss function is employed, which calculates the loss per pixel with uniform weighting, such that the loss at a given pixel is only based on the distance between the current prediction value and the corresponding true label value.

2.5 Difficult Example Selection

In the task of sea-land segmentation, the presence of terrain such as deltas and beaches near the land edge results in lower prediction accuracy for such images. To better distinguish these special terrains, this paper introduces the Difficulty Example Selection (DES) module in the model. During the training process, temporary models are generated, which also have the ability to predict. By predicting the data and selecting low-accuracy sample instances with higher loss values, which are referred to as difficult examples, this approach calculates the loss in the forward propagation process without affecting the model training. Among the instances with a loss value greater than a given threshold n and a specified number N, K (K<N) high-loss samples are selected first for backpropagation. This ensures that similar results to using all the instances can be obtained using fewer difficult examples, effectively reducing computational complexity.

3 Experiment

3.1 Datasets

Our text uses over 2000 self-made high-resolution remote sensing images of land and sea boundaries and ports from around the world. The images and their labels are uniformly randomly cropped to 512x512 as the input size in the training set, and the labels are manually marked with pixel-precision. The dataset contains various types of interference factors, including boats closely connected to land, breakwaters extending into the sea from the land, tidal flats in the sea, etc.

3.2 Accuracy evaluation indicators

(1) Pixel Accuracy, the ratio of correctly classified pixels to total pixels in the image:

$$p_a = \frac{\sum_{i=0}^{n} p_{ii}}{\sum_{i=0}^{n}\sum_{j=0}^{n} p_{ij}}$$

In the equation: p_a is pixel accuracy; n is the number of target classes; p_{ij} is the number of pixels that belong to class i but are predicted as class j; p_{ii} is the number of correctly classified pixels.

(2) Mean Intersection over Union[19], the average ratio of the intersection and union of predicted results reflects the relative position of the buildings.

$$R_{MIoU} = \frac{1}{n+1}\sum_{i=0}^{n} \frac{p_{ii}}{\sum_{j=0}^{n} p_{ij} + \sum_{j=0}^{n} p_{ji} - p_{ii}}$$

(3) Dice，the Dice score is a measurement function used to evaluate the similarity between two samples, with a value between 0 and 1. A higher value indicates greater similarity.

3.3 Comparison Experiments

Select outstanding networks in recent years for semantic segmentation tasks for comparative experiments. For convolutional neural networks, UPerNet[20] and PSPNet[21] are chosen. These networks generally have an "encoder-decoder" structure. As for attention mechanism network models, CCNet[22], DANet[23], OCRNet[24], and ViT[25] are selected. These networks focus on the desired semantic features through attention mechanisms. All models are implemented using open-source code architectures and retrained using the dataset in this paper to compare their strengths and weaknesses.

3.4 Qualitative analysis of results

The comparison results of various methods in different scenes are shown in Figure 3-5. It can be observed that our proposed method achieves clear and coherent segmentation boundaries in various marine and land scenes, demonstrating strong robustness against interference.

Figure 3 shows a scene with a cliff and a coastline, where the terrain is complex and there is a large difference in elevation between the land and the sea. Shadows and waves in the image can affect the boundary extraction. Convolutional neural networks based on the encoder-decoder structure can roughly extract the marine and land boundaries but may have false detections. Models using attention mechanisms produce smoother segmentation results but with lower accuracy and do not perfectly align with the ground truth labels. SegNeXt can accurately extract the marine and land boundaries and even refine them to better match the visual effect perceived by humans, possibly exceeding the ground truth labels. However, there may still be cases of missed classifications. Our proposed method, which incorporates low-level features, reduces the probability of misclassification and retains the fine boundary classification characteristics of the SegNeXt model, as shown in Figure 4.

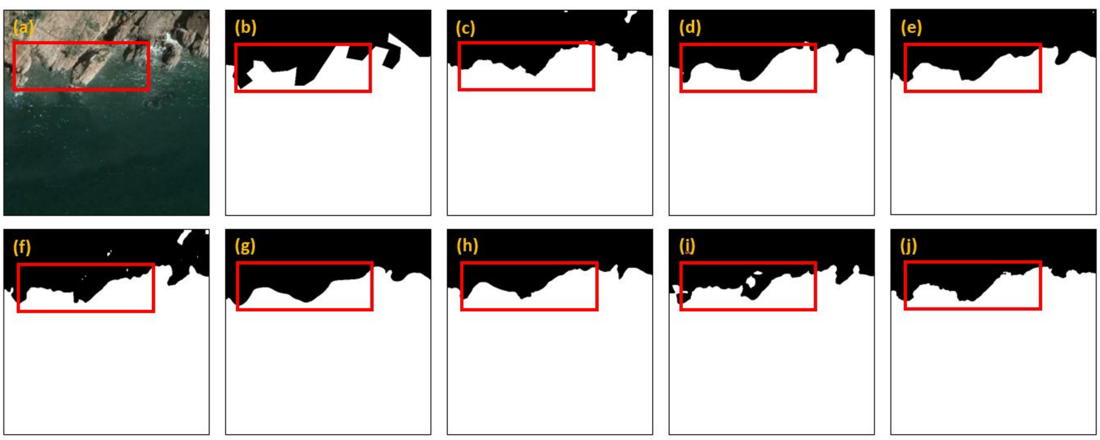

Figure 3. Comparison of network segmentation results for land and sea. (a) Image; (b) Label; (c) CCNet; (d) DANet; (e) UPerNet; (f) PSPNet; (g) ViT; (h) OCRNet; (i) SegNeXt; (j) Ours.

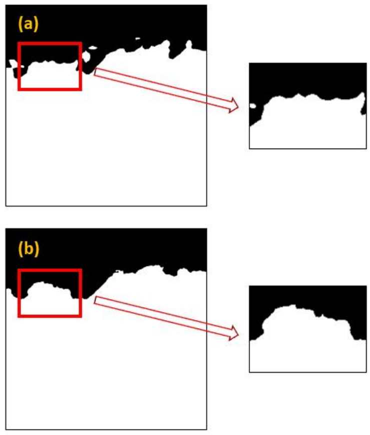

Figure 4. is a comparison of the refined extraction results of the improved network.
(a)SegNeXt; (b)Ours

Figure 5 shows the sea-land segmentation results in a complex military port scene, where CCNet and DANet are both unable to accurately detect the land and distinguish between port land and military ships. OCRNet is influenced by vessels near the shore, leading to issues in extracting the port land as a whole. In recent years, other methods have not been optimized specifically for remote sensing image sea-land segmentation. Their feature extraction is overly focused on small objects, resulting in the mixing of vessel and land features and subsequently misclassifying vessels as land during model prediction.In contrast, the proposed method in this paper demonstrates strong anti-interference capabilities in complex scenes. The use of low-level features can prevent the effect of vessels near the shore on coherent land extraction and maintain the smoothness of the sea-land boundary.

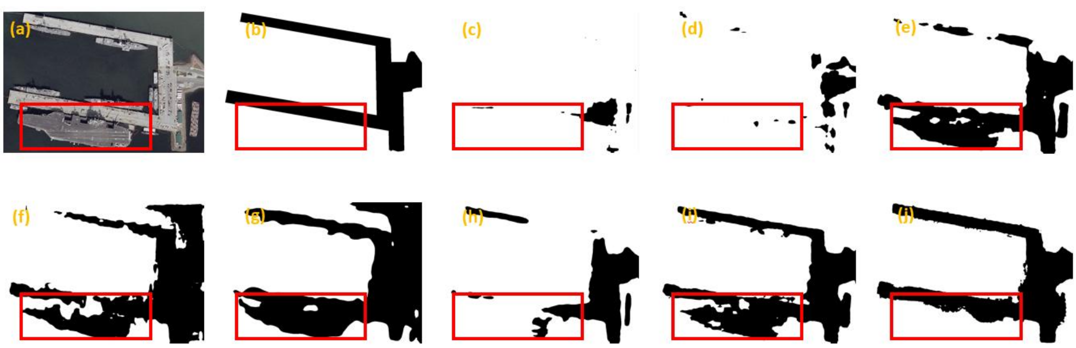

Figure 5. presents a comparison of the sea-land segmentation results among different networks.
(a) Image; (b) Label; (c) CCNet; (d) DANet; (e) UPerNet; (f) PSPNet; (g) ViT; (h) OCRNet; (i) SegNeXt; (j) Ours.

3.5 Quantitative analysis of results

Table 1 presents the accuracy evaluation results of the proposed method and the compared methods. The results indicate that the proposed method performs well in various parameters. It can be observed that CCNet and DANet focus too much on details with their simple attention mechanisms, resulting in poor performance for this kind of large-scale segmentation task like sea-land segmentation. The "Encoder-Decoder" structure convolutional neural network represented by PSPNet accurately extracts sea-land features, but its feature fusion abilities for the shallow and deep-level features are not comprehensive enough, leading to less effective feature utilization. Compared to the proposed method, PSPNet shows lower accuracy in generating mean pixel accuracy (mPA) and mean intersection over union (mIOU) scores, with the proposed method achieving a 5.69% improvement in mPA and an 11.88% improvement in mIOU.

The ViT-based attention mechanism neural network that has excellent performance overly concentrates on details, resulting in a weaker anti-interference ability that may lead to boundary extraction errors when affected by vessels near the shore or nearby land features. In contrast, the proposed method effectively improves boundary recognition accuracy, achieving a 2.70% improvement in mPA and a 9.90% improvement in mIOU compared to ViT.

The SegNeXt model abandons shallow features and mainly uses deep-level features, which may have similar features between vessels near the shore and shoreline features in the sea-land segmentation task. This limitation is addressed by the proposed method, which achieved an 0.86% improvement in mPA and a 1.42% improvement in mIOU over the SegNeXt model.

Table 1. presents the comparison of sea-land segmentation results among different networks.

Methods	mPA	mIOU	mDice
CCNet	82.89	73.19	84.24
DANet	84.66	76.35	86.36
UPerNet	88.74	80.30	88.97
PSPNet	89.11	80.00	88.80
ViT	91.70	81.44	89.73
OCRNet	92.59	87.42	93.24
SegNeXt	93.37	87.17	93.11
Ours	**94.18**	**89.50**	**94.43**

4 Conclusion

This article presents an improvement on the SegNeXt model called DDCANet, which is more suitable for sea-land segmentation tasks. This method combines shallow and deep features in the convolutional network, discarding some features to ensure lightweight network structure and improve resistance to interference. It employs multi-scale rectangular convolutions to form a large-sized rectangular convolution block, triggering spatial attention mechanism to focus on detailed features of land and sea. In the decoding stage, it constructs a dual decoding structure by combining depth separable dilated convolution decoder with the "Hamburger" decoder, enabling multi-scale and deep-level information extraction. The depth separable dilated convolution decoder enlarges the receptive field and captures the overall features of land and sea. However, there is still room for further exploration with this proposed method. Future plans involve applying DDCANet to semantic segmentation of target objects in other remote sensing images to explore the generalizability of this approach.

References

[1] Mohammad A,Reza S,Amirhossein R, et al. Automatic coastline extraction through enhanced

sea-land segmentation by modifying Standard U-Net[J]. International Journal of Applied Earth Observation and Geoinformation,2022,109.

[2] Binge C,Wei J,Ling H, et al. SANet: A Sea-Land Segmentation Network Via Adaptive Multiscale Feature Learning[J]. IEEE JOURNAL OF SELECTED TOPICS IN APPLIED EARTH OBSERVATIONS AND REMOTE SENSING,2021,14.

[3] Y. LeCun, Y. Bengio, and G. Hinton, "Deep learning," Nature, vol. 521, no. 7553, pp. 436 – 444, May 2015.

[4] Chen, L.C., Papandreou, G., Kokkinos, I., Murphy, K., Yuille, A.L.: Semantic image segmen tation with deep convolutional nets and fully connected crfs. arXiv preprint arXiv:1412.7062, 2014

[5] Chen, L.C., Papandreou, G., Kokkinos, I., Murphy, K., Yuille, A.L.: Deeplab: Semantic image segmentation with deep convolutional nets, atrous convolution, and fully connected crfs. IEEE Trans. Pattern Anal. Mach. Intell. 40(4), 834 – 848, 2017

[6] Chen, L.C., Papandreou, G., Schroff, F., Adam, H.: Rethinking atrous convolution for semantic image segmentation. arXiv preprint arXiv:1706.05587 , 2017

[7] Chen, L.C., Zhu, Y., Papandreou, G., Schroff, F., Adam, H.: Encoder-decoder with atrous separable convolution for semantic image segmentation. In: Eur. Conf. Comput. Vis. pp. 801 – 818, 2018.

[8] Zhao, H., Shi, J., Qi, X., Wang, X., Jia, J.: Pyramid scene parsing network. In: IEEE Conf. Comput. Vis. Pattern Recog. pp. 2881 – 2890 , 2017, 11.

[9] Ronneberger, O., Fischer, P., Brox, T. 2015. U-Net: Convolutional Networks for Biomedical Image Segmentation. In: MICCAI. Munich, Germany.234-241. arXiv preprint arXiv:1505.04597, 2015.

[10] Duta, I., Liu, L., Zhu, F., Shao, L.Pyramidal Convolution: Rethinking Convolutional Neural Networks for Visual Recognition. arXiv preprint arXiv:2006.11538, 2020.

[11] Vijay, B., Alex, K.,Roberto, C.SegNet: A Deep Convolutional Encoder-Decoder Architecture for Image Segmentation. TPAMI, 12:2481-2495. arXiv preprint arXiv:1505.07293, 2017.

[12] Guo, M.H., Lu, C.Z., Liu, Z.N., Cheng, M.M., Hu, S.M.: Visual attention network. arXiv preprint arXiv:2202.09741. 2022.

[13] Vaswani, A., Shazeer, N., Parmar, N., Uszkoreit, J., Jones, L., Gomez, A.,et al. Attention is all you need. In: NIPS. Long Beach, CA, USA. 6000 – 6010. arXiv preprint arXiv:1706.03762. 2017.

[14] Fu, J., Liu, J., Tian, H., Li, Y., Bao, Y., Fang, Z., Lu, H.: Dual attention network for scene segmentation. In: IEEE Conf. Comput. Vis. Pattern Recog. pp. 3146 – 3154. 2019.

[15] Gao Hui et al.Multi-Scale Sea-Land Segmentation Method for Remote Sensing Images Based on Res2Net[J].Optics Letters,2022,42(18):155-162.

[16] Guo M H, Lu C Z, Hou Q, et al. Segnext: Rethinking convolutional attention design for semantic segmentation[J]. Advances in Neural Information Processing Systems, 2022, 35: 1140-1156.

[17] Guo, M.H., Xu, T.X., Liu, J.J., Liu, Z.N., Jiang, P .T., Mu, T.J., Zhang, S.H., Martin, R.R.,Cheng, M.M., Hu, S.M. Attention mechanisms in computer vision: A survey. [J]. arXiv preprint arXiv:2111.07624,2021.

[18] Geng, Z., Guo, M.H., Chen, H., Li, X., Wei, K., Lin, Z.: Is attention better than matrix decomposition? In: Int. Conf. Learn. Represent. 2021.

[19] Long J, et al. 2014 Fully convolutional networks for semantic segmentation IEEE Transactions on Pattern Analysis & Machine Intelligence 39 (4) 640-651.
[20] Tete Xiao, Yingcheng Liu, Bolei Zhou, Yuning Jiang, Jian Sun. Unified Perceptual Parsing for Scene Understanding. arXiv preprint arXiv:1807.10221,2018.
[21] Hengshuang Zhao, Jianping Shi, Xiaojuan Qi, Xiaogang Wang, Jiaya Jia. Pyramid Scene Parsing Network[J]. arXiv preprint arXiv:1612.01105,2017.
[22] Zilong Huang, Xinggang Wang, Yunchao Wei, Lichao Huang, Chang Huang, Humphrey Shi, Wenyu Liu and Thomas S. Huang. CCNet: Criss-Cross Attention for Semantic Segmentation[J]. arXiv preprint arXiv:1811.11721,2018.
[23] J. Fu, J. Liu, H. Tian, Y. Li, Y. Bao, Z. Fang and H. Lu. "Dual Attention Network for Scene Segmentation." IEEE Conference on Computer Vision and Pattern Recognition(CVPR). 2019.
[24] YUAN Y, CHEN X, WANG J. Object-contextual representations for semantic segmentation[C]//Proceedings of the European Conference on Computer Vision.Springer, CLoS; Cham, 2020:173.
[25] Alexey Dosovitskiy, et al. An Image is Worth 16x16 Words: Transformers for Image Recognition at Scale[J]. arXiv preprint arXiv:2010.11929,2020.

Cooperative Beam Hopping for LEO Constellation Network

Ren Chaoyu[1], Liu Huijie[2], Tian Feng[3], Wang Wenqian[4]

***Abstract*—LEO constellation network has become a promising approach for global communications, due to its global coverage, lower latency, and flexible construction. However, because of the limited coverage of a single satellite and the high-speed space-ground relative movement, how to leverage the precise satellite resources to satisfy the user terminals' requests is an important issue. Beam hopping technique is an efficient way to handle this issue by scheduling the onboard resource according to the distribution of terminals' requests. In this paper we propose a cooperative beam hopping for LEO constellation network, where multiple satellites provide service for the user terminals in the multi-coverage areas. The problem is innovatively modeled as a LASSO problem considering its sparsity, and machine learning methods are introduced to optimize it. Compared with the fixed beam system, our proposed scheme achieves better performance in terms of resource utilization and average user satisfaction rate.**

***Keywords* — LEO constellation network, beam hopping, resource allocation**

I. INTRODUCTION

Mega LEO constellation communication networks have been an indispensable part of the global network because of the rapid development of advanced satellite manufacturing technology, launch technology, and network technology [1]. LEO constellation has reached unprecedented scale because of its lower cost and smaller size. The largest satellite communications operator SpaceX company has launched 4983 LEO satellites as of August 22, 2023, and 12,000 'StarLink' satellites are expected to be deployed by 2024. Such huge scale will achieve global coverage which can help bridge the "Digital divide" by providing affordable and reliable connectivity services in areas where terrestrial networks are difficult to build [2]. The low latency and small propagation loss of LEO satellites have also earned them ability to provide better global broadband Internet and Internet of Things services [3]. Integrated with ground communication network, LEO constellation network can directly realize 3D global coverage different from traditional 2D 'population coverage' on the surface.

However, due to the uneven distribution of terrestrial user terminals and limited resource on board, the spectrum utilization and service capability of LEO constellation network is lower than terrestrial network [4]. Beam hopping technique in which only a subset of beams is illuminated at a given time for multi-beam satellites [5] is introduced to address this imbalance between system resources and traffic demands in coverage area. In the few past year, beam hopping for single satellite was an appealing issue. An efficient beam hopping based system for single LEO satellite was

This work is supported by Youth Innovation Promotion Association of Chinese Academy of Sciences (great number 2021291).

proposed to allocate onboard resources flexibly according to traffic demand distribution [6]. In order to avoid intra-satellite and inter-satellite interference, a multi-satellite beam hopping algorithm based on load balancing and interference avoidance was proposed for GSO satellite communication system [7]. Nowadays with the increase of LEO satellites, multi-satellite scenarios have attracted much attention. The determinant point process (DPP) is used to solve LEO dual-satellite dynamic beam hopping problem [8].

But there is few research focused on cooperative beam hopping for multi-satellites especially at high latitude where adjacent satellites always create multiple overlapping areas. By analyzing we find that even near the equator there exist double coverage and at 30-degree latitude triple coverage begins to appear based on our assumption. At higher latitudes, the phenomenon of an area covered by more than three satellites becomes frequent as shown in Fig. 3. Thus, to achieve seamless global coverage and construct mage LEO constellation, it is crucial to research multi-satellites cooperating under multiple coverage.

In this paper, we modeled the scenario as a LASSO problem and a cooperative beam hopping solution is proposed for the first time for multiple coverage. Based on this scheme, we propose a multi-satellite cooperative queue management mechanism to balance the demand and supply. In order to demonstrate advantages of this method, a comparison is made with equivalent fixed-beam systems operating within the same system scenario and conditions. After simulation, our scheme has better performance on user satisfaction and system throughput.

The rest of the paper is organized as follows. Section II describes the system model and formulate the multi-satellite beam hopping problem. In section III, we analyze the scenario we have built and make a comparation with fixed beam condition. Section IV presents the simulation result. Section V concludes the work.

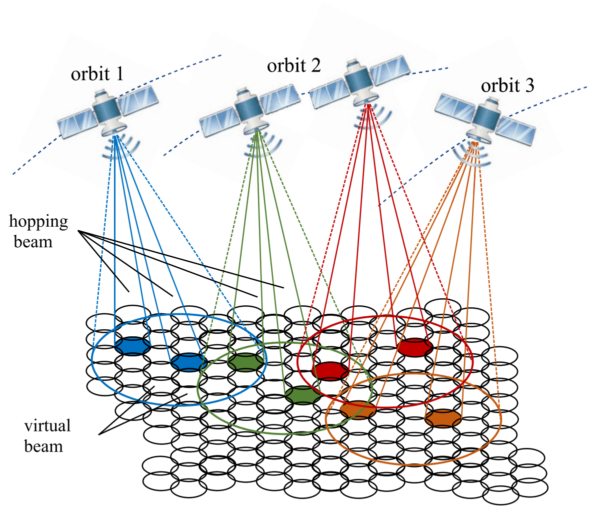

Figure 1 Illustration of cooperative beam hopping of LEO constellation

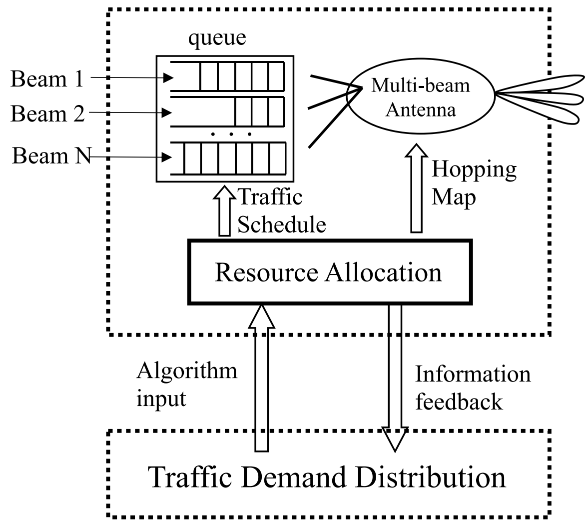

Figure 2 Illustration of beam-hopping satellite communication system

II. SYSTEM MODEL AND PROBLEM FORMULATION

A. System Model

In this paper, we consider the forward link of the LEO constellation network as shown in Fig. 1. According to the coverage of the satellite beams, the region is divided into different cells covered by virtual beams. Only cells illuminated by real satellite beam can be served and satellites dynamically switch beams in accordance with requests in different cells due to the limited on-board resource. The specific process is displayed in Fig. 2. Once terminal users send request to satellites, multi-beam antenna will adjust the beam illuminated regions according to hopping map formed by resource allocation algorithm based on traffic demand distribution. To be noticed, user requests in multiple coverage for resources are cashed in queues on different satellites [9].

For simulation, we take a mega LEO constellation into account, where N satellites serve a specific area. The detailed notations and definitions used are summarized in Table I. To simplify the problem, we assume that each satellite and beam are the same, so suppose that a single multi-beam satellite can provide N_B beams and serve N_V virtual beams.

For one specific satellite, different beams are distributed with time division [10]. Therefore, we divide a period time into time-segments with length T_s where one time-segment is divided into K time slot and the beginning of each time slot denoted as $t, t = 1,2,\ldots,K$. To balance resource supply and demand, we denote vector $\boldsymbol{D}^t$ and $\boldsymbol{X}^t$ to indicate the demand of all covered virtual beam and resource allocated to all beams each satellite at time slot t, where d_j^t and x_k^t respectively representing the demand of j^{th} virtual beam and the capacity of k^{th} beam at time slot t seeing in formula (1). Generally, the lengths of vector $\boldsymbol{D}^t$ and $\boldsymbol{X}^t$ are N_V and N_B, respectively, but if we consider some satellites as a whole, their lengths can be variable.

$$\mathbf{D}^t = \begin{bmatrix} d_1^t \\ d_2^t \\ \cdots \\ d_n^t \end{bmatrix} \quad \mathbf{X}^t = \begin{bmatrix} x_1^t \\ x_2^t \\ \cdots \\ x_n^t \end{bmatrix} \tag{1}$$

According to Shannon's channel capacity theorem, we define P_i^t and B_i^t to respectively indicate the power and bandwidth of i^{th} satellite at time slot t. Assume that the total power and bandwidth on-board are marked by P_0 and B_0. So, we can obtain the following constraints:

$$\sum_{i=1}^{N} B_i^t \le B_0$$
$$\sum_{i=1}^{N} P_i^t \le P_0 \tag{2}$$

Due to the uniform satellite coverage in different region, how to schedule the resources on overlapping

TABLE I:

NOTATIONS AND DEFINATIONS

Notations	Definitions
N	Number of satellites
N_B	Number of beams for each satellite
N_V	Number of virtual beams one satellite served
T_S	Length of time segment
d_i^t	Demand of i^{th} virtual beam at time slot t
x_j^t	Capacity of j^{th} beam at time slot t
$\boldsymbol{D}^t$	Demand of all coverage at time slot t
$\boldsymbol{X}^t$	Resource given to all beams at time slot t
C_j^t	Capacity of beam j at time slot t
$\mathbf{M}_i$	The hopping map of i^{th} satellite
B_i^t	Bandwidth to i^{th} satellite at time slot t
P_i^t	Power to i^{th} satellite at time slot t
B_0	The total bandwidth on-board
P_0	The total power on-board
R_i^t	The real traffic for virtual beam i
r_i	Traffic satisfaction rate of virtual beam i
s	Number of satellites cover the same region
v	Number of overlapping virtual beams

area covered by multiple satellites is a remarkable issue. Therefore, we define C_i^t to represent the whole resource supply capacity for beam i at t time slot where N_0 stands for noise and interference as follow:

$$C_i^t = B_i^t \log_2(1 + p_i^t/N_0) \tag{3}$$

The hopping map denoted as a $pN_V \times pN_B$ matrix $\mathbf{M}_i^t$ for i^{th} satellite where $m_{a,b}$ represents whether at time slot t, the b^{th} virtual beam needs to be illuminated by a^{th} beam for a cluster with p satellites. If $m_{a,b} = 1$, the demand is totally satisfied, otherwise $m_{a,b} = 0$. Ideally it is expected that all resources are allocated to all users, with no surplus and no waste shown as follow:

$$\mathbf{M}_i^t \cdot \mathbf{X}^t = \mathbf{D}^t \tag{4}$$

The real traffic for i virtual beam is defined as $R_i^t = \min\{c_j^t, d_i^t\}$. We use S_i^t to denote the throughput of terminal users in i virtual beam at t time slot shown as follow:

$$S_i^t = \begin{cases} 0, & m_{a,b} = 0 \\ R_i^t, & m_{a,b} = 1 \end{cases} \tag{5}$$

Another measure to evaluate the system performance is average traffic satisfaction rate defined as follow:

$$r_i = \sum_{t=1}^{K} R_i^t / d_i^t \tag{6}$$

B. Problem Formulation

In our cooperative beam hopping system, we pursue higher resource utilizing rate and better services to more users with the limited on-board resources, which means we need to narrow the gap between resources and demand. Considering the overlapping area, we proposed a public resource pool for some satellites to share to avoid resource wasting on public virtual beams. Thus, the resource allocated to each satellite is as less as possible under the condition of satisfying the demand of more users which is represented as:

$$\min \|\mathbf{X}^t\|_1 \tag{7}$$

For single satellite, it is only necessary to ensure the conditions that the capacity each satellite is more than the resource allocated to all beams shown as follow:

$$\sum_{i=1}^{N_B} C_i^t \geq \|\mathbf{X}^t\|_1 \tag{8}$$

But constraint to the overlapping of satellites, public demand should be considered. Suppose that v virtual beams are co-covered by s satellites and traffic in this overlapping area are all stored in queue on-board. Therefore, we only need to guarantee the idle resource of s satellites meet the demand of these virtual beams. The size of matrix $\mathbf{M}_i^t$ are $sN_V \times sN_B$ and the formula of (8) should be looser as:

$$\sum_{i=1}^{sN_B} C_i^t + (s-1)\sum_{i=1}^{v} d_i^t \geq \|\mathbf{X}^t\|_1 \tag{9}$$

In conclude, we construct a LASSO problem to model the scenario as follow:

$$\min \frac{1}{2}\|\mathbf{M}_i^t \cdot \mathbf{X}^t - \mathbf{D}^t\|^2 + \lambda\|\mathbf{X}^t\|_1 \tag{10}$$

For indicators to evaluate the performance of the system shown in formula (5) and (6), the higher maximum of throughput and average traffic satisfaction rate, the better.

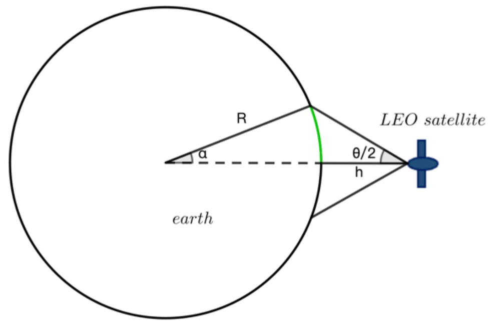

Figure 3 Illustration of LEO satellite coverage

III. SUBPROBLEM ANALYSIS

In this section we analyze the basic coverage of each satellite and the resource allocation algorithm especially focusing on the satellite queues of multiple overlaps.

Assume that the earth is a standard sphere with radius R. The orbit height of satellites is h and the half-open angle is $\theta/2$. The diagram is shown in Fig. 3. The half satellite coverage corresponds to the central angle of the circle is:

$$\alpha = \pi - \theta/2 - \arcsin((h+R)\sin(\theta/2)/R) \tag{11}$$

The radius of satellite coverage area is αR. As the latitude increases, the coverage area of each satellite in different orbits is more likely to overlap. Assume there are M orbits and LEO satellites are evenly distributed in orbit. The critical overlap latitude ϕ satisfies:

$$2\alpha R \cdot M = 2\pi R \cdot \cos\phi \tag{12}$$

We denote the half-open angle of each beam as $\gamma/2$. Thus, according to formula above, the coverage of each beam can be calculated, and the radius of each virtual beam is denoted as βR.

The problem we have built in (8) is a LASSO problem. Because of many constraints of the problem and the sparsity of matrix $\mathbf{M}_i$, we choose Proximal Gradient (PG) to optimize it which is shown as follow:

In the algorithm, s represent the number of satellites in one cluster and K represent the number of cycles. The function of soft-thresholding function [11]:

$$\mathrm{soft}(w_i, \lambda) = \mathrm{sign}(w_i)\max(|w_i| - \lambda, 0) \tag{13}$$

Algorithm 1 Proximal Gradient for LASSO

Problem: $\min \frac{1}{2}\|\mathbf{M}_i^t \cdot \mathbf{X}^t - \mathbf{D}^t\|^2 + \lambda\|\mathbf{X}^t\|_1$, given $\mathbf{D}^t \in \mathbb{R}^{sN_V}, \mathbf{M}_i^t \in \mathbb{R}^{sN_V \times sN_B}$

Input: $\mathbf{x}_0^t \in \mathbb{R}^{sN_B}$ and $L \leq \lambda_{\max}((\mathbf{M}_i^t)^*\mathbf{M}_i^t)$.

repeat

  for $(k = 0, 1, 2, \cdots, K-1)$ do

    $w_k \leftarrow \mathbf{x}_k^t - \frac{1}{L}(\mathbf{M}_i^t)^*(\mathbf{M}_i^t\mathbf{x}_k^t - \mathbf{D}^t)$.

    $\mathbf{x}_{k+1}^t \leftarrow \mathrm{soft}(w_k, \lambda/L)$.

until $\frac{1}{2}\|\mathbf{M}_i^t \cdot \mathbf{x}_k^t - \mathbf{D}^t\|^2 + \lambda\|\mathbf{X}_k^t\|_1 < \varepsilon$

Output: $\mathbf{x}_*^t \leftarrow \mathbf{x}_k^t$

After PG we can get an optimal resource allocation method at time slot t and substituting into formula (5) and (6), the performance of the system can be evaluated.

IV. SIMULATION

In our simulations, there is a mega-constellation of LEO satellites deployed at 1000km consist of 300 LEO satellites, spreading across 15 orbits and 20 satellites each orbit. The details of other simulation parameters and their values are shown in Table II. We Consider a satellites cluster with 15 satellites and the intensity of ground requests is randomly distributed.

The performance compared with fixed beam method is shown in Fig. 4. We can find that as the number of beams increases, both systems have improved performance for the more overlapping areas and beams while fixed beam only improves linearly for their linear increasement of coverage. Cooperative beam hopping system can dynamically allocate the resource to each beam, theoretically it can reach perfect coverage, but constraint to the number of beams and limited resource. In conclusion, cooperative beam hopping improves the throughput of system and average traffic satisfaction rate from users.

V. CONCLUSION AND FUTURE WORK

In this paper we analyze the cooperative beam hopping for LEO constellation scenario, where the onboard resource is limited, and satellites have much overlapping areas. We model it as a LASSO problem and choose throughput of system and average traffic satisfaction rate of users as indicators to evaluate the performance. After simulation, we find that proposed method has better result on the above two measures, while we ignore the interference between satellites which should be our future focus.

TABLE II:
SIMULATION PARAMETERS

Parameters	Values
Number of LEO satellites	300
Number of orbital planes	15
Altitude of the satellite	1000 km
Ka-band frequency f_c	20 GHz
Inclination of orbit	90°
Half-open angle of each satellite $\theta/2$	45°
Half-open angle of each beam $\gamma/2$	2°
Number of beams each satellite	16
Number of virtual beams each satellite	37
Time-segment	60 s
Number of satellites cluster	15

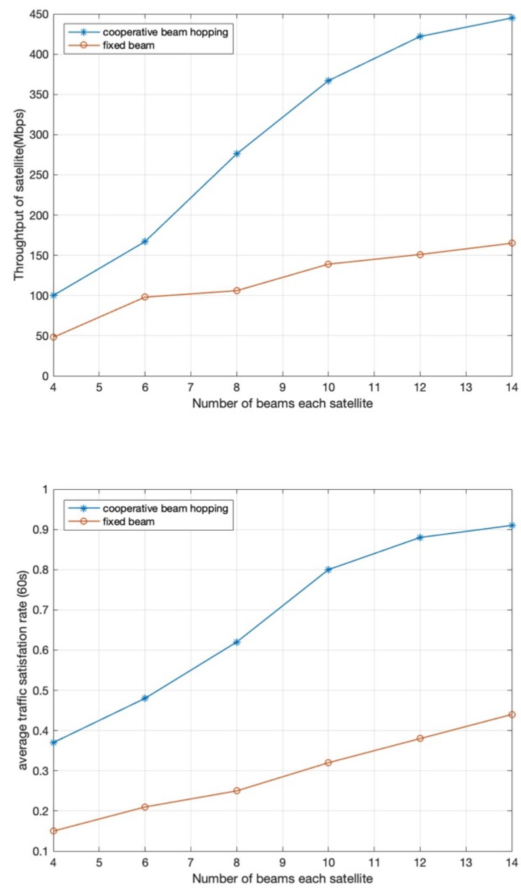

Figure 4 Comparation of two systems performance

References

[1] Sun Z, Li T. Development Prospect of Mega Low Earth Orbit Constellation Satellite Communication Networks [J]. ZTE Technology Journey, 2021, 27(05): 48-51.

[2] Luo H, Shi X, Chen Y, et al. 6G Very Low Earth Orbit satellite network [J]. HuaweiTech, 2022, 12(02):1-4.

[3] Liu S, Lin J, Xu L, et al. A dynamic beam shut off algorithm for LEO multibeam satellite constellation network[J]. IEEE Wireless Communications Letters, 2020, 9(10): 1730-1733.

[4] Tian F, Huang L, Liang G, et al. An efficient resource allocation mechanism for beam-hopping based LEO satellite communication system[C]//2019 IEEE International Symposium on Broadband Multimedia Systems and Broadcasting (BMSB). IEEE, 2019: 1-5.

[5] Anzalchi J, Couchman A, Gabellini P, et al. Beam hopping in multi-beam broadband satellite systems: System simulation and performance comparison with non-hopped systems[C]//2010 5th Advanced Satellite Multimedia Systems Conference and the 11th Signal Processing for Space Communications Workshop. IEEE, 2010: 248-255.

[6] Liu W, Tian F, Jiang Z, et al. Beam-hopping based resource allocation algorithm in LEO satellite network[C]//Space Information Networks: Third International Conference, SINC 2018, Changchun, China, August 9–10, 2018, Revised Selected Papers 3. Springer Singapore, 2019: 113-123.

[7] Lin Z, Ni Z, Kuang L, et al. Multi-Satellite Beam Hopping Based on Load Balancing and Interference Avoidance for NGSO Satellite Communication Systems[J]. IEEE Transactions on Communications, 2022, 71(1): 282-295.

[8] Li W, Zeng M, Wang X, et al. Dynamic Beam Hopping of Double LEO Multi-beam Satellite based on Determinant Point Process[C]//2022 14th International Conference on Wireless Communications and Signal Processing (WCSP). IEEE, 2022: 713-718.

[9] Hou K, Yang J, Liu F, et al. An Active Queue Management Algorithm to Guarantee the QoS of LEO Satellite Network[C]//2023 3rd International Symposium on Computer Technology and Information Science (ISCTIS). IEEE, 2023: 1024-1031.

[10] Ivanov A, Stoliarenko M, Kruglik S, et al. Dynamic resource allocation in LEO satellite[C]//2019 15th International Wireless Communications & Mobile Computing Conference (IWCMC). IEEE, 2019: 930-935.

[11] Wright J, Ma Y. High-Dimensional Data Analysis with Low-Dimensional Models: Principles, Computation, and Applications[M]. Cambridge: Cambridge University Press 2018: 321-323.

About the authors

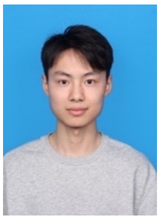

Ren Chaoyu received the B.E. degree in communication engineering from Harbin Institute of Technology in 2018. He is now pursuing for M.E. degree in ShanghaiTech University. His research interests include satellite communication and space network. (Email: renchy2022@shanghaitech.edu.cn)

Tian Feng [corresponding author] received the B.E. degree in electronic information engineering from Northwestern Polytechnical University in 2012 and Ph.D. degree in information and communication engineering from Shanghai Jiao Tong University in 2017. (Email: tianf@microsate.com)

Liu Huijie received the B.E. degree and Ph.D. in communication and information system from Harbin Institute of Technology in1990 and 1996, respectively. He is now a researcher at the Innovation Academy for Microsatellite of Chinese Academy of Science. His research interest on satellite communication.

Wang Wenqian received the B.E. degree in Information Engineering from Xi'an JiaoTong University. She is now a master candidate of University of Chinese Academy of Sciences. Her research interests include satellite network, routing algorithms and optimizing strategy.

IP Tunneling Based for Mobility Management in LEO Constellation Network

WANG Wenqian[1], TIAN Feng[2], YANG Zijian[3], DING Zhaolong[4], REN Chaoyu[5]

***Abstract*—LEO constellation networks, with their advantages of high throughput, wide coverage and strong robustness, have become a key solution to meet future demands for massive data communications and global coverage. However, due to the high-speed movement of low orbit satellites relative to the ground, mobility management is one of the most challenging research topics for enabling mobility service in LEO satellite networks. In this paper, we propose an IP tunneling based scheme for handling the relative mobility between space and ground. The LEO satellite network consists of the access network and the transmission network. The access network includes the user terminals, the space base station on satellite, and the core network in gateway. The transmission network includes the space router, inter-satellite link, feeder link, and the ground router. In the IP tunneling scheme, the access network and the transmission network belong to two networks respectively, where general routing algorithm is used to handle the relative mobility between the satellites and ground stations, and the IP tunneling is used to handle the relative mobility between the satellites and user terminals. Compared with the Mobile IPv6 (MIPv6), the IP tunneling scheme achieves better performance in terms of signaling overhead, memory overhead and switch delay. Analysis result shows that the IP tunneling scheme can greatly reduce the demand of on-board resources.**

***Keywords*—mobility management, IP tunneling, LEO satellite network**

This research was funded by Youth Innovation Promotion Association of Chinese Academy of Sciences (grant number 2021291).

I. INTRODUCTION

The LEO constellation network has become a promising approach for global communication services, due to its wide coverage and rapid construction[1]. Such as, SpaceX company has lunched more than 5000 satellites [https://www.spacex.com/] and the OneWeb company has lunched more than 450 satellites [https://oneweb.net/]. How to leverage the LEO constellation network for global communication has attracted interests from both academy and industry.

Due to the high-speed relative mobility between the satellite and user terminal, and the limited single LEO satellite coverage, the mobility management is an important issue in LEO constellation network. There have been some researches for this issue. As shown in Fig.1, mobility management schemes fall into two categories, centralized and distributed.

Category	*Mobility Management Technology*	*Representitive*
Centralized	*host-based*	*MIPv6, FMIPv6*
	network-based	*PMIPv6, FPMIPv6*
Distributed	*DMM-based*	*DIPS*

Figure 1 Categories of mobility management schemes

In Centralized Mobility Management (CMM), the mobility information is kept at a single mobility anchor. Data packets are transmitted via this anchor. There are some centralized schemes such as MIPv6[2] and Fast Mobile IPv6 (FMIPv6)[3] ,etc., which are the host-based mobility management protocols. Furthermore, the network-based mobility management protocols, for instance, PMIPv6[4], and Fast Proxy Mobile IPv6 (FPMIPv6)[5], have been developed later. The host-based and network-based mobility management protocol are analyzed and compared in terms of handover latency, handover blocking probability, and packet loss in refs.[6]. The result shows that the network-based mobility management outperforms the host-based for the reason that the network-based mobility service provided by Local Mobility Anchor (LMA) and Mobility Access Gate (MAG) reduce the control signals and handover procedures. However, there are some disadvantages of CMM such as non-optimal routes, lack of scalability, single point of failure and duplicate multicast traffic[7].

To solve the problems of CMM, a Distributed Mobility Management (DMM) based scheme in LEO satellites network is proposed in refs.[8]. It deploys the distributed mobility anchors to achieve more optimal routing path, better scalability and robustness. Nevertheless, signaling interactions are frequent in DMM scheme, thus it increases the signaling overhead and complexity of the communication system.

In this paper, we propose an IP tunneling based scheme for handling the relative mobility between space and ground to reduce the demand of on-board resources. The contributes of this paper are summarized as follows:

1. We propose an IP Tunneling Based for Mobility Management (IPTBMM) in LEO constellation network firstly. For a clear description, we design a LEO satellite communication system shown in Fig.2. There are two IP address layer in the proposed LEO satellite communication system. The communication between terminals and data network adopts IP tunnel.
2. We propose for the first time a home satellite maintenance and updating mechanism through cooperation between satellites and ground to reduce the demand of on-board resources.
3. We compare the IP tunneling scheme with the MIPv6 in terms of signaling overhead, memory overhead and switch delay.

The rest of the paper is organized as follows. Section II is an overview of IPTBMM. Section III analyzes the satellite overhead of IPTBMM and compares it with MIPv6 in terms of resource cost. Finally, the conclusions are given in Section IV.

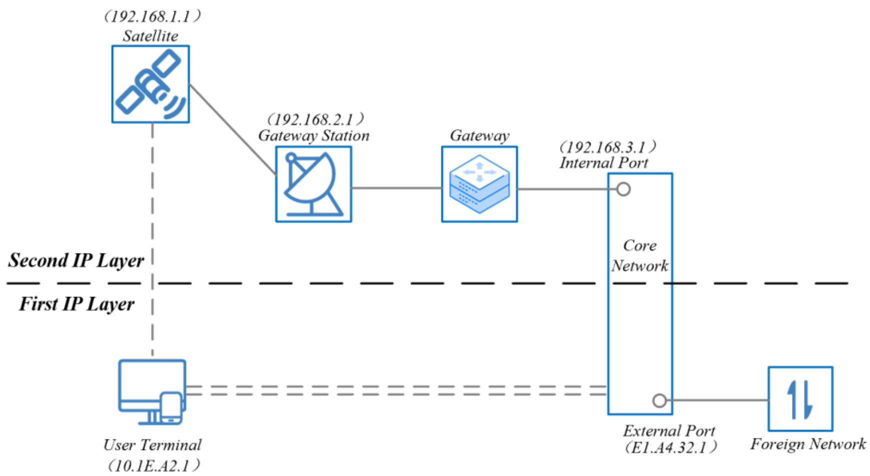

Figure 2 The proposed LEO communication system

II. AN OVERVIWE OF IPTBMM

In IPTBMM scheme, the terminal and the external port of the core network belong to the first layer of IP address, and they have length of 8 bytes, where the first 4 bytes are bound to their home core network. Satellites, gateway stations, and internal ports of the core network have the second layer of IP address, and the length is 4 bytes.

The two layers of IP address are independent of each other. As shown in Fig.3, the data transmission between the terminal and the foreign network is tunnel transmission, in which the satellite and the ground gateway station constitute the transmission layer, and the data transmission process is transparent to the terminal and foreign network.

The step of IPTBMM is as follows:

1. ***Switch.*** After the terminal switches from the first access satellite to the second access satellite, the gateway station notifies the core network of the switching result.
2. ***Update Routing Information.*** The core network maintains the terminal location information, and updates the home satellite table according to the handover result. As shown in Fig.4, the home satellite table includes the IP address of the terminal and the IP address of the home satellite to which the terminal belongs.
3. ***Tunnel Communication.*** When the foreign network needs to transmit data to the satellite terminal, after the data arrives at the core network, the core network obtains the IP address of the satellite that the destination terminal belongs to at the current moment by searching the home satellite table. Then the core network encapsulates the data packet (that is, adds the tunnel transmission head) for tunnel transmission. The new IP head is the same IP address layer as the transport layer. Then, when the new data packet arrives at the gateway station, it is decapsulated (that is, the tunnel transmission head is removed) and transmitted to the access satellite through the satellite link. In the end, the access satellite transmits the data packet to the terminal.

Similarly, when the terminal transmits data to the foreign network, the data packet is first encapsulated by the gateway station for tunnel transmission, and then decapsulated by the core network after reaching the core network. Fig.5 is a schematic diagram of tunnel encapsulation in the LEO satellite communication system proposed in this paper.

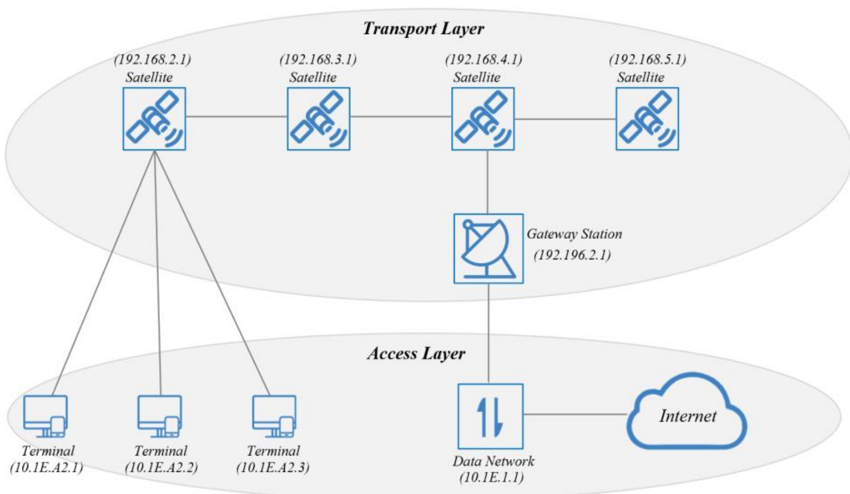

Figure 3 IP address allocation

Terminal IP	*Home Satellite IP*	*Refresh Time*
A1.B2.10.1	*196.168.1.2*	T_0
A1.1H.01.1	*196.168.2.1*	T_0
2B.2C.10.2	*196.168.1.3*	T_0
……	……	……

Figure 4 Home satellite table

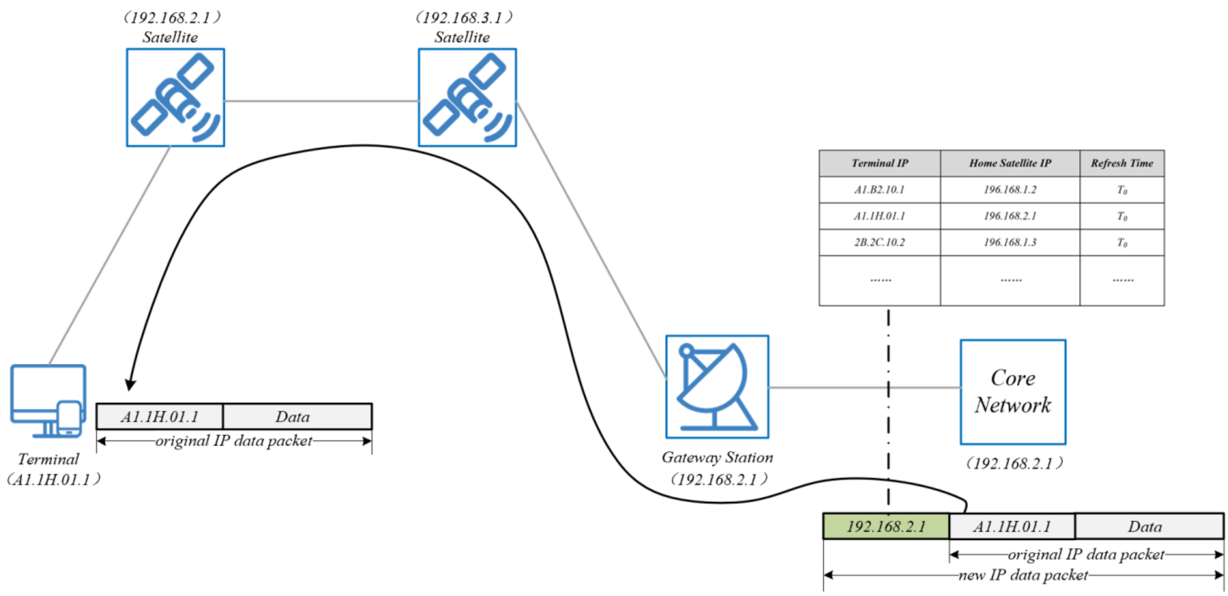

Figure 5 Tunnel encapsulation in the proposed LEO satellite communication

III. COST ANALYSIS

This section will compare IPTBMM and mobility management scheme adopting single IP address layer, for instance, MIPv6 in terms of resource cost.

A. SIGNALING OVERHEAD

Mobility management protocols require various management signaling to provide continuous communication services for terminals that constantly change access points. Signaling overhead is defined as: the sum of control data packets exchanged between the mobile node and the home agent.

The signaling overhead signaling of MIPv6 consists of location registration overhead C^r and location query overhead C^q[9].

In satellite networks, the transmission overhead of datagrams is directly related to the distance from the source node to the destination node, and is proportional to the number of sending location registrations. For the convenience of calculation, it is assumed that the registration and registration confirmation frame sizes are the same as L_r. Define the single bit transmission overhead of control signaling between node *A* and node *B* as $C_{A,B}$, the number of location registrations per unit time is k^r, and the gateway station is represented by *G*. In IPTBMM scheme, the location registration overhead is same as MIPv6. When Mobility Node (MN) corresponds to only one Correspondent Node (CN), the location registration overhead is:

$$C^r_{IPTBMM} = C^r_{MIPv6} = \sum_{i=0}^{k^r} 2 * (C_{MN,G} + C_{MN,CN}) * L_r \quad (1)$$

In MIPv6 scheme, when CN initiates communication with MN for the first time, there is no user terminal table entry in the sending terminal table. Therefore, a location query request needs to be sent to the gateway station; After the communication between CN and MN is established, MN will register the location with CN. At this time, there is no need to initiate a location query request to the gateway station. In IPTBMM scheme, there is no location query overhead. CN directly sends the data packet to the gateway station, which sends the data to MN.

In a single communication between the MN and CN, the cost of location query is:

$$C_{MIPv6}^{q} = 2 * C_{MN,G} * L_r \tag{2}$$

B. MEMORY COST

In MIPv6 scheme, the gateway station updates the routing table, and broadcasts the updated routing table to all satellites. That means every satellite must store the routing table of the whole network.

In IPTBMM scheme, the maintenance and update of the terminal IP address and the terminal's home satellite are delegated to the core network, and each satellite only needs to maintain the routing information of the next-hop satellite. Memory usage is reduced by 1/3.

C. SWITCHING DELAY

In MIPv6 scheme, the handover process can be divided into four stages: link layer handover, mobility detection, duplicate address detection and location update. Fig.5 describes the MIPv6 protocol switching processing diagram[10].

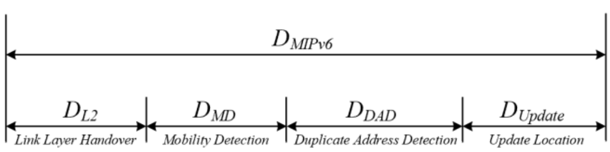

Figure 5

The switching delay of MIPv6 is:

$$D_{MIPv6} = D_{L2}^{MIPv6} + D_{MD}^{MIPv6} + D_{DAD}^{MIPv6} + D_{Update}^{MIPv6} \tag{3}$$

Among them, D_{L2} is the link layer switching delay, D_{MD} is the movement detection process delay, D_{DAD} is the duplicate address detection process delay, and D_{Update} is the location update process delay. In single IP address for mobility management, after the gateway station updates the routing table, it will broadcast the updated routing table to all satellites. Thus, D_{Update} of MIPv6 includes the confirmation delay and the distribution delay as formula (4) shown.

$$D_{Update}^{MIPv6} = D_{confirm} + D_{distribution} \tag{4}$$

It is assumed that the distance between adjacent satellites is about 4000km, the delay of every inter-satellite link transmission is about 12ms.

However, in IPTBMM, there is no need to initiate routing table broadcast, only the core network needs to maintain and update routing information. Thus, the location update process delay of IPTBMM include only the confirm delay, which is shown in formula (5). *D(S(BU))* is the delay of one hop of single binding update packet, *D(S(BAck))* is the delay of one hop of single binding acknowledge packet. *H(MN,HA)* is the numbers of hop between MN and Home Agent (HA). In this way, transmission delay and the demand for on-board resources will be reduced.

$$\begin{aligned} D_{Update}^{IPTBMM} &= D_{confirm} \\ &= (D(S(BU)) + D(S(BAck))) \times H(MN, HA) \end{aligned} \tag{5}$$

IV. CONCLUSION

In this paper, we propose an IP tunneling based scheme for mobility management in LEO constellation network. In this scheme, the access network and the transmission network belong to two networks respectively, and the IP tunneling is used to transport data packets. Analysis in Section III shows that IPTBMM can efficiently reduce or even relieve the work of maintaining terminal routing information of satellites, reduce memory cost and switching delay compared with MIPv6.

References

[1] Al-Hraishawi H, Chougrani H, Kisseleff S, et al. A survey on non-geostationary satellite systems: The communication perspective[J]. IEEE Communications Surveys & Tutorials, 2022.

[2] Johnson D, Perkins C, Arkko J. Mobility support in IPv6[R]. 2004.

[3] Koodli R. Fast handovers for mobile IPv6[R]. 2005..

[4] Gundavelli S. Proxy mobile ipv6[M]//Encyclopedia of Wireless Networks. Cham: Springer International Publishing, 2020: 1120-1128.

[5] Chung J M, Lee D, Song W J, et al. Enhancements to FPMIPv6 for improved seamless vertical handover between LTE and heterogeneous access networks[J]. IEEE Wireless Communications, 2013, 20(3): 112-119.

[6] He D, You P, Yong S. Comparative handover performance analysis of MIPv6 and PMIPv6 in LEO satellite networks[C]//2016 Sixth International Conference on Instrumentation & Measurement, Computer, Communication and Control (IMCCC). IEEE, 2016: 93-98.

[7] Chan H, Liu D, Seite P, et al. Requirements for distributed mobility management[R]. 2014.

[8] Han W, Wang B, Feng Z, et al. Distributed mobility management in IP/LEO satellite networks[C]//2016 3rd International Conference on Systems and Informatics (ICSAI). IEEE, 2016: 691-695.

[9] 郭一然. 低轨道卫星网络移动性支持问题研究[D].西安电子科技大学,2022.DOI:10.27389/d.cnki.gxadu.2021.002404.

[10]丁煜. 低时延低轨卫星移动性管理技术[D].西安电子科技大学,2021.DOI:10.27389/d.cnki.gxadu.2020.001590.

About the authors

WANG Wenqian was born in Jiangsu province. She received the B.E. degree in Information Engineering from Xi'an JiaoTong University. She is now a master candidate of University of Chinese Academy of Sciences. Her research interests include satellite network, routing algorithms and optimizing strategy.
(Email: wangwenqian1011@mail.ustc.edu.cn)

TIAN Feng was born in Hebei province. He received Ph.D degree in Information and Communication Engineering from Shanghai Jiao Tong University. He is now an associated researcher and deputy director in Innovation Academy for Microsatellites of Chinese Academy of Science. His research interests include satellite network communication system design, intelligent space router development, network security protection.(Email:tianf@microsate.com)

YANG Zijian [corresponding author] was born in Suizhou, hubei Province. He received the Ph.D degree in Communication and Information Systems from University of Chinese Academy of Sciences, China. He is now an assistant researcher at the Chinese Academy of Sciences. His research interests include satellite network, routing algorithms and optimizing strategy.
(Email: yanghhh@mail.ustc.edu.cn)

Ren Chaoyu received the B.E. degree in communication engineering from Harbin Institute of Technology in 2018. He is now pursuing for M.E. degree in ShanghaiTech University. His research interests include satellite communication and space network.
(Email: renchy2022@shanghaitech.edu.cn)

Oriented Object Detection Based on Rotated Size-Adaptive Tricube Kernel and Large Receptive Field Mask

Yushan PAN[1],Yang XU[2], Zebin Wu[3], Shangdong Zheng[4], Zhihui Wei[5]

Abstract—Oriented object detection is an important research direction in remote sensing .The detection of oriented objects in remote sensing images is a challenging task due to their complex backgrouds, various sizes, diverse aspect ratios, and especially arbitrary orientations. In recent years, Keypoint-based anchor-freeobject detectors have outstanding performance in this field. However, in existing anchor-free detectors, the keypoint of the object is all generated based on the Gaussian kernel function. However, the geometry of Gaussian kernel function is a circular form, which can not represent the angle and size of the object well. To address the aforementioned issue, this paper innovatively adopts the Tricube kernel, scales and rotates it, to better generate the keypoint heatmap of the object. Besides, to improve the detection performance of the model on large-areaobjects and enhance the perception of the object center points and boundary boxes, we also propose a symmetric feature refine module based on convolution kernel decomposition and supervised by semantic. segmentation mask to reduce background interference and learn more basic features of oriented objects. Taking the BBAVectors method as a baseline, we conducted experiments on multiple remote sensing datasets such as DOTAv1.0, HRSC2016 and SSDD to verify the effectiveness of the proposed method.

Keywords—oriented object detection, keypoint-based detector, feature refinement, convolution neural network, remote sensing

I. INTRODUCTION

Object detection is one of the basic tasks of computer vision. Remote sensing images are typically captured from high resolution satellites in the air with a bird's eye view and are quite different from natural images. The objects in remote sensing images are numerous, densely arranged and complex in background. Additionally, due to different shooting angles, the direction and shape of the objects may vary. The object detection in remote sensing is always the focus and challenge in research and has a broad application prospect. Currently, deep learning-based approaches are the mainstream in object detection. Among them, object detectors can be divided into two categories: two-stage algorithms and one-stage algorithms, depending on whether region proposals need to be generated. They can also be classified into anchor-based algorithms and anchor-free algorithms, depending on whether anchor boxes are needed.

Currently, most oriented object detectors adopt Faster R-CNN[1] or RetinaNet[2] as their baseline models. Based on these models, an additional prediction head is introduced to predict the angles of orientedbounding boxes(OBB), such as RRPN [3], ROITransformer [4], and MORE-Net [5]. However, due to the issue of angular periodicity, these methods using the angle to predict the OBB suffer from the problem of discontinuous boundaries, making it difficult to predict the angle accurately. On the other hand, many oriented object detection methods, such as SCDet [6], LO-Det [7], DAL [8], CenterMap [9], DCL [10], Oriented R-CNN [11], are anchor-based object detection algorithms. A common problem with these algorithms is that the design of anchor boxes is complex, requiring careful adjustment of aspect ratios and sizes. Additionally, the extreme imbalance in the number of positive and negative anchor box samples will lead to slow training and suboptimal performance of the entire model.To solve the above problems, in recent years, the keypoint-based anchor-free algorithm has been proposed and achieved satisfactory results. Algorithms such as CenterNet [12], BBAVectors [13], O2-Dnet [14], etc., have provided a new perspective for object detection by encoding object positions using representative keypoints.

However, existing keypoint-based object detection algorithms generate the heatmap of the keypoint using a Gaussian kernel function. But they lack modeling of object angle and shape information. CHDet [15], on the other hand, better adapts to the features of the object byrotating and scaling the Gaussian kernel function. In this paper, we use Tricube kernel to replace Gaussian kernel and then the heatmap of the keypoint is generated adaptively according to the shape and angle of the object. Different from TricubeNet [16], the former primarily uses the Tricube kernel function to represent the object itself, while this paper uses the Tricube kernel function to generate the heatmap of the object's center point. Additionally, in TricubeNet, the initially generated Tricube kernel have fixed-sized square geometric shapes and are then scaled to represent objects of different shapes. In this paper, however, the parameters of the Tricube kernel function are directly derived from the width and height of the ground truth bounding boxes of the samples, enabling the generation of object keypoint heatmaps that adapt to the shapes of the samples. Compared to the rotated Gaussian kernel function proposed in CHDet, the heatmaps obtained in this paper have a rectangular geometric shape, while the rotated Gaussian kernel function has an elliptical geometric shape. Since the object ground truth labels are rectangles, the proposed method in this paper can more accurately represent the heatmap of the objects. Furthermore, by rotating the Tricube kernel function in a simple way, this paper does not need to use covariance matrices, thus avoiding complex mathematical computations.

The key aspect of keypoint-based remote sensing object detection lies in predicting the centerkeypoint heatmap and bounding box parameters using the prediction head. To enhance the model's perception of the object's center point and bounding box, as well as improve the detection performance for large-area objects, we propose a symmetric feature refinement module based on convolutional kernel decomposition and supervised by semantic segmentation mask.This module is designed to reduce the influence of other objects and complex backgrounds on keypoint heatmap generation. Research has shown that Transformer-based models, such as ViT [17]and Swin Transformer [18], have achieved success in the field of image processing due to their large receptive field. Motivated by this, papers like ConvNeXt [19], Re-pLKNet [20], and SlaK [21]use large convolutional kernels to make CNN networks competitive with Transformer-based models.

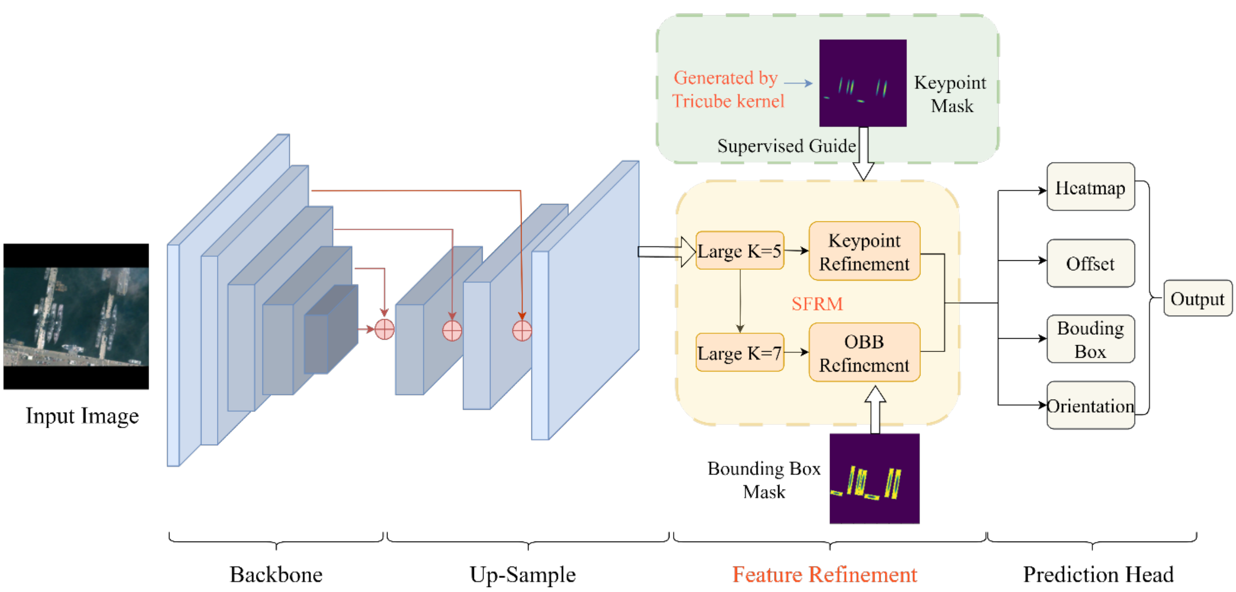

Figure 1the overall framework of proposed method

Referring to the article LskNet[22], we incorporated large kernel decomposition into the feature refinement module, which effectively achieved an equivalent large convolutional kernel, thereby improving the model's receptive field and finally improving the detection performance on large-areaobjects. On the other hand, HSP [23]

proposed using object masks generated from semantic segmentation as a form of supervised learning to enhance the model's feature representation capability. However, the HSP method simply generates a binary mask by labeling pixels inside the bounding box as 1. This mask generation approach does not effectively represent the shape of the object well. Therefore, in this paper, we generate object heatmaps using the Tricube kernel function based on the original mask. And we generate separated heatmap masks for the center point and the bounding box regions of the object to better represent the shape and rotate angle of the oriented objects. To enable the model to simultaneously perceive the bounding box and center point, inspired by CBDA [24], this paper introduces a symmetric feature refinement module. With the supervision of semantic segmentation masks, this module allows the two branches of the module to enhance their feature extraction capabilities for both object keypoints and bounding boxes.

The main contributions of this paper are as follows:

(1) Previously, the generation of keypoint heatmaps was based on Gaussian kernel function. In this paper, to our best knowledge, we are the first to use a rotation and size-adaptive Tricube kernel function to generate heatmaps for objectkeypoints. This approach allows for better feature extraction of object objects.

(2) This paper presents a symmetric feature refinement module that combines kernel decomposition with supervised learning using semantic segmentation mask. The module is designed to enhance the detection performance of large-area objects and improve the model's perception of object center points and bounding boxes.

(3) Using the BBAVectors method as a baseline, we conducted experiments on the DOTAv1.0[25]and HRSC2016[26] remote sensing datasets to validate the effectiveness of the proposed method. Additionally, we performed extra experiments on the SSDD [27]

dataset, which consists of Synthetic Aperture Radar (SAR) data, to verify the applicability of our proposed approach.

II. THE OVERALL FRAMWORK

To validate the effectiveness of the proposed method, we use the anchor-free algorithm BBAVectors as the baseline. Building upon this, we take a size-adaptive Tricube kerneland rotate it to generate the heatmap of object center points. Additionally, as shown in Figure 1, we introduce a Symmetric Feature Refinement Module (SFRM) between the Upsampling part and prediction head of the model to improvethe model’s perception of object keypoints and bounding boxes.

Similar to BBAVectors, the model uses Layer1-5 in ResNet101 as the backbone network, followed by Layer5, a U-shaped structure used to upsample the output features of the backbone network. The final output feature map size of the U-shaped structure is the same as Layer 2, which is a quarter of the input image size. This means that the final sampling stride is 4compared to the original image size. Suppose the size of the input RGB image is $I \in \mathbb{R}^{3\times H\times W}$, where H and W are the height and width of the input image, respectively, the output feature map size after upsampling is $X \in \mathbb{R}^{C\times\frac{H}{s}\times\frac{W}{s}}$(in this paper, C=256，s=4). The prediction head of the model consists of four branches, which are used to predict the heatmap (Heatmap:$P \in \mathbb{R}^{K\times\frac{H}{s}\times\frac{W}{s}}$), offset(Offset: $O \in \mathbb{R}^{2\times\frac{H}{s}\times\frac{W}{s}}$), oriented bounding box(OBB: $B \in \mathbb{R}^{10\times\frac{H}{s}\times\frac{W}{s}}$), orientation(Orientation:$\alpha \in \mathbb{R}^{1\times\frac{H}{s}\times\frac{W}{s}}$), where K is the number of object categories in the dataset and s is the sampling stride of the output feature map compared to the original image. In the Symmetric Feature Refinement Module (SFRM), we also usethe Tricube kernel to generate semantic segmentation masks. These masks are used for supervised learning in the SFRM. The Tricube kernel helps refine the features and enhance the model's perception of semantic information during the refinement process.

III.PROPOSED METHOD

In this section, we first introduce the rotated size-adaptive tricube kernel, which is used to generate heatmaps of object keypoints. Then, a detailed introduction of the proposed Symmetric Feature Refinement Module (SFRM) will be presented, which leverages both the convolution kernel decomposition and semantic segmentation mask information for supervision. The SFRM aims to improve the model's ability to extract features related to object keypoints and bounding boxes. Finally, we introduce the loss function of the entire model, which is used to optimize the overall framework.

A. ROTATED SIZE-ADAPTIVE TRICUBE KERNEL

Indeed, existing keypoint-based object detectors usually use a Gaussian kernel function to generate heatmaps for keypoints. However, the geometric shape of a Gaussian kernel is a circle, which can not effectively represent the orientation and shape of the objects well. In this paper, we propose a new heatmap representation by introducing a rotated size-adaptive Tricube kernel to replace the conventional Gaussian kernel function. This new kernel function is used to generate heatmaps for object keypoints, allowing for better localization of the object's position by capturing both its orientation and shape information.

Assuming that $C = (c_x, c_y)$ is the coordinate of the center point of the object bounding box, we can generate a Gaussian circular heatmap in the vicinity of C in the ground truth values of the heatmap($P \in \mathbb{R}^{K \times \frac{H}{s} \times \frac{W}{s}}$), where $\hat{P} = (p_x, p_y)$ is the sample point. The function expression of this Gaussian circular heatmap is as follows:

$$f(\hat{P}) = exp\left(-\frac{(p_x - c_x)^2 + (p_y - c_y)^2}{2\sigma^2}\right) \#(1)$$

Where σ is the size adaptive standard deviation. Based on Gaussian kernel function, CHDet[15] also proposed a rotated Gaussian kernel function, which was

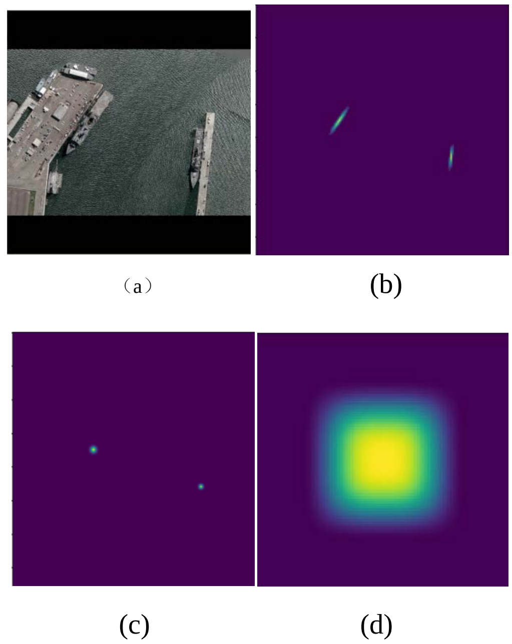

Figure 2(a) input image, (b) Tricube kernel keypoint, (c) Gaussian kernel keypoint, (d) origin Tricube kernel

rotated by a rotation matrix to obtain angle-adaptive Gaussian kernel function.

By taking the width and height of the object-bounding box as parameters x and y, the Tricube kernel function adopted in this paper calculates the object keypoint heatmap and achieving size-adaptivity for the objects. The mathematical expression of the Tricube kernel function is as follows:

$$f(x, y) = (1 - |x|^{\alpha})^{\gamma} * (1 - |y|^{\alpha})^{\gamma} \#(2)$$

In general, the parameter α is set to 3. Following TricubeNet[16], the parameter γ is set to 7. Compared to CHDet [15] where rotation matrixis used to rotate the Gaussian kernel function, this paper providesa novel approach to rotate the Tricube kernel. To rotate the Tricube kernel, we first shift the generated kernel to the center of the heatmap P. Then, we perform rotation on the entire heatmap P, indirectly achieving rotation of the Tricube kernel function. Each channel of the heatmap corresponds to an object category, where a single channel represents the heatmap for that specific class of object.For multiple objectsin a single channel, we rotate each target individually and then shift them back to their original positions. Finally, we add the heatmap of each channel objects separately to get the final rotation keypoint heatmap. This approach avoids complex mathematical computations compared to the use of rotation matrices.

As shown in Fig. 2, (a) is the input image I, (b) represents the heatmap of the object's center points generated by the proposed rotated size-adaptive Tricube kernel, (c) shows the heatmap of the object center points generated by Gaussian kernel function, and (d) depicts the original Tricube kernel without scaling and rotation.

By comparing (b) and (c), we can observe that the geometric shape of the Gaussian kernel function is a circle, which can only locate the position of the object's center point but fails to represent the object’s size and rotation angle. The Gaussian kernel lacks sufficient utilization of prior information about the samples. In contrast, the Tricube kernel used in this paper can represent the size and angle well, to generate a better keypoint heatmap of the object, and finally improve the model's ability to locate the object keypoint.

B. SYMMETRIC FEATURE REFINEMENT MODULE

To enhance the model's perception of objectkeypoints and bounding boxes, as well as improve its detection capability for large-scale targets, we have designed a symmetric feature refinement module(SFRM) based on convolutional kernel decomposition and semantic segmentation masks for supervised learning. As shown in Fig. 3, our proposed SFRM consists of three main components: convolutional kernel decomposition, supervised learning using semantic segmentation information to generate object masksand symmetric feature.

refinement module for object keypoints and bounding boxes feature extraction.

We achieve an equivalent large receptive field by decomposing a large convolutional kernel into a sequence of depth-wise convolutions. In this sequence, the size of each convolution kernel and the dilation rate increase progressively. Specifically, the expansion of the kernel size k, dilation rate d and the receptive field RF, of the i-th depth-wise convolution in the series are defined as follows:

$$k_{i-1} \le k_i; d_1 = 1, d_{i-1} < d_i \le RF_{i-1} \#(3)$$

$$RF_1 = k_1, RF_i = d_i(k_i - 1) + RF_{i-1} \#(4)$$

The increasing of kernel size and dilation rate ensure that the receptive field expands quickly enough. In this paper, unless otherwise specified, the size of convolution kernel Kc is 5 and dilation rate of 1, while the size of convolution kernel Kb is 7 and dilation rate is 3. The equivalent large receptive field is 23. The kernel Kc is used to extract the feature of object key-

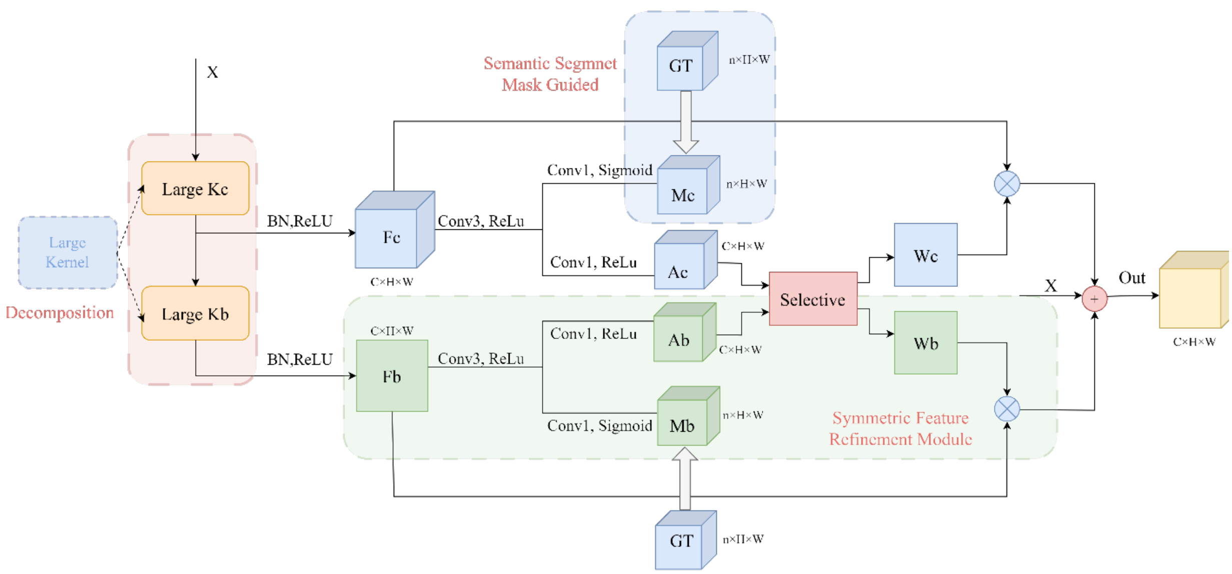

Figure 3the symmetric featurerefinement module based on convolution kernel decomposition and semantic segmentation mask guided supervised learning.

points, while the kernel Kb is used to extract the feature of object bounding boxes. By using convolution kernel decomposition to achieve an equivalent large receptive field, this method provides more flexibility in selecting kernel sizes within the convolution kernel sequence. Additionally, it reduces the number of parameters in the model while achieving the desired receptive field, making it more efficient compared to simply using one large convolution kernel.

As shown in Figure 3, the output feature X passes through the convolution sequences Kc and Kb before entering the symmetric feature refinement module. In the symmetric feature refinement module, we have:

$$\mathrm{Fc} = ReLU\left(BN\left(DWConvc(\mathrm{X})\right)\right)\#(5)$$

$$\mathrm{Ff} = ReLU\left(Conv3(\mathrm{Fc})\right)\#(6)$$

$$\mathrm{Ac} = ReLU\left(Conv1(\mathrm{Ff})\right)\#(7)$$

$$\mathrm{Mc} = Sigmoid\left(Conv1(\mathrm{Ff})\right)\#(8)$$

Among them, DWConvc corresponds to the convolution kernel decomposition for Kc. Conv3 stangds for a 3×3 convolution used for feature extraction. Conv1 stands for a 1×1 convolution used for feature fusion and channel transformation. Fc represents the extracted features of object center points. After applying another 3×3 convolution to the object center point features Fc, we obtain Ff. Following this, two parallel 1×1 convolutions are applied to Ff to generate the object mask Mc and the object center point attention Ac. Where, Mc has dimensions of n×H×W, where n

represents the number of object categories in the dataset, and H and W represent the height and width of the input feature map X, respectively. Similarly, due to the symmetric architecture of the feature refinement module, we can obtain Fb, Ab, and Mb.

As for the Selective mechanism of module, we use the masks of the center points and bounding boxes for supervision to obtain different attention weights, Ac and Ab. The core idea of selection is as follows: at each point in the heatmap, if the value of Ac is greater than Ab, then the weight Wc is set to the value of Ac and then activated through the Sigmoid function. Otherwise, the weight Wc is set to 0. Similarly, we can derive the weight Wb. The mathematical expressions

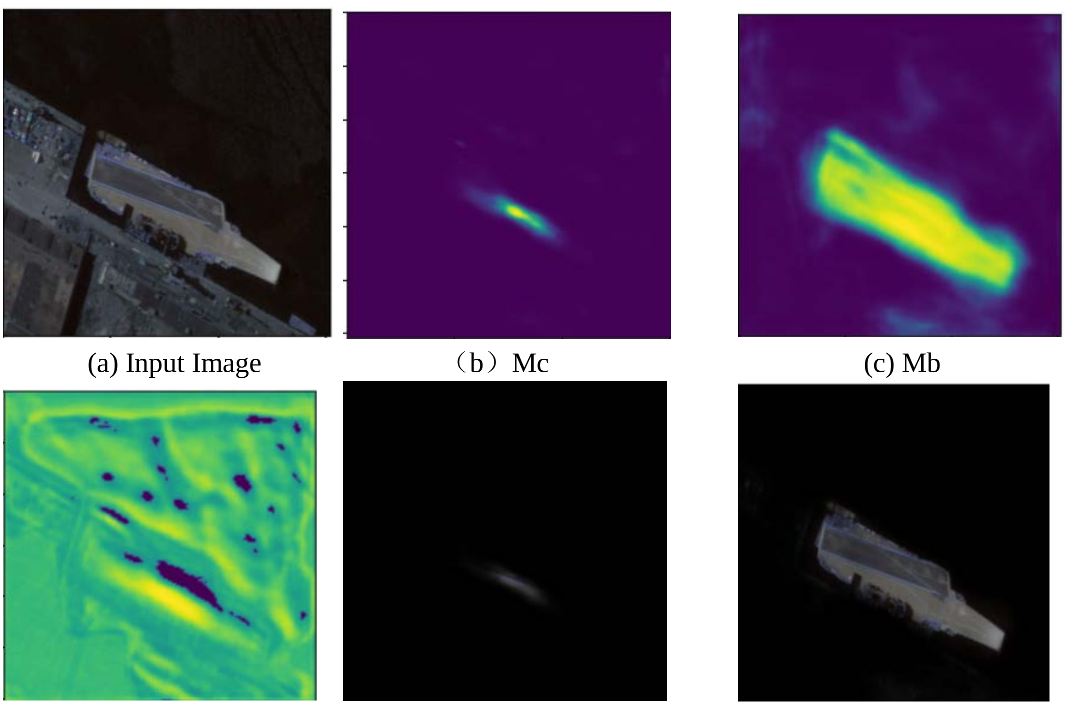

(a) Input Image　（b）Mc　(c) Mb

（d）Wc　（e）Mc×I　（f）Mb×I

Figure 4(a) input image, (b) Mc heatmap, (c) Mb heatmap, (d) center point weight, (e) input image with center point mask, f) input image with bounding box mask are as follows:

$$\mathrm{Wc} = \begin{cases} Sigmoid(\mathrm{Ac}), & if\ \mathrm{Ac} > Ab \\ 0, & else \end{cases} \#(10)$$

$$\mathrm{Wb} = \begin{cases} Sigmoid(\mathrm{Ab}), & if\ \mathrm{Ab} > Ac \\ 0, & else \end{cases} \#(11)$$

Where Wc represents the attention weight for center points, and Wb represents the attention weight for bounding boxes. The final output feature map of the symmetric feature refinement module is:

$$\mathrm{F} = \mathrm{X} + \mathrm{Fc} * \mathrm{Wc} + \mathrm{Fb} * \mathrm{Wb}\#(12)$$

In this paper, image masks generated by semantic segmentation are used for supervised learning in the symmetric feature refinement module. The mask for object center points, Mc, is generated using the proposed Tricube kernel function. By generating the complete object mask M from the ground-truth labels of the samples, the mask for the object bounding box, Mb, can be obtained by simply subtracting Mc from M:

$$\mathrm{Mc} = TricubeKernel(\mathrm{X})\#(13)$$

$$\mathrm{Mb} = \mathrm{M} - \mathrm{Mc}\#(14)$$

To illustrate the effectiveness of using image masks for supervised learning in the symmetric feature refinement module, heatmaps of Mc and Mb corresponding to the module are drawn in Fig 4.

As shown in Figure 4 above, supervised learning of the symmetric feature refinement module using object masks generated by image segmentation effectively enhances the module's perception ability for center points and bounding boxes. Figure 4(e) stand for the visual result obtained by multiplying the predicted center point mask with the original image I, while Figure 4(f) represents the visual result obtained by multiplying the predicted bounding box mask with the original image I.

C. LOSS FUNCTION

To train the proposed method, we adopted loss functions like BBAVectors[13]. The loss function consists of five main components: heatmap loss(L_p), offset loss(L_o), oriented bounding box loss(L_b), orientation loss(L_r), and symmetric feature refinement module supervision loss(L_m). Among them, $L_p$loss is a variant of Focal loss[2], $L_o$and$L_b$are calculatedusing Smooth L1, and L_r is calculatedusing binary cross-entropy loss(BCE Loss). The first four losses are consistent with the baseline model. The $L_m$loss consists of two parts:

$$L_m = L_{Mc} + L_{Mb}\#(15)$$

$$L_{Mc} = -\frac{1}{N_{Mc}}\sum_i \begin{cases} (1-\hat{P}_i)^\alpha log(\hat{P}_i), & if\ \ P_i = 1 \\ (1-P_i)^\beta \hat{P}_i^{\ \alpha} log(1-\hat{P}_i), & otherwise \end{cases} \#(16)$$

$$L_{Mb} = -\frac{1}{N_{Mb}}\sum_i \begin{cases} (1-\hat{P}_i)^\alpha log(\hat{P}_i), & if\ \ P_i = 1 \\ \hat{P}_i^{\ \alpha} log(1-\hat{P}_i), & otherwise \end{cases} \#(17)$$

Where L_{Mc} is the loss for the center point mask, which is calculated in the same way as L_p. L_{Mb} is the loss for the bounding box mask and is calculated using Focal Loss. N_{Mc} and N_{Mb} are normalization terms used to reduce the influences of different object sizes and scales on the loss function. N_{Mc} are the number of sampled boxes for loss calculation during training process, while N_{Mb} is related to the size of the predicted mask. In this paper, the value of N_{Mb} is:

$$N_{Mb} = (W/4) * (H/4)\#(18)$$

The hyper-parameters λ_1, λ_2,λ_3,$\lambda_4$and $\lambda_5$are the balance factors of the five loss terms and the final loss function of the model is as follows:

$$L = \lambda_1 L_p + \lambda_2 L_o + \lambda_3 L_b + \lambda_4 L_r + \lambda_5 L_m\#(19)$$

Unless otherwise specified, for simplicity we set $\lambda_1 = \lambda_2 = \lambda_3 = \lambda_4 = \lambda_5$.

IV. EXPERIMENTAL EVALUATION

Using the BBAVectors[13] method as the baseline, we conducted experiments on the HRSC2016[26] dataset to validate the effectiveness of the proposed method. Additionally, experiments were performed on the SSDD dataset [27], which consists of SAR-type data, to validate the generalizability of the proposed method.

A. DATASET

HRSC2016 is a large ship detection dataset consisting of 1,061 images and 2,970 object instances. Each instance in the dataset has two types of annotations: rotated bounding box annotations and rectangular bounding box annotations. The image sizes vary from 700 to 1100 pixels and the dataset is divided into three parts: training set, test set, and validation set, with 444, 436, and 181 images, respectively. We only used the training set to train the model and evaluated the effectiveness of the proposed method on the test set.

The SSDD dataset is a publicly available dataset designed for ship detection in SAR (Synthetic Aperture Radar) images. It consists of 1,160 images including 2,456ships, making it suitable for validating the detection performance of models on SAR-type images. We randomly divided the dataset into training and test sets in a ratio of 7:3, resulting in 870 images for training and 290 images for testing.

B. EVALUATION CRITERION

To be consistent with the baseline model BBAVectors, we use the VOC07 standard to calculate mAP (mean Average Precision) for HRSC2016. and use the VOC12 standard to calculate mAP for another dataset. In VOC07, AP is calculated using eleven-point interpolation, while in VOC12, AP is obtained by calculating the area under the precision-recall curve (PR curve). Precision (P) and recall (R) are defined as follows:

$$P = \frac{TP}{TP + FP} \#(20)$$

$$R = \frac{TP}{TP + FN} \#(21)$$

TP, FP and FN stand for true positive, false positive and false negative respectively. mAP is the average AP of objects in all categories:

$$\mathrm{mAP} = \frac{1}{N_{cls}} \sum_{i=1}^{N} \mathrm{AP_i} \#(22)$$

Where $AP_i$is the AP in the i-th class and $N_{cls}$is the total number of classed being evaluated.

C. INPLEMENTATION DETAILS

The images inputted to the network are resized to 608×608. The resolution of the output feature map of the upsampling module is 152×152. The backbone ResNet101 weights are pre-trained on the ImageNet dataset. In terms of dataset augmentation, we adopt the standard data augmentations to the images in the training process, which involve random flipping and random cropping. Adam [40] is used as the optimizer for the model, with an initial learning rate set to 1.25e-4. On the HRSC2016 dataset, we trained the model for 100 epochs using a batch size of 4 on an NVIDIA GeForce RTX 2080 Ti. On the SSDD dataset, we used Titan V for training, keeping the number of epochs and batch size consistent with HRSC2016. To ensure reproducibility, we fixed the random seed to 317 and replaced the bilinear interpolation used in BBAVectors with the default interpolation algorithm provided by PyTorch for upsampling, ensuring that the model produces consistent results after each training schedule.

D. ABLATION STUDY

To validate the effectiveness of the proposed module, we conducted experiments on the HRSC2016 and SSDD datasets, and obtained the above results. As can be seen from Tab. 1, we can find that the proposed Tricube kerneland symmetric feature refinement module both improve the mAP (mean Average Precision) for object detection. The fusion of these two methods further enhances the detection accuracy of the network. In this paper, SFRM(Gaussian)represents the symmetric feature refinement module usingthe Gaussian kernel to generate semantic segmentation masks for objects, while SFRM(Tricube) represents the use of Tricube kernel in the module to generate masks. The

Table 1　　Ablation studies on HRSC2016 and SSDD dataset

Method	+Tricube Kernel	+SFRM（Gaussian）	+SFRM（Tricube）	mAP(VOC07) HRSC2016	mAP(VOC12) SSDD
Baseline				88.20	90.03
	√			89.00	90.63
Our Methods		√		89.54	90.20
	√		√	**89.60**	**90.79**

combined experiments of the two modules both usetheTricube function to generate the required heatmaps.

To maintain consistency with the baseline network BBAVectors, mAP is calculated using the VOC07 standard on the HRSC2016 dataset and using VOC12 on the SSDD dataset. Compared to BBAVectors, the proposed Tricube kernel improves the model's detection accuracy by 0.8% on HRSC2016 and by 0.63% on SSDD. The symmetric feature refinement module improves the model's accuracy by 1.34% and 0.20% on the two datasets, respectively. The combination of these two methods leads to an improvement of 1.4% and 0.79% in the model's detection accuracy, respectively.

Table 4 Experiment results on HRSC2016 dataset

Type	Methods	Backbone	Input size	mAP
Two-Stage	R2CNN[28]	ResNet101	800×800	73.07
	RoI-Transformer[4]	ResNet101	512×800	86.20
	Gliding Vertex[29]	ResNet101	512×800	88.20
	ReDet[30]	ResNet101	512×800	90.46
	Oriented R-CNN[11]	ResNet101	1333×800	**90.5**
One-Stage	RSDet[31]	ResNet50	800×800	86.50
	CPS-Det[32]	ResNeXt50	800×800	89.12
	R3Det[33]	ResNet101	800×800	89.26
	KFIOU[34]	ResNet50	500×800	89.43
	DCL[10]	ResNet101	800×800	89.46
	AOPDet[35]	ResNet101	1024×1024	88.50
	GRS-Det[36]	ResNet101	800×800	89.57
	BBAVectors[13]	ResNet101	612×612	88.60
Ours		ResNet101	612×612	**89.60**

Tab. 2 illustrates the impact of parameters α and β in the Tricube kernel. When α is set to 3, the parameter β has trivial effect on the experimental results. However, when α is set to 2, there is a significant decrease in the model's detection accuracy. For the remaining experiments in this paper, they were conducted under the conditions of α=3 and β=7.

Table 2 the influence of α and β in Tricube kernel

(α, β)	mAP(VOC07) HRSC2016
(2, 10)	88.10
(3, 3)	88.90
(3, 7)	**89.00**

To verify the influence of different convolution kernel sizes in the symmetric feature refinement module, we conducted experiments on the HRSC2016 dataset using four sets of convolution sequences with increasing receptive fields. The experiments were performed on a Titan V GPU, and the results are shown in Table 3.

Table 3 the influence of kernel size and dilation rate in symmetric feature refinement module

(K, D) Sequence	Receptive Field	mAP(VOC07)
(3, 1) → (3, 1)	5	89.58
(3, 1) → (5, 2)	11	89.28
(5, 1) → (7, 3)	23	89.68
(5, 1) → (7, 4)	29	89.58

Where, the receptive field is calculated as follows:

$$RF_{out} = RF_{in} + (KernelSize - 1) * Dilation \#(23)$$

In remaining experiments, convolution kernel sequences were all used (5, 1) and (7, 3), whose equivalent receptive field was 23.

E. COMPARE WITH THE-STATE-OF-THE-ART METHODS

e compared the proposed model with currently popular two-stage and one-stage algorithms on the HRSC2016 dataset, and the experimental results are shown in Tab 4. Our proposed module improved the detection performance of the network by 1.4% compared to the baseline (local reproduction, BBAVectors's mAP is 88.20%). This surpasses many mainstreams two-stage algorithms and most of the one-stage algorithms, validating the effectiveness and state-of-the-art performance of our proposed module. The partial detection results visualization of our algorithm on the HRSC2016 dataset is shown in the Fig. 5.

The performance of the proposed module on the

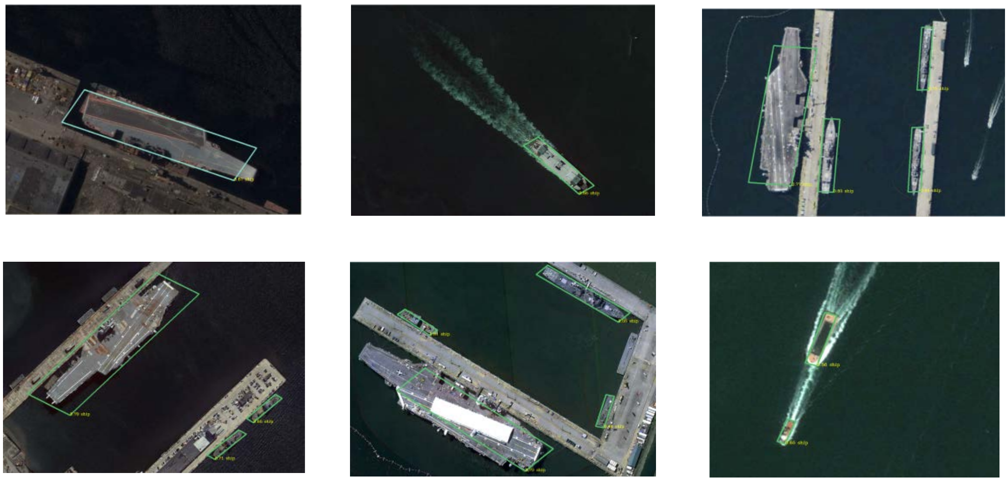

Figure 5 Visual detection results of HRSC2016 dataset

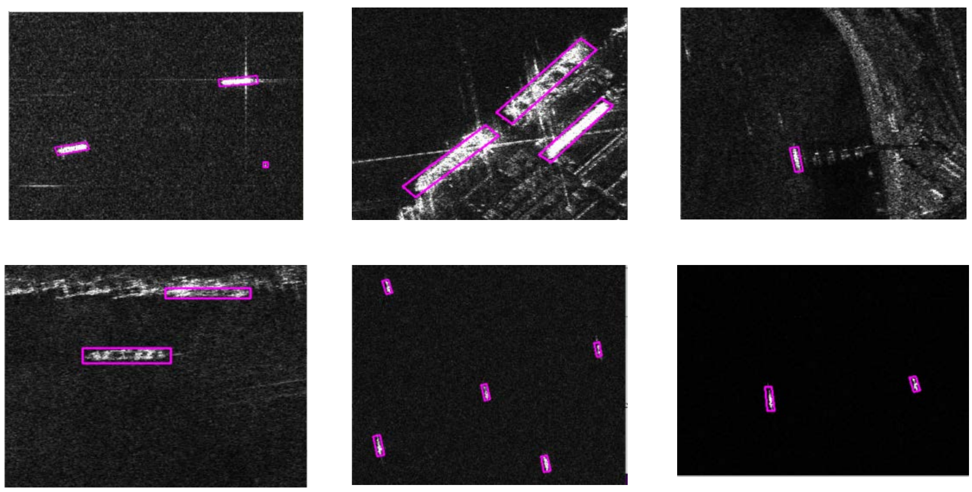

Figure 6 Visual detection results of SSDD dataset

SSDD dataset is shown in Tab. 5. In the experiment, compared with the existing horizontal boundary box detection algorithm, the detection accuracy of this paper is significantly improved.

Table 5　Experiment results of SSDD dataset

Method	Object type	mAP
LFO-Net[37]	HBB	80.12
The method of Cui, Li et al.[38]	HBB	89.8
The method of Chen et al[39]	HBB	79.78
DAPN[40]	HBB	83.4
BBAVectors[13]	OBB	90.03
Ours	OBB	**90.79**

SAR (Synthetic Aperture Radar) images are different from optical remote sensing images. Figure 6 shows partial detection results of the proposed algorithm on the SSDD dataset, demonstrating the versatility of our algorithm in effectively handling diverse types of remote sensing image datasets.

V. CONCLUSION AND FUTURE WORK

In this paper, we innovatively use the rotated size- adaptive Tricube kernel to generate object keypoint heatmaps instead of Gaussian kernel, which solves the problem that Gaussian kernel can not represent the size and angle of object well due to the circular form. Furthermore, to enhance the model's detection performance for large-area objects and improve its perception of object keypoints and bounding boxes, we propose the symmetric feature refinement module based on convolutional kernel decomposition and supervised learning using semantic segmentation masks. The combination of these two approaches not only fully utilizes prior information from the samples but also reduces background interference and improves the model's feature extraction ability for rotated objects. Experimental results on the HRSC2016 and SSDD datasets demonstrate the effectiveness and generality of the proposed methods.

For future work, the symmetric feature refinement module proposed in this paper performs poorly in detecting small-sized objects. Additionally, the Tricube kernel has limited improvement in detecting densely arranged objects. Addressing these issues would greatly enhance the performance of the model.

References

[1] Ren S, He K, Girshick R, et al. Faster r-cnn: Towards real-time object detection with region proposal networks[J]. Advances in neural information processing systems, 2015, 28.

[2] Lin T Y, Goyal P, Girshick R, et al. Focal loss for dense object detection[C]//Proceedings of the IEEE international conference on computer vision. 2017: 2980-2988.

[3] Ma J, Shao W, Ye H, et al. Arbitrary-oriented scene text detection via rotation proposals[J]. IEEE transactions on multimedia, 2018, 20(11): 3111-3122.

[4] Ding J, Xue N, Long Y, et al. Learning RoI transformer for oriented object detection in aerial images[C]//Proceedings of the IEEE/CVF Conference on Computer Vision and Pattern Recognition. 2019: 2849-2858.

[5] Zhu K, Zhang X, Chen G, et al. Multi-Oriented Rotation-Equivariant Network for Object Detection on Remote Sensing Images[J]. IEEE Geoscience and Remote Sensing Letters, 2022, 19: 1-5.

[6] Yang X, Yang J, Yan J, et al. Scrdet: Towards more robust detection for small, cluttered and rotated objects[C]//Proceedings of the IEEE/CVF international conference on computer vision. 2019: 8232-8241.

[7] Zhou L, Wei H, Li H, et al. Arbitrary-oriented object detection in remote sensing images based on polar coordinates[J]. IEEE Access, 2020, 8: 223373-223384.

[8] Ming Q, Zhou Z, Miao L, et al. Dynamic anchor learning for arbitrary-oriented object detection[C]//Proceedings of the AAAI Conference on Artificial Intelligence. 2021, 35(3): 2355-2363.

[9] Wang J, Yang W, Li H C, et al. Learning center probability map for detecting objects in aerial images[J]. IEEE Transactions on Geoscience and Remote Sensing, 2020, 59(5): 4307-4323.

[10] Yang X, Hou L, Zhou Y, et al. Dense label encoding for boundary discontinuity free rotation detection[C]//Proceedings of the IEEE/CVF conference on computer vision and pattern recognition. 2021: 15819-15829.

[11] Xie X, Cheng G, Wang J, et al. Oriented R-CNN for object detection[C]//Proceedings of the IEEE/CVF international conference on computer vision. 2021: 3520-3529.

[12] Zhou X, Wang D, Krähenbühl P. Objects as points[J]. arXiv preprint arXiv:1904.07850, 2019.

[13] Yi J, Wu P, Liu B, et al. Oriented object detection in aerial images with box boundary-aware vectors[C]//Proceedings of the IEEE/CVF Winter Conference on Applications of Computer Vision. 2021: 2150-2159.

[14] Wei H, Zhang Y, Chang Z, et al. Oriented objects as pairs of middle lines[J]. ISPRS Journal of Photogrammetry and Remote Sensing, 2020, 169: 268-279.

[15] Zhang F, Wang X, Zhou S, et al. Arbitrary-oriented ship detection through center-head point extraction[J]. IEEE Transactions on Geoscience and Remote Sensing, 2021, 60: 1-14.

[16] Kim B, Lee J, Lee S, et al. TricubeNet: 2D kernel-based object representation for weakly-occluded oriented object detection[C]//Proceedings of the IEEE/CVF Winter Conference on Applications of Computer Vision. 2022: 167-176.

[17] Dosovitskiy A, Beyer L, Kolesnikov A, et al. An image is worth 16x16 words: Transformers for image recognition at scale[J]. arXiv preprint arXiv:2010.11929, 2020.

[18] Liu Z, Lin Y, Cao Y, et al. Swin transformer: Hierarchical vision transformer using shifted windows[C]//Proceedings of the IEEE/CVF international conference on computer vision. 2021: 10012-10022.

[19] Liu Z, Mao H, Wu C Y, et al. A convnet for the 2020s[C]//Proceedings of the IEEE/CVF conference on computer vision and pattern recognition. 2022: 11976-11986.

[20] Ding X, Zhang X, Han J, et al. Scaling up your kernels to 31x31: Revisiting large kernel design in cnns[C]//Proceedings of the IEEE/CVF conference on computer vision and pattern recognition. 2022: 11963-11975.

[21] Liu S, Chen T, Chen X, et al. More convnets in the 2020s: Scaling up kernels beyond 51x51 using sparsity[J]. arXiv preprint arXiv:2207.03620, 2022.

[22] Li Y, Hou Q, Zheng Z, et al. Large Selective Kernel Network for Remote Sensing Object Detection[J]. arXiv preprint arXiv:2303.09030, 2023.

[23] Xu C, Li C, Cui Z, et al. Hierarchical semantic propagation for object detection in remote sensing imagery[J]. IEEE Transactions on Geoscience and Remote Sensing, 2020, 58(6): 4353-4364.

[24] Liu S, Zhang L, Lu H, et al. Center-boundary dual attention for oriented object detection in remote sensing images[J]. IEEE Transactions on Geoscience and Remote Sensing, 2021, 60: 1-14.

[25] Xia G S, Bai X, Ding J, et al. DOTA: A large-scale dataset for object detection in aerial images[C]//Proceedings of the IEEE conference on computer vision and pattern recognition. 2018: 3974-3983.

[26] Liu Z, Yuan L, Weng L, et al. A high resolution optical satellite image dataset for ship recognition and some new baselines[C]//International conference on pattern recognition applications and methods. SciTePress, 2017, 2: 324-331.

[27] Zhang T, Zhang X, Li J, et al. SAR ship detection dataset (SSDD): Official release and comprehensive data analysis[J]. Remote Sensing, 2021, 13(18): 3690.

[28] Jiang Y, Zhu X, Wang X, et al. R 2 cnn: Rotational region cnn for

arbitrarily-oriented scene text detection[C]//2018 24th International conference on pattern recognition (ICPR). IEEE, 2018: 3610-3615.

[29] Xu Y, Fu M, Wang Q, et al. Gliding vertex on the horizontal bounding box for multi-oriented object detection[J]. IEEE transactions on pattern analysis and machine intelligence, 2020, 43(4): 1452-1459.

[30] Han J, Ding J, Xue N, et al. Redet: A rotation-equivariant detector for aerial object detection[C]//Proceedings of the IEEE/CVF Conference on Computer Vision and Pattern Recognition. 2021: 2786-2795.

[31] Qian W, Yang X, Peng S, et al. Learning modulated loss for rotated object detection[C]//Proceedings of the AAAI conference on artificial intelligence. 2021, 35(3): 2458-2466.

[32] Li X, Li Z, Lv S, et al. Ship detection of optical remote sensing image in multiple scenes[J]. International Journal of Remote Sensing, 2022, 43(15-16): 5709-5737.

[33] Yang X, Yan J, Feng Z, et al. R3det: Refined single-stage detector with feature refinement for rotating object[C]//Proceedings of the AAAI conference on artificial intelligence. 2021, 35(4): 3163-3171.

[34] Yang X, Zhou Y, Zhang G, et al. The KFIoU loss for rotated object detection[J]. arXiv preprint arXiv:2201.12558, 2022.

[35] Zhu Z, Sun X, Diao W, et al. AOPDet: Automatic organized points detector for precisely localizing objects in aerial imagery[J]. IEEE Transactions on Geoscience and Remote Sensing, 2021, 60: 1-16.

[36] Zhang X, Wang G, Zhu P, et al. GRS-Det: An anchor-free rotation ship detector based on Gaussian-mask in remote sensing images[J]. IEEE Transactions on Geoscience and Remote Sensing, 2020, 59(4): 3518-3531.

[37] Zhang X, Wang H, Xu C, et al. Lightweight Feature Optimizing Network for Ship Detection in SAR Image[J]. IEEE Access. 2019, 7:141662-141678.

[38] Cui Z, Li Q, Cao Z, et al. Dense Attention Pyramid Networks for Multi-Scale Ship Detection in SAR Images[J]. IEEE Transactions on Geoscience and Remote Sensing, 2019, 57(11): 8983-8997.

[39] Chen C, He C, Hu C, et al. A Deep Neural Network Based on an Attention Mechanism for SAR Ship Detection in Multiscale and Complex Scenarios[J]. IEEE Access, 2019, 7:104848-104863

[40] Li Q, Min R, Cui Z, et al. Multiscale Ship Detection Based on Dense Attention Pyramid Network in Sar Images[C]. In Proceedings of IEEE International Geoscience and Remote Sensing Symposium, 2019, 5-8

About the authors

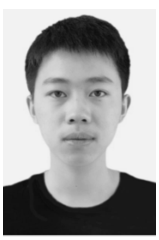

Yushan Pan was born in Anhui, China, in 2000. He received the B.Sc. degree in computer science and technology from Nanjing University of Science and Technology(NUST). He is currently pursuing the M.Sc. degree in NUST, Nanjing. His research interests include object detection and deep learning.

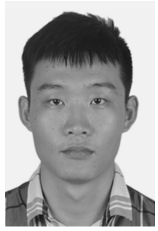

Yang Xu(Member IEEE) received the B.Sc. degree in applied mathematics and the Ph.D. degree in pattern recognition and intelligence systems from the Nanjing University of Science and Technology(NUST), Nanjing, China, in 2011 and 2016, respectively.

He is currently a Professor with the School of Computer Science and Engineering, NUST. His research interests include hyperspectral image classification, image processing, and machine learning.

Zebin Wu(Senior Member, IEEE) received the B.Sc. and Ph.D. degrees in computer science and technlogy from the Nanjing University of Science and Technology, Nanjing, China, in 2003 and 2007, respectively.

He is currently a Professor with the School of Computer Science and Engineering, Nanjing University of Science and Technology. His research interests include hyperspectral image processing, parallel computing, and big data processing.

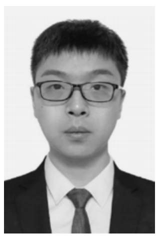

Shangdong Zheng was born in Jiangsu, China,in 1995. He received the B.Sc. degree in software engineering from the School of Computer andCommunication, Lanzhou University of Technology,Lanzhou, China, in 2017. He is currently pursuingthe Ph.D. degree with the Nanjing University ofScience and Technology, Nanjing, China.

His research interests include object detection,remote-sensing object detection, image processing,and deep learning.

Zhihui Wei (Member, IEEE) was born in Jiangsu,China, in 1963. He received the B.Sc. and M.Sc.degrees in applied mathematics and the Ph.D. degreein communication and information systems fromSoutheast University, Nanjing, China, in 1983, 1986,and 2003, respectively.

He is currently a Professor and a Doctoral Supervisor with the Nanjing University of Science andTechnology (NUST), Nanjing. His research interests include partial differential equations, mathematical image processing, multiscale analysis, sparserepresentation, and compressive sensing

A Multi-Resolution Image Fusion Method for Hyperspectral and SAR images Based on Multi-Task Convolutional Neural Networks

Yifan ZHANG, Yang XU, Zebin WU, Biqi WANG, Zhihui WEI
School of Computer Science and Engineering, Nanjing University of Science and Technology, Nanjing, China

Abstract—**In recent years, a single sensor can no longer satisfy the expanding needs due to the diversification of remote sensing imaging techniques. To provide more accurate and thorough remote sensing earth observation, multi-source remote sensing image fusion may fully utilize image information obtained from different sensors. However, integrating complementary advantages is still difficult because of the variance in imaging techniques and the informational imbalance among data from multiple sources. Furthermore, real-world situations frequently involve varied data resolution, and the outcomes of straightforward super-resolution preprocessing are not always helpful for performing subsequent tasks. In this paper, we propose a multi-task convolutional network framework for super-resolution reconstruction and fusion of hyperspectral images, which can be applied to the multi-resolution fusion classification task of low-resolution hyperspectral images (LR-HSIs) and SAR images. The minimization of the proposed joint loss function in the generative adversarial network (GAN) framework, including super-resolution and classification objective functions, can effectively achieve the multi-task goals. Experimental results on the super-resolution and classification of real LR-HSIs and SAR images demonstrate the effectiveness of the proposed method visually and quantitatively.**

Keywords — **data fusion, multi-resolution image fusion, multimodal-cross attention, super-resolution, multi-task GAN**

I. INTRODUCTION

With the development of remote sensing earth observation technologies such as multispectral, hyperspectral, infrared, synthetic aperture radar, and night light, remote sensing imaging methods have shown a trend of diversification[1], and multi-source remote sensing image fusion has also become a research hotspot in the field of remote sensing. The ground objects captured by multi-source remote sensing images of the same scene are the same, but the image resolution, field of view and target characteristics reflected by the image are different.

Several studies aimed at combining multi-sensor data have been carried out. For example, Byun Y. et al. [2] proposed a multi-sensor image fusion method based on texture fusion rules. Currently, methods based on feature fusion have been proposed to obtain more recognizable fusion features. Cao Q. et al.[3] presented a fusion algorithm that combines the semantic information expressed by traditional artificial features with the abstract information extracted by convolutional neural networks (CNNs). Mohla et al.[4] developed a dual attention-based spectral-spatial multimodal fusion network for HSI and LiDAR classification.

In some cases, optical and SAR images are strongly complimentary[5], and fusion of optical and SAR images for remote sensing classification is considered to be a promising method to improve classification accuracy[6]. Among them, hyperspectral images (HSIs) can give detailed descriptions of the spectral signatures of ground covers but have low spatial resolution, whereas Synthetic Aperture Radar (SAR) data provides rich target scattering information coupled with severe speckle noise. Compared with the limitations of a single source of data, the fusion of hyperspectral data and SAR data can take advantage of the unique advantages of optical imaging and active imaging to generate higher-quality fused images.

However, there are still many challenges in the fusion of multi-source remote sensing images. For example, different basic principles of imaging lead to excessive image structural differences; information imbalance between multi-source data makes it difficult to combine complementary advantages; and differences in image resolution hinder practical applications. Specifically, the proportion of spectral information in hyperspectral data is much higher than that in SAR data, and some symmetric feature fusion methods are not suitable because they can’t fully combine complementary advantages[7]. In addition, considering the low spatial resolution of hyperspectral images, hyperspectral images need to be super-resolution processed before fusion to match the size of SAR data, and the goal of the super-resolution task is not only to make the hyperspectral images clear, but also to make them easier to fuse and classify. However, from sparse dictionary learning or low-rank approximation[8][9] to deep convolutional neural networks[10][11], super-resolution reconstruction methods focus only on the reconstruction of fine textures in hyperspectral images. Very little work has been done to combine reconstruction and fusion classification tasks.

To address the problems above, we propose a multi-task convolutional network framework. This end-to-end framework includes a super-resolution branch and a fusion classification branch, and integrates the super-resolution and fusion classification tasks into the GAN framework through a joint loss function, which can improve the fusion classification performance for LR-HSIs and SAR images in real-world situations.

The main contributions of this work are summarized as follows.

1) Considering the existing problems in hyperspectral and SAR image fusion tasks, a novel end-to-end unified framework for joint super-resolution and fusion classification tasks is designed. It selects a reasonable and efficient super-resolution method, designs a fully interactive fusion classification module, and innovatively integrates these two tasks into the GAN framework through a unified joint loss function.

2) The hyperspectral image super-resolution branch is implemented by alternating serial 2D and 3D convolutions, combined with information from SAR images. The fusion classification branch includes three core modules: multi-scale feature extraction module, asymmetric feature propagation module, and multi-modal cross-attention module to achieve the extraction of effective information and full interaction between HSI and SAR data, and generate accurate classification result.

3) Finally, we demonstrate the effectiveness of the network in two tasks. Extensive experiments on two real-world datasets show that our method can guarantee the quality of hyperspectral image super-resolution while also achieving better classification results than state-of-the-art fusion classification methods.

This paper is organized as follows: Section II and Section III describe the details of our proposed framework. Section IV presents extensive experiments and a comprehensive analysis of the proposed method. Section V draws the conclusion.

II. THE PROPOSED METHOD

The overall structure of the proposed framework is shown in Fig.1, and the details of the super-resolution and fusion sub-networks are shown in Fig.2. First, we use serial 2D and 3D convolution alternately for HSI super-resolution without increasing network parameters, and we incorporate information from high-resolution SAR images. Second, the same blocks are employed for feature extraction of the super-resolution HSI and SAR images, and an additional multi-scale feature information extraction module is adopted for the SAR branch to enhance the richness of feature extraction. The entire fusion interaction between HSI and SAR data is then achieved using the asymmetric feature propagation module and multi-modal cross-attention module, and we put the fusion features into the classifier to obtain the final classification result. Finally, we integrate the above tasks into a unified GAN network through a joint loss function.

A. HYPERSPECTRAL SUPER-RESOLUTION

In view of the inherent characteristics of hyperspectral images, researchers have designed various methods using 2D convolution with reference to the natural image super-resolution method[12]. Unlike 2D convolution, conventional 3D convolution is implemented by convolving 3D kernels and feature maps. It results in a significant increase in network parameters. Considering this shortcoming, researchers modified the filter $k \times k \times k$ to $k \times 1 \times 1$ and $1 \times k \times k$ [10]. Typical algorithms include SSRNet[11] and MCNet[10]. In order to effectively combine 2D and 3D convolution in hyperspectral super-resolution networks, 2D and 3D convolution units can be used alternately in serial to overcome the redundancy problem caused by parallel structures in previous super-resolution networks and learn spatial domain information better under the premise of sharing spatial information. At the same time, split adjacent spatial and spectral convolution[13] are introduced to fully explore the information between the spectrum and the horizontal or vertical direction of the space. Furthermore, in order to make full use of the existing prior information, we add related information from the SAR image to the end of the super-resolution network to obtain more abundant reconstruction information and better reconstruction image quality.

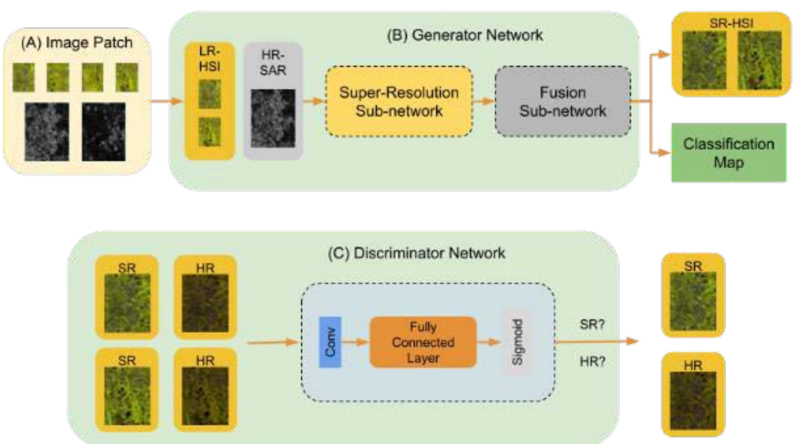

Figure 1 Overall architecture of the model

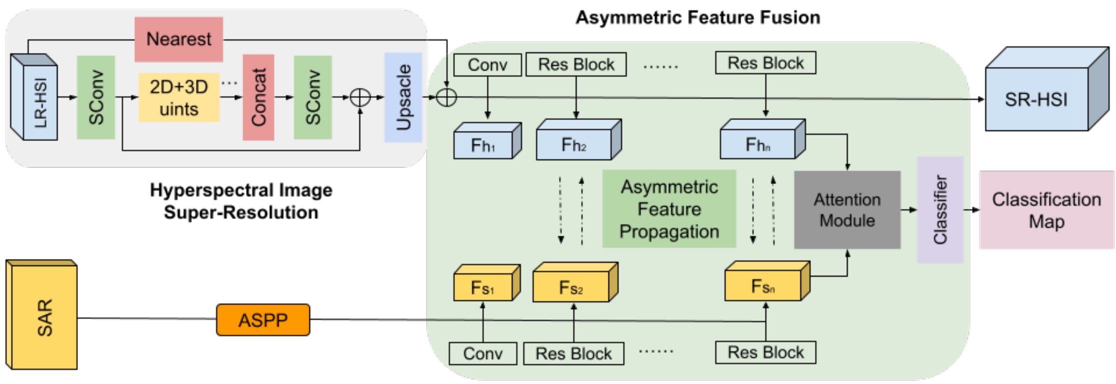

Figure 2 Details of the super-resolution and fusion sub-networks

B. ASYMMETRIC FEATURE PROPAGATION

The imbalance of multi-source data tends to reduce the effect of feature interaction. Instead of generating features with the same expressive capacity, a more effective method is to use the form of asymmetric feature propagation to integrate complementary advantages. Before feature propagation and fusion, we divide the super-resolution HSI and SAR images into the same image blocks for feature extraction and use an additional multi-scale feature information extraction module for the SAR branch to enhance the richness of feature extraction. When using the weight-share residual blocks for feature extraction, an independent batch normalization (BN) layer is maintained, and the redundancy of the current channel is determined by the scale factor in the BN. The specific feature fusion algorithm is formulated as follows:

$$y_{h,c} = \begin{cases} \gamma_{h,c}\dfrac{x_{h,c}-\mu_{h,c}}{\sqrt{\sigma_{h,c}^2+\epsilon}} + \beta_{h,c}, \text{if } \gamma_{h,c} > \theta \\ \gamma_{s,c}\dfrac{x_{s,c}-\mu_{s,c}}{\sqrt{\sigma_{s,c}^2+\epsilon}} + \beta_{s,c}, \text{else} \end{cases}$$

Where *h, c*, and *s, c* are the BN parameters of the c_{th} channel in the HSI and SAR branches, $x_{h,c}$ and $x_{s,c}$ are the c_{th} channel features from X_h and X_s, respectively, and θ is a self-set threshold close to 0.

C. CROSS-ATTENTION MODULE

Most traditional attention mechanisms don’t have the ability to generate high-dimensional joint features. In order to improve the joint feature expression ability, we use a module combining single source self-attention and multi-modal cross-attention to effectively capture the position relationship of a single data source feature map, and carry out feature map interaction of HSI and SAR images in two-dimensional space.

The flow chart of this module is shown in Fig.3. The specific steps are as follows:

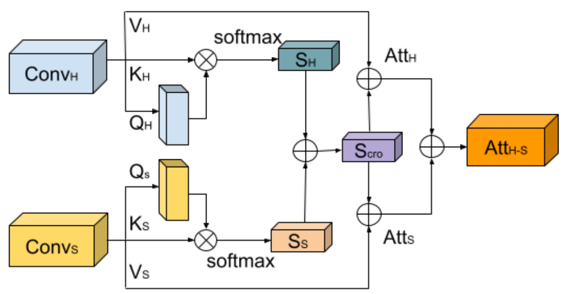

Figure 3 Flowchart of the cross-attention module

(1) Input HSI and SAR patches, and extract the feature maps V_H, Q_H, K_H of HSI and V_S, Q_S, K_S of SAR data respectively with three 1×1 convolution.

(2) Calculate the self-attention of HSI and SAR data respectively, and the context can be modeled effectively by capturing the internal correlation of features and obtaining the long-range dependencies between features. The calculation formula is as follows:

$$S_H = softmax(Q_H \otimes K_H)$$
$$S_S = softmax(Q_S \otimes K_S)$$

(3) Calculate multi-modal cross attention and joint attention of HSI and SAR image patches to obtain weighted feature maps:

$$S_{cro} = S_H \odot S_S$$
$$Att_H = S_{cro} \odot V_H$$
$$Att_S = S_{cro} \odot V_S$$

(4) Cross the weighted feature maps of HSI and SAR image patches to obtain the final joint attention map:

$$Att_{H-S} = Att_H \odot Att_S$$

III. NETWORK DETAILS

In the above fusion task, in order to match the size of SAR data, hyperspectral super-resolution preprocessing can be directly introduced. However, we not only need to reconstruct HSI with fine texture but also construct high-resolution images with strong discriminative information to complete the fusion classification task. Therefore, we propose a unified multi-task convolutional neural network to simultaneously complete super-resolution and fusion classification tasks by integrating these two tasks into GAN through a joint loss function.

A. GENERATOR NETWORK

As shown in Fig.1, the generator network consists of two sub-networks, namely the HSI super-resolution sub-network and the asymmetric feature fusion sub-network. The super-resolution network takes low-resolution HSI patches as input and outputs $2\times$ super-resolution HSI patches. Then, the second sub-network cascaded with it fuses the features of the reconstructed HSI and SAR data in the form of asymmetric feature propagation and cross-attention, and finally outputs the classification map.

B. DISCRIMINATOR NETWORK

We add a true or false classification branch at the end of the discriminator network, which consists of a convolutional layer, a fully connected layer, and a sigmoid function. Its function is to reflect the probability that the input image is a real image or a generated super-resolution image. Furthermore, the classification loss function is backpropagated to the generator to obtain high-resolution images with discriminative information for better classification.

C. LOSS FUNCTION

Let $\{I_i^{LR}, i = 1,2,\dots,N\}$ and $\{I_i^{HR}, i = 1,2,\dots,N\}$ represent the low-resolution blurred HSIs and the real high-resolution HSIs as the input images, respectively. The parameters $\{y_i, i = 1,2,\dots,N\}$ represent the corresponding labels of land classification. Multi-task learning of network structure is achieved by mixing multiple losses, and the overall loss is mainly divided into pixel-wise loss, adversarial loss, and classification loss.

Pixel-wise loss is a simple method for compelling the super-resolution images generated by the generator to be similar to real HSIs is to use the pixel-level mean square error (MSE) loss. The similar level MSE loss function is composed of the differences between the super-resolution HSIs and real HSIs. The formula is given by:

$$L_{MSE} = \frac{1}{N}\sum_{i=1}^{N} \|G_w(I_i^{LR}) - I_i^{HR}\|^2$$

The adversarial loss function is added to the target loss function in order to diminish the visual disparities between the real and super-resolution HSIs. This forces the generator to produce super-resolution HSIs that are sufficiently similar to the real HSIs to deceive the discriminator. The adversarial loss is defined as:

$$\frac{1}{N}\sum_{i=1}^{N} \log\left(1 - D_\theta\left(G_w(I_i^{LR})\right)\right) + \log D_\theta(I_i^{HR})$$

To allow the generator to recover more details of the object content for easier classification, we introduce the classification loss to the object function. The classification loss function is:

$$\frac{1}{N}\sum_{i=1}^{N} \log\left(y_i - G_{cls}(I_i^{LR})\right)$$

For better gradient behavior, we optimize the objective function through alternate training and define the loss function of generator G and the discriminator D as follows:

$$\min_{w} \frac{1}{N}\sum_{i=1}^{N} \left(\alpha \log\left(1 - D_\theta\left(G_w(I_i^{LR})\right)\right)\right.$$
$$\left. -\beta \log\left(y_i - G_{cls}(I_i^{LR})\right) + \|G_w(I_i^{LR}) - I_i^{HR}\|^2\right)$$

$$\min_{\theta} \frac{1}{N}\sum_{i=1}^{N} -\left(\log D_\theta\left(G_W(I_i^{LR})\right) + \log D_\theta\left(G_W(I_i^{HR})\right)\right)$$

Here, the α and β parameters represent the trade-off weights. $G_w(I_i^{LR})$ and $D_\theta\left(G_w(I_i^{LR})\right)$ are the generated high-resolution HSIs and the probability of the reconstructed HSIs, respectively. And $G_{cls}(I_i^{LR})$ denotes the probabilities of the generated super-resolved HSIs belonging to the true category y_i.

IV. EXPERIMENTAL EVALUATION

In order to verify the effectiveness of this method, we select two real HSI and SAR datasets for experimental verification. Among them, Python 3.8 is used to complete the training of the network, and the Pytorch version is 1.9.0. In the experiment, the CPU uses an Intel(R) Core(TM) i7-9700K CPU @ 3.60GHz, 8 cores, 32GB of memory, Windows 10 64-bit system, and the GPU used an NVIDIA GeForce RTX 2080Ti with 11GB of available video memory.

A. EXPERIMENTAL DATASET

The HSI and SAR data used in the experiments are publicly available datasets. The first dataset consists of spaceborne hyperspectral and dual-polarization PolSAR images from Augsburg, Germany, collected by the HySpex sensor and the Sentinel-1 sensor[14][15]. The spatial resolution of both data is 30 m GSD and the size is 332×485. The HSI contains 180 spectral bands (0.4~2.5 μm) and the SAR contains four features based on polarization decomposition. In order to facilitate subsequent experiments, we cut the data set into a size of 320×480; and the HSI of the second Berlin data set is simulated EnMAP data synthesized based on the HyMap HS data, with a wavelength range of 244 bands from 400 to 2500 nm[16], we also crop it to 800×440 for the convenience of subsequent calculations.

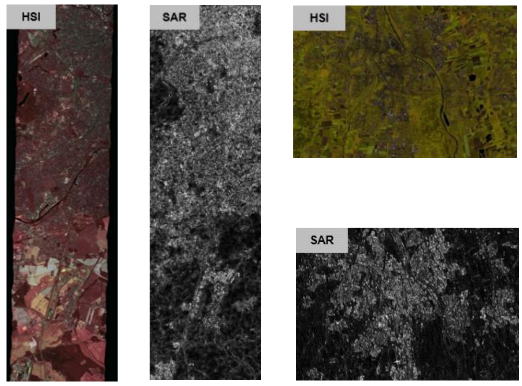

(a)　　(b)

Figure 4 Multisource remote sensing dataset. (a) Berlin dataset. (b) Augsburg dataset.

B. Evaluation Metrics

We use six quantitative indicators to evaluate various models. To be specific, we adopt Peak Signal-to-Noise Ratio (PSNR), Spectral Angle Mapper (SAM) and Structural SIMilarity (SSIM) to evaluate the performance of reconstructed HSI. And we select the Overall Accuracy (OA), the Average Accuracy (AA) and the Kappa Coefficient (Kappa) as the metrics for the evaluation of the fusion classification task.

C. EXPERIMENTAL DETAILS

For SAR and HSI data, we use half of the images for training and the other half for testing. First, 5000 image patches with a patch size of 16 are randomly selected from the SAR images and HSI at the same time. After adding noise, rotation, and other data enhancement operations, the training set and verification set are divided into a training set and a verification set in a ratio of 4:1. Taking the $2\times$ magnification as an example, the HR-HSI in the training sample needs to be bicubic interpolated and downsampled to half the original image resolution to obtain the low-resolution image LR-HSI during the training process. Before inputting these data, we subtract the average of all image patches and finally send the training samples of SAR and LR-HSI to the cascaded generator network for training.

Taking the Augsburg dataset as an example, the specific input and test sample numbers are as shown in the following table:

Table 1 Number of samples in Augsberg dataset

Class		Number of Sample	
No.	Name	Training	Testing
1	Forest	7124	5650
2	Residential Area	17348	12410
3	Industrial Area	1481	2319
4	Low Plants	10261	14411
5	Allotment	276	219
6	Commercial Area	963	664
7	Water	680	781
	Total	38133	36454

C. EXPERIMENTAL RESULTS AND ANALYSIS

To verify the effectiveness of our method, we compare our model with other models using sup er-resolution methods and classification methods.

(1) Effect on the super-resolution.

We compare our approach with Bicubic, EDSR[17], MCNet[10] respectively to prove the super-resolution performance of our method. It demonstrates that the proposed method achieves better performance on the three indicators listed in Tab.2. Compared with those of Bicubic, EDSR, and MCNet, this method achieves 2.19, 0.53, and 0.24 higher PSNR, respectively. The results above show that the super-resolution image reconstruction of the proposed method ensures the quality of image generation and offers discriminative images for fusion classification tasks that follow.

Table 2 Comparison of different super-resolution methods

Method	Augsberg			Berlin		
	PSNR	PSNR	SSIM	SAM	SSIM	SAM
Bibubic	31.23	0.81	7.67	37.12	0.93	2.31
EDSR	32.89	0.84	7.47	39.03	**0.97**	**2.05**
MCNet	33.18	0.85	7.63	39.26	**0.97**	2.15
Proposed	**33.42**	**0.86**	**7.32**	**39.65**	**0.97**	2.15

(2) Effect on the classification.

To evaluate the classification performance, the SVM classifier with radial basis function (RBF) kernels and the DFINet[18] are applied in our experiments. Tab.3 shows the results obtained from the experiments. It can be found that our proposed method performs the best, the overall accuracy is 6.61% and 1.82% better than SVM and the DFINet on the Augsberg dataset, and there is an increase of 4.39% and 4.24% on the Berlin dataset. For visual comparisons, we also show the classification maps of the aforementioned methods on the two datasets in Fig.5. The classification map generated by SVM is rather noisy since less spatial information is taken into account in the classifiers, and the DFINet obtains more clear classification results comparatively. In general, our method obtains the best global performance.

Table 3 Comparison of different classification methods

Method		Augsberg			Berlin		
		OA	AA	Kappa	OA	AA	Kappa
	HSI	88.89	57.19	86.61	84.15	51.72	78.25
SVM	SAR	89.78	48.02	85.88	61.81	32.78	50.24
	H+S	90.31	55.73	86.69	85.04	50.24	79.40
DFINet	H+S	95.10	61.50	92.53	85.19	47.76	79.48
Proposed	H+S	**96.92**	**71.40**	**95.40**	**89.43**	**56.36**	**85.39**

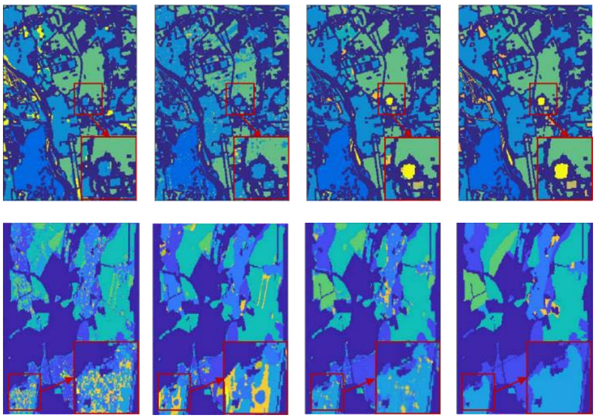

(a) (b) (c) (d)

Figure 5 Classification maps using different methods. (a) SVM. (b) DFINet. (c) Proposed. (d) Ground Truth.

(3) Ablation Studies and Running Time Comparisons.

The effectiveness of each proposed module for ensuring super-resolution quality and improving classification accuracy is verified through a series of ablation experiments, and the specific experimental results are listed in Tab.4. We choose ERCSR[13] and Asyffnet[7] as baseline methods. Initially, these two methods are trained independently of one another. Then, since cascaded ERCSR+ Asyffnet is only used as a pre-processing super-resolution method, it does not consider the discriminative information required for downstream classification tasks. Hence, although it does get good SR results, the performance improvement for subsequent classification tasks is limited. To improve downstream classification performance, we organically combine them into a GAN network. which uses the joint loss function method to train them to achieve information complementarity jointly.

It can be seen from the experimental results in Tab.4 that the proposed structure further enhances the classification performance on the basis of preserving the quality of HSI super-resolution.

V. CONCLUSION AND FUTURE WORK

In order to solve the problem of the large difference in resolution between HSI and SAR data in practical application scenarios and the imbalance of information between multi-source data, this paper proposes a multi-task convolutional neural network framework which can be applied to the fusion of multi-resolution HSIs and SAR images. First, this paper combines super-resolution reconstruction and fusion tasks and achieves super-resolution reconstruction of HSIs at any multiple through serial 2D and 3D convolution modules, while achieving fusion of HSI and SAR data of different resolutions. Secondly, a mechanism combining self-attention and cross-attention is introduced to learn the two-dimensional spatial relationship between different features and improve the visual expression of the image. At the same time, a unified joint loss function is proposed to integrate the above tasks into a GAN framework for alternate optimization training. Experimental results show that the method proposed in this paper provides discriminative images for subsequent fusion classification tasks while ensuring the quality of hyperspectral super-resolution reconstruction, making the overall classification result reach high accuracy. However, the performance of the algorithm in this paper is limited when the resolution of HSI and SAR data differs by too many multiples, and there is still room for improvement in the fusion effect at high magnifications.

Table 4 Ablation study on the components of the network

Method		Training time(s)	Testing time(s)	PSNR	PSNR	SSIM	SAM	SSIM	SAM
Augsberg	Asyffnet	352	390	-	-	-	96.15	71.84	94.13
	ERCSR	40732	4129	33.22	0.85	7.63	-	-	-
	Cascade	52204	4818	**33.46**	**0.86**	**7.22**	96.60	68.82	94.80
	Proposed	50893	4033	33.42	**0.86**	7.32	**96.92**	**71.40**	**95.40**
Berlin	Asyffnet	356	993	-	-	-	87.00	51.14	82.00
	ERCSR	58609	13845	39.66	**0.97**	**2.02**	-	-	-
	Cascade	75497	16779	**39.74**	**0.97**	2.18	88.70	50.77	84.25
	Proposed	71913	13476	39.65	**0.97**	2.15	**89.43**	**56.36**	**85.39**

References

[1] Sun W W, Yang G, Chen C, et al. Development status and literature analysis of China's earth observation remote sensing satellites[J]. Journal of Remote Sensing, 2020, 24(5): 479-510.

[2] Byun Y. A texture-based fusion scheme to integrate high-resolution satellite SAR and optical images[J]. Remote sensing letters, 2014, 5(2): 103-111.

[3] Cao Q, Zhong Y, Ma A, et al. Urban land use/land cover classification based on feature fusion fusing hyperspectral image and LiDAR data[C]//IGARSS 2018-2018 IEEE International Geoscience and Remote Sensing Symposium. IEEE, 2018: 8869-8872.

[4] Mohla S, Pande S, Banerjee B, et al. Fusatnet: Dual attention based spectrospatial multimodal fusion network for hyperspectral and lidar classification[C]//Proceedings of the IEEE/CVF Conference on Computer Vision and Pattern Recognition Workshops. 2020: 92-93.

[5] Liu J, Gong M, Qin K, et al. A deep convolutional coupling network for change detection based on heterogeneous optical and radar images[J]. IEEE transactions on neural networks and learning systems, 2016, 29(3): 545-559.

[6] Mou L, Zhu X, Vakalopoulou M, et al. Multitemporal very high resolution from space: Outcome of the 2016 IEEE GRSS data fusion contest[J]. IEEE Journal of Selected Topics in Applied Earth Observations and Remote Sensing, 2017, 10(8): 3435-3447.

[7] Li W, Gao Y, Zhang M, et al. Asymmetric feature fusion network for hyperspectral and SAR image classification[J]. IEEE Transactions on Neural Networks and Learning Systems, 2022.

[8] Huang H, Yu J, Sun W. Super-resolution mapping via multi-dictionary based sparse representation[C]//2014 IEEE International Conference on Acoustics, Speech and Signal Processing (ICASSP). IEEE, 2014: 3523-3527.

[9] Wang Y, Chen X, Han Z, et al. Hyperspectral image super-resolution via nonlocal low-rank tensor approximation and total variation regularization[J]. Remote Sensing, 2017, 9(12): 1286.

[10] Li Q, Wang Q, Li X. Mixed 2D/3D convolutional network for hyperspectral image super-resolution[J]. Remote Sensing, 2020, 12(10): 1660.

[11] Wang Q, Li Q, Li X. Spatial-spectral residual network for hyperspectral image super-resolution[J]. arXiv preprint arXiv:2001.04609, 2020.

[12] Arun P V, Buddhiraju K M, Porwal A, et al. CNN-based super-resolution of hyperspectral images[J]. IEEE Transactions on Geoscience and Remote Sensing, 2020, 58(9): 6106-6121.

[13] Qiang Li, Qi Wang, and Xuelong Li. Exploring the relationship between 2d/3d convolution for hyperspectral image super-resolution. IEEE Transactions on Geoscience and Remote Sensing, 59(10):8693–8703, 2021.

[14] Kurz F, Rosenbaum D, Leitloff J, et al. Real time camera system for disaster and traffic monitoring[C]//Proceedings of International Conference on SMPR 2011. 2011: 1-6.

[15] Baumgartner A, Gege P, Köhler C, et al. Characterisation methods for the hyperspectral sensor HySpex at DLR's calibration home base[C]//Sensors, Systems, and Next-Generation Satellites XVI. SPIE, 2012, 8533: 371-378.

[16] Okujeni A, van der Linden S, Hostert P. Berlin-urban-gradient dataset 2009-an enmap preparatory flight campaign[J]. 2016.

[17] Lim B, Son S, Kim H, et al. Enhanced deep residual networks for single image super-resolution[C]//Proceedings of the IEEE conference on computer vision and pattern recognition workshops. 2017: 136-144.

[18] Gao Y, Li W, Zhang M, et al. Hyperspectral and multispectral classification for coastal wetland using depthwise feature interaction network[J]. IEEE Transactions on Geoscience and Remote Sensing, 2021, 60: 1-15.

About the authors

Yifan ZHANG was born in Nanjing. She received the B.E. degree in computer science and technology from Nanjing Normal University. She is now a Ph.D. candidate in engineering. Her research interests include remote sensing data fusion and model compression.
(Email: yfzhang@njust.edu.cn)

Yang XU [corresponding author] received the Ph.D. degree in pattern recognition and intelligence systems from the Nanjing University of Science and Technology, China. He is now a Professor with the School of Computer Science and Engineering. His research interests include hyperspectral image classification and image processing. (Email: xuyangth90@njust.edu.cn)

Zebin WU received the Ph.D. degree in computer science and technology from the Nanjing University of Science and Technology, China. He is now a Professor with the School of Computer Science and Engineering, Nanjing University of Science and Technology. His research interests include hyperspectral image processing, parallel computing, and big data processing. (Email: wuzb@njust.edu.cn)

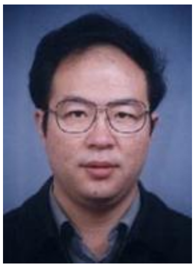

Zhihui WEI was born in Jiangsu, China, in 1963. He received the Ph.D. degree in communication and information systems from Southeast University, Nanjing, China. He is currently a Professor and a Doctoral Supevisor with the Nanjing University of Science and Technology, Nanjing. His research interests include multiscale analysis, mathematical image processing, and partial differential equations. (Email: gswei@njust.edu.cn)

Biqi WANG received the B.Admin. degree in Information Management and Information System from the School of Information Engineering, Nanjing University of Finance and Economics, Nanjing, China, in 2019. She is currently pursuing the Ph.D. degree with the Nanjing University of Science and Technology, Nanjing, China. Her research interests are transfer learning and hyperspectral image processing. (Email: wangbiqi@njust.edu.cn)

空间信息网络天基接入网无线资源管理研究

赵瑜 [1]，李悦 [1]，班亚明 [2]，马宁 [2]
（1.91977 部队，北京 100036；2.中国电子科技集团公司第 54 研究所，河北 石家庄 050081）

摘 要：针对空间信息网络天基接入网，提出一种集中与分布式相结合的星地协同无线资源管理架构。基于该架构对无线资源管理的相关过程和算法进行了设计与实现，并对算法进行了仿真分析。结果表明，所述无线资源管理方法在资源利用率及用户间公平性等方面均具备较高的性能水平。

关键词：空间信息网络；天基接入网；无线资源管理

Research of radio resource management of space-based access network in space information networks

ZHAO Yu[1]，LI Yue[1]，BAN Ya Ming[2]，MA Ning[2]
（1. THE PLA army 91977，Beijing 100036，China；
2.The 54th Research Institute of CETC，Shijiazhuang 050081，China)

Abstract: Aiming at the space-based access network of space information networks, a satellite-ground collaborative radio resource management architecture combining centralized and distributed is proposed. Based on this architecture, the relevant processes and algorithms of radio resource management are designed and implemented, the algorithm is simulated and analyzed. The results show that the proposed radio resource management method has a high performance level in terms of resource utilization and fairness between users.

Key words：space information networks；space-based access network；radio resource management

1 序言

空间信息网络，是以空间平台（如同步卫星或中地轨卫星、平流层气球、飞机等）为载体，结合地面网络节点，完成空间信息的获取、预处理、传输、再处理任务的网络化系统。空间信息网络由不同轨道上不同种类、不同性能的卫星、星座、航天器等天基基础设施结合地面设施，通过星间、星地链路构成。按照网络功能不同，空间信息网络划分为核心网、接入网和各类应用子网[1]。

天基接入网是由布设在太空中的多颗卫星组成的低轨卫星通信网络，这些卫星之间通过星间链路构成卫星星座，保证在任意时间、全球任意地点均有不少于 1 颗卫星对地可见，可为用户提供全球无缝的随遇接入能力，并可通过多星接力提供持续可靠的宽带移动通信服务能力。由于低轨卫星高速运动，单颗卫星对地面特定区域的过顶时间有限，其运行轨迹覆盖区域内用户分布不断变化[2]，这都给无线资源的管理造成一定的困难。通过增加收发天线数量，虽然可以获得更广的覆盖和更强的鲁棒性，但是硬件设施成本的增加以及功耗的增加在此方面形成了巨大的限制[3]。考虑到宽带卫星频谱资源宝贵、业务需求多变、信道衰落严重等特点，对系统无线资源管理技术的性能和技术水平都提出了较高的要求。

本文主要对天基接入网低轨宽带卫星无线资源管理的相关技术进行了研究，提出了一种集中与分布式相结合的星地协同无线资源管理架构，并对具体过程和算法进行了设计与实现。最后，通过仿真验证了方案的可行性。

2 天基接入网无线资源管理设计

2.1 无线资源管理架构设计

天基接入网的无线资源管理架构由部署在地基节点网信关站中的地面网控、部署在天基接入网各低轨宽带卫星中的星载网控，以及部署在各卫星

终端中的网控代理组成，采用集中与分布式相结合的星地协同管理模式。

地面网控集中受理卫星终端的业务接入申请，统筹管理卫星终端的各类业务，并生成初始带宽需求；由各星星载网控独立完成本星无线资源的 BoD 动态分配，实现对上行链路和下行链路的建立。其中，上行链路指的是用户链路的终端发送到卫星接收方向的链路[4,5]，下行链路指的是用户链路的卫星发送到终端接收方向的链路[6]。天基接入网无线资源管理架构如图 1 所示。

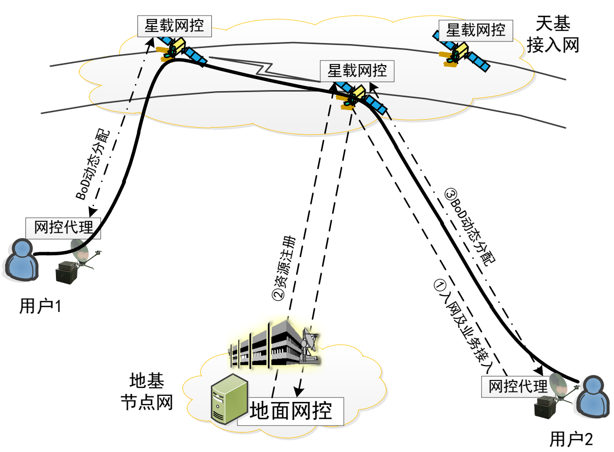

图 1　天基接入网无线资源管理架构示意图

2.2　无线资源管理流程设计

2.1.1　入网认证流程

入网认证主要完成对用户身份的确认，并授予用户资源使用的权限。入网认证过程包括入网注册和身份认证等环节。

入网注册需要入网申请、入网许可和入网确认共三次交互过程，主要完成信道单元的身份识别，并为后续阶段分配控制信道。入网申请由信道单元开机搜索到的波束发出，携带着信道单元序列号，网控识别信道单元序列号是否与网络配置过程中所备案的信息一致，若信息一致，则执行入网权限控制。入网权限包括允许入网和禁止入网，可提前配置在备案信息中。

入网注册后即开始身份认证，身份认证用于用户终端的合法性验证，由用户终端与安全保密系统交互，网控负责信令透传。网控据认证结果确认信道单元的合法身份，并向其发送入网完成。信道单元利用入网完成信令中携带的网络认证响应信息对网络的合法性进行认证，完成双向认证。

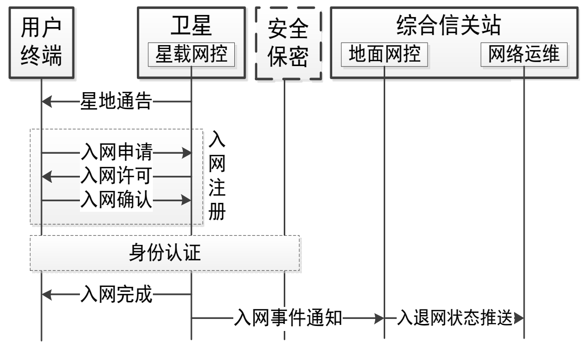

图 2　入网认证

2.1.2　业务接入流程

业务接入流程根据使用场景分为单星通信和跨星通信两种业务模式。

（1）单星通信

单星通信建立链路流程如图 3 所示。

1）用户通过拨号方式启动面向连接业务，主叫用户终端向星载网控发送建链申请，请求建立通信连接。

2）星载网控执行业务接入控制，并向被叫用户发送对端寻呼。

3）被叫用户终端返回寻呼响应，星载网控分配密钥及通信资源，并通过建链应答和建链通知信令通知主被叫。

4）星载网控向地面网控发送建链事件通知，地面网控向网络运维推送链路状态报告。

（2）跨星通信

跨星通信建链流程如图 4 所示。

1）用户通过拨号方式启动面向连接业务，主叫用户终端向星载网控发送建链申请，请求建立通信连接。

2）主叫星载网控执行业务接入控制，分配资源，协商通信密钥，并向被叫星载网控发送星间协同建链申请。

3）被叫星载网控向被叫用户终端发送对端寻呼。

4）被叫用户终端返回寻呼响应，被叫星载网控执行资源分配，向被叫用户终端发送建链通知，并向主叫星载网控返回星间协同建链响应。

5）被叫星载网控向被叫地面网控发送建链事件通知，被叫地面网控向被叫网络运维推送链路状态报告。

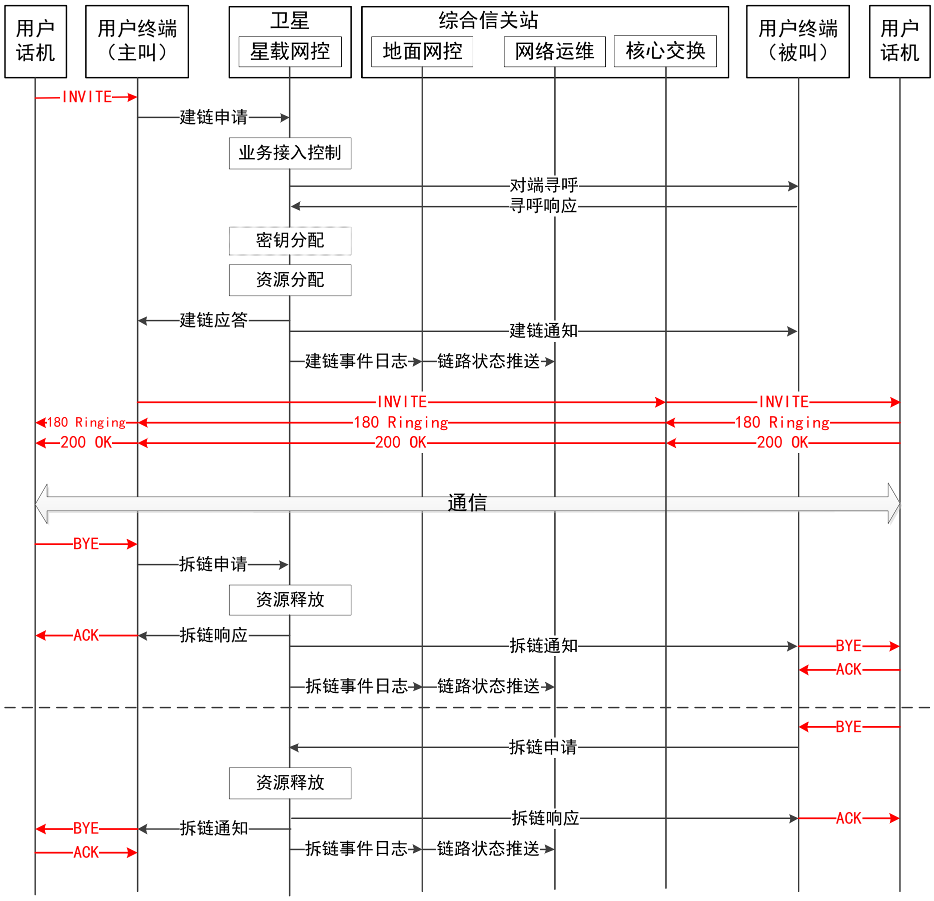

图 3 单星通信流程

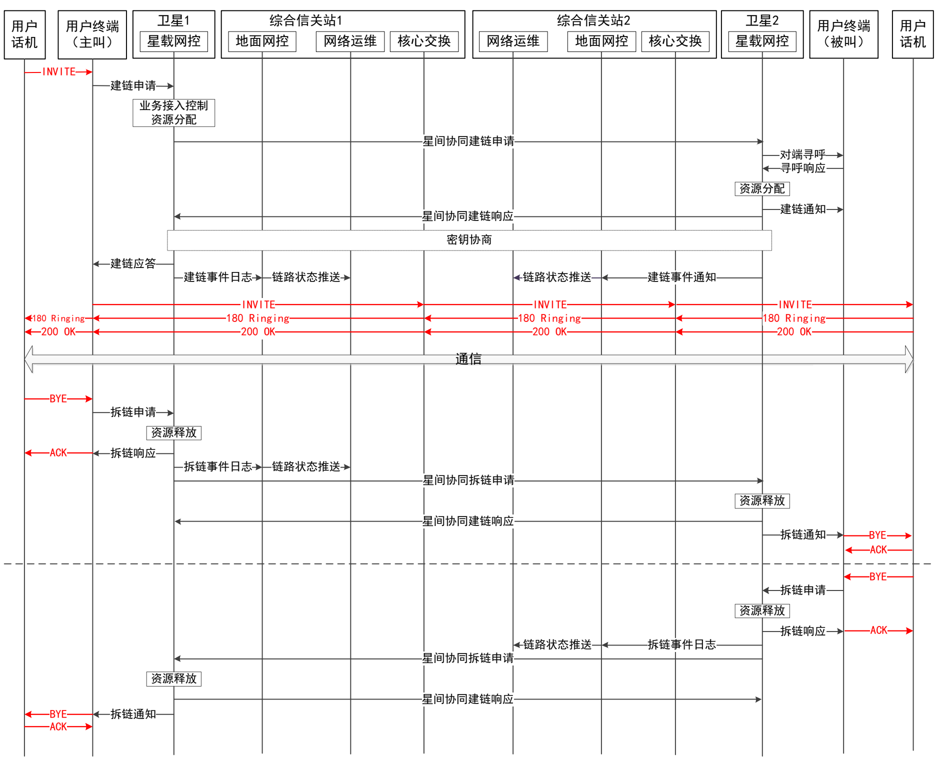

图 4 跨星通信流程

6）主叫星载网控向主叫地面网控发送建链事件通知，主叫地面网控向主叫网络运维推送链路状态报告。

2.1.3　资源分配流程

资源管理的对象，包括卫星波束的波位，星地上行链路的载波和时隙，星地下行链路的突发VTDM、星间链路的带宽和星载处理交换的链路标签等。资源分配方式包括预分配和按需分配。

资源预分配为系统提供静态分配方式，具有最高优先级，当预分配资源与动态分配的资源出现冲突时，应通过资源抢占优先满足预分配的资源需求。

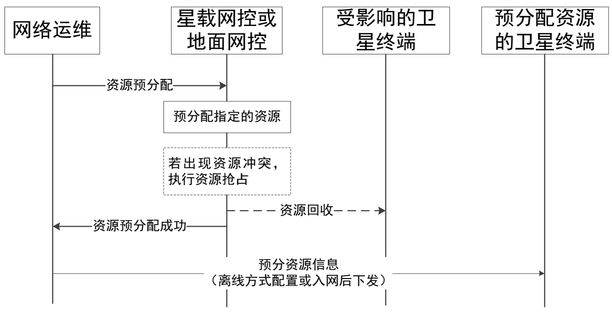

图 5 预分配流程

按需分配随业务保障流程执行，基于申请中的业务需求对资源动态分配。

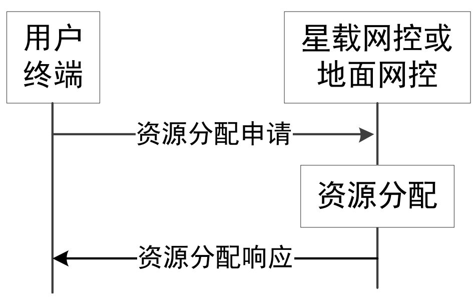

图 6 按需分配流程

3　天基接入网无线资源管理实现

3.1　无线资源管理过程设计

无线资源管理过程主要包括业务接入和资源分配。业务接入过程完成同一卫星波束内、波束间，以及不同卫星间业务的接入控制及接续管理。其中接入控制包括对通信双方信道单元在线状态、通信状态等检查，对用户信道单元通信使用端口、资源等信息确认。接续管理实现通信链路建立，包括通信双方星地链路标签和端口分配、星间链路标签端口分配、星地链路接续关系配置、星间路由转发表配置、星地/星间资源预留通知等。

3.1.1　业务接入过程设计

业务按 QoS 等级分为保障业务和非保障业务，相应的接入过程如图 7 所示。

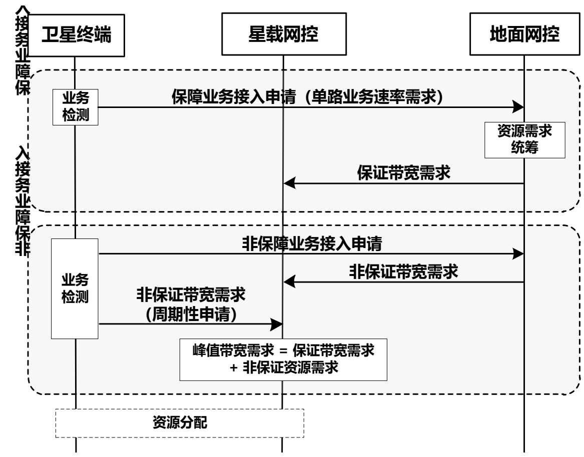

图 7　业务接入过程

（1）保障业务接入

保障业务承诺业务的保证速率，基于业务驱动，接入申请以卫星终端的单路业务为单位，按保证速率计算资源需求。保障业务接入申请集中提交至地面网控，地面网控根据接入申请中的卫星终端信息，查询与该卫星终端关联的所有保障业务（包含当前正在申请的业务），将这些业务的资源需求进行求和，得到卫星终端的保证带宽（CIR）需求，并将其发送至卫星终端当前接入卫星的星载网控。

（2）非保障业务接入

非保障业务基于容量进行周期性申请，尽力而为保障。接入申请以卫星终端为单位，按其数据缓存深度计算资源需求，地面网控仅在卫星终端首次接入时受理申请，此后卫星终端可直接向星载网控周期性提交非保证带宽需求，由星载网控将该资源需求与卫星终端的保证带宽（CIR）需求进行求和后获得峰值带宽（PIR）需求。

3.1.2　资源分配过程设计

资源分配过程分为需求收集、资源计算和帧计划下发三步，采用流水线作业方式，周期性执行，如图 8 所示。

（1）需求收集

需求收集是在 1 个帧周期中采集本周期内各用户的带宽需求，以供下个帧周期的资源计算使用。需求收集通常采用双缓存模式，当前缓存采用读写模式，接收并记录在本周期产生的用户带宽需求；

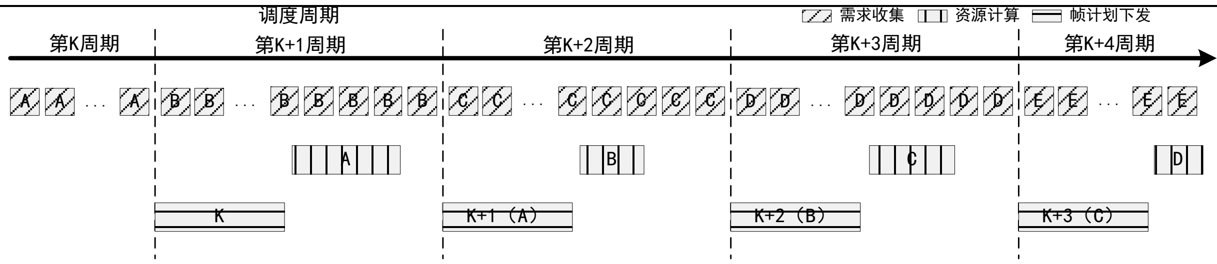

图 8　资源分配过程

备用缓存采用只读模式，输出上一个周期已收集完的用户带宽需求供资源计算使用。两个缓存的角色每经历 1 个帧周期互换一次。

（2）资源计算

资源计算是根据上一帧周期采集到的各用户的带宽需求，确定各用户的时隙个数和时隙位置，分为时隙分配和时隙调度。时隙分配基于优先级进行多轮分配，每轮次在所有未满足需求的用户中，选择优先级最大的用户分配 1 个时隙的基本带宽，直到所有用户的带宽需求均被满足或资源池中再无可用资源为止。时隙调度是按照各用户分配的时隙数量，确定各用户业务时隙的具体位置，调度结果满足以下条件：

- 某个时隙只能够分配给一个卫星终端。
- 一个卫星终端在同一时隙内只能占用一条载波。
- 一个载波组内允许一个卫星终端的多个时隙位置离散并跨载波分布。

（3）帧计划下发

帧计划下发是将上一周期计算生成的资源分配结果（即帧计划）以广播方式通告给本波束下的所有卫星终端。

3.2　无线资源管理算法实现

常见的 QoS 调度机制分为紧急调度机制、平均水平保障调度机制和按优先级调度机制三种[7]。资源分配算法包含时隙分配算法和时隙调度算法两部分。时隙分配算法旨在确定在当前分配周期各卫星终端应分配的时隙个数；时隙调度算法旨在确定在当前分配周期各卫星终端所分配时隙的具体位置。

3.2.1　时隙分配算法

在天基接入网中，卫星终端的空口信令可与业务数据一起复接在同一时隙中打包传输。对于那些接入后长期无业务通信的卫星终端，系统会经历过一段时间后，主动分配 1 个 KeepAlive 时隙，以保证其日常的在线保持及定时同步。

KeepAlive 时隙分配在整个分配过程的一开始执行，星载网控为每个卫星终端维护一个阈值时刻，若当前时刻超出阈值时刻，则需要为该卫星终端分配 KeepAlive 时隙，星载网控按照超时时间从高到低对卫星终端进行排序，在不超出 1 帧允许的 KeepAlive 时隙分配上限的前提下，依顺序为各卫星终端分配时隙资源。对于获得 KeepAlive 时隙的卫星终端，如果在本轮分配周期内有业务需求，该时隙也可用于业务传输，并计入其业务时隙分配的配额。

业务时隙分配以综合优先级和累积满足度为评价指标，采取多轮次分配方案，每次为一个卫星终端分配 1 个时隙，直到所有时隙分配完或所有卫星终端完成分配。

综合优先级以 4 比特表示，由用户优先级和申请优先级组成，数值越小代表的资源分配等级越高。

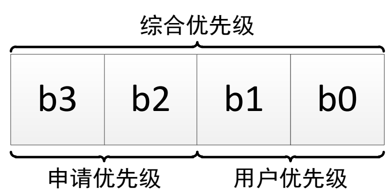

图 9　优先级组成示意图

用户优先级分为一般、重要、核心、顶层四级，由网络管理系统按用户的重要程度统一配置，取值如表 1 所示。

表 1　用户优先级取值表

用户优先级	取值
一般	3
重要	2
核心	1
顶层	0

申请优先级分为非实时、实时两级，非实时申请为 1，实时申请为 0，随卫星终端所得带宽的变化而动态变化，确定规则如下：

- 卫星终端维护两种带宽需求：保证带宽（CIR）和峰值带宽（PIR）。保证带宽是该用户所有已经接入的保障业务的带宽需求之和；峰值带宽是保证带宽与该用户的非保障业务的带宽需求之和。不难发现，保证带宽≤峰值带宽。
- 将卫星终端当前已获得带宽与保证带宽和峰值带宽进行比较，若已获得带宽＜保证带宽，则申请优先级为实时优先级；若保证带宽≤已获得带宽＜峰值带宽，则申请优先级为非实时优先级。

累积满足度是在综合优先级相同的情况下，为体现公平性原则而引入的评价因子，用来衡量卫星终端接入期间其带宽需求的累积满足情况，星载网控应优先为累积满足度低的卫星终端分配资源，从而保证所有卫星终端的累计满足度大体一致。累积满足度按轮次进行累积，由于每个轮次只会为一个卫星终端分配 1 个时隙，故只会更新 1 个卫星终端的累积满足度，计算公式如下：

$$S = S + \frac{1}{C_{PIR}} \times Factor$$

其中：

S为卫星终端的累积满足度；

C_{PIR}为卫星终端峰值带宽转换后的时隙个数；

$Factor$为满意度因子，一般取载波的最大时隙数。

根据上式，不难发现满足度具有以下性质：

- 一个分配周期内，卫星终端增长的满足度不超过$Factor$。
- 卫星终端的峰值带宽与其在每个轮次中增长的满足度成反比。

综上，业务时隙分配过程中，各轮次需按以下规则对卫星终端进行排序：

1）首先，比较综合优先级，数值约小，排名越靠前；

2）若综合优先级一致，比较累积满足度，数值约小，排名越靠前；

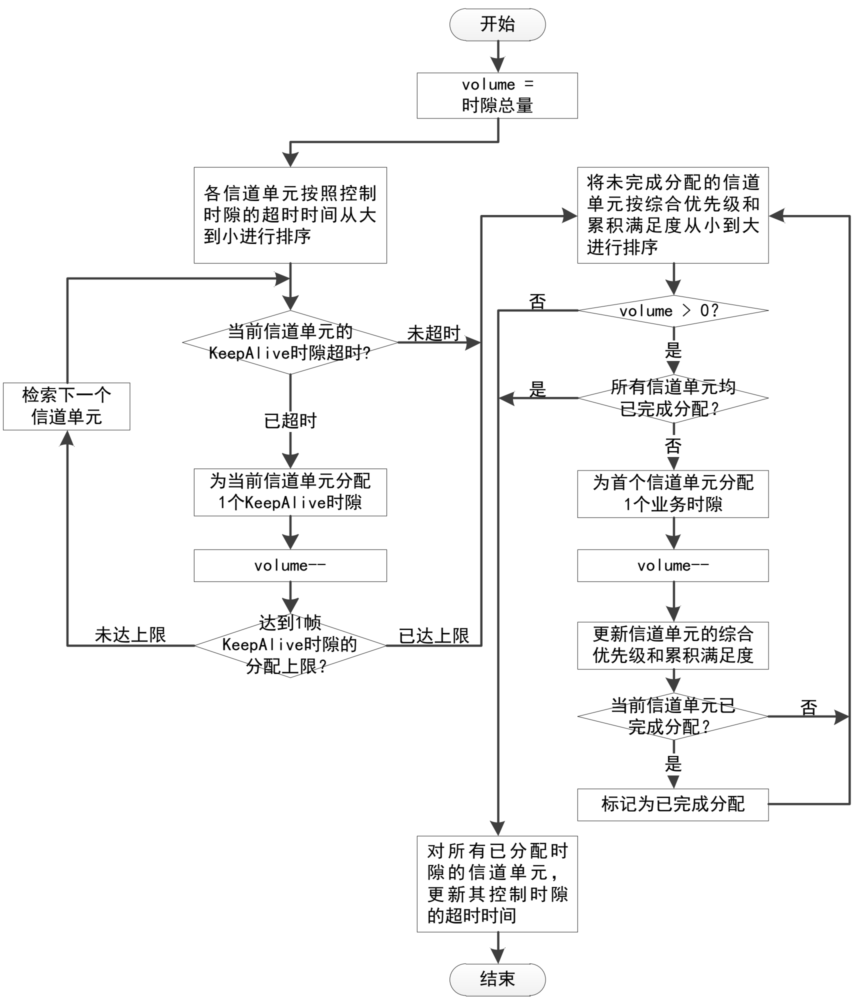

图 10　时隙分配算法过程

3）每轮次分配完成后，对于获得时隙的卫星终端，需要动态更新其综合优先级中的申请优先级以及其累积满足度。

最后，给出时隙分配算法的具体过程，如图 10 所示。

3.2.2 时隙调度算法

时隙调度算法的主要思想是将卫星终端按时隙分配算法所确定的时隙个数划分等价类，并按等价类中单个成员的时隙个数由多至少进行排序分级。各级等价类具有单独的遍历空间和轮询周期，一个轮询周期最多可包含调度段和非调度段（可选）两个区段。调度过程将所有时隙进行一次遍历。每个时隙从第 1 级等价类开始执行递归检查，若时隙处于当前等价类轮询周期的调度段内，则将其指派给等价类中的对应成员；否则向下一级等价类递归。算法原理如图 11 所示。

具体实现时，算法包含等价类划分、轮询周期确定和递归轮询遍历等关键步骤。

（1）等价类划分

算法中各卫星终端的时隙个数是时隙分配算法的计算结果，其具备以下性质：

- 单个卫星终端的时隙个数不会超过单条载波的时隙个数，从而满足“一台卫星终端在同一个时隙内只能占用一条载波”的分配约束。
- 所有卫星终端的时隙个数之和≤载波个数×单条载波的时隙个数

另一方面，算法中等价类划分需满足以下要求：

- 同一个等价类中卫星终端的时隙个数相同；同一个等价类中卫星终端的时隙个数之和，称为该等价类的时隙个数
- 所有等价类的时隙个数之和=载波个数×单条载波的时隙个数

不难发现，时隙分配结果不满足等价类划分的等式要求，需要通过添加“伪卫星终端”的方式对结果进行扩展，具体方法如下：

令 C 为载波个数，S 为单条载波的时隙个数，N 为所有卫星终端的时隙个数之和。

为了与实际的卫星终端进行区分，伪卫星终端使用负数标识，共分两类：

第 1 类伪卫星终端的时隙个数等于单条载波的时隙个数。

第 2 类伪卫星终端仅在上式无法整除时设置，数量为 1，时隙个数=（$C\times S-N$）mod S。

伪卫星终端添加完毕后，与实际的卫星终端一起按照时隙个数由多至少进行排序，将时隙个数相同的多个连续卫星终端归为一个等价类，等价类的生成顺序对应等价类的等级。

（2）轮询周期确定

等价类划分过程中，可同步确定各等价类的遍历空间和轮询周期，具体规则如下：

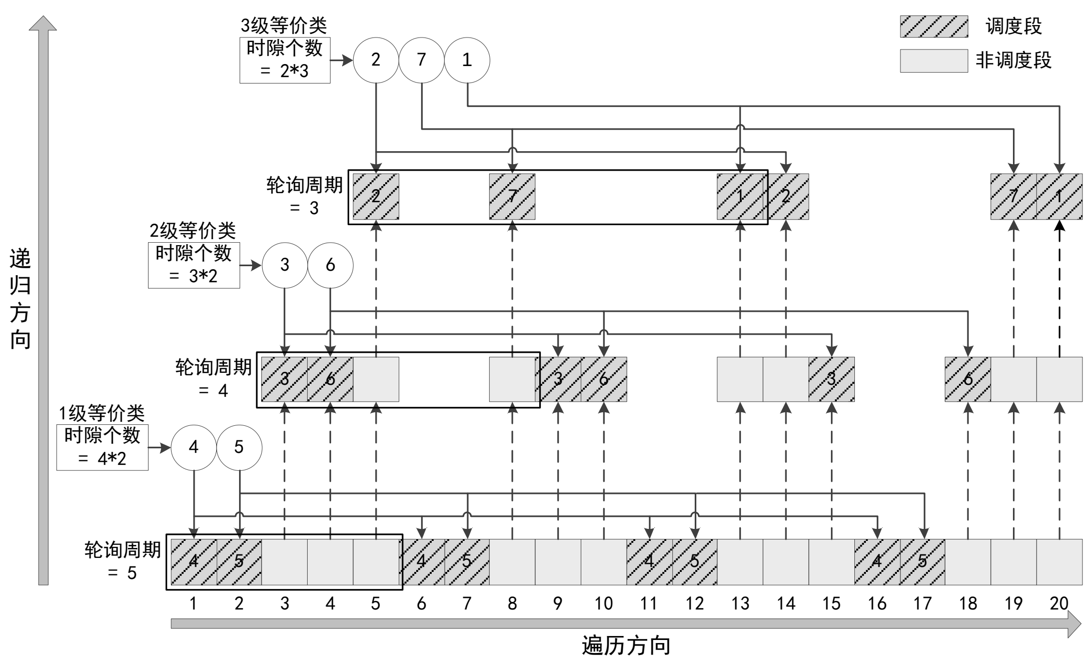

图 11 时隙调度算法原理

- 第 1 级等价类的遍历空间=载波个数×单条载波的时隙个数
- 其他等价类的遍历空间=前一级等价类的遍历空间－前一级等价类的时隙个数
- 等价类的轮询周期视情况决定：

令 B 为等价类的遍历空间，P 为等价类中单个卫星终端的时隙个数，$T=B/P$，$M=B \bmod P$。

若 M=0，则所有轮次的轮询周期均为 T；否则，前 M 轮的轮询周期为 T+1，后续轮次的轮询周期为 T。

（3）递归轮询遍历

等价类及其轮询周期确定以后，为各等价类分别维护一个游标，并开展递归轮询遍历过程，具体流程如图 12 所示。

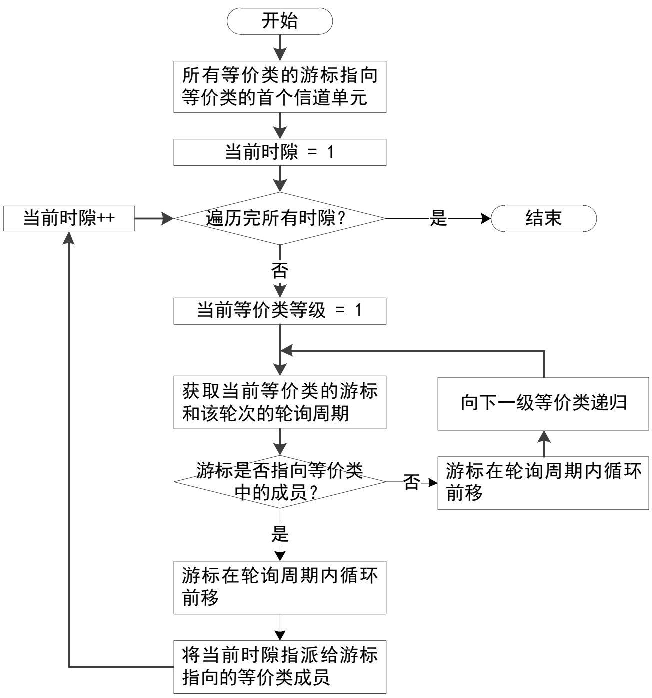

图 12　递归轮询遍历过程

4　仿真与分析

针对天基接入网的无线资源管理，使用 Matlab 对文中的网控资源分配机制进行了仿真，算法的性能指标为资源利用率和用户间公平性。

设定 100 个用户接入卫星的场景。其中，卫星配置 1 个 8 条载波的载波组，每条子载波包含 8 个时隙；20 个用户中包含 5 个顶级用户、5 个核心用户、5 个重要用户和 5 个一般用户。所有用户的保证带宽（CIR）和峰值带宽（PIR）需求服从泊松分布。

模拟 100 台终端 30 秒内的资源分配情况，所有终端以 1:1:2:6 的比例划分顶层、核心、重要、一般用户优先级。宽带网控以 100ms 为周期进行帧计划计算，30 秒内共进行 3000 次资源分配。在每个资源分配周期内，按当前资源池容量的 70%~110% 产生业务量，并将该业务量划分成模拟话音、SIP 话音、IP 数据、同步数据、异步数据随机指派给各终端，生成各终端的资源申请，所有终端的保证带宽（CIR）和峰值带宽（PIR）需求服从泊松分布。网控按照该资源申请进行资源分配，并计算资源分配效率，仿真结果如图 13 所示。

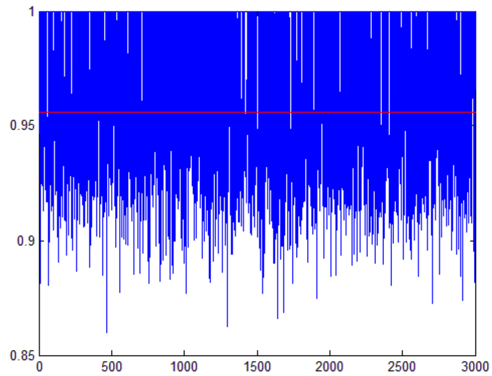

图 13　资源分配利用率仿真结果

仿真结果表明，地面网控的平均资源分配利用率约为 95.59%。

5　结束语

本文针对空间信息网络天基接入网的低轨卫星通信网络无线资源分配策略展开研究，主要提出了一种集中与分布式相结合的星地协同无线资源管理架构。本文首先介绍了该架构的设计方案和具体的资源管理流程，然后对具体的资源分配过程进行了阐述，并且详细介绍了对时隙资源进行分配的算法及其原理。最后，通过仿真实验验证了该架构的可行性，证明了该方法在资源利用率及用户间公平性等方面均具备较高的性能水平。在未来的研究中，拟考虑更大规模的用户资源申请场景，并且需要提升资源分配算法的性能，降低时间复杂度，提升实时资源分配的效率。

参考文献

[1]　任勇，姜春晓，杜军，王景璟．空间信息网络体系架构及其应用

[M].北京：人民邮电出版社,2018:1-6.
[2] Yitao L, Na D, Wuyang Z. A Hierarchical Approach to Resource Allocation in Extensible Multi-Layer LEO-MSS[J].IEEE Access,2020,8.
[3] 陈娅婷.空天地一体化网络无线资源管理与传输协议优化研究[D].北京交通大学,2020.DOI:10.26944/d.cnki.gbfju.2019.000512.
[4] Lutz E.Co-channel interference in high-throughput multibeam satellite systems[C]//Proceedings of the 2015 IEEE International Conference on Communications(ICC). London,UK,2015:885-891.
[5] Fonseca N J G, Sombrin J. Multi-beam reflector antenna system combining beam hopping and size reduction of effectively used spots[J].IEEE Antennas and Propagation Magazine,2012,54(2):88-89.
[6] Ahmad I, Nguyen K, Letzepis N. Performance analysis of high throughput satellite systems with optical feeder links[C]//Proceedings of the 2017 IEEE Global Communications Conference (GLOBECOM),Singapore,2017:1-7.
[7] Kim Y, Son K, Chong S. QoS scheduling for heterogeneous traffic in OFDMA-based wireless systems[C]//Proceedings of the 2009 IEEE Global Communications Conference (GLOBECOM), Honolulu, USA, 2009:1-6.

[作者简介]

赵瑜，（1974− ），女，硕士，正高级工程师，主要研究方向：通信网络管理

李悦，（1977− ），女，硕士，高级工程师，主要研究方向：卫星通信

班亚明（1984− ），男，硕士，高级工程师，主要研究方向：卫星通信系统和运维管控

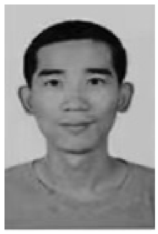

马宁（1986− ），男，硕士，高级工程师，主要研究方向：卫星通信系统和运维管控

基于光照感知分级特征融合的多模态遥感目标检测方法

田涛，徐洋，吴泽彬，何承迅，韦志辉

（南京理工大学计算机科学与工程学院）

摘　要：遥感图像中的目标检测在民用和军事领域都发挥着重要作用。近年来，许多遥感图像目标检测算法都表现出了优异的能力。然而，这些方法是为单一的可见光模态设计的，无法应对光照不足或雾天场景的挑战。针对上述问题，本文引入红外模态，红外图像能够体现被拍摄目标的温度，以此避免低光照和雾天的影响，并提出了一种新型的多模态遥感图像目标检测方法来应对这些挑战。该方法由图像光照感知模块和光照分级特征融合模块构成，其中，光照感知模块通过可见光图像将光照情况量化得到光照评分。光照分级特征融合模块以光照评分为先验进行光照分级并融合提取自两个模态的特征。我们在真实多模态数据集上进行了充足的实验，证明了我们的方法在多模态遥感图像目标检测任务中的优越性。

关键词: 目标检测；多模态遥感图像；光照感知；特征融合

Illumination aware and feature fusion for RGB-infrared multi-modal remote sensing object detection

Tao Tian, Yang Xu, Zebin Wu, Chengxun He, Zhihui Wei

(School of Computer Science and Engineering, Nanjing University of Science and Technology)

Abstract: Object detection in remote sensing images (RSIs) plays an important role both in civil and military fields. In recent years, many object detection algorithms in RSIs have shown the excellent capability. However, these methods are designed for the single RGB modality, which cannot cope with the challenges in insufficient illumination or foggy scenarios. Regarding the issue above, this paper introduces infrared images, which can reflect the temperature of the objects, thereby avoiding the influence of low light or fog. Then, this paper proposes a new multi-modal remote sensing object detection method to address these challenges. The method includes an illumination aware module and an illumination judgment and feature fusion module. First, the input RGB image is embedded into the illumination aware module to get an illumination score. Then the illumination judgment and feature fusion module utilize the score as the priori to regulate the interaction between the RGB modality and the infrared modality. We conduct extensive experiments on two rgb-infrared multi-modal remote sensing image object detection datasets and the results demonstrate the superiority of our proposed method.

Keywords: object detection, multi-modal remote sensing image, illumination aware, feature fusion

1　引言

现代遥感技术主要包括信息的获取、传输、存储和处理等环节，指运用现代化的遥感平台和传感器，从远距离感知目标反射或自身辐射的电磁波、可见光、红外线，将这些信息回传地面并对目标进行探测和识别。遥感图像是指通过遥感平台和传感器获取的能够表示地球表面各种物体的图像，例如机场、车辆、建筑物等。遥感图像中的目标检测是备受研究人员关注的一个课题，其在军用和民用应用领域都有着十分重要的意义，是军事侦察、城市规划、交通疏导、土地勘测等应用的重要基础。近年来，遥感技术得到飞速发展，通过遥感平台能够获得大量高分辨率遥感图像，为遥感目标检测的研究提供了充足的数据支撑,也表明遥感大数据时代已然来临[1-3]。然而，由于复杂的背景和多样的成像方法，在遥感图像上进行目标检测仍然具有挑战性。

近年来，研究人员致力于开发各种遥感图像目标检测方法，例如 Cheng 等人[4]在 R-CNN（region-convolutional neural network）框架上，提出

了学习旋转不变卷积网络模型（RICNN, rotation-invariant convolutional neural network），通过在现成的 CNN 模型中添加一个新的旋转不变层实现。Zhong 等人[5]利用位置敏感平衡 (PSB, position-sensitive balancing) 方法来提高生成区域 Proposals 的质量，在提出的 PSB 框架中，引入了基于残差网络的全卷积网络（FCN, fully convolutional network），以解决目标检测中平移变化与图像分类中平移不变的矛盾。而为了实现实时目标检测，Tang 等人[6]使用基于回归的目标检测器来检测车辆目标，该方法的检测框通过每个特征图位置采用一组具有不同比例的默认框来生成。

尽管上述方法都取得了显著成果，但它们都是从为自然场景图像设计的方法中迁移而来的，而且针对的都是可见光图像这一单模态。由于遥感图像复杂的背景以及成像环境的多样性，在单模态遥感图像上进行目标检测依旧具有挑战性。可见光图像具有丰富的颜色信息与更多的纹理信息，却易受到光照条件影响。红外图像具有热辐射信息，对光照不敏感，却缺乏纹理细节信息。因此，可见光图像与红外图像具有极强的互补性。近年来，利用可见光图像与红外图像的互补信息，这两个模态已经被广泛应用于计算机视觉领域的多个任务中，例如目标检测、目标跟踪、语义分割等。Fang 等人[7]结合卷积神经网络与 Transformer 各自的优势，设计了双分支特征提取网络与多模态特征融合模块进行行人目标检测。Lan 等人[8]利用稀疏表示的鲁棒性和模态相关性来表示不同模态的特征，将可见光与红外模态的目标特征结合进行目标跟踪。虽然可见光图像与红外图像具有互补信息，但如果无区别地进行多模态信息交互，可能会因冗余信息造成更差的效果。在遥感图像目标检测领域中，若光照条件差，可见光图像信息丢失严重，无法很好地检测目标，在这种情况下，红外图像能提供更有效的目标类别与位置信息。而在光照条件良好的环境下，由于缺乏颜色信息，红外图像中可能会出现与真实目标外观相似的虚假目标，带来冗余信息。因此，在不同光照条件下，可见光图像和红外图像对目标检测的贡献不同。在良好的光照条件下，可见光图像和红外图像相辅相成；在恶劣的光照条件下，红外图像提供的信息更有作用。

针对上述现象，为了更好地利用红外图像，本章提出了一种基于光照感知分级特征融合的多模态遥感目标检测方法。该方法由图像光照感知模块和光照分级特征融合模块构成，其中，光照感知模块通过对光照更为敏感的可见光图像，将光照情况量化得到光照评分。光照分级特征融合模块以光照评分为先验进行光照分级，根据不同级别采取不同方法对两种模态的特征进行融合。最后，将经过充分融合后得到的特征图送入检测出进行目标检测。我们在两个可见光红外多模态遥感图像目标检测数据集 Drone Vehicle[8]和 VEDAI（vehicle detection inaerial imagery）[9]上进行实验，验证了该方法的可行性和优越性。

2 本文所提方法

2.1 整体概述

卷积神经网络（CNN, convolutional neural network）通过连续采用卷积层来提取局部特征,提取高频信息能力强，但受限于卷积核感受野大小，它在获取全局上下文信息方面缺乏效率；Transformer 中的自注意力机制能学习长距离依赖，使得模型有选择地聚焦于输入的某些部分，可以有效地获取全局信息，但在捕获细粒度细节方面存在局限性。过去对 CNN 和 Transformer 结合的研究主要集中在用 Transformer 层替换卷积层或者将两者按顺序堆叠，例如 Detection Transformer(DETR)[10]。而本方法以 CNN 和 Transformer 并行作为双分支骨干网络，由于可见光图像具有清晰的纹理细节和阴影，我们将其输入至 CNN 分支中提取局部特征；而对于物体边界模糊、缺少纹理信息的红外图像，我们将其输入 Transformer 分支提取全局特征，更充分地结合了两者的优势。网络的整体框架如图 1 所示，包含两个模块：图像光照感知模块和光照分级特征融合模块。网络以可见光与红外图像对作为输入进行目标检测的大致步骤如下：

(1)首先，将可见光图像输入光照感知模块(IA, Illumination Aware)得到光照量化评分，此评分能够反映图像的光照情况，并将光照评分作为先验信息输入光照分级特征融合模块，用于控制和调节两个模态之间的相互作用。

(2)之后，通过双分支骨干网络提取两种模态的多尺度特征并选择原尺度的$\{\frac{1}{16}，\frac{1}{8}，\frac{1}{4}\}$的特征图送入光照分级特征融合模块(IRFF, Illumination Judgment and Feature Fusion)中，根据光照评分对图

像的光照条件进行分级，按照不同光照级别对多模态特征图进行不同的融合处理,以此调节不同模态在不同光照情况下的作用。

(3)最后，将经过充分融合后得到的特征图送入检测层进行目标检测。

本节接下来将对光照感知模块和光照分级特征融合模块进行详细介绍。

2.2　图像光照感知模块

图像处理中常应用的彩色坐标系统有两种：一种是 RGB 彩色系统，由三原色红、绿、蓝组成；另一种是 HIS 彩色系统，由色调(H)、亮度(I)、饱和度(S)组成。计算机上定量处理色彩时通常采用 RGB 彩色系统，而 HIS 系统更加符合人眼对色彩的感知，所以从视觉上定性描述色彩时常用 HIS 系统。HIS 色彩表征系统能清楚地表现色调、饱和度和亮度的变化情形,对图片的颜色与亮度信息做了很好的区分，能很好地识别图像的亮度情况。对于一对可见光与红外图像，我们通常利用可见光图像来感知光照情形，而依赖红外图像处理低光照场景。由于没有先验表明越亮的区域越可能出现待检测目标,我们只需要获取描述图像整体光照情况的全局光照值。图像光照感知模块通过彩色变换将可见光图像从 RGB 颜色空间变换到 HIS 颜色空间，进而表征图像的光照情况。图像亮度评分的转换方程如下：

$$I=\frac{R+G+B}{3}, R、G、B\in[0,255]\#(1)$$

$$I'=\frac{\sum_{i=0}^{m}\sum_{j=0}^{n}I}{h\times w}\#(2)$$

其中，R、G、B分别表示可见光图像某像素点中 RGB 空间的像素值，I表示该像素点的亮度值。h、、w分别代表可见光图像的高度与宽度。I'表示可见光图像的全局光照值，并对I'进行归一化计算来得到图像的全局光照量化评分。并将评分送入光照分级特征融合模块作为先验信息，控制和调节两个模态之间的相互作用。

2.3 光照分级特征融合模块

通过光照感知模块得到的光照评分，我们将图像的光照情况分为三个不同的等级。当光照值范围在 0.75~1 之间时，表示图像光照条件充足，可见光图像相比于红外图像包含更丰富的对目标检测有效的信息，在此条件下对可见光模态特征进行一次额外的特征增强。与之相反，当光照值范围在 0~0.35 之间时，表示图像光照条件较差，红外图像相比可见光图像能提供更有效的图像类别及位置信息，在此条件下对红外模态特征进行一次额外的特征增强。在以上两种情况下，我们通过对其中一种模态进行特征增强，进一步获取在该光照条件下对目标检测更有帮助的模态信息。特征增强方法参考 LSKNet[11]网络结构，LSKNet 的核心思想是动态调整空间感受野区分背景信息，以便更准确地检测和分类，LSK 模块由一连串的大内核卷积和一个空间核选择机制组成，通过大内核卷积增大感受野处理特征，再由空间核选择机制对特征进行有效加权然

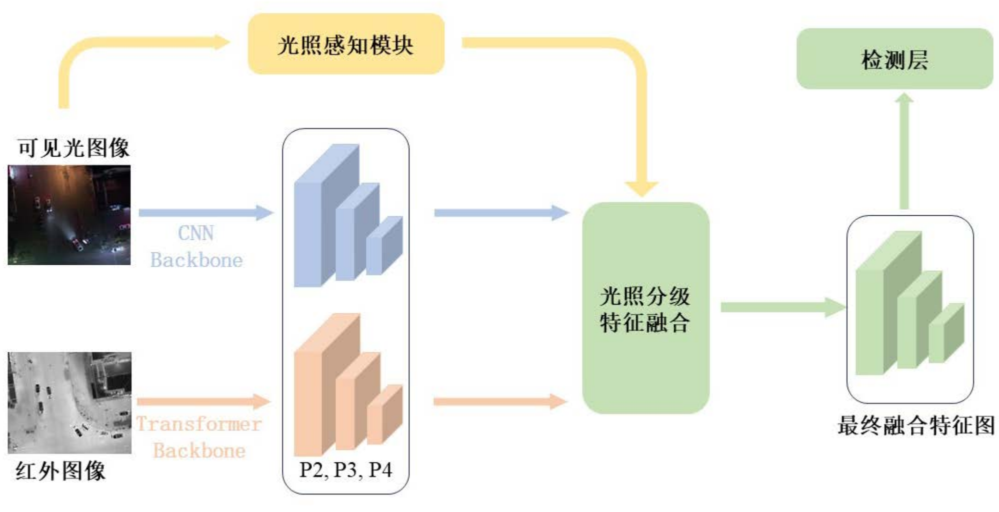

图 1　网络结构图

后在空间上进行合并，以此提高网络关注目标的最相关区域。本文主要修改了 LSK 模块中空间选择方法，在光照条件充足或较差情况下对其中一种模态特征进行特征增强，再将经过增强的模态特征与未增强的另一模态特征进行拼接并卷积得到最终的融合特征图。

而当光照值在 0.35~0.75 之间时，表示图像光照条件良好，可见光图像与红外图像都将对目标检测起到重要作用，所包含的互补信息相辅相成，在此条件下对两种模态特征作交叉注意力(Cross-Attention)[12]处理实现融合。交叉注意力思想基于以 Query，Key 和 Value 向量为计算主体的注意力机制，用于处理两个不同模态序列之间的关联，以一种模态信息为 Q，另一种模态信息为 K 和 V，通过注意力的形式来计算两个模态不同区域之间的关联程度。本文分别以可见光模态特征与红外模态特征作为查询向量进行两次交叉注意力处理，将两种模态数据进行交互处理以实现融合，并分别与原特征图进行残差连接，最后再拼接并卷积得到最终的融合特征图。以可见光模态特征作为查询向量为例，通过计算其与红外模态特征各个位置的关联程度得到相似度矩阵，将相似度矩阵归一化后得到权重矩阵，最终与红外模态特征相乘进行加权求和得到加入条件注意力的新特征图。经过交叉注意力处理后，两类模态特征进行了充分的信息交互以及有效的融合。

三种光照条件下的特征融合方式如图 2 所示。在光照分级特征融合模块中，我们通过光照值控制和调节可见光模态与红外模态的相互作用，将图像光照情况分为了三个不同等级，在不同光照条件下对两种模态特征采取合适的处理方法以实现充分有效融合。

3 实验结果及分析

为了验证本文方法的有效性，本文选用了两个真实可见光和红外配对数据集进行了实验验证。其中，使用 Python 3.9 完成生成对抗网络训练的部分，Pytorch 版本为 1.9.1。实验中 CPU 采用 Intel(R) Core(TM) i7-9700K CPU @ 3.60GHz，8 内核，32G 内存，Windows 10 64 位系统，GPU 采用 NVIDIAGeForceRTX3090Ti，可用显存为 24GB。

3.1 实验数据集

实验中采用的可见光和红外数据是公开的数据集。第一个数据集是由天津大学推出的大型无人机航拍车辆数据集 Drone vehicle[8]，包含了 28439 对可见光和红外图像，其中 17990 对图像为训练集，1469 对图像为验证集，剩下 8980 对图像为测试集。该数据集涵盖了包括街道、停车场、居民区等在内的多种场景和包括白天、夜晚、深夜在内的不同光照条件，目标种类包括轿车、公共汽车、卡车等五种类型。第二个数据集是一个卫星图像车辆检测数据集 VEDAI[9]，包含了 1296 对可见光和红外图像，其采用 K 折交叉验证法并取 K=10，将其中一份作为测试集，剩下的九份作为训练集。该数据集包含草地、高速公路、城镇等多个复杂场景。为了便于比较，在本实验中，我们采用与 Li 等[16]相同的设置，将多个车辆类别视为一种类别，保留轿车、皮卡、卡车和货车四种类别。

3.2 评价指标

对于目标检测的评价，通常使用多类平均准确率（mAP, mean average precision）作为指标，多类平均准确率是通过单类平均准确率（AP, average precision）得到的综合指标，单类平均准确率则通过召回率（Recall）、准确率（Precision）计算得到。

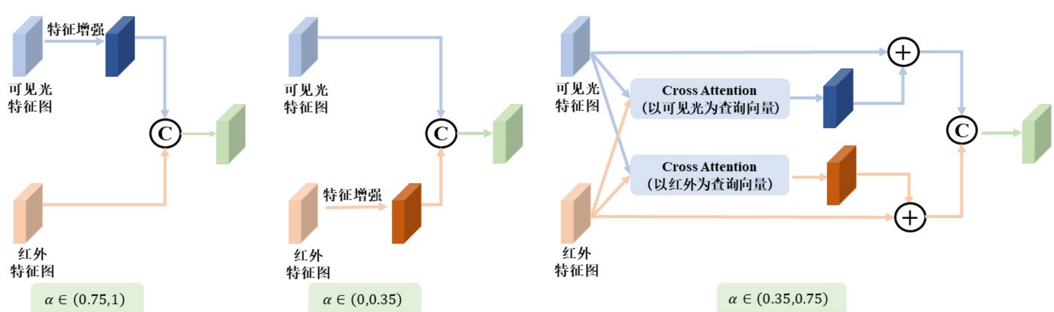

图 2　分级特征融合模块

召回率和准确率的计算定义如下：

$$Precision=\frac{TP}{TP+FP}\#(3)$$

$$Recall=\frac{TP}{TP+FN}\#(4)$$

其中，真正样本（TP）和真负样本（TN）表示预测正确，假正样本（FP）和假负样本（FN）表示预测错误。平均准确率采用积分法计算出所有类别的召回率——回归率曲线和坐标轴所围成的面积得到，其计算公式如下：

$$mAP=\frac{AP}{N}=\frac{\int_0^1 p(r)dr}{N}\#(5)$$

其中，p 表示准确率，r 表示召回率，N 表示目标类别数量。

3.4　实验结果

1)　对比实验

为了验证本文提出的方法的有效性，我们分别将本文方法在 Drone Vehicle 数据集上与 UA-CMDet[9]、Halfway Fusion(OBB)[13]、CIAN(OBB)[14]、AR-CNN(OBB)[15] 以及 Cascade-TSFADet[16]进行比较，结果如表 1 所示，在 VEDAI 数据集上与 DPM 等[9]以及 R³-Net[17]进行比较，结果如表 2 所示。从实验结果可知，本文方法在 Drone Vehicle 数据集上 mAP 可达到 76.27%，在 VEDAI 数据集上可达到 75.21%，明显高于其他方法取得的 mAP，从直观的角度看来本文方法具有更优异的性能。

表 1　Drone Vehicle 上不同方法 mAP 比较

Methods	Drone Vehicle
UA-CMDet	64.01
HalfwayFusion(OBB)	68.19
CIAN(OBB)	70.23
AR-CNN(OBB)	71.58
Cascade-TSFADet	73.90
本文算法	76.27

表 2　VEDAI 上不同方法 mAP 比较

Methods	4-cls VEDAI
DPM	45.85
SVM+HOG31+LBP	50.23
SVM + LTP	51.15
R³-Net	69
本文算法	75.21

图 3 给出了本文方法在 DroneVehicle 数据集上的一些检测结果，不同颜色的检测框代表不同的类别。从可视化结果可以看出，本文方法有效地融合了可见光图像与红外图像的信息，无论是在白天还是夜晚都能将目标很好地检测出来，再一次证明了本方法的有效性。

2)　消融实验

为了说明本文提出的方法中加入的每个模块的都能促进模型性能的提升，我们在 VEDAI 数据集上进行消融实验。本文方法的主要创新在于：对

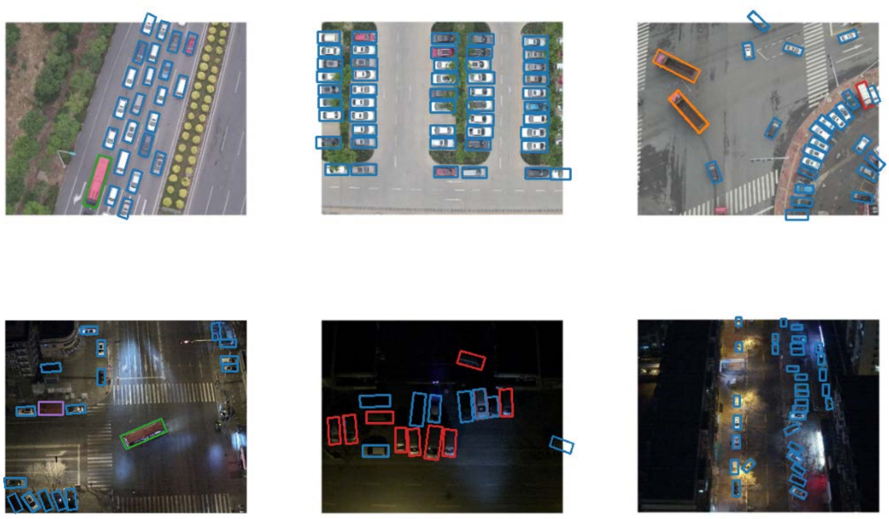

图 3　检测结果可视化

图像进行光照感知，获得图像光照评分并判断光照情况，以此为先验信息根据不同的光照条件对多模态特征采取不同的融合处理方式，避免引入冗余信息，使有效的特征信息得到了充分利用。

表 3　在 VEDAI 数据集上的消融结果

	光照感知分级	特征增强与交叉融合	mAP%
基准方法			67.88
		√	70.04
基准方法+	√		72.99
	√	√	75.21

我们以简单的多模态特征拼接并卷积为融合方法的双分支网络作为基准方法，分别验证了光照分级、特征增强与交叉融合的效果，结果如表 3 所示。基准方法在 VEDAI 数据集上的 mAP 为 67.88％，当直接采用特征增强与交叉注意力融合方法时，mAP 提升至 70.04％，而只引入光照感知时，mAP 提升至 72.99％。在利用光照感知分级并采用特征增强与交叉注意力融合方法即本文提出的方法后，将 mAP 提升至 75.21％。通过消融实验进一步证明了本文提出的创新方法的有效性。

4　结束语

大多数现有的遥感图像目标检测方法都是为单一的可见光模态设计的，在光照条件较差时对可见光图像进行目标检测具有挑战性，而在光照充足条件下引入红外图像可能会带来冗余信息。针对上述问题，我们思考光照条件影响，在本文提出了一种新型的多模态遥感图像目标检测方法，方法包含光照感知模块与光照分级特征融合模块。光照感知模块通过可见光图像获取全局光照量化评分，光照分级特征融合模块针对不同光照条件对可见光模态特征与红外模态特征进行不同融合处理，调控两类模态之间的相互作用，以更好地利用可见光与红外图像在遥感目标检测中的互补信息。最后我们在真实多模态遥感数据集 DroneVehicle 和 VEDAI 上进行了充分的实验，验证了我们的方法在多模态遥感图像目标检测中具有优异的性能。

参考文献：

[1] 陶超, 阴紫薇, 朱庆,等. 遥感影像智能解译:从监督学习到自监督学习[J]. 测绘学报, 2021.

[2] 何国金, 王力哲, 马艳,等. 对地观测大数据处理:挑战与思考[J]. 科学通报, 2015(5):9.

[3] 李德仁, 张良培, 夏桂松. 遥感大数据自动分析与数据挖掘[J]. 测绘学报, 2014(12):6.

[4] Gong C, Zhou P, Han J. Learning Rotation-Invariant Convolutional Neural Networks for Object Detection in VHR Optical Remote Sensing Images[J]. IEEE Transactions on Geoscience and Remote Sensing, 2016, 54(12):7405-7415.

[5] Zhong Y, Han X, Zhang L. Multi-class geospatial object detection based on a position-sensitive balancing framework for high spatial resolution remote sensing imagery[J]. ISPRS Journal of Photogrammetry and Remote Sensing, 2018, 138:281-294.

[6]Tang T, Zhou S, Deng Z, et al. Arbitrary-Oriented Vehicle Detection in Aerial Imagery with Single Convolutional Neural Networks[J]. Remote Sensing, 2017, 9(11):1170.

[7] Lan X, Ye M, Zhang S, et al. Modality-correlation-aware sparse representation for RGB-infrared object tracking[J]. Pattern Recognition Letters, 2020, 130: 12-20.

[8] Sun Y, Cao B, Zhu P, et al. Drone-based RGB-infrared cross-modality vehicle detection via uncertainty-aware learning[J]. IEEE Transactions on Circuits and Systems for Video Technology, 2022, 32(10): 6700-6713.

[9] Razakarivony S, Jurie F. Vehicle detection in aerial imagery: A small target detection benchmark[J]. Journal of Visual Communication and Image Representation, 2016, 34: 187-203.

[10] Carion N, Massa F, Synnaeve G, et al. End-to-end object detection with transformers[C]//European conference on computer vision. Cham: Springer International Publishing, 2020: 213-229.

[11] Li Y, Hou Q, Zheng Z, et al. Large Selective Kernel Network for Remote Sensing Object Detection[J]. arXiv preprint arXiv:2303.09030, 2023.

[12] Chen C F R, Fan Q, Panda R. Crossvit: Cross-attention multi-scale vision transformer for image classification[C]//Proceedings of the IEEE/CVF international conference on computer vision. 2021: 357-366.

[13] Liu J, Zhang S, Wang S, et al. Multispectral deep neural networks for pedestrian detection[J]. arXiv preprint arXiv:1611.02644, 2016.

[14] Zhang L, Liu Z, Zhang S, et al. Cross-modality interactive attention network for multispectral pedestrian detection[J]. Information Fusion, 2019, 50: 20-29.

[15]Zhang L, Zhu X, Chen X, et al. Weakly aligned cross-modal learning for multispectral pedestrian detection[C]//Proceedings of the IEEE/CVF international conference on computer vision. 2019: 5127-5137.

[16]Yuan M, Wang Y, Wei X. Translation, Scale and Rotation: Cross-Modal Alignment Meets RGB-Infrared Vehicle Detection[C]//European Conference on Computer Vision. Cham: Springer Nature Switzerland, 2022: 509-525.

[17] Li Q, Mou L, Xu Q ,et al.R3-Net: A Deep Network for Multioriented Vehicle Detection in Aerial Images and Videos[J].IEEE transactions on geoscience and remote sensing : a publication of the IEEE Geoscience and Remote Sensing Society, 2019.DOI:10.1109/TGRS.2019.2895362.

[作者简介]

田涛（1998−），男，南京理工大学硕士生，主要研究方向为遥感图像目标检测。

徐洋（1990−），男，南京理工大学教授、博士生导师，主要研究方向为图像处理、机器学习等

吴泽彬（1981−），男，南京理工大学教授、博士生导师，主要研究方向为多源信息融合、遥感大数据处理、云计算及应用技术等

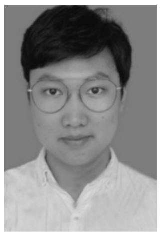

何承迅（1995−），男，南京理工大学博士生，主要研究方向为高光谱图像处理

韦志辉（1963−），男，南京理工大学教授、博士生导师，主要研究方向为稀疏分解与压缩感知理论及应用等

面向多任务的宽带卫星通信资源调度研究

陈志坤，赵瑜，王璐
91977 部队，北京 100036

摘　要：相比传统卫星通信系统，宽带卫星通信系统可实现卫星通信容量的大幅扩展。随着卫星通信用户数以及宽带卫星规模的持续增长，通信任务需求也随之增加，面向多任务的资源调度可有效提升卫星资源利用率，已成为目前的一个研究热点。首先详细介绍了宽带卫星通信系统架构，明确了资源调度在整个通信系统中的作用。然后从方案设计和算法设计两方面梳理了目前宽带卫星通信资源调度的研究进展，总结了现有研究仍然存在的问题。接着，提出了一种多星、跨网、异站场景下的多域异构资源联合调度方案，对星、网、地等资源进行统一描述，建立了任务需求的描述模型，探讨了资源与任务需求之间的匹配约束关系，并进一步给出了一种强化学习驱动的智能调度算法框架。最后，对全文进行了总结，给出了未来的研究方向。
关键词：宽带卫星通信；多任务；资源建模；智能调度；

Multi-task-oriented resource scheduling for broadband satellite communications

CHEN ZhiKun，ZHAO Yu，WANG Lu
THE PLA army 91977，Beijing 100036，China

Abstract: Compared with traditional satellite communications, broadband satellite communications can greatly improve satellite communication capacity. With the continuous growth of the number of satellite communication users and broadband satellites, the number of communication tasks has increased. Multi-task-oriented resource scheduling can effectively improve the utilization rate of satellite resources, which has become a research hotspot. First, the architecture of broadband satellite communication system is introduced, and the role of resource scheduling in the whole system is clarified. Then, the related works on broadband satellite communication resource scheduling are presented and summarized from the aspects of scheme design and algorithm design, based on which the challenges of resource scheduling is analyzed. Consequently, a joint scheduling scheme for multi-domain heterogeneous resources in a multi-satellite, cross-network and heterogeneous scenario is proposed, where the available resources including satellites, networks and ground stations, along with the tasks, are described and modeled, the matching constraint relationship between resources and task requirements are discussed, and further a reinforcement learning-driven intelligent scheduling algorithm framework is developed. Finally, the paper is summarized and the future research directions are given.
Key Words: broadband satellite communications; multiple tasks; resource modelling; intelligent scheduling

0　引言

当今世界，空间已成为未来战争的主战场之一，是世界各国布局下一代信息化网络作战的重要考虑因素[1]。卫星通信在空间信息网络建设中具有举足轻重的地位，目前已被广泛应用在军事国防、海洋渔政、抗震救灾等各个领域[2]。宽带卫星通信，又称为高通量卫星通信，具有比传统卫星通信更大的通信容量，可为分布在陆、海、空、天的各类用户提供语音、数据、图像等高速数据传输服务。针对用户提交的通信任务请求，目前大多数宽带卫星系统都是采用预规划或静态调度等方式进行资源分配。然而，这种资源调度方式仅在任务请求较少时可行，随着卫星用户和通信任务数量的增多，若仍采用原来的调度方式，会导致没有可用资源分配给新的任务，而已占用的卫星资源的利用率却很低的问题[3]。因此，需研究面向多任务的宽带卫星资源调度，在有限的资源内支持更多的通信任务，提

高卫星资源利用率。

本文首先对宽带卫星通信系统进行介绍，总结了现有资源调度方案及算法的研究进展。然后通过分析现有研究存在的问题，设计了多星、跨网、异站场景下的面向多任务的多域异构资源联合调度方案，最后总结了全文，并展望了未来宽带卫星网络下资源调度的研究方向。

1　宽带卫星通信系统

宽带通信卫星通常作为中继节点为各类地面网系的用户提供所需要的卫星资源，并进行数据转发服务，主要使用 Ku 频段和 Ka 频段。宽带卫星通信系统体系架构如图 1 所示，由空间段、控制段和用户段组成。空间段指在空间中运行的卫星星座。宽带通信卫星主要包括平台和有效载荷两部分。平台保障了卫星和有效载荷的正常运行，提供动力支持和电力支持等。有效载荷是卫星实现通信必不可少的设施，主要包括星载天线和转发器，星载天线用来发送和接收遥测信号和数据传输信号，转发器可接收并转发地面站发送的数据信号。控制段包括地面站和一些运行控制中心。地面站接收卫星转发的信号，同时也会向卫星发射信号。卫星的运行控制系统主要包括卫星测控、综合管理、仿真决策等模块，负责对卫星资源、地面站型、不同网系的各类用户进行综合管理，执行卫星状态监控、资源使用情况监控、地面信息状态采集、网系使用控制、资源调度决策等功能[4]。用户段主要由各种用户终端组成，包括手持机、固定站、车载站等等，这些用户终端可能接入不同的地面网系，以支持不同类型的业务数据传输。

本文主要聚焦宽带卫星通信系统中控制段的资源调度管理功能。目前国外宽带卫星网络中的星上载荷管理、地面站网控制以及异构资源规划管理等功能都是通过运行控制系统实现的，而最成熟的卫星运控系统还属美军，其航天测控网络可实现全球覆盖，且在任务规划、资源调度等方面都实现了较高的自动化，可根据任务需求对全球卫星通信资源进行分布式按虚调度。我国的卫星运控系统与之相比仍有差距，目前我国的卫星运控系统主要实现对卫星网络的规划和管理，在任务管理以及资源的统筹规划上仍有欠缺[5]。此外，对星上载荷和地面网系执行独立且分离的管理调度，而且尚未实现对多星的统一运行管理，已实现的功能仅适用于单星或单系列卫星，还未从真正意义上形成一个卫星通信综合管理体系[6]。

2　资源调度技术研究进展

面对多样化的通信任务需求，如何设计资源调度方案可在有限的可用卫星资源的条件下满足尽可能多的通信任务是当前宽带卫星通信网络面临的挑战之一。一般来说，卫星资源调度的对象依次是卫星、波束、转发器和带宽。由于通信任务具有时效性要求，在进行卫星资源调度时不仅要考虑频率资源的分配，还需考虑时间上的规划调度。目前

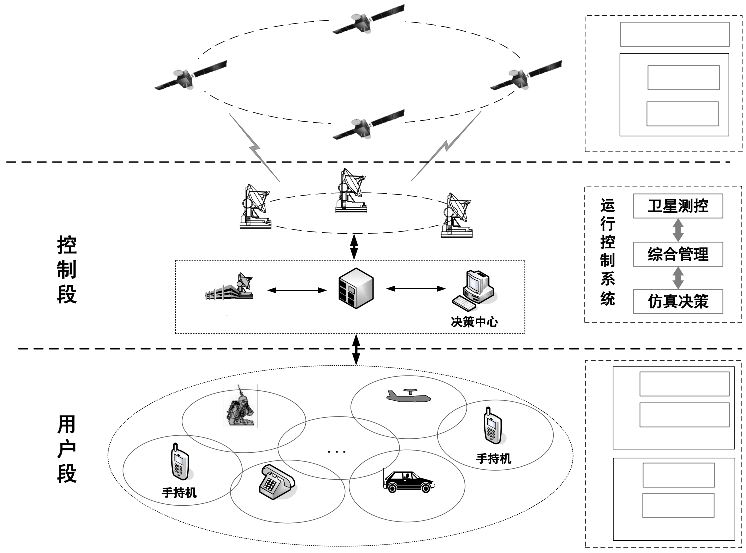

图 1. 宽带卫星通信系统体系架构

宽带卫星网络资源调度大多采用静态配置和动态调度相结合的思路，先根据任务需求配置满足条件的卫星、波束和转发器资源，再建立业务需求约束条件下的带宽、时间二维资源优化问题，来实现卫星资源的高效利用[7]。

根据资源调度涉及的卫星数量，现有方案可分为单星资源调度和多星资源调度方案[8]。文献[9]中针对单星场景提出一种基于前向搜索和蒙特卡洛树搜索的方法来进行基于任务的资源调度。然而，单星场景下的研究局限性较强，无法应用于当前包含多个卫星星座的空间信息网络。文献[10]以最小化任务响应时间为优化目标进行了多星场景的资源调度，文献[11]考虑了不同任务的权重，为最大化完成任务的总权重为目标进行优化。此外，文献[12]以最小化总开销为目标进行通信资源调度规划。然而，这些方案都没有考虑卫星高度、地面站设备等约束，不能直接应用于实际的卫星通信场景。

在资源调度算法方面，文献[13]针对空军卫星控制网，对地面资源进行了优化问题建模，并利用遗传算法进行了求解。文献[14]分别采用了启发式算法、局部搜索算法和遗传算法对卫星资源调度问题进行求解，证明了遗传算法相比其它两种算法的优越性。此外，文献[15]针对 SPOT5 卫星下的资源调度问题，分别采用完全搜索算法（动态规划、深度优先搜索）和非完全搜索算法（禁忌搜索、贪婪搜索）进行了仿真实验，结果证明算法优劣与问题规模密切相关，问题规模较小时，完全搜索算法性能更优。此外，国内陈荣光等人比较了贪婪算法和遗传算法在卫星资源调度方面的性能，证明了遗传算法相比贪婪算法性能更好[16]。中科院潘泳鸰等人分析了国内外有效载荷规划方案的研究情况，并将其与调度问题进行对比，将二者抽象为同一个数学模型，并采用智能规划算法思想设计了一个软件平台，可同时为空间飞行器进行有效载荷的规划和调度[17]。文献[18]针对预警卫星的资源使用问题进行了研究，在满足多约束条件下设计了基于改进粒子群算法的资源优化配置方案。

上述针对卫星资源调度问题的研究大都是针对星上载荷或地面资源进行的。然而，在宽带卫星通信中，卫星仅仅只是一个中继设备，而宽带卫星系统包含卫星、地面站等多类基础设施，对于不同任务需求，选择合适的基础设施可以有效提高整个系统的资源使用效能。因此，可调度资源不应仅仅局限于星上有效载荷资源，还应考虑地面网系、地面站等资源。面向多任务的资源调度问题应从整个通信系统所有可用资源的角度去考虑，通过分析任务具体需求，设计基于卫星、网系、站型等多维异构资源的高效合理匹配调度方案。此外，目前常用的启发式算法通常只能收敛到一个局部最优解，而且时间开销大，并不适用于大规模用户场景，也很难满足实际应用场景对时延的需求，因而设计低复杂度、高自动化的资源调度算法也是面临的一个重大挑战。

3 面向多任务的多域异构资源联合调度

宽带通信卫星是用户进行数据传输的空间中继点，为执行通信任务的用户提供可用卫星资源。由于频率资源有限，资源扩展申请非常困难，卫星通信经常处于资源不足的状态，需要进行高效的资源调度，以提高资源利用率，支持更多的卫星通信任务。考虑到用户段存在不同的地面网系，不同网系具有不同的特点，且通信业务类型不同，对卫星、地面站型等资源的需求也不同。在实际宽带卫星系统运行过程中，若采用人工方式针对不同通信任务给用户预分配所需的卫星、网系和地面站型等资源，系统运行自动化程度较低，且无法对资源进行最优资源配置。针对这一问题，本节提出面向多任务的多域异构资源联合调度方案，首先对任务需求进行分析和建模，然后对星、网、站等多域异构资源进行虚拟化统一描述。在分析了任务需求与资源利用的匹配约束的基础上，提出一种强化学习驱动的智能调度机制，对系统接收到的通信任务进行高效资源分配。

3.1 任务和资源建模

本小节通过分析通信任务需求以及宽带卫星通信网络中需要进行资源调度的所有可用资源，分别对任务、卫星资源、通信网系、地面站资源进行建模。

3.1.1 任务建模

面对宽带卫星通信系统下多样复杂的通信任务，精确完整地描述任务需求是进行基于任务的资源调度的基础。

在进行资源调度时，需要考虑任务的传输业务类型、所需带宽、任务区域、移动性等需求。因此，在对具有不同特征和需求任务进行建模时，也要将这些

因素考虑进去。具体而言，将任务需求建模如下：

$$Task=\{N^{\mathrm{T}},T_{\mathrm{start}}^{\mathrm{T}},T_{\mathrm{end}}^{\mathrm{T}},f^{\mathrm{T}},I^{\mathrm{T}},R^{\mathrm{T}},M^{\mathrm{T}},S^{\mathrm{T}}\},$$

其中，N^{T}、$T_{\mathrm{start}}^{\mathrm{T}}$、$T_{\mathrm{end}}^{\mathrm{T}}$、$f^{\mathrm{T}}$、$I^{\mathrm{T}}$分别表示任务编号、开始时间、结束时间、频段要求及是否使用抗干扰模式等基本信息，R^{T}、M^{T}分别表示任务区域和移动性要求，S^{T}表示卫星的业务相关需求。对任务区域和移动性要求的建模可为后续为通信任务分配卫星波束资源提供参考信息。这里，用边缘点的经纬度信息来描述不规则区域的范围，用中心点的经纬度和半径来表示圆形任务区域。当任务区域随时间变化时，需在任务区域上增加一个时间戳。假设任务区域为圆形区域，可将其表示为$R^{\mathrm{T}}=\{(Lo,La),r,time\}$，其中$(Lo,La)$表示中心点的经纬度坐标，$r$表示半径，$time$表示时间戳信息。此外，对于业务相关的需求，需要考虑业务类型、带宽需求、业务量、保密性要求、传输速率要求等。为了简化模型同时不影响任务需求描述的完整性，本文考虑将业务根据这些需求进行分类，并设置不同的编号，每个编号代表其中一类业务。

3.1.2　卫星资源建模

如图 1 所示，卫星上的资源包括平台和有效载荷资源，而有效载荷又包括星载天线和转发器资源，因此，在对卫星资源进行描述时，需综合考虑这些因素进行建模。由于在对任务进行资源调度时，不仅需要选择中继卫星，还需要对该卫星上的具体波束和转发器进行匹配，在对卫星资源进行建模时，需综合考虑卫星、平台、天线及转发器等资源要素，可表示为

$$\begin{aligned}Satelite=\{&N^{\mathrm{S}},f^{\mathrm{S}},B^{\mathrm{S}},I^{\mathrm{S}},O^{\mathrm{S}},P^{\mathrm{S}},Antenna_1,\cdots,\\&Transponder_1,\cdots,Transponder_{k^{\mathrm{T}}},\cdots,\\&Antenna_{k^{\mathrm{A}}},\cdots,Antenna_{K^{\mathrm{A}}},\\&Transponder_{K^{\mathrm{T}}}\}\end{aligned},$$

其中，N^{S}、f^{S}、B^{S}、I^{S}分别表示卫星编号、支持的频段、是否支持多波束和抗干扰模式，O^{S}和P^{S}分别表示平台的剩余燃料和输出功率。假设在该卫星上共配备了K^{A}根星载天线和K^{T}个转发器，$Antenna_{k^{\mathrm{A}}}$表示第k^{A}个星载天线资源模型，$Transponder_{k^{\mathrm{T}}}$表示第$k^{\mathrm{T}}$个转发器资源模型。星载天线主要包括遥测天线和通信天线，其中通信天线具有波束覆盖区域和移动性等属性，可根据不同配置分为全球波束天线、区域赋性波束天线等。考虑到不同通信任务对天线资源的需求，可将其表示为

$$Antenna_{k^{\mathrm{A}}}=\{k^{\mathrm{A}},f_{k^{\mathrm{A}}}^{\mathrm{A}},R_{k^{\mathrm{A}}}^{\mathrm{A}},M_{k^{\mathrm{A}}}^{\mathrm{A}},J_{k^{\mathrm{A}}}^{\mathrm{A}}\},$$

其中，$f_{k^{\mathrm{A}}}^{\mathrm{A}}$表示第$k^{\mathrm{A}}$个星载天线的工作频段，$R_{k^{\mathrm{A}}}^{\mathrm{A}}$表示覆盖区域，$M_{k^{\mathrm{A}}}^{\mathrm{A}}$表示可移动性，$J_{k^{\mathrm{A}}}^{\mathrm{A}}$表示极化特性。相应地，可将转发器资源表示为

$$Transponder_{k^{\mathrm{T}}}=\{k^{\mathrm{T}},f_{k^{\mathrm{T}}}^{\mathrm{start}},f_{k^{\mathrm{T}}}^{\mathrm{end}},BW_{k^{\mathrm{T}}}^{\mathrm{T}}\},$$

其中，$f_{k^{\mathrm{T}}}^{\mathrm{start}}$和$f_{k^{\mathrm{T}}}^{\mathrm{end}}$分别表示第$k^{\mathrm{T}}$个转发器的起始频点和终止频点，$BW_{k^{\mathrm{T}}}^{\mathrm{T}}$表示可用带宽。

3.1.3　地面通信网系资源建模

根据所采用的传输体制或者业务类型等可将地面网系分为不同的种类，比如，根据传输体制可将其分为频分多址接入（Frequency Division Multiple Access，FDMA）网系、时分多址接入（Time Division Multiple Acces，TDMA）网系、码分多址（Code Division Multiple Access，CDMA）网系等；根据用户拓扑结构可将其分为星型网、树状网、混合拓扑网络等，如表 1 所示。

表 1　地面通信网系分类

分类标准	网系名称
传输体制	FDMA 网系、TDMA 网系、CDMA 网系等
网络拓扑	星型网、网状网、树状网、混合拓扑网络等
星上处理模式	透明模式网系、处理模式网系等
是否跨星、跨波束	单星网系、跨星网系、单波束网系、多波束网系等
业务类型	广播分发网系、综合业务网系、数据通信网系等
是否抗干扰	调频抗干扰网系、隐蔽通信网系等

根据任务需求的不同，用户需要选择合适的地面通信网系进行数据传输。网系资源可建模为

$$Network=\{N^{\mathrm{N}},f^{\mathrm{N}},S^{\mathrm{N}},D^{\mathrm{N}}\},$$

其中，N^{N}表示网系编号，以便用户查询和调度结果确认，f^{N}表示支持的通信频段，S^{N}表示业务相关需求，D^{N}表示可支持的卫星。其中，对S^{N}的建模与 3.1.1 节类似，通过不同的业务编号来对应不同的需求，包括传输体制、传输速率、保密性需求等要素。

3.1.4 地面站资源建模

地面站主要包括天线射频和信道终端。天线射频一方面将要发射的射频信号转化为定向辐射的电磁波，另一方面接收卫星信号，并将其传给信道终端处理。对应地，信道终端也分为发射端和接收端，发射端将要发送的信息转化为适合卫星通信体制的信息形式，接收端将接收到的卫星信道还原为用户所需的业务信息。卫星通信系统会根据之前选定的通信体制来确定对应的信道终端。地面站资源可建模为

$$Station = \{N^{G}, L^{G}, f^{G}, I^{G}, S^{G}\},$$

其中，N^{G} 表示地面站编号，L^{G} 表示地面站的位置信息，f^{G} 指支持的频段，I^{G} 表示地面站的抗干扰能力，S^{G} 表示业务相关需求，包括传输体制、业务类型等要素。

3.2 任务与资源的匹配约束分析

根据上述任务和资源的描述模型，结合实际应用需求，可知任务与卫星、网系和地面站型等资源模型的匹配约束条件主要包括：

（1）卫星资源：主要对通信任务与卫星的时效性、频段、是否支持单波束/多波束组网、抗干扰模式等条件进行资源匹配。

（2）波束资源：主要对任务区域与波束覆盖区域、任务频段与波束频段、移动性以及抗干扰模式等要素是否匹配。

（3）转发器资源：主要针对可用频段、需求带宽、移动性、是否使用抗干扰模式等约束选择合适的转发器资源。

（4）网系资源：主要针对可用频段、保密性要求、传输速率要求，业务类型需求等约束选择合适的网系资源。

（5）地面站资源：通过任务区域、移动性、使用频段、是否使用抗干扰模式、传输体制、业务类型等和地面站资源进行匹配。

需要注意是，在传统的利用人工方式进行资源预分配的过程中，考虑任务和资源的匹配约束时，需要首先将通信任务与卫星资源进行匹配，获得符合条件的卫星列表，进而对波束资源和转发器资源进行匹配；在所选卫星资源上，再将通信任务需求与地面网系资源进行匹配，得到符合条件的网系列表；在此基础上，通过将任务需求与地面站资源进行匹配，得到符合条件的地面站资源结果。最后，再通过遍历算法或者一些启发式算法对带宽资源进行调度管理。然而，这种分配方式自动化程度差，耗时长，且无法得到最优的全局调度结果。

3.3 智能资源联合调度机制

前两小节对卫星、网系、地面站型等资源和任务需求进行了建模，并分析构建了通信任务与各类型资源之间的匹配约束条件。在此基础上，需进一步明确任务执行所需占用的转发器起始、终止频点，在多任务并存的情况下，在一个调度周期内进行资源的全局规划和合理分配，使任务的完成情况最好，卫星资源利用率最高。当前卫星通信网络资源调度大多是先根据匹配约束确定星、网、地资源，再利用遗传算法和粒子群算法等启发式算法对转发器资源进行两维资源规划。也有一些工作进行星地资源和转发器资源的联合调度优化，但并未考虑地面网系的选择问题。为了降低计算开销，加快资源调度速度，本小节提出一种强化学习驱动的智能联合调度框架，将涉及的多域异构资源相关要素和任务需求属性作为强化学习算法的输入，通过训练好的深度神经网络模型后，直接输出所选择的星、网、地资源及对应的转发器带宽资源，在满足约束的前提下，最大化资源占用率和任务完成率。

由于网络中用户终端数目较大，采用集中式资源调度方案会导致计算量过大、灵活性不足的问题。因此，本文提出基于深度Q网络（Deep Q-Network）的多智能体分布式资源调度框架，每个用户拥有一个独立的 DQN 网络来得到其资源调度策略，但在网络训练时需采用系统整体收益作为回报函数，从而达到优化系统整体资源调度的目的。具体而言，DQN 网络的五大组件设置如下:

（1）智能体：用户本身作为智能体，执行资源调度决策；

（2）状态空间：包括所有可用卫星、网系、地面站三类资源的资源要素以及要执行的通信任务的需求要素，即状态空间为

$$\begin{aligned} state = & \{\text{All } Satellite\} \cup \{\text{All } Network\} \cup \\ & \{\text{All } Station\} \cup Task \end{aligned};$$

（3）动作空间：执行该通信任务时，智能体可以选择的所有资源要素的排列组合；

（4）回报函数：整个 GEO 宽带卫星网络的资源利用率或任务完成率等优化目标。需要注意的是，当为用户分配的资源与任务需求不匹配时，即不满

足 3.2 节给出的匹配约束条件时，回报值应设为 0 或者负值，从而促使智能体学到更多有用的经验。

（5）探索策略：采用 ε 贪婪策略。智能体以 ε 的概率从动作空间中随机选择一个动作来进行探索，以 1-ε 的概率选择具有最大 Q 值的动作，从而实现动作探索与利用的折中。

DQN 网络的具体训练过程如下。首先，该方法中存在两个全连接 DNN 网络，一个是评估网络，一个是目标网络。评估网络根据输入的状态值输出所有动作下的估计 Q 值，目标网络根据输入的状态值输出所有动作下的目标 Q 值。每经过 T 次迭代，目标网络的权重 $\overline{\boldsymbol{\theta}}$ 会更新为评估网络的权重 $\boldsymbol{\theta}$。此外，将每一步得到的状态转移关系 $e_t=(s_t,a_t,r_t,s_{t+1})$ 存储在经验池中，其中 s_t 表示第 t 步训练时的状态，a_t 表示第 t 步训练时选取的动作，r_t 表示第 t 步训练时获得的回报。智能体会每次从经验池中随机选取一部分数据作为训练数据，对评估网络进行训练，损失函数可表示为：

$$Loss(\boldsymbol{\theta})=\mathbb{E}[(r_t+\alpha\max Q(s_{t+1},a_{t+1}\,|\,\overline{\boldsymbol{\theta}})-Q(s_t,a_t\,|\,\boldsymbol{\theta}))^2]\text{，（1）}$$

其中，α 表示折扣因子，网络权重 $\boldsymbol{\theta}$ 采用梯度下降法进行优化。

4　结论

本文针对宽带卫星系统下面向多任务需求的资源调度方案展开研究。首先给出了宽带卫星系统的架构及组成，对比了我军与美军在卫星运行控制系统上的现状，指出了我军卫星通信系统在资源调度方面的不足。然后分析了目前卫星通信资源调度问题面临的挑战与困难，介绍了目前在调度方案和具体算法设计上的研究进展，总结了现有方案的不足。接着，提出了一种面向多任务需求的多域异构智能资源调度方案，对卫星、网系、地面站等资源以及任务需求进行统一描述，分析了资源与任务需求之间的匹配关系，并提出一种强化学习驱动的分布式资源调度算法，可根据资源使用情况及任务需求为用户合理高效分配资源。

由于当前很多卫星通信系统下，卫星运控系统和测控系统是相互独立的，本文工作主要针对卫星运行控制系统下的通信任务进行资源调度研究。然而，运控任务和测控任务都需使用频率资源进行数据传输，对二者进行统一规划调度势必会带来更大的性能增益，未来需要在同时考虑运控任务和测控任务的情况下进行资源优化方案设计与评估。此外，考虑到卫星通信系统中用户的动态拓扑特性，需要设计适用于移动场景的多星多网多站资源实时动态调度技术。

参考文献

[1] H. Guo, Q. Yang, H. Wang, et al., SpaceDML: Enabling distributed machine learning in space information networks[J]. IEEE Network, 2021, 35(4): 82-87.

[2] P. Zhang, Y. Zhang, N. Kumar and M. Guizani, Dynamic SFC embedding algorithm assisted by federated learning in space–air–ground-integrated network resource allocation scenario[J]. IEEE Internet of Things Journal, 2023, 10(11): 9308-9318.

[3] X. Mi, C. Yang and Z. Chang, Multi-Resource Management for Multi-Tier Space Information Networks: A Cooperative Game[C]//2019 15th International Wireless Communications & Mobile Computing Conference (IWCMC), Tangier, Morocco, 2019: 948-953.

[4] 秦鹏，刘海蛟，陆洲．基于天基信息网络综合管控系统建设的思考[J]．中国电子科学研究院学报，2017.

[5] 安辰．我国首颗高通量通信卫星实践十三号投入使用[J]．计算机与网络，2018(03).

[6] 汪春霆，翟立君．关于天地一体化信息网络典型应用示范的思考[J]．电信科学，2017，12：37-42.

[7] 刘悦．国外高通量卫星系统与技术发展[J]．国际太空，2017，11：42-47.

[8] Y. Wang, D. Zhou, N. Song, et al., Concurrent reconfiguration of resource-oriented emergency TT&C mission planning for space information networks[J]. Journal of Communications and Information Networks, 2021, 6(2): 142-152.

[9] D. Eddy and M. Kochenderfer. Markov decision processes for multi-objective satellite task planning[C]//2020 IEEE Aerospace Conference. New York: IEEE Communications Society, 2020: 1-12.

[10] Z. Yang, W. Zhong, XI Tao, et al. Imaging reconnaissance satellites single mission integrated scheduling for emergency requirements[J]. Systems Engineering and Electronics, 2018, 40(9): 2000-2006.

[11] M. Wang, G. Dai, M. Vasile. Heuristic scheduling algorithm oriented dynamic tasks for imaging satellites[J]. Mathematical Problems in Engineering, 2014(5): 1-11.

[12] J. Wang, X. Zhu, D. Qiu, et al. Dynamic scheduling for emergency tasks on distributed imaging satellites with task merging[J]. IEEE Transactions on Parallel and Distributed Systems, 2014, 25(9): 2275-2285.

[13] D.A. Parish. A genetic algorithm approach to automating satellite range scheduling[D]. USA: Air Force Institute of Technology,1994.

[14] L. Barbulescu, L.D. Whitley, and A.D. Howe. Leap before you look:An effective strategy in an oversubscribed problem[C]. Nineteenth National Conference on Artificial Intelligence,2004: 143-148.

[15] E. Bensana, G. Verfaillie, J.C. Agnese, et al. Exact and inexact methods for the daily management of an earth observation satellite[J].Symposium on Space Mission Operations and Ground Data

Systems,1996.
[16] 陈荣光，李春升，陈杰，于泽．基于贪婪算法的近空间平台区域覆盖优化设计[J]. 北京航空航天大学学报，2009，35(05)：547-550.
[17] 潘泳鸽，钟红恩．空间飞行器有效载荷规划与调度软件平台[J]．微计算机信息，2008，30：25-27.
[18] 冯明月，汤绍勋，何俊．基于改进粒子群算法的天基预警系统资源调度方法[J]. 中国电子科学研究学院学报，2010，5(1)：97-101.

[作者简介]

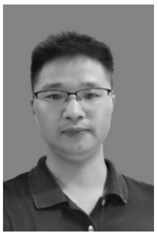

陈志坤，（1985－ ），男，博士，工程师，主要研究方向：信息通信网络

赵瑜，（1974－ ），女，硕士，正高级工程师，主要研究方向：通信网络管理

王璐（1981－ ），女，硕士，工程师，主要研究方向：通信网络管理

于 Retinex 模型和注意力混合机制的遥感图像融合方法

叶永旭[1]，汪婷婷[1]，方发明[1]，张桂戌[1]
1.华东师范大学计算机科学与技术学院，上海 200062

摘　要: 全色锐化是一种融合多光谱图像（LRMS）和全色图像（PAN）从而获得高分辨率多光谱图像（HRMS）的技术。基于 PAN 和 LRMS 在成像过程中分别具有 HRMS 进行 Retinex 分解后的照度分量和反射分量特点这一观察，引入 Retinex 模型指导构建全色锐化网络（AIRNet）。具体而言，提出了基于空间注意力的照度模块（SAIM），将 PAN 转换为 HRMS 的照度分量。此外使用基于混合通道-空间注意力机制的反射模块（HARM）将 LRMS 转换为 HRMS 的反射分量。最终基于 Retinex 模型将得到的 HRMS 相应的照度分量和反射分量融合得到 HRMS。在多个遥感图像数据集上与最先进的全色锐化方法进行的定性和定量的对比实验结果表明，AIRNet 具有显著突出的性能。此外，多个消融实验也表明，提出的 SAIM 和 HARM 是 AIRNet 用于全色锐化的有效模块。

关键词: 全色锐化；遥感图像融合；空间注意力机制；通道注意力机制；Retinex 模型

Remote sensing image fusion method based on Retinex model and hybrid attention mechanism

Ye Yongxu[1], Wang Tingting[1], Fang Faming[1], Zhang Guixu[1]

1. School of Computer Science and Technology, East China Normal University, Shanghai 200062, China

Abstract: Pansharpening is a technique that fuses a multispectral image (LRMS) and a panchromatic image (PAN) to obtain a high-resolution multispectral image (HRMS). Based on the observation that PAN and LRMS respectively have the characteristics of illumination component and reflection component of HRMS after Retinex decomposition, this paper proposes an inverse Retinex model guided pansharpening network, termed as AIRNet. Specifically, a Spatial Attention based Illuminance Module (SAIM) is proposed to convert the PAN to the illuminance component of HRMS. And a Hybrid Attention-based Reflectance Module (HARM) is used to convert the LRMS to the reflection component of the HRMS. Finally, based on the inverse Retinex model, the corresponding illuminance component and reflection component of the obtained HRMS are fused to obtain HRMS. Qualitative and quantitative comparison experiments with state-of-the-art pansharpening methods on multiple remote sensing image datasets show that AIRNet has significantly outstanding performance. In addition, multiple ablation experiments also show that the proposed SAIM and HARM are effective modules of AIRNet for pansharpening.

Key words: Pansharpening, Remote sensing image fusion, Spatial attention mechanism, Channel attention mechanism, Inverse Retinex model

1　介绍

遥感图像在地物分类[7]、地理数据[9]等领域发挥着重要作用。在遥感图像成像过程中，全色图像（PAN）是由卫星传感器响应整个全色波段的光得到的混合图像，空间分辨率较高，但是只有单个波段的光谱信息。多光谱图像（LRMS）则是由卫星传感器对多个不同波段的光作出响应得到的多波

收稿日期:；　预印本:
基金项目:国家自然科学基金青年项目(编号: 62202173)；中国博士后科学基金面上资助(编号: 2021M701215)
第一作者简介：叶永旭，硕士研究生，研究方向为遥感图像全色锐化。E-mail: 51215901060@stu.ecnu.edu.cn
通信作者简介:方发明，教授，研究方向为计算机视觉、图像处理。E-mail: fmfang@cs.ecnu.edu.cn

段图像，因此具有多个波段的光谱信息，但空间分辨率较低。为了得到具有高空间分辨率的多光谱图像（HRMS），研究者们提出一种融合 LRMS 和 PAN 的技术，称为全色锐化[5]。全色锐化方法主要可以分为组分替换（CS）方法、多尺度分析（MRA）方法和变分优化（VO）方法以及深度学习（DL）方法[23]。

CS 方法的核心思想是先对 LRMS 进行变换得到空间分量和光谱分量，再对其空间分量使用 PAN 进行替换，最后逆变换得到目标 HRMS。代表性方法主要有：主成分分析（PCA）[21]和自适应 Gram-Schmidt（GSA）[2]等。一般来说，CS 方法计算复杂度较小，但容易造成严重的光谱信息丢失。MRA 方法的主要思想是在多分辨率下对 LRMS 进行分解，并用 PAN 替换其空间分量，最终逆分解后得到目标图像。经典方法有：加性小波亮度比例法（AWLP）[19]、平滑滤波强度调制法（SFIM）[20]和“àtrous”小波变换法（ATWT）[24]等。与 CS 方法相比，MRA 方法具有更好的光谱保持能力，但通常会导致显著的空间畸变。VO 方法通过假设观测图像与目标图像之间存在潜在的关系来构建变分模型，并利用图像的先验信息来约束该模型，模型的最优解即对应全色锐化结果。具体方法可以分为贝叶斯方法[27]和变分方法[10]等。VO 方法可以均衡地保持 HRMS 图像的空间信息和光谱信息，但如何建立观测图像与目标图像之间的潜在关系并选择合适的先验项是一个很大的挑战。

近年来，卷积神经网络（CNN）被广泛应用于不同的计算机视觉任务中，同时也在全色锐化任务中大放异彩[12]。[18]首次提出利用 CNN 进行全色锐化。在此之后，Hu 等[11]提出了一种多尺度多深度卷积神经网络（MSDCNN），在不同尺度下提取更丰富的特征用于全色锐化。Xu 等[31]为全色锐化任务建立了一个高效的观测模型，并展开为深度网络进行求解，即 GPPNN。此外，Cai 和 Huang[6]将全色锐化看成基于超分引导的任务，并提出了一种渐进式全色锐化网络 SRCNN。Wang 等[28]为了充分利用多尺度信息中的浅层特征，采用了“U”型网络进行全色锐化。此外，为了提高模型的泛化能力，有多个方法应用了生成对抗模型[17]等无监督策略进行全色锐化。

此外，一种比较有趣的想法是将 Retinex 模型引入全色锐化[8]。Retinex 模型将图像分解为反射分量和照度分量[15]，其中，反射分量反映了物体对不同光线的反射率，照度分量通常被认为是环境光源与几何结构相互作用的结果。一般来说，基于 Retinex 模型的全色锐化方法首先对 LRMS 进行 Retinex 分解，获得其照度分量，然后利用照度分量与 PAN 进行加权融合得到新的照度分量，再与原始 LRMS 相加得到 HRMS。从本质上讲，这类方法仍然属于 CS 方法。因此，光谱信息的丢失不可避免。

受基于 Retinex 模型的全色锐化方法启发，本文提出了一种 Retinex 模型引导的基于注意力的全色锐化网络（Attention-based Inverse Retinex Network，AIRNet）。如图 1 所示，AIRNet 分别将 PAN 和 LRMS 输入基于空间注意力的照度模块（Spatial Attention-based Illumination Module，SAIM）和基于混合注意力的反射模块（Hybrid Attention based Reflectance Module，HARM），获得 HRMS 相应的照度分量和反射分量，然后通过 Retinex 分解得到 HRMS。AIRNet 有效地利用了 PAN 中丰富的空间信息和 LRMS 中丰富的光谱信息。

本文的主要贡献如下：

1.首次使用 Retinex 模型用于全色锐化。提出了

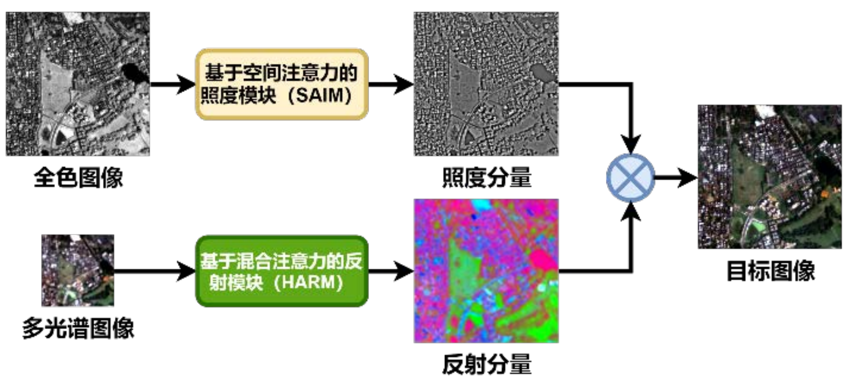

图 1　本文提出的全色锐化方法的实例

一种新颖的全色锐化架构，从 PAN 和 LRMS 分别推导出 HRMS 的照度分量和反射分量，再由 Retinex 分解得到 HRMS。

2.提出了基于空间注意力的照度模块（SAIM），将具有丰富空间信息的 PAN 转化为 HRMS 相应的照度分量。

3.结合通道注意力和空间注意力提出了基于混合注意力的反射模块（HARM），用于将包含大量光谱信息的 LRMS 转换为 HRMS 相应的反射分量。

4.在多个卫星数据集上与多种最先进方法的实验结果对比表明了所提方法的优越性。

2　相关工作和动机

2.1　注意力机制

人类的视觉感知系统不会同时处理整个场景，为了更好地捕捉视觉结构，注意力会选择性地捕捉突出的部分[16]。基于该特性所设计的基于注意力的网络可以更有效地利用图像中有用的信息。

空间注意力机制如图 2（a）所示，空间注意力模块将输入特征$\mathbf{F} \in \mathbb{R}^{H \times W \times C_{in}}$的最大池化和平均池化沿通道维度进行拼接，并送入卷积层得到中间输出$\tilde{\mathbf{F}} \in \mathbb{R}^{H \times W \times C_{in}}$，再经由 Sigmoid 函数后与原始特征图相乘得到空间注意力图。具体如下：

$$SA(\mathbf{F}) = \mathbf{F} \cdot g(\sigma(\mathbf{W} \otimes [MAX(\mathbf{F}), AVG(\mathbf{F})]))\#(1)$$

其中$g(\cdot)$和$\sigma(\cdot)$分别表示 Sigmoid 函数和 ReLU 函数，$\mathbf{W} \in \mathbb{R}^{2 \times k \times k \times C_{out}}$为$C_{out}$个大小为$k \times k \times 2$的

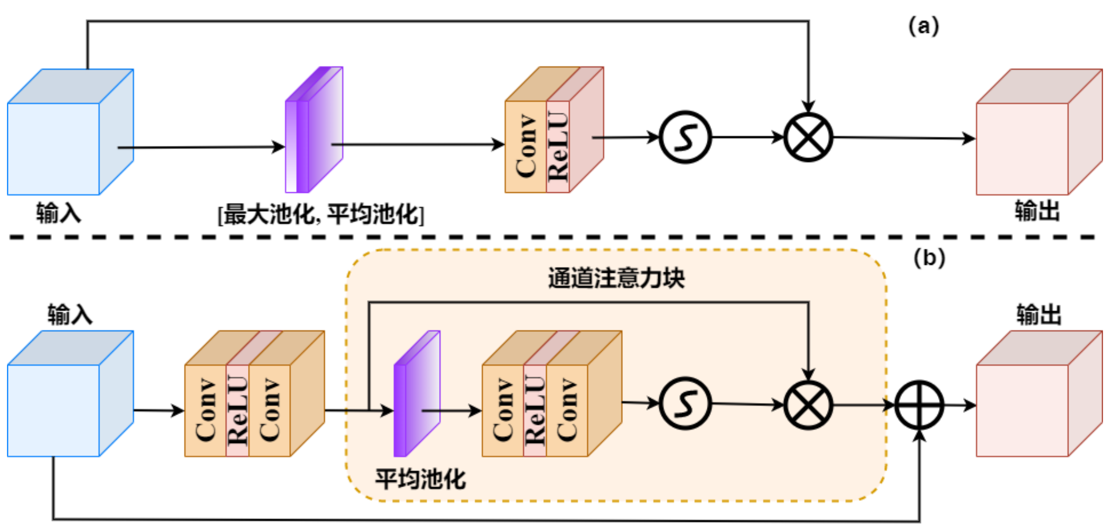

图 2　不同注意力机制的整体结构。（a）空间注意力模块；（b）残差通道注意力块

卷积核，$\otimes$表示卷积运算，$[\cdot]$，$MAX(\cdot)$，$AVG(\cdot)$分别表示沿通道拼接、最大池化和平均池化操作，$\cdot$代表逐元素乘法。

残差通道注意力块由于低分辨率空间中具有丰富的低频信息和部分有价值的高频信息，而卷积层中的每个卷积核都只对空间维度上有局部感受野，因此使用通道注意力机制可以利用特征通道之间的相互依赖，使网络专注于通道维度上更有价值的特征。Wang 等[26]提出了残差通道注意力块（Residual Channel Attention Block，RCAB），如图 2（b）所示。残差块和长跳跃连接可以使主干网络保留部分原始特征信息；通道注意力机制通过提取通道之间的依赖关系，可以进一步增强网络的拟合能力。具体地，RCAB 的结构可以表示成：

$$RCAB(\mathbf{F}) = \mathbf{F} + CA\left(\mathbf{W}^1 \otimes \sigma(\mathbf{W}^2 \otimes \mathbf{F})\right)\#(2)$$

其中$\mathbf{W}^1 \in \mathbb{R}^{C_{in} \times k \times k \times C_{out}}$，$\mathbf{W}^2 \in \mathbb{R}^{C_{in} \times k \times k \times C_{out}}$分别表示两个由$C_{out}$个大小为$k \times k \times C_{in}$的卷积核堆叠而成的卷积层。$CA(\cdot)$为通道注意力模块，其结构如下：

$$CA(\mathbf{F}) = \hat{\mathbf{F}} \cdot g\left(\mathbf{W}_U \otimes \sigma(\mathbf{W}_D \otimes AVG(\mathbf{F}))\right)\#(3)$$

其中，$\hat{\mathbf{F}}$表示 RCAB 中通道注意力模块输入的中间特征图，$\mathbf{W}_U$和$\mathbf{W}_D$分别表示在通道注意力模块中用于通道缩放的卷积核。

2.2　Retinex 模型

Retinex 模型是一种模拟人类视觉系统的颜色感知模型，目标是将一个观测图像$\mathbf{O} \in \mathbb{R}^{H \times W \times C}$分解

为它的照度分量和反射分量，即：

$$\mathbf{O}=\mathbf{I}\cdot\mathbf{R}\#(4)$$

式中，$\mathbf{I}\in\mathbb{R}^{H\times W\times C}$表示图像代表场景中物体亮度的照度分量，$\mathbf{R}\in\mathbb{R}^{H\times W\times C}$表示图像物体对光的反射率的反射分量。

在文献[30]的研究中，照度分量往往认为是环境光源与几何结构相互作用的结果，即拥有大量的空间信息。反射分量包含更多关于物体对不同光的反射率的信息，即丰富的光谱信息。正因为如此，Retinex 模型可以作为光谱信息和空间信息的有效特征提取器。同时 Retinex 模型也被广泛应用于图像暗光增强等任务中[22]。

2.3　动机

在遥感图像成像过程中，PAN 是通过吸收全色波段的光而获得的单波段图像，同时具有光源信息和丰富的几何结构信息；LRMS 则是通过吸收多个不同波长范围的光而获得的多光谱图像，含有丰富的光谱信息，即反映了场景物体对不同的光的反射率。结合 Retinex 模型将图像分解为反映环境光源和几何结构相互作用的照度分量以及包含物体不同光反射率的反射分量这一事实，自然而然地，可以认为 PAN 和 LRMS 分别是 HRMS 照度分量和反射分量固有的先验信息。因此，利用神经网络强大的拟合能力，将 PAN 和 LRMS 转化为 HRMS 的照度分量和反射分量，即可得到 HRMS。

得益于注意力机制中的空间注意力和通道注意力，可以有效地实现上述图像变换。一方面，从 PAN 得到 HRMS 照度分量，更注重环境光源和几何的组合效果，因此可以基于空间注意力来构建照度模块；另一方面，为了获得场景物体对不同波长的光的反射率信息，需要逐通道处理 LRMS，为此构建了一个基于混合通道注意力和空间注意力的反射模块。

3　研究方法

本节将详细介绍提出的 AIRNet。如图 3 所示，整个网络架构包含两个分支：一个分支用于将 PAN 转换为照度分量，另一个将 LRMS 转换为反射分量。最后基于 Retinex 模型将照度分量和反射分量相乘，即可得到待求的 HRMS。

3.1　基于 Retinex 模型的融合框架

将待求 HRMS 表示成$\mathbf{X}\in\mathbb{R}^{H\times W\times C}$，PAN 和 LRMS 分别表示成$\mathbf{P}\in\mathbb{R}^{H\times W\times 1}$和$\mathbf{MS}\in\mathbb{R}^{h\times w\times C}$，$\mathbf{MS}_{\uparrow\times 4}\in\mathbb{R}^{H\times W\times C}$表示对$\mathbf{MS}$上采样 4 倍。根据 Retinex 模型的定义，只要得到相对应的照度分量$\bar{\mathbf{I}}\in\mathbb{R}^{H\times W\times C}$和反射分量$\bar{\mathbf{R}}\in\mathbb{R}^{H\times W\times C}$，即可得到目标图像$\mathbf{X}$。由于$\mathbf{P}$和$\mathbf{MS}$通道数不一致，为了从$\mathbf{P}$得到$\bar{\mathbf{I}}$，首先通过卷积对$\mathbf{P}$的通道数进行扩展。即：

$$\hat{\mathbf{P}}=Conv_{\times 1}(\mathbf{P})\#(5)$$

其中，$Conv_{\times 1}(\cdot)$表示卷积层，下标表示卷积层的数量，$\hat{\mathbf{P}}\in\mathbb{R}^{H\times W\times C}$表示通道扩展后的图像。然后将$\hat{\mathbf{P}}$遍历$\mathrm{N}_1$个密集连接的照度模块 SAIM，最后通过一个卷积层和一个带有 Tanh 激活函数的1x1卷积层，即可得到$\bar{\mathbf{I}}$。整个过程可以表示为：

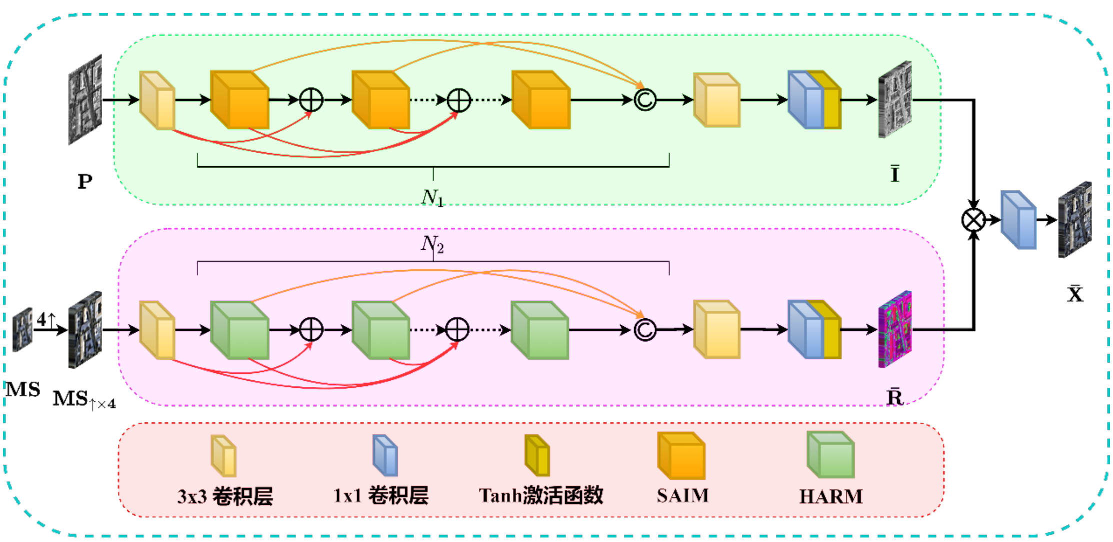

图 3　本文提出的 AIRNet 的整体架构

$$\bar{\mathbf{I}} = Conv_{\times 2}\left(\mathbf{F}_{\times N_1}^{SAIM}(\widehat{\mathbf{P}})\right)\#(6)$$

其中$\mathbf{F}_{\times N_1}^{SAIM}(\cdot)$表示$N_1$个密集连接的照度模块。

另一方面，$\mathbf{MS}$首先使用双三次插值得到$\mathbf{MS}_{\uparrow\times 4}$，然后通过上述类似的过程得到$\bar{\mathbf{R}}$，

$$\mathbf{MS}_{\uparrow\times 4} = Bicubic_{\times 4}(\mathbf{MS})\#(7)$$

$$\bar{\mathbf{R}} = Conv_{\times 2}\left(\mathbf{F}_{\times N_2}^{HARM}(\mathbf{MS}_{\uparrow\times 4})\right)\#(8)$$

其中$\mathrm{Bicubic}_{\times 4}(\cdot)$表示使用双三次插值进行 4 倍上采样，$\mathbf{F}_{\times N_2}^{\mathrm{HARM}}(\cdot)$表示$N_2$个密集连接的反射模块 HARM。最后基于 Retinex 模型得到估计的 HRMS，

$$\bar{\mathbf{X}} = Conv_{\times 1}(\bar{\mathbf{I}} \odot \bar{\mathbf{R}})\#(9)$$

整个网络架构采用了密集连接策略来增加模型训练的稳定性。此外对多个照度模块和反射模块获得的中间特征图进行沿通道拼接操作，从而可以更好地利用浅层特征。

3.2　基于空间注意力的照度模块（SAIM）

Jin 等[13]的研究发现，$\bar{\mathbf{I}}$对$\bar{\mathbf{R}}$的每个通道的关系不应该由同一个简单函数来刻画，而应该由相互独立的复杂函数来表示。因此所设计的 SAIM 在保持环境光源与几何结构的交互的前提下，对$\bar{\mathbf{I}}$的不同通道进行不同的处理。SAIM 的详细结构如图 4（a）所示。对于通道扩展后的$\widehat{\mathbf{P}}$，首先执行通道分离操作：

$$\{\widehat{\mathbf{P}}_1,\cdots,\widehat{\mathbf{P}}_C\} = split\left(\widehat{\mathbf{P}}^{in}\right)\#(10)$$

其中$\widehat{\mathbf{P}}^{in}$表示输入特征图。$split(\cdot)$表示通道分离操作。$\{\widehat{\mathbf{P}}_1,\cdots,\widehat{\mathbf{P}}_C\} \in \mathbb{R}^{H\times W\times 1}$表示通道分离后的单通道特征图。然后使用空间注意力机制和多层卷积层来实现环境光源与几何结构的交互：

$$SAIM_i(\widehat{\mathbf{P}}_i) = Conv_{\times 3}\left(SA(\widehat{\mathbf{P}}_i)\right)\#(11)$$

$$\widehat{\mathbf{P}}^{out} = Conv_{\times 1}([Conv_{\times 1}(SAIM_1),\cdots,Conv_{\times 1}(SAIM_C)])\#(12)$$

其中$SA(\cdot)$表示空间注意力模块，$\widehat{\mathbf{P}}^{out}$表示输出的交互结果特征图。这个过程模拟了环境光源和几何结构的交互作用，实现了从$\mathbf{P}$到$\bar{\mathbf{I}}$的转换。SAIM 使用了参数共享的策略，不仅减少了训练参数，还能有效地避免网络过拟合。

3.3　基于混合注意力的反射模块（HARM）

HARM 的结构如图 4（b）所示，首先对输入特征图$\mathbf{MS}_{\uparrow\times 4}^{in}$进行特征预提取操作：

$$\widetilde{\mathbf{MS}}_{\uparrow\times 4} = Conv_{\times 1}\left(\mathbf{MS}_{\uparrow\times 4}^{in}\right)\#(13)$$

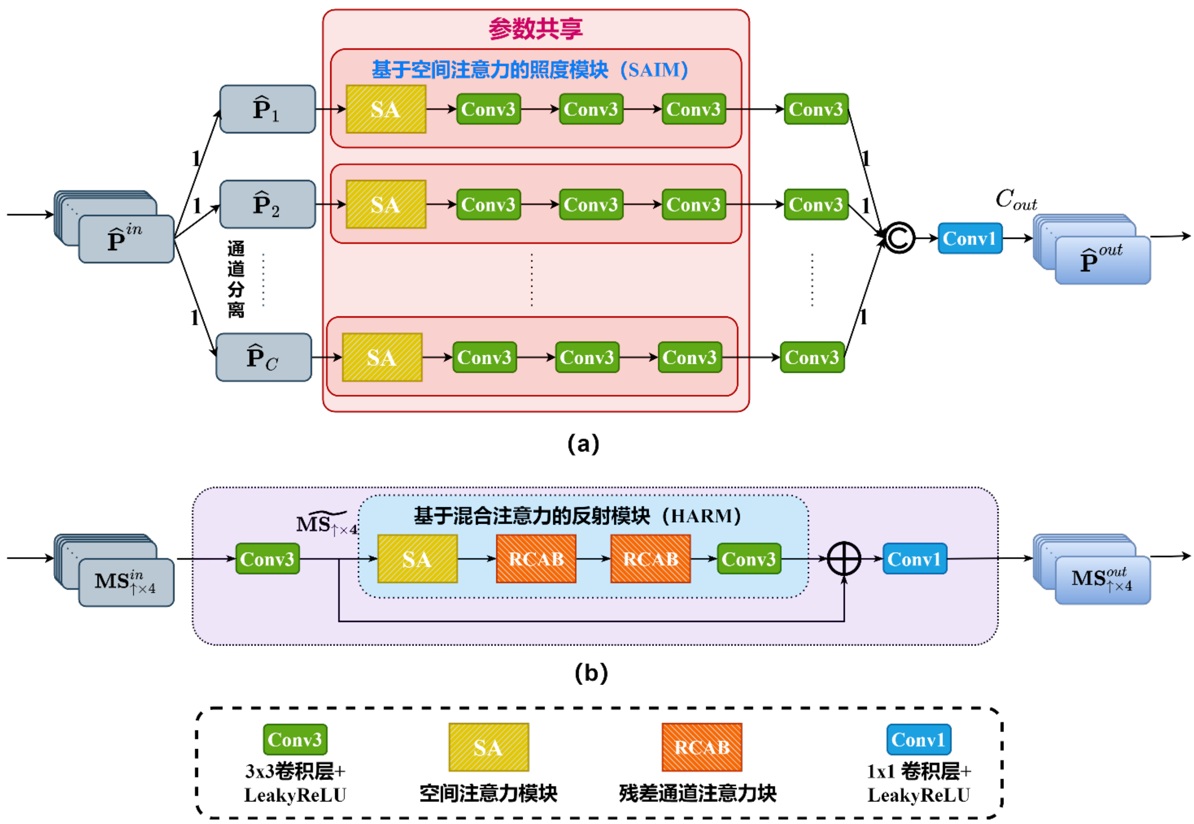

图 4　（a）基于空间注意力的照度模块（SAIM）；（b）基于混合注意力的反射模块（HARM）

其中$\widetilde{\mathbf{MS}_{\uparrow\times4}}$表示预提取的特征图。由于$\overline{\mathbf{R}}$包含了物体对不同波段的光的反射信息，所以使用 SA 模块聚焦于特定物体，并结合 RCAB 来筛选相应的通道。Woo 等[29]的工作表明将 SA 和 RCAB 结合起来可以在某些任务中获得更好的结果。最后使用残差连接来保留更多的输入信息。具体过程可以表示为：

$$HARM(\widetilde{\mathbf{MS}_{\uparrow\times4}}) = Conv_{\times1}\left(RCAB_{\times2}\left(SA(\widetilde{\mathbf{MS}_{\uparrow\times4}})\right)\right)\#(14)$$

$$\mathbf{MS}_{\uparrow\times4}^{out} = Conv_{\times1}\left(\widetilde{\mathbf{MS}_{\uparrow\times4}} + HARM(\widetilde{\mathbf{MS}_{\uparrow\times4}})\right)\#(15)$$

其中$RCAB_{\times2}(\cdot)$表示执行两次 RCAB，$\mathbf{MS}_{\uparrow\times4}^{out}$表示输出特征图。

3.4　损失函数

提出的 AIRNet 网络采用平均绝对误差函数（MAE）作为损失函数，即：

$$\mathcal{L} = \frac{1}{N}\sum_{i=1}^{N}\left\|\overline{\mathbf{X}}_{\boldsymbol{\Theta}_{AIRNet(i)}} - \mathbf{X}_i\right\|_1\#(16)$$

其中N表示训练样本数，$\overline{\mathbf{X}}_{\boldsymbol{\Theta}_{AIRNet(i)}}$表示 AIRNet 经过参数$\boldsymbol{\Theta}$得到的第$i$个融合结果 HRMS，$\mathbf{X}_i$代表第$i$个真实标签数据。

4　实验

4.1　实验设置

数据集实验中使用的数据集分别是从 MS 图像为 4 波段的 QuickBird（QB）和 8 波段的 WorldView-2（WV2）卫星上获取的遥感图像。所有遥感图像被裁剪成大小为 64×64 的 MS 图像和 256×256 的 PAN 图像，然后根据 Wald 协议[25]将获得的 PAN/MS 图像的分辨率降低 4 倍。得到用于训练的 LRMS/PAN 图像块大小为16×16/64×64，真实标签数据 GT 的图像块大小为64×64。从 QB/WV2 数据集中获得的图像对数量为 10596/9118 对，以 90%/10%的比例分离数据集分别用于训练/验证。

评估指标为了验证所提出的网络的性能，分别执行存在参考图像的降分辨率评估以及使用真实遥感数据的全分辨率评估。降分辨率评估选择了五个广泛使用的定量指标，即 SAM[32]， SCC[33]，QAVE[1]， ERGAS[4] 和通用图像质量指数Q4/Q8[14]。全分辨率评估中则使用 QNR[3]指标及其两个分量D_λ和D_S。

训练细节实验使用 Pytorch 框架在 Nvidia GTX 2080ti GPUs 上实现。在训练过程中，epoch 设置为700，学习率为 6.5e-4，每 40 个 epoch 学习率下降0.5 倍，训练批次大小为 16，使用权值衰减、β_1、β_2分别为 9.5e-5、0.9 和 0.999 的 Adam 优化器。

4.2　实验比较

本节将提出的 AIRNet 与其他先进的全色锐化方法进行比较，其中包括四种传统方法：即 GSA[2]，ATWT[24]， AWLP[19]和 SFIM[20]，另外还比较了五种基于深度学习的方法：PNN[18]、MSDCNN[11]、MUCNN[28]、SRPPNN[6]、GPPNN[31]。除此之外，我们对上采样版本的 LRMS（EXP）也进行了定性对比实验。

降分辨率评估：表 1 和表 2 的 2-6 列分别显示了每种方法在 QB 和 WV2 降分辨率数据集上的平均定量结果。从表中数据可以看出，本文提出的方

表 1　　QB 数据集上的平均定量指标结果

	降分辨率评估				全分辨率评估			
	Q4↑	QAVE↑	SAM↓	ERGAS↓	SCC↑	D_λ↓	D_S↓	QNR↑
GSA	0.8723	0.8721	3.0938	2.0194	0.9088	0.0640	0.1027	0.8407
AWLP	0.8665	0.8664	3.1087	2.0155	0.9164	0.0679	0.0948	0.8440
ATWT	0.8611	0.8652	3.2040	2.0378	0.9134	0.0793	0.1106	0.8191
SFIM	0.8542	0.8599	3.2438	2.0966	0.9099	0.0635	0.0870	0.8553
PNN	0.7787	0.7732	3.5218	2.6695	0.8235	0.0523	0.0468	0.9031
MSDCNN	0.8878	0.8895	2.7394	1.9609	0.8989	0.0443	0.0331	0.9244
MUCNN	0.8995	0.8993	2.5666	1.8615	0.9082	0.0506	0.0485	0.9040
SRPPNN	0.9117	0.9137	2.4376	1.7578	0.9131	0.0257	0.0349	0.9407
GPPNN	0.9146	0.9142	2.3593	1.7897	0.9167	0.0546	0.0449	0.9030
本文方法	0.9297	0.9301	2.1758	1.6218	0.9287	0.0255	0.0318	0.9427

注：**粗体**为最好的结果，<u>下划线</u>为第二好的结果

表 2　　WV2 数据集上的平均定量指标结果

	降分辨率评估				全分辨率评估			
	Q8↑	QAVE↑	SAM↓	ERGAS↓	SCC↑	D_λ↓	D_S↓	QNR↑
GSA	0.9190	0.9135	6.7579	4.0076	0.8967	0.0524	0.1287	0.8258
AWLP	0.8932	0.8920	6.7229	4.4648	0.8855	0.0611	0.1060	0.8394
ATWT	0.8949	0.8951	6.6278	4.4232	0.8869	0.0694	0.1150	0.8237
SFIM	0.8798	0.8819	6.7435	4.6349	0.8878	0.0510	0.1074	0.8471
PNN	0.9485	0.9483	4.8106	2.9017	0.9368	0.0376	0.1031	0.8633
MSDCNN	0.9529	0.9530	4.6903	2.7662	0.9419	0.0364	0.0802	0.8863
MUCNN	0.9517	0.9512	4.6655	2.8446	0.9426	0.0425	0.1033	0.8564
SRPPNN	0.9608	0.9608	4.2076	2.5060	0.9527	0.0559	0.0577	0.8867
GPPNN	0.9563	0.9556	4.3993	2.6939	0.9481	0.0429	0.0798	0.8807
本文方法	0.9639	0.9641	3.9955	2.4312	0.9579	0.0410	0.0754	0.8896

注：　**粗体**为最好的结果，下划线为第二好的结果

法要明显优于其他方法。此外，基于模型展开的方法如 GPPNN 和 SRPPNN 在 QB 数据集上略优于其他方法。同时，SRPPNN 在 WV2 数据集中表现更好。图 5 和图 6 分别展示了每种方法融合一对 QB 测试数据的结果以及该融合结果与真实图像之间的误差图，可以发现本文方法在空间信息恢复和光谱信息保持上都有更好的表现。

全分辨率评估：表 1 和表 2 的最后三列给出了各种方法在 QB 和 WV2 全分辨率数据集上的平均定量度量结果。可以看到在 QB 数据集上，本文方法三个指标均获得了最佳结果。在 WV2 数据集上，尽管D_λ和D_S指标结果不是最优的，但是 QNR 仍然优于其他方法。图 7 给出了每种方法融合一对 WV2 真实数据的结果，本文方法仍然具有良好的视觉效果。

4.3　消融实验

N_1和N_2的数量为了探讨N_1和N_2的数量对网络性能的影响，在 WV2 数据集上进行消融实验。如表 3 所示，在$N_1=2$，$N_2=2$时网络性能最好，在$N_1=3$，$N_2=1$和$N_1=3$，$N_2=3$时网络性能相对较差。因此，在实验中均采用$N_1=2$，$N_2=2$的设置。

SAIM 和 HARM 的有效性为了验证 SAIM 和 HARM 两个模块的有效性，同样在 WV2 数据集上进行了消融实验。该消融实验考虑了四种情形，I. HARM 和 SAIM 都使用；II. 不使用 HARM 使用 SAIM；III. 使用 HARM 但不使用 SAIM 以及 IV. HARM 和 SAIM 都不使用。如图 8 所示，I 的表现

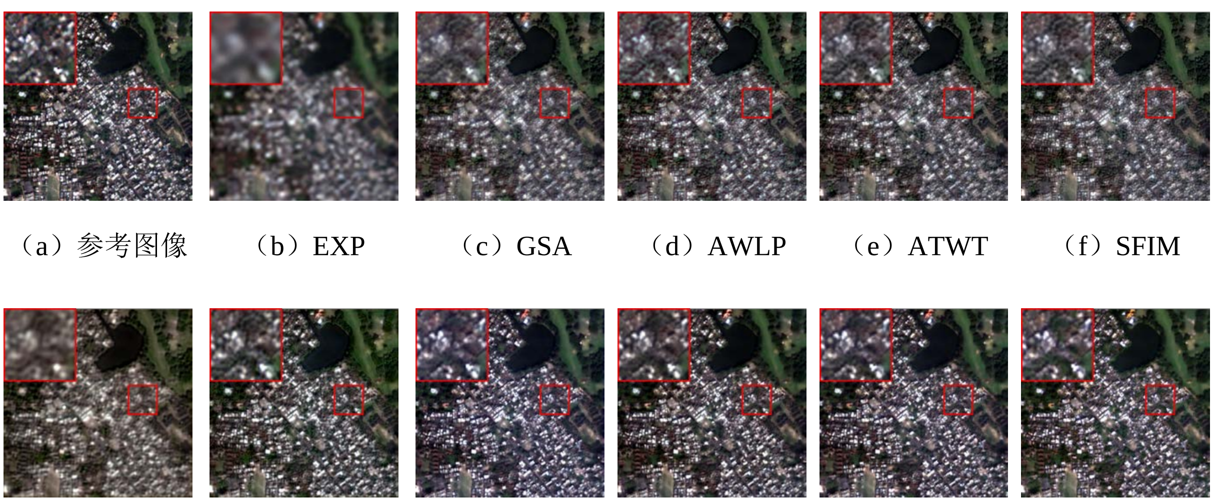

（a）参考图像　（b）EXP　（c）GSA　（d）AWLP　（e）ATWT　（f）SFIM

（g）PNN　（h）MSDCNN　（i）MUCNN　（j）SRPPNN　（k）GPPNN　（l）本文方法

图 5　在降分辨率的 QB 数据集上的定性比较，左上角的红框是图像中红框对应区域的放大图

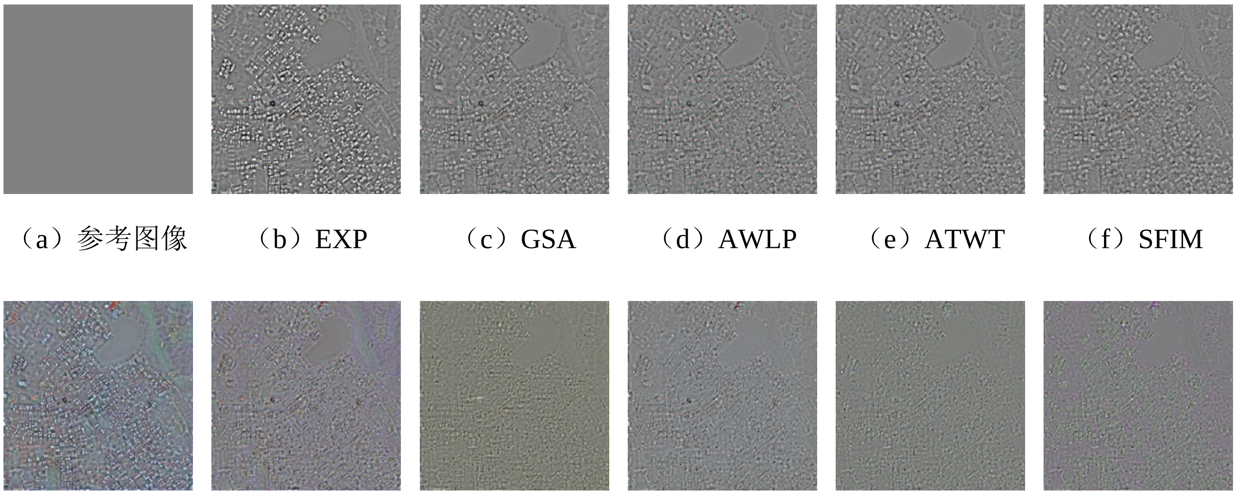

（a）参考图像　（b）EXP　（c）GSA　（d）AWLP　（e）ATWT　（f）SFIM

（g）PNN　（h）MSDCNN　（i）MUCNN　（j）SRPPNN　（k）GPPNN　（l）本文方法

图 6　图 5 中的结果所对应的误差图。为了更好的可视化，所有的误差图都通过在每个像素上加 0.5 来重新缩放显示

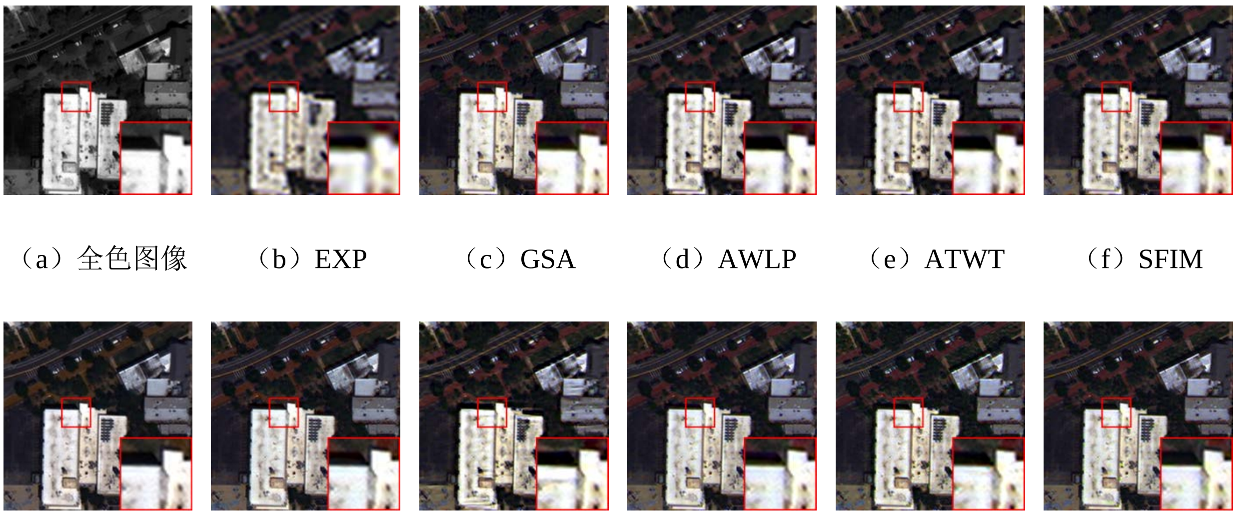

（a）全色图像　（b）EXP　（c）GSA　（d）AWLP　（e）ATWT　（f）SFIM

（g）PNN　（h）MSDCNN　（i）MUCNN　（j）SRPPNN　（k）GPPNN　（l）本文方法

图 7 在全分辨率的 WV2 数据集上的定性比较，右下角的红框是图像中红框对应区域的放大图

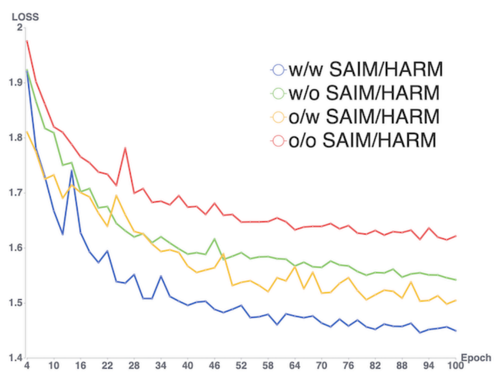

（a）训练过程中的 LOSS 曲线

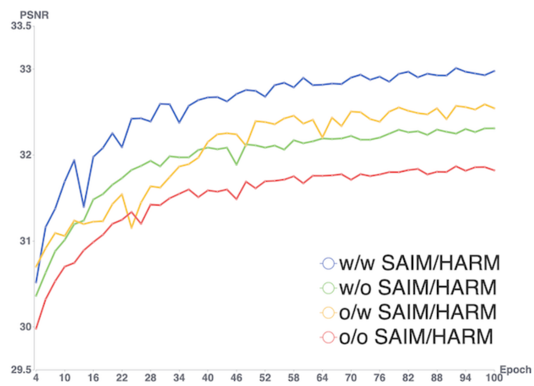

（b）训练过程中的 PSNR 曲线

图 8 有效性消融实验中的 PSNR 和 LOSS 曲线

最佳。相比之下，训练过程中 II 和 III 的 PSNR 和 LOSS 曲线表现较差。同时，III 表现出比 II 更好的性能，也就是说，SAIM 对模型的影响比 HARM 小。IV 的表现最差，说明提出的 SAIM 和 HARM 是有效的模块。

5　结论

本文在 Retinex 模型的指导下设计了一种基于注意力的全色锐化方法 AIRNet。具体而言，AIRNet 使用基于空间注意力的照度模块（SAIM）将 PAN 转换为 HRMS 相应的照度分量，使用基于混合注意力的反射模块（HARM）将 LRMS 转换为 HRMS 相应的反射分量，最终根据 Retinex 模型将照度分量和反射分量相乘得到待求的 HRMS。与其他先进方法的对比实验结果表明，提出的方法在定性和定量比较中更有优势。未来工作将集中在如何使用 Retinex 模型建立观测图像与目标图像的关系并提出更具有解释性的变分模型，与此同时，也将探索使用无监督策略来增加全色锐化模型的泛化能力，并将此框架应用到更广泛的遥感图像融合应用中，提高不同源遥感图像质量，为后续的地物识别、植被监测等任务做贡献。

参考文献

[1] Aiazzi B, Alparone L, Baronti S, et al. MTF-tailored multiscale fusion of high-resolution MS and Pan imagery[J]. Photogrammetric Engineering & Remote Sensing, 2006, 72(5): 591-596.

[2] Aiazzi B, Baronti S, Selva M. Improving component substitution pansharpening through multivariate regression of MS $+ $ Pan data[J]. IEEE Transactions on Geoscience and Remote Sensing, 2007, 45(10): 3230-3239.

[3] Alparone L, Aiazzi B, Baronti S, et al. Multispectral and panchromatic data fusion assessment without reference[J]. Photogrammetric Engineering & Remote Sensing, 2008, 74(2): 193-200.

[4] Alparone L, Wald L, Chanussot J, et al. Comparison of pansharpening algorithms: Outcome of the 2006 GRS-S data-fusion contest[J]. IEEE Transactions on Geoscience and Remote Sensing, 2007, 45(10): 3012-3021.

[5] 肖亮, 刘鹏飞, 李恒. 多源空—谱遥感图像融合方法进展与挑战[J]. 2020.
Xiao L, Liu P F, Li H. Progress and challenges in the fusion of multisource spatial-spectral remote sensing images[J]. Journal of Image and Graphics, 2020, 25(5): 851-863.

[6] Cai J, Huang B. Super-resolution-guided progressive pansharpening based on a deep convolutional neural network[J]. IEEE Transactions on Geoscience and Remote Sensing, 2020, 59(6): 5206-5220.

[7] Cao X, Yao J, Xu Z, et al. Hyperspectral image classification with convolutional neural network and active learning[J]. IEEE Transactions on Geoscience and Remote Sensing, 2020, 58(7): 4604-4616.

[8] Dong W, Xiao S, Li Y, et al. Hyperspectral pansharpening based on intrinsic image decomposition and weighted least squares filter[J]. Remote Sensing, 2018, 10(3): 445.

[9] Du P, Liu S, Xia J, et al. Information fusion techniques for change detection from multi-temporal remote sensing images[J]. Information Fusion, 2013, 14(1): 19-27.

[10] Fang F, Li F, Shen C, et al. A variational approach for pan-sharpening[J]. IEEE Transactions on Image Processing, 2013, 22(7): 2822-2834.

[11] Hu J, Hu P, Kang X, et al. Pan-sharpening via multiscale dynamic convolutional neural network[J]. IEEE Transactions on Geoscience and Remote Sensing, 2020, 59(3): 2231-2244.

[12] 杨勇, 苏昭, 黄淑英, 等. 基于深度学习的像素级全色图像锐化研究综述[J]. Journal of Remote Sensing, 2022, 26(12).
Yong Y. Deep-learning approaches for pixel-level pansharpening[J]. National Remote Sensing Bulletin, 2023, 26(12): 2411-2432.

[13] Jin X, Gu Y, Liu T. Intrinsic image recovery from remote sensing hyperspectral images[J]. IEEE Transactions on Geoscience and Remote Sensing, 2018, 57(1): 224-238.

[14] Krizhevsky A, Sutskever I, Hinton G E. Imagenet classification with deep convolutional neural networks[J]. Advances in neural information processing systems, 2012, 25.

[15] Land E H, McCann J J. Lightness and retinex theory[J]. Josa, 1971, 61(1): 1-11.

[16] Larochelle H, Hinton G E. Learning to combine foveal glimpses with a third-order Boltzmann machine[J]. Advances in neural information processing systems, 2010, 23.

[17] Ma J, Yu W, Chen C, et al. Pan-GAN: An unsupervised pan-sharpening method for remote sensing image fusion[J]. Information Fusion, 2020, 62: 110-120.

[18] Masi G, Cozzolino D, Verdoliva L, et al. Pansharpening by convolutional neural networks[J]. Remote Sensing, 2016, 8(7): 594.

[19] Otazu X, González-Audícana M, Fors O, et al. Introduction of sensor spectral response into image fusion methods. Application to wavelet-based methods[J]. IEEE Transactions on Geoscience and Remote Sensing, 2005, 43(10): 2376-2385.

[20] Schowengerdt R A. Remote sensing: models and methods for image processing[M]. elsevier, 2006.

[21] Shah V P, Younan N H, King R L. An efficient pan-sharpening method via a combined adaptive PCA approach and contourlets[J]. IEEE transactions on geoscience and remote sensing, 2008, 46(5): 1323-1335.

[22] Song X, Huang J, Cao J, et al. Multi-scale joint network based on Retinex theory for low-light enhancement[J]. Signal, Image and Video Processing, 2021: 1-8.

[23] Vivone G, Alparone L, Chanussot J, et al. A critical comparison among pansharpening algorithms[J]. IEEE Transactions on Geoscience and Remote Sensing, 2014, 53(5): 2565-2586.

[24] Vivone G, Restaino R, Dalla Mura M, et al. Contrast and error-based fusion schemes for multispectral image pansharpening[J]. IEEE Geoscience and Remote Sensing Letters, 2013, 11(5): 930-934.

[25] Wald L, Ranchin T, Mangolini M. Fusion of satellite images of different spatial resolutions: Assessing the quality of resulting images[J]. Photogrammetric engineering and remote sensing, 1997, 63(6): 691-699.

[26] Wang F, Jiang M, Qian C, et al. Residual attention network for image classification[C]//Proceedings of the IEEE conference on computer vision and pattern recognition. 2017: 3156-3164.

[27] Wang T, Fang F, Li F, et al. High-quality Bayesian pansharpening[J]. IEEE Transactions on Image Processing, 2018, 28(1): 227-239.

[28] Wang Y, Deng L J, Zhang T J, et al. SSconv: Explicit spectral-to-spatial convolution for pansharpening[C]//Proceedings of the

29th ACM International Conference on Multimedia. 2021: 4472-4480.
[29] Woo S, Park J, Lee J Y, et al. Cbam: Convolutional block attention module[C]//Proceedings of the European conference on computer vision (ECCV). 2018: 3-19.
[30] Xu J, Hou Y, Ren D, et al. Star: A structure and texture aware retinex model[J]. IEEE Transactions on Image Processing, 2020, 29: 5022-5037.
[31] Xu S, Zhang J, Zhao Z, et al. Deep gradient projection networks for pan-sharpening[C]//Proceedings of the IEEE/CVF Conference on Computer Vision and Pattern Recognition. 2021: 1366-1375.
[32] Yuhas R H, Goetz A F H, Boardman J W. Discrimination among semi-arid landscape endmembers using the spectral angle mapper (SAM) algorithm[C]//JPL, Summaries of the Third Annual JPL Airborne Geoscience Workshop. Volume 1: AVIRIS Workshop. 1992.
[33] Zhou J, Civco D L, Silander J A. A wavelet transform method to merge Landsat TM and SPOT panchromatic data[J]. International journal of remote sensing, 1998, 19(4): 743-757.

[作者简介]

叶永旭（2000− ），男，硕士研究生，研究方向为遥感图像全色锐化。

汪婷婷（1992− ），女，博士，博后，主要研究方向为遥感图像处理和自然图像恢复。

方发明（1987− ），男，博士，教授，主要研究方向为基于深度学习和变分法的图像处理。

张桂戌（1970− ），男，博士，教授，主要研究方向为图像处理与模式识别。

基于上行 NOMA 的卫星通信系统半免授权传输性能分析

郭焱，林敏，谈苗苗，孔槐聪，程铭

（南京邮电大学通信与信息工程学院，江苏，南京，210003）

摘　要：本文考虑卫星通信系统中的多用户接入场景，其中卫星点波束覆盖范围内的一个地球站和多个移动终端共同接入卫星网络。首先，根据卫星通信的特点，利用用户的统计信道状态信息，提出了基于上行非正交多址（NOMA）的半免授权（SGF）传输方案，以提高系统频谱效率，同时减少用户接入的信令开销。其次，假设卫星链路服从阴影莱斯分布，在移动终端采用分布式争用策略的条件下，推导出地球站和移动终端的中断概率以及系统吞吐量的闭合表达式。最后，计算机仿真验证了理论分析的正确性和所提方案相比免授权 NOMA 和正交多址接入方案的优越性，同时定量分析了用户数、目标数据速率等典型参数对系统性能的影响。

关键词：卫星通信系统，统计信道状态信息，非正交多址接入，半免授权传输，阴影莱斯衰落

Performance Analysis of Semi-Grant-Free Transmission in Uplink NOMA-Based Satellite Communication Systems

GUO Yan, LIN Min, TAN Miaomiao, KONG Huaicong, CHENG Ming

(School of Communications and Information Engineering, Nanjing University of Posts and Telecommunications, Nanjing 210003, China)

Abstract: This paper investigates a multi-user access scenario in satellite communication systems, where one earth station together with multiple mobile terminals covered by satellite spot beam has access to the satellite. According to the feature of satellite communication and the available statistical channel state information, a NOMA-based semi-grant-free transmission scheme is first proposed to improve spectrum efficiency and reduce signaling overhead. Next, by assuming that the satellite channels undergo shadowed-Rician distribution, the closed-form outage probability expressions of earth station and mobile terminals and system throughput expression of the considered system are derived under the condition that the mobile terminals use distributed contention strategy. Finally, simulation results validate the effectiveness of the theoretical analysis and quantitatively analyze the benefits of the proposed scheme over grant-free NOMA and orthogonal multiple access scheme. Besides, the effect of typical parameters on the system performance such as user number and target data rate is also revealed.

Key words: satellite communication systems, statistical channel state information, non-orthogonal multiple access, semi-grant-free transmission, shadowed-Rician fading

1　引言

卫星通信具有覆盖范围广、不受地理条件限制等优点，在偏远地区通信、应急救援等领域得到了广泛应用。将卫星通信网与地面无线网相互融合，共同构建覆盖全球的空天地一体化网络成为大势所趋，并将在第六代移动通信系统（the 6-th generation wireless systems, 6G）中将扮演不可或缺的角色[1]-[4]。然而，随着业务数量及种类的增多，卫星与地面用户之间存在大传输时延和庞大的控制信令开销的问题日益凸显，使得用户的通信质量无法得到保证，同时也会增加卫星接收机的功耗。因此，如何以低时延和低信令开销应对大规模终端的接入，成为当前卫星通信亟待解决的问题[5]-[6]。在这种情况下，时隙 ALOHA、分集时隙 ALOHA 等随机接入协议能够通过简化接入流程来降低接入时延和信令开销，因而在卫星通信中得到研究[7]-[8]。然而这些随机接入方案的性能会受到碰撞的影响，如何解决卫星系统大规模接入的碰撞问题仍是一个难题。非正交多址接入（non-orthogonal multiple access, NOMA）技术以其频谱利用率高的独特优势，已经成为极具发展前景的新型多址技术，将 NOMA 应用于卫星上行接入场景中，

通过允许多个用户共享同一资源块，有望减少碰撞[9]。国内外学者已经围绕中断概率、遍历容量方面来证实理论分析的可行性，例如，文献[10]针对一个采用 NOMA 的卫星上行接入场景，分析了采用连续干扰消除（successive interference cancellation, SIC）技术和联合解码（joint decoding, JD）技术的中断概率；文献[11]进一步考虑了地面用户的位置分布，并分析了星地传输系统的遍历容量；文献[12]将速率分割技术与上行 NOMA 相结合，进一步提高了卫星通信系统的吞吐量。

然而在有限的频谱资源前提下，随着连接需求的激增，更多的用户将接入同一时频资源块，卫星执行 SIC 的复杂度大大提升，从而造成性能的衰减[13]。为了进一步提高频谱效率，文献[14]提出了一种半免授权（semi-grant-free, SGF）传输方案。该方案针对地面网络中的多用户上行接入场景，其中数据速率需求高的授权（grant-based, GB）用户和数据突发、数据量小的免授权（grant-free, GF）用户共存，考虑到 GF 用户的传输时间短，为其分配单独的资源块将带来资源的浪费，因此 GF 用户与 GB 用户共享频谱资源。该方案包含三个步骤：（1）GB 用户采用授权协议与基站建立连接后，将自己的发射功率和信道状态信息发送给基站；（2）基站根据 GB 用户的信息，广播一个接入阈值给所有的 GF 用户。（3）满足阈值条件的 GF 用户将利用 NOMA 技术接入 GB 用户的资源块中，从而提升了频谱资源的利用率。之后，SGF 方案在地面网络中的应用得到了一系列的研究。文献[15]在文献[14]提出的 SGF 方案的基础上引入了基于接入阈值的混合 SIC，从而保证了 GB 用户的服务质量需求（quality-of-service, QoS），并推导了系统中断概率的闭合表达式以及高信噪比条件下的渐进表达式；文献[16]进一步考虑用户位置分布，在 SGF 方案中提出了一种动态接入阈值，为 GF 用户提供更灵活的接入，并从系统吞吐量的角度分析了方案的优越性；文献[17]将功率控制引入 SGF 方案，通过 GB 用户对自身的发射功率进行自适应调控，在保证可靠连接的前提下降低了系统功耗，并分析了系统的中断概率和渐进性能。

尽管上述研究都证明了 SGF 方案在提升通信系统性能中的优势，但它们还存在以下问题：一是现有的文献仅研究了地面网络中的 SGF 方案，而在卫星通信领域中的 SGF 方案设计仍处于起步阶段；二是上述文献都需要获取 GB 用户的瞬时信道状态信息（channel state information, CSI），不仅带来大量的功耗和信令开销，而且在实际的卫星通信网络中获取瞬时 CSI 是不实际的；三是大多数文献在信道建模时仅考虑了小尺度衰落，忽略了路径损耗、天线增益等实际参数的影响。在这种情况下，本文研究了一个卫星通信系统的多用户接入场景，其中静止轨道卫星（Geostationary satellite, GEO）点波束覆盖范围内的一个地球站和多个移动终端共同接入卫星网络，并将具有更高数据速率需求的地球站视为 GB 用户，将数据量小、数据突发的移动终端视为 GF 用户。首先，利用用户的统计 CSI 提出了一种基于上行 NOMA 的 SGF 传输方案，以实现在保证 GB 用户 QoS 的前提下允许 GF 用户接入同一时频资源，从而在提高频谱效率的同时减少信令开销。其次，假设卫星信道服从阴影莱斯衰落，并在 GF 用户采用分布式争用策略的条件下，推导了中断概率和系统吞吐量的闭合表达式。最后，仿真结果验证了理论分析的正确性和所提方案相比免授权 NOMA 方案和正交多址接入（orthogonal multiple access, OMA）的优越性，并分析了实际参数对系统性能的影响。

2　系统模型

如图 1 所示，考虑卫星通信系统的多用户接入场景，其中 GEO 卫星点波束覆盖范围内，一个固定的地球站和 M 个移动终端采用基于上行 NOMA 的 SGF 传输方案接入卫星，以获得更高的频谱效率和接入能力。其中，作为 GB 用户的地球站配备高增益的抛物面天线，具有更高的传输优先级；作为 GF 用户的移动终端配备单天线，具有数据量小、数据突发、需要即时传输的特点。为了便于理解，接下来将分别介绍信道模型和信号模型。

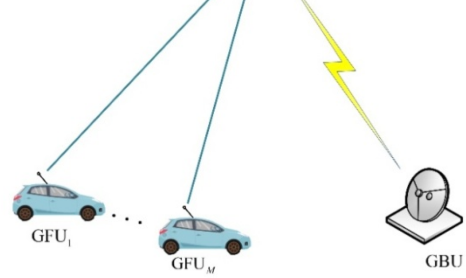

图 1　多用户卫星通信系统模型图

2.1　信道模型

在对卫星信道进行建模时，需要考虑无线信道的衰落特性，以及星载天线增益、卫星链路损耗等实际参数的影响[18]，因此，信道模型可写作

$$h_v = \ell_v \tilde{h}_v \tag{1}$$

其中，角标 $v \in \{k,b\}$ 表示 GB 用户和第 k 个 GF 用户；$\tilde{h}_v$ 表示卫星链路的小尺度衰落，ℓ_v 表示卫星链路的信道系数，其表达式为：

$$\ell_v = \frac{\sqrt{G_v G_s}\lambda}{4\pi d_v} \tag{2}$$

其中，λ 表示载波的波长；d_v 表示卫星与地面用户之间的距离；G_s 表示星载天线增益，通常建模为[19]：

$$G_s = G_s^{\max}\left(\frac{J_1(q_s)}{2q_s} + 36\frac{J_3(q_s)}{q_s^{\ 3}}\right)^2 \tag{3}$$

其中，$G_s^{\max}$ 表示最大卫星天线增益；$J_n(x)$ 是第一类 n 阶贝塞尔函数；$q_s = 2.07123\sin\theta_s / \sin\theta_{\text{3dB}}$，$\theta_s$ 表示波束中轴线和地面节点之间的夹角，θ_{3dB} 表示天线增益衰减 3dB 的角度。式（2）中，G_v 表示用户的发射天线增益，由于作为 GB 用户的地球站配备抛物面天线，其天线增益 G_b 可表示为[20]：

$$G_b = \begin{cases} G_b^{\max} - 2.5\times 10^{-3}\left(D_b\bar{\theta}_b / \lambda\right)^2, 0 < \bar{\theta}_b < \hat{\theta} \\ 2 + 15\log(D/\lambda), \hat{\theta} \leqslant \bar{\theta}_b < \tilde{\theta} \\ 32 - 25\log\bar{\theta}, \tilde{\theta} \leqslant \bar{\theta}_b < 48^\circ \\ -10, 48^\circ \leqslant \bar{\theta}_b \leqslant 180^\circ \end{cases} \tag{4}$$

其中 $G_b^{\max}$ 表示天线最大增益，D_b 表示天线口径，$\bar{\theta}_b$ 表示离轴角，$\hat{\theta}$ 和 $\tilde{\theta}$ 的表达式分别为 $\hat{\theta} = \frac{20}{D}\sqrt{G_v^{\max} - \left(2 + 15\log\frac{D}{\lambda}\right)}$，$\tilde{\theta} = 15.82\left(\frac{D_v}{\lambda}\right)^{-0.6}$。

此外，式（1）中 $\tilde{h}_v$ 表示卫星链路的小尺度衰落，通常服从阴影莱斯分布[11]，即 $\left|\tilde{h}_v\right| \sim SR(m_v, \sigma_v, \Omega_v)$，其中 Ω_v 为直达径分量的平均功率；$2\sigma_v$ 为多径分量的平均功率；$m_v \in \mathrm{N}^+$ 为 Nakagami-m 分布的衰落参数。

2.2　信号模型

如图 1 所示，在第 k 个时隙内，GB 用户和第 k 个 GF 用户同时向卫星发送信号 $x_v(t), v \in \{b,k\}$，卫星接收到的信号表示为

$$y(t) = \sqrt{P_b}h_b x_b(t) + \sqrt{P_k}h_k x_k(t) + n(t) \tag{5}$$

式中，P_b 和 P_k 分别表示 GB 用户和第 k 个 GF 用户的发射功率，$n_k(t)$ 表示均值为 0，方差为 σ^2 的加性高斯白噪声（additive white gaussian noise, AWGN）。

由于 GB 用户是固定的地球站，具有更高的传输优先级，因此相比 GF 用户而言，GB 用户具有更大的发射功率和天线增益，即满足 $P_b > P_k$，$|h_b|^2 > |h_k|^2$。根据 NOMA 的解码策略，首先对 GB 用户的信号进行解码，此时第 k 个 GF 用户的信号将被视为干扰。因此卫星解码 GB 用户的信号 $x_b(t)$ 的可达速率表示为：

$$R_b = \log_2\left(1 + \frac{P_b|h_b|^2}{P_k|h_k|^2 + \sigma^2}\right) \tag{6}$$

其次采用 SIC 技术将 GB 用户的信号 $x_b(t)$ 从叠加信号中减去，从而第 k 个 GF 用户的的可达速率表示为：

$$R_k = \log_2\left(1 + \frac{P_k|h_k|^2}{\sigma^2}\right) \tag{7}$$

3　半免授权传输方案

本节针对如图 1 所示卫星通信系统中的上行多用户接入场景，提出了一种基于上行 NOMA 的半免授权传输方案。该方案能够在满足 GB 用户 QoS 的前提下，为 GF 用户提供通信服务。首先，GB 用户与卫星建立连接后，卫星获取 GB 用户的统计 CSI、发射功率和发射天线增益，随后，为了筛选出可以接入的 GF 用户，卫星向所有的 GF 用户广播一个接入阈值 τ，计算方法如下：

为了满足 GB 用户的 QoS，在卫星已知 GB 用户统计 CSI 的情况下，GB 用户的数据速率应满足如下的不等式：

$$\log_2\left(1 + \frac{E\left[P_b|h_b|^2\right]}{\tau^* + \sigma^2}\right) \geq R_b^{th} \tag{8}$$

其中，R_b^{th} 表示 GB 用户的目标数据速率，τ^* 表示来自 GF 用户的干扰。

由式（8）可以得到，来自 GF 用户的干扰应该满足 $\tau^* \leq \tau$，其中 τ 即为所求的接入阈值，其表达式为：

$$\tau = \max\left\{0, \frac{P_b \ell_b^2 \left(\Omega_b + 2\sigma_b\right)}{\varepsilon_b} - \sigma^2\right\} \tag{9}$$

其中 $\varepsilon_b = 2^{R_b^{th}} - 1$。

GF 用户在收到接入阈值后，将自己的信号强度与接入阈值比较，如果满足 $P_k \left|h_k^2\right| \le \tau$，该用户可以在不影响 GB 用户 QoS 的前提下接入 GB 用户的信道。用 S 表示允许接入的 GF 用户的集合，M 个 GF 用户共有 2^{M-1} 个子集，因此集合 S 的样本空间表示为 $\left\{\varnothing, S_1, S_2, ..., S_i, ..., S_{2^M-1}\right\}$，其中 $\varnothing$ 为空集，表示没有满足条件的 GF 用户，此时 GB 用户将独占信道资源传输数据。子集的大小为 $\left|S_i\right| = K$。因此可以定义：

$$\begin{cases} S = \varnothing, P_k \left|h_k^2\right| > \tau, k \in \{1, 2, ..., K\} \\ S = S_i, P_k \left|h_k^2\right| \le \tau, k \in S_i \end{cases} \tag{10}$$

其中，$S = S_i$ 表示集合 S 非空，此时在 GB 用户的传输周期内，每个时隙内 GF 用户将采用分布式争用的策略接入卫星，争用策略表示如下：

为了避免 GF 用户碰撞，每个用户在争用开始前需要各自等待一个退避时间，再向卫星发送信号，卫星将成功接收最先到达的用户信号。GF 用户的退避时间与自身的信号强度成反比，即在每个时隙内，信号强度最强的 GF 用户能够争用成功并接入卫星，接入的用户可以表示为 $k = \arg\max\limits_{k^* \in S_i}\left(P_{k^*}\left|h_{k^*}\right|^2\right)$。

需要指出的是，与文献[15]-[16]中基于瞬时 CSI 的 SGF 传输方案不同，本文利用 GB 用户的统计 CSI 计算接入阈值 τ，因此由式（9）可知接入阈值在 GB 用户的数据传输周期内是常数，避免了频繁更新阈值带来的信令开销，从而更加适用于卫星通信场景。接下来，将进一步对系统的中断性能和吞吐量进行分析。

4　系统性能分析

中断概率和吞吐量是衡量无线通信系统的重要指标，中断概率通常定义为用户信号的可达数据速率小于目标数据速率的概率，系统的吞吐量定义为系统无中断解码条件下的可达数据速率。因此，GB 用户的中断发生在以下两种情况：（1）当 S 为空集时，GB 用户独自传输数据未达到目标数据速率；（2）当 S 非空集时，GB 用户在受到 GF 用户干扰的情况下传输数据未达到目标数据速率。数学表示为：

$$\begin{aligned} P_{out}^b = & 1 - \Pr\{S = \phi\}\underbrace{\Pr\left\{\log_2\left(1+\gamma_b\right) \ge R_b^{th}\right\}}_{\mathrm{I}_1} - \\ & \sum_{i=1}^{2^M-1}\Pr\{S = S_i\}\underbrace{\sum_{k^* \in S_i}\Pr\left\{k = k^* \left| S = S_i\right.\right\}\Pr\left\{\log_2\left(1+\frac{\gamma_b}{\gamma_k+1}\right) \ge R_b^{th}\left| k = k^*\right.\right\}}_{\mathrm{I}_2} \end{aligned} \tag{11}$$

其中 $\gamma_b = \bar{\gamma}_b\left|h_b\right|^2 = \frac{P_b \ell_b^2}{\sigma^2}\left|\tilde{h}_b\right|^2$，$\gamma_k = \bar{\gamma}_k\left|h_k\right|^2 = \frac{P_k \ell_k^2}{\sigma^2}\left|\tilde{h}_k\right|^2$。

类似地，第 k 个 GF 用户的中断发生在以下两种情况：（1）S 为非空集情况下，GB 用户传输数据未达到目标数据速率；（2）S 为非空集情况下，GB 用户无中断传输，但 GF 用户未达到目标数据速率。数学表示为：

$$\begin{aligned} P_{out}^k = & 1 - \sum_{i=1}^{2^M-1}\Pr\{S = S_i\} \\ & \underbrace{\sum_{k^* \in S_i}\Pr\left\{k = k^*\left| S = S_i\right.\right\}\Pr\left\{\log_2\left(1+\frac{\gamma_b}{\gamma_k+1}\right) \ge R_b^{th}, \log_2\left(1+\gamma_k\right) \ge R_f^{th}\left| k = k^*\right.\right\}}_{\mathrm{I}_3} \end{aligned} \tag{12}$$

接下来，为了计算中断概率的闭合表达式，需要得到 γ_b 和 γ_k 的概率密度函数（Probability Density Function, PDF）和累积分布函数（Cumulative distribution function, CDF）。由下式给出[18]：

$$f_{\gamma_v}(x) = \alpha_v \sum_{i=0}^{m_v-1}\frac{\left(1-m_v\right)_i\left(-\delta_v\right)^i}{\bar{\gamma}_v^{i+1}\left(i!\right)^2}\exp\left(-\frac{l_v x}{\bar{\gamma}_v}\right)x^i \tag{13}$$

$$\begin{aligned} F_{\gamma_v}(x) = & \int_0^x f_{\gamma_v}(x)dx = \\ & \alpha_v \sum_{i=0}^{m_v-1}\frac{\left(1-m_v\right)_i\left(-\delta_v\right)^i}{l_v^{i+1} i!}\left[1 - \exp\left(-\frac{l_v x}{\bar{\gamma}_v}\right)\sum_{j=0}^{i}\frac{1}{j!}\frac{x^j l_v^j}{\bar{\gamma}_v^j}\right] \end{aligned} \tag{14}$$

其中，$v \in \{b, k\}$，$\alpha_v = \frac{1}{2\sigma_v}\left(\frac{2\sigma_v \mu_v}{2\sigma_v \mu_v + \Omega_v}\right)^{\mu_v}$，

$\delta_v = \dfrac{\Omega_v}{2\sigma_v\left(2\sigma_v\mu_v + \Omega_v\right)}$，$l_v = \dfrac{1}{2\sigma_v} - \delta_v$，$m_v \in \mathbb{N}^+$

利用γ_k的 CDF，可以计算式（11）、（12）中用户集S的各种情况出现的概率，则$\Pr\{S = S_i\}$计算为：

$$\Pr\{S = S_i\} = \prod_{q\in S_i}\Pr\left\{\gamma_q \le \frac{\tau}{\sigma^2}\right\}\prod_{p\notin S_i}\Pr\left\{\gamma_p > \frac{\tau}{\sigma^2}\right\} = \\ \sum_{i=1}^{2^M-1}\prod_{q\in S_i}\left\{\sum_{n_1=0}^{m_q-1}\Phi_{m_q,n_3,l_q}\left[1-\Lambda\left(\frac{l_q\tau}{\bar{\gamma}_q\sigma^2},n_1\right)\right]\right\} \\ \prod_{p\notin S_i}\left\{\sum_{n_2=0}^{m_p-1}\Phi_{m_p,n_4,l_p}\Lambda\left(\frac{l_q\tau}{\bar{\gamma}_q\sigma^2},n_2\right)\right\} \tag{15}$$

其　中　$\Phi_{m_p,n,l_p} = \alpha_p\dfrac{\left(1-m_p\right)_n\left(-\delta_p\right)^n}{l_p^{n+1}n!}$　，$\Lambda(a,n) = \exp(-a)\sum_{t=0}^{n}\dfrac{1}{t!}(a)^t$，令$S_i$为空集即可得到$\Pr\{S=\phi\}$的表达式。

根据式（14），式（11）中I_1可以计算为：

$$\mathrm{I}_1 = 1 - F_{\gamma_b}\left(\varepsilon_b\right) = \sum_{n=0}^{m_b-1}\Phi_{m_b,n,l_b}\Lambda\left(\frac{l_b\varepsilon_b}{\bar{\gamma}_b},n\right) \tag{16}$$

在 GF 用户采用分布式争用策略的情况下，I_2可以表示为：

$$\mathrm{I}_2 = \Pr\left\{k = \arg\max_{k^*\in S_i}\left(\gamma_{k^*}\right),\frac{\gamma_b}{\gamma_k+1}\ge\varepsilon_b, 0\le\gamma_k<\frac{\tau}{\sigma^2}\right\} = \\ \int_0^{\bar{\gamma}_1}\prod_{j=1}^{|S_i|}F_{\gamma_j}\left(\frac{y}{\varepsilon_b}-1\right)f_{\gamma_b}(y)dy + \\ \int_{\bar{\gamma}_1}^{\infty}\prod_{j=1}^{|S_i|}F_{\gamma_j}\left(\frac{\tau}{\sigma^2}\right)f_{\gamma_b}(y)dy \tag{17}$$

其中$\bar{\gamma}_1 = \varepsilon_b\left(\dfrac{\tau}{\sigma^2}+1\right)$。将式（13），（14），代入式（17），并利用牛顿二项展开公式，可以将式（17）写为：

$$\mathrm{I}_2 = \sum_{n_3=0}^{m_b-1}\frac{\Phi_{m_b,n_3,\bar{\gamma}_b}}{n_3!}\left\{\Xi_1\int_0^{\bar{\gamma}_1}y^{\sum_{j=1}^{|S_i|}u_j+n_b}\right. \\ \exp\left(-\left(\sum_{j=1}^{|S_i|}\frac{n_j\eta_{k_j}}{\bar{\gamma}_j\varepsilon_b}+\frac{l_b}{\bar{\gamma}_b}\right)y\right)dy + \\ \left.\Xi_2\left(\frac{\tau}{\sigma^2}\right)\int_{\bar{\gamma}_1}^{\infty}y^{n_b}\exp\left(-\frac{l_b}{\bar{\gamma}_b}y\right)dy\right\} \tag{18}$$

其中，

$$\Xi_1 = \sum_{k_1=0}^{m_1}\sum_{n_1-0}^{k_1}\sum_{u_1=0}^{n_1\eta_{k_1}}\cdots\sum_{k_{|S_i|}}^{m_{|S_i|}}\sum_{n_{|S_i|}}^{k_{|S_i|}}\sum_{u_{|S_i|}}^{n_{|S_i|}\eta_{k_{|S_i|}}}\left[\prod_{j=1}^{|S_i|}\psi_{k_j}\left(\frac{l_j^{\,n_j}}{n_j!\bar{\gamma}_j^{\,n_j}}\right)^{\eta_{k_j}}\right. \\ \left.\exp\left(\frac{\eta_{k_j}l_j}{\bar{\gamma}_j}\right)\binom{n_j\eta_{k_j}}{u_j}\frac{(-1)^{n_j\eta_{k_j}-u_j}}{\varepsilon_b^{u_j}}\right]$$

$$\Xi_2(a) = \prod_{j=1}^{|S_i|}\left[\sum_{k_j}^{m_j}\sum_{n_j}^{k_j}\psi_{k_j}\left(\frac{l_j^{\,n_j}a^{n_j}}{n_j!\bar{\gamma}_j^{\,n_j}}\right)^{\eta_{k_j}}\exp\left(-\frac{\eta_{k_j}l_j}{\bar{\gamma}_j}a\right)\right]$$

利用[21]求解式（18）中的积分，可以得到I_2的闭合表达式为：

$$\mathrm{I}_2 = \sum_{n_3=0}^{m_b-1}\frac{\Phi_{m_b,n_3,\bar{\gamma}_b}}{n_3!}\left\{\Xi_1\Theta_1\left(\bar{\gamma}_1,\sum_{j=1}^{|S_i|}u_j+n_b,\sum_{j=1}^{|S_i|}\frac{n_j\eta_{k_j}}{\bar{\gamma}_j\varepsilon_b}+\frac{l_b}{\bar{\gamma}_b}\right)+\right. \\ \left.\Xi_2\left(\frac{\tau}{\sigma^2}\right)\Theta_2\left(\bar{\gamma}_1,n_b,\frac{l_b}{\bar{\gamma}_b}\right)\right\} \tag{19}$$

其　中　，　$\Theta_1(u,n,\mu) = \mu^{-n-1}\gamma(n+1,\mu u)$　，$\Theta_2(u,n,\mu) = \mu^{-n-1}\Gamma(n+1,\mu u)$。$\gamma(\bullet,\bullet)$表示不完全 Gamma 函数，$\Gamma(\bullet,\bullet)$表示上不完全 Gamma 函数。

进一步，将式（16），式（19）带入式（11），可以得到 GB 用户中断概率的闭合表达式为：

$$P_{out}^{b} = 1 - \prod_{p=1}^{M}\left\{\sum_{n_1=0}^{m_p-1}\Phi_{m_p,n_1,l_p}\Lambda\left(\frac{l_p\tau}{\bar{\gamma}_p\sigma^2},n_1\right)\right\}\bullet\mathrm{I}_1 - \\ \sum_{i=1}^{2^M-1}\prod_{q\in S_i}\left\{\sum_{n_3=0}^{m_q-1}\Phi_{m_q,n_3,l_q}\left[1-\Lambda\left(\frac{l_q\tau}{\bar{\gamma}_q\sigma^2},n_3\right)\right]\right\} \\ \prod_{p\notin S_i}\left\{\sum_{n_4=0}^{m_p-1}\Phi_{m_p,n_4,l_p}\Lambda\left(\frac{l_q\tau}{\bar{\gamma}_q\sigma^2},n_4\right)\right\}\bullet\mathrm{I}_2 \tag{20}$$

接着推导 GF 用户的中断概率。类似地，式（12）中I_3可以表示为：

$$\mathrm{I}_3 = \Pr\left\{k = \arg\max_{k^*\in S_i}\left(\gamma_{k^*}\right),\frac{\gamma_b}{\gamma_k+1}\ge\varepsilon_b,\gamma_k\ge\varepsilon_k\right\} = \\ \int_{\bar{\gamma}_2}^{\bar{\gamma}_1}\int_{\varepsilon_k}^{\frac{y}{\varepsilon_b}-1}f_{\gamma_k}(x)dxf_{\gamma_b}(y)dy + \int_{\bar{\gamma}_1}^{\infty}\int_{\varepsilon_k}^{\frac{\tau}{\sigma^2}}f_{\gamma_k}(x)dxf_{\gamma_b}(y)dy \tag{21}$$

其中$\bar{\gamma}_2 = \varepsilon_b\left(\varepsilon_k+1\right)$。将式（13）带入式（21）并求解积分，$\mathrm{I}_3$的表达式计算为：

$$\mathrm{I}_3 = \sum_{n_b}^{m_b-1}\frac{\Phi_{m_b,n_b,\bar{\gamma}_b}}{n_b!}\left\{\Xi_1\exp\left(-\left(\sum_{j=1}^{|S_i|}\frac{n_j\eta_{k_j}}{\bar{\gamma}_j\varepsilon_b}+\frac{l_b}{\bar{\gamma}_b}\right)\bar{\gamma}_2\right)\right.$$

$$\sum_{z=0}^{\sum_{j=1}^{|S_i|}u_j+n_b}\binom{\sum_{j=1}^{|S_i|}u_j+n_b}{z}\overline{\gamma}_2^{\sum_{j=1}^{|S_i|}u_j+n_b-z}$$
$$\Theta_1\left(\overline{\gamma}_1-\overline{\gamma}_2,z,\sum_{j=1}^{|S_i|}\frac{n_j\eta_{k_j}}{\overline{\gamma}_j\varepsilon_b}+\frac{l_b}{\overline{\gamma}_b}\right)-$$
$$\Xi_2(\varepsilon_k)\exp\left(-\frac{l_b\overline{\gamma}_2}{\overline{\gamma}_b}\right)\sum_{z=0}^{n_b}\binom{n_b}{z}\overline{\gamma}_2^{n_b-z} \tag{22}$$
$$\Theta_2\left(\overline{\gamma}_1-\overline{\gamma}_2,z,\frac{l_b}{\overline{\gamma}_b}\right)+\sum_{n_b}^{m_b-1}\frac{\Phi_{m_b,n_b,\overline{\gamma}_b}}{n_b!}$$
$$\left.\left[\Xi_2\left(\frac{\tau}{\sigma^2}\right)-\Xi_2(\varepsilon_k)\right]\Theta_2\left(\overline{\gamma}_1,n_b,\frac{l_b}{\overline{\gamma}_b}\right)\right\}$$

最终，第 k 个 GF 用户的中断概率可以计算为：

$$P_{out}^k=1-\sum_{i=1}^{2^M-1}\prod_{q\in S_i}\left\{\sum_{n_1=0}^{m_q-1}\Phi_{m_q,n_1,l_q}\left[1-\Lambda\left(\frac{l_q\tau}{\overline{\gamma}_q\sigma^2},n_1\right)\right]\right\}$$
$$\prod_{p\notin S_i}\left\{\sum_{n_2=0}^{m_p-1}\Phi_{m_p,n_2,l_p}\Lambda\left(\frac{l_q\tau}{\overline{\gamma}_q\sigma^2},n_2\right)\right\}\bullet \mathrm{I}_3 \tag{23}$$

为进一步分析所提方案的优越性，本文接着给出了系统吞吐量的表达式：

$$R_{sum}=\left(1-P_{out}^b\right)R_b^{th}+\frac{1}{K}\sum_{k=1}^{K}\left(1-P_{out}^k\right)R_f^{th} \tag{24}$$

其中 P_{out}^b 和 P_{out}^k 由式（20）和式（23）给出。

5　仿真结果与分析

本节通过计算机仿真验证理论分析的正确性，同时定量分析了目标数据速率、用户数等典型参数对系统性能的影响。此外，为了验证本文所提出的传输方案的优越性，还与免授权 NOMA 方案和 OMA 方案进行了对比。假设 GF 用户的卫星链路经历轻度阴影衰落（Light Shadowing，LS）、平均阴影衰落（Average Shadowing，AS）和重度阴影衰落（Heavy Shadowing，HS），GB 用户的卫星链路经历 AS；假设所有 GF 用户的发射功率相同，即 $P_k=P$。GB 用户和 GF 用户的目标数据速率设置为 $R_b^{th}=2R_k^{th}=2\,\text{bps/Hz}$，相关仿真参数设置见表 1[12]、[15]。

图 2 对比了分别采用三种不同传输方案下的 GF 用户的中断概率随 GF 用户发射功率的变化情况，其中 GF 用户数为 M=4，GB 用户发射功率为 P_b=40 dBm。可以看出，闭合表达式得到的结果与蒙特卡洛仿真高度吻合，从而验证了理论分析的正确性。此外，由图 2 我们发现，与免授权 NOMA 方案相比，所提出的 SGF 方案有明显的性能提升，这是因为在免授权 NOMA 方案中，所有的 GF 用户接入同一资源块中，在执行 SIC 时会受到严重的干扰；另外，与 OMA 方案相比，由于所提出的 SGF 方案在保证 GB 用户的 QoS 的条件下允许 GF 用户接入同一时频资源，提高了频谱效率，因此有一定的性能提升。

表 1　仿真参数

参数	数值
卫星轨道	GEO
载波频率	2 GHz
3dB 角度	0.4°
玻尔兹曼常数	1.38×10^{-23} J/m
噪声温度	300 K
噪声带宽	5 MHz
最大卫星天线增益	53 dB
GB 用户最大发射天线增益	20 dB
信道参数（LS）	$\{m_i,b_i,\Omega_i\}_{LS}=\{10,0.126,1.29\}$
信道参数（AS）	$\{m_i,b_i,\Omega_i\}_{AS}=\{5,0.251,0.279\}$
信道参数（HS）	$\{m_i,b_i,\Omega_i\}_{HS}=\{2,0.0007,0.063\}$

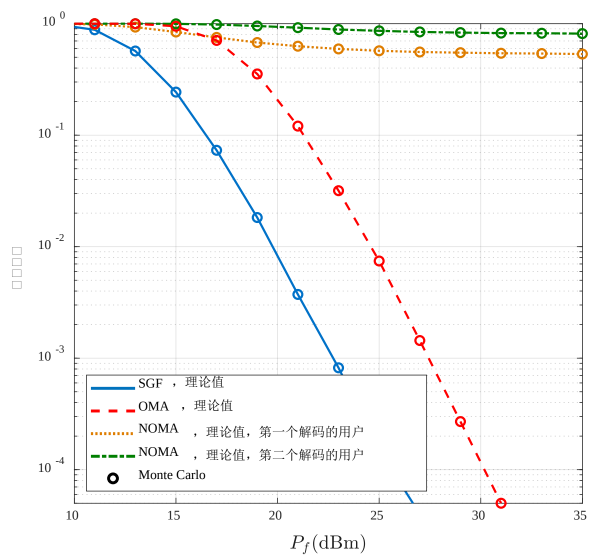

图 2　不同方案下 GF 用户中断概率随 GF 用户发射功率变化曲线

图 3 和图 4 分别分析了 GF 用户数对 GF 用户的中断概率和系统吞吐量的影响，其中，图 4 中 GF 用户发射功率为 P_k=20 dBm。可以看出，在相同的发射功率条件下，GF 用户的中断性能随着用户数的增加有明显的性能提升，这说明分

布式争用策略能充分利用用户的分集增益，在多用户接入的场景中更具有适应性。此外，从图 4 中可以看到，所提方案的系统吞吐量相比 OMA 方案有明显的性能提升，说明该方案在提升系统吞吐量方面具有优势。

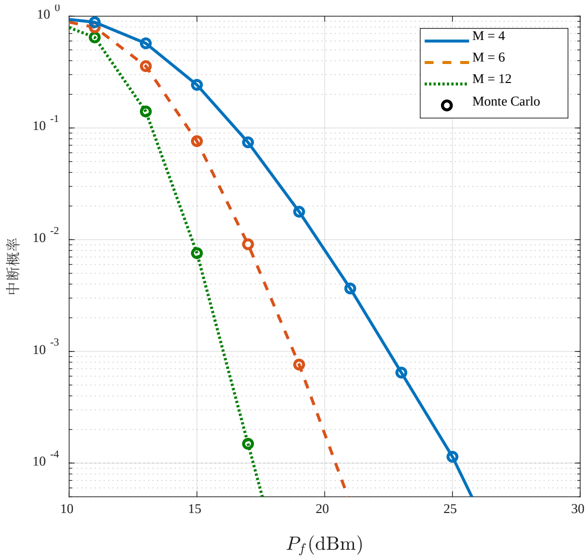

图 3　不同用户数下 GF 用户中断概率随 GF 用户发射功率变化曲线

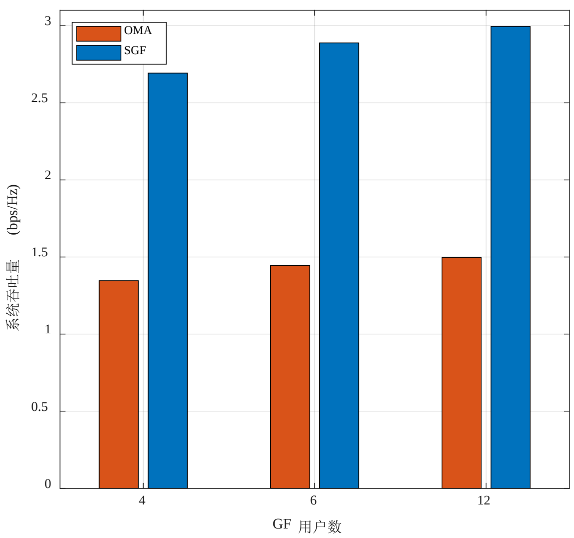

图 4　不同方案下 GF 用户数对系统吞吐量的影响

图 5 给出了系统吞吐量随 GB 用户和 GF 用户目标数据速率的变化情况。从图中可以看出，系统吞吐量随 GB 用户的数据速率增加几乎呈线性变化；这说明在所提出的 SGF 方案中，GB 用户的数据速率在一定范围内增加时，GB 用户的 QoS 始终能被保证。当 GF 用户数据速率增加时，系统吞吐量呈先上升再下降的趋势，这是因为在高数据速率区间内，随着数据速率的增加，GF 用户中断发生的概率会变大，从而影响系统的吞吐量。

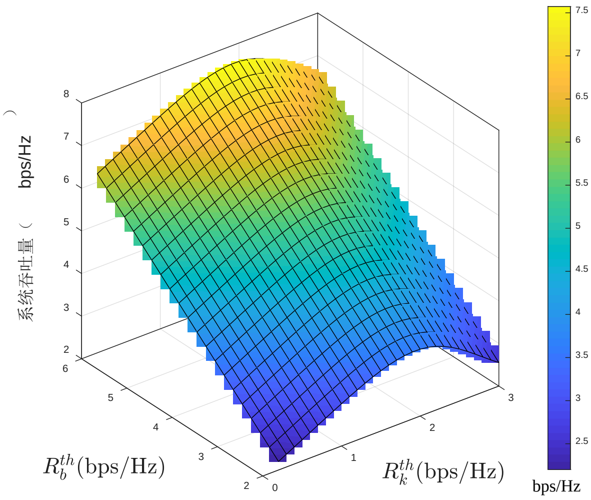

图 5　系统吞吐量随目标数据速率变化图

6　结束语

本文研究了一个卫星通信系统中的多用户接入场景，其中 GEO 卫星点波束覆盖范围内的一个地球站作为 GB 用户，多个移动终端作为 GF 用户，共同接入卫星网络。首先，根据地面用户的统计 CSI，提出了一种基于上行 NOMA 的 SGF 传输方案，该方案能够在不影响 GB 用户 QoS 的前提下允许 GF 用户与 GB 用户共享信道，从而在提升频谱资源利用率的同时减少信令开销。其次，假设卫星信道经历阴影莱斯衰落，并考虑天线增益和卫星链路损耗的影响，在 GF 用户采用分布式争用接入策略的情况下，推导出中断概率和系统吞吐量的闭合表达式。最后，计算机仿真验证了理论分析的正确性和所提方案相比免授权 NOMA 方案和 OMA 方案的优越性，分析了用户数、目标数据速率等典型参数对系统性能的影响。

参考文献：

[1]　赛迪智库无线电所. 6G 概念及愿景白皮书[R]. 2020.
[2]　安建平,李建国,于季弘等.空天通信网络关键技术综述[J].电子学报, 2022, 50(02): 470-479.
[3]　D. C. Nguyen, M. Ding, P. N. Pathirana et al., 6G Internet of Things: A Comprehensive Survey[J]. IEEE Internet of Things Journal, 2022, 9(1): 359-383.
[4]　IMT-2030(6G)推进组. 6G 典型场景和关键能力白皮书[R]. 2022.
[5]　D. Jiang, F. Wang, Z. Lv et al., QoE-Aware Efficient Content Distribu-

tion Scheme For Satellite-Terrestrial Networks[J]. IEEE Transactions on Mobile Computing, 2023, 22(1): 443-458.

[6] 朱立东,张勇,贾高一.卫星互联网路由技术现状及展望[J].通信学报, 2021, 42(08): 33-42.

[7] T. Zhu, J. Li, Z. Liu and G. Zhang, Diversity Slotted ALOHA with Power Accumulation for Satellite IoT Networks[C]. 2021 13th International Conference on Wireless Communications and Signal Processing (WCSP), Changsha, China, 2021, pp. 1-5.

[8] R. Kassab, A. Munari, F. Clazzer, and O. Simeone, Grant-free coexistence of critical and non-critical IoT services in two-hop satellite and terrestrial networks[J]. IEEE Internet of Things Journal, 2022, 9(16): 14829-14843.

[9] Z. Ding, X. Lei, G. K. Karagiannidis, R. Schober, J. Yuan, and V. K. Bhargava, A survey on non-orthogonal multiple access for 5G networks: Research challenges and future trends[J]. IEEE Journal on Selected Areas in Communications, 2017, 35(10): 2181–2195.

[10] S. A. Tegos, P. D. Diamantoulakis, J. Xia, L. Fan and G. K. Karagiannidis, Outage Performance of Uplink NOMA in Land Mobile Satellite Communications[J] IEEE Wireless Communications Letters, 2020, 9(10): 1710-1714.

[11] X. Yan, H. Xiao, K. An, G. Zheng and S. Chatzinotas, Ergodic Capacity of NOMA-Based Uplink Satellite Networks With Randomly Deployed Users[J]. IEEE Systems Journal, vol. 14, no. 3, pp. 3343-3350, Sept. 2020.

[12] H. Kong, M. Lin, Z. Wang, J.-Y. Wang, W.-P. Zhu and J. Wang, Performance Analysis for Rate Splitting Uplink NOMA Transmission in High Throughput Satellite Systems[J]. IEEE Wireless Communications Letters, 2022, 11(4): 816-820.

[13] AMMAR Z, MOHAMMAD S, ALOUINI, et al. On multiple users scheduling using superposition coding over Rayleigh fading channels[J]. IEEE Communications. Letters., 2013, 17(04): 733–736.

[14] Z. Ding, R. Schober, P. Fan and H. V. Poor, Simple Semi-Grant-Free Transmission Strategies Assisted by Non-Orthogonal Multiple Access[J]. IEEE Transactions on Communications, 2019, 67(6): 4464-4478.

[15] Z. Ding, R. Schober and H. V. Poor, A New QoS-Guarantee Strategy for NOMA Assisted Semi-Grant-Free Transmission[J]. IEEE Transactions on Communications, 2021, 69(11): 7489-7503.

[16] C. Zhang, Y. Liu and Z. Ding, Semi-Grant-Free NOMA: A Stochastic Geometry Model[J]. IEEE Transactions on Wireless Communications, 2022, 21(2): 1197-1213.

[17] Z. Yang, P. Xu, J. Ahmed Hussein, Y. Wu, Z. Ding and P. Fan, Adaptive Power Allocation for Uplink Non-Orthogonal Multiple Access With Semi-Grant-Free Transmission[J]. IEEE Wireless Communications Letters, 2020, 9(10): pp. 1725-1729.

[18] 林敏,朱丽文,孔槐聪等.基于协作非正交多址的无人机辅助卫星通信系统中断性能分析[J].电子与信息学报, 2022, 44(09): 3033-3042.

[19] Z. Wang, M. Lin, S. Sun, M. Cheng, W-P. Zhu, Robust Beamforming for Enhancing User Fairness in Multibeam Satellite Systems With NOMA[J]. IEEE Transactions on Vehicular Technology, 2022, 71(1): 1010-1014.

[20] 林敏,张健,林志等.多播传输模式下的卫星通信安全波束成形算法[J].电子学报, 2022, 50(01): 98-105.

[21] GRADSHTEYN I S, RYZHIK I M. Table of integrals, series, and products[M]. New York: Academic Press, 2014.

[作者简介]

郭焱（2000− ）：女，博士研究生。研究方向为空天地一体化高效协同传输技术等。

林敏（1972− ）：男，博士、教授、博士生导师。研究方向为无线通信系统、智能信号处理、天线新技术等。

谈苗苗（1999− ）:女，硕士研究生。研究方向为卫星通信、非正交多址接入技术等。

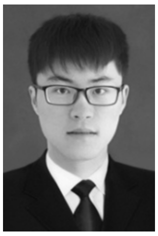

孔槐聪（1995− ）：男，博士研究生。研究方向为无线通信、通信信号处理等。

程铭（1991− ）：男，博士、讲师。研究方向为星地融合网络、无线通信中的性能评估、人工智能等。

针对高光谱大数据集的超像素子空间聚类方法

黄坤[1]；李欣[1,*]；皮英冬[2]
[1] 遥感信息工程学院，武汉大学，武汉，湖北，40072，中国
[2] 测绘遥感信息工程国家重点实验室，武汉大学，武汉，湖北，40072，中国

摘　要：高光谱影像由于其成像机制的独特性使其拥有着更多的光谱信息，但也导致了高光谱影像的数据量庞大。此外高光谱影像数据标签的缺乏限制了高光谱影像的实际应用。子空间聚类作为一种无监督的方法且高度兼容高光谱影像的高维特性而逐渐受到研究人员的关注，但在实际的工程应用中，子空间聚类的内存消耗是巨大且难以接受的。为了解决上述问题，本文提出一种基于超像素的子空间聚类方法，该方法通过超像素分割技术使得高光谱影像的数据总量大幅降低，且该方法通过联合利用超像素空间信息和光谱信息的聚类方法，大幅提升聚类性能。在高光谱两个公共数据集的实验证明了本文方法的有效性。
关键词：超像素；高光谱影像；子空间聚类

Superpixel Subspace Clustering Method for Large Hyperspectral Datasets

Kun huang[1]; Xin Li[1,*]; Yingdong Pi[2]
[1] The School of Remote Sensing and Information Engineering, Wuhan University, Wuhan, Hubei, 430072, China
[2] State Key Laboratory of Information Engineeringin Surveying, Mapping and Remote Sensing, Wuhan University, Wuhan, Hubei, 430072, China

Abstract: Due to the uniqueness of its imaging mechanism, hyperspectral images (HSI) have more spectral information, but this leads to a huge amount of data in hyperspectral images. In addition, the lack of hyperspectral image data labels also limits the practical application of hyperspectral imagery. As an unsupervised method and highly compatible with the high-dimensional characteristics of hyperspectral images, subspace clustering has gradually attracted the attention of researchers, but the memory consumption of subspace clustering in applications greatly restricts its application. In order to solve the above problems, this paper proposes a subspace clustering method based on superpixels. This method greatly reduces the total amount of hyperspectral image data through superpixel segmentation technology, and this method jointly utilizes superpixel spatial information and spectral information. The clustering method greatly improves the clustering performance. Experiments on two public hyperspectral data sets demonstrate the effectiveness of this method.
Key words:superpixel; hyperspectral image; subspace clustering

1　引言

高光谱成像通过将传统成像技术和光谱探测技术相结合，进而获取目标地物的空间位置信息和光谱信息[1,2]。由于高光谱影像可以获取目标地物的光谱细节信息，因此高光谱影像在环境检测、精准农业、植被生物量估算等诸多领域都有应用[3]。尽管高光谱影像的应用前景十分广泛，但前期的影像标注流程极大的限制了高光谱影像的实际应用。为了克服此问题，聚类技术逐渐受到研究人员的注意力。

常见的聚类方法可以分为三种：第一种为基于质心的聚类方法，如 Kmeans、FCM；第二种为基于层次聚类（Hierarchical Clustering）的方法；第三种方法为基于图的聚类算法，如谱聚类（Spectral Clustering）。此外，子空间聚类作为一种基于谱聚类的方法，由于其对高维数据的高度兼容性和对数据底层结构的强捕捉性，在高光谱聚类领域有着广泛的应用和极佳的效果。子空间聚类的原理是通过寻找表现数据结构的低维子空间，并计算数据点与子空间的距离进行聚类。目前子空间聚类在小数据集的高光谱影像上有着广泛的应用和可靠的精度，

如文献[4]提出了一种结合光谱相关性和空间信息的高光谱遥感影像的光谱空间聚类算法（S^4C）。文献[5]通过在稀疏子空间聚类中添加ι_2正则化提取光谱空间信息从而提升聚类性能。

随着图卷积的逐步发展，研究人员开始注意到数据内在的图结构信息，文献[6]提出了一种图卷积子空间聚类框架，该框架将子空间聚类和数据内在图结构信息进行融合，从而增强聚类的性能及鲁棒性。此外，随着深度学习的发展，文献[7]提出了一种基于图正则化残差子空间聚类网络，该网络通过将图正则化添加到联合损失中从而捕捉数据的内在图信息。

尽管子空间聚类在高光谱影像取得了较好的效果，但随着数据量的增长其内存消耗会急剧增加，这是因为对于含有N个数据的数据集，子空间聚类需要创建一个$N \times N$的自表达矩阵，此外对自表达矩阵的计算操作也会消耗内存，这意味着子空间在大数据集上的内存消耗是十分巨大的。为了解决针对大型高光谱影像子空间聚类的内存消耗问题，一些研究通过对图像进行预处理来降低数据总量。文献[8]提出了一种基于稀疏编码的聚类方法。该方法避免了学习整个图像的大规模邻接矩阵和图划分，从而降低了计算复杂度以及时间和内存开销。并通过基于联合稀疏编码的聚类（JSCC）模型进一步利用 HSI 的像素间相关性来提高聚类性能。文献[9]利用熵率超像素(ERS)[10]分割算法将 HSI 划分为超像素，并分别构建全局和局部信息的相似图，后通过权重将它们组合起来，输入谱聚类得到聚类结果。此外，一些研究[11,12]通过构建锚图将 HSI 中的像素映射到锚点，从而减少计算量并提高计算效率。

超像素将连续像素分组为具有一定空间连续性的紧凑区域，从而将 HSI 中相似的像素分组为单个超像素。此外，超像素很好的利用了图像内在的空间关联信息，具体来说，从像素的角度来看，其周围的像素与其往往是同类地物，因此利用好这部分先验信息是十分有效且重要的。许多研究已将超像素分割纳入到数据预处理中[13–16]，然而，这些研究倾向于只将超像素应用于预处理阶段，并没有充分挖掘超像素内部含有的丰富信息。

超像素分割算法作为一种利用了图像空间相关性先验知识的方法，在减少数据总量且保障分类精度方面具有一定的优势。本文提出了一种利用超像素空间邻接图和光谱邻接图的聚类方法，该方法通过同时利用超像素的空间信息和光谱信息有效地提高了聚类性能。在 WHU_Hi_HongHu 和 QUH-Pingan 的实验证明了本文方法的有效性和优势性。

2　本文方法

图 1 是本文方法的流程图，首先通过 PCA（Principal Component Analysis，PCA）对高光谱数据进行降维处理，再使用 SLIC（Simple Linear Iterative Clustering，SLIC）超像素分割算法对其进行分割操作。后将获得的超像素分割图与原始的高光谱影像进行融合得到超像素的特征，并分别在空间域和光谱域提取超像素的图结构，最后得到自表达矩阵的一致性部分，并输入谱聚类中得到聚类结果。

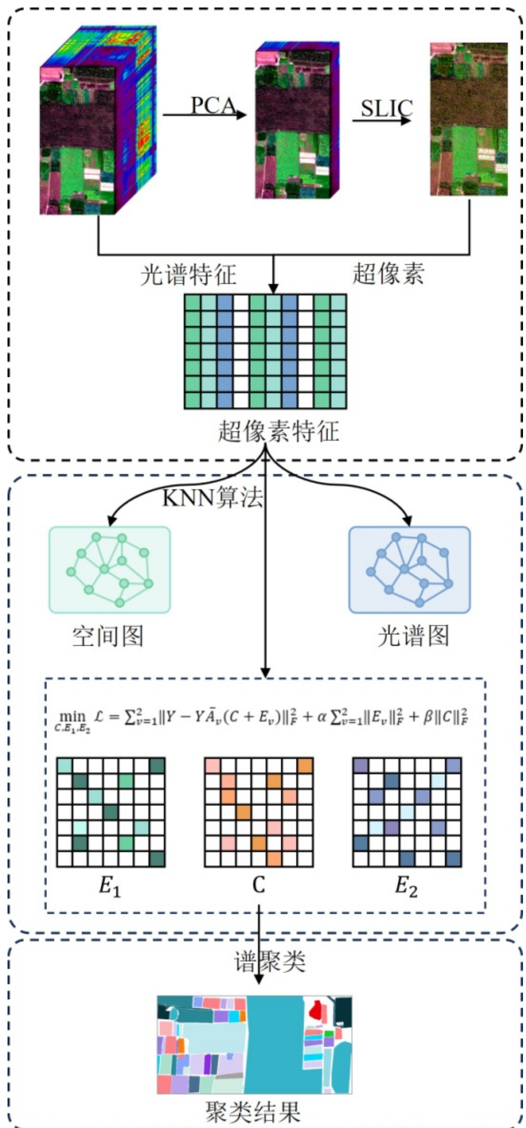

图 1　本文方法流程图

2.1　稀疏子空间聚类

子空间聚类是一种图聚类模型，它认为同一类数据位于同一子空间中，并且同一子空间中的数据可以相互表示。假设数据集$X \in R^{m\times n}$包含n个维度为m的数据。对于X中的任意$x_i \in R^m$，子空间聚类旨在通过数据集中其他数据的线性组合来恢复x_i，问题可以表述为：

$$\min_C \|C\|_p s.t.\ X = XC, diag(C) = 0 \quad (1)$$

式中C表示自表达系数矩阵。通过强制C的对角线元素为 0 避免出现平凡解的情况是一种常见的限制方法。以这种方式，每个数据将被数据集中的其他数据恢复和重建。$\|C\|_p$表示系数矩阵C的p范数。由于ι_0范数的非凸性质，矩阵C不能通过交替方向乘子法（alternating direction method of multipliers, ADMM[17]）求解。因此，ι_1范数和ι_2范数通常用于稀疏子空间聚类（SSC），例如$\|C\|_1$（SSC[18]）和$\|C\|_2$（ι_2-SSC[5]）。具体来说，稀疏子空间聚类模型公式表述为：

$$\min_C \|X - XC\|_F + \lambda\|C\|_* s.t. diag(C) = 0 \quad (2)$$

式中$\|\cdot\|_F$代表 Frobenius 范数，$\|C\|_*$代表矩阵 C 的ι_1, ι_2范数。式（2）可以通过 ADMM 工具进行求解。此外，图卷积的发展致使高光谱聚类和图结构的融合方法逐渐发展。文献[19]提出了一种针对高光谱图像的无监督广泛学习（unsupervised broad learning，UBL）方法，该方法将图正则化引入到映射特征中，以保存数据内在流形结构。文献[6]将图嵌入到子空间聚类，并提出了图卷积子空间聚类模型，具体问题可表述为式（3），其中$\bar{A}$表示具有自环的归一化邻接矩阵。该模型通过将自表达特性嵌入到非欧式空间中，从而获得更为强大的图嵌入字典，大大提高了聚类性能，也证明了图结构的重要性。

$$\min_C \frac{1}{2}\|X\bar{A}C - X\|_F^2 + \frac{\lambda}{2}\|C\|_F^2 \quad (3)$$

2.2　超像素分割算法

超像素分割算法将图像划分为具有相似特征的紧密区域，称为超像素。这些超像素区域通常是图像中连续的像素块，具有相似的颜色、纹理或亮度等特征。超像素分割算法的目标是减少图像中的冗余信息，并以更高级别的语义信息表示图像内容。相比于传统的基于像素的图像处理方法，超像素分割算法在计算效率和图像分析任务上具有更好的性能。本文采用 SLIC[20]超像素分割算法，该算法有着简单易实现、速度快以及能够产生紧凑且均匀的超像素，且能够很好的保留边界信息的优点。

给定一个高光谱影像数据$X\epsilon\mathbb{R}^{m\times n\times B}$，其中$m$和$n$分别表示高光谱影像的宽和高，$B$表示高光谱影像的光谱维度。在超像素分割之后得到超像素集SP，其中$SP = \{SP_1, \dots SP_{nums}\}$。$SP_k$是超像素集中第$k$个超像素，其是一个像素的集合并可以被描述为：$SP_k = \{x_1^k, \dots x_{n_k}^k\}$，$x_i^k \in \mathbb{R}^B$表示单个像素的光谱特征。为了更好的描述超像素，$Y$和$P$被用来分别表示超像素的光谱特征和空间特征。$Y_i, P_i$可由式（4）计算所得，其中$pos()$表示像素在图像上的位置。

$$\begin{cases} Y_i = \frac{1}{n_k}\sum_i^{n_k} x_i^k \\ P_i = \frac{1}{n_k}\sum_i^{n_k} pos(x_i^k) \end{cases} \quad (4)$$

正如每个像素都有空间位置和光谱特征，超像素作为像素的集合，理应同样含有这两个特征。本文使用超像素中所有像素的光谱平均值作为超像素的光谱特征，并使用所有像素的质心坐标作为超像素的空间位置。这两种方式可以有效的描述超像素的空间位置和光谱特征。

2.3　超像素图建立

大量研究表明，数据之间的内在图结构对于聚类至关重要，并且可以增强深度亲和力矩阵的生成。目前，主流方法是研究超像素之间的光谱图结构[6]。然而，这忽略了超像素之间的空间相关性。在超像素实际分割过程中，将单个特征划分为一个单一超像素是很困难的。超像素分割的结果往往是过分割的，因此，超像素通常与其周围的超像素属于同一类地物。这意味着考虑超像素之间的空间相关性是十分有必要的。

为了表示超像素之间的光谱图结构，我们使用 k 最近邻（k-nearest neighbor，KNN）方法来计算欧式距离并创建超像素光谱邻接图。具体来说，数据集中的每个点被视为图的一个节点，节点之间的边关系定义如式（5）所示。同理，使用 KNN 算法计算每个超像素在图像位置上的邻接点，获得超像素的空间邻接图，其中$\mathcal{N}(Y_i)$表示为Y_i的邻域。

$$A_{ij} = \begin{cases} 1 & Y_j \in \mathcal{N}(Y_i) \\ 0 & Y_j \notin \mathcal{N}(Y_i) \end{cases} \quad (5)$$

2.4　目标函数

文献[6]证明了图结构在子空间聚类中的有效性。然而，该文献中所提出的方法是单视图像素级聚类方法，其在大数据集上的应用受到限制。为了更好地利用超像素之间的空间和光谱信息，本文提

出了一种双视图超像素图子空间聚类方法。通过结合光谱邻接图和空间邻接图的信息，以此更有效地捕获数据结构并提高聚类准确性。

具体来说，认为双视图自我表达矩阵必须存在一致部分[21]，这意味着自我表达矩阵可以分解为两部分，一部分是两者之间的一致部分C视图，另一部分是两个视图之间不一致的部分E。因此最终的目标函数如式（6）所示。

$$\min_{C,E_1,E_2} \mathcal{L} = \sum_{v=1}^{2} \|Y - Y\bar{A}_v(C + E_v)\|_F^2 + \alpha \sum_{v=1}^{2} \|E_v\|_F^2 + \beta \|C\|_F^2 \tag{6}$$

其中C表示双视图自我表达矩阵之间的一致部分，E_1, E_2表示自我表达矩阵之间的不一致部分。通过约束E_1, E_2的 Frobenius 范数，使自表达矩阵之间的不一致部分最小化，从而使它们的自表达矩阵之间的一致部分最大化。此外，我们也对一致性部分C施加稀疏性约束。我们注意到目标函数式（3）是非凸的，因此可以使用交替迭代法来求解。

$$\begin{cases} C = (\sum_{v=1}^{2} \bar{A}_v^T Y^T Y \bar{A}_v + \beta I)^{-1} (\sum_{v=1}^{2} \bar{A}_v^T Y^T Y - \sum_{v=1}^{2} \bar{A}_v^T Y^T Y \bar{A}_v E_v) \\ E_v = (\bar{A}_v^T Y^T Y \bar{A}_v + \alpha I)^{-1} (\bar{A}_v^T Y^T Y - \bar{A}_v^T Y^T Y \bar{A}_v C) \end{cases} \tag{7}$$

具体来说，先固定C值，使用式（7）更新E_v，后固定E_v，使用式（7）更新C。不停迭代下去，直至C值的变化量小于 0.001，或者是迭代次数达到 1000。最后将C输入到谱聚类中获得聚类结果。

3　实验

3.1　数据集简介

本次实验选用两个高光谱公共数据集，分别是 WHU_Hi_HongHu[22]（HongHu）和 QUH-Pingan[23]（PingAn）。HongHu 数据集是典型的农业场景，种植棉花、油菜、卷心菜等 17 种作物。无人机飞行高度为 100m，影像尺寸为940×475像素，在 400~1000nm 波段范围内有 270 个波段，无人机载高光谱影像空间分辨率约为 0.043m。PingAn 数据集是典型的城市场景，有船、海水，汽车、道路等典型地物。无人机飞行高度为 200m，无人机载高光谱图像空间分辨率约为 0.10m。影像尺寸为1230×1000像素，在波长范围为 400-1000nm 内含有 176 个波段。表 1 是实验所用数据集的简介，图 2 和图 3 是数据的彩色图及地物覆盖图。

3.2　对比方法和评价指标

本文选用了两种经典的聚类方法（Kmeans[24]、FCM[25]）进行对比，这两种方法都是基于质心的像素级聚类方法。此外本文还选用了一种超像素级的高光谱聚类方法：SGLSC[9]。

表 1　　实验所用数据集介绍

数据集	图像大小	波段数	空间分辨率/(m)	类别数	样本数
HongHu	940 × 475	270	0.0043	22	386,693
PingAn	1230 × 1000	176	0.1	10	1,140,937

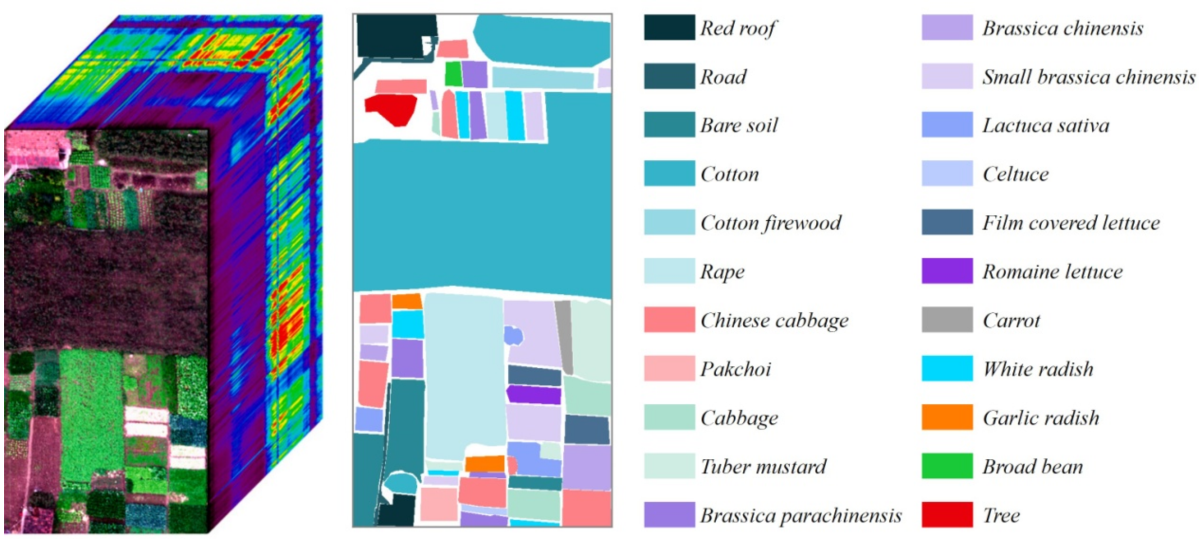

图 2　HongHu 数据集假彩色图片和地物覆盖图

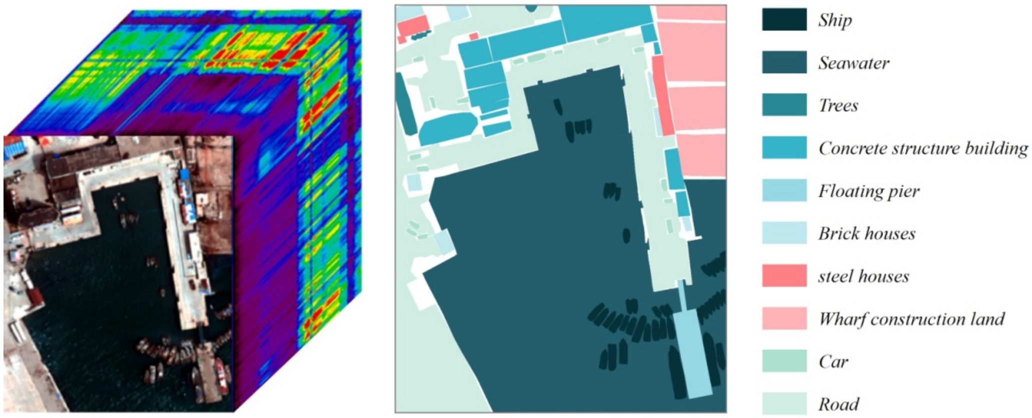

图 3　PingAn 数据集假彩色图片和地物覆盖图

本实验中使用的定量评价指标包括生产者准确度(producer accuracy, PA)、总体准确度(overall accuracy, OA)、标准化互信息(normalized mutual information, NMI) 和 kappa 系数(kappa)。这些指标的值都在 0-1 之间，数值越大说明聚类效果越好。

3.3　实验结果

表 2 为对比实验的定量结果，可以看出，本文方法在 HongHu 和 PingAn 数据集有着巨大的领先

表 2　　对比实验定量结果（最佳结果加粗表示）

方法	HongHu					PingAn				
	类	Kmeans	FCM	SGLSC	Ours	类	Kmeans	FCM	SGLSC	Ours
PA	1	0.3584	0.4842	0.6785	**0.7433**	1	0.2796	0.2550	0.0172	**0.7373**
	2	**0.5034**	0.0000	0.0000	0.1162	2	**0.9725**	0.6519	0.3676	0.9718
	3	0.8957	0.8916	**0.9950**	0.8771	3	0.0036	0.0029	0.0000	**0.9723**
	4	0.2434	0.1329	0.2761	**0.9830**	4	0.3238	0.3624	0.0089	**0.8188**
	5	0.3712	0.4151	0.6748	**0.8480**	5	**0.4752**	0.4684	0.0000	0.0000
	6	0.3301	0.2396	0.7774	**0.9273**	6	0.1470	0.1570	0.0000	**0.2809**
	7	0.2801	0.2976	0.5056	**0.6420**	7	0.4389	0.0957	0.0000	**0.7675**
	8	0.1290	0.1818	0.0126	**0.3416**	8	0.2283	0.2012	0.0000	**0.9262**
	9	0.2869	0.2751	0.6797	**0.7835**	9	0.1744	0.0773	0.0000	**0.2070**
	10	0.1144	0.1184	**0.8648**	0.6886	10	0.3151	0.2709	**0.9718**	0.8323
	11	0.1789	0.1697	0.5169	**0.6797**					
	12	0.4476	0.4609	0.0000	0.0132					
	13	0.3059	0.2481	0.4566	**0.6853**					
	14	0.4976	0.5148	0.0000	**0.6287**					
	15	**0.3453**	0.1766	0.0050	0.0000					
	16	0.3578	0.8067	**0.9850**	0.9811					
	17	0.5296	0.0007	**0.6963**	0.0399					
	18	0.0000	0.1131	0.0071	**0.9888**					
	19	0.0986	0.0697	0.6635	**0.8231**					
	20	0.3528	0.1268	0.0003	**0.5100**					
	21	**0.0068**	0.0015	0.0000	0.0000					
	22	0.3502	0.221	0.2931	**0.8146**					
	OA	0.3090	0.2516	0.4595	**0.8308**	OA	0.6401	0.4620	0.4232	**0.8785**
	NMI	0.4396	0.3943	0.5545	**0.7691**	NMI	0.4808	0.4250	0.3044	**0.7442**
	Kappa	0.2572	0.2126	0.4091	**0.7861**	Kappa	0.4890	0.3195	0.2270	**0.8208**

幅度，在 HongHu 数据集上，本文提出的方法在 OA、NMI 和 Kappa 可以达到 0.8308、0.7691 和 0.7861。在 PingAn 数据集上，本文提出的方法在 OA、NMI 和 Kappa 可以达到 0.8785、0.7442 和 0.8208。两个数据集上的结果均证明了本文方法的优势性。此外，在 HongHu 数据集上的 22 类地物覆盖中，本文方法有 14 类地物的分类准确性最佳；在 PingAn 数据集上的 10 类地物覆盖中，本文方法有 7 类地物的分类准确性最佳。

图 4 和图 5 分别是 HongHu 和 PingAn 数据集的可视化结果图。从图 4 中可以看出，Kmeans 和 FCM 在图像上的错分现象比较明显，具体表现在图像上为含有的噪声较多，SGLSC 在图像中间最大的区域分类效果不好，而本文方法在上述区域表现较好，错分现象较少。从图 5 可以看出，FCM 和 SGLSC 在海水区域的分类效果不好，有着明显的错分现象，Kmeans 和本文方法在海水区域表现良好，得益于超像素的使用，本文方法在海水区域没有椒盐噪声的存在，而 Kmeans 方法存在着部分椒盐噪声。总的来说，本文方法在两个数据集的分类表现远超其他对比方法，有着较大的优势。

3.4　参数敏感性分析

图 6 和图 7 分别是 PCA 降维之后的数据维度D和超像素数量对聚类精度的影响。从图 6 中可以看出，维度的适当增加对聚类精度的提升有益，但当维度过大时又容易出现“维度灾难”，这点在 PingAn 数据集上表现尤为明显，HongHu 数据集在维度为 15、17、19、21 的时候显著比维度为 7、9、11、13 高，在维度为 13 和 15 之间有一个大幅增长。超像素分割数量也是影响聚类精度的重要参数，图 7 为 HongHu 数据集和 PingAn 数据集聚类精度受超像素数量的影响变化图，可以看出，对于 HongHu 数据集而言，其在超像素分割数量为 5000-6000 时有着较好的聚类精度，过多和过少的超像素都会降低其精度。PingAn 数据集呈现随超像素数量增加而缓慢降低的趋势，不过 OA 值总体在 80%以上，衰减幅度不大。

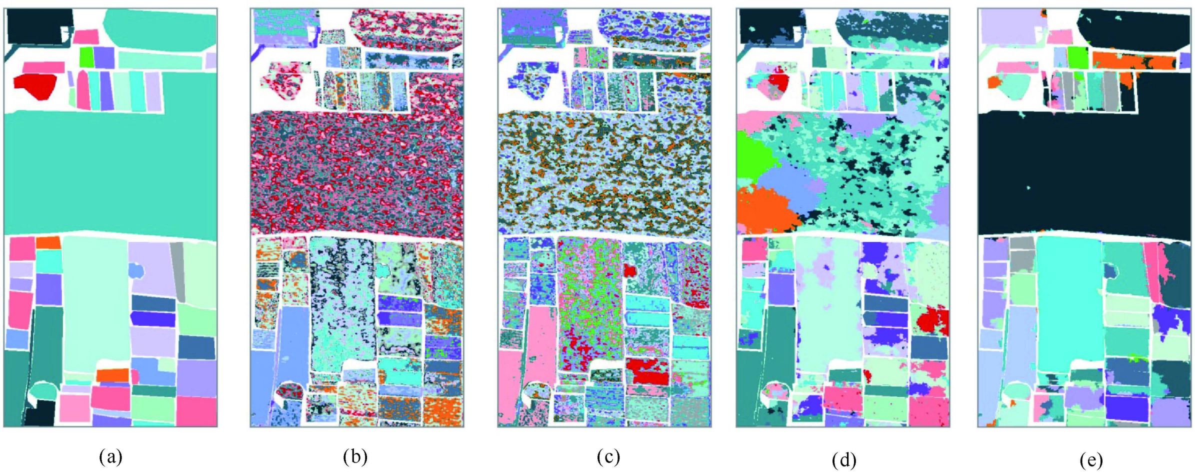

图 4　HongHu 数据集可视化结果图，(a)地面真值；(b)Kmeans；(c)FCM；(d)SGLSC；(e)Ours

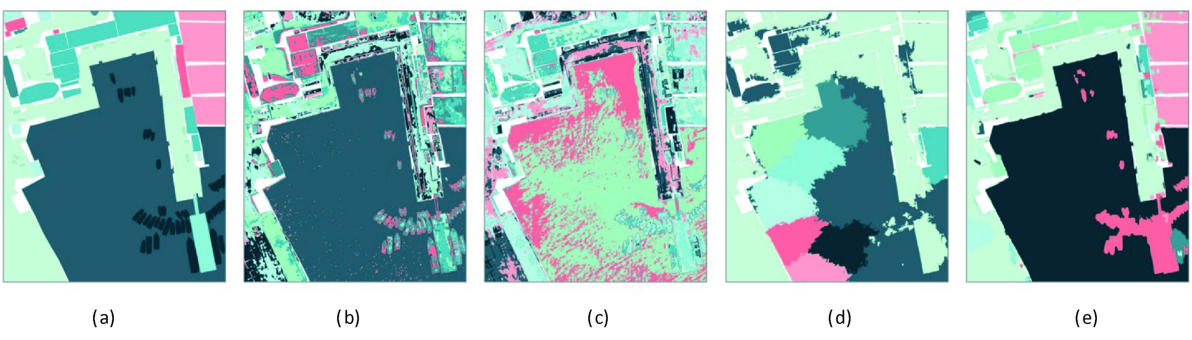

图 5　PingAn 数据集可视化结果图，(a)地面真值；(b)Kmeans；(c)FCM；(d)SGLSC；(e)Ours

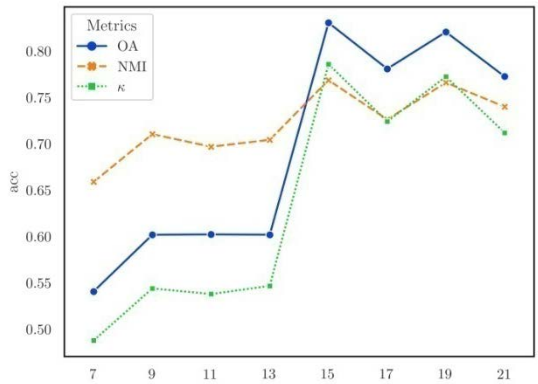

（a）

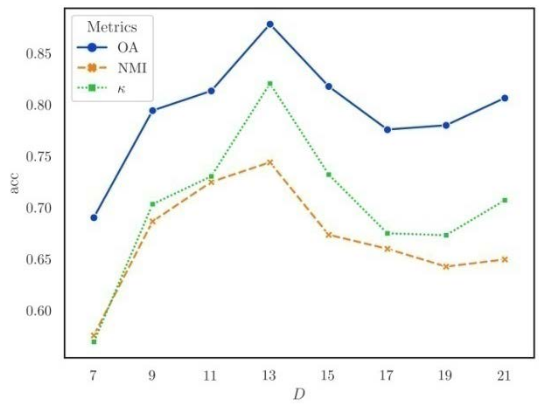

（b）

图 6　PCA 降维维度D对聚类精度的影响（a）HongHu；（b）PingAn

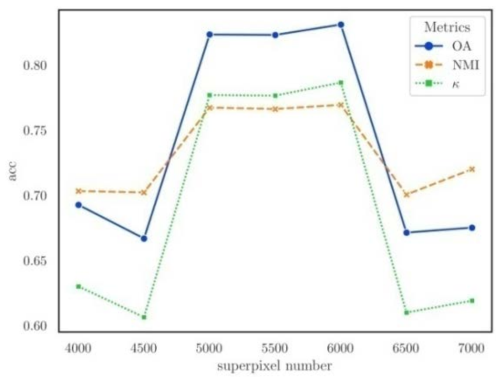

（a）

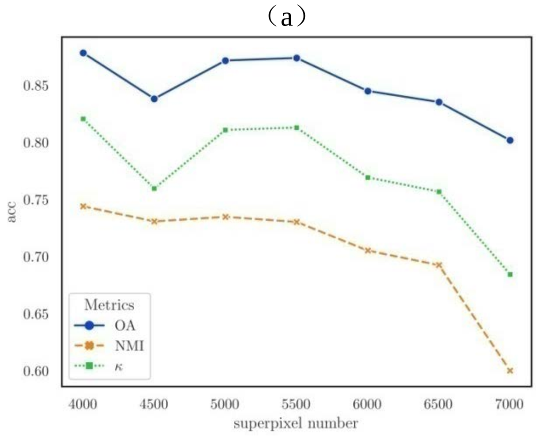

（b）

图 7　超像素数量对聚类精度的影响（a）HongHu；（b）PingAn

4　结论

本文提出了一种适用于大型高光谱数据集的子空间聚类方法，首先通过引入超像素对高光谱影像做预处理操作，从而大幅减少了数据量，于此同时，超像素空间信息和光谱信息的合理利用极大的提升了聚类性能。本文方法相比于经典的聚类方法在 HongHu 和 PingAn 数据集上的表现有着较大幅度的领先，证明了本文方法的有效性。

参考文献：

[1] 童庆禧，张兵，张立福．中国高光谱遥感的前沿进展[J]．遥感学报，2016, 20(5): 19.

[2] 张良培，李家艺．高光谱图像稀疏信息处理综述与展望[J]．遥感学报，2016, 20(5): 11.

[3] 杜培军，夏俊士，薛朝辉，等．高光谱遥感影像分类研究进展[J]．遥感学报，2016, 20(2): 21.

[4] ZHANG H, ZHAI H, ZHANG L, et al. Spectral–Spatial Sparse Subspace Clustering for Hyperspectral Remote Sensing Images[J/OL]. IEEE Transactions on Geoscience and Remote Sensing, 2016, 54(6): 3672-3684. DOI:10.1109/TGRS.2016.2524557.

[5] ZHAI H, ZHANG H, ZHANG L, et al. A New Sparse Subspace Clustering Algorithm for Hyperspectral Remote Sensing Imagery[J/OL]. IEEE Geoscience and Remote Sensing Letters, 2017, 14(1): 43-47. DOI:10.1109/LGRS.2016.2625200.

[6] CAI Y, ZHANG Z, CAI Z, et al. Graph Convolutional Subspace Clustering: A Robust Subspace Clustering Framework for Hyperspectral Image[J/OL]. IEEE Transactions on Geoscience and Remote Sensing, 2021, 59(5): 4191-4202. DOI:10.1109/TGRS.2020.3018135.

[7] CAI Y, ZENG M, CAI Z, et al. Graph Regularized Residual Subspace Clustering Network for hyperspectral image clustering[J/OL]. Information Sciences, 2021, 578: 85-101. DOI:https://doi.org/10.1016/j.ins.2021.07.003.

[8] ZHAI H, ZHANG H, ZHANG L, et al. Sparsity-Based Clustering for Large Hyperspectral Remote Sensing Images[J/OL]. IEEE Transactions on Geoscience and Remote Sensing, 2021, 59(12): 10410-10424. DOI:10.1109/TGRS.2020.3032427.

[9] ZHAO H, ZHOU F, BRUZZONE L, et al. Superpixel-Level Global and Local Similarity Graph-Based Clustering for Large Hyperspectral Images[J/OL]. IEEE Transactions on Geoscience and Remote Sensing, 2022, 60: 1-16. DOI:10.1109/TGRS.2021.3132683.

[10] LIU M Y, TUZEL O, RAMALINGAM S, et al. Entropy rate superpixel segmentation[C/OL]//CVPR 2011. 2011: 2097-2104. DOI:10.1109/CVPR.2011.5995323.

[11] WANG R, NIE F, WANG Z, et al. Scalable Graph-Based Clustering With Nonnegative Relaxation for Large Hyperspectral Image[J/OL]. IEEE Transactions on Geoscience and Remote Sensing, 2019, 57(10): 7352-7364. DOI:10.1109/TGRS.2019.2913004.

[12] WANG R, NIE F, YU W. Fast Spectral Clustering With Anchor Graph for Large Hyperspectral Images[J/OL]. IEEE Geoscience and Remote Sensing Letters, 2017, 14(11): 2003-2007. DOI:10.1109/LGRS.2017.2746625.

[13] TU B, ZHOU C, HE D, et al. Hyperspectral Classification With Noisy Label Detection via Superpixel-to-Pixel Weighting Distance[J/OL]. IEEE Transactions on Geoscience and Remote Sensing, 2020, 58(6): 4116-4131. DOI:10.1109/TGRS.2019.2961141.

[14] YANG C, BRUZZONE L, ZHAO H, et al. Superpixel-Based Unsupervised Band Selection for Classification of Hyperspectral Images[J/OL]. IEEE Transactions on Geoscience and Remote Sensing, 2018, 56(12): 7230-7245. DOI:10.1109/TGRS.2018.2849443.

[15] CAI Y, ZHANG Z, GHAMISI P, et al. Superpixel Contracted Neighborhood Contrastive Subspace Clustering Network for Hyperspectral Images[J/OL]. IEEE Transactions on Geoscience and Remote Sensing, 2022, 60: 1-13. DOI:10.1109/TGRS.2022.3179637.

[16] ZHAO H, BRUZZONE L, GUAN R, et al. Spectral-Spatial Genetic Algorithm-Based Unsupervised Band Selection for Hyperspectral Image Classification[J/OL]. IEEE Transactions on Geoscience and Remote Sensing, 2021, 59(11): 9616-9632. DOI:10.1109/TGRS.2020.3047223.

[17] BOYD S, PARIKH N, CHU E, et al. Distributed optimization and statistical learning via the alternating direction method of multipliers[J]. Foundations and Trends® in Machine learning, 2011, 3(1): 1-122.

[18] ELHAMIFAR E, VIDAL R. Sparse subspace clustering: Algorithm, theory, and applications[J]. IEEE transactions on pattern analysis and machine intelligence, 2013, 35(11): 2765-2781.

[19] KONG Y, CHENG Y, CHEN C P, et al. Hyperspectral image clustering based on unsupervised broad learning[J]. IEEE Geoscience and Remote Sensing Letters, 2019, 16(11): 1741-1745.

[20] ACHANTA R, SHAJI A, SMITH K, et al. SLIC superpixels compared to state-of-the-art superpixel methods[J]. IEEE transactions on pattern analysis and machine intelligence, 2012, 34(11): 2274-2282.

[21] CAI X, HUANG D, ZHANG G Y, et al. Seeking commonness and inconsistencies: A jointly smoothed approach to multi-view subspace clustering[J]. Information Fusion, 2023, 91: 364-375.

[22] ZHONG Y, HU X, LUO C, et al. WHU-Hi: UAV-borne hyperspectral with high spatial resolution (H2) benchmark datasets and classifier for precise crop identification based on deep convolutional neural network with CRF[J/OL]. Remote Sensing of Environment, 2020, 250: 112012. DOI:https://doi.org/10.1016/j.rse.2020.112012.

[23] FU H, SUN G, ZHANG L, et al. Three-dimensional singular spectrum analysis for precise land cover classification from UAV-borne hyperspectral benchmark datasets[J/OL]. ISPRS Journal of Photogrammetry and Remote Sensing, 2023, 203: 115-134. DOI:https://doi.org/10.1016/j.isprsjprs.2023.07.013.

[24] MACQUEEN J B. Some methods for classification and analysis of multivariate observations[J]. Proceedings of the fifth Berkeley symposium on mathematical statistics and probability, 1967, 1(14): 281-297.

[25] BEZDEK J C. Pattern recognition with fuzzy objective function algorithms[J]. Plenum Press, New York, 1981, 1(1): 121-163.

[作者简介]

黄坤 1999 年出生于中国江西省丰城市。现在他是武汉大学遥感信息工程学院的一名硕士研究生。他的研究方向是高光谱无监督聚类、高光谱超像素分割和图神经网络。

李欣，武汉大学遥感信息工程学院教授，博士生导师，摄影测量系副主任，主要研究方向为近景摄影测量、无人机可见光、高光谱影像处理、工业测量、卫星遥感影像处理。

皮英冬，武汉大学测绘遥感信息工程国家重点实验室特聘副研究员，主要从事卫星遥感数据高精度处理与应用工作。

QFL: Quantization-aware Federated Learning over Heterogeneous Devices

XIE Weiying[1] , CHEN Xiaoyu[2], LI Yunsong[3]

Abstract—**In recent years, there seems to be a trend from single-satellite to multi-satellite cooperative processing. Meanwhile, with the rapid development of machine learning techniques, the space industry, which is also experiencing rapid growth, is ready to utilize recent advancements in ML to process complicated tasks. However, data collected by satellites may be partially private, which prevents downlinking it to the ground and processing it with high-performance computing devices. Federated learning (FL) is a significant approach to training global models using decentralized data while preserving privacy. Traditional FL techniques typically assign the same model to all clients directly, assuming that they have the same computing and storage capacities. However, in practical scenarios, satellites can be heterogeneous in terms of those capabilities. Assigning different models to heterogeneous devices seems a feasible way but problems may arise due to the difference in model structure. In this paper, we propose a fresh framework called QFL. QFL assigns distinct quantization bit widths for strong and weak clients, enabling all clients to contribute to the training of a global model stored on the server. Moreover, we establish a criterion to evaluate the contribution of each client model to the global model using information from quantization bit width and local gradient. Additionally, we introduce a quantization module featuring trainable scaling factors, which enhances the performance of parameter quantization. Comprehensive experiments reveal the effectiveness of our framework. We achieve around 96% BOPs reduction and more than 1.6× compression rate in communication amount while the decrease in accuracy is less than 1% in most experimental setups.**

Keywords—**federated learning, distributed learning, network compression, parameter quantization**

I. INTRODUCTION

The last years have witnessed the great development of satellite techniques, especially low-orbit satellites, which have attracted a succession of satellite launches by different organizations in different countries[1-3]. This explosive growth in the number of satellites has made it easier to serve a variety of reconnaissance or remote-sensing missions. Therefore, how to analyze the large amount of data acquired becomes a problem. A data-sharing model to exchange data from different on-orbit parties and train collaboratively sounds attractive and practical. However, for on-orbit applications, some of the data is protected by law, and their disclosure can lead to serious consequences. Federate learning (FL) provides a scenario where multiple clients can learn jointly while preserving data privacy, thus has been widely used in privacy-sensitive scenes, including finance [4] and healthcare [5]. In FL, sampled clients are asked to train and update their local models through a given number of rounds and then upload their local model parameters to the server to aggregate a global model.

Most of the federated learning methods[6,7] make an ideal assumption that all the clients contain the same amount of computing and storage resources. In fact, in real-world scenarios, satellites on different orbits, or even on the same orbit, are usually heterogeneous in computing power and memory size. Meanwhile, due to the growing computational power of satellites, it is increasingly attractive to push network training to the edge. However, these on-orbit devices are still limited in computing and storage resources compared with the computing equipment on the ground.

In order to solve the heterogeneity problem, Bonawitz et al. [8] proposed a way to directly drop the poorly performing clients and only aggregate the model parameters of those strongly performing clients into a global model. Such an approach sounds unfair since poorly performing clients may also contain some valuable information. In addition, considering the heterogeneity of different devices, some methods use different sizes of local models. For example, FedMD [9] proposed a knowledge-distillation-based framework that enables participants to build their own models. The server does not control or participate in the construction of these models. Liu et al. [10] proposed a method to effectively deploy federated learning over heterogeneous clients, while a momentum knowledge distillation method is proposed to share the information of large models with small models. Although the methods above take into account the resource heterogeneity among different clients, due to the diversity of heterogeneous models, problems may arise in the process of global model fusion, leading to a degradation of model accuracy.

We conceive a new perspective to address the above issues: exploring quantization-aware federated learning. In a nutshell, we dynamically select the appropriate quantization bit width for each participant in federated learning according to their difference in computing resources. In this way, all the local clients of federated learning can effectively participate in the training of the global model and make their own contributions.

In this paper, we propose a novel heterogeneous federated learning framework called QFL, to address the above critical challenges caused by heterogeneous devices and quantization. According to computing and storage capabilities, clients are classified into two classes, strong clients and weak clients, and quantized with different quantization bit widths. We also introduce a trainable scaling factor during network parameter quantization in order to achieve higher accuracy than the ordinary neural network parameter quantization method. The key contributions of our work are as follows:

- We propose QFL for effective federated learning over heterogeneous devices. Clients with different computing and memory capabilities are assigned different quantization bit widths, all of which can contribute to training a global model stored on the server.
- We introduce a trainable scaling factor during network parameter quantization to achieve better quantization performance.
- We implement and evaluate our QFL in different experimental settings, verifying the effectiveness of the proposed method in learning an accurate global model from heterogeneous clients in the FL framework.

II. RELATED WORK

A. FEDERATED LEARNING

Since the concept of federated learning was first proposed by FedAvg [7] in 2017, federated learning has received a lot of attention. Unlike traditional distributed machine learning, federated learning enables multiple participants to train a same global model without data sharing. After that, Liu et al. [11] proposed a framework known as federated transfer learning (FTL). FTL is able to share knowledge among different participants, which protects user privacy. Smith et al. [6] apply the idea of multi-task learning to federated learning so that the clients can complete separate tasks, which ensures data security. Wang et al. [12] proposed FedMA, an algorithm that performs layer-wise matching and averaging to obtain a global model. Some of the FL methods concern about the problem of data heterogeneity. Sattler et al. [13] improves the performance of Non-IID data by training a small part of data among edge devices. Liang et al. [14] proposed a method to jointly learn compact local representations of each client together with the global model, based on the analysis that the combination reduces the variance. Li et al. [15] provide Ditto to allow each client to gain information from the global model while training its personalized model. Zhang et al. [16] proposed an Adaptive Local Aggregation module to adaptively combine global with each local objective on clients. As for federated learning on heterogeneous devices, early works mainly focus on offering models with different sizes. Some of them [9,17] are based on knowledge distillation to generate student models. Besides, some methods focus on reducing communication costs to settle the problems due to edge devices. Konečný et al. [18] provide two strategies to reduce communication costs, i.e., structured updates and sketched updates. Both of them reduce the cost significantly while reducing the amount of information transmitted. Caldas et al. [19] use the concept of dropout [20], where instead of training a global model, a smaller sub-model (a subset of the global model) is trained to update the global one. FedKD [21] combines adaptive mutual knowledge distillation and dynamic gradient compression techniques and achieves salient communication cost reduction. In general, all the methods based on communication costs reduce the exchange loss of information for reduced communication costs. Overall, existing approaches do not take into account the limited computing power and storage capabilities of edge devices, and heterogeneous-model-based approaches may create computational problems when different models are aggregated. To address these issues, we propose to introduce parameter quantization in federated learning to solve the problem that heterogeneous edge devices have different computational and storage resources and they are all limited.

B.QUANTIZATION

For some resource-constrained edge devices, the ordinary operations based on FP32 may exceed their computing capacity. In this case, quantization is a kind of technique that is commonly used in neural network compression. Generally speaking, quantization is implemented by converting the FP32 values to INT8 ones. But it is also practicable to use a lower bit width, such as XNOR [22], binary [23], or ternary [24] quantization. Based on whether it is deployed during the training phase, quantization is mainly divided into two categories, post-training quantization (PTQ) and quantization-aware training (QAT). For the first kind of quantization, PTQ usually quantizes the pre-trained models at the very beginning of the inference stage directly. He et al. [25] proved that 4-bit-quantized networks do not need to retrain, and proposed a Quasi-Lloyd-Max algorithm to minimize the error caused by 4-bit quantization. Fang et al. [26] provide a piecewise linear quantization (PWLQ) scheme for pre-trained models, to decompose the entire quantization range into non-overlapping regions of each tensor. However, some research [27,28] have shown that PTQ methods may not ensure the performance of the pre-trained model after quantization.

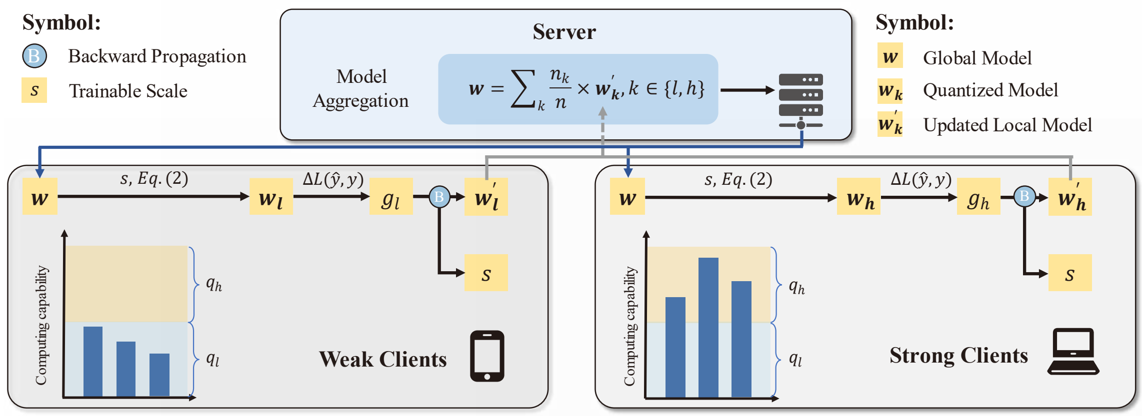

Figure 1 Workflow of QFL framework. The server first transmits a global model to all the selected clients (including strong ones and weak ones). Then, the selected clients quantize and train their local models by minimizing the loss between output $\hat{y}$ and ground truth y. Finally, the updated models from heterogeneous devices are uploaded to the server and aggregated to a new global model.

Different from PTQ, QAT applies quantization throughout the whole training process, that is, models in INT8 format or even lower bit width have been optimized during the model training process. Zhou et al. [29] designed a new quantization method called Explicit Loss-error-aware Quantization (ELQ) according to Taylor expansion, while a novel training strategy called incremental quantization is proposed. Dong et al. [30] proposed HAWQ, a method based on the Hessian matrix for fully automatic determination of mixed-precision quantization. The main idea of HAWQ is to make use of the second-order information provided by the Hessian matrix to determine the relative quantization precision of each block. Zhao et al. [31] observed that the distribution of gradients cannot be regarded as Gaussian in the same way as weights. Based on this observation, they proposed Gradient Vectorized Quantization to capture the gradient distribution. Zhen et al. [32] proposed General Quantizer (GQ) with self-adjustable centroids in a mu-Law constrained space, to overcome the limitation that the quantization centroids have to be predetermined and fixed.

III. METHODOLOGY

A.PROBLEM FORMULATION

In this paper, we focus on how to implement federated learning on heterogeneous devices. Suppose we have N clients, including N_{m1} large clients and N_{m2} small ones with $N = N_{m1} + N_{m2}$. Each of the participated clients has its own dataset $D = \{D_1^h, D_2^h, \dots, D_{m1}^h, D_1^l, D_2^l, \dots, D_{m2}^l\}$ that is inaccessible to all the other clients. Here, h and l stand for high-performance client and low-performance client respectively. Our aim is to collectively train individual models $\{\varphi_1^h, \varphi_2^h, \dots, \varphi_{m1}^h, \varphi_1^l, \varphi_2^l, \dots, \varphi_{m2}^l\}$ for each client, utilizing their local datasets $\{D_1^h, D_2^h, \dots, D_{m1}^h, D_1^l, D_2^l, \dots, D_{m2}^l\}$, with the assistance of the central server, while maintaining data privacy by not exchanging sensitive information. The goal is to train the local models and minimize their local losses to obtain a convincing global model

$$\{\varphi_1^h, \dots, \varphi_{m1}^h\} = argmin\ \sigma\{L_1^h, \dots, L_{m1}^h\}$$
$$\{\varphi_1^l, \dots, \varphi_{m2}^l\} = argmin\sigma\{L_1^l, \dots, L_{m2}^l\} \quad (1)$$

where $L_i^t = L(\varphi_i^t, D_i^t; \boldsymbol{w}), i \in [1, max(m1, m2)], t \in \{h, l\}$, with $L(\cdot)$ representing the loss function, φ_i^t representing a local model on client i with type t, and $\boldsymbol{w}$ representing the global model.

B. QFL FRAMEWORK

Next, we introduce the details of our QFL framework to address the heterogeneity problem. The workflow of our framework is shown in Figure 1. The core concept of our framework is to allocate varying degrees of quantization to different clients based on their computing capabilities. Stronger clients make a higher-bit-width quantization to their network parameters, while weaker clients make a lower-bit-width one. In other words, we further reduce the bit width available for network parameters so that the model could be deployed on those clients with less computing and storage capacity. The heterogeneous clients with different capacities are assigned two different kinds of bit widths q_l and q_h accordingly, with $q_l < q_h$.

Algorithm 1 summarizes the overall framework of QFL. For the i-th round of communication, the server holds a global model $\boldsymbol{w_i}$. The server randomly selects m clients to form a random set N_i (m is determined jointly by C and N, and the number of elements in set N_i is equal to m). It's worth noting that the proportion for weak clients and strong clients is uncertain since N_i is randomly selected. The server transmits the global model $\boldsymbol{w_i}$ to all the clients in the random set N_i. Then, for a weak client k_s in the random set N_i, the first thing to do is to quantize the model and the input to q_s bits, and the quantization process can be described as:

$$w_{i_{quant}} = round(clamp\left(\frac{\boldsymbol{w_i}}{s}, B_n, B_p\right) \times s \qquad (2)$$

where $round(\cdot)$ means rounding the number to the nearest integer, and $clamp(x, a, b)$ sets values greater than b to b and values less than a to a. B_p and B_n is determined by the quantization bit. Given a quantization bit q_s, we have $B_p = 2^{q_s - 1} - 1$ and $B_n = -2^{q_s - 1}$. s stands for quantization scale, and we'll talk about how do to determine the value of s later. After the computing parameters are properly quantized, we apply optimization methods to train the network parameters. To be more specific, in the course of E rounds' local training, the training process can be formulated as:

$$w \leftarrow w - \eta g(w) - \beta w \qquad (3)$$

where η denotes the current learning rate, and β denotes the weight decay. For a selected strong client k_h, all procedures are the same as above, except that the quantization parameter is set to q_h with $q_h > q_l$.

Algorithm 1: The framework of FedHQ

Input: learning rate η, weight decay β, number of clients N, communication rounds R, local training epochs E, proportion of clients selected in each round C, local training batch size B, proportion of weak clients S, proportion of strong clients L $(S + L = 1)$, quantization bit widths q_s and q_l for weak and strong clients, local dataset for each client D_i^t.

Server executes:
  Initialize $\boldsymbol{w_0}$
  for each round $r = 1,2, \dots, R$ **do**
    $m \leftarrow max(C \times N, 1)$
    $N_r \leftarrow$ (random set of m clients)
    for each weak client $k_l \in N_r$ in parallel **do**
      $w_{r+1}^{k_l} \leftarrow ClientUpdate(k_l, \boldsymbol{w_r}, q_l, D^l)$
    end for
    for each strong client $k_h \in N_r$ in parallel **do**
      $w_{r+1}^{k_h} \leftarrow ClientUpdate(k_h, \boldsymbol{w_r}, q_h, D^h)$
    end for
    $\boldsymbol{w_{r+1}} \leftarrow WeightAgg(w_{r+1}^{k_s}, w_{r+1}^{k_l}, k_s, k_l \in N_r)$
  end for
  $\boldsymbol{ClientUpdate}(k_t, \boldsymbol{w}, q_t, D^t)$:
    $\boldsymbol{B} \leftarrow$ (split D^t into batches of size B)
    for each local epoch j from 1 to E **do**
      for batch $b \in \boldsymbol{B}$ **do**
        $w_{quant} \leftarrow Quant(w, q_t)$
        $w_{quant} \leftarrow w_{quant} - \eta g(w_{quant}) - \beta w_{quant}$
        Return w_{quant} to server
      end for
    end for

After all the selected clients finished their local training of E rounds, the server collects all the m local models and aggregate them to a new global model $\boldsymbol{w_{i+1}}$ and directly replace $\boldsymbol{w_i}$ with $\boldsymbol{w_{i+1}}$.

C. QUANTIZATION MODULE WITH TRAINABLE SCALES

In this section, we introduce our quantization strategy with trainable scaling factor. As we mentioned before, the quantization process of network parameter can be described as

$$x_{quant} = round(clamp\left(\frac{x}{s}, min, max\right) \times s. \qquad (4)$$

Algorithm 2: Trainable-scale quantization

Input: learning rate η, weight decay β, quantization bit width q, number of network layers Λ, local training epochs E, reminder term ϵ, input x, weight $\boldsymbol{w}$, output y.

Client executes:

for each layer in a network λ=1,2,…, Λ **do**

  Initialize $s_\lambda^0 = \frac{|\max(\lambda)|}{2^{q-1}-1}$

  $q_{max} = 2^{q-1} - 1$

  $q_{min} = -2^{q-1}$

end for

for each local training epoch e=1,2,…,E **do**

  for each layer in a network λ=1,2,…, Λ **do**

    $x_q \leftarrow round(clamp\left(\frac{x}{s_\lambda^{e-1}+\epsilon}, q_{min}, q_{max}\right) \times s$

    $w_q \leftarrow round(clamp\left(\frac{w_\lambda}{s_\lambda^{e-1}+\epsilon}, q_{min}, q_{max}\right) \times s$

    $y \leftarrow w_q \odot x_q$

  end for

  while in backward propagation **do**

    for each layer in a network λ=1,…, Λ **do**

      $g(s_\lambda^{e-1}) \leftarrow \nabla L$

      $s_\lambda^e \leftarrow s_\lambda^{e-1} - \eta g(s_\lambda^{e-1}) - \beta s_\lambda^{e-1}$

    end for

  end while

end for

Then, we start to introduce our quantization module, as shown in Algorithm 2. First of all, the initial scaling factor s needs to be determined according to each layer in a neural network, which can be denoted as:

$$s_\lambda^0 = \frac{|\max(\lambda)|}{2^{q-1}-1} \tag{5}$$

where λ represents the λ-th layer in the network, and q refers to the quantization bit width. After initialization, for the i-th epoch of a local training on a client, in the λ-th layer, the input and weight are quantized using scaling factor s_λ^{i-1} together with Eq.(2). Then, the quantized parameters are used to perform the corresponding operation (convolution or matrix multiplication) to obtain an output matrix for transmission to the next layer of the network.

The process of backward propagation demonstrates the particularity of the trainable scaling factors. In detail, our scaling factor is not considered as a hyperparameter like the learning rate, but as a parameter that can be updated like the weights of neural networks. In this case, in backward propagation, for each layer of a neural network, the gradient of scaling factors with respect to the overall loss function is obtained. And the gradient, combined with an optimizer, is used to update scaling factors for each layer. It is worth mentioning that, the rounding function used in neural network quantization usually rounds a number to the nearest integer. On this occasion, during the gradient computation in the process of backward propagation, the gradient is usually counted as 0 and therefore affects the weight update process of the whole model. One common way to address this issue would be approximating the gradient by straight-through estimator (STE) [33], which regards the gradient of the rounding function as one:

$$\frac{\partial round(x)}{\partial x} \approx 1 \tag{6}$$

Combined with the quantization process formula, the gradient of the scaling factors in each layer can be defined as:

$$\begin{aligned}\frac{\partial x_{quant}}{\partial s} &= \frac{\partial\, round(clamp\left(\frac{x}{s}, min, max\right)}{\partial s} \times s \\ &\quad + round(clamp\left(\frac{x}{s}, min, max\right) \\ &\approx \frac{\partial\, clamp\left(\frac{x}{s}, min, max\right)}{\partial s} \times s \\ &\quad + round(clamp\left(\frac{x}{s}, min, max\right) \\ &= \begin{cases} -\left(\frac{x}{s}\right) + round\left(\frac{x}{s}\right), min < \frac{x}{s} < max \\ max, \frac{x}{s} \geq max \\ min. \frac{x}{s} \leq min \end{cases}\end{aligned} \tag{7}$$

Guided by Eq.(7), backward propagation blocking caused by the round function can be resolved and the weights and scaling factors for each layer of the neural network can be updated normally by backward

Table 1 Experimental results on MNIST and Fashion-MNIST datasets

Dataset	Network	Method	Top-1 Acc.(%)	BOPs(G)	BOPs Redu.(%)	Comm. Amount(GB)	Comp. Rate
MNIST	2NN	FedAvg	**96.99**	9.61×10^6	-	7.58×10^3	-
		FedProx	96.74	9.61×10^6	-	7.58×10^3	-
		FQL	96.77	$\mathbf{3.76 \times 10^5}$	**96.09**	$\mathbf{4.5 \times 10^3}$	**1.69**×
	CNN1	FedAvg	**98.68**	4.65×10^8	-	6.34×10^4	-
		FedProx	98.39	4.65×10^8	-	6.34×10^4	-
		FQL	98.55	$\mathbf{1.82 \times 10^7}$	**96.09**	$\mathbf{3.77 \times 10^4}$	**1.681**×
Fashion-MNIST	2NN	FedAvg	**87.57**	9.61×10^6	-	7.58×10^3	-
		FedProx	87.24	9.61×10^6	-	7.58×10^3	-
		FQL	87.30	$\mathbf{3.76 \times 10^5}$	**96.09**	$\mathbf{4.5 \times 10^3}$	**1.69**×
	CNN1	FedAvg	**90.05**	4.65×10^8	-	6.34×10^4	-
		FedProx	89.36	4.65×10^8	-	6.34×10^4	-
		FQL	89.42	$\mathbf{1.82 \times 10^7}$	**96.09**	$\mathbf{3.77 \times 10^4}$	**1.681**×

propagation combined with the optimizer.

IV. EXPERIMENTAL RESULTS

A. EXPERIMENTAL SETTING

a. Datasets and Models

We evaluate our QFL framework on three different datasets, MNIST [34], Cifar10 [35], and Fashion-MNIST[36], all of which are widely used to verify the effectiveness of methods for image classification tasks.

We use four different models, two for MNIST and Fashion-MNIST, and three for Cifar10 (we adopted a model on all of the datasets): (1) A three-layer Multi-Layer Perception (MLP) with 784 input features and 200 hidden features, which we denote as 2NN. (2) A model with two convolutional layers and two linear layers, which we denote as CNN1. More specifically, both of the convolutional layers adopt a 5×5 convolutional kernel, and the first convolutional layer contains 32 output channels and the second one contains 64 output channels. The number of hidden features for linear layer is 512. (3) A model with three convolutional layers and two linear layers, which we denote as CNN2. More specifically, all of the convolutional layers adopt a 5×5 convolutional kernel, and the first convolutional layer contains 32 output channels and the second and third one contains 64 output channels. The number of hidden features for linear layer is 512. (4) A modified model based on VGG11 network, which we denote as VGG11M. Compared to VGG11, the model Compared with VGG11, the number of output channels for each convolutional layer of the model is reduced to half of the original number. In addition, the number of in and out features for the three linear layers is changed to (128, 128), (128, 128), and (128, 10), respectively, and all the ReLu and dropout layers between linear layers are removed.

b. Evaluation Metrics

To quantitively evaluate the performance of our proposed QFL framework, we apply overall accuracy, together with bit operations (BOPs) and communication amount. For overall accuracy, we demonstrate the Top-1 accuracy for MNIST and Cifar10 datasets. The bit operations (BOPs) criterion, proposed by [37] has been adopted by some early work [38-41]. For a convolutional layer, BOPs can be formulated by

$$BOPs = k^2 * C_{in} * C_{out} * B_w * B_a * X_{out} * Y_{out} \quad (8)$$

where C_{in} and C_{out} refer to the number of input channels and output channels of the convolutional layer, and k^2 refers to the kernel size. B_w and B_a represents the bit width for weight and activation, and $X_{out} * Y_{out}$ represents the size of the output feature map. While, for a linear layer, BOPs can be formulated by

$$BOPs = C_{in} * C_{out} * B_w * B_a \quad (9)$$

where C_{in} and C_{out} refer to the number of input features and output features of the linear layer.

As for communication amount, it can reflect the performance of a federated learning framework to some extent by comparing the amount of information transferred between the server and the clients.

c. Implementation Details

Table 2 Experimental results on Cifar10 dataset

Network	Partition	Method	Top-1 Acc.(%)	BOPs(G)	BOPs Redu.(%)	Comm. Amount(GB)	Comp. Rate
CNN1	IID	FedAvg	**70.95**	6.98×10^8	-	8.22×10^4	-
		FedProx	64.34	6.98×10^8	-	8.22×10^4	-
		FQL	70.05	$\mathbf{2.73 \times 10^7}$	**96.10**	4.88×10^4	**1.683**×
	Non-IID	FedAvg	59.19	6.98×10^8	-	8.22×10^4	-
		FedProx	**60.55**	6.98×10^8	-	8.22×10^4	-
		FQL	59.03	$\mathbf{2.73 \times 10^7}$	**96.10**	4.88×10^4	**1.683**×
CNN2	IID	FedAvg	**72.93**	8.01×10^8	-	2.61×10^4	-
		FedProx	63.22	8.01×10^8	-	2.61×10^4	-
		FQL	72.45	$\mathbf{3.13 \times 10^7}$	**96.09**	1.55×10^4	**1.683**×
	Non-IID	FedAvg	65.84	8.01×10^8	-	2.61×10^4	-
		FedProx	**67.07**	8.01×10^8	-	2.61×10^4	-
		FQL	65.12	$\mathbf{3.13 \times 10^7}$	**96.09**	1.55×10^4	**1.683**×
VGG11M	IID	FedAvg	**74.8**	4.65×10^8	-	3.23×10^4	-
		FedProx	71.94	4.65×10^8	-	3.23×10^4	-
		FQL	72.15	$\mathbf{1.82 \times 10^7}$	**81.25**	1.92×10^4	**1.682**×
	Non-IID	FedAvg	56.71	4.65×10^8	-	3.23×10^4	-
		FedProx	62.34	4.65×10^8	-	3.23×10^4	-
		FQL	**62.75**	$\mathbf{1.82 \times 10^7}$	**81.25**	1.92×10^4	**1.682**×

The proposed framework is implemented on NVIDIA GeForce RTX 3090 Ti using PyTorch. Among the four types of backbone, 2NN and CNN1 are used for training and testing on MNIST dataset, while CNN1, CNN2 and VGG11M are trained and tested on Cifar10 dataset. Both of the datasets are equally divided among weak and strong clients. In all of our experiments, number of clients in total K is set to 100. The proportion of clients selected in each round C is set to 0.1. The number of local training epochs E is 10. The number of communication rounds R is set to 500. Quantization bit widths q_l and q_h for weak and strong clients are set to 4 and 8, accordingly. The proportion of weak clients S and that of strong clients L are both set to 0.5. As for optimizer, we adopt Adam optimizer. We set learning rate $\eta = 0.001$, and weight decay $\beta = 0.0005$.

B. EXPERIMENTS AND COMPARISONS ON DATASETS

Detailed experimental results, including overall accuracy, number of BOPs and the communication amount for 2NN and CNN1 on MNIST and Fashion-MNIST datasets, are shown in Table 1. As observed from the table, by quantizing the weights and activation functions, the computational cost of both the two types of networks can be significantly reduced (about 4% of the original BOPs), with only a marginal decrease in accuracy. In addition, since all the client quantizes the weights in the model before uploading the updated local model, the amount of communication between the client and the server is also significantly reduced.

Table 2 shows the above-mentioned overall accuracy, number of BOPs and the communication amount for CNN2 and VGG11M on Cifar10 dataset. From Table 2, we can see that due to trade-off considerations, both BOPs and communication amount are reduced significantly, with only a small decrease in accuracy. Besides, our QFL framework even exceeds the accuracy of FedAvg and FedProx on some networks with Non-IID data distribution.

V. CONCLUSION AND FUTURE WORK

Based on two challenging questions, this paper presents a framework, called QFL, to solve the problems caused by client-side heterogeneity and data noise due to low bit-width quantization. QFL allocate different quantization bit widths for strong and weak clients, and all of the clients can contribute to training a global model stored on the server. In addition, we introduce a quantization module with trainable scaling factors, which improves the performance of parameter quantization. Our approach is extensively validated through experiments, showcasing its effectiveness and sophistication.

For future work, we will take into account that heterogeneous nodes will produce different quantization errors, and adopt a better aggregation method to replace average aggregation.

References

[1] J. A. Ruiz-de Azua, L. Fernandez, J. F. Munoz, M. Badia, R. Castella, ˜ C. Diez, A. Aguilella, S. Briatore, N. Garzaniti, A. Calveras, A. Golkar, and A. Camps, “Proof-of-concept of a federated satellite system between two 6-unit cubesats for distributed earth observation satellite systems,” in IGARSS 2019 - 2019 IEEE International Geoscience and Remote Sensing Symposium, 2019, pp. 8871–8874.

[2] A. Singh and K. Gaurav, “Deep learning and data fusion to estimate surface soil moisture from multi-sensor satellite images,” Scientific Reports, vol. 13, no. 1, p. 2251, 2023.

[3] A. Toker, Q. Zhou, M. Maximov, and L. Leal-Taixe, geo-localization,” in Proceedings of the IEEE/CVF Conference on Computer Vision and Pattern Recognition, 2021, pp. 6488–6497.

[4] Dash, B.; Sharma, P.; and Ali, A. 2022. Federated learning for privacy-preserving: A review of PII data analysis in Fintech. International Journal of Software Engineering & Applications (IJSEA), 13(4).

[5] Xu, J.; Glicksberg, B. S.; Su, C.; Walker, P.; Bian, J.; and Wang, F. 2021. Federated learning for healthcare informatics. Journal of Healthcare Informatics Research, 5: 1–19.

[6] Smith, V.; Chiang, C.-K.; Sanjabi, M.; and Talwalkar, A. S. 2017. Federated multi-task learning. Advances in Neural Information Processing Systems, 30.

[7] McMahan, B.; Moore, E.; Ramage, D.; Hampson, S.; and y Arcas, B. A. 2017. Communication-efficient learning of deep networks from decentralized data. In Proceedings of Artificial Intelligence and Statistics, 1273–1282.

[8] Bonawitz, K., Eichner, H., Grieskamp, W., Huba, D., Ingerman, A., Ivanov, V., ... & Roselander, J. (2019). Towards federated learning at scale: System design. *Proceedings of machine learning and systems*, *1*, 374-388.

[9] Li, D.; and Wang, J. 2019. FedMD: Heterogenous federated learning via model distillation. arXiv preprint arXiv:1910.03581.

[10] Liu, R.; Wu, F.; Wu, C.; Wang, Y.; Lyu, L.; Chen, H.; and Xie, X. 2022. No one left behind: Inclusive federated learning over heterogeneous devices. In Proceedings of the 28th ACM SIGKDD Conference on Knowledge Discovery and Data Mining, 3398–3406.

[11] Liu, Y.; Kang, Y.; Xing, C.; Chen, T.; and Yang, Q. 2020. A secure federated transfer learning framework. IEEE Intelligent Systems, 35(4): 70–82.

[12] Wang, H.; Yurochkin, M.; Sun, Y.; Papailiopoulos, D.; and Khazaeni, Y. 2020. Federated learning with matched averaging. arXiv preprint arXiv:2002.06440.

[13] Sattler, F.; Wiedemann, S.; Muller, K.-R.; and Samek, W. ¨ 2019. Robust and communication-efficient federated learning from non-iid data. IEEE Transactions on Neural Networks and Learning Systems, 31(9): 3400–3413.

[14] Liang, P. P.; Liu, T.; Ziyin, L.; Allen, N. B.; Auerbach, R. P.; Brent, D.; Salakhutdinov, R.; and Morency, L.-P. 2020. Think locally, act globally: Federated learning with local and global representations. arXiv preprint arXiv:2001.01523.

[15] Li, T.; Hu, S.; Beirami, A.; and Smith, V. 2021. Ditto: Fair and robust federated learning through personalization. In International Conference on Machine Learning, 6357–6368.

[16] Zhang, J.; Hua, Y.; Wang, H.; Song, T.; Xue, Z.; Ma, R.; and Guan, H. 2023. Fedala: Adaptive local aggregation for personalized federated learning. In Proceedings of the AAAI Conference on Artificial Intelligence, volume 37, 11237– 11244.

[17] Itahara, S.; Nishio, T.; Koda, Y.; Morikura, M.; and Yamamoto, K. 2021. Distillation-based semi-supervised federated learning for communication-efficient collaborative training with non-iid private data. IEEE Transactions on Mobile Computing, 22(1): 191–205.

[18] Konečný, J., McMahan, H. B., Yu, F. X., Richtárik, P., Suresh, A. T., & Bacon, D. (2016). Federated learning: Strategies for improving communication efficiency. *arXiv preprint arXiv:1610.05492*.

[19] Caldas, S.; Konecny, J.; McMahan, H. B.; and Talwalkar, ˇ A. 2018. Expanding the reach of federated learning by reducing client resource requirements. arXiv preprint arXiv:1812.07210.

[20] Hinton, G. E.; Srivastava, N.; Krizhevsky, A.; Sutskever, I.; and Salakhutdinov, R. R. 2012. Improving neural networks by preventing co-adaptation of feature detectors. arXiv preprint arXiv:1207.0580.

[21] Wu, C.; Wu, F.; Lyu, L.; Huang, Y.; and Xie, X. 2022. Communication-efficient federated learning via knowledge distillation. Nature communications, 13(1): 2032.

[22] Rastegari, M.; Ordonez, V.; Redmon, J.; and Farhadi, A.

2016. XNOR-Net: Imagenet classification using binary convolutional neural networks. In Proceedings of the European Conference on Computer Vision (ECCV), 525–542. Springer.

[23] Kim, M.; and Smaragdis, P. 2016. Bitwise neural networks. arXiv preprint arXiv:1601.06071.

[24] Zhu, C.; Han, S.; Mao, H.; and Dally, W. J. 2016. Trained ternary quantization. arXiv preprint arXiv:1612.01064.

[25] He, C.; Ceyani, E.; Balasubramanian, K.; Annavaram, M.; and Avestimehr, S. 2022. SpreadGNN: Decentralized multitask federated learning for graph neural networks on molecular data. In Proceedings of the AAAI Conference on Artificial Intelligence, volume 36, 6865–6873.

[26] Fang, J.; Shafiee, A.; Abdel-Aziz, H.; Thorsley, D.; Georgiadis, G.; and Hassoun, J. H. 2020. Post-training piecewise linear quantization for deep neural networks. In Computer Vision–ECCV 2020: 16th European Conference, Glasgow, UK, August 23–28, 2020, Proceedings, Part II 16, 69–86. Springer.

[27] Jacob, B.; Kligys, S.; Chen, B.; Zhu, M.; Tang, M.; Howard, A.; Adam, H.; and Kalenichenko, D. 2018. Quantization and training of neural networks for efficient integer-arithmetic-only inference. In Proceedings of the IEEE conference on Computer Vision and Pattern Recognition, 2704–2713.

[28] Krishnamoorthi, R. 2018. Quantizing deep convolutional networks for efficient inference: A whitepaper. arXiv preprint arXiv:1806.08342.

[29] Zhou, A.; Yao, A.; Wang, K.; and Chen, Y. 2018. Explicit Loss-Error-Aware Quantization for Low-Bit Deep Neural Networks. In Proceedings of the 2018 IEEE/CVF Conference on Computer Vision and Pattern Recognition (CVPR), 9426–9435.

[30] Dong, Z.; Yao, Z.; Gholami, A.; Mahoney, M. W.; and Keutzer, K. 2019. HAWQ: Hessian aware quantization of neural networks with mixed-precision. In Proceedings of the IEEE/CVF International Conference on Computer Vision (ICCV), 293–302.

[31] Zhao, K.; Huang, S.; Pan, P.; Li, Y.; Zhang, Y.; Gu, Z.; and Xu, Y. 2021. Distribution adaptive int8 quantization for training cnns. In Proceedings of the AAAI Conference on Artificial Intelligence, volume 35, 3483–3491.

[32] Zhen, K.; Radfar, M.; Nguyen, H.; Strimel, G. P.; Susanj, N.; and Mouchtaris, A. 2023. Sub-8-bit quantization for on-device speech recognition: a regularization-free approach. In 2022 IEEE Spoken Language Technology Workshop (SLT), 15–22. IEEE.

[33] Bengio, Y.; Leonard, N.; and Courville, A. 2013. Estimat- ´ ing or propagating gradients through stochastic neurons for conditional computation. arXiv preprint arXiv:1308.3432.

[34] LeCun, Y.; Bottou, L.; Bengio, Y.; and Haffner, P. 1998. Gradient-based learning applied to document recognition. Proceedings of the IEEE, 86(11): 2278–2324.

[35] Krizhevsky, A.; Hinton, G.; et al. 2009. Learning multiple layers of features from tiny images.

[36] Xiao, H.; Rasul, K.; and Vollgraf, R. 2017. Fashion-MNIST: a novel image dataset for benchmarking machine learning algorithms. arXiv preprint arXiv:1708.07747.

[37] Baskin, C.; Liss, N.; Schwartz, E.; Zheltonozhskii, E.; Giryes, R.; Bronstein, A. M.; and Mendelson, A. 2021. UNIQ: Uniform noise injection for non-uniform quantization of neural networks. ACM Transactions on Computer Systems (TOCS), 37(1-4): 1–15.

[38] Hawks, B.; Duarte, J.; Fraser, N. J.; Pappalardo, A.; Tran, N.; and Umuroglu, Y. 2021. Ps and Qs: Quantization-aware pruning for efficient low latency neural network inference. Frontiers in Artificial Intelligence, 4: 676564.

[39] Pappalardo, A.; Umuroglu, Y.; Blott, M.; Mitrevski, J.; Hawks, B.; Tran, N.; Loncar, V.; Summers, S.; Borras, H.; Muhizi, J.; et al. 2022. QONNX: Representing Arbitrary Precision Quantized Neural Networks. arXiv preprint arXiv:2206.07527.

[40] Yao, Z.; Dong, Z.; Zheng, Z.; Gholami, A.; Yu, J.; Tan, E.; Wang, L.; Huang, Q.; Wang, Y.; Mahoney, M.; et al. 2021. HAWQ-V3: Dyadic neural network quantization. In Proceedings of the International Conference on Machine Learning (ICML), 11875–11886.

[41] Xie, W.; Fan, X.; Zhang, X.; Li, Y.; Sheng, M.; and Fang, L. 2023. Co-Compression via Superior Gene for Remote Sensing Scene Classification. IEEE Transactions on Geoscience and Remote Sensing, 61: 1–12.

A Multi-Branch Hierarchical Feature Extraction Network Combining Sentinel-1 and Sentinel-2 for Yellow River Delta Wetlands Classification

LI Xinhao[1], LIU Mingwei[1], Dou Qingwen[2],XU Mingming[1],LIU Shanwei[1],SHENG Hui[1]

Abstract—**The classification of wetlands in the Yellow River Delta is important for the monitoring of vegetation dynamics, rational resource utilization, and ecosystem protection. In this paper, the multi-temporal Sentinel-1 and Sentinel-2 data from 2021 are used to extract 168 features about spectral, index, texture, and polarization scattering. And based on the multi-source features, a novel multi-branch hierarchical feature extraction network (MHFE) is designed to classify the wetlands in the Yellow River Delta. By virtue of the multi-branch characteristics, the proposed MHFE can target the processing data with different features. The network includes the attention convolution module and fuzzy information module designed according to the characteristics of the data. The results show that the overall accuracy of multi-source features can reach 87.55% when classifying collaboratively, which is significantly higher than that of single-source features, and the fusion of multi-source data helps to improve the accuracy of wetland classification. Comparing with a variety of advanced deep learning classifiers, the proposed MHFE has the highest overall accuracy, which verifies that the application of this model to classify the wetlands in the Yellow River Delta has validity.**

Li Xinhao, Liu Mingwei, XU Mingming,Liu Shanwei,Sheng Hui are with the College of Oceanography and Space Informatics, China University of Petroleum (East China), Qingdao 266580, China

Qingwen Dou is with the Land Surveying and Mapping Institute of Shandong Province, Jinan 250102, China

This work was supported by the National Natural Science Foundation of China under Grant 62071492.

Keywords — **Multi-source data fusion; Self-attention mechanism; Wetland classification; Yellow River estuary**

I. INTRODUCTION

Wetlands, along with oceans and forests, comprise the three major global ecosystems. Wetlands are renowned as the kidneys of the Earth, natural reservoirs, and biodiversity hotspots. Coastal wetlands, located in the transitional zones between land and sea, demonstrate distinctiveness in terms of maintaining ecological balance, providing resource support, improving environmental quality, reducing disaster risks, and promoting socio-economic development. The Yellow River Delta wetlands are one of the world's largest, most well-preserved, and youngest temperate coastal wetlands. However, under the dual influence of human activities and climate change, the Yellow River Delta wetlands are facing increasingly serious threats, including shrinking in size, systematic degradation, and deteriorating habitats. Therefore, conducting detailed classification and accurate monitoring of the wetlands in the Yellow River Delta is an essential prerequisite for subsequent management and protection efforts.

As a result of the launching and networking of Earth observation satellites, multi-source remote sensing data have been gradually applied to the classification of coastal wetlands. Optical imagery provides rich spectral information but is limited by cloudy, rainy, and foggy conditions, resulting in reduced availability and making it challenging to distinguish land cover with similar spectral reflectance. Synthetic Aperture Radar (SAR) has strong penetration capabilities and is less affected by weather conditions. It can reflect vegetation structural features, detect hydrological features, and also overcome the limitations of optical images in monitoring coastal wetlands. Single-temporal remote sensing data are not seasonal and cyclical, supplemented with multi-time-phase remote sensing data can reflect the climatic and temporal nature. Studies have shown that integrating multi-temporal images results in higher overall classification accuracy compared to single-temporal images[1]. This indicates that the collaborative classification of multi-temporal optical data and radar data is a favorable choice for enhancing the accuracy of wetland land cover classification [2].

Before the rise of deep learning technology, wetland classification was often constrained by methods that combined feature information with machine learning classification. Wetland classification in the Yellow River Delta region was achieved through the collaborative use of radar data and multispectral data using methods such as Maximum Likelihood, Decision Trees, and Support Vector Machine[3]. Zhang[4] used a random forest algorithm combined with object-oriented to realize the accurate classification of typical wetland vegetation in the Yellow River Mouth Protected Area. By integrating multispectral remote sensing data, SAR data, and topographic data, wetlands were accurately extracted using the Random Forest algorithm, and the classification map can be directly employed for sustainable management, ecological conservation, and evaluation of coastal wetlands[5].

With the development of relevant technologies, deep learning has gained widespread attention and is being applied in various fields. Therefore, constructing deep classification architectures to achieve fine-grained classification of coastal wetlands has distinct advantages and development potential. To fully exploit the multi-source data features, researchers often extract the potential information of the image using preprocessing, such as vegetation index, red edge index, texture features, polarization features. Based on the five types of feature indicators, such as water body index extracted from Sentinel-1 and Sentinel-2 time-series data, the Random Forest algorithm, Support Vector Machine algorithm, and Deep Neural Network algorithm were used for comparative classification, and the purpose of the exploration was to find the optimal combination of features and classification strategies for wetland vegetation classification[6]. Han[7] conducted feature exploration using a Convolutional Neural Network (CNN) based on feature intersection learning. The research indicates that this model exhibits good effectiveness and generalization in the scenario of coastal wetland classification with high spectral and multispectral fusion.

However, existing deep learning networks often do not do feature differentiation for the input feature data, and extract features according to the unified features directly, and lack of network design for feature extraction of different data. Designing a network suitable for multi-source data containing various features is essential for wetland classification. Therefore, we have proposed a multi-branch hierarchical feature extraction network (MHFE)designed for different feature data. The different branches of the network can handle input data with different features, enabling targeted and efficient feature extraction. At the same time, we have designed two modules based on the characteristics of the data. These are the attention convolution module(ACM), which increases the focus on high-weight pixels, and the fuzzy information module(FIM), which reduces the impact of noisy data. The main contributions can be summarized as follows:

1) MHFE has the ability to branch to process multiple feature data through multiple branches. It can selectively handle data with a large amount of information and rich details,data with low information content and simplicity, data with prominent features, and data with high noise levels and unclear information.

2) The ACM possesses efficient capability for

extracting detailed features. It can enhance the attention to important information and is suitable for processing feature data rich in details.

3) The FIM can extract global information from feature data and effectively reduce the introduction of noise. It can be used for processing feature data with blurred details and high levels of noise.

The remaining sections of this paper are organized as follows: In Section II, the extent of wetlands in the Yellow River Delta and the use of multi-source data are expounded. Section III describes the details of proposed method MHFE. The experimental evaluation are presented in Section IV. Finally, section V provides a conclusion to this paper.

II. STUDY AREA AND DATA

A. STUDY AREA

This study selected the entrance of the Yellow River Delta into the sea(119°4′E-119°18′E,37°38′N-37°49′N) as the research area. It is located between Bohai Bay and Laizhou Bay in a mid-latitude region with a temperate continental monsoon climate characterized by cold winters and hot summers, with rainfall occurring during the warm season. The annual average precipitation in this area is 560 mm. The common wetland vegetation types include native vegetation such as Phragmites australis, Tamarix chinensis, Suaeda and willow forests, as well as the introduced exotic species of Spartina alterniflora. Fig.1 shows the geographical location of the study area.

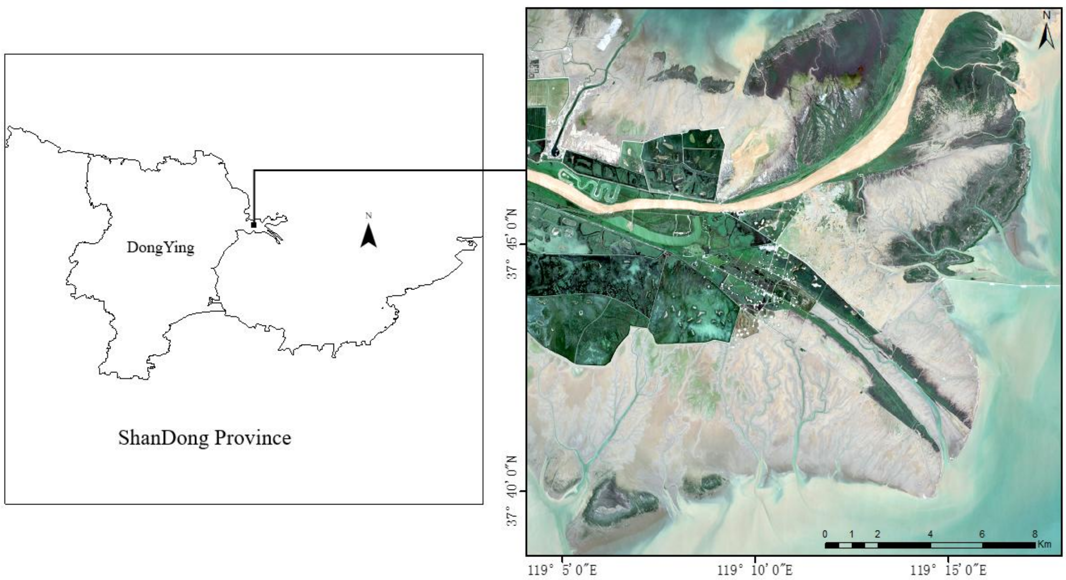

Figure 1 The geographical location of the study area

B. DATA

This study utilizes two main categories of data: satellite data and sample point data.

The satellite data includes Sentinel-1 and Sentinel-2 data, all of which were downloaded from the Copernicus Open Access Hub. Sentinel-1 consists of two satellites, S1A and S1B, which orbit at an altitude of approximately 700 km. They have a spatial resolution of 5 m × 20 m and revisit the same area every 6 days. Sentinel-1 is equipped with a SAR that provides C-band radar data in dual polarization. It is not restricted by cloud cover, rainfall, or lighting conditions, enabling it to provide images regardless of the time of day or weather conditions. Sentinel-2 carries the Multispectral Imager (MSI), which provides high-resolution multispectral imagery up to 290 km wide, covering 13 spectral bands. Sentinel 2 parameters for each band are shown in Tab.1.

C. DATA PREPROCESSING

Get 2021 Sentinel-1 IW Level-1 Ground Range Detected (GRD)data for 4 views in spring, summer, autumn and winter. Extraction of backward scattering coefficients and polarisation features from Sentinel-1 data, with pre-processing operation steps including Orbit Correction, Thermal Noise Removal, Radiometric Calibration, Refined Lee Filtering, Terrain Correction, Polarisation Decomposition, and Cropping. To acquire cloud-free or low-cloud Sentinel-2 Multi Spectral Instrument(MSI) Level-2A data for the year 2021, covering all four seasons, and perform preprocessing operations including Resampling, Band Synthesis, and Cropping.Project the spectral data and SAR data into the WGS 1984 UTM Zone 50N coordinate system. Finally, the spectral data were aligned with the SAR data pixel by pixel to obtain a multi-source feature dataset. Sample point data, combined with on-site survey photos, high-resolution images from Google Earth, and historical records, were manually interpreted. Pure image elements were selected to classify eight wetland feature types, namely, Suaeda salsa, Natural willow forests, Miscanthus, Reeds, Tamarisks, Arable land, Water bodies, Tidal flats, with a total number of 16,102 samples. Tab.2 provides detailed information about the research data, while Tab.3 presents details about the training, validation, and testing samples.

Table 1 Sentinel-2 Spectral Band Information

Waveband Number	Sentinel-2A		Sentinel-2B		Spatial Resolution (m)	Main Application
	Centre Wavelength (nm)	Bandwidth (nm)	Centre Wavelength (nm)	Bandwidth (nm)		
1	442.7	21	442.7	21	60	Aerosol
2	492.4	66	492.1	66	10	Blue
3	559.8	36	559.0	36	10	Green
4	664.6	31	664.9	31	10	Red
5	704.1	15	703.8	16	20	Red Edge 1
6	740.5	15	739.1	15	20	Red Edge 2
7	782.8	20	779.7	20	20	Red Edge 3
8	832.8	106	832.9	106	10	NIR
8A	864.7	21	864.0	22	20	Narrow NIR
9	945.1	20	943.2	21	60	Water vapour
10	1373.5	31	1376.9	30	60	SWIR–Cirrus
11	1613.7	91	1610.4	94	20	SWIR 1
12	2202.4	175	2185.7	185	20	SWIR 2

Table 2 Detailed information on the study data

Seasonality	Sentine-1	Sentine-2
Winter	2021-02-20	2021-02-24
Spring	2021-05-06	2021-05-06
Summer	2021-07-25	2021-07-23
Autumn	2021-10-13	2021-10-15

Table 3 The detailed information of training, testing and validation sample

Ground Truth	No.	Color	Class	Train.	Val.	Test.
Yellow River Delta Dataset	1		Water body	355	355	6395
	2		Spartina alterniflora	128	128	2300
	3		Phragmites australis	68	68	1224
	4		Tamarix chinensis	5	6	97
	5		Suaeda salsa	35	35	632
	6		Tidal flat	187	187	3370
	7		Natural willow forest	20	19	346
	8		Cultivated land	7	7	128
			Total	805	805	14492

III. THE PROPOSED METHOD

A. FEATURE EXTRACTION

Spectral bands provide detailed surface information. Vegetation index, water body index can effectively differentiate between different types of land cover. Differences in vegetation growth in response to the red-edge index. Texture features describe the properties of the spatial distribution and arrangement of various details and structures in an image. Radar images are not easily disturbed by the external environment and are sensitive to information on vegetation structure. Polarisation features improve accuracy of land cover classification. Coastal wetlands are mainly composed of vegetation and water. Therefore, in order to characterise the wetland vegetation, hydrology and soil, this study uses preprocessed four Sentinel-1 images and four Sentinel-2 images to extract the spectral bands, water index, vegetation index, red-edge index, texture features and polarisation features for each image. In this case, except for the radar backscatter coefficient and polarisation features extracted from the Sentinel-1 data, the rest of the features are extracted or calculated from the Sentinel-2 data. Specific information for each categorical feature is shown inTab.4.

Table 4 Introduction of Characteristic Variables

Feature index	Index abbreviation	Description of features	Number of features
Spectral feature group	Band	B2,B3,B4,B5,B6,B7,B8,B8a,B11,B12	40
Water body-vegetation-soil index group	NDVI	(B8-B4)/(B8+B4)	28
	DVI	B8-B4	
	RVI	B8/B4	
	EVI	2.5(B8-B4)/(B8+6.0B4-7.5B2+1)	
	SAVI	(B8-B)/(B8+B4+0.5)×(1+0.5)	
	NDWI	(B3-B8)/(B3+B8)	
	MNDWI	(B3 - B11)/(B3 + B11)	
Red border index group	NDVI_re1	(ρREG4-ρREG1)/(ρREG4+ρREG1)	40
	NDVI_re2	(ρREG4-ρREG2)/(ρREG4+ρREG2)	
	NDVI_re3	(ρREG4-ρREG3)/(ρREG4+ρREG3)	
	ND_re1	(ρREG2-ρREG1)/(ρREG2+ρREG1)	
	ND_re2	(ρREG3-ρREG1)/(ρREG3+ρREG1)	
	CI_re	B8/ρREG3-1	
	CI_Green	B8/B3-1	
	RNDVI	(ρREG1-B4)/(ρREG1+B4)	
	RRI_1	B8/ρREG1	
	RRI_2	ρREG1/B4	
Texture feature group	GLCM_M	Mean	32
	GLCM_V	Variance	
	GLCM_H	Homogeneity	

	GLCM_C	Contrast	
	GLCM_D	Dissimilarity	
	GLCM_E	Entropy	
	GLCM_SM	Second Momen	
	GLCM_C	Correlation	
Radar polarisation feature group	S1_VV	VV	28
	S1_VH	VH	
	S1_VV-VH	VV-VH	
	S1_VV/VH	VV/VH	
	S1_A	Alpha	
	S1_ α	Anisotropy	
	S1_ H	Entropy	

Extracted ten spectral bands of Sentinel-2, with the removal of the coastal/aerosol B1 band, the water vapour B9 band and the cirrus B10 band. Seven vegetation, water, and soil indices reflecting the growth status, health, and climatic cycle of green vegetation, water distribution, and soil coverage were extracted. Extraction of 10 red-edge indices expressing plant leaf area and chlorophyll sensitivity. Extracted 8 texture features that present inter-pixel relationships and patterns. In order to avoid data redundancy, after principal component analysis of the spectral bands, the first principal component with the most information content was taken to do the grey scale covariance matrix GLCM processing. Seven polarisation features mapping the structure and spatial distribution of plant communities were extracted. There are a total of 168 features. The combination of multi-source remote sensing data and multi-feature information data complements each other, enhances the distinguishability of features, and has the prospect of stable reliability and wide application.

B.INTRODUCTION TO THE MHFE NETWORK

The multi-feature combination of feature data in this paper consists of multiple sources of satellite imagery, texture, polarization, and other multiple-feature information superimposed on the same spatial location. However, the design of existing deep learning classification networks tends to focus on single-feature data, which is challenging to fit the multi-feature data requirements and cannot effectively perform feature extraction. To better carry out feature extraction, we designed an MHFE that can be more targeted to multi-feature data for feature extraction based on the data characteristics, which contains an ACM and a FIM designed based on the data characteristics.

1) Introduction of the general network

The MHFE network structure is shown in Fig.3. The input data can be roughly categorized into four types of feature data superimposed as shown in Fig.2, which are $\boldsymbol{A} \in \mathrm{R}^{H\times W\times A1}$, $\boldsymbol{B} \in \mathrm{R}^{H\times W\times A2}$, $\boldsymbol{C} \in \mathrm{R}^{H\times W\times A3}$, $\boldsymbol{D} \in \mathrm{R}^{H\times W\times A4}$, where H is the image length and W is the image width; $A1$,$A2$,$A3$,$A4$ is the number of bands of the four types of data. First, we preprocess the data, respectively, the four types of data in accordance with the proportion of their bands, the dimensionality reduction. The feature maps after dimensionality reduction are $\boldsymbol{A}'$, $\boldsymbol{B}'$, $\boldsymbol{C}'$, $\boldsymbol{D}'$, where the bands of $\boldsymbol{A}'$,$\boldsymbol{B}'$,$\boldsymbol{C}'$,$\boldsymbol{D}'$ are $B1$,$B2$,$B3$,$B4$;$B1$：$B2$：$B3$：$B4$ =$A1$：$A2$：$A3$：$A4$.

(a) Spectral bands in July -Band8

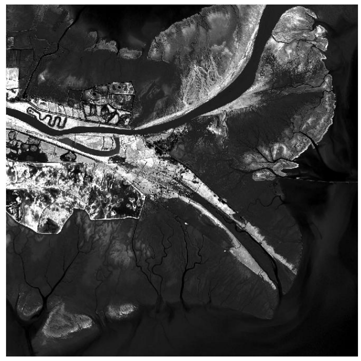

(b) Vegetation index in July -RRI2

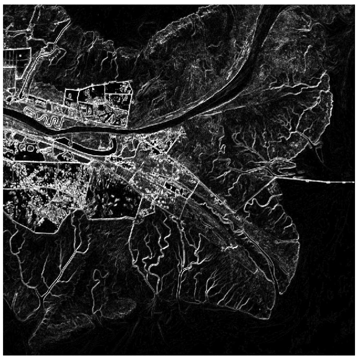

(c) Texture feature in July -Dissimilarity

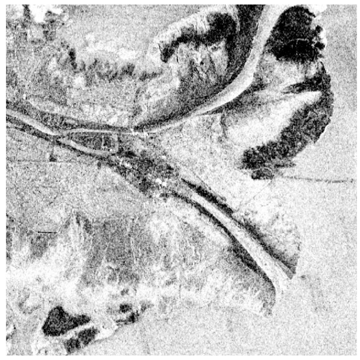

(d) Polarization feature in July -Anisotropy

Figure 2 Representative maps of the four types of feature images

Subsequently, a total of four branches were designed to handle different multi-featured data better. The input data for branch 1 is $\boldsymbol{A}'$,respectively, passed through the convolution module and the ACM, and the output feature matrices are operated on each other. Branch 1 is designed mainly for feature maps with more details, such as Fig.2(a), where the main information extraction is carried out by convolution and ACM , focusing on the ACM to highlight the important information, which ensures that more information is extracted and reduces the missing information.The input data for branch 2 is $\boldsymbol{B}'$, which is subjected to the convolution module, multi-head self-attention module, and batch normalization, respectively. Branch 2 mainly targets the data with more prominent features, as in Fig.2(b).The input data of branch 3 are $\boldsymbol{C}'$, respectively, through the spatial attention module, the multi-head self-attention module, and the convolution module. Branch 3 is mainly for the image data that is more single prominent data, such as texture information, as in Fig.2(c). The input data of branch 4 are $\boldsymbol{D}'$,respectively, through the ACM, FIM. Branch 4 mainly focuses on feature data with fuzzy data, as in Fig.2(d), and extracts only its global features, while reducing the noise in the extracted data.The input data of branch 5 is the non-preprocessed data $\boldsymbol{X}$,which passes through the convolution module, the multi-head self-attention module, and the fully-connected layer. Branch 5 makes up for the missing global information due to the classification process and the lost information such as spatial due to dimensionality reduction by processing the unprocessed image data.

The feature maps obtained through each of the five branches are $\boldsymbol{A}' \in \mathrm{R}^{H\times W\times C}$, $\boldsymbol{B}' \in \mathrm{R}^{H\times W\times C}$, $\boldsymbol{C}' \in \mathrm{R}^{H\times W\times 1}$, $\boldsymbol{D}' \in \mathrm{R}^{H\times W\times 1}$, $\boldsymbol{X}' \in \mathrm{R}^{H\times W\times C}$. Subsequently, the $\boldsymbol{A}'$, $\boldsymbol{B}'$ is spliced in the spectral dimension and combined with $\boldsymbol{C}'$, $\boldsymbol{D}'$, $\boldsymbol{X}'$,respectively. The network

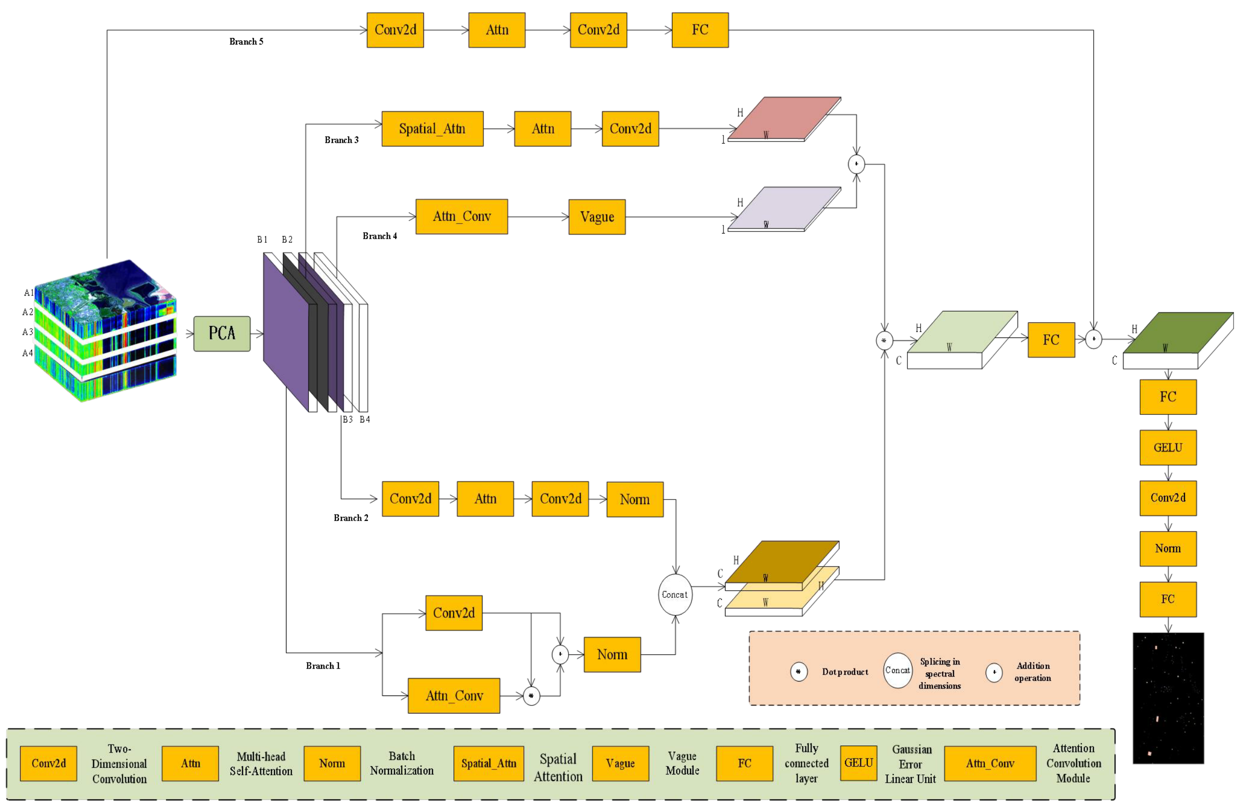

Figure 3 Structural design of MHFE

2) Attention Convolution Module

For informative images, single or simple convolutional kernel superposition is not good enough to extract effective information, so designing the attention convolutional module to ensure the efficient extraction of information. As shown in Fig.4, the ACM is composed of three branches, a, b, and c, respectively, which play an important information extraction, comprehensive information extraction, play the role of residuals, set the input feature map represented by $\boldsymbol{X}$, the specific operation is as follows:

The branch a consists of a convolutional kernel, a batch normalization, an activation function Relu, and a fully connected layer as follows:

$$\boldsymbol{X}_1 = \mathrm{FC}\big(\mathrm{Relu}(\mathrm{Batch\_norm}\big(\mathrm{Conv2D}(\boldsymbol{X})\big))\big) \tag{1}$$

where $\boldsymbol{X}_1$ is the feature matrix of the output of branch 1; Conv2D(●)is a 2D convolution operation; Batch_norm(●)is the batch normalization; Relu(●) is an abbreviation for modified linear unit, an activation function commonly used in neural networks; FC(●) is operated through the full connectivity layer. The purpose of the branch design is to focus on the important information by using the activation function Relu to mask the negative values in the feature map after the convolution operation with a value of 0 and retain only the non-zero value information.

The branch b consists of a convolutional, a batch normalization, and a fully connected layer, and the branch c plays the role of the residuals, with a moderating role using the FC linearization layer. Finally, the feature maps of the three branches are summed up and the network structure is shown in Fig.3. The specific operations are as follows:

$$\boldsymbol{X}_2 = \mathrm{FC}\left(\mathrm{Conv2D}\big(\mathrm{Batch\_norm}(\boldsymbol{X})\big)\right) \tag{2}$$

$$\boldsymbol{X}_3 = \mathrm{FC}(\boldsymbol{X}) \tag{3}$$

$$\boldsymbol{X} = \boldsymbol{X}_1 + \boldsymbol{X}_2 + \boldsymbol{X}_3 \tag{4}$$

Where $\boldsymbol{X}_2$, $\boldsymbol{X}_3$ are the feature matrices of the outputs of branches b, c.

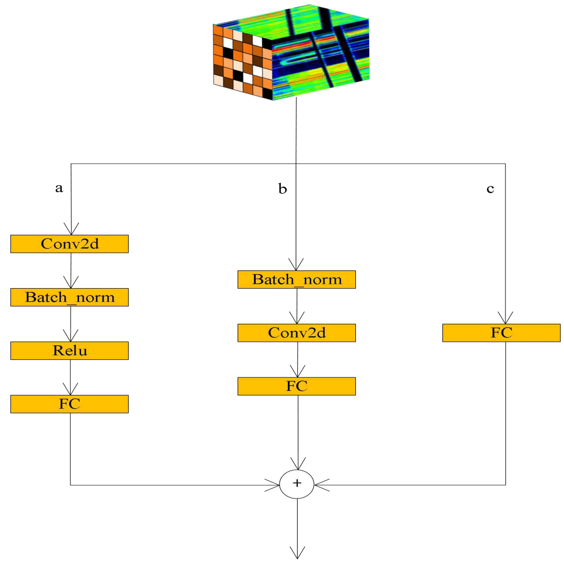

Figure 4 Attention convolution module design

3) Fuzzy Information Module

In processing images with little information and a lot of noise in the data, too much noise is often introduced if the information is extracted directly. Therefore, the fuzzy information module is designed with the aim of extracting the main information of the data to minimize the effect of noise as much as possible. As shown in Fig.5, the core idea of this module is to reduce the spatial size of the feature map patch while extracting the features by convolution, and at the same time, bilinear interpolation is carried out, which is used to recover the spatial size of the feature map patch, so as to realize the role of expanding the main features of the patch and reducing the influence of the noise, which is operated as follows:

$$\boldsymbol{X}' = \mathrm{GELU}\big(\mathrm{Conv2d}(\boldsymbol{X})\big) \tag{5}$$

$$\boldsymbol{X} = \mathrm{Interpolate}(\boldsymbol{X}') \tag{6}$$

$$\boldsymbol{X} = \mathrm{Interpolate}\big(\mathrm{Conv2d}(\boldsymbol{X})\big) \tag{7}$$

where GELU(●) is a Gaussian error linear unit, which is often used as a nonlinear transformation function in deep learning, and Interpolate(●) is a bilinear interpolation operation; $\boldsymbol{X}$ is a feature patch with a spatial size of 7×7, and is a patch that has been convolved with a spatial size of 5×5.

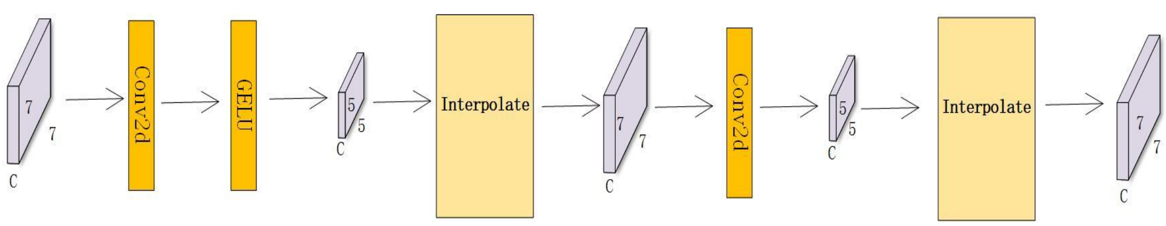

Figure 5 Fuzzy information module design

IV. EXPERIMENTAL EVALUATION

A.CLASSIFICATION AND ACCURACY ASSESSMENT

In order to explore the effectiveness of multi-source feature data, the classical machine learning random forest algorithm was used to design three comparison schemes, as shown in Tab.5. Sentinel-1 feature data, Sentinel-2 feature data, Sentinel-1 and Sentinel-2 feature data were used as the input dataset to classify the wetland features in the Yellow River estuary using the random forest algorithm, respectively. Confusion matrix is usually calculated to visualize and evaluate the performance of the classification model quantitatively, and in this part, the confusion matrix is used to calculate four indexes, namely, Overall Accuracy (OA), Kappa coefficient, Producer Accuracy (PA), and User Accuracy (UA), to evaluate the accuracy of the classification results of the experimental scheme. The Sentinel-1 features are backscattering coefficients and polarization features, and the Sentinel-2 features are raw spectral bands, vegetation index, water index, soil index, red edge index, and texture features

Table 5 Design of data set input scheme

Input dataset	Characteristics
Features data for Sentinel-1	S1(backscattering coefficient,polarization characteristics)
Features data for Sentinel-2	S2(original spectral bands,vegetation index,water index,soil index,red edge index,texture characteristics)
Features data for Sentinel-1 and Sentinel-2	S1_S2(backscattering coefficient,polarization characteristics,original spectral bands,vegetation index,water index,soil index,red edge index,texture characteristics)

The overall accuracies of the three different input datasets are shown in Tab.6. The overall classification accuracies of the multi-source data over the single-source data increased by 11.82% and 2.22%, respectively, and the Kappa coefficients increased by 16.26% and 2.82%, respectively. Tamarix chinensis is the feature with the lowest precision in the single Sentinel-1 SAR data. The low classification accuracy of a feature also lowers the overall accuracy. The large field area of spartina alterniflora can reach 96.79% in PA and 89.40% in UA because spartina alterniflora usually grows in water and has abundant branches and leaves, and its branching structure and wet environment cause the scattering characteristics of radar waves to be different from those of the surrounding water or other features, thus showing distinctive features in the radar data; the classification accuracy of the four types of features, namely, natural willow forest, tamarix chinensis, cultivated land, and tidal flats, in the single Sentinel-2 optical data is greatly improved compared with that of the single SAR data, and the PA can reach up to 88.23% on average, and the UA can reach up to 75.31% on average. The reason is that high-resolution optical data are rich in spectral and textural features, which make it relatively easy to identify and distinguish feature types with different color tones, structural morphology, and coverage forms; in Sentinel-1 and Sentinel-2 multi-source feature data, there are considerable PAs and UAs for each feature type, which neutralizes the inadequacy of a single source of data for classifying a feature.

Table 6 Evaluation of classification accuracy of different datasets

Feature category	Sentinel-1		Sentinel-2		Sentinel-1+Sentinel-2	
	PA%	UA%	PA%	UA%	PA%	UA%
Suaeda salsa	89.21	89.58	95.44	88.80	95.85	92.77
natural willow	66.37	70.75	88.50	78.13	89.38	75.37
spartina alterniflora	96.79	89.40	100.00	98.90	99.51	99.63
phragmites australis	73.87	80.99	87.65	94.13	89.31	93.07
tamarix chinensis	13.89	45.45	69.44	62.50	63.89	71.88
cultivated land	72.22	35.14	100.00	100.00	100.00	100.00
tidal flat	69.50	51.01	94.98	60.06	97.85	65.65
water	71.51	84.99	73.23	97.68	78.37	98.87
OA%	75.73%		85.33%		87.55%	
Kappa coefficient%	66.97%		80.41%		83.23%	

Overall, multi-source feature data classification is greatly improved compared with single optical data and single SAR data classification. Optical remote sensing data provide rich visual information of the earth's surface, and when optical remote sensing data are limited, radar data can be used as an effective supplementary data source, and radar features can be integrated into the optical features to improve the classification accuracy. At the same time, multi-source data can be combined in many ways and multi-temporal data can be acquired conveniently, so the application of wetland classification in the Yellow River Delta under multi-source feature data is more flexible and more widely applicable. Therefore, based on the multi-source feature remote sensing data, the research on the classification method of wetlands in the Yellow River Delta is carried out.

B. COMPARISON OF DIFFERENT METHODS

To evaluate the effectiveness and superiority of MHFE, several advanced and widely used deep learning methods are used for comparison based on multi-source feature datasets. The methods include multi-scale 3-D deep convolutional neural network (M3D-DCNN) [8], a CNN-based 3-D deep learning approach(3D-CNN)[9], an attention-based bidirectional long short-term memory network (AB-LSTM) [10], a deep feature fusion network (DFFN)[11], a transformer-based backbone network named SpectralFormer (SPEFORMER) [12], SSFTT [13] and Group-Aware Hierarchical Transformer (GAHT) [14].

To ensure fair performance across models, all deep learning classification methods were run within the Pytorch framework. The minimum batch size and epoch were set to 300 and 300, respectively, to update all model parameters. The optimizer and learning rate scheduler are the same as the original settings in order to obtain the best performance of the other models reported in their papers. For MHFE, we used a stochastic gradient descent (SGD) optimizer with a momentum of 0.9 and a weight decay of 0.0001 to update the training parameters and set the learning rate to a constant of 0.001. The experiments were accelerated using NVIDIA GeForce RTX 3060 GPUs equipped with 12 GB of memory. The classification performance of each model on the Yellow River Delta dataset was evaluated using three metrics: overall accuracy (OA), average accuracy (AA) and Kappa coefficient (Kappa). The classification results of different methods are shown in Tab.7.

Table 7 Classification results of different classification methods on multi-source feature dataset

Class	M3D-DCNN	3D-CNN	AB-LSTM	DFFN	SPEFORMER	SSFTT	GAHT	Proposed
1	99.06	98.80	98.62	99.31	97.14	99.94	99.52	99.47
2	100.00	99.74	96.91	99.83	100.00	100.00	100.00	100.00
3	95.26	94.36	89.46	88.24	89.13	92.97	95.67	96.25
4	84.54	5.15	9.28	80.41	83.51	83.51	81.44	92.59
5	95.25	95.89	93.35	96.52	97.78	95.25	93.51	96.30
6	96.26	80.86	89.44	97.39	98.28	96.41	96.44	99.97
7	86.71	49.13	88.15	84.39	78.61	89.60	85.55	82.86
8	100.00	100.00	84.38	100.00	100.00	100.00	100.00	97.89
OA(%)	97.69%	92.47%	94.24%	97.41%	96.70%	97.98%	97.84%	98.80%
AA(%)	94.63%	77.99%	81.20%	93.26%	93.06%	94.71%	94.02%	95.67%
K×100	96.77%	89.35%	92.01%	96.38%	95.41%	97.17%	96.98%	98.33%

The experimental results show that MHFE outperforms other classification methods.3D-CNN extracts features in three dimensions, which is one more dimension of feature extraction than 2DCNN.M3D-DCNN captures different levels of information through multi-scale modules, and the densely connected layer in the structure promotes the transfer of information and the reuse of features, and the OA of the two classification methods is 92.47% and 97.69%, respectively; AB- LSTM improves the modeling ability of key information by introducing an attention mechanism to enhance the model's attention to different locations of the input data, thus improving the modeling ability of key information, with an OA of 94.24%; DFFN utilizes dense connections in the network to promote information transfer and feature fusion ability, with the OA increasing to 97.41%; SPEFORMER combines the self-attention mechanism of Transformer and the CNN's spatial information processing, with an OA of 96.70%; SSFTT features a self-supervised learning approach, with a performance excellent classification effect, with an OA exceeding SPEFORMER's by 1.28%; GAHT utilizes a generative adversarial network model, with a higher performance and classification advantage, with an OA of up to 97.84%; MHFE designed a multibranch structure, including an ACM and a FIM, with the highest accuracy among several methods, with an OA as high as 98.80%. In AA, MHFE improves 1.04%, 17.68%, 14.47%, 2.41%, 2.61%, 0.96%, and 1.65% compared to M3D-DCNN, 3D-CNN, AB-LSTM, DFFN, SPEFORMER, SSFTT, and GAHT, respectively; and in Kappa coefficients, MHFE compares favorably with M3D- DCNN, 3D-CNN, AB-LSTM, DFFN, SPEFORMER, SSFTT, and GAHT by 1.56%, 8.98%, 6.32%, 1.95%, 2.92%, 1.16%, and 1.35%, respectively, and AA also presents the same enhancement results. It can be seen that the multi-branch feature module obtains enough feature information, and branch-by-branch information extraction facilitates the improvement of classification accuracy of multi-source feature data.

C.ABLATION EXPERIMENTS

We performed ablation experiments on our dataset in order to visualize the role of different modules. This section focuses on the following two main modules: the ACM, and the FIM.

Table 8 Effect of different modules on classification accuracy

Vague Module	Attention Convolution Module	AA	OA	Kappa
√	√	95.67%	98.80%	98.33%
√	×	95.20%	98.18%	97.46%
√	×	89.47%	98.28%	97.60%
×	√	93.50%	98.03%	97.24%
×	×	91.24%	97.55%	96.57%

1) Attentional Convolution Module

Explore the contribution of the ACM to the MHFE. In order to verify the advancement of the attentional convolution module, the attentional convolution module was removed and replaced with the normal convolution module (shown in green) and the removal of this module (shown in red). As shown in Tab.8, both types of experiments showed a significant decrease in accuracy after removing the LMHSA. This phenomenon indicates that the ACM possesses more powerful feature extraction ability than the ordinary convolution module, and also proves that the design of the structure of the ACM is reasonable.

2) Fuzzy Information Module

Explore the contribution of the FIM to MHFE. The FIM is removed from the whole network. As shown in Tab.8, there is a significant reduction in the classification accuracy after removing the FIM. The results show that the FIM allows the model to extract the main information and reduce the introduction of noise when confronted with less informative and noisy data. Therefore, the FIM has a positive contribution to MHFE.

V. CONCLUSION

This study first demonstrates the positive effect of multi-source feature data fusion on improving classification accuracy. Secondly, based on multi-source feature data, a multi-branch hierarchical feature extraction network MHFE is proposed for wetland classification in the Yellow River Delta. The proposed network utilizes multiple branches to mine the feature distribution, which solves the problem of a single network structure being too deep. The network uses an ACM to extract more representational features, which amplifies the details of the features, and a FIM to reduce the introduction of noise and enhance feature discrimination. Extensive experiments on the Yellow River Delta coastal wetland dataset show that the proposed method outperforms several other leading classification methods.

References

[1] Xie S Y, Fu L B, Li Y, et al. Classification Method on Marsh Wetlands in Honghe National Nature Reserve based on Multi-dimensional Remote Sensing Images[J]. Wetland Science, 2021, 19(01):1-16.

[2] Ming Y S, Liu Q H, Bai H, et al. Classification and change detection of vegetation in the Ruoergai Wetland using optical and SAR remote sensing data[J]. National Remote Sensing Bulletin, 2023, 27(6):1414-1425.

[3] Li P, Li D H, Li Z H, et al. Wetland Classification Through Integration of GF-3 SAR and Sentinel-2B Multispectral Data over the Yellow River Delta [J]. Geomatics and Information Science of Wuhan University, 2019, 44(11):1641-1649.

[4] Zhang C Y, Chen S L, Li P, et al. Spatiotemporal dynamic remote sensing monitoring of typical wetland vegetation in the Current Huanghe River Estuary Reserve[J]. Haiyang Xuebao, 2022, 44(1):125-136.

[5] Xing H, Niu J, Feng Y, et al. A coastal wetlands mapping approach of Yellow River Delta with a hierarchical classification and optimal feature selection framework[J]. Catena, 2023, 223: 106897.

[6] Zhang L, Luo W T, Zhang H H, et al. Classification scheme for mapping wetland herbaceous plant communities using time series Sentinel-1 and Sentinel-2 data[J]. National Remote Sensing Bulletin, 2023, 27(06):1362-1375.

[7] Han Z, Gao Y, Jiang X, et al. Multisource remote sensing classification for coastal wetland using feature intersecting learning[J]. IEEE Geoscience and Remote Sensing Letters, 2022, 19: 1-5.

[8] He M, Li B, Chen H. Multi-scale 3D deep convolutional neural network for hyperspectral image classification[C]//2017 IEEE International Conference on Image Processing (ICIP). IEEE, 2017: 3904-3908.

[9] Hamida A B, Benoit A, Lambert P, et al. 3-D deep learning approach for remote sensing image classification[J]. IEEE Transactions on geoscience and remote sensing, 2018, 56(8): 4420-4434.

[10] Mei S, Li X, Liu X, et al. Hyperspectral image classification using attention-based bidirectional long short-term memory network[J]. IEEE Transactions on Geoscience and Remote Sensing, 2021, 60: 1-12.

[11] Song W, Li S, Fang L, et al. Hyperspectral image classification with deep feature fusion network[J]. IEEE Transactions on Geoscience and Remote Sensing, 2018, 56(6): 3173-3184.

[12] Hong D, Han Z, Yao J, et al. SpectralFormer: Rethinking hyperspectral image classification with transformers[J]. IEEE Transactions on Geoscience and Remote Sensing, 2021, 60: 1-15.

[13] Sun L, Zhao G, Zheng Y, et al. Spectral–spatial feature tokenization transformer for hyperspectral image classification[J]. IEEE Transactions on Geoscience and Remote Sensing, 2022, 60: 1-14.

[14] Mei S, Song C, Ma M, et al. Hyperspectral image classification using group-aware hierarchical transformer[J]. IEEE Transactions on Geoscience and Remote Sensing, 2022, 60: 1-14.

LI Xinhao was born in 2000. He received the B.S. degree in 2022 from Shandong Agricultural University, Taian, China, with a degree in surveying and mapping engineering. He is currently pursuing a degree in surveying and mapping science and technology at China University of Petroleum (East China), Qingdao, China, His research interests include hyperspectral image classification.(Email:lxh17866703382@163.com)

LIU Mingwei was born in 1999. She received the B.S. degree inengineering from the Inner Mongolia University of Science and Technology, Baotou, China, in 2022,where she is currently pursuing the master ’ s degree surveying and mapping science and technology from the China University of Petroleum (East China), Qingdao, China. Her research direction is remote sensing of wetlands. (E-mail：s22160005@s.upc.edu.cn.)

Dou Qingwen was born in 1969. He is currently the vice president of Land Surveying and Mapping Institute of Shandong Province. He is mainly engaged in natural resources law enforcement, satellite remote sensing technology development and application. His research interests include technical support and guarantee of satellite remote sensing images for natural resources management.

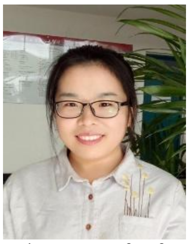

XU Mingming received the B.S. degree in surveying and mapping engineering from the China University of Petroleum (East China), Qingdao, China, in 2011, and the Ph.D. degree in photogrammetry and remote sensing from the State Key Laboratory of Information Engineering in Surveying, Mapping, and Remote Sensing, Wuhan University, Wuhan, China, in 2016. She is currently an Associate Professor with the College of Oceanography and Space Informatics, China University of Petroleum. Her research interests include hyperspectral image processing and wetland remote sensing. (Email:xumingming@upc.edu.cn)

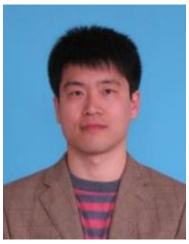

LIU Shanwei received the B.S. degree and the Master's degree in surveying and mapping engineering from China University of Petroleum (East China), Qingdao, China, in 2005 and 2008, respectively. He received the Ph.D. degree in environmental science from the Yantai Institute of Coastal Zone Research, Chinese Academy of Sciences, Yantai, China, in 2011. He is a Professor with the College of Oceanography and Space Informatics, China University of Petroleum (East China), Qingdao, China. His research interests include remote sensing of marine, GIS development and application.(Email:shanweiliu@163.com)

SHENG Hui received the B.S. degree in Photogrammetry and Remote Sensing from Wuhan Technical University of Surveying and Mapping and the Master's degree in Geodesy and Surveying Engineering from Wuhan University, Wuhan, China, in 1995 and 2002, respectively. He received the Ph.D. degree in Geological Resources and Geoengineering from China University of Petroleum (East China), Qingdao, China, in 2010. He is an Associate Professor with the College of Oceanography and Space Informatics, China University of Petroleum (East China), Qingdao, China. His research interests include marine remote sensing, the application of photogrammetry and remote sensing in geology, and the smart oil field.(Email:sheng@upc.edu.cn)

特定于类别的原型自完善对比学习用于小样本高光谱图像分类

刘泉涌[1]，彭江涛[1，2]

1,2. 湖北大学数学与统计学院湖北应用数学重点实验室，武汉 430062

摘 要： 深度学习已被广泛应用于高光谱图像分类，并取得了显著的成功，但对于标注样本量有限的高维高光谱图像数据集的分类仍然是一个巨大的挑战。小样本学习（Few-shot learning）在解决少样本分类问题方面表现出色，然而，大多数现有的 FSL 方法通常都存在原型不稳定和域偏移的问题。为了解决这些问题，本文提出了一种特定于类别的原型自完善对比学习方法用于跨域高光谱图像分类。我们的方法采用监督对比学习策略促进度量空间中的特征的类内紧凑性和类间分散性。为了稳定和完善支持集的原型，我们设计了一个特定于类别的原型自完善模块，它能够利用查询集中丰富的标记信息自适应地学习不同类别原型的不同更新规则。此外，我们还构建了一种局部判别域适应方法用来调整源域和目标域之间的全局分布，同时保留特定域的判别信息。在四个公共 HSI 数据集上的实验结果表明，我们的算法在高光谱图像分类方面的表现优于现有的小样本和深度学习方法。

关键词： 高光谱图像分类、对比学习、原型网络、小样本学习

1 引 言

高光谱图像是由数百个连续光谱波段组成的三维数据立方体，它包含丰富的地理空间信息和光谱信息，因此在地面物体识别和分类方面具有独特的优势[1], [2]。高光谱图像分类旨在根据图像固有的光谱或空间特征，将每个像素划分为一个独特的类别[3]。近几十年来，高光谱图像被广泛应用于生态环境监测、城市规划、精准农业等多个领域 [4], [5]。

在早期的研究中，一些侧重于手工特征提取器和分类器的传统算法被用于高光谱图像分类，如 k-最近邻（KNN）[6]、支持向量机（SVM）[7]、联合稀疏表示[8]和 Gabor 小波[9]等。这些算法都能实现良好的分类性能，但人为设置的参数使其对不同应用场景的适应性较差。

过去几年来，随着计算能力的提高，深度学习在高光谱图像分类中得到了广泛应用，并取得了很好的效果 [10-12]。与传统分类方法相比，基于深度学习的方法可以通过一系列堆叠层提取样本的高级特征，并在反向传播过程中自动更新参数。2004 年，Chen 等人首次提出了基于堆叠自动编码器（SAE）的深度高光谱图像分类网络[13]，揭示了深度学习网络在其分类领域的强大潜力。为了减少参数数量，他们进一步引入了具有稀疏连接性和权重共享的卷积网络（CNN）[14]来提取特征。并且，一些改进的基于 CNN 的方法，如 3D-CNN [15]、HybirdSN [16]也被陆续提出。随后，Zhong 等人提出了一种光谱空间残差网络（SSRN）[17]，该方法缓解了随着网络层数增加而出现的梯度消失或梯度爆炸问题。此外，为了进一步提高模型的性能，一些改进策略如多尺度结构[18]、[19]和注意力机制[20]、[21]也被应用到高光谱图像分类算法中。然而，基于深度学习的算法的卓越性能取决于大量的标记样本。实际上，收集标注样本费时费力，而且所提供的标注样本有限。因此，高精度小样本分类越来越受到关注。

为了解决标注样本稀缺的问题，人们针对基于深度学习的高光谱图像分类提出了一些小样本分类策略。一些数据增强策略如随机高斯噪声[22]、随机旋转或裁剪[23]的提出是为了在现有样本的基础上直接增加标注样本的数量，扩大训练集。轻量级网络可以通过深度卷积 [24] 或点卷积 [25] 来减少模型的可训练参数，从而降低模型对标注样本的依赖性。此外，自监督学习可以通过对比损失[26-28]或其他借口任务[29][30]来挖掘未标记样本的监督信息，从而利用自身信息训练网络。这些方法都能在只有少量标记样本的情况下实现良好的分类性能。

小样本学习（FSL）因其能有效利用少量标记样本识别新的未知类别而备受关注，它使用已知数据集中的标记样本进行训练，然后对新数据集中的未标记样本进行分类，训练数据集和测试数据集之间的类别不要求相同。Liu 等人[31]提出了一种深度小样本学习（DFSL）方法，利用少量标记数据对高光谱图像进行分

类。DFSL 首次将情景训练的方式应用于高光谱图像分类，它通过深度三维残差网络从四个源域数据集学习度量空间。Gao 等人[32]提出了一种用于高光谱图像小样本分类的深度关系网络，它利用目标数据集的少量标记样本对训练好的模型进行微调，从而减少了两个域之间的差异。随后，Li 等人[33]提出了一种深度跨域小样本分类（DCFSL）方法，进一步研究了小样本学习中存在的域偏移问题，该方法利用基于对抗域的自适应模块来缓解域偏移现象。Xi 等人[34]提出了一种基于类协方差度量的小样本学习（CMFSL）方法，该方法设计了一个谱先验细化模块来减少域间差异，并使用类协方差作为分类度量。Zuo 等人[35]提出了一种边缘标记图神经网络（FSL-EGNN），首次将 EGNN 嵌入到 FSL 框架中，通过循环更新节点特征和边缘特征来实现未知样本的分类。Zhang 等人[36]提出了图信息聚合跨域小样本分类（Gia-CFSL）方法，该方法采用基于图信息聚合的域对齐策略来抑制域偏移。

目前，小样本中存在的域偏移问题最受关注，现有的基于小样本学习的高光谱图像分类方法试图通过设计或应用域适应（DA）策略来缩小域差异。然而，小样本学习和域适应二者之间存在显著差异，域适应中源域和目标域之间的特征空间和标签空间是相同的，而小样本学习中的两个域具有完全不同的类别和特征。如图 1 (a) 所示，传统的 DA 策略可能对 FSL 无效，因为它们会将两个域中不同类别的特征对齐，这可能会影响分类器的性能。此外，现有的基于度量的 小样本分类方法在计算支持集原型时也存在一些缺陷，直接计算特征均值获取的支持集原型受噪声样本的影响较大，可能会降低模型的性能。为了解决这个问题，人们提出了许多基于原型的小样本分类优化方法 [37-39]。Cheng 等人[40] 提出了一种连体原型网络，通过自校准和互校准模块对原型进行校准，从而获得更稳定的支持集原型。Yu 等人[41]提出了一种用于小样本高光谱图像分类的多视图校准原型学习（MCPL），通过校准聚合网络（CAN）将从平均向量获得的原型转换为局部高光谱图像补丁特征。Liu 等人[42]提出了一种精炼原型对比学习（RPCL）方法，该方法利用对比学习和查询集中丰富的样本信息对原型施加三重限制，并在不增加模型参数的情况下精炼原型。Xu 等人[43]提出了一种基于原型自我更新的小样本分类方法，该方法设计了一个原型自我更新（PSU）模块，用于修正支持集的原型。如图 1 (b)所示，这些方法使用统一策略优化所有类别原型，这可能会导致其中一些原型偏离真实原型。

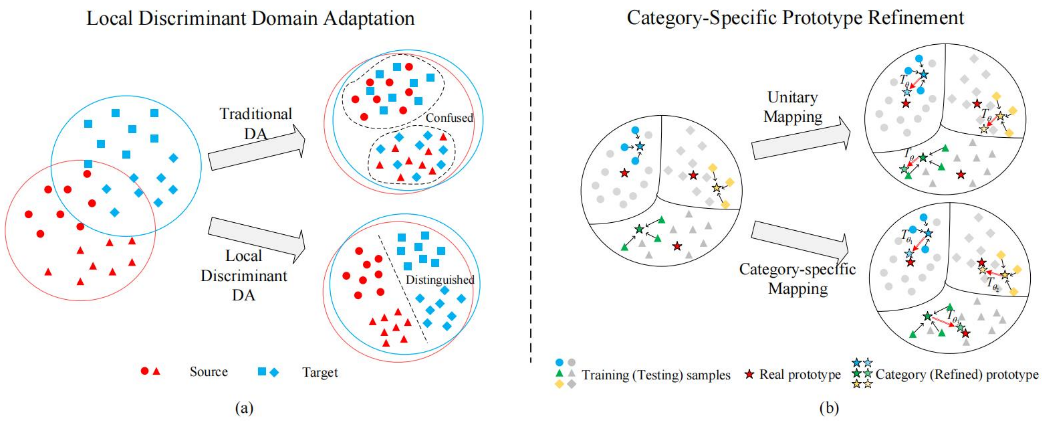

图 1 领域适应和原型完善模块图解。(a) 红色和蓝色大圆圈分别代表源域和目标域的总体分布，小标记代表两个域中的四个不同类别。传统的域适应方法在调整域之间的总体分布（例如，红圈和蓝圈几乎重合）的同时，也会强行调整两个域中的不同类别。而局部判别域适应方法则试图对齐全局分布，同时保留两个域中特定类别的分布和判别信息。(b) 原始的基于度量的 FSL 方法直接使用平均特征作为类别原型，得到的原型通常偏离真实原型，如左图所示。现有的原型完善方法采用单元映射来更新所有原型，只能完善部分原型。而针对不同类别的原型细化策略则针对不同的原型制定不同的更新映射。细化后的原型更接近真实原型。

根据上述表述的问题，如图 1 所示，我们提出了一种特定类别原型自完善对比学习用于跨域高光谱图像小样本分类。与之前的研究不同，我们使用了有监督的对比学习来强调特征的类间变异性，然后针对跨域问题引入了局部判别域适应策略，并设计了一个特定类别原型细化网络，允许原型随着网络的迭代而自适应更新。具体来说，自适应映射层和空间光谱特征提取器用于提取源域和目标域样本的特征。随后，通过最小化支持集和查询集样本原型之间的距离来学习度量空间，其中相同类别的样本距离较近，不同类别的样本距离较远。为了缓解小样本学习中的域偏移问题，我们通过嵌入模块学习了一个特征嵌入空间，在该空间中，源域和目标域的全局分布被对齐，同时保留了特定域的判别信息。此外，我们还引入了一个特定于类别的原型校准网络，该网络从不同类别中提取汇总信息，并用于更新支持集的相应类别原型。所有映射层、特征提取网络、嵌入层和原型校准网络都在统一的框架下进行训练。为了证明算法的有效性，我们在四个公开数据集上进行了实验，结果表明我们的方法优于现有算法。文章中提出的算法的主要贡献如下：

(1)我们设计了一个模块，使用类别聚合信息来细化支持集的原型。它可以生成特定类别的特征映射，指导各类别原型的更新，从而进一步提高支持集原型的稳定性和有效性。

(2)我们引入了一种改进的域适应策略来缓

解跨域小样本分类中的域偏移问题，该策略可以调整源域和目标域之间的全局分布，同时保持特定域的鉴别信息。

(3)我们通过构建对比支持集，将监督对比学习纳入小样本学习的框架，以进一步强调特征的类内相似性和类间变异性。

2　算法介绍

2.1 总体框架

为了解决上文提到的两个基本问题，我们提出了一种特定于类别的原型自完善对比学习方法，算法的整体框架如图 2 所示，它设计了一个特定类别的映射模块，允许支持集的原型在网络迭代过程中不断自我更新，以解决原型不稳定问题，并通过局部判别域适应策略缓解域偏移。

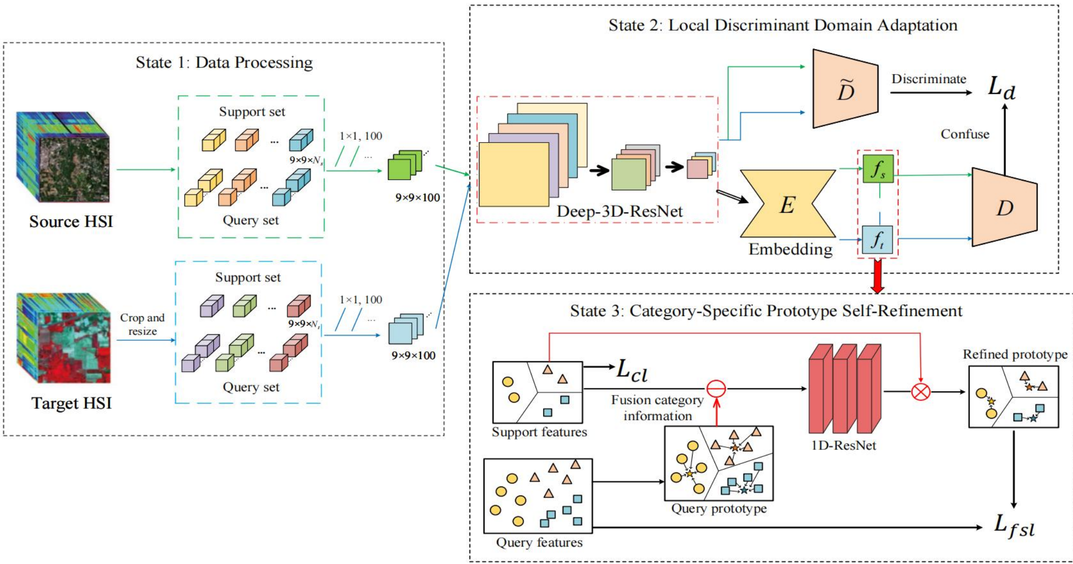

图 2 算法主体框架图

如图 2 所示，在元训练阶段，我们在源域和目标域上交替使用小样本，每个训练过程有三个阶段。首先，使用数据增强层和自适应映射层确保源域和目标域的光谱维度和标记样本数量相同。其次，局部域判别域适应策略被用来减少源域和目标域之间的差异。最后，我们设计了一种作用于支持集的特定于类别的映射，用于细化支持集的原型，使原型在网络迭代过程中得到自适应更新，同时使用监督对比学习策略来提高特征提取器的特征学习能力，增加同类样本之间的相似性和不同类样本之间的不相似性。

目标数据集中的标注样本和未标注样本依次进入映射层、深度特征提取模型和嵌入层提取嵌入特征。值得注意的是，此时的特征具有类内收敛和类间分离的特点。因此，最终使用 1-NN 分类器对未标记样本进行分类，并生成分类映射图。

2.2 数据处理

高斯噪声、随机旋转和裁剪操作等数据增强策略被广泛用于扩展有限的训练集，并能有效提高模型的性能。由于用于小样本分类的目标域标注样本数量有限，我们采用了数据增强策略（随机裁剪和调整大小）来扩展目标域的训练集。我们使用长宽比为 3：4、大小范围为原始图像 8%-100%的矩形对原始图像进行裁剪，然后将裁剪后的图像还原为原始大小(9×9)。此时，目标域训练集扩展为每类 200

个标注样本，源域训练集直接选择为每类 200 个标注样本，两者都用于模型的交替训练。

源域和目标域的支持集和查询集的构建过程相同。以目标数据集为例，首先从训练数据集中随机抽取N个类别，然后从这N个类别中的每个类别中随机抽取 2 个标注样本形成支持集$S_s=\{(x_i,y_i)\}_{i=1}^{n_s}$，并从剩余样本中各随机抽取 19 个标注样本形成查询集$Q_s=\{(x_j,y_j)\}_{j=1}^{n_q}$其中$N=C_s$，$n_s=2\times C_s$和 $n_q=19\times C_s$。我们将支持集中来自同一类别的两个标注样本放入不同的集合中，然后得到对比支持集，这为后续监督对比学习的应用提供了便利。

由于成像传感器的不同，源域数据和目标域数据的光谱尺寸通常是不同的。我们采用自适应映射层[37]来统一光谱维数。自适应映射层通过c个大小为$1\times1\times h$的卷积核进行简单的卷积操作，其中h是输入的维数，ch是输出的维数（实验中的$ch=100$）。

2.3 小样本学习领域自适应

自适应层之后，带有嵌入模块的深度三维残差网络用于提取输入样本的空间-光谱嵌入特征。如图 3 所示，特征提取网络由两个残差块和一个嵌入块组成，其中每个残差块包含三个大小为 3 的三维卷积层，嵌入块包含两个线性层。输入样本的中间特征和最终特征分别在嵌入块之前和之后提取。

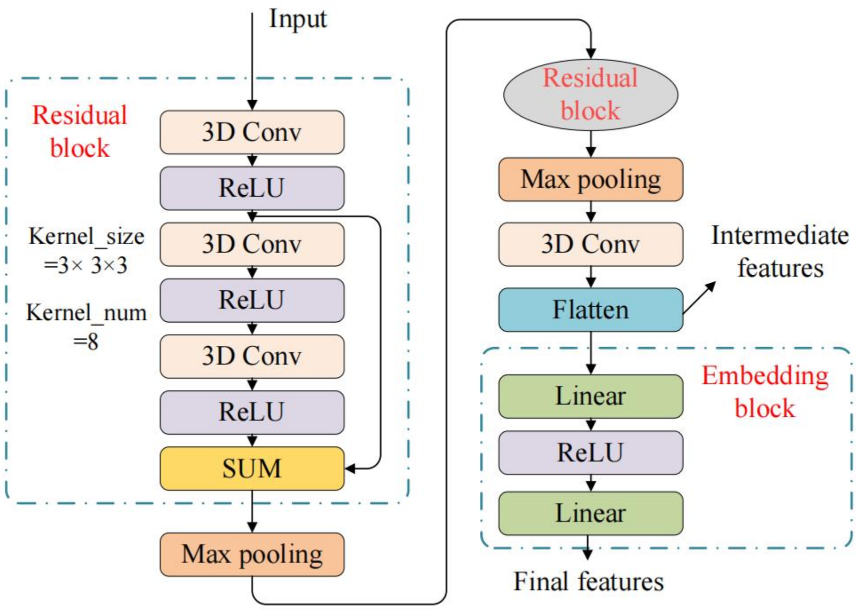

图 3 模型框架图

考虑到小样本学习中的源域和目标域具有完全不同的类别，而传统的领域自适应策略可能本质上不适合跨域小样本分类问题。我们希望模型能学习一个特征嵌入空间，在这个空间中，源域和目标域的全局分布是一致的，而特定域的判别信息仍被保留。因此，我们在嵌入块之前和之后分别对特征进行域判别和域对齐。

2.3.1 域对齐损失

为了调整目标域和源域的全局数据分布，一些域适应策略仍可广泛应用于跨域小样本分类问题。受条件域对抗网络（CDAN）的启发，我们使用条件域判别器D跨越源分布

$P_s(x)$和目标分布 $P_t(x)$以减少域偏移。根据最终特征$f=F(x)$ 和分类器预测结果 $g=G(x)$，域对抗损失函数L定义如下：

$$\min_{D}\max_{F,G} L =- E_{x_i\sim P_s(x)}\log\left[D(f_i^s,g_i^s)\right] - E_{x_j\sim P_t(x)} log\left[1-D\left(f_j^t,g_j^t\right)\right]$$

其中$D(,)$代表判别器预测样本 x属于源域的概率。我们选择多线性映射 $T_{\otimes}(h)=f\otimes g$，其中 $h=(f,g)$和 $T_{\otimes}(h)$ 定义为多个随机向量的外积。多线性图 $T_{\otimes}(h)$可以更详细地捕捉复杂数据分布背后的多模态结构，但当d_f和 $d_g g$较大时，容易出现维度爆炸。因此，用随机多线性图代替多线性图可以解决这个问题，而内积 $T_{\otimes}(h)$ 可以近似为点积 $T_{\odot}(h)=\left(\frac{1}{\sqrt{d}}\right)\left(R_f f\right)\left(R_g g\right)$，其中$\odot$为元素内积，$R_f f$和 $R_g g$是两个随机矩阵，在训练阶段只采样一次并固定不变，且 $d\ll d_f\times d_g$ 。最后，调整策略如下：

$$T(h)=\begin{cases}T_{\otimes}(h), & d_f\times d_g\le d_{fea}\\ T_{\odot}(h), & \text{otherwise}\end{cases}$$

其中 d_{fea}代表全连接层的输出维度，本文将其设置为 1024。也就是说，当多线性图的维数为 1024 时，随机多线性图的策略为$T_{\odot}$的策略。因此，域对齐损耗 L_{da} 由方程演化如下：

$$L_{da} =- E_{x_i\sim P_s(x)}\log\left[D\left(T(h_i^s)\right)\right] - E_{x_j\sim P_t(x)} log\left[1-D\left(T\left(h_j^t\right)\right)\right]$$

其中，用于进行域配准的域判别器 D 是一个多层感知器（MLP），由五个全连接层和整流线性单元（ReLU）组成。

2.3.2 域判别损失

当源域和目标域的类别分布相同时，上述域对齐策略可以有效缓解域偏移，但对于像小样本学习这样不共享任何共同类别的域偏移问题，过多的域对齐操作可能会导致模型失去对新类别的一些判别性能。因此，我们引入了一种局部域判别方法，旨在限制嵌入层之前的中间特征，使其保持一定的域判别能力。判别器$\widetilde{D}$用于源分布$P_s(x)$和目标分布$P_t(x)$。与之前不同的是，我们希望两个域中的类别分布彼此不同。那么类似地，我们可以在判别器$\widetilde{D}$上定义一个域判别损失函数：

$$\min_{\widetilde{D},\widetilde{F},\widetilde{G}} \tilde{L} =- E_{x_i\sim P_s(x)}\log\left[\widetilde{D}\left(\tilde{f}_i^s,\tilde{g}_i^s\right)\right] - E_{x_j\sim P_t(x)} log\left[1-\widetilde{D}\left(\tilde{f}_j^t,\tilde{g}_j^t\right)\right]$$

然后让$\tilde{h}=\left(\tilde{f},\tilde{g}\right)$，域判别损失 L_{da} 为

$$L_{dd} =- E_{x_i\sim P_s(x)}\log\left[\widetilde{D}\left(T\left(\tilde{h}_i^s\right)\right)\right] - E_{x_j\sim P_t(x)} log\left[1-\widetilde{D}\left(T\left(\tilde{h}_j^t\right)\right)\right]$$

值得注意的是，我们将领域分类器$\widetilde{G}$作为域判别器$\widetilde{D}$并直接计算不同领域样本的分类损失。算法的域适应损失 L_d 最终可以表示为

$$L_d=L_{da}+L_{dd}$$

2.4 监督对比学习

基于原型网络的小样本学习是通过最小化支持集原型与查询集样本之间的距离来训练的，它能使同一类别的样本在新的嵌入空间中聚类更紧密。然而，我们认为原型网络只考虑了样本的类内相似性，而忽略了类间差异性，这可能会导致相似类别的混淆。为了缓解上述问题，我们采用了一种基于监督对比学习的策略来提高模型的判别性能。

对于具有N-way K-shot 设置的每个元任务，支持集的每个类别都包含两个标注样本，在构建对比支持集时可以得到两个单独的组，其中每个组都有 N 不同类别的标注样本。我们将这两个集合分别记为 $S_1=\{x_1,x_3,x_5\cdots,x_{2N-1}\}$和 $S_2=\{x_2,x_4,x_6\cdots,x_{2N}\}$，其中 x_{2k-1}和 x_{2k}来自同一类别，这意味着两组样本中的每个样本都只有一个来自同一类别的阳性样本，而其余的 $2N-1$ 为负样本。因此，对比损失函数 $l_{m,n}$之间的 $F(x_m)$和 $F(x_n)$如下：

$$l_{m,n}=-\log\frac{exp\left(\frac{s\left(F(x_m),F(x_n)\right)}{\tau}\right)}{\sum_{k=1}^{2N}1_{[k\neq m]}exp\left(\frac{s\left(F(x_m),F(x_k)\right)}{\tau}\right)}$$

其中 $x_m,x_n\in S_s$属于同一类别，而 $s(,)$代表欧氏距离。τ是温度系数，实验中设定为0.5。考虑到 $l_{2k-1,2k}\neq l_{2k,2k-1}$，每个元任务的最终平均对比度损失为 L_{cl}每个元任务的最终平均对比度损失如下:

$$L_{cl}=\frac{1}{2N}\sum_{k=1}^{N}\left(l_{2k-1,2k}+l_{2k,2k-1}\right)$$

2.5 特定于类别的自我完善策略

原型网络的类别原型被认为是引导查询样本完成分类的辅助样本，其质量在很大程度上影响着模型的性能。然而，在标注样本较少的情况下，直接通过特征平均得到的支持集原型会受到噪声像素的影响，导致分类结果不稳定。为了实现原型的自我更新，我们设计了一种特定于类别的原型自我更新策略，将原型添加到网络训练中，使原型随着网络的迭代而不断更新。算法模块的框架如图 4 所示。首先，我们将查询集的类别原型与支持集的样本特征相结合。其次，将组合特征输入嵌入网络 $T_\theta(\cdot)$ 提取特定类别的聚合信息。最后，将聚合

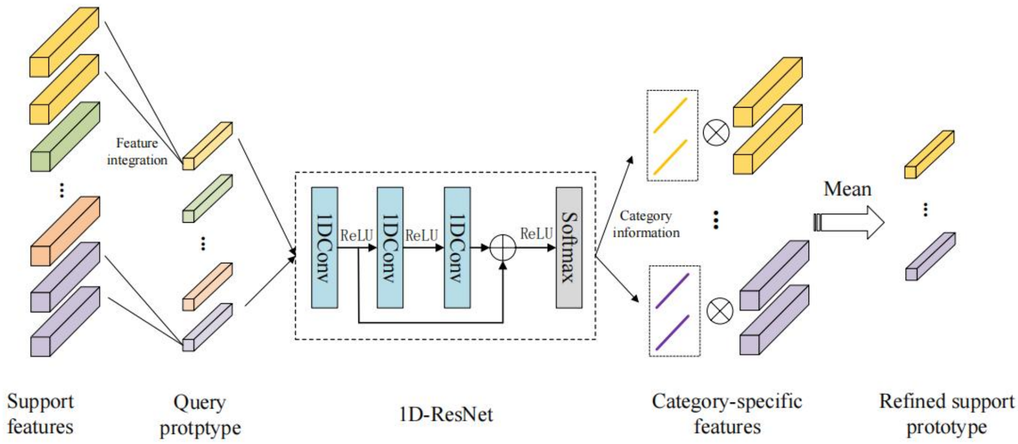

图 4 特定于类别的原型自完善模块的说明

信息分配给原始支持集特征，从而得到支持集的更新原型。

查询集中第c的类别原型计算公式为

$$P_q^c=\frac{1}{M_q}\sum_{x_j\in Q_s^c}F(x_j)$$

其中Q_s^c代表查询集合中属于c的样本集合，M_q是查询集中每个类别的样本数量。我们可以用查询集的类别原型构建一个 $T_{\theta_n}(\cdot)$并将其添加到网络训练中，这样就能对不同类别的样本进行自适应转换。因此，支持集特征 ω_i 的聚合信息 $F(x_i)$的计算公式为:

$$\omega_i=T_{\theta_{y_i}}\left(F(x_i)\right)$$

其中 y_i是 x_i的标签，并且

$$T_{\theta_k}\left(F(x_i)\right)=T_\theta\left(P_q^k-F(x_i)\right)$$

通过上述变换，我们可以得到每个支持集样本的相应聚合信息，然后更新原始支持集特征，计算公式如下：

$$F_{new}(x_i)=\sum_{i=1}^{n_s}F(x_i)\cdot\omega_i$$

因此，支持集中第c的修正原型计算如下：

$$P_s^c=\frac{1}{n_s}\sum_{x_i\in S_s^c}F_{new}(x_i)$$

其中 S_s^c代表支持集中属于*第* c-类的样本集合，n_s是支持集中每个类别的样本数。因此，

每个元任务的小样本分类损失函数如下：

$$L_{fsl} = -\frac{1}{n_q}\sum_{j=1}^{n_q}\frac{exp\left(-d\left(F(x_j), P_s^{y_j}\right)\right)}{\sum_{c=1}^{N} exp\left(-d\left(F(x_j), P_s^{c}\right)\right)}$$

其中 $d(\cdot)$代表欧氏距离，y_j是 x_j的标签。最后，模型训练过程的总损失函数为：

$$L_{total} = L_{fsl} + L_d + L_{cl}$$

3　实验结果分析

34.1 数据集

为了评估 CPSCL 的分类性能，实验使用了四个公共数据集，包括筑西、印度松树（IP）、帕维亚大学（UP）、萨利纳斯（SA）。在实验设置中，筑西数据集被选为源域数据集，其他三个数据集被选为目标域数据集。

筑西数据集由东京大学制作并公开，于 2014 年 7 月 29 日在日本伊巴列市筑成由高光谱可见光/近红外相机（Hyperspec-VNIR-C）采集。该数据集包含 128 个光谱波段，范围从 343 到 1018nm的 128 个光谱波段，空间大小为 2517×2335，空间分辨率为 2.5 米。数据集包含 19 个土地覆被等级，涵盖城市和农村地区。图 5 显示了伪彩色图像和相应的地面实况图。

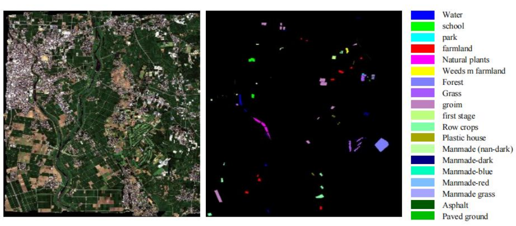

图 5 筑西数据集伪彩色图像和相应的地面实况图

IP 数据集是 1992 年由机载可见光/红外成像分光仪（AVIRIS）传感器在印第安纳州西北部的印第安纳松树试验场收集的。该数据集包含 200 个光谱波段，范围从 400 到 2500nm的 200 个光谱波段，空间大小为 145×145，空间分辨率为 20 米。它有 16 个土地覆盖类别，包含各种农作物。伪彩色图像和相应的地面实况图如图 6 所示。

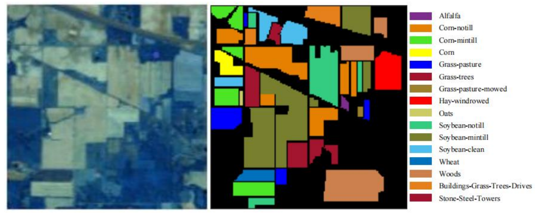

图 6 IP 数据集伪彩色图像和相应的地面实况图

UP 数据集由意大利北部帕维亚大学试验场的反射光学光谱图像系统（ROSIS）收集。该数据集包含 103 个光谱波段，范围从 430 到 860nm的 103 个光谱带，空间大小为 610×340，空间分辨率为 1.3 米。它包含 9 种不同类型的土地覆被类别。伪彩色图像和相应的地面实况图如图 7 所示。

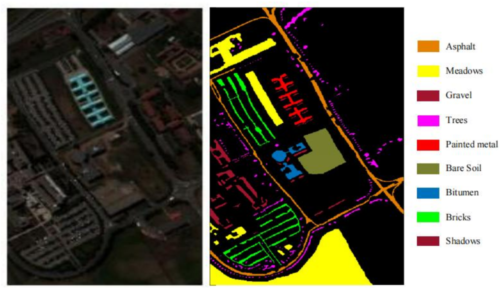

图 7 UP 数据集伪彩色图像和相应的地面实况图

3.2 实验设置

为了验证我们方法的优越性，我们将算法与几种最先进的基于深度学习和小样本分类的算法进行了比较，包括 HybirdSN、SSRN、A2S2K、SSCL、DFSL、DCFSL、CMFSL 和 Gia-CFSL。其中前四种算法属于基于深度学习的监督式方法，它们不需要源领域数据集的参与，直接在四个目标领域数据集上进行实验，每个类随机选取五个标注样本作为训练集，其余样本作为测试集。其余四种算法属于基于小样本学习的监督方法，其中 DFSL 和 CMFSL 融合了（休斯顿大学 2013 年、筑成、肯尼迪航天中心和博茨瓦纳）四个数据集作为源域数

据集，波段选择策略统一了源域和目标域数据集的维度，DCFSL 和 Gia-CFSL 使用了与本文相同的源域数据集和维度统一方法。对于基于 FSL 的算法，我们采用了相同的实验设置，从源域数据集中每个类别随机抽取 200 个标注样本（不包括样本少于 200 个的类别），并从目标域数据集中每个类别抽取 5 个标注样本用于实验。

在 CPSCL 中，输入立方体的窗口大小设为 9 × 9，学习率为 0.001，源域和目标域数据集的交替训练迭代次数设为 3000，这足以训练网络。在 N-way K-shot 集训练中，N 设置为目标域数据集的类别数（例如，IP 和 SA 的 N=16，UP 的 N=9），K 设置为 2。此外，我们

从剩余样本的每个类别中选择 19 个标记样本作为查询集。所有算法的分类性能均采用总体准确率（OA）、平均准确率（AA）和 K 系数，每个实验运行十次后报告平均结果。

3.3 分类结果

表 1 显示了不同方法在 IP 数据集上的分类结果。可以看出，我们的算法在 OA 和 IP 数据集上的 OA 和 k 系数比其他算法高出约 10%。对于第 2、5、7、9 和 12 类，我们提出的算法分类结果非常出色。值得注意的是，与基于 FSL 的四种方法相比，我们的算法对 第 11 类“Soybean-mintill”的分类准确率提高了 30%以上，这也是 IP 数据集中样本数量最多的类别。这可能是因为特定于类别的原型修正

模块校准的原型更准确，能够在样本数量较多的情况下获得更严格的分类边界。图 9 显示了不同方法的分类图，这也清楚地表明了我们算法的优越性。

表 1 不同算法在 IP 数据集上的实验结果

Class	HybirdSN	SSRN	A2S2K	SSCL	DFSL	DCFSL	CMFSL	Gia-CFSL	CPSRCL
1	89.39	80.28	36.19	87.3	80.24	90.17	94.67	**100**	98.78
2	63.82	44.18	68.28	36.82	30.17	54.23	49.21	66.37	**71.05**
3	61.27	48.38	65.34	54.33	79.24	72.88	**84.19**	80.13	64.06
4	42.85	50.52	49.25	34.61	87.17	83.72	**93.27**	75.18	92.03
5	50.31	92.37	87.68	73.17	85.33	**93.27**	92.31	91.08	86.19
6	78.29	96.51	97.21	89.95	88.48	92.68	**97.35**	96.28	86.90
7	78.58	47.29	20.73	**100**	**100**	**100**	**100**	**100**	**100**
8	91.11	99.75	47.85	97.72	**100**	98.85	99.11	99.76	97.67
9	27.28	28.42	25.18	**100**	**100**	**100**	**100**	**100**	**100**
10	55.51	45.28	64.29	49.26	54.81	67.24	67.28	68.38	**76.01**
11	71.32	71.73	74.39	34.27	42.32	40.38	38.13	37.18	**73.20**
12	45.73	45.73	56.27	43.37	37.28	30.60	48.92	49.38	**56.80**
13	90.55	64.64	76.19	98.48	97.66	97.47	96.18	**98.57**	96.25
14	69.17	**95.82**	92.27	73.28	73.12	83.15	84.37	72.39	93.21
15	31.28	21.38	51.11	65.58	58.37	66.52	64.57	**81.34**	64.04
16	25.62	24.41	57.53	96.18	**100**	**100**	99.19	**100**	99.43
OA	62.16	61.28	69.76	56.81	60.12	64.87	67.07	66.27	**77.65**
AA	60.76	59.79	60.64	70.9	75.89	79.45	81.80	82.25	**84.73**
Kappa	61.37	56.87	66.84	49.85	55.91	60.95	62.83	63.19	**74.63**

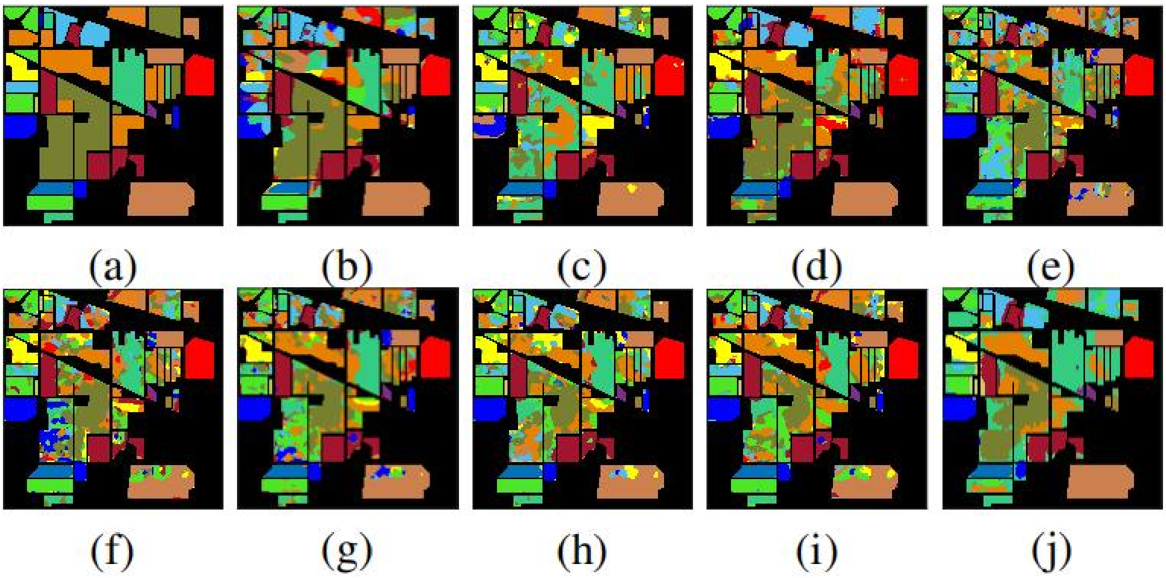

图 8　不同算法在 IP 数据集上的分类图。(a)地物真值；(b) HybirdSN（62.16%）；(c) SSRN（61.28%）；(d) A2S2K（69.76%）；(e) SSCL（56.81%）；(f) DFSL（60.12%）；(g) DCFSL（64.87%）；(h) CMFSL（67.07%）；(i) Gia-CFSL（%）；(j) CPSRCL（77.65%）

表 2 显示了 UP 数据集的实验结果。从表中可以看出，所提出的方法在 OA、AA 和系数方面都取得了最佳结果，在所有三个指标上都比排名第二的 CMFSL 高出近 3%。并且，基于小样本学习的算法的分类性能普遍优于基于深度学习的方法，这可能是因为在没有其他数据集信息辅助的情况下，45 个标注样本包含的信息太少。图 10 显示了不同方法的分类图，可以看出我们的算法在第 4 类和第 8 类上的结果更好。

表 2 不同算法在 UP 数据集上的实验结果

Class	HybirdSN	SSRN	A2S2K	SSCL	DFSL	DCFSL	CMFSL	Gia-CFSL	CPSRCL
1	89.39	80.28	36.19	87.3	80.24	90.17	94.67	**100**	98.78
2	63.82	44.18	68.28	36.82	30.17	54.23	49.21	66.37	**71.05**
3	61.27	48.38	65.34	54.33	79.24	72.88	**84.19**	80.13	64.06
4	42.85	50.52	49.25	34.61	87.17	83.72	**93.27**	75.18	92.03
5	50.31	92.37	87.68	73.17	85.33	**93.27**	92.31	91.08	86.19
6	78.29	96.51	97.21	89.95	88.48	92.68	**97.35**	96.28	86.90
7	78.58	47.29	20.73	**100**	**100**	**100**	**100**	**100**	**100**
8	91.11	99.75	47.85	97.72	**100**	98.85	99.11	99.76	97.67
9	27.28	28.42	25.18	**100**	**100**	**100**	**100**	**100**	**100**
10	55.51	45.28	64.29	49.26	54.81	67.24	67.28	68.38	**76.01**
11	71.32	71.73	74.39	34.27	42.32	40.38	38.13	37.18	**73.20**
12	45.73	45.73	56.27	43.37	37.28	30.60	48.92	49.38	**56.80**
13	90.55	64.64	76.19	98.48	97.66	97.47	96.18	**98.57**	96.25
14	69.17	**95.82**	92.27	73.28	73.12	83.15	84.37	72.39	93.21
15	31.28	21.38	51.11	65.58	58.37	66.52	64.57	**81.34**	64.04
16	25.62	24.41	57.53	96.18	**100**	**100**	99.19	**100**	99.43
OA	62.16	61.28	69.76	56.81	60.12	64.87	67.07	66.27	**77.65**
AA	60.76	59.79	60.64	70.9	75.89	79.45	81.80	82.25	**84.73**
Kappa	61.37	56.87	66.84	49.85	55.91	60.95	62.83	63.19	**74.63**

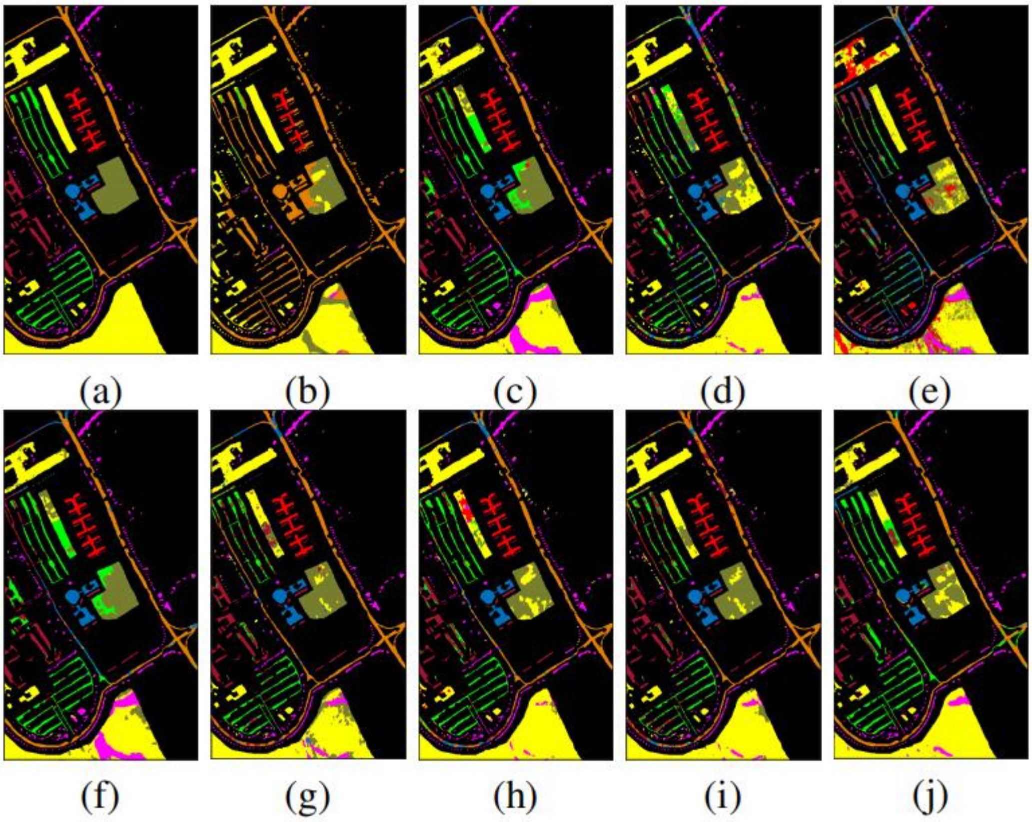

图 9 不同算法在 UP 数据集上的分类图。(a)地物真值；(b) HybirdSN（74.11%）；(c) SSRN（79.81%）；(d) A2S2K（68.43%）；(e) SSCL（62.28%）；(f) DFSL（78.24%）；(g) DCFSL（82.24%）；(h) CMFSL（85.38%）；(i) Gia-CFSL（83.72%）；(j) CPSRCL（87.74%）

4 结论

在本文中，我们提出了一个特定类别的原型自细化对比学习网络，并将该模型应用于小样本高光谱图像分类。我们设计了一种类别特定的映射来更新支持集的原型，允许原型与类别信息一起自适应地进行优化，有效地缓解了噪声样本造成的原型不稳定问题。为了处理源域和目标域的分布差异和类别差异，设计了一个局部判别域适应模块，在保持特定域信息的同时对齐两个域的全局分布。此外，我们利用监督对比学习来增强样本特征的类内紧密性和类间离散性。在两个个公共数据集上的分类结果证明了算法的可行性。

参考文献

[1] A. Plaza, J. A. Benediktsson, J. W. Boardman, J. Brazile, L. Bruzzone,G. Camps-Valls, J. Chanussot, M. Fauvel, P. Gamba, A. Gualtieri,M. Marconcini, J. C. Tilton, and G. Trianni, “Recent advances in techniques for hyperspectral image processing,” *Remote Sens. Environ.*, vol. 113, pp. S110–S122, 2009.

[2] P. Ghamisi, N. Yokoya, J. Li, W. Liao, S. Liu, J. Plaza, B. Rasti, and A. Plaza, “Advances in hyperspectral image and signal processing: A comprehensive overview of the state of the art,” *IEEE Geoscience and Remote Sensing Magazine*, vol. 5, no. 4, pp. 37–78, 2017.

[3] J. M. Bioucas-Dias, A. Plaza, G. Camps-Valls, P. Scheunders, N. M.Nasrabadi, and J. Chanussot, “Hyperspectral remote sensing data analysis and future challenges,” *IEEE Geosci. Remote Sens. Mag.*, vol. 1, no. 2, pp. 6–36, Jun. 2013.

[4] X. Yang and Y. Yu, “Estimating soil salinity under various moisture conditions: An experimental study,” *IEEE Trans. Geosci. Remote Sens.*, vol. 55, no. 5, pp. 2525–2533, 2017.

[5] S. Mei, X. Li, X. Liu, H. Cai, and Q. Du, “Hyperspectral image classification using attention-based bidirectional long short-term memory network,” *IEEE Trans. Geosci. Remote Sens.*, vol. 60, pp. 1–12, 2022.

[6] L. Samaniego, A. B´ardossy, and K. Schulz, “Supervised classification of remotely sensed imagery using a modified *k*-nn technique,” *IEEE Trans. Geosci. Remote Sens.*, vol. 46, no. 7, pp. 2112–2125, 2008.

[7] F. Melgani and L. Bruzzone, “Classification of hyperspectral remote sensing images with support vector machines,” *IEEE Trans. Geosci. Remote Sens.*, vol. 42, no. 8, pp. 1778–1790, 2004. [8] J. Peng, W. Sun, and Q. Du, “Self-paced joint sparse representation for the classification of hyperspectral images,” *IEEE Trans. Geosci. Remote Sens.*, vol. 57, no. 2, pp. 1183–1194, 2019.

[9] L. Shen and S. Jia, “Three-dimensional gabor wavelets for pixel-based hyperspectral imagery classification,” *IEEE Trans. Geosci. Remote Sens.*, vol. 49, no. 12, pp. 5039–5046, 2011.

[10] S. Li, W. Song, L. Fang, Y. Chen, P. Ghamisi, and J. A. Benediktsson, “Deep learning for hyperspectral image classification: An overview,” *IEEE Trans. Geosci. Remote Sens.*, vol. 57, no. 9, pp. 6690–6709, 2019.

[11] L. Wu, L. Fang, J. Yue, B. Zhang, P. Ghamisi, and M. He, “Deep bilateral filtering network for point-supervised semantic segmentation in remote sensing images,” *IEEE Trans. Image Process.*, vol. 31, pp. 7419–7434, 2022.

[12] L. Ma, M. M. Crawford, L. Zhu, and Y. Liu, “Centroid and covariance alignment-based domain adaptation for unsupervised classification of remote sensing images,” *IEEE Trans. Geosci. Remote Sens.*, vol. 57, no. 4, pp. 2305–2323, 2019.

[13] B. Tu, X. Liao, Q. Li, Y. Peng, and A. Plaza, “Local semantic feature aggregation-based transformer for hyperspectral image classification,” *IEEE Trans. Geosci. Remote Sens.*, vol. 60, pp. 1–15, 2022.

[14] M. Zhang, W. Li, Y. Zhang, R. Tao, and Q. Du, “Hyperspectral and lidar data classification based on structural optimization transmission,” *IEEE Trans. Cybernetics*, vol. 53, no. 5, pp. 3153–3164, 2023.

[15] Y. Chen, Z. Lin, X. Zhao, G. Wang, and Y. Gu, “Deep learning-based classification of hyperspectral data,” *IEEE J. Sel. Top. Appl. Earth Observ. Remote Sens.*, vol. 7, no. 6, pp. 2094–2107, 2014.

[16] Y. Chen, H. Jiang, C. Li, X. Jia, and P. Ghamisi, “Deep feature extraction and classification of hyperspectral images based on convolutional neural networks,” *IEEE Trans. Geosci. Remote Sens.*, vol. 54, no. 10, pp. 6232– 6251, 2016.

[17] S. Ji, W. Xu, M. Yang, and K. Yu, “3d convolutional neural networks for human action recognition,” *IEEE Transactions on Pattern Analysis and Machine Intelligence*, vol. 35, no. 1, pp. 221–231, 2013.

[18] S. K. Roy, G. Krishna, S. R. Dubey, and B. B. Chaudhuri, “Hybridsn: Exploring 3-d–2-d cnn feature hierarchy for hyperspectral image classification,” *IEEE Geosci. Remote Sens. Lett.*, vol. 17, no. 2, pp. 277–281, 2020.

[19] M. He, B. Li, and H. Chen, “Multi-scale 3d deep convolutional neural network for hyperspectral image classification,” in *2017 IEEE International Conference on Image Processing (ICIP)*, 2017, pp. 3904–3908.

[20] Z. Xu, H. Yu, K. Zheng, L. Gao, and M. Song, “A novel classification framework for hyperspectral image classification based on multiscale spectral-spatial convolutional network,” in *2021 11th Workshop on Hyperspectral Imaging and Signal Processing: Evolution in Remote Sensing (WHISPERS)*, 2021, pp. 1–5.

[21] Z. Zhao, D. Hu, H. Wang, and X. Yu, “Center attention network for hyperspectral image classification,” *IEEE Journal of Selected Topics in Applied Earth Observations and Remote Sensing*, vol. 14, pp. 3415– 3425, 2021.

[22] H. Sun, X. Zheng, X. Lu, and S. Wu, “Spectral–spatial attention network for hyperspectral image classification,” *IEEE Trans. Geosci. Remote Sens.*, vol. 58, no. 5, pp. 3232–3245, 2020.

[23] H. Zhou, L. Fulin, H. Zhuang, Z. Weng, X. Gong, and Z. Lin, “Attention multi-hop graph and multi-scale convolutional fusion network for hyperspectral image classification,” *IEEE Trans. Geosci. Remote Sens.*, vol. PP, pp. 1–1, 01 2023.

[24] Y. Duan, F. Luo, M. Fu, Y. Niu, and X. Gong, “Classification via structure-preserved hypergraph convolution network for hyperspectral image,” *IEEE Trans. Geosci. Remote Sens.*, vol. 61, pp. 1–13, 2023.

[25] T. Guo, R. Wang, L. Fulin, X. Gong, L. Zhang, and X. Gao, “Dual-view spectral and global spatial feature fusion network for hyperspectral image classification,” *IEEE Trans. Geosci. Remote Sens.*, vol. PP, pp. 1– 1, 01 2023.

[26] J. M. Haut, M. E. Paoletti, J. Plaza, A. Plaza, and J. Li, “Hyperspectral image classification using random occlusion data augmentation,” *IEEE Geosci. Remote Sens. Lett.*, vol. 16, no. 11, pp. 1751–1755, 2019.

[27] W. Li, C. Chen, M. Zhang, H. Li, and Q. Du, “Data augmentation for hyperspectral image classification with deep CNN,” *IEEE Geosci. Remote Sens. Lett.*, vol. 16, no. 4, pp. 593–597, 2019.[28] B. Cui, X.-M. Dong, Q. Zhan, J. Peng, and W. Sun, “Litedepthwisenet: A lightweight network for hyperspectral image classification,” *IEEE Trans. Geosci. Remote Sens.*, vol. 60, p. 5502915, 2022.

[29] H. Zhang, Y. Li, Y. Jiang, P. Wang, Q. Shen, and C. Shen, “Hyperspectral classification based on lightweight 3-D-CNN with transfer learning,” *IEEE Trans. Geosci. Remote Sens.*, vol. 57, no. 8, pp. 5813–5828, 2019.

[30] L. Zhao, W. Luo, Q. Liao, S. Chen, and J. Wu, “Hyperspectral image classification with contrastive self-supervised learning under limited labeled samples,” *IEEE Geosci. Remote Sens. Lett.*, vol. 19, p. 6008205, 2022.

[31] B. Liu, A. Yu, X. Yu, R. Wang, K. Gao, and W. Guo, “Deep multiview learning for hyperspectral image classification,” *IEEE Trans. Geosci. Remote Sens.*, vol. 59, no. 9, pp. 7758–7772, 2021.

[32] Q. Liu, J. Peng, G. Zhang, W. Sun, and Q. Du, “Deep contrastive learning network for small-sample hyperspectral image classification,” *Journal of Remote Sensing*, vol. 3, p. 0025, 2023.

[33] K. Li, Y. Qin, Q. Ling, Y. Wang, Z. Lin, and W. An, “Self-supervised deep subspace clustering for hyperspectral images with adaptive self-expressive coefficient matrix initialization,” *IEEE J. Sel. Top. Appl. Earth Observ. Remote Sens.*, vol. 14, pp. 3215–3227, 2021.

[34] Y. Peng, Y. Liu, B. Tu, and Y. Zhang, “Convolutional transformer-based few-shot learning for cross-domain hyperspectral image classification,” *IEEE J. Sel. Top. Appl. Earth Observ. Remote Sens.*, vol. 16, pp. 1335– 1349, 2023.

[35] B. Liu, X. Yu, A. Yu, P. Zhang, G. Wan, and R. Wang, “Deep few-shot learning for hyperspectral image classification,” *IEEE Trans. Geosci. Remote Sens.*, vol. 57, no. 4, pp. 2290–2304, 2019.

[36] K. Gao, B. Liu, X. Yu, J. Qin, P. Zhang, and X. Tan, “Deep relation network for hyperspectral image few-shot classification,” *Remote Sens.*, vol. 12, no. 6, p. 923, 2020.

[37] Z. Li, M. Liu, Y. Chen, Y. Xu, W. Li, and Q. Du, “Deep cross-domain few-shot learning for hyperspectral image classification,” *IEEE Trans. Geosci. Remote Sens.*, vol. 60, p. 5501618, 2022.

[38] B. Xi, J. Li, Y. Li, R. Song, D. Hong, and J. Chanussot, “Few-shot learning with class-covariance metric for hyperspectral image classification,” *IEEE Trans. Image Process.*, vol. 31, pp. 5079–5092, 2022.

[39] X. Zuo, X. Yu, B. Liu, P. Zhang, and X. Tan, “Fsl-egnn: Edge-labeling graph neural network for hyperspectral image few-shot classification,” *IEEE Trans. Geosci. Remote Sens.*, vol. 60, pp. 1–18, 2022.

[40] Y. Zhang, W. Li, M. Zhang, S. Wang, R. Tao, and Q. Du, “Graph information aggregation cross-domain few-shot learning for hyperspectral image classification,” *IEEE Trans. Neur. Netw. Learn. Syst.*, 2022.

[41] Y. Huang, J. Peng, W. Sun, N. Chen, Q. Du, Y. Ning, and H. Su, “Two-branch attention adversarial domain adaptation network for hyperspectral image classification,” *IEEE Trans. Geosci. Remote Sens.*, vol. 60, pp. 1– 13, 2022.

[42] J. Peng, Y. Huang, W. Sun, N. Chen, Y. Ning, and Q. Du, “Domain adaptation in remote sensing image classification: A survey,” *IEEE J. Sel. Top. Appl. Earth Observ. Remote Sens.*, vol. 15, pp. 9842–9859, 2022.

[43] Y. Huang, J. Peng, N. Chen, W. Sun, Q. Du, K. Ren, and K. Huang, “Cross-scene wetland mapping on hyperspectral remote sensing images using adversarial domain adaptation network,” *ISPRS Journal of Phtogrammetry and Remote Sensing, vol. 203, pp. 37–54, 2023.*

Improved YOLOv5s with Coordinate Attention for Small and Dense Object Detection from Optical Remote Sensing Images

Qinggang Wu[1], Yonglei Wu[1], Wei Huang[1*](Corresponding Author), Yang Li[1]
[1] College of Computer and Communication Engineering, Zhengzhou University of Light Industry, Zhengzhou 450000, China.

Abstract — **The objects in optical HRRSI (High-Resolution Remote Sensing Image) are characterized by tiny, dense, and complex backgrounds, which bring great challenges to accurate object detection. This research presents an enhanced YOLOv5s network-based remote sensing object recognition technique to overcome these issues. Firstly, we present an enhanced YOLOv5s architecture that prunes unnecessary residual modules and incorporates Coordinate Attention (CA) to effectively detect densely packed small objects in remote sensing images. Secondly, since the differences of object sizes in remote sensing images are huge, an optimized anchor box generation algorithm of Differential Evolution (DE) is adopted to produce various anchor box sizes, especially for small objects. Thirdly, we replace the commonly used CIoU loss function in YOLOv5s with a new α-Wise-IoU loss function inspired by both α-IoU and Wise-IoU. This substitution accelerates bounding box regression and concentrates more on regular anchor boxes in our approach. Finally, the SioU Soft-NMS instead of NMS (Non-Maximum Suppression) is utilized to remove the redundant duplicate boxes in our model to detect the dense objects in remote sensing images. Experimental results on NWPU VHR-10 dataset show that the object detection accuracy of the proposed YOLOv5s method significantly increases compared with state-of-the-art algorithms.**

Keywords — **High-Resolution Remote Sensing Image (HRRSI), Differential Evolution (DE), SIoU Soft-NMS (SCYLLA-IOU Soft-NMS), Coordinate Attention (CA), α-Wise-IoU Loss Function.**

Manuscript received 09. 12, 2023.

The authors are with the College of Computer and Communication Engineering, Zhengzhou University of Light Industry, Zhengzhou 450000, China.

Corresponding Author: Wei Huang.

I. INTRODUCTION

In recent years, with the advancements of remote sensing technology, HRRSIs now contain significantly more information than in past, which plays a vital role in diverse applications, for example, precision agriculture, traffic monitoring, and military reconnaissance. Object detection from HRRSIs has been one of the key topics in these applications. However, the remote sensing objects are usually small-sized and densely distributed, resulting in miss detection or incorrect detection as other categories, particularly for those with intricate backgrounds influenced by various factors like weather, illumination and oceanic conditions [1][2]. Consequently, these difficulties may impede the feature extraction of HRRSIs, reduce the object detection accuracy, and hardly meet the object detection requirements.

There have been numerous solutions to tackle the aforementioned challenges in remote sensing object detection [3]. Conventional object detection methods have often utilized machine learning techniques, but the feature extraction process typically entails manual tuning [4]. The advent of deep learning technologies has revolutionized the field of computer vision, significantly advancing object detection and further improving the accuracy of remote sensing object detection. Currently, the mainstream object detection algorithms can be divided into two categories: two-stage algorithms and one-stage algorithms [5]. The conventional two-stage algorithms include R-CNN (Region Convolutional Neural Networks) [6], Fast R-CNN [7], Faster R-CNN [8], and Mask R-CNN [9]. Although these algorithms possess high object detection accuracy, they suffer from the drawbacks of slow speed and losing spatial information of local objects in the entire image. On the other hand, the one-stage algorithm involves SDD (Single Shot

MultiBox Detector) [10], [11], YOLO (You Only Look Once) methods [12], [13], [14], etc. These algorithms are fast in detecting objects, but the object accuracy is not very high. There are five versions of object detection methods for the YOLOv5, in which the small model of YOLOv5s achieves a better balance between object detection speed and accuracy. In recent years, transformers-based methods [15], [16], [17] have emerged as a novel approach to object detection.

Although YOLOv5s method has made great achievements in remote sensing object detection, the small and dense objects are prone to be missed or erroneously categorized as other classes when it is applied to detect objects from HRRSIs with complex backgrounds. For example, the car in the bottom shadow of Figure 1 (a) is missed in the object detection results by YOLOv5s due to the low contrast intensities of the image. Meantime, some bare stones in Figure 1 (b) are erroneously detected as ships for the sea-like scenarios with deep green colors. Thus, the feature extraction process of the YOLOv5s detection network can be challenging, leading to the missed or false detections, particularly when dealing with densely scattered tiny objects in complex environments. To tackle these issues, this paper proposes an enhanced YOLOv5s algorithm. The main contributions of this paper can be summarized as follows:

(1) We propose an improved YOLOv5s network by pruning some redundant residual blocks in the original CSP (Cross-Stage-Partial Network) [18] layer to detect the densely distributed small objects from HRRSIs. Besides, to enhance object detection accuracy, Coordinate Attention (CA) is incorporated into the backbone to achieve a broader receptive field without increasing extra parameters.

(2) A new anchor box generation algorithm based on Differential Evolution (DE) is adopted to replace the original K-means anchor box generation algorithm, which can produce various-sized anchor boxes and helps to improve object detection accuracy in HRRSIs.

(3) We proposed a new loss function of α-Wise-IoU to replace the commonly used CIoU loss in YOLOv5s. The α-Wise-IoU not only focuses on most regular anchor boxes other than extremely good or bad anchor boxes but also accelerates the convergence speed of the proposed method.

(4) In the proposed method, the SIoU Soft-NMS is introduced to replace NMS, which mitigates the duplicated object detection, especially for small and dense targets in remote sensing images.

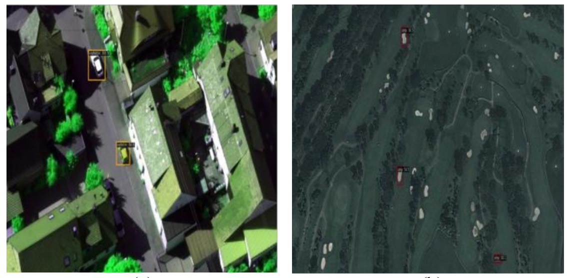

(a) (b)

Figure 1 Difficulties existed in the small and dense object detection results by YOLO from HRRSIs with complex background. (a) The car in the bottom shadow of the image is missed due to the low contrast intensities. (b) Some bare stones are erroneously detected as ships for the sea-like scenarios with deep green colors.

The structure of this paper is as follows: Section II presents a brief introduction to the related works. Section III elaborates on the proposed algorithm of YOLOv5s. Section IV conducts a comparative analysis of experimental results achieved by state-of-the-art methods. Section V summarizes the conclusions of the paper and suggests the research directions in the future.

II. RELEATED WORK

As the mainstream method, deep learning attracts large number of researchers to detect objects from HRRIs. This section mainly reviews the deep learning based object detection methods in terms of two-stage and one-stage. Due to its efficiency, the YOLO series method related to our work are reviewed in detail.

A. Object Detection from HRRIs based on deep learning

According to the steps involved in the deep learning based object detection methods for HRRIs, they can be roughly divided into two categories: two-stage and one-stage. In the former kind of two-stage object detection methods, the first step is region proposal, which is followed by the second step of classifying the samples by CNN. The representatives of the two-stage methods in remote sensing object detection are R-CNN [6], Fast R-CNN [7], Faster R-CNN [8], and Mask R-CNN [9], R2-CNN [19], etc. Pang et al. [19] proposed a Remote Sensing R-CNN (R2-CNN) object detection method which utilizes the Tiny-Net to extract features efficiently and powerfully. Besides, it subsequently incorporates a global attention mechanism to efficiently extract features while suppressing the false detections. Fu et al. [20] built a unified framework based two-stage method which proposed a feature fusion structure to generate multi-scale feature hierarchies to form a powerful multi-scale object feature representation. Generally, the two-stage object detection methods are characterized by the high accuracy and have been widely employed in numerous object detection tasks. However, the computational cost makes it impractical for the real-time object detection from HRRIs.

In contrast, the one-stage method completes the object detection by unifying the bounding box localization and regression in an end-to-end network. The representatives of such kind of method are SSD [10], YOLO [12], [13], [14]. Lu et al. [21] proposed AF-SSD (Attention and Feature fusion SSD) which uses multi-layer feature fusion structure to enhance the semantic information of the shallow features. Additionally, they introduced a dual-path attention module to highlight the key features. Wang et al. [22] introduced the FMSSD (Feature-Merged Single-Shot Detection) network to fuse the contextual information of multi-scale features. Moreover, it accomplishes the ASFP (Atrous Spatial Feature Pyramid) module and also introduces a new area loss function, which monotonically decreases with respect to area to increase the weight of the loss function. The area loss can emphasize the smaller objects and improve the prediction speed. Compared with the two-stage method, the one-stage method is superior mainly in terms of object detection speed with slight improvement in accuracy. Thus, many researchers are prone to utilize the one-stage algorithm to detect objects from HRRSIs.

B. Object Detection from HRRIs based on YOLO series

Due to the lightweight and efficiency, many researchers focus on the YOLO series methods in remote sensing object detection. Xu et al. [23] proposed an improved YOLOv3 object detection method which utilizes DenseNet (Densely Connected Network) to enhance the feature extraction ability. C. Cao et al. [24] proposed an enhanced object detection method for HRRIs based on YOLOv4 [25] by incorporating the Pyramid Pooling Module (PPM) [26] and replacing the original activation function with Mish [27]. Zhang et al. [28] proposed a SuperYOLO method by incorporating a multi-modality fusion module that integrates the RGB and Infrared images, in which a Super-Resolution (SR) branch is added to assist the small object detection in remote sensing images. Generally, a lightweight network can accelerate the inference process, but the object detection accuracy is not satisfactory when the background in HRRIs is more complex.

To overcome above problems, attention mechanism is employed to enhance the object detection performance of YOLO methods by paying more attention on important information. Liu et al. [29] proposed a YOLO-extract method by integrating CA into the backbone network using a dilated convolution [30] after pruning operation. In addition, the Focal-DIoU loss function is employed to replace CIoU and address the imbalance between positive and negative samples. Zhu et al. [31] introduced an object detection framework of TPH-YOLOv5, in which an additional Transformer Prediction Head (TPH) is designed and an CBAM module is introduced to mitigate the negative effects of abrupt changes in object size and achieve more accurate object localization in high-density scenes. Although above method achieves great improvements in remote sensing images, the false or missed object detections are inevitable in YOLO series based methods. Aiming at these problems that encountered by YOLOv5s method for the densely distributed small objects in complex remote sensing images, we propose an improved YOLOv5s algorithm by introducing a CA module and designing a better loss function, which can not only improve the object detection accuracy, but also do not increase any additional parameters.

III. Proposed YOLOv5s Network

The architecture of the proposed YOLOv5s network is shown in Figure 2, which incorporates the CA module into the backbone to enhance object detection accuracy by increasing the receptive field. In addition, the redundant residual blocks in the CSP layer are pruned to detect the densely distributed small objects from remote sensing images. To improve the feature fusion performance, the SPPF and FPN+PAN modules in the Neck component of the YOLOv5s network are retained. Different from the loss function in the prediction head of the original YOLOv5s network, a novel α-Wise-IoU loss function is designed in the proposed YOLOv5s network.

A. Backbone Network Optimization

Generally, the low-level features in CNN-based object detection methods possess high-resolution and rich location information, while the semantic information is low. On the contrary, the high-level feature resolution is low, resulting in scant location information but abundant semantic information. Given abundant small and dense objects in remote sensing

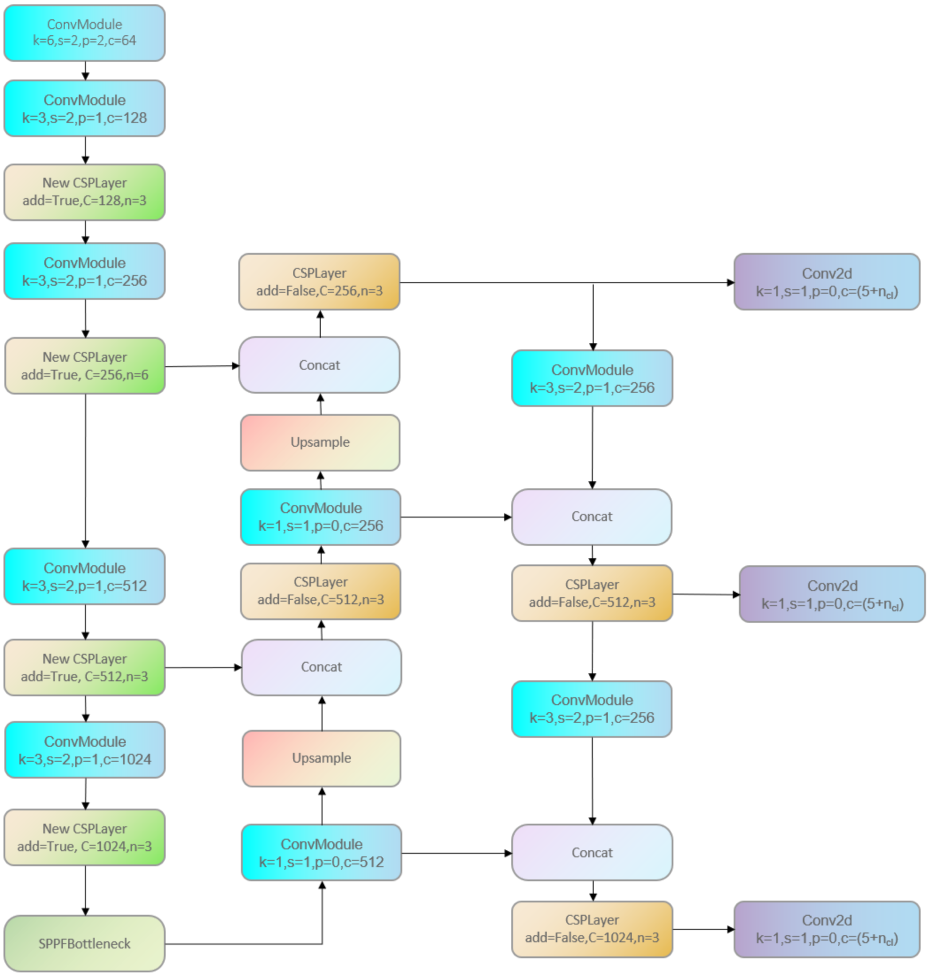

Figure 2 Architecture of the improved YOLOv5s network proposed in this paper.

images, the network layers can't be excessively deep. In the YOLOv5s method, the CSP layer plays a critical role in enhancing feature expression ability which consists of both the main and auxiliary branches, with each branch performing a 1x1 convolution at the outset to decrease the channel numbers. In both branches, a 1x1 convolution is firstly operated to reduce the number of channels. In the main branch, the semantic features are extracted through a residual block, which is concatenated with the auxiliary branch. During this process, the CSP layer facilitates the extraction and fusion of distinct features between the main and auxiliary branches while decreasing the number of parameters and calculation load of the network, consequently accelerating the network training speed. The number of residual blocks in the CSP layer affects the complexity of the network. In original YOLOv5s, the number of residual blocks in CSP is 3, 6, 9, and 3, respectively. Through our experiments, the number of residual blocks in the last two CSP layers has little boost effect on the network in detecting objects from HRRSIs. Therefore, the number of residual blocks in each CSP layer is reduced to 3, 6, 3, and 3, respectively. In other words, six residual blocks are pruned compared with the original third layer, but there is no obvious decrease in object detection accuracy.

To enhance object detection accuracy in complex backgrounds, the proposed YOLOv5s network integrates the Coordinated Attention (CA) module into its backbone. This module enables the network to concentrate on larger receptive fields without significantly increasing computational overhead compared with other attention modules. The CA module captures essential information, including cross-channel, directional, and positional information. Incorporating the CA module into the network backbone enhances its ability to accurately detect and locate objects of interest. Therefore, we add CA to each CSP layer in the backbone network, and the structure of the proposed CSP layer is shown in Figure 3.

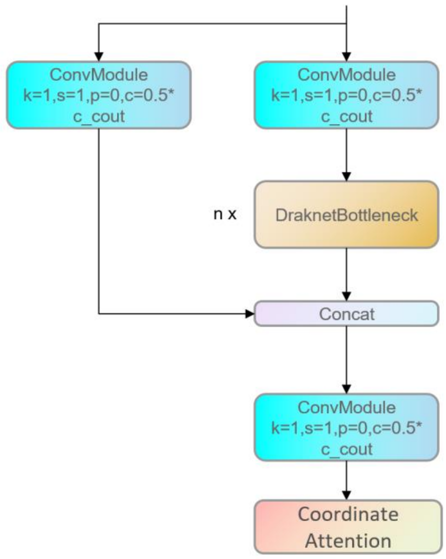

Figure 3 Structure of the proposed CSP layer.

B. Optimize Anchor Generation

The anchor box, generated by k-means in the original YOLOv5s network, demonstrates good detection accuracy on the COCO dataset but is not suited for remote sensing imagery. In this paper, the idea of the Differential Evolution (DE) algorithm [32] is used to generate the anchor boxes, which is a heuristic random search algorithm proposed by Store and Price for solving Chebyshev polynomials based on a theory of gene evolution. The DE algorithm exhibits strong robustness and requires minimal parameters. It operates through a four-step process, including initialization, mutation, crossover, and selection. Figure 4 displays the flowchart of the DE algorithm. The traditional loss function, namely IoU, was employed in our termination criteria. Once the DE algorithm achieves the predetermined threshold, it will terminate and generate an optimized anchor box size.

The comparison of object detection results by YOLOv5s with anchor box generation method of k-means and DE algorithm from NWPU VHR-10 remote sensing images are shown in Figure 5. The left image is the object detection result by the original YOLOv5s algorithm with k-means as anchor box generation method, while the right one is obtained by the proposed YOLOv5s algorithm with DE algorithm. It can be observed that the ground track field is missed by the original YOLOv5s algorithm, while the proposed algorithm with the DE method successfully detects this object. The reason mainly lies in that the target with a large size cannot be detected well by the original anchor box due to its fixed size, while the

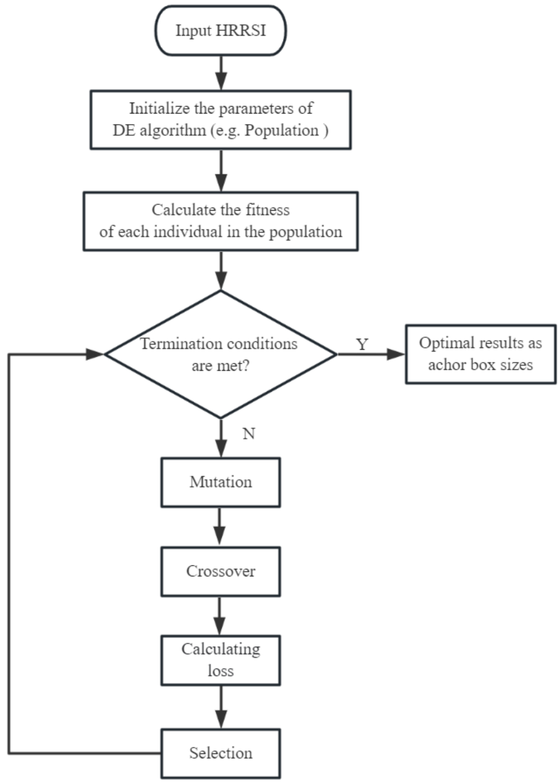

Figure 4 Flowchart of Differential Evolution (DE) algorithm.

Figure 5 Comparison of object detection results by YOLOv5s with k-means (left) and DE algorithm(right) on NWPU VHR-10 remote sensing images.

anchor box generated by the DE algorithm varies to a great extent and mitigates the problem of detecting objects from remote sensing images where the sizes of interested objects are with large differences.

C.α-Wise-IoU Loss

Bounding box regression is a vital step in object detection for accurate object localization. The success of this approach heavily relies on the selection of an appropriate loss function. YOLOv5s is widely recognized as one of the most advanced techniques for object detection, leveraging the CIoU loss function for bounding box regression. The CIoU function is an enhancement of DIoU [33], which exacts a penalty on the length-to-width ratio of the predicted box versus the ground-truth box. Formula (1) shows the calculation method of the CIoU:

$$L_{CIoU}=1-IoU+\frac{\rho^2\left(b,b^{gt}\right)}{c^2}+\left(\frac{v}{\left(1-IoU\right)+v}\right)v \quad (1)$$

$$v=\frac{4}{\pi^2}\left(arc\ \tan\frac{w^{gt}}{h^{gt}}-arc\ \tan\frac{w}{h}\right)^2 \quad (2)$$

The variables b and b^{gt} correspond to the predicted and ground-truth box center points, respectively. The meaning of other symbols can refer to the literature [33]. Remote sensing images often contain challenging samples, but CIoU fails to consider the balance between difficult and easy samples. Influenced by geometric factors such as distance and aspect ratio, the penalty on hard samples can be exacerbated, thereby reducing the generalization ability of the object detection method on other remote sensing images. A suitable loss function must minimize the impact of these geometric factors when the predicted anchor box closely aligns with the ground-truth anchor box.

We propose to replace the original CIoU with the Wise-IoU v3 [34], which effectively solves the problem of the aforementioned hard examples. At the same time, we integrate the idea of α-IoU into Wise-IoU, which not only accelerates the convergence speed of the proposed YOLOv5s model but also provides stronger robustness to object detection in remote sensing images. For the Wise-IoU, there are three versions. The first one is Wise-IoU v1 and calculated as formulas (3) and (4):

$$L_{WIoUv1}=R_{WIoU}L_{IoU} \quad (3)$$

$$R_{WIoU}=\exp\left(\frac{\left(x-x_{gt}\right)^2+\left(y-y_{gt}\right)^2}{\left(W_g^2+H_g^2\right)^*}\right) \quad (4)$$

where variables W_g and H_g denote the width and height of the smallest enclosing box. The ground-truth box's width and height are represented by x_{gt} and y_{gt} respectively, while the predicted boxes' width and height are represented by x and y.

As is commonly understood, the Focal Loss [35] function implements a monotonic focusing mechanism for cross-entropy, thereby decreasing the weight attributed to simple samples in the calculation of the overall loss values. This facilitates the model in concentrating on more challenging samples and ultimately achieving better classification performance. Similarly, Wise-IoU v2 constructs the monotonic focusing coefficient of Wise-IoU v1 as formula (5).

$$L_{WIoUv2}=\left(\frac{L_{IoU}^*}{L_{IoU}}\right)^\gamma L_{WIoUv1} \quad (5)$$

Further, Wise-IoU v3 uses a dynamic non-monotonic focusing mechanism, which defines outliers to describe the quality of the anchor box as formula (6):

$$\beta=\frac{L_{IoU}^*}{L_{\alpha IoU}}\in\left[0,+\infty\right) \quad (6)$$

A higher quality is attained by the YOLOv5s model as the outlier degree of the anchor box decreases. To make the bounding box regression (BBR) towards regular-quality anchor boxes, a small gradient gain should be assigned to the one with a lower or high outlier degree, which can effectively prevent large gradients from hard samples. It utilizes a non-monotonic focusing coefficient β to modify WIoU v1 in formula (7).

$$L_{WIoUv3}=rL_{WIoUv1},\ r=\frac{\beta}{\delta\alpha^{\beta-\delta}} \quad (7)$$

To accelerate the convergence speed of object detection model, we introduce the idea of α-IoU [36] to improve the performance of Wise-IoU v3. On this basis, we design the α-Wise-IoU loss function, which makes the object detection algorithm focus more on regular-quality anchor boxes. Specifically, we allocate a small gradient gain to the anchor boxes with higher and lower quality. The α-Wise-IoU loss function proposed in this paper is shown in formula (8).

$$L_{\alpha WIoU}=\exp\left(\frac{\left(x-x_{gt}\right)^2+\left(y-y_{gt}\right)^2}{\left(W_g^2+H_g^2\right)^*}\right)\gamma\left(1-IoU^t\right) \quad (8)$$

where t plays the same role as α in $\alpha-IOU$ (here the reason we term it as t is to differ from the α in γ) and set to be 3. γ is the same meaning as that of formula (7), where the parameter α in γ is set to 1.9, δ set to 3. The computational graph detaches W_g and H_g (the detach operation is indicated by the superscript *).

As shown in Figure 6, the object detection results by the original YOLOv5s method with CIoU as the loss function is shown on the left, while the proposed method with α-Wise-IoU as the loss function is shown on the right. By comparison, the duplicate detection

Figure 6 Comparison of object detection results by YOLOv5s with CIoU (left) and α-Wise-IoU (right) on NWPU VHR-10 remote sensing images.

boxes of small and dense aircrafts on the left are effectively avoided by the improved YOLOv5s method with α-Wise-IoU as the loss function on the right.

D. SIoU Soft-NMS

Non-Maximum Suppression (NMS) is a frequently employed post-processing approach in object detection algorithms. But NMS usually results in the following problems. When the threshold is too small, the bridge (as shown in Figure 7) inside the green box is easily suppressed. Otherwise, it is easy to cause false positive detection, i.e., the suppression effect is not significant. As an improved version of NMS, Soft-NMS is designed to overcome the problems of NMS. The main idea of Soft-NMS [37] is to modify the score of the traditional NMS algorithm in overlapping regions, which is suppressed in a reduced probability. Specifically, the steps of the Soft-NMS algorithm are as follows.

(1) All the detected objects are sorted from the highest score to the lowest score.

(2) The object with the highest score is chosen, and the overlap between it and the remaining objects is calculated using IOU values. The weights of the remaining objects are adjusted accordingly.

(3) The confidence of the bounding box is reduced based on the adjusted weights, where the confidence is computed using the original score weighted by the updated weights.

(4) Repeat steps (2) and (3) for all the objects.

Due to the small and dense targets in remote sensing images, NMS may result in detecting duplicate targets. To overcome this problem, we use the SIoU [38] to combine with Soft-NMS instead of the original IoU.

Figure 7 The problem existing in NMS.

IV. Experimental Results and Analysis

The experiments are conducted on the platform configured with hardware including AMD Ryzen 7 5800 H, NVIDIA GeForce RTX 3070 (8GB), and software including Operating System Win10, PyTorch 1.12.1 + cu116, and the frameworks of MMYOLO and MMDetection are used. The object detection results are compared with the cutting-edge two-stage approach of Faster R-CNN and the one-stage techniques of SSD, YOLOv3, and YOLOv5.

A. Experimental Dataset and Parameter Settings

The NWPU VHR-10 dataset [39] is adopted to conduct experiments and comparisons in this paper, which includes 800 remote sensing images and 10 classes. All the remote sensing images are divided into three subsets of training, validation, and testing with a ratio of 6:2:2. As for the parameters in the training process of the YOLOv5s network, an initial learning rate of 0.0025, a batch size of 16, and a total of 200 training rounds are set.

B. Evaluating Metric

In this paper, mAP (mean Average Precision) is utilized as an evaluation metric to describe the performance of each object detection method, the calculation of which is based on *Precision* and *Recall.*

Precision measures the prediction accuracy based on the percentage of true positives in all the predicted targets. It can be calculated using formula (9):

$$P = \frac{TP}{TP+FP} \tag{9}$$

Recall measures the number of correct predictions that were detected in the samples. It can be calculated using formula (10):

$$R = \frac{TP}{TP+FN} \tag{10}$$

The two equations above incorporate TP (True Positive), FN (False Negative), FP (False Positive), and TN (True Negative). As both above commonly used performance evaluation metrics, *Precision* and *Recall* are often contradictory. Therefore, the mAP parameter is introduced to evaluate the performance of the object detection method by using both parameters simultaneously. The calculation for AP and mAP is given by formula (11):

$$AP = \int_0^1 P(R)dr\,, \quad mAP = \frac{1}{N}\sum_{i=1}^{N} AP_i \tag{11}$$

C. Comparison with original YOLOv5

To evaluate the effectiveness of the proposed YOLOv5s method, the object detection results on remote sensing images are obtained by the YOLOv5s algorithm with a confidence level of 0.65. Figure 8 shows the comparisons of the object detection results between the proposed YOLOv5s method (right) and the original YOLOv5s method (left) for the dense and small targets. The image in the first row contains many dense storage tanks, which clearly shows that there are many duplicate and inaccurate prediction boxes obtained by the original YOLOv5s method (such as the storage tanks in the second and third columns of the second row inside the red circle), while the storage tanks in the right image are detected and located more accurate without duplicate detection results. The reason lies in that the SIoU Soft-NMS suppresses more duplicate bounding boxes compared to the commonly used NMS in the original YOLOv5s method. The images in the second row depict the densely distributed small aircrafts. It is evident that the left image comprises numerous inaccurate prediction boxes and redundant detections, e.g. the aircrafts at the bottom-left of the image. In contrast, the object detection results in the right image are more accurate with no duplicate bounding boxes, which successfully locates and identifies the aircrafts. The images in the third row are more complex than the above two images since there are not only storage tanks but also small-sized aircrafts. When detecting storage tanks on the left side, there are many duplicate and inaccurate prediction boxes, but the boxes of the storage tanks and aircrafts in the right image are more accurate and there is no re-detection for the densely distributed small targets (for example the small aircraft in the center of the image which is also partially occluded by a large aircraft). Thus, the frequently occurring problem in the original YOLOv5s method does not exist in the proposed algorithm. The reason lies in that the introduced SIoU Soft-NMS can suppress more duplicate bounding boxes and the DE algorithm generates varied sizes of anchor boxes which help to detect the objects with large size differences in remote sensing images.

Figure 8 Comparison of small and dense object detection results on NWPU remote sensing images between the proposed YOLOv5s method and the original YOLOv5s algorithm.

Figure 9 illustrates the miss and erroneous object detection results of the original YOLOv5s model in complex remote sensing images. As shown in the left image of the first row, the overpass is erroneously classified as a bridge, since the overpass is very similar to a bridge in the scene. In contrast, such a problem does not occur in the object detection result of the proposed model. Similarly, the original YOLOv5s model makes a mistake since the watermark is recognized as a ship at the bottom of the second row and the reef as a ship in the bottom-left of the third row, which highlights the challenges of detecting targets with blurred visual appearance. In contrast, both of these two blurred objects are not deemed as the wrong objects by the proposed YOLOv5s method. The reason is that the CIoU commonly used in the original YOLOv5s allocates nearly average weights to all the bounding boxes, while the α-Wise-IoU proposed in this paper pays more attention to the regular bounding boxes. All the above object detection results demonstrate that the introduced CA module improves

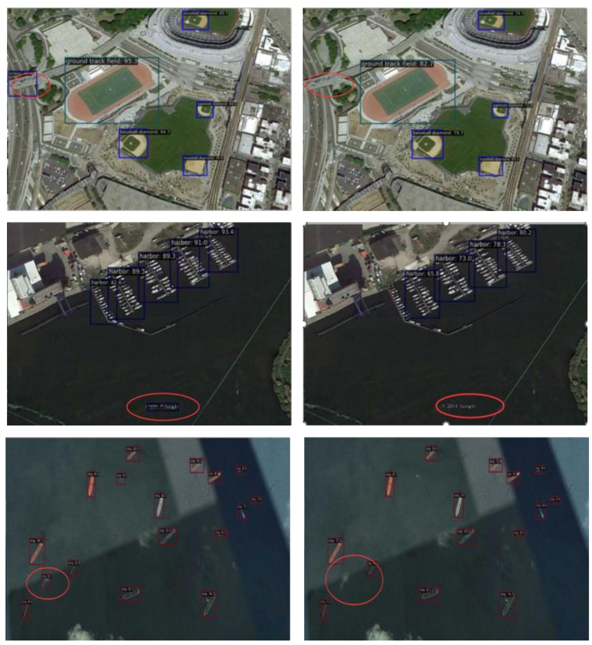

Figure 9 Comparison of object detection results on NWPU VHR-10 remote sensing images with complex backgrounds between the proposed YOLOv5s method and the original YOLOv5s network.

the feature extraction ability in detecting remote sensing objects.

Table 1 shows the *AP* values for each category of objects in the NWPU VHR-10 dataset, and it can be observed that the *AP* values of the nine kinds of objects except for vehicle increase compared to the original method. For the small and dense characteristics of airplane, ship, and storage tank, there is a significant increase obtained by the proposed algorithm in terms of *AP* since our method focus more on densely distributed small objects. For the large and medium objects, e.g. baseball diamond and tennis court, etc., the *AP* values are also increased compared to the original YOLOv5s method. This shows that our method achieves better object detection results in most cases. It can also be observed that there is a slight decrease in vehicles, the reason lies in that they are easily affected by the complex light circumstance and severe occlusion, which is still a challenging problem in the field of remote sensing object detection.

Table 1 Comparison of the proposed yolov5s method and the original yolov5s in terms of ap for object detection of each category in the NWPU VHR-10 remote sensing dataset.

Object Category	YOLOv5s(AP)	Proposed YOLOv5s(AP)
Airplane	69.5	71.4
Ship	61.7	64.4
Storage tank	49.4	57.7
Baseball diamond	75.0	78.1
Tennis court	71.7	73.4
Basketball court	66.0	67.9
Ground track field	81.7	83.6
Harbor	55.8	58.3
Bridge	34.6	36.5
Vehicle	61.0	59.4

D. Comparison with More State-of-the-art Methods

To further verify the efficacy of the newly proposed YOLOv5s technique, additional experiments were performed on the NWPU VHR-10 remote sensing dataset, and the resulting object detection results were compared against the cutting-edge methods, as depicted in Figure 10. In this figure, the first five rows are the object detection results obtained by Faster R-CNN, SSD, YOLOv3, YOLOv5, and the proposed YOLOv5 in this paper, while the last row is the Ground Truth. As observed in the first column, the bare land in the lower right corner is recognized as a baseball field by Faster R-CNN, SSD, and YOLOv5, and such false detection does not occur in YOLOv3 possibly due to its weak feature extraction. It is noticed that the improved YOLOv5s algorithm avoids these false detections. Similarly, Faster R-CNN and SSD occur false positive detections since they mistakenly deem the lawn as a baseball diamond in the second column, and YOLOv3 failed to detect some airplanes. In contrast, there are no miss or false detection for any objects by YOLOv5s and our improved YOLOv5s method which demonstrates that the proposed YOLOv5s obtains better object detection accuracy and performance. In the remote sensing images with complex backgrounds, the advantage of our improved method is also obvious. For example, there is a large shadow in the central area of the image in the third column. Although the two-stage algorithm Faster R-CNN detects most cars, it also had the issue of duplicate detections. Our proposed algorithm only missed one car that was partially located in the shadow on the left center of the image, while the other algorithms had more miss detections. Similarly, in the last column image with a more challenging scenario, there is a gray car in the shadow which is difficult to discern even with the naked eyes. The methods of SSD, YOLOv3 and the original YOLOv5s fail to recognize this car in the shadow, but the two-stage method of Faster R-CNN and the proposed YOLOv5s algorithm successfully detect and accurately locate the car since the introduced Coordinate Attention module in our method improves the feature extraction ability in the shadow area with low contrast. Regarding object detection speed, the enhanced one-stage algorithm outperforms the two-stage method, signifying the superiority of our enhanced technique in handling densely-packed small objects in complex background remote sensing images.

Table 2 Comparison of the proposed yolov5s method with state-of-the-art object detection methods in terms of *mAP* on the NWPU VHR-10 remote sensing dataset.

Model	*mAP*
Faster R-CNN	58.4
SSD	60.1
YOLOv3	51.4
YOLOv5s	62.6
Improved YOLOv5s	65.1

Table 2 shows the comparisons with other existing algorithms in terms of *mAP* which are obtained on the same platform. It can be observed that the *mAP* value of the proposed algorithm is better than those of the mainstream two-stage algorithm of Faster R-CNN and one-stage algorithms of SSD, YOLOv3, and YOLOv5s. While the detection accuracy of the two-stage Faster R-CNN algorithm is comparable to

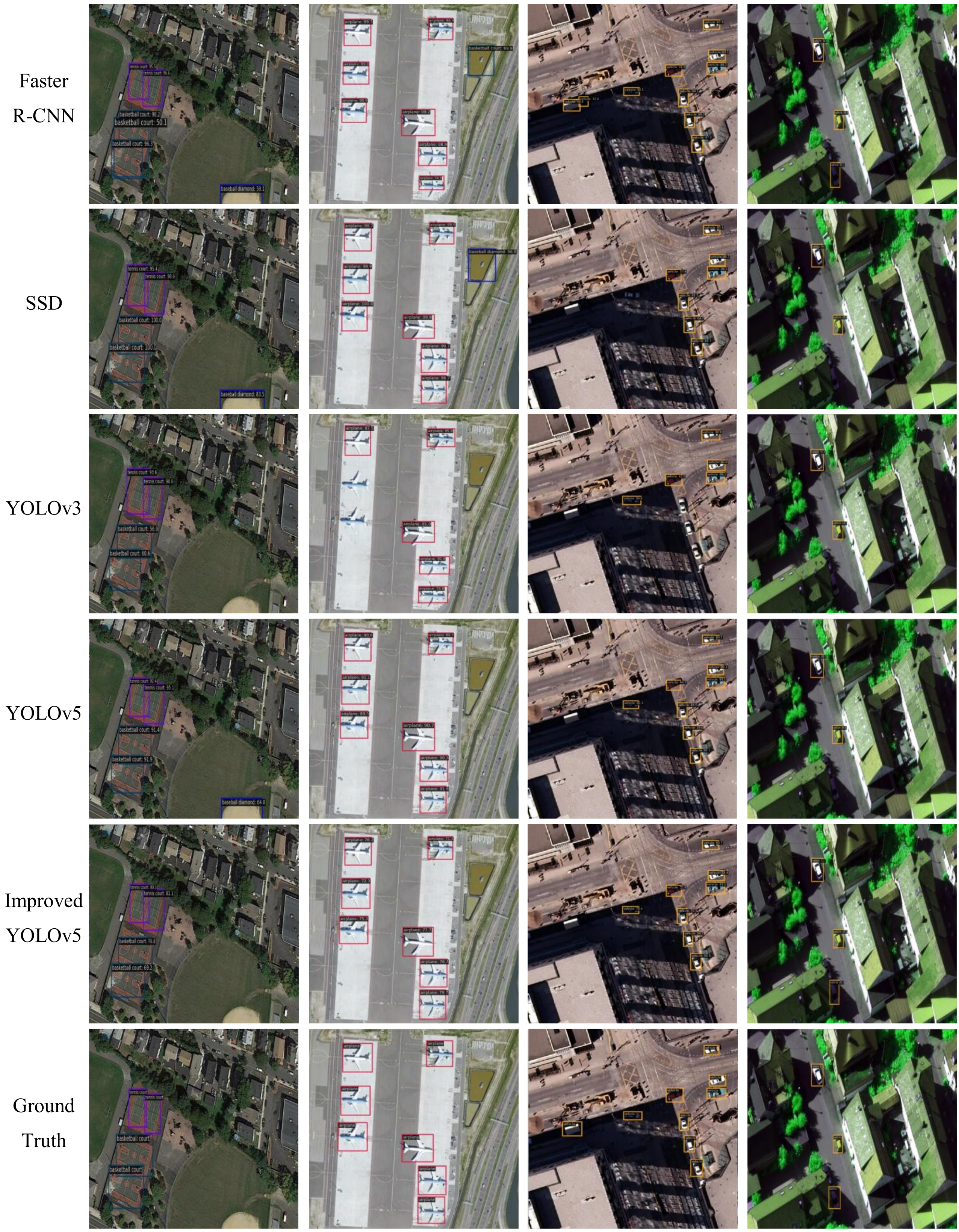

Figure 10 Comparison on the detection performance of small and dense objects in NWPU VHR-10 remote sensing images with complex backgrounds between the proposed YOLOv5s approach and state-of-the-art methods of Faster R-CNN (two-stage), and SSD, YOLOv3, and YOLOv5 (one-stage).

that of the one-stage SSD algorithms, it is not as fast as the one-stage algorithms in object detecting speed.

E. Ablation Study

To verify the effects of the modifications in the proposed YOLOv5s method, Table 3 shows the ablation experimental results compared with the original YOLOv5s on the test set. For convenience, all the medium models are termed as abbreviated name in the first column. The original YOLOv5s method achieves 62.6 *mAP* on the test set. On this basis, the *mAP* of YOLOv5s-V1 method increases 1.1 by introducing the DE algorithm to replace the K-means algorithm, which enhances the detection ability for objects with large size differences. In addition, a new loss function of α-Wise-IoU is adopted in YOLOv5s-V2 to replace the commonly used CIoU in the original YOLOv5s method. This not only enables the network to focus more on common anchor boxes but also accelerates the convergence speed. We can observe that the YOLOv5s-V2 method improves by 0.3 *mAP* compared to the YOLOv5s-V1 method. Furthermore, the YOLOv5s-V3 method is improved with an enhanced backbone network that boosts the feature extraction ability, which leads to a 0.2 *mAP* improvement versus the YOLOv5s-V2 method. Finally, our proposed model YOLOv5s-V4 utilizes SIoU Soft-NMS instead of NMS based on YOLOv5-V3 to remove redundant anchor boxes of dense targets, resulting in an improvement of an additional 0.8 *mAP* Thus, our proposed model YOLOv5s-V4 outperforms the original YOLOv5s method by 2.5 *mAP* on the NWPU VHR-10 dataset, demonstrating the effectiveness of the proposed method.

Table 3 model ablation analysis on NWPU VHR-10 remote sensing dataset in terms of *mAP* .

Abbreviated Model Name	Improved Model	*mAP*
YOLOv5s	YOLOv5s	62.6
YOLOv5s-V1	+DE	63.7(+1.1)
YOLOv5s-V2	+α-Wise-IoU	64.0 (+0.3)
YOLOv5s-V3	+CA	64.2(+0.2)
YOLOv5s-V4	+ SIoU Soft-NMS	65.1(+0.8)

V. Conclusion

This paper proposes a deep neural network to detect small objects that are densely packed in remote sensing images with complex backgrounds. The proposed network mainly contains four aspects: optimized backbone network, Differential Evolution (DE) based anchor box generation algorithm, α-Wise-IoU loss function, and SIoU Soft-NMS. We prune some redundant residual blocks in the CSP layer from the original YOLOv5s network and integrate the CA mechanism to the backbone network to detect the densely distributed small objects from remote sensing images by enlarging the receptive field. The DE-based anchor box generation algorithm is adopted to replace the original K-means algorithm to produce various-sized anchor boxes. We design a new loss function of α-Wise-IoU to focus on most regularanchor boxes and accelerate the convergence speed of the proposed method. The proposed approach employs SIoU Soft-NMS to reduce the occurrence of duplicate object detection in small and densely-packed objects in remote sensing images. This method is effective for accurately detecting small objects within complex backgrounds, resulting in improved detection accuracy when compared to state-of-the-art algorithms. In future work, the data augmentation method could be optimized by incorporating prior knowledge of complex backgrounds to enhance feature extraction capabilities in even more intricate environments. anchor boxes and accelerate the convergence speed of the proposed method. The proposed approach employs SIoU Soft-NMS to reduce the occurrence of duplicate object detection in small and densely-packed objects in remote sensing images. This method is effective for accurately detecting small objects within complex backgrounds, resulting in improved detection accuracy when compared to state-of-the-art algorithms. In future work, the data augmentation method could be optimized by incorporating prior knowledge of complex backgrounds to enhance feature extraction capabilities in even more intricate environments.

References

[1] G. Cheng, J. Han, “A survey on object detection in optical remote sensing images,” ISPRS J. Photogramm. Remote Sens, vol. 117, pp. 11–28, 2016.

[2] C. Li, R. Cong, C. Guo, H. Li, C. Zhang, F. Zheng, Y. Zhao, “A parallel down-up fusion network for salient object detection in optical remote sensing images,” Neurocomputing, vol. 415, pp. 411–420, 2020.

[3] J. Wang, Z. Gong, X. Liu, H. Guo, D. Yu, L. Ding, “Object detection based on adaptive feature-aware method in optical remote sensing images,” Remote Sens, vol. 14, no. 3616, 2022.

[4] W. Han, J. Li, S. Wang, Y. Wang, J. Yan, R. Fan, X. Zhang, L. Wang, “A context-scale-aware detector and a new benchmark for remote sensing small weak object detection in unmanned aerial vehicle images,” Int. J. Appl. Earth Obs. Geoinf, vol. 112, no. 102966, 2022.

[5] G. Hinton, N. Srivastava, A. Krizhevsky, I. Sutskever, and R. Salakhutdinov, “Improving neural networks by preventing coadaptation of feature detectors,” 2012, arXiv:1207.0580.

[6] R. Girshick, J. Donahue, T. Darrell, and J. Malik, “Rich feature

hierarchies for accurate object detection and semantic segmentation," in Proc. IEEE Conf. Comput. Vis. Pattern Recognit., Jun. 2014, pp. 580–587.
[7] R. Girshick, "Fast R-CNN," in Proc. IEEE Int. Conf. Comput. Vis., Dec. 2015, pp. 1440–1448.
[8] S. Ren, K. He, R. Girshick, and J. Sun, "Faster R-CNN: towards real-time object detection with region proposal networks," in Proc. Adv. Neural Inf. Process. Syst., vol. 28, pp. 1–15, 2015.
[9] K. He, G. Georgia, D. Piotr, and B. Girshick. "Mask R-CNN," in Proc. IEEE Int. Conf. Comput. Vis., Dec. 2017, pp. 2980-2988.
[10] W. Liu, D. Anguelov, D. Erhan, C. Szegedy, S. Reed, C. Fu, and A. Berg, "SSD: single shot multibox detector," in Proc. Eur. Conf. Comput. Vis., Oct. 2016, pp. 21–37.
[11] C. Fu, W. Liu, A. Ranga, A. Tyagi, and A. Berg, "DSSD: deconvolutional single shot detector," 2017, arXiv:1701.06659.
[12] J. Redmon, S. Divvala, R. Girshick, and A. Farhadi, "You only look once: unified, real-time object detection," in Proc. IEEE Conf. Comput. Vis. Pattern Recognit., Jun. 2016, pp. 779–788.
[13] J. Redmon and A. Farhadi, "YOLO9000: better, faster, stronger," in Proc. IEEE Conf. Comput. Vis. Pattern Recognit., Jul. 2017, pp. 7263–7271.
[14] J. Redmon and A. Farhadi, "YOLOv3: an incremental improvement," 2018, arXiv:1804.02767.
[15] A. Vaswani, M. Shazeer, N. Parmar, U. Jakob, J. Llion, N. Aidan, K. Lukasz, and P. Illia, "Attention is all you need," in Proc. Adv. Neural Inf. Process. Syst., Dec. 2017, pp. 5998-6008..
[16] N. Carion, M. Francisco, S. Gabriel, U. Nicolas, K. Alexander and Z. Sergey, "End-to-end object detection with transformers," 2020, ArXiv abs/2005.12872.
[17] A. Dosovitskiy, B. Lucas, K. Alexander, W. Dirk, etc., "An image is worth 16x16 words: transformers for image recognition at scale," 2020, ArXiv abs/2010.11929.
[18] C. Wang, H. Liao, Y. Wu, P. Chen, J. Hsieh, I. Yeh, "CSPNet: a new backbone that can enhance learning capability of CNN," in Proc. IEEE Conf. Comput. Vis. Pattern Recognit., Jun. 2020, pp. 390–391.
[19] J. Pang, C. Li, J. Shi, Z. Xu, and H. Feng, "R^2 -CNN: Fast Tiny Object Detection in Large-Scale Remote Sensing Images," IEEE Trans. Geosci. Remote Sens., vol. 57, no. 8, pp. 5512–5524, Aug. 2019, doi: 10.1109/TGRS.2019.2899955.
[20] K. Fu, Z. Chang, Y. Zhang, G. Xu, K. Zhang, and X. Sun, "Rotation-aware and Multi-scale Convolutional Neural Network for Object Detection in Remote Sensing Images," Isprs J. Photogramm. Remote Sens., vol. 161, pp. 294–308, Mar. 2020, doi: 10.1016/j.isprsjprs.2020.01.025.
[21] X. Lu, J. Ji, Z. Xing, and Q. Miao, "Attention and Feature Fusion SSD for Remote Sensing Object Detection," IEEE Trans. Instrum. Meas., vol. 70, pp. 1–9, 2021, doi: 10.1109/TIM.2021.3052575..
[22] P. Wang, X. Sun, W. Diao, and K. Fu, "FMSSD: Feature-Merged Single-Shot Detection for Multiscale Objects in Large-Scale Remote Sensing Imagery," IEEE Trans. Geosci. Remote Sens., vol. 58, no. 5, pp. 3377–3390, May 2020, doi: 10.1109/TGRS.2019.2954328.
[23] D. Xu and Y. Wu, "Improved YOLO-V3 with DenseNet for Multi-Scale Remote Sensing Target Detection," Sens., vol. 20, no. 15, p. 4276, Jul. 2020, doi: 10.3390/s20154276.
[24] C. Cao, J. Wu, X. Zeng, Z. Feng, T. Wang, X. Yan, Z. Wu, Q. Wu, and Z. Huang, "Research on airplane and ship detection of aerial remote sensing images based on convolutional neural network," Sensors, vol. 20, no. 17, vol. 4696, 2020.
[25] A. Bochkovskiy, C. Wang, and H. Liao, "YOLOv4: optimal speed and accuracy of object detection," 2020, arXiv:2004.10934.
[26] H. Zhao, J. Shi, X. Qi, X. Wang, and J. Jia, "Pyramid scene parsing network," in Proc. IEEE Conf. Comput. Vis. Pattern Recognit., Jul. 2017, pp. 2881–2890.
[27] D. Misra, "Mish: a self regularized non-monotonic neural activation function," 2019, ArXiv abs/1908.08681.
[28] J. Zhang, J. Lei, W. Xie, Z. Fang, Y. Li, and Q. Du, "SuperYOLO: Super Resolution Assisted Object Detection in Multimodal Remote Sensing Imagery," IEEE Trans. Geosci. Remote Sens., vol. 61, pp. 1–15, 2023, doi: 10.1109/TGRS.2023.3258666.
[29] Z. Liu, Y. Gao, Q. Du, M. Chen, W. Lv, "YOLO-extract: improved YOLOv5s for aircraft object detection in remote sensing images," IEEE Access, vol. 11, pp. 1742–1751, 2023.
[30] F. Yu, K. Vladlen, and A. Thomas. "Dilated residual networks," in Proc. IEEE Conf. Comput. Vis. Pattern Recognit., Jul. 2017, pp. 636-644.
[31] X. Zhu, S. Lyu, X. Wang, and Q. Zhao, "TPH-YOLOv5: Improved YOLOv5 Based on Transformer Prediction Head for Object Detection on Drone-captured Scenarios." arXiv, Aug. 25, 2021. doi: 10.48550/arXiv.2108.11539.
[32] K. Price, and R. M. Storn, "Differential Evolution: a simple and efficient heuristic for global optimization over continuous spaces," J. Global Optim., vol. 11, no. 4, 341-359, 1997.
[33] Z. Zheng, P. Wang, W. Liu, J. Li, R. Ye, and D. Ren, "Distance-IoU loss: faster and better learning for bounding box regression," in AAAI Conf. Artif. Intell., Feb. 2020, pp. 12993–13000.
[34] Z. Tong, Y. Chen, Z. Xu, and R. Yu, "Wise-IoU: bounding box regression loss with dynamic focusing mechanism," Jan. 2023. arXiv:2301.10051.
[35] T. Lin, P. Goyal, R. Girshick, K. He, and P. Dollar, "Focal loss for dense object detection," in Proc. IEEE Int. Conf. Comput. Vis., Oct., 2017, pp. 2999–3007.
[36] J. He, M. Sarah, X. Ma, B. James, C. Ying, and X. Hua. "Alpha-IoU: a family of power intersection over union losses for bounding box regression," in Proc. Adv. Neural Inf. Process. Syst., Dec. 2021, pp. 20230-20242.
[37] B. Navaneeth, B. Singh, R. Chellappa, and L. Davis. "Soft-NMS-improving object detection with one line of code," in Proc. IEEE Int. Conf. Comput. Vis., Oct. 2017, pp. 5562-5570.
[38] Z. Gevorgyan, "SIoU loss: more powerful learning for bounding box regression,". 2022, arXiv:2205.12740.
[39] G. Cheng and J. Han. "A survey on object detection in optical remote sensing images," ISPRS J. Photogramm. Remote Sens., vol. 117, pp. 11-28, Jul. 2016.

A Reliability-Amended-Based Controller Placement Method for LEO Satellite Networks

WEI Shuotong[1,2], DONG Tao[1,2*], DI Hang[1,2],LIU Zhihui[1,2], JINShichao[1,2]

1. State Key Laboratory of Space-Ground Integrated Information Technology, Space Star Technology Co., Ltd., Beijing 100095, China;

2. Beijing Institute of Satellite Information Engineering, Beijing 100095, China

Abstract: LEO satellite networks are becoming research hot and the utilization of software defined network (SDN) technology brings benefits in flexible network control. Controller placement is important for SDN-enabled networks. In this paper, the impact of delay and reliability on controller placement for SDN-enabled LEO satellite networks is analyzed firstly, following which a reliability-amended model is proposed based on programmable switches distributed on some satellites. The latency-reliability utility function and programmable switch-based enhanced controller placement algorithm are presented. Finally, the effectiveness of the proposed method is demonstrated through simulation and the results show that about 10% reliability can be improved compared to that without amendment.

Keywords: LEO satellite networks, software defined network (SDN), controller placement, joint delay and reliability optimization, reliability amendment

I INTRODUCTION

Low earth orbit (LEO) satellite networks own relatively low altitudes, guaranteeing low latency compared with geostationary orbit (GEO) satellites. In the last decade, the number of deployed satellites has increased dramatically and the 3rd Generation Partnership Project proposes non-terrestrial network to take advantage of the convergence of satellite networks and terrestrial 5G networks to incorporate a hybrid satellite network to overcome the limitations in terms of smaller coverage of terrestrial cellular communications and greater terrain restrictions, in which LEO satellite networks are indispensable [1].However, with the increasingly various services in demand, a huge amount of data is generated, which features fast speed, diversity, sophistication, and heterogeneity. Compared with the terrestrial network, LEO satellite networks computing, storage and other resources are limited. The dynamically changing topology causes frequent routing switching, resulting in difficulties in flexible network control and efficient resource utilization.

Software defined network (SDN) technology is an approach to solve above problems, by decoupling the data plane and control plane [2]. SDN enables communication between controllers and switches by OpenFlow protocol. From the perspective of network architecture, SDN is endowed with flexibility, open interfaces, and centralized control, which solves the problem of rigidity of satellite networks, simplifying network management.

Constrained by on-satellite limited resources and LEO satellite network scale, choosing a suitable set of controllers is of great significance for network performance improvement [3]. Many factors, such as the harsh space environment, frequent link switch and unbalancing traffic, affect the reliability of nodes and links, which will lead to network failure. Therefore, the reliability problem for the control plane is prominent. In order to improve the reliability of satellite networks, SDN-based satellite networks are mainly faced with the controller placement problem (CPP), which directly affects the performance of the network, and at the same time, it is crucial to achieve the minimization of the node-to-controller latency. In summary, it is of important significance to determine the impact of latency and reliability on networks by optimiz-

Manuscript received XX. XX, 2023; accepted XX. XX, 2023.

This work is supported by the National Key Research and Development Program (No. 2021YFB2900604), and Young Elite Scientists Sponsorship Program by CAST (No. 2022QNRC001).

ing the location of the controllers in the LEO satellite network topology.

Latency and reliability are important factors affecting controller placement, due to network latency affects the data processing efficiency and real-time performance. Meanwhile, considering the high dynamics of LEO satellites, the stability of LEO satellite networks will be vulnerable to deterioration. However, unlike the terrestrial CPP, the dynamics of satellite networks and the limited processing resources of satellites prevent existing research on terrestrial CPP from being applied to LEO satellite networks.

To tackle the CPP for LEO satellite networks, researchers conduct some studies that mainly focus on minimizing the average network latency, maximizing network reliability, or optimizing load balancing[2-12]. Research [2] presented an entirely new problem of joint placement optimization for satellite gateways and controllers to maximize network reliability. It obtained the maximum average reliability, given the latency constraint. However, it is only focusing on GEO satellite and terrestrial networks. Study [4] focused on minimizing the average failure probability of the control path, ensuring reliability with certain latency constraints. However, it only considered the satellite network with a few LEO satellite nodes. D. K. Luong et al. in [5] accomplished optimal network reliability with latency constraints by state-of-the-art simulated annealing (SASA), while inter-satellite links are neglected. On the aspects of minimizing network latency, Cheng Chi et al. in [3] considered control latency and load balance to evaluate the average network response control latency, without reliability factors. In research [6], it achieved network reliability maximization and proposed simulated annealing partition-based K-Means (SAPKM),while just considering propagation latency in networks. Study [7] comprehensively investigated the influence of overall latency and proposed a clustering-based network partition algorithm (CNPA) to shorten the maximum end-to-end latency, while seldomly considering the reliability. B. Li et al. in [8] proposed based on a multi-agent deep Q-learning networks method to optimize CPP including latency, load balancing, and path reliability. But they only considered the network in terrestrial networks. Research [9] constructed an optimal space control network to improve the temporal effectiveness of network control, just minimizing the number of controllers with a reliability guarantee. J. Guo et al. in [10] only considered the latency's influence. In [11] they proposed a static placement with a dynamic assignment (SPDA) method to reduce switch-controller latency and optimize load balancing performance, leaving reliability out of consideration. In [12], the controller placement with traffic load was considered to ensure the delivery latency, without reliability considered.

Although providing significant insights, most research separated the latency and reliability to evaluate their impact on CPP. We couple the reliability and latency in the SDN-enabled LEO satellite network. This paper maximizes the joint latency-reliability utility function, with the failure probability decay model. The main contributions of this paper are as follows.

1. A reliability-amendment CPP model is provided for LEO satellite networks, in which programmable switches are distributed to conduct network monitoring and load balancing, hence enhancing reliability.

2. A joint latency-reliability utility function (LRUF) is introduced to characterize the overall performance of the satellite network in terms of CPP, in which the correlation between latency and reliability is analyzed, formulating the failure probability as a function of latency.

3. A programmable switch-based enhanced controller placement algorithm (PECPA) is proposed to achieve the maximum of LRUF.

This paper is organized as follows: Section IIintroduces the system model. In Section III, we formulate the problem and propose PECPA. Section Ⅳ describes the simulation and analysis and concludes the paper and looks forward to future work in Section Ⅴ.

II SYSTEMMODEL

A. LEO Satellite Network Scenario

The investigated satellite network scenario is software defined network (SDN)-based LEO satellite networks, in which the functions of network control and network switch are separately forming the control plane and data plane respectively, as shown in Fig.1. Meanwhile, in the LEO satellite networks, some nodes in the data plane possess programmability are called as programmable switching nodes (PSNs)in this paper.

The satellite network is denoted as an undirected graph $\mathbf{G}(\mathbf{V},\mathbf{E})$, where the node set is $\mathbf{V}=\{\mathbf{V},\mathbf{Con}\}$, representing the set of all satellite nodes with the number of satellite nodes N. And the set of links is $\mathbf{E}$, in which the weight of the link presents the distance between nodes.

The satellite switch node set is denoted as $\mathbf{V}_s$ with each element v_s and the total number is n_s. The collection of satellite SDN controllers is $\mathbf{Con}$, and the number is m. The satellite nodes with programmability forming the set $\mathbf{V}_{\text{INT}}=\{v_{\text{INT}}\}$ with total number $|\mathbf{V}_{\text{INT}}|=n_{\text{INT}}$.

In this paper, the controller placement problem (CPP) is studied considering the reliability of nodes and links in LEO satellite networks. The failure probability of node s and link l are denoted as P_s and P_l respectively.

The detailed notations and definitions used in this paper are summarized in Table I.

Table 1　Notations and definitions

Notation	Definition
$\mathbf{G}(\mathbf{V},\mathbf{E})$	satellite network with node set $\mathbf{V}$ and edge set $\mathbf{E}$
N	number of satellites
$\mathbf{V}_s$	set of satellite switch nodes
$\mathbf{Con}$	set of SDN controllers
$\mathbf{V}_{\text{INT}}$	set of PSNs
v_s	satellite switch node
v_{INT}	PSN
m	number of SDN controller
n_s	number of satellite switch nodes
n_{INT}	number of PSNs
P_s	the failure probability of node
P_l	the failure probability of link
nor_{R}	normalized reliability
nor_{L}	normalized delay
η	latency reliability utility function

B. Network Model

1) Latency among controllers and switches

In SDN-enabled LEO satellite networks, for many services with low latency requirements, the control plane requires control data to be processed within a short period. Therefore, the latency between nodes and controllers needs to be considered when performing satellite network controller placement. Besides, the distance between different satellite nodes

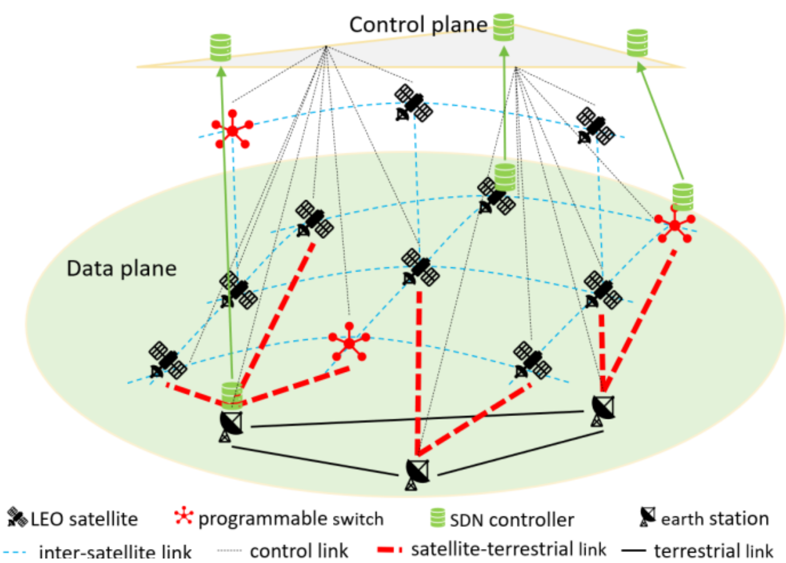

Figure 1　LEO satellite network scenario

is relatively large, as the propagation latency increases by 3ms for every 1000km. The queuing latency and transmission latency are diversified from different satellite nodes and controllers with traffic loads. Therefore, in this paper, we comprehensively consider the impact of propagation latency, transmission latency, and queuing latency on SDN CPP.

Propagation latency: In the control plane, controllers are placed in a distributed manner, which leads to longer data propagation distances from node-to-controller and controller-to-controller [9]. In SDN-enabled satellite networks, the propagation of control data is subject to higher latency, which in turn prevents the controller from processing and distributing control data timely. Therefore, the propagation latency is an important factor in controller placement.

In this paper, the propagation latency between node a and node b is defined as

$$\tau_{a,b}^{\mathrm{p}} = \frac{dis_{a,b}}{v_{a,b}}, \forall(a,b) \in \boldsymbol{E}. \tag{1}$$

In (1), $dis_{a,b}$ denotes the propagation distance between node a and node b. $v_{a,b}$ denotes the propagation rate between node a and node b. Besides, $dis_{i,j} = \sum dis_{a,b}$ represents the general propagation distance from a node i to a non-adjacent node j, where the number of inter-satellite links passing through is n_p, and the propagation rate is $v_{i,j} = \sum v_{a,b} / n_p$. The corresponding propagation latency is $\tau_{i,j}^{\mathrm{p}} = dis_{i,j} / v_{i,j}$. Furthermore, we define the average propagation latency from node i to other $N-1$ nodes as

$$\tau_i^{\mathrm{p}} = \frac{1}{N-1} \sum \tau_{i,j}^{p}. \tag{2}$$

It represents the property of the node i in propagation latency. Assuming the maximum average propagation latency as $dlp = \max\{\tau_i^{\mathrm{p}}\}$.

Transmission latency: Due to the uneven distribution of service flows and data received, some switches have higher loads and need to transmit larger amounts of data to corresponding nodes. In case of state synchronization, more data needs to be transmitted between controllers. When the control plane manages the data plane, there is a high transmission latency in both controllers and nodes. Therefore, the transmission latency is also an important factor that affects the overall performance of the network in CPP.

In LEO satellite networks, the transmission latency from node a to node b is defined as

$$\tau_{a,b}^{\mathrm{t}} = \frac{D_{a,b}}{B_{a,b}}, \forall(a,b) \in \boldsymbol{E}, \tag{3}$$

where $D_{a,b}$ denotes the data size from node a to node b, and $B_{a,b}$ represents the transmission rate from node a to node b, defined as follow

$$\begin{aligned} B_{a,b} &= f\left(B_{\mathrm{band}}, P_{\mathrm{trans}}, N_0, G_{\mathrm{gain}}\right) \\ &= B_{\mathrm{band}} \log_2\left(1 + P_{\mathrm{trans}} \frac{G_{\mathrm{gain}} g_{a,b}}{dis_{a,b}^2} / \left(N_0 B_{\mathrm{band}}\right)\right). \end{aligned} \tag{4}$$

G_{gain} denotes the interline-of-sight communication coefficient. $g_{a,b}$ means the channel power gain. B_{band} represents the channel bandwidth of inter-satellite link. P_{trans} denotes the transmission power. N_0 is channel power spectral density[13].

Assuming the satellite node i needs to transmit data to n_t nodes, the average node transmission latency as a measure of the average amount of data that the node i needs to transmit during the time period to express the property of the node i in transmission latency, defined as

$$\tau_i^{\mathrm{t}} = \frac{1}{n_t} \sum \tau_{i,j}^{\mathrm{t}}. \tag{5}$$

Besides, set the maximum average transmission latency as $dlt = \max\{\tau_i^{\mathrm{t}}\}$.

Queuing model: In LEO satellite networks, assuming that there are n nodes and m controllers connected in a satellite network, controller requests are sent randomly from any node, and the probability of a request arriving at the controller is Poisson distributed[14]. Assuming the arrival rate be λ_i, and the total arrival rate of the system is $\lambda = \sum \lambda_i$. Before a request is sent to a processor in a controller, it is stored in the controller's queue. Let the service rate of each controller be μ_i, and the total service rate be

$\mu = \sum \mu_i$. Since both service time and arrival time follow an exponential distribution and the number of controllers is m , the number of servers is m , and the system in the SDN-enabled satellite network is a $M/M/m$ queuing model[7]. In this paper, assume that the service rate of all controllers is same, then the service intensity is $\rho = \lambda / m\mu$. The steady-state probability is denoted as

$$p_k = p_0 \left(\frac{\lambda}{\mu}\right)^k \frac{1}{m! m^{k-m}}, k \le m. \tag{6}$$

As $\sum P_k = 1$, p_0 can be expressed as

$$p_0 = \left[\sum_{k=0}^{m-1} \frac{(m\rho)^k}{k!} + \frac{(m\rho)^m}{m!(1-\rho)}\right]^{-1}. \tag{7}$$

Queuing latency: In LEO satellite networks, controllers and nodes need to process data streams from multiple nodes simultaneously without instantaneity due to limited capacity. Assuming the stream arrivals in satellite networks obey the Poisson process, the queuing latency of the whole network is the $M/M/m$ model. The queuing latency of the node i is expressed as

$$\tau_i^{\text{que}} = \frac{L_i}{\lambda} = \frac{(m\rho)^m \rho}{m!(1-\rho)^2 \lambda} p_0, \tag{8}$$

where L_i denotes the length of queue in node i . More details of the $M/M/m$ model and correlation formula derivation can be referred to [14]. We define the maximum queueing latency is $dlq = \max\{\tau_i^{\text{que}}\}$.

2) *Reliability among controllers and switches*

Not only low latency but also high reliability is required when evaluating the performance of satellite networks. The better the reliability of the control plane, the longer the entire network is able to transfer data between nodes without errors. Reliability involves node reliability and link reliability, and controller placement should be placed on nodes with high node reliability and high reliability of links to other nodes[9].

Nodes and links reliability: In this paper, the overall reliability of a node is related to the node reliability and the link reliability of other nodes connected to it. Assume the number of inter-satellite links passing between node u to controller node c is n_l , the number of satellite nodes passing through them is n_r , the failure probability of satellite nodes is P_s , the failure probability of inter-satellite links is P_l , then the reliability of links from node i to node c is

$$R_{ic} = \prod_{e \in E_{i\to c}}^{n_l} \left(1 - P_l^e\right) \prod_{v \in V_{i\to c}}^{n_{no}} \left(1 - P_s^v\right). \tag{9}$$

Furthermore, the number of node i to other nodes is n_u , and the average reliability of node i is

$$R_i = \frac{1}{n_u} \sum R_{iu}. \tag{10}$$

When a controller node is placed on a node with high reliability, it is able to send control flow stably in real time and relatively close to other nodes with low propagation and transmission latency, guaranteeing the real-time performance of control flow. In this paper, in order to better measure the reliability of the satellite node i , the normalized reliability is defined as

$$nor_{Ri} = \frac{R_i}{R_{\max}}, \tag{11}$$

where $R_{\max} = \max\{R_i\}$ is the maximum average reliability under a certain time slice of satellite network topology.

Reliability decay: With each additional hop of the link, the nodes have to reallocate more resource to ensure the same reliability as the previous one. In time slices, the latency grows linearly as the number of nodes on the end-to-end link increases and the end-to-end latency unreliability increases exponentially[15]. It further follows that the reliability of nodes and links decreases exponentially as the latency grows linearly where the probability of not being able to transmit properly is a latency-dependent function. The failure probability of node after decay is expressed as

$$P_v^{'} = f\left(P_v, \tau\right) = \left[P_v + \theta_v e^{\tau_v^{\text{que}} + \tau_v^{\text{t}}}\right]_0^1, \tag{12}$$

where θ_v denotes the coefficient of node failure probability with latency, and function $[f]_0^1$ denotes that its value is 1 if $f \ge 1$ and otherwise its value equals to f itself. The failure probability of node increases exponentially as its queuing latency and transmission latency increase. Similarly, the failure probability of link after decay is expressed as

$$P_l^{'} = f\left(P_l, \tau\right) = \left[P_l + \theta_l e^{\tau_{a,b}^{\mathrm{p}} + \left(\tau_a^{\mathrm{t}} + \tau_b^{\mathrm{t}}\right)/2}\right]_0^1, \qquad (13)$$

where θ_l denotes the coefficient of link failure probability with latency. As a link connect node a and node b, the failure probability of a node increases exponentially with propagation latency and transmission latency increase.

III THE PROPOSED METHOD

A. Problem Formulation

Reliability amendment: To accurately real-time sense network performance, optimize load balancing, effectively reduce congestion, and further improve the reliability of the entire network, the PSNs are considered to distribute in LEO satellite networks.PSN possesses in-band network telemetry (INT) ability and can achieve network monitoring with low bandwidth consumption. Owing to the programmability, it has prowess in flexibly configurating the network and accurately adjusting traffic load[16]. Therefore, nodes endowed with programmable switch can reduce the failure probability of satellite networks.

In this paper, PSNs are deployed in the satellite network and balance the traffic load to improve the reliability of the nodes and links. There are n_{INT} PSNs, the set of nodes is $\mathbf{V}_{\mathrm{INT}}$. Assuming it has the ability to correct the failure probability of nodes and links up to N_{INT} hops, the farther apart, the smaller the amendment of the failure probability. Therefore, the amended failure probability can be expressed as

$$P_{\mathrm{new}} = P_{\mathrm{old}} - \delta(P), \qquad (14)$$

where $\delta(P)$ is amendatory factor with $\delta(P) < 1$, $\delta(P)$ is a function of the latency and the number of hops, as shown in (15). Δ is the amendatory increment, θ_2 denotes the decay coefficient with latency. With the certainty of hops, amendatory factor decreases with the increase of latency.

$$\delta(P) = \Delta - (n - N_{\mathrm{INT}})e^{-\tau}\theta_2. \qquad (15)$$

Therefore, node-amended failure probability is a function of queuing latency and transmission latency

$$P_{v,\mathrm{new}} = \left[P_{v,\mathrm{old}} - \Delta + (n - N_{\mathrm{INT}})e^{-(\tau_v^{\mathrm{que}} + \tau_v^{\mathrm{t}})}\theta_2\right]^+. \quad (16)$$

Similarly, link-amended failure probability is a function of propagation latency and transmission latency

$$P_{e,\mathrm{new}} = \left[P_{e,\mathrm{old}} - \Delta + (n - N_{P4})e^{-(\tau_{a,b}^{\mathrm{p}} + (\tau_a^{\mathrm{t}} + \tau_b^{\mathrm{t}})/2)}\theta_2\right]^+. \quad (17)$$

Latency-reliability utility function: In SDN-enabled LEO satellite networks, the CPP is a joint optimization of latency and reliability. Different from previous studies, this paper firstly proposes the latency-reliability utility function to comprehensively measure the impact of latency and reliability on LEO satellite network performance. The LRUF of node i is expressed as

$$\eta_i = \alpha \bullet nor_{Ri} + \beta \bullet \frac{1}{nor_{Li}}, \qquad (18)$$

where nor_{Ri} and nor_{Li} respectively denote normalized reliability and normalized latency, α and β signify the coefficient of normalized reliability and normalized latency, respectively. Normalized latency is defined as the sum of average propagation latency, average transmission latency and queuing latency of node i, divided by the maximum latency, shown as follows

$$nor_{Li} = \frac{L_i}{L_{\max}}, \qquad (19)$$

where $L_i = \tau_i^{\mathrm{p}} + \tau_i^{\mathrm{t}} + \tau_i^{\mathrm{que}}$ and $L_{\max} = dlp + dlt + dlq$.

Controller placement problem: CPP is solved in two steps: firstly, the number and location of PSNs are calculated in the network. Secondly, controller placement is performed based on the results of the node and link reliability amendment.

The deployment of PSNs is carried out first, through which INT is performed to improve the overall reliability of the network. Calculate the normalized reliability of all nodes in LEO satellite networks. Then, sort the nodes according to the size of the normalized reliability and select the node with the smallest normalized reliability as the deployment nodes for PSNs.

According to Eq.(16) and (17), amend the reliability of the links and nodes as described above. Cycle until all nodes and links in the network are amended.

Based on the results of PSN deployment, with nodes and links reliability amended, controllers are placed on the nodes with the highest LRUF, so that the reliability of the set of controllers reach a large value. Based on the optimal enumeration algorithm, the set of controllers $\mathbf{Con}$ is placed on the m nodes with the highest LRUFs. The optimization objective is to achieve the maximum sum of LRUF of the set of controllers

$$\begin{aligned} &\max \ \eta = \sum \eta_i, \\ &\text{subject to: C1: } \alpha+\beta=1 \\ &C2\text{: } i \in \boldsymbol{Con} \end{aligned} \tag{20}$$

where C1 is the constraint for coefficients of latency and reliability and C2 restrains the elements belonging to controller set.

B. Programmable Switch-based Enhanced Controller Placement Algorithm (PECPA)

In this paper, we propose programmable switch-based enhanced controller placement algorithm (PECPA). The detailed steps contain calculating the average reliability under the shortest path from each node to the others in LEO satellite networks, deploying PSNs at the nodes with the lowest reliability, and then deploying PSNs cyclically until the network is covered. Finally, calculate the LRUF of the nodes in the network according to the amendment results, and select the nodes with the largest LRUFs as the set of controllers.

Algorithm 1Programmable Switch-based Enhanced Controller Placement Algorithm (PECPA)

Input: satellite network topology $\mathbf{G}(\mathbf{V},\mathbf{E})$, controller number m

Output： PSN topology $\mathbf{V}_{\text{INT}}$， PSN number n_{INT}, controller topology $\mathbf{Con}$

Initialize： $\mathbf{V}_{\text{tem}} = \varnothing$， $\mathbf{E}_{\text{tem}} = \varnothing$， $R_i = 0$

Compute R_i of nodes

Sort R_i at descending order

While $\{\mathbf{V}_{\text{tem}} \cap \mathbf{V}_{\text{P4}}\} \neq \mathbf{V}$ && $\mathbf{E}_{\text{tem}} \neq \mathbf{E}$ do

Select minimum R_i ， add node to $\mathbf{V}_{\text{INT}}$ ，

$n_{\text{INT}} = n_{\text{INT}} + 1$

Amend reliability of nodes and links, add to $\mathbf{V}_{\text{tem}}$ $\mathbf{E}_{\text{tem}}$

for $e \in \{\mathbf{E} / \mathbf{E}_{\text{tem}}\}$ do

If e adjacent nodes involved $\mathbf{V}_{\text{tem}}$

amend the reliability of e, $\mathbf{E}_{\text{tem}} = \mathbf{E}_{\text{tem}} \cup \{e\}$

End if

End for

End while

Compute η_i of nodes

Select maximum m as $\mathbf{Con}$

return $\mathbf{V}_{\text{INT}}$， n_{INT}， $\mathbf{Con}$

IV SIMULATION AND ANALYSIS

In this section, we show the results of the comparison between proposed amended and unamended methods. Simulations focus on nodes and links before and after amendment in terms of controller topology, overall network reliability and LRUF.

In the simulation, we simulate a constellation with 66 satellite nodes. The constellation has a total of 6 orbital planes, with 11 satellites on each plane. The altitude of orbit is 780km, with inclination of 86.4°, and the orbital plane spacing is 30°. To calculate the reliability of the network, the failure probability of the network components is randomly generated from [0.05, 0.2]. To evaluate proposed method, the simulation is conducted in 9 successive time slices, while the interval among slices is 100s.

Figure 2(a) illustrates the deployment of PSNs and amended nodes in the amended satellite network topology. Where the red diamonds represent the deployment of PSNs, the green triangles represent the amended nodes, and the blue lines indicate the amended links. Fig.2(b) represents the placement of the satellite network controllers before amendment, where the pink pentacles are the nodes placed with controllers and the blue dots are satellite switch nodes. Fig.2(c) represents the placement of controllers after reliability amendment, where the changed controllers are highlighted by cyan pentacles. In other words, the set of controllers has been re-selected after the deployment of PSNs.

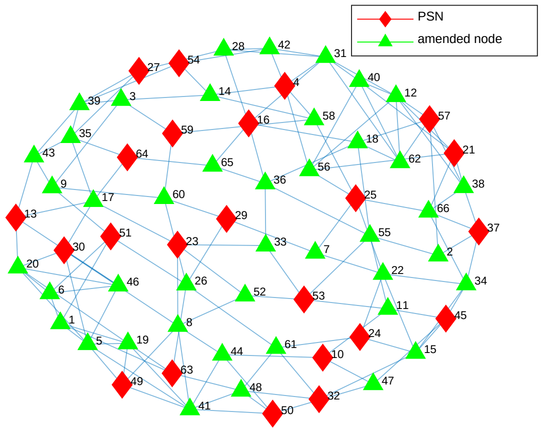

(a)PSNdeployment

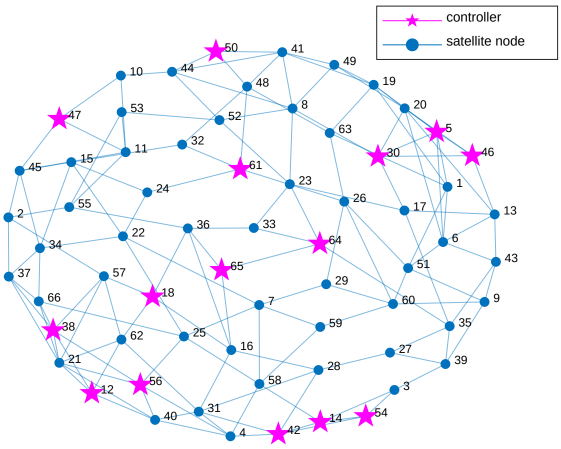

(b)Controller placement before amendment

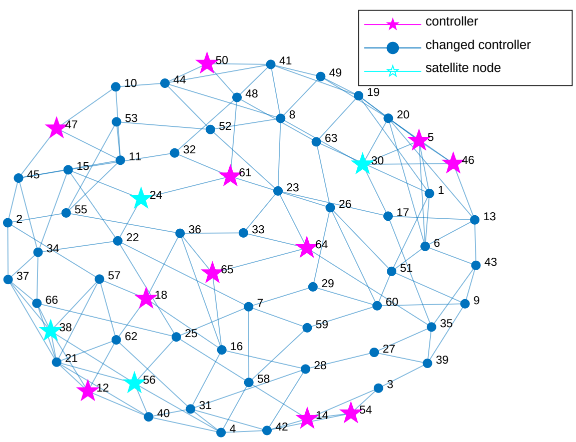

(c)Controller placement after amendment

Figure 2 Comparisons of topology

Figure 3(a) illustrates the comparison of the overall reliability of LEO satellite networks before and after amendment, where the overall reliability of the network is improved by around 20% after amendment compared to that before at the same network topology. Besides, in different time slices, the increased amplitude of overall reliability of the network remains essentially the same over time. Fig.3(c) illustrates the comparison of the normalized reliability of the set of controllers before and after amendment, and the normalized reliability after amendment will be improved around 0.1, which is about 10% normalized reliability of controllers can be enhanced. Additionally, the normalized latency of controller barely changes as shown inFig.3(b).

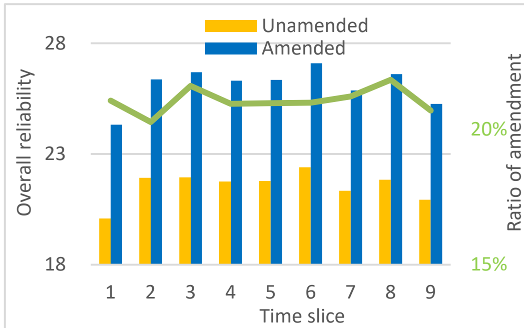

(a) Reliability of satellite network

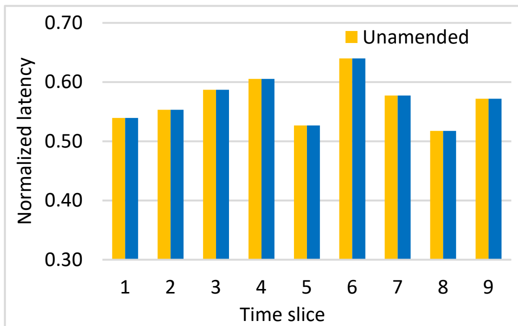

(b) Normalized latency of controllers

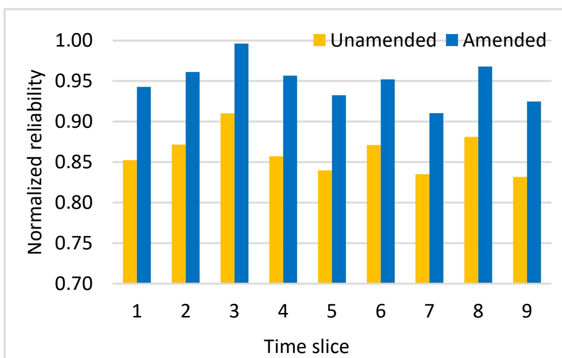

(c) Normalized reliability of controllers

Figure 3 Comparison of reliability

All graphs reflect the effectiveness of proposed amendment method, stably improving the reliability of controllers. Combing Fig.3(b) and Fig.3(c), it is indicated that PECPA can increase reliability of controllers in LEO satellite networks without altering those latencies.

Figure 4 illustrates the comparisons of LRUFs of LEO satellite networks before and after the amendment, where the latency and reliability are endowed with the same weight $\alpha = \beta = 0.5$. It can be seen that the overall LRUF after amended increases by about 1 compared to that before amended. Besides, in different time slices, though the satellite topology has changed, the values of LRUF are improved stably, proving the feasibility of PECPA.

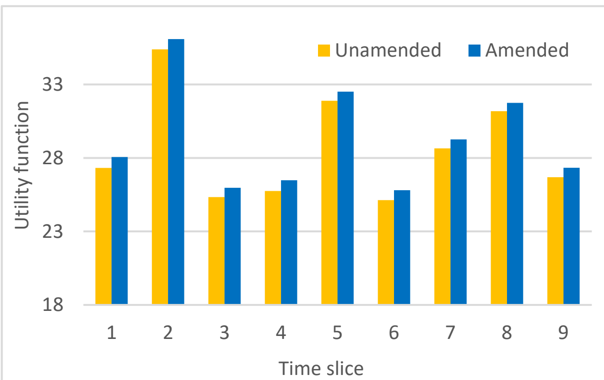

Figure 4　Latency-reliability utility function of controllers

V　CONCLUSIONS

This paper investigates CPP in LEO satellite networks and proposes node and link reliability amendment based on perceptual enhancement. The LRUF is firstly proposed and PSNs are deployed in the network, achieving the reliability amendment. To maximize LRUF, we propose PECPA and simulation results prove the effectiveness.

As part of our future work, we intend to further investigate the controller and switch migration problem under dynamic topologies considering the combined controller placement problem for both terrestrial and satellite networks.

References

[1] F. Rinaldi et al., "Non-Terrestrial Networks in 5G & Beyond: A Survey," in IEEE Access, vol. 8, pp. 165178-165200, 2020.

[2] J. Liu, Y. Shi, L. Zhao, Y. Cao, W. Sun and N. Kato, "Joint Placement of Controllers and Gateways in SDN-Enabled 5G-Satellite Integrated Network," in IEEE Journal on Selected Areas in Communications, vol. 36, no. 2, pp. 221-232, Feb. 2018.

[3] C. Chi, L. Yang, Q. Huang and Y. Qi, "Optimal Placement of Multi-Controller Considering Load Balance and Control Delay in Software Defined Satellite Network," 2022 34th Chinese Control and Decision Conference (CCDC), Hefei, China, 2022, pp. 2123-2128.

[4] N. Torkzaban and J. S. Baras, "Controller Placement in SDN-enabled 5G Satellite-Terrestrial Networks," 2021 IEEE Global Communications Conference (GLOBECOM), Madrid, Spain, 2021, pp. 1-6.

[5] D. K. Luong, Y. -F. Hu, J. -P. Li and M. Ali, "Metaheuristic Approaches to the Joint Controller and Gateway Placement in 5G-Satellite SDN Networks," ICC 2020 - 2020 IEEE International Conference on Communications (ICC), Dublin, Ireland, 2020, pp. 1-6.

[6] K. Yang, B. Zhang and D. Guo, "Controller and Gateway Partition Placement in SDN-Enabled Integrated Satellite-Terrestrial Network," 2019 IEEE International Conference on Communications Workshops (ICC Workshops), Shanghai, China, 2019, pp. 1-6.

[7] G. Wang, Y. Zhao, J. Huang and Y. Wu, "An Effective Approach to Controller Placement in Software Defined Wide Area Networks," in IEEE Transactions on Network and Service Management, vol. 15, no. 1, pp. 344-355, March 2018.

[8] B. Li, X. Deng, X. Chen, Y. Deng and J. Yin, "MEC-Based Dynamic Controller Placement in SD-IoV: A Deep Reinforcement Learning Approach," in IEEE Transactions on Vehicular Technology, vol. 71, no. 9, pp. 10044-10058, Sept. 2022.

[9] S. Ji, D. Zhou, M. Sheng and J. Li, "Mega Satellite Constellation System Optimization: From a Network Control Structure Perspective," in IEEE Transactions on Wireless Communications, vol. 21, no. 2, pp. 913-927, Feb. 2022.

[10] J. Guo et al., "SDN Controller Placement in LEO Satellite Networks Based on Dynamic Topology," 2021 IEEE/CIC International Conference on Communications in China (ICCC), Xiamen, China, 2021, pp. 1083-1088.

[11] J. Guo, L. Yang, D. Rincón, S. Sallent, Q. Chen and X. Liu, "Static Placement and Dynamic Assignment of SDN Controllers in LEO Satellite Networks," in IEEE Transactions on Network and Service Management, vol. 19, no. 4, pp. 4975-4988, Dec. 2022.

[12] L. Chen, F. Tang and X. Li, "Mobility- and Load-Adaptive Controller Placement and Assignment in LEO Satellite Networks," IEEE INFOCOM 2021 - IEEE Conference on Computer Communications, Vancouver, BC, Canada, 2021, pp. 1-10.

[13] LIU Zhihui, WEI Huan, YIN Jie,"Management of MEC Service and Optimization of Mission Migration in LEO Satellite Networks LEO," in Space-Integrated-Ground Information Networks, vol.3, no.3, pp. 72-80, 2022.

[14] Gross, Donald, et al. "Fundamentals of Queueing Theory" Wiley-Interscience Wiley-Interscience, 2008,pp.49-115.

[15] B. Yu, X. Chi, S. Li, X. Liu and S. Ren, "Martingale-based URLLC Slice Customization for the Provisioning of Reliability Regard to End-to-end Latency," in IEEE Internet of Things Journal.

[16] LV Hong-Run, LIN Qing, SHEN Geng-Biao,"Survey on In-band Network Telemetry," in Journal of Software, vol.34, no.8, pp:3870-3890.

About the authors

WEI Shuotong was born in 2000. He receivedthe B.S. degree in communication engineeringfrom Chongqing University. He is pursing a M.S degree at China Academy of Space Technology. His research interests include satellite networks and communication. (Email: 18696667121@163.com)

DONG Tao [corresponding author] was born in 1975. He received the B.S. and Ph.D. degrees in electronics science and technology from Beijing Institute of Technology in 1999 and 2004, respectively. He is currently a professor with State Key Laboratory of Space-Ground Integrated Information Technology, Space Star Technology Co.,Ltd.. His research interests include satellite communication and networks. (Email: dongtaoandy@163.com)

DI Hang was born in 1996. He received his B.S. degree in electrical engineering and automation from Xi'an Jiaotong University, Xi'an, Shanxi, in 2018, and his M.S. degree in electrical and computer engineering from Northeastern University, Boston, Massachusetts, in 2020. And now he is pursing a Ph.D. degree at China Academy of Space Technology. His research interests include satellite communication and networks.(E-mail: dihang2020@sina.com)

LIU Zhihui was born in 1989. She received her M.S. degree in computational mathematics, Xiangtan University, Xiangtan, Hunan, in 2012, and her Ph.D. degree at the School of Information and Communication Engineering from Beijing University of Posts and Telecommunications (BUPT), Beijing, China, in signal and information processing. She is currently a senior engineer in State Key Laboratory of Space-Ground Integrated Information Technology, Space Star Technology Co.,Ltd.. Her research interests include space communication and networks.(E-mail: liuzhihui1225@163.com)

JIN Shichao was born in 1980. He received the B.S.degree inphysics from Lanzhou University, and the Ph.D. degree in physics from Tsinghua University. He is currently a professor with State Key Laboratory of Space-Ground Integrated Information Technology, Space Star Technology Co.,Ltd.. His research interests include satellite communication and networks.(E-mail：jinshch@spacestar.com.cn)

A Model-Driven Approach to Enhance Faster-than-Nyquist Signaling over Nonlinear Channels

Tongzhou Yu*, Baoming Bai*, Ruimin Yuan*, and Chao Chen*
*State Key Lab. of ISN, Xidian University, Xi'an, China
Email: tzyu@stu.xidian.edu.cn, bmbai@mail.xidian.edu.cn

***Abstract*—In order to increase the capacity of future satellite communication systems, faster-than-Nyquist (FTN) signaling is increasingly considered. Existing methods for compensating for the high power amplifier (HPA) nonlinearity require perfect knowledge of the HPA model. To address this issue, we analyze the FTN symbol distribution and propose a complex-valued deep neural network (CVDNN) aided compensation scheme for the HPA nonlinearity, which does not require perfect knowledge of the HPA model and can learn the HPA nonlinearity during the training process. A model-driven network for nonlinearity compensation is proposed to further enhance the performance. Furthermore, two training sets based on the FTN symbol distribution are designed for training the network. Extensive simulations show that the Gaussian distribution is a good approximation of the FTN symbol distribution. The proposed model-driven network trained by employing a Gaussian distribution to approximate a FTN signaling can achieve a performance gain of 0.5dB compared with existing methods without HPA's parameters at the receiver.**

***Index Terms*—Faster-than-Nyquist signaling, high power amplifier, nonlinear compensation, complex-valued neural network.**

I. INTRODUCTION

Future wireless communication systems, such as beyond 5G and 6G, have been getting a larger demand for higher transmission rates and spectral efficiency [1], which require integration of non-terrestrial networks. To this end, faster-than-Nyquist (FTN) signaling, a non-orthogonal waveform technology, has been considered as a promising candidate to improve the spectrum efficiency without the requirement of additional bandwidth or antennas [2]. FTN signaling was first proposed by Mazo in 1975 [3], which breaks the orthogonality between transmitted symbols by compressing the symbol period to effectively improve the spectral efficiency. More importantly, FTN signaling is able to achieve the ultimate capacity for the signal power spectral density (PSD) [4]. As a result, the option of using faster-than-Nyquist signaling in DVB-S2X satellite application systems have been actively considered [2], [5], [6].

One challenge in FTN signaling is the presence of Inter-Symbol Interference (ISI), which occurs when symbols overlap with each other. In the downlink of satellite communication systems such as DVB-S2X, higher-order constellations are adopted for achieving higher spectral efficiency [7]. This can make it more difficult and accurate to detect the transmitted signal in the FTN transmission system. The BCJR algorithm [8] is an efficient maximum a posteriori probability (MAP) algorithm whose complexity is exponential in the number of ISI taps. A common approach for reduced-complexity MAP detection is a simplification of trellis search within the BCJR algorithm [9], [10]. With the factor graph representation of ISI channels, a sum product algorithm and its variants [11] are considered, which have a computational complexity linear in the number of ISI taps compared to the exponential complexity of the BCJR algorithm. Another challenge is nonlinear distortion in the transmit signal caused by the satellite's high power amplifier. HPA often operates near saturation to maximize the power efficiency and introduces amplitude and phase distortion [12]. ISI will be further increased when the FTN signaling passes through the HPA compared to the Nyquist signaling. Hence one of the key issues is designing FTN signaling with low Peak-to-Average Power Ratio (PAPR), which helps minimize the nonlinear distortion [13], [14].

Fewer works available have considered HPA nonlinearity compensation for FTN transmission. In [7], the authors study the Forney observation model and apply theme to nonlinear channel through a linearized Volterra series approach. For better performance, the estimation of the nonlinear channel is required. Ref. [15] proposes a synchroization scheme for FTN signaling in a satellite context. The approach is based on a Volterra decomposition of the received signal to accommodate both linearized and non-linearized amplifiers present in the satellite payload. And channel estimation is employed to address time offset issues in the proposed schemes. The authors in [12] propose a post-distortion detection scheme for memoryless power amplifiers with a perfect knowledge of the HPA's input-output characteristics.

Motivated by the above observations, in this paper we propose a model-driven compensation scheme for FTN transmission without HPA's parameters at the receiver. We analyze the FTN symbol distribution, and use the Kullback-Leibler (KL) divergence to measure the difference between the symbol distribution and Gaussian distribution. A CVDNN-aided compensation scheme is then proposed to compensate for the nonlinear distortion of the HPA with unknown parameters of HPA. A model-driven CVDNN network for compensation is designed for a better performance. Furthermore, we train the models by assuming a Gaussian distribution to approximate the FTN signaling.

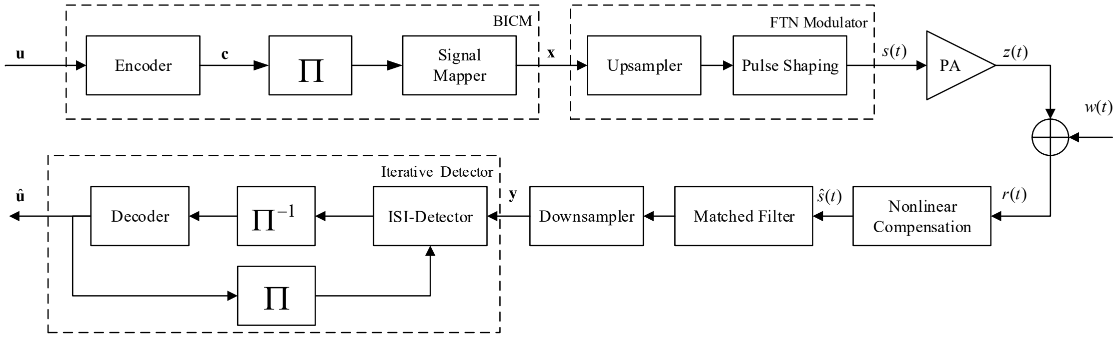

Fig. 1. System model of the proposed coded FTN with HPA.

This paper is organized as follows. In Section II, we introduce a coded FTN system with the high power amplifier. FTN signaling generation and power amplifier model are discussed in detail. In Section III, we first derive the expression of FTN symbol and use a method to measure the difference between FTN symbol distribution and Gaussian distribution. Then, we propose a CVDNN-based compensation scheme. For better performance, by unfolding iterative process, we propose a model-driven CVDNN network for compensation. The training process and training data are also discussed in detail. In Section IV, we evaluate the performance of the proposed scheme by simulation. The proposed scheme can achieve a better performance than the existing scheme.

II. System Model

A. FTN Signaling Generation

Consider the downlink transmission of a satellite communication system as shown in Fig. 1. Assume that the sequence $\mathbf{u}$ of information bits is encoded into a codeword $\mathbf{c}$ by a forward error correction (FEC) encoder. The code bits are then interleaved and mapped into modulated symbol sequence $\mathbf{x} = \{x_n\}$ with x_n taking on values in alphabet $\mathcal{X}$. The baseband FTN signal $s(t)$ is generated by upsampling the symbol sequence $\mathbf{x}$ of length N and pulse shaping [3] with the following expression.

$$s\,(t) = \sum_{n=0}^{N-1} x_n p\,(t - n\tau T), \tag{1}$$

where $p\,(t)$ is assumed be the T-orthogonal root raised cosine (RRC) pulse with a roll-off factor β, and $\tau < 1$ is the FTN time-compression factor. Note that the symbol period τT of the FTN signaling is shorter than that of the Nyquist signaling. When $\tau = 1$, the FTN signaling is degraded to the Nyquist signaling.

B. Power Amplifier Model

Before transmission, the FTN signal $s(t)$ is amplified by an HPA. In order to obtain the efficient power amplification, the HPA usually operates in the saturation region and the output signal is nonlinearly distorted. The general HPA model for describing the nonlinear distortion is the well known Volterra series [16]. A simplified model, commonly used to describe an HPA is the following memoryless polynomial model [17]:

$$z(t) = \sum_{d=1}^{D} \alpha_{2d-1} s(t) |s(t)|^{2(d-1)}, \tag{2}$$

where α_{2d-1} is the complex coefficient of the $(2d-1)$-th order nonlinearity, which contains the amplitude and phase distortion effects. The $s(t)$ and $z(t)$ are the input and output signals of the HPA, respectively. For the model of (2), $D = 2$ is usually assumed [12], which takes into account the nonlinear influence each timeslot, and ignores the inter-modulation component. It has been widely used because its fitting accuracy for nonlinear effects and memory effects is moderate.

Suppose that $z(t)$ is transmitted over the AWGN channel. The receiver gets the signal $r(t) = z(t) + w(t)$, where $w(t)$ represents a circularly-symmetric Gaussian random process with a one-sided PSD of N_0. At the receiver side, the nonlinear detector is performed upon $r(t)$ to compensate for the nonlinear distortion and recover the original signal, resulting in $\hat{s}(t)$. We consider $\hat{s}(t)$ as a biased estimate of $s(t)$, and the bias is denoted by $w_{\text{bias}}(t)$. As a result, the output of the nonlinear detector is

$$\hat{s}(t) = s(t) + w_{\text{bias}}(t). \tag{3}$$

Moreover, to simplify the analysis, the detector noise $w_{\text{bias}}(t)$ is assumed to be a complex circularly-symmetric Gaussian noise with two-sided power spectral density of σ^2_{bias} which is proportional to N_0 and independent of FTN signal $s(t)$.

C. FTN Signal Detection

After nonlinear compensation, the signal $\hat{s}(t)$ is first passed through a matched filter with impulse response $p^*(t)$ and is then sampled for detection at the rate of $1/(\tau T)$. We obtain the discrete-time signal sequence as

$$\begin{aligned} y_n &= \int_{-\infty}^{\infty} \hat{s}(t) p^*(t - n\tau T)\,\mathrm{d}t \\ &= \sum_m g_{n-m} x_m + \eta_n, \end{aligned} \tag{4}$$

where

$$g_{n-m}=\int_{-\infty}^{\infty} p^*(t-n\tau T)p(t-m\tau T)\,\mathrm{d}t, \tag{5}$$

and

$$\eta_n=\int_{-\infty}^{\infty} w_{\text{bias}}(t)p^*(t-n\tau T)\,\mathrm{d}t. \tag{6}$$

Let L represent the number of channel taps with significant power on one side. The rest ISI terms with insignificant energy are therefore neglected and then set to zero in the following analysis, i.e., $g_l=0$ for $|l|>L$. The term $\eta[k]$ in (4) and (6) represents the colored noise due to a matched filter, whose autocorrelation function satisfies $\mathbb{E}[\eta\eta^H]=\sigma^2_{\text{bias}}\mathbf{G}$, where $(\cdot)^H$ denotes the conjugate transpose and $\mathbf{G}$ is a Toeplitz matrix of full rank [18] given by

$$\mathbf{G}=\begin{pmatrix} 1 & g_{-1} & \cdots & g_{-L} & 0 & 0 & 0 & 0 & \cdots & 0\\ g_1 & 1 & \cdots & g_{-(L-1)} & g_{-L} & 0 & 0 & 0 & \cdots & 0\\ \vdots & \vdots & \vdots & \vdots & \vdots & \vdots & \vdots & \vdots & \ddots & \vdots\\ g_L & \cdots & g_1 & 1 & g_{-1} & g_{-2} & g_{-3} & g_{-4} & \cdots & 0\\ 0 & g_L & \cdots & g_1 & 1 & g_{-1} & g_{-2} & g_{-3} & \cdots & 0\\ \vdots & & \ddots & & & & & & \ddots & \vdots \end{pmatrix}. \tag{7}$$

We can express (4) in matrix form as $\mathbf{y}=\mathbf{G}\mathbf{x}+\boldsymbol{\eta}$. An iterative soft information detection between ISI detector and FEC decoder is performed to recover the transmitted symbols based on the sequence $\mathbf{y}$. In this work, we will utilize the sum product algorithm (SPA) for ISI detection [11]. Such detector has a relatively low complexity and can achieve a near-optimal performance in high-order constellations.

Note that the nonlinear detector performs symbol sequence detection prior to the ISI detector. It is a challenging task to compensate for nonlinear distortion, which will be discussed in the next section.

III. Nonlinear Distortion Compensation

A. FTN Symbol Distribution

Due to the receiver's limited knowledge of the accurate nonlinear input-output characteristics of the HPA, we consider AI-aided nonlinear compensation. We first need to know the distribution of FTN symbol to train the nonlinear compensation module better. For QAM modulation, the real and imaginary parts are independent and identically distributed. It could be shown that the real and imaginary parts of FTN symbol are also independent and identically by Eq. (1). The distribution of real part of FTN symbol is considered in the following discussion. Without loss of generality, the real part of FTN signal is sampled at the time instant $t=0$, and we obtain the following expression:

$$\Re\{s_0\}=\Re\{s(t=0)\}=\sum_{l=-L}^{L}\Re\{x_l\}\,p(-l\tau T) \tag{8}$$

where $\Re\{\cdot\}$ denotes the real part of a complex value. With $x_l\in\mathcal{X}\subset\mathbb{C}$, $\Re\{x_l\}$ corresponds to the l-th PAM symbol. The expression $p(-l\tau T)$ varies with l slowly and may be approximated as a constant if τ or β is sufficiently small. In this case, $\Re\{s_0\}$ is a linear combination of independent and identically distributed (i.i.d.) random variables. According to the central limit theorem, $\Re\{s_0\}$ can approximate a Gaussian random variable. The imaginary part of FTN symbol $\Im\{s_0\}$ can be analyzed in the same way. Therefore, the FTN symbol s_0 is a complex Gaussian-like random variable.

We use KL divergence as a metric to measure the difference between the distribution p of $\Re\{s_0\}$ and a standard normal distribution q, which is defined as follows:

$$D_{\text{KL}}(p||q)=\sum_i p(i)\log\frac{p(i)}{q(i)}. \tag{9}$$

The detailed results are discussed in Section IV for ensuring the accuracy of the approximation.

B. CVDNN-Aided Nonlinear Detection Scheme

Algorithm 1 Nonlinear detection(NLD)

Require: $\{r_n\}$, $\{\alpha_{2d-1}\}$, $\{\mathbb{E}\left[|s_n|^{2(d-1)}\right]\}$

Initialize $h_n^{(0)}=\sum_d \alpha_{2d-1}\mathbb{E}\left[|s(n)|^{2d-2)}\right]$, $s_n^{(0)}=r_n/h_n^{(0)}$

for $k=1$ to K **do**

  Update the term $h_n^{(k)}=\sum_d \alpha_{2d-1}\left|s_n^{k-1}\right|^{2(d-1)}$

  Update the estimation $s_n^{(k)}=r_n/h_n^{(k)}$.

end for

return $\hat{s}_n=s_n^{(K)},\ n=1,2,\ldots$

Algorithm 2 CVDNN-aided nonlinear detection(Net-Aided)

Require: $\{r_n\}$, a CVDNN network $\mathrm{CVDNN}(\cdot)$

Initialize $s_n^{(0)}=r_n$

for $k=1$ to K **do**

  Vectorize $s_n^{(k-1)}$ as $\left[1,s_n^{(k-1)},\cdots,(s_n^{(k-1)})^{2D-2}\right]$

  Feed above vectors into $\mathrm{CVDNN}(\cdot)$

$$h_n^{(k)}=\mathrm{CVDNN}\left(\left[1,s_n^{(k-1)},\cdots,(s_n^{(k-1)})^{2D-2}\right]\right)$$

  Update $s_n^{(k)}=r_n/h_n^{(k)}$.

end for

return $\hat{s}_n=s_n^{(K)},\ n=1,2,\ldots$

By Eq. (2), we have the following expression for brevity:

$$\begin{aligned}\mathbf{r}&=\mathbf{z}+\mathbf{w}\\ &=\mathbf{H}\mathbf{s}+\mathbf{w}.\end{aligned} \tag{10}$$

For memoryless HPA, $\mathbf{H}$ in (10) is a diagonal matrix. A more specific form is given below.

$$\begin{aligned}r_n&=h_n s_n+w_n\\ &=\left(\sum_{d=1}^{D}\alpha_{2d-1}|s_n|^{2(d-1)}\right)s_n+w_n.\end{aligned} \tag{11}$$

It is obvious that $h_n=\sum_d\alpha_{2d-1}|s_n|^{2(d-1)}$ depends on instantaneous power of s_n and the HPA's parameters $\{\alpha_1,\alpha_3,\ldots,\alpha_{2D-1}\}$. Perfect knowledge of the above parameters is required for the nonlinear detection. The nonlinear detection algorithm 1 in [12] is based on perfect knowledge of the HPA model. However, in practice, the HPA's parameters $\{\alpha_1, \alpha_3, \ldots, \alpha_{2D-1}\}$ are unknown and the instantaneous power of s_n is not available. For this issue, we propose a complex-valued deep neural network aided nonlinear detection scheme and combine estimation and detection together for a better performance. CVDNN is a neural network with complex-valued weights and activations. It has been shown that CVDNN can achieve better performance than real-valued deep neural network in handling the natural complex-valued and signals [19]. We use CVDNN to estimate above parameters and instantaneous power $\{|s_n|^2, |s_n|^4, \ldots, |s_n|^{2D-2}\}$.

As is shown in Fig. 2, the CVDNN in this work is a fully connected neural network with 2 hidden layers. The first layer extracts the features of the input signal, and the second hidden layer combines the features and further extracts the features of the input signal. The last output layer predicts h_n in this study. The training and parameter optimization will be discussed in Section III-D. As is shown in Algorithm 2, CVDNN works as a part of the nonlinear detection. The CVDNN performs different functions during the training and testing phase.

During the training phase, the CVDNN is trained to estimate the unknown key parameters of HPA model offline. Once the training is done, the estimated parameters are fixed. The network can perform the nonlinear detection directly to compensate for the nonlinear distortion. Just one tiny CVDNN is needed to implement the nonlinear detection for all the received signals for memoryless HPA.

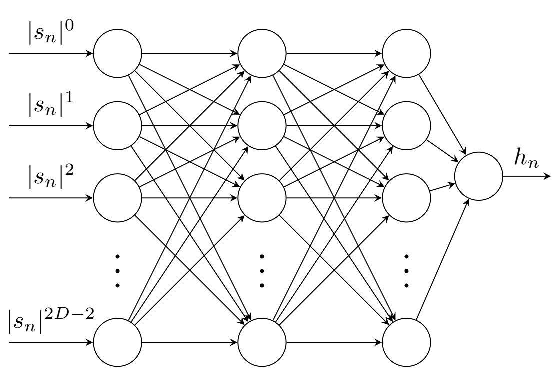

Fig. 2. The structure of CVDNN.

C. Model-Driven CVDNN Network for Nonlinearity Compensation

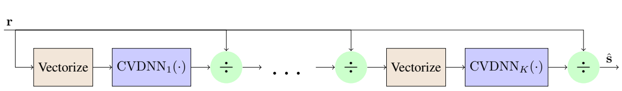

Fig. 3. The model-driven CVDNN network for nonlinear compensation.

It is clear that the CVDNN-aided nonlinear detection is an iterative process and adopts the same CVDNN for each iteration. By the use of deep unfolding first introduced in [20], the iterative algorithm 2 can be converted to a deep neural network, which is called model-driven CVDNN network. Fig. 3 illustrates that the model-driven (MD) network. Networks $\mathrm{CVDNN}_1(\cdot), \mathrm{CVDNN}_2(\cdot), \ldots, \mathrm{CVDNN}_K(\cdot)$ have the same connection but different weights and share a common connectivity pattern as shown in Fig. 2. It is important that we map the input signal s_n in a higher dimensional space $\left[1, |s_n|, \cdots, |s_n|^{2D-2}\right]$ to deal with the nonlinear distortion. In this way, the network can be controlled and fine-tuned in a more precise manner for a better performance.

This adjustment is based on the feedback received from training samples, enabling the network to minimize the discrepancy between its actual output and the expected output. In the case of the large network depicted in Fig. 3, each small module has its own relative optimal weights to better perform its respective subtask. Its connectivity is designed according to the expression of h_n. This connectivity ensures that the model maintains interpretability while achieving improved performance with less data.

D. Training and Parameter Optimization

Sampled FTN symbols have a very large alphabet size $|\mathcal{X}|^{2L-1}$ and could be considered approximately continuous if τ is small enough. For example, the alphabet size is $16^5 = 1048576$ for $L = 3$ and $|\mathcal{X}| = 16$. Our approach focuses on compensating for the HPA effect on the FTN symbols, which will output hard decision values on the FTN symbols instead of providing the log likelihood ratio values for each FTN symbol. Therefore, we optimize the parametrization towards a minimum mean-square error (MMSE) between HPA inputs $\mathbf{s}$ and desired outputs $\hat{\mathbf{s}}$ as follows:

$$\min \mathcal{L} = \sum_{n=0}^{N-1} \|s_n - \hat{s}_n\|_2^2, \tag{12}$$

where complex-valued s_n and $\hat{s}_n$ are the n-th element of $\mathbf{s}$ and $\hat{\mathbf{s}}$, respectively. MMSE here used for loss function more focus on the amplitude distortion.

When training complex-valued networks, the gradient computation follows a similar process to real-valued networks. However, the loss function Eq. (12) is non-holonomic and may not have complex differentiablity. Wirtinger developed a framework that simplifies the process of the derivative of complex valued functions with respect to both holomorphic and nonholomorphic functions [21]. By doing this, the devrivatives to the loss can be computed in the complex domain. An identity function [19] is used as activation function. We use the Adam algorithm [22], a stochastic gradient descent method, to minimize the loss function. All weights are initialized with a Xavier Gaussian distribution [23].

These are two different ways to generate training data. The first one is more accurate on a certain FTN system, while the second one is more general. By the analysis in Section III-A, we can obtain that it is more robust to τ and β.

1) Generate FTN symbols using the given parameters τ, β and channel output $\mathbf{r}$ according to Eq. (11). Then $\mathbf{r}$ is fed

into the network to recover the FTN symbols. Finally, the parametrization on training is performed.

2) Sample a complex Gaussian distribution i.i.d. as a good approximation of FTN signaling and optimize the network parameters.

IV. Simulation Results and Analysis

Without loss of generality, we choose RRC with a roll-off factor $\beta = 0.3$ as the shaping pulse. Set $\tau = 0.8$ and the length of the truncated ISI $L = 5$. Meanwhile, 5G NR LDPC codes are chosen as the FEC code, where the length of the sequence of information bits in one block is set 1024 and the code rate is $R_c = 1/2$ and $R_c = 2/3$. 16-QAM mapping is used in this study because the nonlinearity of HPA is more severe for higher order modulations. Furthermore, the HPA parameters, as stated in [24], are given by $\alpha_1 = 0.9798 - 0.2887j$ and $\alpha_3 = -0.2901 + 0.4350j$. We do not consider using power backoff to reduce the nonlinear distortion as it is a negative measure. The HPA input back-off (IBO) is set to 0dB. We consider worse-case scenario, where the HPA is driven to its saturation point. The maximum iteration number is set to $K = 3$.

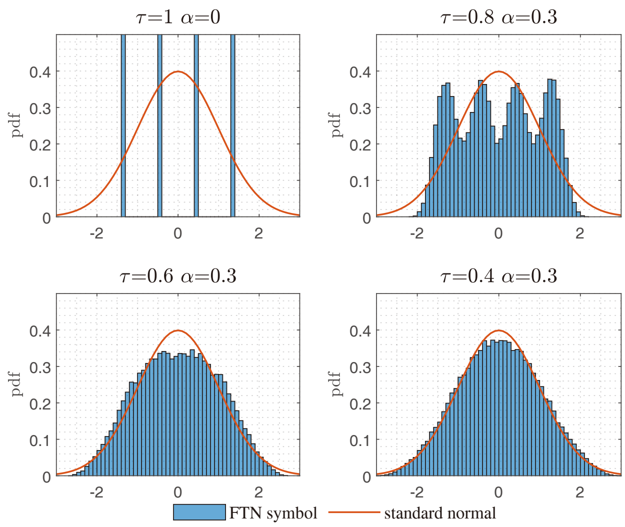

Fig. 4. PDFs of FTN symbol and standard normal distribution.

First, we analyze the distribution of the FTN symbol and compared it to the standard Gaussian distribution. The KL divergence between these two distributions is shown in Table I. To perform this analysis, we sample the standard Gaussian distribution from -10 to 10 with a step of 0.01. The results indicate that as the roll-off factor β and the time-compression factor τ decrease, the KL divergence tends to become smaller, possibly even approaching zero. This suggests that the Gaussian distribution can effectively approximate the FTN symbol distribution. To further illustrate this, Fig. 4 provides a visualization of the two distributions at specific values of β and τ. These results give us a better understanding of the FTN symbol distribution and guide us to use the complex Gaussian distribution as training data set for the neural network.

TABLE I
KL DIVERGENCE BETWEEN THE FTN SYMBOL DISTRIBUTION AND THE GAUSSIAN DISTRIBUTION.

D_{KL}(bit) \ τ / β	1.0	0.8	0.6	0.4	0.2
0.3	3.3792	0.0936	0.0258	0.0104	0.0020
0.2	3.3791	0.0797	0.0217	0.0081	0.0020
0.1	3.3786	0.0680	0.0206	0.0074	0.0019
0	3.3752	0.0584	0.0174	0.0068	0.0019

The proposed approaches under two different training data sets for nonlinear compensation are compared in Fig. (5). Note that ”No HPA” here means that the HPA is not used in the simulation, and we keep the same power level as the HPA case. In the figure, the proposed model-driven approach outperforms the CVDNN-aided scheme and nearly approaches the performance nonlinear detection scheme in [12] with perfect knowledge of the HPA’s parameters. Our approach has no need for these parameters and is more practical. Especially, the model-driven approach trained with the Gaussian distribution as the training data is proved to be effective. Even though the proposed CVDNN-aided scheme is not as good as the model-driven approach, it still compensates for the nonlinear distortion effectively and outperforms the FTN system without compensation.

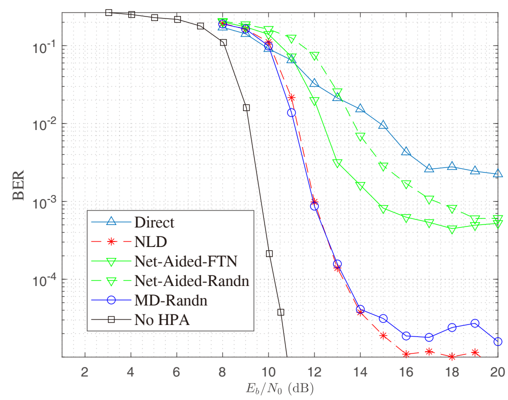

Fig. 5. BER performance of proposed nonlinear compensation schemes for coded FTN System under different training sets with $R_c = 2/3$. where Direct means no compensation is applied, ‘-Randn’ and ‘-FTN’ are the proposed schemes with Gaussian and FTN training sets, respectively.

A lower rate of the coded FTN system is also considered in Fig. 6. In this case, the model-driven approach outperforms the NLD approach. And the E_b/N_0 gap about 0.5 dB at BER $= 10^{-6}$ is observed. The gap between the two approaches is larger than that in the higher rate case. Also, the error floor is lower than that in the higher rate case. So the model-driven approach is more suitable for the case of lower rates.

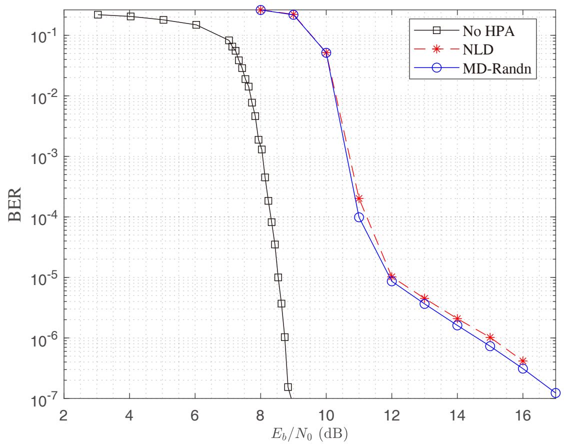

Fig. 6. BER performance of model-driven approach working in lower rate with $R_c = 1/2$.

V. Conclusion

In this study, we design CVDNN-aided compensation schemes for the coded FTN system with HPA under unknown HPA's parameters condition at the receiver. Based on it, we propose a model-driven approach to compensate for the HPA nonlinearity for better performance. We analyze the distribution of FTN symbol and find the Gaussian distribution is a good approximation. Then we design two training sets for the CVDNN-aided and the model-driven schemes. The proposed model-driven CVDNN scheme can achieve a better performance than the NLD approach. Especially, the model-driven approach obtains about 0.5 dB E_b/N_0 gap at BER $= 10^{-6}$ for the case of low rate $R_c = 1/2$. And FTN with HPA can work well in future Wireless Communication systems.

References

[1] C.-X. Wang, X. You, X. Gao *et al.*, "On the road to 6G: Visions, requirements, key technologies, and testbeds," *IEEE Communications Surveys & Tutorials*, vol. 25, no. 2, pp. 905–974, 2023.

[2] Q. Li, F.-K. Gong, P.-Y. Song, G. Li, and S.-H. Zhai, "Beyond DVB-S2X: faster-than-Nyquist signaling with linear precoding," *IEEE Transactions on Broadcasting*, vol. 66, no. 3, pp. 620–629, Sep. 2020.

[3] J. E. Mazo, "Faster-than-Nyquist signaling," *The Bell System Technical Journal*, vol. 54, no. 8, pp. 1451–1462, Oct. 1975.

[4] F. Rusek and J. B. Anderson, "Constrained capacities for faster-Than-Nyquist Signaling," *IEEE Transactions on Information Theory*, vol. 55, no. 2, pp. 764–775, Feb. 2009.

[5] Q. Li, F.-K. Gong, P.-Y. Song, and S.-H. Zhai, "Pre-equalized interference cancellation for faster-than-Nyquist signaling," *IEEE Access*, vol. 7, pp. 77 868–77 876, 2019.

[6] Q. Li, F.-K. Gong *et al.*, "Symbol-based multi-layer iterative successive interference cancellation for Faster-than-Nyquist signalling," *IET Communications*, vol. 14, no. 2, pp. 243–250, 2020.

[7] P. Mohr, R. Grünheid, and G. Bauch, "Forney observation models for faster-than-Nyquist Signaling on nonlinear satellite links," in *Proc. 2022 IEEE 96th Vehicular Technology Conference (VTC2022-Fall)*, Sep. 2022, pp. 1–6.

[8] G. Colavolpe and G. Germi, "On the application of factor graphs and the sum-product algorithm to ISI channels," *IEEE Transactions on Communications*, vol. 53, no. 5, pp. 818–825, May 2005.

[9] J. B. Anderson and A. Prlja, "Turbo equalization and an M-BCJR algorithm for strongly narrowband intersymbol interference," in *Proc. 2010 International Symposium On Information Theory & Its Applications*, Oct. 2010, pp. 261–266.

[10] S. Li, B. Bai, J. Zhou, P. Chen, and Z. Yu, "Reduced-complexity equalization for faster-than-Nyquist signaling: New methods based on Ungerboeck observation model," *IEEE Transactions on Communications*, vol. 66, no. 3, pp. 1190–1204, Mar. 2018.

[11] G. Colavolpe, D. Fertonani, and A. Piemontese, "SISO detection over linear channels with linear complexity in the number of interferers," *IEEE Journal of Selected Topics in Signal Processing*, vol. 5, no. 8, pp. 1475–1485, Dec. 2011.

[12] Z. Alina and O. Amrani, "Post-distortion for memoryless power amplifiers," in *Proc. 2014 IEEE 28th Convention of Electrical & Electronics Engineers in Israel (IEEEI)*, Dec. 2014, pp. 1–4.

[13] Q. Li, Y. Gao *et al.*, "PAPR analysis for faster-than-Nyquist signaling in satellite communications," in *Proc. 2020 International Conference on Wireless Communications and Signal Processing (WCSP)*, Oct. 2020, pp. 708–711.

[14] S. B. Makarov, M. Liu, A. S. Ovsyannikova, S. V. Zavjalov, Il. Lavrenyuk, W. Xue, and Y. Xu, "A reduction of peak-to-average power ratio based faster-than-Nyquist quadrature signals for satellite communication," *Symmetry*, vol. 13, no. 2, p. 346, Feb. 2021.

[15] J.-A. Lucciardi, N. Thomas, M.-L. Boucheret, C. Poulliat, and G. Mesnager, "Receiver for FTN signaling in non-linear channel: Joint channel estimation and synchronization," in *Proc. 2017 IEEE 28th Annual International Symposium on Personal, Indoor, and Mobile Radio Communications (PIMRC)*, Oct. 2017, pp. 1–7.

[16] R. de Figueiredo, "The Volterra and Wiener theories of nonlinear systems," *Proceedings of the IEEE*, vol. 70, no. 3, pp. 316–317, 1982.

[17] G. Zhou, H. Qian, L. Ding, and R. Raich, "On the baseband representation of a bandpass nonlinearity," *IEEE Transactions on Signal Processing*, vol. 53, no. 8, pp. 2953–2957, Aug. 2005.

[18] Y. J. Daniel Kim, "Properties of faster-than-Nyquist channel matrices and folded-spectrum, and their applications," in *Proc. 2016 IEEE Wireless Communications and Networking Conference*, 2016, pp. 1–7.

[19] C. Lee, H. Hasegawa, and S. Gao, "Complex-valued neural networks: A comprehensive survey," *IEEE/CAA Journal of Automatica Sinica*, vol. 9, no. 8, pp. 1406–1426, Aug. 2022.

[20] K. Gregor and Y. LeCun, "Learning fast approximations of sparse coding," in *Proceedings of the 27th International Conference on International Conference on Machine Learning*, ser. ICML'10. Madison, WI, USA: Omnipress, Jun. 2010, pp. 399–406.

[21] K. Kreutz-Delgado, "The complex gradient operator and the CR-Calculus," arXiv:0906.4835, Jun. 2009.

[22] D. P. Kingma and J. Ba, "Adam: A method for stochastic optimization," arXiv:1412.6980, Jan. 2014.

[23] X. Glorot and Y. Bengio, "Understanding the difficulty of training deep feedforward neural networks," in *Proceedings of the Thirteenth International Conference on Artificial Intelligence and Statistics*, Mar. 2010, pp. 249–256.

[24] V. A. Bohara and S. H. Ting, "Theoretical analysis of OFDM signals in nonlinear polynomial models," in *Proc. 2007 6th International Conference on Information, Communications & Signal Processing*, Dec. 2007, pp. 1–5.

极化码的最大似然译码性能分析

郑湘萍，姚忻圆梦，马啸

摘　要：极化码作为 5G 增强移动宽带场景下的控制信道编码方案，通常采用串行抵消列表译码算法。随着列表大小增加，译码性能逐渐逼近最大似然译码性能，但译码复杂度也随之显著提高。因而分析极化码的最大似然译码性能有助于我们选择列表大小以实现性能与复杂度之间的合理折中。文中利用改进的联合界技术和基于 Bonferroni 不等式的下界技术评估极化码的最大似然译码性能。前者的计算仅需要截断重量谱而后者的计算仅依赖于部分码字集合。为了计算极化码的重量谱，引入了随机交织技术。基于串行抵消列表译码算法，可以得到极化码的部分码字集合。仿真结果表明，该上下界技术可以有效地估计极化码的最大似然译码性能并指导极化码的串行抵消列表译码的参数选择。特别地，对于 5G 极化码[128, 64]，[256, 128]和[512, 256]，串行抵消列表译码算法设定列表大小为 2 即可，而级联长度为 4 的 5G 循环冗余校验级联极化码[128, 16]对应的串行抵消列表译码算法列表设定为 8 即可。

关键词：Bonferroni 不等式；最大似然译码；极化码；串行抵消列表译码；截断重量谱

Performance Analysis of Maximum-Likelihood Decoding of Polar Code

ZHENG Xiangping，YAO Xinyuanmeng，MA Xiao

Abstract: As the standard coding scheme for 5G enhanced Mobile Broadband (eMBB) control channels, polar codes are usually decoded by the successive cancellation list (SCL) decoding algorithm. As the list size increases, the SCL decoding performance improves and tends to the ML decoding performance, while leading to significantly increased complexity. Therefore, analyzing the ML decoding performance is helpful for us to select a suitable list size and hence to trade off the performance and the complexity of the SCL decoding of polar codes. In this paper, we employ improved union bounds and lower bounding techniques based on Bonferroni inequality to evaluate the ML performance of polar code. The former requires only truncated weight spectra and the latter can rely only on a subset of the codebook. To calculate the weight spectrum of a polar code, random interleavers are introduced. In contrast, a subset of the codebook can be obtained by performing the SCL decoding algorithm. Simulation results show that the proposed techniques can effectively predict the ML performance of the polar codes and provide guidelines on the choice of the parameters of the SCL decoding. Specifically, the SCL decoding with list size of 2 is sufficient to approach the ML performance of the 5G polar codes [128, 64]，[256, 128], and [512, 256]. By contrast, for the 5G polar code [128,16] with 4-bit Cyclic Redundancy Check, the list size is required to be 8 for obtaining near ML performance.

Key words: Bonferroni inequality；maximum likelihood decoding；polar code；successive cancellation list decoding；truncated weight spectrum

1　引言

信道编码是空间网络信息传输的物理层关键技术，而空间信息网络通信场景具有多样性，包括星地通信与星间通信等。因此，我们有必要研究多类编码技术以适应不同场景的需求。卷积码、RS（Reed-Solomon）码、RM（Reed-Muller）码、Turbo码、LDPC（Low-Density Parity-Check）码等纠错码技术相继被引入空间通信各场景。极化码由 Arıkan 于 2009 年提出，是一类可渐近逼近信道容量的构造性纠错编码[1]，目前已成为 5G 增强移动宽带场景（eMBB, Enhanced Mobile Broadband）控制信道编码的方案。针对极化码的译码，Arıkan 提出了串行抵消译码算法（SC，Successive Cancellation）[1]

通信作者：马啸，maxiao@mail.sysu.edu.cn
基金项目：国家重点研发计划资助项目（No.YFA1000500）

和置信传播译码算法（BP, Belief Propagation）[2]。SC 算法在中短长码的场景中性能较差，而 BP 算法虽然改善了极化码的译码性能，但与最大似然（ML, Maximum Likelihood）译码算法相比还是存在一定的差距。为了进一步提升极化码的性能，文献[3-5]提出了循环冗余校验（CRC, Cyclic Redundancy Check）协助的串行抵消列表（SCL, Successive Cancellation List）译码算法，即 CA-SCL 译码算法。与 CRC 级联极化码相似，WANG 等[6]提出了基于奇偶校验（PC, Parity Check）辅助的 PC-SCL 译码算法。可以验证的是，在列表大小较大时，SCL 译码算法可以实现 ML 译码的性能。

对于 SC 译码性能，可以采用高斯逼近法（GA, Gaussian approximation）[7]评估，其基本思想是利用简化的密度进化算法计算各个子信道的译码错误概率，并根据码的信息比特位置计算得到 SC 译码算法的译码错误概率的估计。对于 SCL 译码性能，可以采用蒙特卡罗仿真方法评估。蒙特卡罗仿真通过大量的样本可以对译码错误概率进行估计，其估计的精确度取决于仿真的样本数量。然而，蒙特卡罗仿真方法在高信噪比区域所需计算时间长，且无法指导码设计时的系统参数选择。对于 ML 译码性能，可以采用上下界技术评估。当上下界贴近时，ML 译码性能可以通过上下界近似估计。由于在码字发送概率相等的情况下 ML 译码是误帧率（FER, Frame Erasure Rate）最小的最佳译码算法，所以该上下界可用以指导设计性能好的编译码算法。联合界是目前最简单的 ML 译码的上界技术。但是，它在低信噪比区域发散。Gallager 提出了第一上界技术（GFBT, Gallager's First Bounding Technique）[8-9]，其基本思想是把接收向量划分为两个区域，当接收向量处于 Gallager 区域内时，采用联合界等技术进行上界；当接收向量处于 Gallager 区域外时，视为译码错误事件。由此利用全概率公式可以得到该 GFBT 上界。设计不同几何形状的 Gallager 区域，并通过数值积分的方法可以得到不同的 GFBT 上界，例如切面界（TB, Tangential Bound）[10]，球形界（SB, Sphere Bound）[11]，切面球形界（TSB, Tangential-Sphere Bound）[12]等。然而数值积分受限于设计区域的几何形状以及积分的计算复杂度。利用汉明距离来优化设计 Gallager 区域，Ma 等在文献[13]和文献[14]中提出了基于截断重量谱的 ML 上界技术和基于三角形谱和四面体谱的 ML 上界技术，通过减少码字参与个数在一定程度上降低了计算复杂度。关于 ML 译码的性能下界，传统的有球包界（SPB, Sphere Packing Bound）[15]。1998 年，Seguin[16]利用 De Caen 下界[17]提出了基于成对错误概率的 ML 译码性能下界。Behnamfar 等[18]则利用 KAT 下界[19]对 ML 译码进行下界分析。Cohen 等[20]利用柯西-施瓦茨不等式给出了更普适的 ML 译码下界，此外还提出了仅针对一个相同汉明重量的码字集合的 ML 译码下界。最近，针对极化码，Shuval 等[21]提出了基于码字比特相关性的算法来计算码字之间的成三错误概率，进一步给出了基于码字的成对和成三错误概率的 ML 译码下界。

本文采用改进的联合界技术和基于部分码字集合的 Bonferroni 下界技术分析极化码的 ML 性能。对于未知全局重量谱的极化码而言，改进的联合界技术利用截断重量谱进行 ML 性能估计。下界的计算只需选取码表中的部分码字。当选取的部分码字的汉明重量较轻时，紧致的 ML 下界可以利用二阶 Bonferroni 不等式计算得到。文中基于该上下界技术对 5G 极化码进行了评估。结果表明，改进的联合界技术和基于部分码字集合的 Bonferroni 下界技术计算复杂度低，在仿真区域内，上下界比较贴近，可以准确地估计极化码的 ML 译码性能，从而得到 SCL 译码逼近 ML 译码性能所需的最小列表大小。

2　极化码的上下界技术

2.1　极化码

2.1.1　极化码介绍

信道极化可以分成信道分裂和信道联合。当码长 N 足够大时，经过信道极化得到的 N 个子信道会呈现两极分化，部分信道的容量趋于 1（无噪信道），部分信道的容量趋于 0（有噪信道）。因此，可以通过在可靠性度量高的子信道上传输消息比特，在可靠性度量低的子信道传输冻结比特来完成消息传输。基于此，极化码可进行如下构造。令 $\mathcal{P}[N,K,\mathcal{A}]$ 表示一个码长为 N（$N=2^n, n\ge 1$），信息长为 K，码率为 $R=K/N$ 的极化码。这里，$\mathcal{A}\subseteq\{0,1,\dots N-1\}$ 是传输信息比特的子信道位置的集合。记信息序列为 $\boldsymbol{u}_0^{N-1}=(\boldsymbol{u}_{\mathcal{A}},\boldsymbol{u}_{\mathcal{A}^c})$，其中，$\boldsymbol{u}_{\mathcal{A}}$ 包含 K 个信息比特，$\boldsymbol{u}_{\mathcal{A}^c}$ 包含 $N-K$ 个冻结比特。记 $\boldsymbol{c}_0^{N-1}=(c_0,c_1,\dots,c_{N-1})$ 为码字序列，$\boldsymbol{G}_N=\boldsymbol{F}^{\otimes n}$ 为生成矩阵，其中 $\boldsymbol{F}^{\otimes n}$ 为矩阵 $\boldsymbol{F}=\begin{bmatrix}1 & 0\\ 1 & 1\end{bmatrix}$ 的 n 阶克罗内克

积（Kronecker Product）。极化码的编码过程可以表示为

$$\boldsymbol{c}_0^{N-1}=\boldsymbol{u}_0^{N-1}\boldsymbol{G}_N \quad 。 \tag{1}$$

基于矩阵 $\boldsymbol{F}$，极化码可以通过递归的形式实现编码。令 $\boldsymbol{c}_{m-1,2j}$ 、$\boldsymbol{c}_{m-1,2j+1}$ 分别表示在递归的第 $m-1$ 阶段得到的第 $2j$ 和第 $2j+1$ 个码字，$\boldsymbol{c}_{m,j}$ 表示在递归的第 m 阶段得到的第 j 个码字。在已知码字 $\boldsymbol{c}_{m-1,2j}$ 和 $\boldsymbol{c}_{m-1,2j+1}$ 的情况下，码字 $\boldsymbol{c}_{m,j}$ 可通过式(2)得到。记初始状态满足 $\boldsymbol{c}_{0,j}=u_j$（$0\le j\le N$）。

$$\boldsymbol{c}_{m,j}=(\boldsymbol{c}_{m-1,2j}+\boldsymbol{c}_{m-1,2j+1},\boldsymbol{c}_{m-1,2j+1}) \quad , \tag{2}$$

其中，$\boldsymbol{c}_{m,j}$ 为长度为 2^m 的码字，$m=1,2,...,n,\ j=0,1,...,2^{n-m}-1$。当递归至 $m=n$ 时，码字 $\boldsymbol{c}_{n,0}$ 即是编码之后的极化码 $\mathcal{P}[N,K,\mathcal{A}]$ 的码字。公式(2)的加法为二进制加法运算。以长度为 8 的信息序列为例，极化码编码示意图如图 1 所示。

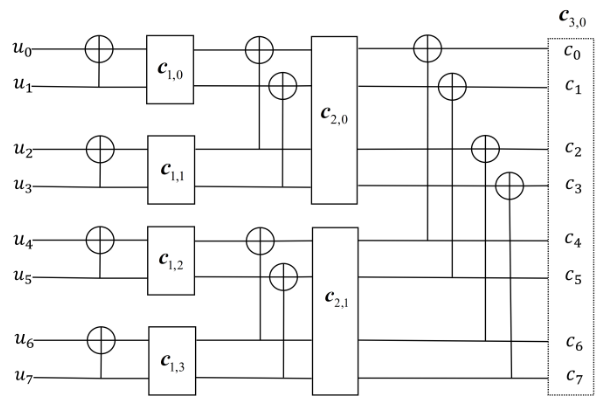

图 1　长度为 8 的信息序列编码示意图

2.1.2　极化码重量谱分布

设极化码 $\mathcal{P}[N,K,\mathcal{A}]$ 的重量谱为 $A(Y)=\sum_{0\le j\le N}A_jY^j$，其中 Y 代表哑变量，A_j 代表汉明重量为 j 的码字个数。由于极化码的重量谱不易计算，本文采用随机交织极化码[22]的重量谱的计算方法近似估计极化码的重量谱，具体如下。

交织极化码[22]的基本思想是在极化码的编码过程中，引入交织器 $\prod$ 打乱式(2)中的码字 $\boldsymbol{c}_{m-1,2j}$。此时，根据文献[22]，均匀随机交织极化码簇的重量谱可以通过递归计算得到，其基本思想如下。

已知码字 $\boldsymbol{c}_{m-1,2j}$ 和 $\boldsymbol{c}_{m-1,2j+1}$ 的重量谱分别为 $A_{\boldsymbol{c}_{m-1,2j}}(Y)$ 和 $A_{\boldsymbol{c}_{m-1,2j+1}}(Y)$，则码字 $\boldsymbol{c}_{m,j}$ 的重量谱 $A_{\boldsymbol{c}_{m,j}}(Y)$ 可如式(3)计算，其中，初始状态如式(4)所示。当递归至 $m=n$ 时，$A_{\boldsymbol{c}_{n,0}}(Y)$ 即为随机交织极化码簇的重量谱。

$$A_{\boldsymbol{c}_{m,j}}(Y)=\sum_{d_1,d_2}A_{\boldsymbol{c}_{m-1,2j},d_1}A_{\boldsymbol{c}_{m-1,2j+1},d_2}G(d_1,d_2,m) \quad , \tag{3}$$

$$A_{\boldsymbol{c}_{0,j}}(Y)=\begin{cases}1+Y, & j\in\mathcal{A}\\ 1, & j\in\mathcal{A}^c\end{cases} \quad , \tag{4}$$

其中，

$$G(d_1,d_2,m)=\sum_{k=\max(0,d_1+d_2-2^{m-1})}^{\min(d_1,d_2)}\frac{\binom{d_2}{k}\binom{2^{m-1}-d_2}{d_1-k}}{\binom{2^{m-1}}{d_1}}Y^{d_1+2d_2-2k} \tag{5}$$

2.1.3　极化码部分码字集合

通常情况下，译码错误一般发生在发送码字被错译成离它汉明距离最近的码字。为了得到最小汉明重量码字集合，Zhang 等[23]提出了一种基于 SCL 译码的方法。在假设接收端接收到全零码字的情形下，Zhang 等[23]根据 SCL 译码器选取可靠性大的译码路径对应的码字集合，作为最小汉明重量码字集合的近似估计。更一般地，假设在有噪信道上发送全零码字，在仿真 SCL 译码算法的过程中保留所有候选路径对应的非零码字，从而可以得到极化码的部分码字集合。

2.2　改进的联合界技术

基于不失一般性，假设发送端发送全零码字 $\boldsymbol{c}^{(0)}$ 并对它采用二进制相移键控调制（BPSK, Binary Phase Shift Keying）调制。调制信号经过加性高斯白噪声（AWGN, Additive White Gaussian Noise）信道，接收端收到接收向量 $\boldsymbol{y}_0^{N-1}=(-1)^{c^{(0)}}+\boldsymbol{w}_0^{N-1}$，其中 $\boldsymbol{w}_0^{N-1}$ 表示 N 维高斯随机向量（每一维随机变量服从均值为 0，方差为 σ^2 的高斯分布）。

根据文献[14]，ML 译码的性能上界可通过式(6)进行计算，表达式如下：

$$\Pr\{E\}\le\min_{1\le d^*\le N}\left\{\sum_{d\le 2d^*}h(A_d)+B(p_b,N,d^*+1,N)\right\} \tag{6}$$

其中，表示 A_d 汉明重量为 d 的码字的数量，

$$h(A_d)=\min\{p_1(A_d),p_2(A_d)\} \quad , \tag{7}$$

$$B(p_b,N_l,N_s,N_f)\triangleq\sum_{m=N_s}^{N_f}\binom{N_l}{m}p_b^m(1-p_b)^{N_l-m} \quad , \tag{8}$$

$$p_b\triangleq Q\left(\frac{1}{\sigma}\right) \quad , \tag{9}$$

其中，

$$p_1(A_d)=A_dQ\left(\frac{\sqrt{d}}{\sigma}\right)B(p_b,N-d,0,d^*-1) \quad , \quad (10)$$

$$p_2(A_d)=\left(A_d-1\right)\left(Q\left(\sqrt{d}/\sigma\right)-\frac{1}{2}Q^2\left(\sqrt{d}/\sigma\right)\right) B(p_b,N-2d,0,d^*-1)+Q\left(\sqrt{d}/\sigma\right) \quad (11)$$

$$Q(x)\triangleq\int_x^{+\infty}\frac{1}{\sqrt{2\pi}}e^{-\frac{z^2}{2}}dz \quad 。 \quad (12)$$

可以看出，该改进的联合界的求解仅依赖于码本中汉明重量不超过 $2d^*$ 的截断重量谱。基于任意的 $d^*\ge 0$，只要已知极化码的截断重量谱 $A(Y)=\sum_{0\le j\le 2d^*}A_jY^j$，就可以计算得到对应的改进的联合界。其次，可以优化 d^* 来获得更紧致的改进的联合界。

2.3 基于部分码字集合的 Bonferroni 下界技术

对于极化码 $\mathcal{P}[N,K,\mathcal{A}]$，极化码的码本 $\left\{\boldsymbol{c}^{(i)},i=0,1,\dots 2^K-1\right\}$ 包含 2^K 个码字，其中 $\boldsymbol{c}^{(0)}$ 是全零码字。此时，ML 译码错误概率为 $\Pr\{E\}=\Pr\left\{\bigcup_{i=1}^{2^K-1}\varepsilon_{0\to i}\right\}$。这里，$\varepsilon_{0\to i}$ 表示 $\boldsymbol{c}^{(0)}$ 错译为码字 $\boldsymbol{c}^{(i)}$ 的概率。任意选取一个有 J 个元素的子集 $\mathcal{J}\subseteq\{1,2,\dots 2^K-1\}$，$\Pr\left\{\bigcup_{i=1}^{2^K-1}\varepsilon_{0\to i}\right\}\ge\Pr\left\{\bigcup_{j\in\mathcal{J}}\varepsilon_{0\to j}\right\}$。根据二阶 Bonferroni 不等式[24]，可以得到 $\Pr\left\{\bigcup_{j\in\mathcal{J}}\varepsilon_{0\to j}\right\}\ge\sum_{i\in J}\Pr\{\varepsilon_{0\to i}\}-\sum_{i<j(i,j\in J)}\Pr\left\{\varepsilon_{0\to i}\cap\varepsilon_{0\to j}\right\}$。由此，基于部分码字集合，ML 译码错误概率下界可如式(13)计算得到，记为 Bonferroni 下界。

$$\Pr\{E\}\ge\sum_{i\in\mathcal{J}}\Pr\{\varepsilon_{0\to i}\}-\sum_{i<j(i,j\in\mathcal{J})}\Pr\left\{\varepsilon_{0\to i}\cap\varepsilon_{0\to j}\right\} \quad (13)$$

其中，$\Pr\{\varepsilon_{0\to i}\}$ 和 $\Pr\left\{\varepsilon_{0\to i}\cap\varepsilon_{0\to j}\right\}$ 可通过有限积分[25]计算得到，即，

$$\Pr\{\varepsilon_{0\to i}\}=\frac{1}{\pi}\int_0^{\pi/2}\exp\left[-\frac{W_H\left(\boldsymbol{c}^{(i)}\right)}{\sigma^2\sin^2\theta}\right]d\theta \quad , \quad (14)$$

$$\Pr\left\{\varepsilon_{0\to i}\cap\varepsilon_{0\to j}\right\}=\psi\left(\frac{\sqrt{W_H\left(\boldsymbol{c}^{(i)}\right)}}{\sigma},\frac{\sqrt{W_H\left(\boldsymbol{c}^{(j)}\right)}}{\sigma}\right) \quad (15)$$

其中，$W_H\left(\boldsymbol{c}^{(i)}\right)$ 表示码字 $\boldsymbol{c}^{(i)}$ 的汉明重量，

$$\psi(x,y)=\frac{1}{2\pi}\int_0^{\frac{\pi}{2}-\tan^{-1}\left(\frac{y}{x}\right)}\frac{\sqrt{1-\rho_{ij}}}{1-\rho_{ij}\sin 2\theta}\exp\left[-\frac{x^2}{2}\frac{1-\rho_{ij}\sin 2\theta}{(1-\rho_{ij}^2)\sin^2\theta}\right]d\theta+\frac{1}{2\pi}\int_0^{\tan^{-1}\left(\frac{y}{x}\right)}\frac{\sqrt{1-\rho_{ij}}}{1-\rho_{ij}\sin 2\theta}\exp\left[-\frac{y^2}{2}\frac{1-\rho_{ij}\sin 2\theta}{(1-\rho_{ij}^2)\sin^2\theta}\right]d\theta \quad (16)$$

其中，ρ_{ij} 与码字 $\boldsymbol{c}^{(i)}$ 与码字 $\boldsymbol{c}^{(j)}$ 之间的汉明距离 $W_H\left(\boldsymbol{c}^{(i)}-\boldsymbol{c}^{(j)}\right)$ 有关，

$$\rho_{ij}=\frac{W_H\left(\boldsymbol{c}^{(i)}\right)+W_H\left(\boldsymbol{c}^{(j)}\right)-W_H\left(\boldsymbol{c}^{(i)}-\boldsymbol{c}^{(j)}\right)}{2\sqrt{W_H\left(\boldsymbol{c}^{(i)}\right)W_H\left(\boldsymbol{c}^{(j)}\right)}} \quad (17)$$

2.4 极化码性能分析

通过计算得到极化码的近似重量谱及部分码字集合后，极化码的改进的联合界可通过式(6)计算，极化码的基于 Bonferroni 公式的下界可通过式(13)计算，从而估计极化码的 ML 译码的性能界。接下来以 5G 极化码为例进行仿真实验和分析。

3 极化码的上下界技术

3.1 5G 极化码的上下界性能仿真

本小节给出 5G 极化码[128, 64], [256, 128]和[512, 256]的上下界仿真结果及分析。实验中均采用 SCL 译码算法。

图2给出了计算5G极化码改进的联合界所需用到的截断谱参数 d^* 信息。在仿真中，在信噪比 $E_b/N_0=3\text{dB}$ 时，5G 极化码[128, 64], [256, 128]和[512, 256]所需截断重量谱的参数分别为 45，8 和 104。从图中可以看到，随着信噪比的增大，优化参数 d^* 减小。这个是符合预期的，因为当信噪比增大的时候，主要错误还是发生在较小 $E_b/N_0=6\text{dB}$ 对应的汉明球内。

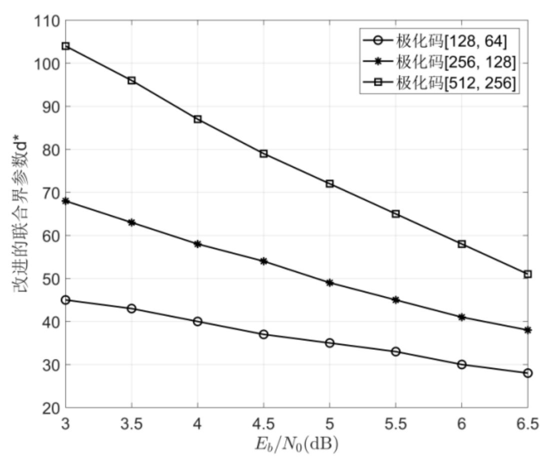

图 2 计算极化码改进的联合界所需的截断重量谱参数 d^*

图 3 给出了计算 5G 极化码 Bonferroni 下界时所需的码字两两之间的汉明距离分布。在仿真中，基于极化码的近似重量谱，SCL 译码器列表大小设定为重量谱中最小汉明重量码字的数量，从而得到一个汉明重量较轻的码字集合。值得说明的是，为获得紧致的 Bonferroni 下界，在不同信噪比下可以选取不同的码字集合进行计算。根据式(15)，Bonferroni 下界的计算复杂度主要来自概率 $\Pr\left\{\varepsilon_{0\to i}\cap\varepsilon_{0\to j}\right\}$ 的积分计算。当码字集合的汉明重量相同时，概率 $\Pr\left\{\varepsilon_{0\to i}\cap\varepsilon_{0\to j}\right\}$ 的计算主要与码字两两汉明距离有关。从图中可以看到，选取 5G 极化码[128, 64]的部分码字集合为 275 个汉明重量为 8 的码字时，码字之间的汉明距离可归为三类，分别是 8，12，16。 选取 5G 极化码[256, 128]部分码字集合为 96 个汉明重量为 8 的码字时，码字之间的汉明距离可归为两类，分别是 8 和 16。选取 5G 极化码[512, 256] 的部分码字集合为 64 个汉明重量为 8 的码字时，码字之间的汉明距离均为 16。可以看出码字集合中的码字两两之间的距离分布具有稀疏性，此时，对应的概率 $\Pr\left\{\varepsilon_{0\to i}\cap\varepsilon_{0\to j}\right\}$ 的计算次数也大大减少。例如，5G 极化码[128, 64]仅需计算三类概率，对应的概率 $\Pr\left\{\varepsilon_{0\to i}\cap\varepsilon_{0\to j}\right\}$ 的计算也仅需三次。因此，基于 Bonferroni 的下界的计算复杂度也较低。

图 4、5、6 给出了 5G 极化码采用列表为 1，2 的 SCL 译码算法的 FER 仿真性能，以及给出了它的联合界、改进的联合界以及 Bonferroni 下界。这里，当不采用下界技术时，SCL 译码性能的评估需要通过不断改变列表大小来实现。从图中可以发现列表为 2 时 SCL 译码算法已经逼近 ML 译码性能。由于列表大小为 4 对于性能的进一步改进收效甚微，而其所需的计算复杂度更高，所以在实际中列表大小设为 2 即可。当采用改进的联合界以及 Bonferroni 下界技术时，从图中可以看出，上界和下界在高信噪比区域贴近，由此我们可以估计极化码在 ML 译码下的 FER 性能。

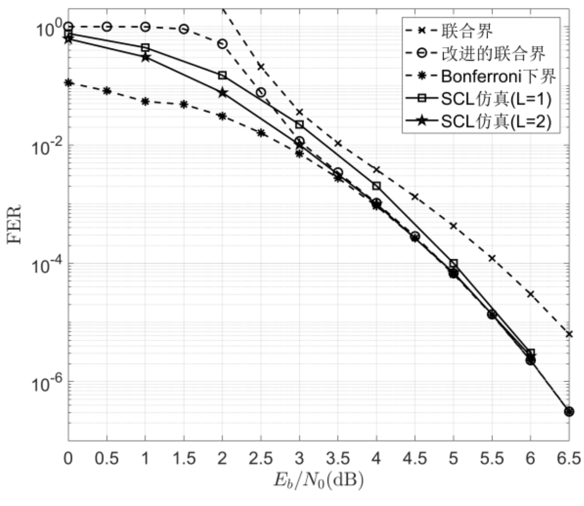

图 4　极化码[128, 64]的性能曲线

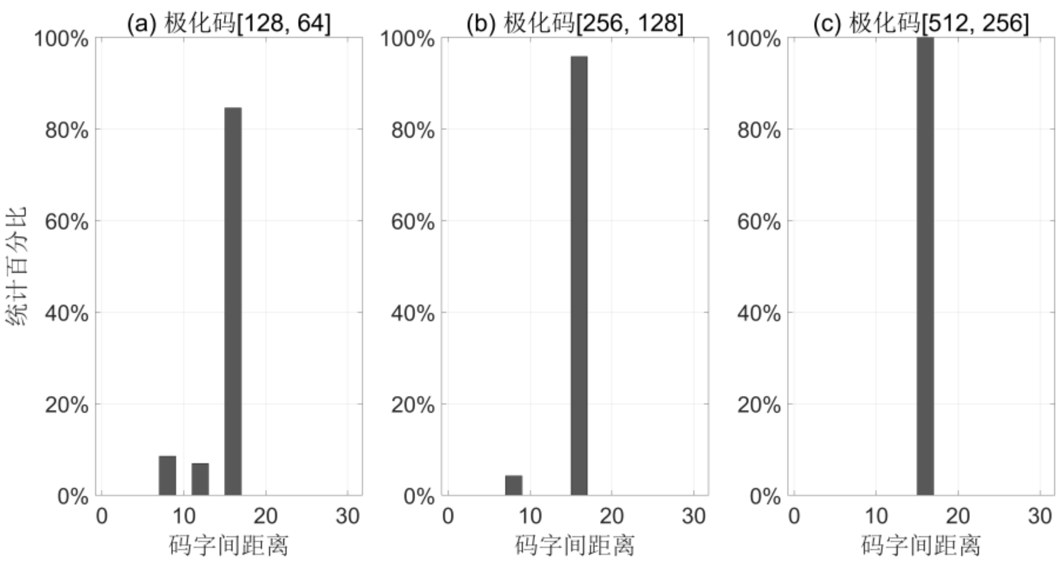

图 3　5G 极化码部分码字两两之间的汉明距离分布

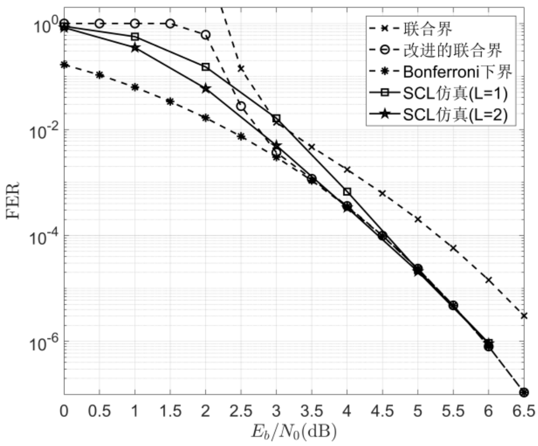

图 5　极化码[256, 128]的性能曲线

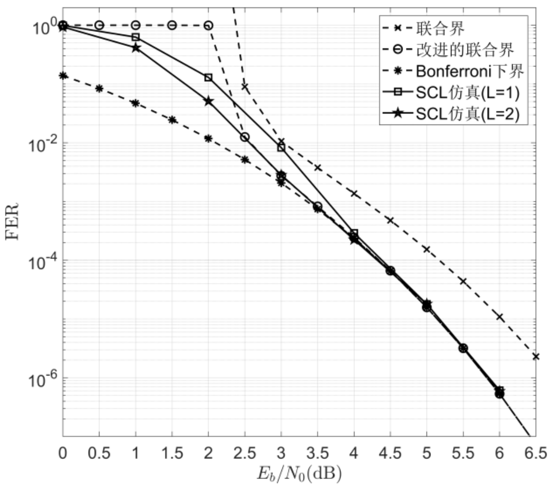

图 6　极化码[512, 256]的性能曲线

3.2　5G CRC 极化码的下界性能仿真

在实际应用中，极化码通常是与 CRC 级联的。此时，重量谱就难以估计，因而没有简单的上界技术。但是极化码的部分码字集合总是可以通过 CA-SCL 仿真得到，基于此可以计算 Bonferroni 下界。当 CA-SCL 译码性能逼近下界时，该下界技术可以用于指导列表参数大小的选择。在本小节中，对 5G CRC 级联极化码[128, 16]进行仿真实验。实验采用 CA-SCL 译码算法，CRC 级联长度为 4。

图 7 给出了 5G CRC 级联极化码[128, 16]采用 CA-SCL 译码算法的 FER 仿真性能，以及给出了它的 Bonferroni 下界。由仿真结果可以看出，随着列表大小的增加，CA-SCL 译码性能逐步逼近 ML 译码性能。当信噪比为 $E_b / N_0 = 6\text{dB}$ 时，CA-SCL(L=8)已经逼近 ML 译码性能。因此，可以推测 CA-SCL(L=8)在高信噪比区域具有近 ML 译码性能的特性，在实际中设置 CA-SCL 列表大小为 8 即可。此外，与没有 CRC 级联的极化码相比，可以看到级联极化码的 CA-SCL 算法逼近 ML 译码性能所需列表大小通常较大，例如，5G 极化码[128, 64]的 SCL 列表实际大小设为 2，而 5G CRC 级联极化码[128, 16]的 CA-SCL 列表大小设为 8。

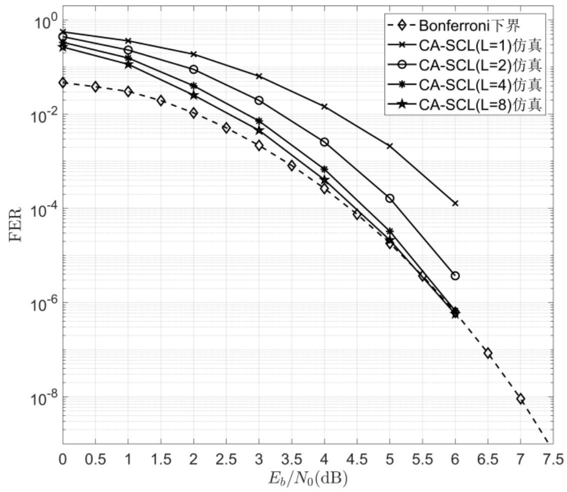

图 7　极 CRC 级联极化码[128, 16]的 CA-SCL 译码性能曲线以及对应的下界性能曲线

4　结束语

本文针对极化码的最大似然译码性能，采用了改进的联合界技术和基于部分码字集合的 Bonferroni 下界技术。数值仿真结果表明，该上下界贴近，从而可以有效估计极化码的最大似然译码性能，进一步指导 SCL 译码算法列表参数的选择。特别地，对于 5G 极化码[128, 64]，[256, 128]和[512, 256]，SCL 译码算法设定列表大小为 2 即可，而对于级联长度为 4 的 5G CRC 级联极化码[128, 16]，CA-SCL 译码算法列表设定为 8 即可。

参考文献：

[1] ARIKAN E. Channel Polarization: A Method for Constructing Capacity-Achieving Codes for Symmetric Binary-Input Memoryless Channels[J]. IEEE Transactions on Information Theory, 2009, 55(7): 3051-3073.

[2] ARIKAN E. A Performance Comparison of Polar Codes and Reed-Muller Codes[J]. IEEE Communications Letters, 2008, 12(6): 447-449.

[3] TAL I, VARDY A. List Decoding of Polar Codes[C]//Proceedings of the IEEE International Symposium on Information Theory. St Peters-

burg, Russia: IEEE, 2011: 1-5.

[4] TAL I, VARDY A. List Decoding of Polar Codes[J]. IEEE Transactions on Information Theory, 2015, 61(5): 2213-2226.

[5] NIU K, CHEN K. CRC-Aided Decoding of Polar Codes[J]. IEEE Communications Letters, 2012, 16(10): 1668-1671.

[6] WANG T, QU D, JIANG T. Parity-Check-Concatenated Polar Codes[J]. IEEE Communications Letters, 2016, 20(12): 2342-2345.

[7] TRIFONOV P. Efficient Design and Decoding Of Polar Codes[J]. IEEE Transactions on Communications, 2012, 60(11): 3221-3227.

[8] GALLAGER R. Low-Density Parity-Check Codes[J]. IRE Transactions on Information Theory, 1962, 8(1): 21-28.

[9] SHAMAI S, SASON I. Variations on the Gallager Bounds, Connections, and Applications[J]. IEEE Transactions on Information Theory, 2002, 48(12): 3029-3051.

[10] BERLEKAMP E R. The Technology of Error-Correcting Codes[J]. Proceedings of the IEEE, 1980, 68(5): 564-593.

[11] HERZBERG H, POLTYREV G. Techniques of Bounding the Probability of Decoding Error for Block Coded Modulation Structures[J]. IEEE Transactions on Information Theory, 1994, 40(3): 903-911.

[12] DIVSALAR D. A Simple Tight Bound on Error Probability of Block Codes with Application to Turbo Codes[J]. TMO progress report, 1999, 19: 42-139.

[13] MA X, LIU J, BAI B. New Techniques for Upper-Bounding the ML Decoding Performance of Binary Linear Codes[J]. IEEE Transactions on Communications, 2013, 61(3): 842-851.

[14] MA X, LIU J, ZHUANG Q, et al. New Geometrical Spectra of Linear Codes with Applications to Performance Analysis[C]//2013 IEEE Information Theory Workshop (ITW). IEEE, 2013: 1-5.

[15] SHANNON C E. Probability of Error for Optimal Codes in A Gaussian Channel[J]. Bell System Technical Journal, 1959, 38(3): 611-656.

[16] SEGUIN G E. A Lower Bound on the Error Probability for Signals in White Gaussian Noise[J]. IEEE Transactions on Information Theory, 1998, 44(7): 3168-3175.

[17] DE CAEN D. A Lower Bound on the Probability of A Union[J]. Discrete mathematics, 1997, 169(1-3): 217-220.

[18] BEHNAMFAR F, ALAJAJI F, LINDER T. Improved Lower Bounds for the Error Rate of Linear Block Codes[C]//43rd Allerton Conference on Control, Computing and Communications, Monticello, Illinois, USA. 2005.

[19] KUAI H, ALAJAJI F, TAKAHARA G. Tight Error Bounds for Nonuniform Signaling over AWGN Channels[J]. IEEE Transactions on Information Theory, 2000, 46(7): 2712-2718.

[20] COHEN A, MERHAV N. Lower Bounds on the Error Probability of Block Codes Based on Improvements on De Caen's Inequality[J]. IEEE Transactions on Information Theory, 2004, 50(2): 290-310.

[21] SHUVAL B, TAL I. A Lower Bound on the Probability of Error of Polar Codes over BMS Channels[J]. IEEE Transactions on Information Theory, 2018, 65(4): 2021-2045.

[22] CHIU M C. Interleaved Polar (I-Polar) Codes[J]. IEEE Transactions on Information Theory, 2020, 66(4): 2430-2442.

[23] ZHANG Q, LIU A, PAN X, et al. CRC Code Design for List Decoding of Polar Codes[J]. IEEE Communications Letters, 2017, 21(6): 1229-1232.

[24] HOPPE F M. Iterating Bonferroni Bounds[J]. Statistics & Probability Letters, 1985, 3(3): 121-125.

[25] SASON I, SHAMAI S. Performance Analysis of Linear Codes under Maximum-Likelihood Decoding: A Tutorial[J]. Foundations and Trends® in Communications and Information Theory, 2006, 3(1–2): 1-222.

[作者简介]

郑湘萍（2000− ），女，中山大学硕士研究生，主要研究方向为极化码译码。（E-mail：zhengxp23@mail2.sysu..edu.cn）

姚忻圆梦（1997− ），女，中山大学博士研究生，主要研究方向为极化码、信道编码。（E-mail：yaoxym@mail2.sysu.edu.cn）

马啸（1968− ），男，博士，中山大学教授、博士生导师，主要研究方向为信息与编码理论、编码调制技术、无线通信、光通信等。（E-mail：maxiao@mail.sysu.edu.cn）

An Efficient Transmission-Reception Scheme for LoRa-Based Uplink Satellite IoT Communications

Zhongyang Yu, Mengmeng Xu, Yuanyuan Wang, and Jixun Gao
School of Computer Science, Henan University of Engineering, Zhengzhou, P. R. China
Email: xd_yzy2013@sina.com

***Abstract*—Due to the impact of the superposition of noises and interferences caused by the users using the long range (LoRa) modulation with large spreading factors (SFs) for uplink satellite IoT communications, the other users using the LoRa with relatively small SFs are hard to detect without the aid of the power allocation and interference cancellation. To this end, we propose a simple but efficient transmission-reception scheme including selective repetition transmission and superposition reception. In specific, the selective repetition can support two cases of full repetition and partial repetition in order to achieve a good tradeoff between detection performance and transmission rate, and the superposition reception can mitigate the negative effect of the superposition of the noises and interferences. Simulation results validate the efficiency of the proposed scheme.**

I. Introduction

Satellite Internet of Things (IoT) networks will be capable of solving the issue of massive users' connectivity especially in remote areas [1], [2]. Unlike terrestrial access networks such as long range (LoRa) technology with multiple gateways, satellite-based networks perhaps need to consider joint orthogonal "time-frequency-code" division multiple access technology such as the classical time division multiple access (TDMA), frequency division multiple access (FDMA), and code division multiple access (CDMA). For this reason, we try to design a joint "frequency-code" orthogonal multiple access scheme, combining pseudo-noise (PN) or Walsh coding and LoRa modulation with different spreading factors (SFs). First of all, this letter will deal with the problem of detecting superposed LoRa signals without the use of the power allocation and interference cancellation strategy.

For the LoRa modulation, it can be described as the frequency shift chirp modulation (FSCM) [3], where the initial frequency shift carries the user information unlike the pure chirp spread spectrum (CSS) modulation [4] but similar to a kind of high-order CSS. In [5], the authors provided a detailed analysis of LoRa waveform property and its spectral, where they proved that the LoRa waveforms are asymptotically orthogonal for large SFs. In other words, those with relatively small SFs exhibit weak orthogonality. Considering two LoRa signals simultaneously received with the same SFs, Ref. [6] showed that the reception can be successful as long as one signal is received at least 6 dB above the other while Ref. [7] presented a different result and further indicated that packet loss would occur in the packets modulated with different SFs if the interference is strong enough. However, these results were obtained under the noise-free environment. Indeed, only the LoRa signal with a high SF is possible to detected from the superposed LoRa signals in the presence of Gaussian noises [8], which potentially proves the LoRa waveform property derived in [5]. For the superposed LoRa signals with the same SFs, Temim *et al.* addressed the corresponding reception based on the well-known successive interference cancellation (SIC) algorithm [9]. Furthermore, Noreen *et al.* investigated the capture effect of the LoRa based system with different SFs and its combination with the SIC algorithm [10]. In order to maximize energy efficiency of the system, Su *et al.* studied the corresponding energy efficient resource allocation which includes the power allocation [11]. However, the performance of the LoRa based systems in these researches is determined by the energy threshold selection in the power allocation and SIC strategy regardless of using the same SFs or different SFs, where in this case the strategy seems complicated.

In this letter, we deal with the issue of uplink multiuser transmission based on the LoRa modulation with different SFs without the use of the power allocation and SIC strategy. At the transmitter, we propose a selective repetition transmission scheme for the users with small SFs. Accordingly, a superposition reception scheme is provided to detect those users at the receiver. Taking two-user and three-user simultaneous transmissions for examples, simulation results demonstrate that the proposed scheme can perform well especially for the multiuser transmission with far SFs. Meanwhile, fading performance evaluation and massive-user transmission design are also given.

II. System Model

Consider an uplink (satellite) IoT system with N users sharing an available bandwidth B, where each user adopts the LoRa modulation with an unique SF. In other words, $SF_1 \sim SF_N$ are assigned in turn to *User* $1 \sim N$, restricting $SF_1 < SF_2 < \cdots < SF_N$ without loss of generality. Under such conditions, the l-th received signal, taken at the chirp rate B, can be expressed as

$$y_N(l,k) = \sum_{m=1}^{N} s_m(l,k)\, e^{\mathrm{j}(2\pi f_d^m k/B+\theta_m)} + n_m(l,k), \quad (1)$$

where f_d^m and θ_m are the frequency offset and phase offset, respectively, k is the chirp index, whose specific range will be given latter, $s_m(l,k)$ is the LoRa signal with the average energy $E_s = \mathbb{E}\{|s_m(l,k)|^2\} = 1$, whose specific form will be given in the next section, and $n_m(l,k)$ is the additive white Gaussian noise (AWGN) with zero mean and variance σ_m^2.

Since the noncoherent detection will be used, the impact of the phase offset is thus not considered. Furthermore, we will consider in simulation the frequency offset $|f_d^m| < 0.5B/2^{SF_m}$ according to the interval between the two adjacent chirps.

III. Proposed Scheme

In general, the users using the LoRa modulation with small SFs are susceptible to the impact of the noises and interferences from other users using the LoRa with relatively large SFs. This is because the LoRa modulation with small SFs is unsatisfactory in terms of both noise-immune ability and orthogonality [5]. If not consider the power allocation and SIC strategy, our selective repetition transmission and superposition reception scheme can be selected.

A. Selective Repetition Transmission

To start with, we define the chirp number $M_i = 2^{SF_i}$ for *User* i, followed by a varying number of repeats K_i $(i \neq N)$. Clearly, $K_i \leq (M_N - M_i)/M_i$ in terms of the chirp number $M_N = 2^{SF_N}$ for *User* N. Furthermore, we denote by $K_i = (M_N - M_i)/M_i$ the number of full repetition and $K_i < (M_N - M_i)/M_i$ the number of partial repetition, designated as K_i^{fr} and K_i^{pr} respectively.

Based on repeating the original symbols generated by the LoRa modulation with small SFs, we put forward a selective repetition transmission scheme, as shown in Fig. 1 with (a) no repetition case, (b) full repetition case, and (c) partial repetition case. For the *no repetition case*, there are M_N/M_i original LoRa symbols to be transmitted. For the *full repetition case*, it carries only one original symbol along with the same K_i^f symbols obtained by repeating this original symbol. For the *partial repetition case*, it supports one current original symbol and its K_i^p repeated symbols as well as other symbols and their $\tilde{K}_i^p$ repeated symbols. Surprisingly, for *User* i, the latter two cases can mitigate the other users' interferences in different degrees at the expense of some transmission rate, compared to the case (a). However, it is known from the existing literatures [9-11] that the power allocation and SIC strategy is required for the case (a).

For *User* i, the original LoRa symbol can be represented as [3]

$$s_i^o(l,k) = \frac{e^{\mathrm{j}2\pi\left[\left(d_l^i + \frac{k}{2}\right) \bmod M_i\right]\frac{k}{M_i}}}{\sqrt{M_i}},\ k \in \{0,1,\ldots,M_i-1\}, \tag{2}$$

where $d_l^i \in \{0,1,\ldots,M_i-1\}$ is the decimal number determined by SF_i binary digits, the term *mod* denotes the modulo operator.

In the following, we will explain the three cases above.

1) No repetition case: The modulation signal $s_i(l,k)$ in (1) consists of M_N/M_i different original symbols, each having similar form of $s_i^o(l,k)$ in (2)

$$s_i(l,k) = \left[\underbrace{s_i^o(l,k)}_{\text{current symbol}}\ \overbrace{s_i^o(l+1,k)\cdots}^{(M_N/M_i-1)\text{ other symbols}}\right]. \tag{3}$$

The corresponding transmission rate is thus $R_{b,i}^{nr} = \frac{B \cdot SF_i}{M_i}$.

2) Full repetition case: The current symbol $s_i^o(l,k)$ is repeated K_i^f times, yielding a new version of the modulation signal $s_i(l,k)$:

$$s_i(l,k) = \left[\underbrace{s_i^o(l,k)}_{\text{current symbol}}\ \overbrace{s_i^o(l,k)\cdots s_i^o(l,k)}^{K_i^f\text{ repeated symbols}}\right], \tag{4}$$

where these repeated symbols will be fully explored during the noncoherent detection. But the corresponding transmission rate is reduced by a factor of $(K_i^f + 1)$ denoted by $R_{b,i}^{fr} = \frac{R_{b,i}^{nr}}{K_i^f+1}$, compared to the no repetition case.

3) Partial repetition case: The current symbol $s_i^o(l,k)$ and other symbols such as $s_i^o(l+1,k)$ are repeated K_i^p times and $\tilde{K}_i^p$ times, respectively, obtaining another new version of the modulation signal $s_i(l,k)$:

$$s_i(l,k) = \left[\underbrace{s_i^o(l,k)}_{\text{current symbol}}\ \overbrace{s_i^o(l,k)\cdots}^{K_i^p\text{ repeated symbols}}\ \underbrace{s_i^o(l+1,k)\ \overbrace{\cdots}^{\tilde{K}_i^p\text{ repeated symbols}}}_{\text{other symbols}}\right], \tag{5}$$

where partial repeated symbols are utilized, which equivalently improves the loss of transmission rate against the full repetition case. In this sense, the corresponding transmission rate becomes $R_{b,i}^{pr} = R_{b,i}^{fr} \cdot \frac{K_i^f+1}{K_i^p+1}$.

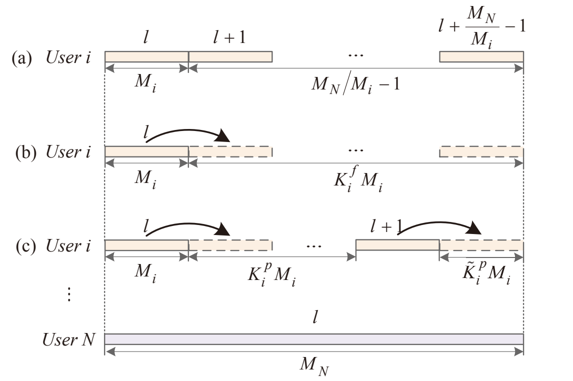

Fig. 1. Schematic diagram of the proposed transmission scheme for *User* i, where the solid box and the dashed box denote the original LoRa symbol and its repeated version, respectively.

B. Superposition Reception

For the full repetition case or partial repetition case, we will consider the *superposition* of the current symbol and its repeated symbols, as revealed in Fig. 2, in order to enhance

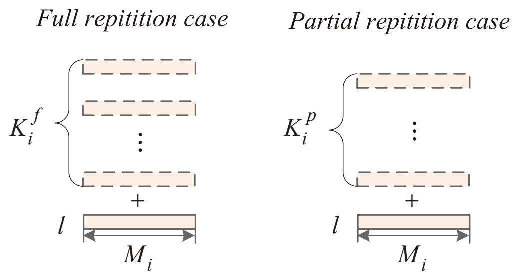

Fig. 2. Schematic diagram of the corresponding reception scheme for *User i*.

the ability of anti-interference and anti-noise especially for the users using the LoRa modulation with fairly small SFs. For simplicity, we will omit the frequency offset and phase offset in the following discussion.

For *User i*, other users are considered as interferences such that (1) can be rewritten as

$$y_N(l,k) = s_i(l,k) + \underbrace{\sum_{m=1, m\neq i}^{N} s_m(l,k)}_{\text{other user's interferences}} + \underbrace{\tilde{n}(l,k)}_{\text{superposed noises}}, \tag{6}$$

where $\tilde{n}(l,k) \triangleq \sum_{m=1}^{N} n_m(l,k)$.

1) No repetition case: We consider (2) and (3) into (6), and multiply by a down chirp with the form of $e^{-j\pi k^2/M_i}$ such that a dechirped signal can be derived as

$$\tilde{y}_N^{nr}(l,k) = \frac{1}{\sqrt{M_i}} e^{j2\pi \frac{d_l^i}{M_i} k} + s_I(l,k) + \tilde{\tilde{n}}(l,k), \tag{7}$$

where $s_I(l,k) \triangleq \sum_{m=1, m\neq i}^{N} s_m(l,k) e^{-j\pi k^2/M_i}$ is the superposition of $N-1$ LoRa-like signals, each having a wide-band spectrum with low spectral density [7], $\tilde{\tilde{n}}(l,k) \triangleq \tilde{n}(l,k) e^{-j\pi k^2/M_i}$ is the rotation version of $\tilde{n}(l,k)$.

Then, we can compute (7) via the discrete Fourier transform (DFT) using M_i orthogonal chirps, given by

$$R_l^{nr}(q) = \delta\left(q - d_l^i\right) + S_I(q) + N(q), q = 0, 1, \ldots, M_i - 1, \tag{8}$$

where $S_I(q)$ is the DFT of $s_I(l,k)$, $N(q)$ is the DFT of $\tilde{\tilde{n}}(l,k)$. One can observe that it is hard to detect the desired symbol d_l^i from the signal $R_l^{nr}(q)$ due to the effect of the interference $S_I(q)$ and the noise $N(q)$.

2) Full repetition case: Similarly, we have after some calculations

$$\tilde{y}_N^{fr}(l,k) = \frac{K_i^f + 1}{\sqrt{M_i}} e^{j2\pi \frac{d_l^i}{M_i} k} + \sum_{v=0}^{K_i^f} s_I(l+v,k) + \tilde{\tilde{n}}(l+v,k), \tag{9}$$

and

$$R_l^{fr}(q) = \left(K_i^f + 1\right)\delta\left(q - d_l^i\right) + \sum_{v=0}^{K_i^f} \left[S_I(q) + N(q)\right] e^{j2\pi qv}, \quad q = 0, 1, \ldots, M_i - 1. \tag{10}$$

Actually, one can find from (10) that the superposition of the current symbol and its repeated symbols can mitigate the negative impact of both interference and noise from other users, which helps to capture the expected symbol d_l^i.

3) Partial repetition case: Like the full repetition case, we also have

$$\tilde{y}_N^{pr}(l,k) = \frac{K_i^p + 1}{\sqrt{M_i}} e^{j2\pi \frac{d_l^i}{M_i} k} + \sum_{v=0}^{K_i^p} s_I(l+v,k) + \tilde{\tilde{n}}(l+v,k), \tag{11}$$

and

$$R_l^{pr}(q) = \left(K_i^p + 1\right)\delta\left(q - d_l^i\right) + \sum_{v=0}^{K_i^p} \left[S_I(q) + N(q)\right] e^{j2\pi qv}, \quad q = 0, 1, \ldots, M_i - 1. \tag{12}$$

Due to $K_i^p < K_i^f$, the partial superposition reception can guarantee a good compromise between the detection performance and the transmission rate.

Finally, the transmitted symbol d_l^i can be estimated after taking the amplitude of (8), (10), or (12) and looking for the location of the maximum [3], [5], [12]. Obviously, such noncoherent detection is not affected by the phase offset in (1) owing to taking the *amplitude* rather than the *real* part.

With regard to *User N* assigned to the largest SF, the corresponding anti-noise ability and orthogonality are the strongest such that the transmitted symbol can easily be detected, which will be verified in the latter simulation.

IV. Simulation Results

In this section, we will evaluate the performance of the proposed scheme to detect simultaneously received LoRa signals with different SFs under the AWGN channel. The basic parameters are listed in Table I.

TABLE I
BASIC PARAMETERS

Bandwidth (kHz)	$B = 125$
Spreading factor	$SF = 7, 9, 12$
Chirp number	$M = 128, 512, 4096$
Number of users	$N = 2, 3$

A. Two Users with Near or Far SFs

1) The case of two users with near SFs: Assume that *User 1* and *User 2* use $SF_1 = 7$ and $SF_2 = 9$, respectively. The specific simulation parameters are reported in Table II. Fig. 3 presents the detection performance of the two-user simultaneous transmission using $SF_1 = 7$ and $SF_2 = 9$, with (a) no frequency offsets and (b) the default frequency offsets.

As observed from Fig. 3(a), for *User 1* the corresponding performance improvement seems remarkable when considering the full repetition case ($K_1^f = 4$) or the partial repetition case ($K_1^p = 1$), compared to the no repetition case. In Specific, the performance of $K_1^f = 4$ can achieve the performance near to the single user transmission with $SF = 7$ [12], but at the

TABLE II
SIMULATION PARAMETERS FOR *User* 1 AND *User* 2

No repetition case	$512/128 = 4$ symbols transmitted
Full repetition case	$K_1^f = (512-128)/128 = 3$
Partial repetition case	$K_1^p = 1$
Frequency offset (Hz)	$f_d^1 = 0, 65$ and $f_d^2 = 0, 60$
Phase offset (rad)	$\theta_1 \in [-\pi, \pi)$ and $\theta_2 \in [-\pi, \pi)$

TABLE III
SIMULATION PARAMETERS FOR *User* 1 AND *User* 2

No repetition case	32 symbols and 8 symbols transmitted
Full repetition case	$K_1^f = 31$ and $K_2^f = 7$
Partial repetition case	$K_1^p = 15$ and $K_2^p = 3$

expense of the transmission rate (where $R_{b,1}^{fr} \approx 1709$ bps and $R_{b,1}^{nr} \approx 6835$ bps). Although the performance loss of $K_1^p = 1$ approaches 2.5 dB at the BER of 10^{-3}, the corresponding transmission rate can be increased to $R_{b,1}^{pr} \approx 3418$ bps. Moreover, the performance loss of *User* 2 is near 1.3 dB compared to the single user transmission with $SF = 9$ [12]. On the other hand, the two users are still capable of being detected well under small frequency offsets (and random phase offsets), which has reflected in Fig. 3(b).

2) The case of two users with far SFs: Assume that *User* 1 and *User* 2 adopt $SF_1 = 7$ and $SF_2 = 12$, respectively. For *User* 1, we consider the no repetition case with 32 symbols transmitted, the full repetition case with $K_1^f = 31$, and the partial repetition case with $K_1^p = 7, 15$. Fig. 4 presents the corresponding detection performance.

It is found from Fig. 4 that the performance of $K_1^f = 31$ can achieve the best performance thanks to the superposition of up to 31 repeated symbols, but resulting in a great sacrifice of the transmission rate (note that $R_{b,1}^{fr} \approx 214$ bps and $R_{b,1}^{nr} \approx 6835$ bps). Conversely, the performance losses of $K_1^p = 15$ and $K_1^p = 7$ can approach 0.5 dB and 1.5 dB against the single user transmission with $SF = 7$ [12], while the corresponding transmission rates are enhanced to 428 bps and 856 bps, respectively. Moreover, considering the single user transmission with $SF = 12$ [12], the performance loss of *User* 2 is actually negligible, which proves the previous discussion on the user with the largest SF.

B. Three Users with Different SFs

Suppose that *User* 1, *User* 2, and *User* 3 utilize $SF_1 = 7$, $SF_2 = 9$, and $SF_3 = 12$, respectively. The corresponding simulation parameters for *User* 1 and *User* 2 are presented in Table III. The detection performance of the three-user simultaneous transmission based on the proposed scheme is provided in Fig. 5.

In addition to the similar results to Fig. 3(a) and Fig. 4, one can also find that the performance loss of *User* 3 becomes larger compared to the performance of the single user with $SF = 12$ [11] due to the double interferences from *User* 1 and *User* 2. Also, increased performance losses have happened for *User* 1 and *User* 2, regardless of considering the full repetition

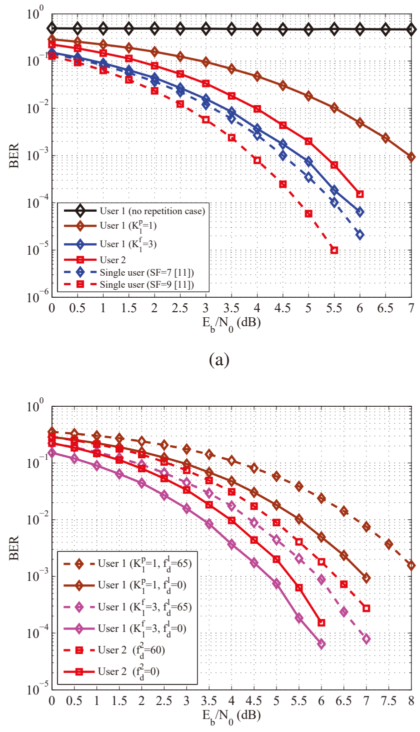

Fig. 3. Detection performance of the two-user simultaneous transmission using $SF_1 = 7$ and $SF_2 = 9$ with (a) no frequency offsets and (b) the default frequency offsets.

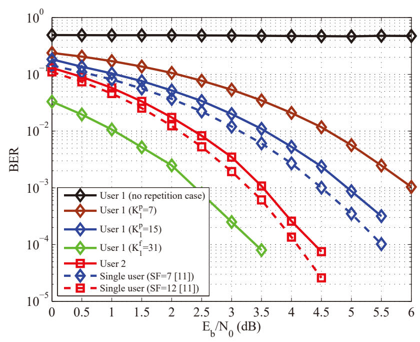

Fig. 4. Detection performance of the two-user simultaneous transmission with $SF_1 = 7$ and $SF_2 = 12$.

case ($K_1^f = 31$ and $K_2^f = 7$) or the partial repetition case ($K_1^p = 15$ and $K_2^p = 3$). These results allow us to know the limit of the proposed scheme, though there is no need to consider the power allocation and SIC strategy.

C. Fading Performance Evaluation

Taking the two-user transmission using far SFs for an example, we will evaluate the performance of the proposed scheme over a frequency-flat Rician fading channel with different K factors $K = 5$ dB, $K = 10$ dB and $K = 15$ dB, where *User* 1 and *User* 2 adopt $SF_1 = 7$ and $SF_2 = 12$, respectively. For *User* 1, the full repetition case with $K_1^f = 31$ is considered. The corresponding performance curve is depicted in Fig 6.

We note that for *User* 2 with $SF_2 = 12$ the corresponding performance under the Rician channel with $K = 10$ dB and $K = 15$ dB is almost close to that under the AWGN channel (from Fig. 4), while the performance with $K = 5$ dB starts to become poor. For *User* 1 with $SF_2 = 7$ and $K_1^f = 31$, the overall performance under the Rician channel with different K factors seems much worse than that under the AWGN channel (from Fig. 4). In other words, these results tells us to know that the impact of fading on the user assigned to the small SF is greater than that on the user assigned to the large SF.

D. Massive-User Transmission Design

As mentioned in the introduction, we will consider the combination of a PN (or Walsh) code with L offsets (or rows) and a LoRa modulation with N SFs (typically $L = 512$ and $N = 2$). In general, $U = L \times N$ users are divided into L groups, each group having an unique offset. All N users in each group are modulated by the N-SF LoRa modulators, respectively. Based on the match-filtering method [13], [14] and our proposed scheme, these U users may be successfully detected even in the present of large frequency offsets. Further research will be carried out in our extended work.

V. Conclusion

In the letter we have shown that, for uplink satellite IoT communications with the LoRa modulation the user assigned the largest SF can easily be captured even when simultaneously transmitting several other users assigned small SFs. To detect these users, we designed a selective repetition transmission and superposition reception scheme. By considering the two cases of the full repetition case and partial repetition case, a good tradeoff can be achieved between the detection performance and transmission rate. Simulation results indicate that, the proposed scheme for two-user transmission with near SFs can provide higher transmission rates but unsatisfactory performances, compared to that for two-user transmission with far SFs; and more users' transmission will reduce the overall performance of our scheme. Nevertheless, the proposed scheme because of its simplicity and efficiency may be a potential alternative of the widely-used power allocation and SIC strategy.

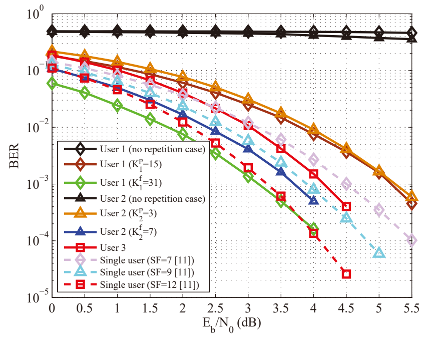

Fig. 5. Detection performance of the three-user simultaneous transmission using $SF_1 = 7$, $SF_2 = 9$, and $SF_3 = 12$

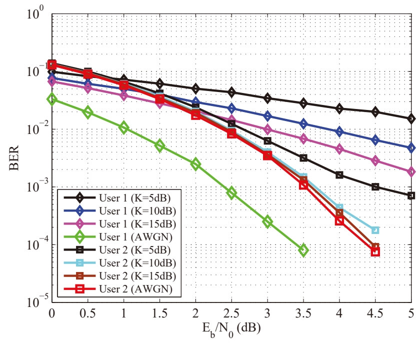

Fig. 6. Detection performance of the two-user simultaneous transmission using $SF_1 = 7$ and $SF_3 = 12$ over the frequency-flat Rician fading channel

References

[1] G. M. Capez, S. Henn, J. A. Fraire and R. Garello, "Sparse satellite constellation design for global and regional direct-to-satellite IoT services," *IEEE Trans. Aero. Elec. Sys.*, vol. 58, no. 5, pp. 3786-3801, Oct. 2022.

[2] C. Guo, X. Chen, J. Yu and Z. Xu, "Design of joint device and data detection for massive grant-free random access in LEO satellite Internet of Things," *IEEE Internet Things J.*, vol. 10, no. 8, pp. 7090-7099, Apr. 2023.

[3] L. Vangelista, "Frequency shift chirp modulation: The LoRa modulation," *IEEE Signal Process. Lett.*, vol. 24, no. 12, pp. 1818-1821, Dec. 2017.

[4] X. Ouyang and J. Zhao, "Orthogonal chirp division multiplexing," *IEEE Trans. Commun.*, vol. 64, no. 9, pp. 3946-3957, Sept. 2016.

[5] M. Chiani and A. Elzanaty, "On the LoRa modulation for IoT: Waveform properties and spectral analysis," *IEEE Internet Things J.*, vol. 6, no. 5, pp. 8463-8470, Oct. 2019.

[6] C. Goursaud and J.-M. Gorce, "Dedicated networks for IoT: PHY/MAC state of the art and challenges," *EAI Endorsed Trans. Internet Things*, vol. 1, Oct. 2015.

[7] D. Croce, M. Gucciardo, S. Mangione, G. Santaromita and I. Tinnirello, "Impact of LoRa imperfect orthogonality: Analysis of link-level performance," *IEEE Commun. Lett.*, vol. 22, no. 4, pp. 796-799, April 2018.

[8] G. Colavolpe, T. Foggi, M. Ricciulli, Y. Zanettini and J. Mediano-Alameda, "Reception of LoRa signals from LEO satellites," *IEEE Trans. Aerosp. Electron. Syst.*, vol. 55, no. 6, pp. 3587-3602, Dec. 2019.

[9] M. A. Ben Temim, G. Ferr, B. Laporte-Fauret, D. Dallet, B. Minger and L. Fuche, "An enhanced receiver to decode superposed LoRa-like signals," *IEEE Internet Things J.*, vol. 7, no. 8, pp. 7419-7431, Aug. 2020.

[10] U. Noreen, L. Clavier and A. Bounceur, "LoRa-like CSS-based PHY layer, capture effect and serial interference cancellation," in *Proc. 24th European Wireless Conf.*, Catania, Italy, 2018, pp. 1-6.

[11] B. Su, Z. Qin and Q. Ni, "Energy efficient uplink transmissions in LoRa networks," *IEEE Trans. Commun.*, vol. 68, no. 8, pp. 4960-4972, Aug. 2020.

[12] T. T. Nguyen, H. H. Nguyen, R. Barton and P. Grossetete, "Efficient design of chirp spread spectrum modulation for low-power wide-area networks," *IEEE Internet Things J.*, vol. 6, no. 6, pp. 9503-9515, Dec. 2019.

[13] T. Sibbett, H. Moradi and B. Boroujeny, "Normalized matched filter for blind interference suppression in filter bank multicarrier spread spectrum systems," *IEEE Access*, vol. 10, pp. 64270-64282, 2022.

[14] J. Shi, X. Liu, X. Fang, X. Sha, W. Xiang and Q. Zhang, "Linear canonical matched filter: Theory, design, and applications," *IEEE Trans. Signal Process.*, vol. 66, no. 24, pp. 6404-6417, Dec. 2018.

Remote sensing landslide hazard risk analysis based on attention fusion

LITong[1]，LIULiping[1]，WANG Yu[1]，JIN Yiming[1*]，LIUYu[1]，QIAO Feng[1]

Abstract: As one of the most serious geologic disasters, landslides cause great losses to human lives and properties, so the reliable and timely identification of landslide hazards is of great social and economic significance. In this paper, by adding the attention fusion remote sensing image landslide identification method, using PS-InSAR and SBAS-InSAR two kinds of time series InSAR technology to extract the surface deformation information in the study area, combined with the results of the time series deformation of the algorithm identified in this paper for the risk assessment of landslide potential points, focusing on the analysis of the northern part of the village of Wenbao in Lund County, the western part of the village of Guanglian landslide potential areas, and the use of time series deformation curve quantitatively describe the landslide potential areas. With the help of time series deformation curves, the deformation of the landslide hazardous areas is quantitatively described, which provides a new idea for the identification and risk analysis of landslide hazards.

Keywords: Remote sensing images, Landslide identification, Image recognition, deep learning

I INTRODUCTION

As a serious threat to the safety and sustainable development of human society, geologic disasters, including landslide disasters, have been attracting much attention because of their sudden occurrence and great threat to people's property.

In recent years, with the rapid development of deep learning technology, the introduction of the attention mechanism has brought new ideas and methods for remote sensing data analysis. Through the application of self-attention mechanism, key surface features can be extracted from massive remote sensing data, and potential areas of landslide hazards can be identified more accurately.

The purpose of this paper is to explore the method based on improved attention fusion, combining multi-source remote sensing data and surface information, to realize the comprehensive risk analysis of landslide potential. With the powerful capability of deep learning, we will aim to accurately identify potential landslide hazard areas, analyze their geomorphic features and environmental context, and integrate the spatial and temporal trends to reveal the potential landslide risks in a more comprehensive way. Through this research, we aim to provide a scientific basis for geohazard prevention and control and risk early warning to meet the challenges posed by landslide hazards.

LitongLiulipinJinyimin-LiuyuQiaofengNingxia750021, China;

This work is supported by 《A study on vertical structure modeling and inversion method for satellite-borne L/P dual-band Po-InSAR vegetation》(No.62061038)

II Landslide Recognition from Remote Sensing Images Based on Attention Fusion

In the self-attention mechanism, the sequence length dominates the self-attention computation, and it is proved theoretically that the feature space matrices Q, K, V formed by the self-attention mechanism are low-rank, so we propose an improved self-attention mechanism that linearly maps the combination of the serialized data K', V' of the original self-attention mechanism to the low-rank matrices K', $V'_{s\times d}$, where $s \ll n$ and the self-attentive output transformation is:

$$f_{att}\left(Q',K'',V''\right)=softmax\left(\frac{Q'K''^{\mathrm{T}}}{\sqrt{d}}\right)V'' \qquad (1)$$

The improved self-attention can shorten the sequence length of the original serialized data K', V', so as to achieve the goal of reducing the model parameters and light weighting the model.

According to the improved self-attention mechanism to design self-attention coding module[1], the structure is shown in Figure 2-1. The module inputs semantic feature map $X \in R_{C\times H\times W}$, generates three spatial matrices Q, K, V, and obtains$Q^{'}$, $K^{'}$, V' after convolution operation, and then obtains low-rank matrices $K'^{'}$, $V'^{'}$, after linear mapping, and utilizes Q' to make a query on K' to obtain the query result $Q'K'^{'T}$, and then combines the query result with the randomized position matrix is summed and softmax processed to obtain matrix $V'^{'}$ correlation weight between sequence data, in which the random position matrix can be trained by the model to obtain the position-related information between sequence data[2], and finally the correlation weight matrix is multiplied with the value matrix $V'^{'}$ to obtain the self-attention of the semantic feature map. The improved self-attention coding module can reduce the feature map scale from both channel and space, which reduces the computational cost and realizes the self-attention mechanism inside the feature map.

The structure of the improved self-attentive decoding module is shown in Fig. 2-2, which utilizes the low-level semantic feature $X \in R_{C\times H\times W}$ to generate the query input Q, and utilizes the high-level semantic feature $Y \in R_{C\times h\times w}$to generate the key and value inputs K and V. After the convolution and linear mapping of the similar coding module to obtainQ',$K'^{'}$,$V'^{'}$, and obtains the correlation weights among sequence data under two semantic scales through the query result $Q'K'^{'T}$ to obtain the correlation matrix between the sequence data under the two semantic scales, add the position information and softmax processing to obtain the correlation weight of feature X reflected on feature Y, and finally multiply the correlation weight with the value $V^{'}$matrix to obtain the self-attention feature map[3]. On the basis of inheriting the advantages of the encoding module, the decoding module is able to capture the correlation of different spatial location features of different feature maps and realize the self-attention mechanism among feature maps.

III.InSAR-based Landslide Hazard Risk Analysis

In this section, permanent scatterer interferome-

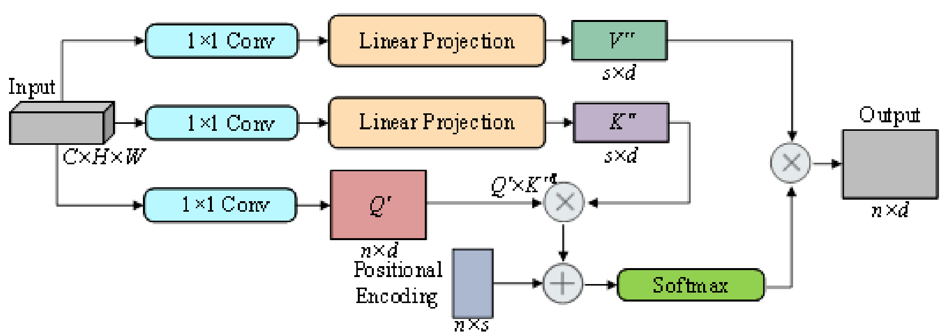

Figure 2-1　Improved Self-Attention Coding Module

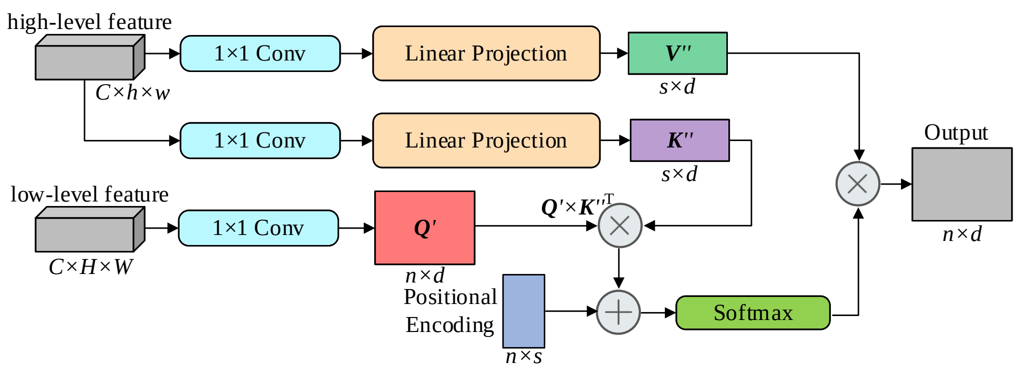

Figure 2-2　Improved Self-Attention Decoding Module

try and short baseline set interferometry are used to extract deformation information in the study area, and the key deformation areas are calibrated and analyzed, and then the time-series InSAR deformation extraction results are combined with this paper's remotely sensed landslide identification algorithm to analyze potential landslide hazards in the study area.

A. Definition of key deformation zones in the study area

Combining the PS-InSAR and SBAS-InSAR time-series deformation results[4,5], a total of 185 key deformation areas are circled, as shown in Figure 1-1, which correlate the geomorphic features of the study area with the key deformation areas, and analyze the deformation of the study area in terms of geotectonic aspects.

Figure 3-1 shows that the key deformation zones are mainly distributed in the middle and low mountainous areas, loess hilly areas and red rocky hilly areas, the number of which accounted for 56.22%, 21.62% and 20.00%, respectively, and the development of the key deformation zones in the river valley plain area is less, which accounted for 2.16%, and the statistics are shown in Table 3-1.

According to Figure 3-1 and Table 3-1, it can be found that the middle and low mountainous areas account for the largest proportion of key deformation areas, which are distributed in the west side of Liupan Mountain, mainly affected by the movement of crustal plates, and the surface deformation is intense. The distribution of key deformation areas in loess hilly areas is the second largest, accounting for 21.62% of the total[6]. Due to the loess has homogeneity and uprightness, under the action of wind and rain, its microfissure extends and expands, greatly reducing the integrity of loess, coupled with the action of gravity, by the tensile stress and shear stress, along the existing fissures, vertical joints, tectonic joints or loess layer and the weak interface between the ancient soil constantly produce slip, pull off and tracking shear, gradually forming a sliding surface, under the action of earthquakes and heavy rainfall Under the action of

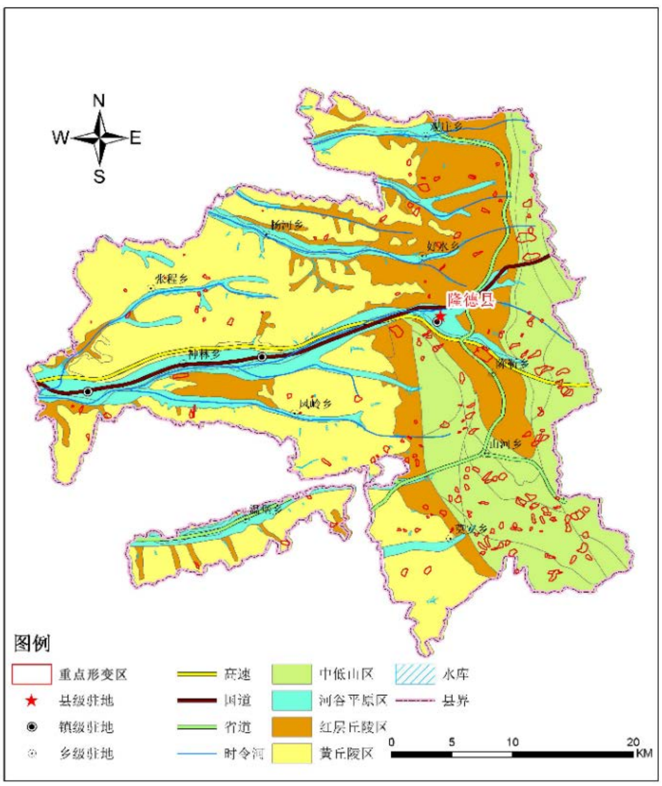

Figure 3-1　Distribution of key deformations

Table **3-1** Statistics of geomorphological features of deformation zones

Serial number	Landform type	Hazard class for key deformation zones	Number of priority deformation zones	Subtotal	Percentage
1	River valley plains region	Low	2	4	2.16%
		High	2		
2	Red layer hilly area	Low	10	37	20.00%
		Middle	18		
		High	9		
3	Hilly area	Low	17	40	21.62%
		Middle	22		
		High	1		
4	Mid-to-low mountain area	Low	47	104	56.22%
		Middle	7		
		High	50		
	Total	-	185	185	100%

earthquakes and strong rainfall, landslides and avalanches eventually occur. The key deformation area in the red rocky hills area accounts for 20.00% of the total. The topography of this area is highly undulating, and the weathering of the mudstone is serious, so landslides, avalanches, and unstable slopes (landslide hazards and avalanche hazards) are found in this area[7]. The distribution of key deformation zones in the river valley plain area is smaller, accounting for only 2.16% of the total number of disasters, which is mainly due to the fact that its terrain is flat and open, and thus the geo-environmental conditions for the occurrence of landslides, avalanches and other disasters are weaker.

C. Landslide risk analysis

The surface deformation inversion results from PS-InSAR and SBAS-InSAR show that the western foothills of Liupan Mountain and the southern part of Lund County in Lund County show a subsidence trend along the radar line-of-sight direction, while the northwestern part of Lund County, which is far away from the Liupan Mountain, mainly shows an uplift trend. Taking the deformation areas in the northern part of Wenbao Village, the western part of Guanglian Village, and the northern part of Xujiazhuang in Lund County as examples, we analyze whether there are landslide hazards in these areas by combining the deformation extracted from the time-series InSAR.

The deformation zone in the northern part of Wenbao Village is located at 35°27'38.66 "N, 105°56'48.86 "E, with an elevation of 2013 meters, and the deformation zone has a northeast-southwest orientation, and the annual average deformation rate of this area is 22 mm/y according to the deformation information of SBAS-InSAR. The deformation area in the northern part of Wenbao village is shown in Fig. 3-2(a), and Fig. (b) corresponds to the potential landslide hazard area detected by the recognition algorithm in this paper, from which it can be seen that the predicted area of landslide hazard is smaller compared to the deformation area, and it is mainly concentrated in the part of the deformation area that is at a higher altitude, which is mainly due to the fact that when slow landsliding occurs, the deformation is the first to occur in the high altitude of the landslide body, and thus the topographic characteristics of the landslide hazard are consistent with the model's estimation of landslide targets[8]. Table 3-2 shows the length-area correspondence between the landslide hazard area and the deformation area, where the landslide hazard area accounts for 24.5% of the deformation area.

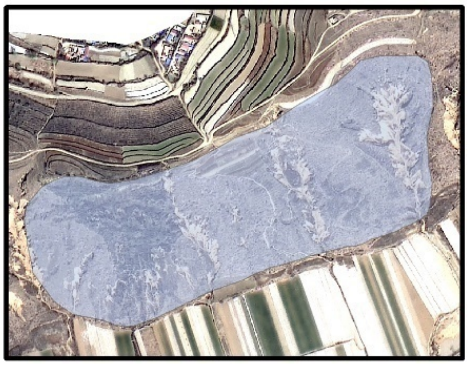

(a) Deformation areas

(b) Landslide hazards

Figure 3-2　Deformation Area North of Winnebago Village

Table **3-2**　Parameters of deformation zone in the northern part of Winborough Village

Area	Maximum north-south length/m	Maximum east-west length/m	Area cov ered/m^2
Landslide hazard	133.3	433.6	39680.9
Region of deformation	269.7	733.5	162109.8

From the SBAS-InSAR time-series deformation results, Figure 3-3 shows the time-series deformation curves of the landslide hazard area. The horizontal axis represents the date time, ranging from January 2019 to May 2021, corresponding to the data acquisition period for deformation extraction. The vertical axis represents the deformation variables in mm/12d, as the revisit period of Sentinel I data is 12 days, and the deformation variables of neighboring revisits are accumulated together. The figure shows an overall sinking trend, but an uplifting phenomenon from December 2019 to May of the following year. This phenomenon is mainly caused by two factors: first, on December 13, 2019 Lund County received snowfall, and the C-band microwaves had difficulty penetrating the snow layer, resulting in temporary topographic uplift; second, the temperature in Lund County continued to be sub-zero in January 2020, and the moisture condensed into frost, which also resulted in temporary topographic uplift. As the temperature rises, vegetation growth affects after March, and the terrain lifts again briefly[10]. After the vegetation growth saturated, around August, the area again appeared to subside. In summary, the landslide hazard area in the northern part of the village of Winborough has always been in a subsidence trend, and the area should be given priority attention.

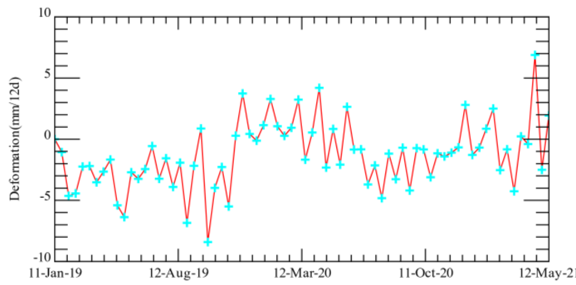

Figure 3-3　Temporal deformation curve of the landslide hazard area in the northern part of Wenbao village

The deformation zone in the western part of Guanglian Village is located at 35°36'22.92 "N, 106°1'6.66 "E, with a sea wave of 2034 meters, and the deformation zone generally shows a northeast-southwest direction, and the annual average deformation rate of the area is 36mm/y as shown by the results of the SBAS-InSAR deformation.

The deformation area in the western part of Guanglian Village is shown in Figure 3-4(a), and Figure (b) corresponds to the potential landslide hazard area of the recognition algorithm. It can be seen that the landslide prediction area is more dispersed compared to the deformation area, and it is mainly distributed in the slope area with obvious optical features, which is caused by two reasons, namely, the optical and elevation aspects. First of all, the western part of Guanglian Village is a complex hilly structure, which is similar to the edge structure of the landslide target in terms of optical features; from the perspective of elevation, the deformation area has experienced a long subsidence process, and the terrain tends to be similar to that of the landslide target in the shape of a tongue or a funnel, so to some extent, part of the subsidence area in the deformation area can be regarded as a slow-change landslide target[11]. In order to qualitatively analyze the landslide hazard identification area, the above hazard area is divided into seven parts, and the location of each part is shown in Figure 3-5.

(a) Deformation areas

(b) Landslide hazards

Figure 3-4 Western Deformation Zone of Kwang Luen Village

Figure 3-5 Distribution of landslide hazards in thewestern part of Guanglian Village

Table 3-2 shows the length and area information of deformation areas and landslide hazards. By analyzing Figure 4-12 and Table 4-3, it can be found that the area of the No. 4 and No. 5 hazards accounts for the largest proportion of the total area of the landslide hazards, reaching 48.3% of the total area of the landslide hazards, and the length of landslide hazards is in the order of one hundred meters, which reflects that this paper's landslide recognition algorithm is able to extract the landslide hazards of the order of square kilometers.

Table 3-2 shows the time-sequence deformation curves of the seven landslide potential points in the region. From the time-varying curves, it can be seen that the trend of the deformation curves of Point 3 and Point 7 near Guanglian Village are basically the same, and they all briefly lifted up during the period of February to April, 2019, which is mainly related to the continuous snowfall situation in that period

It can be seen that the seven potential points have been lifted up to varying degrees in this period of time, and each potential point Point 2 is located in the high-elevation slope area, and the time-varying curve shows that the deformation characteristics of this area are obvious, and it shows an accelerated subsidence trend, which should be listed as a key area of concern. points 1, 4 and 6 showed a sudden elevation during April and May 2020, which is due to the existence of continuous rainfall in Lunde County during the same period, and in May 2020, the number of days of rainfall in Lunde County reached 1,000 days, and the number of days of rainfall in Lunde County reached 1,000 days. The number of rainfall days in Lund County reached 14 days, which greatly accelerated the growth process of the local vegetation, which in turn affected the temporal curves of these hidden points. As a whole, the landslide hazard sites in this deformation zone show a subsidence trend, and measures need to be taken to prevent landslide risks in this area.

Table **3-2**　　Parameters of deformation area in the west of Guanglian village

Area	Maximum north-south length /m	Maximum east-west length /m	Area covered /m^2
Landslide Hazard #1	392.2	410.8	126369.5
Landslide Hazard #2	736.4	535.0	243256.1
Landslide Hazard #3	535.1	692.7	258604.4
Landslide Hazard #4	778.8	612.4	354414.2
Landslide Hazard #5	769.1	764.5	512941.0
Landslide Hazard #6	325.0	291.6	65421.4
Landslide Hazard #7	726.2	668.8	233716.2
Region of deformation	2627.4	2417.6	3779366.1

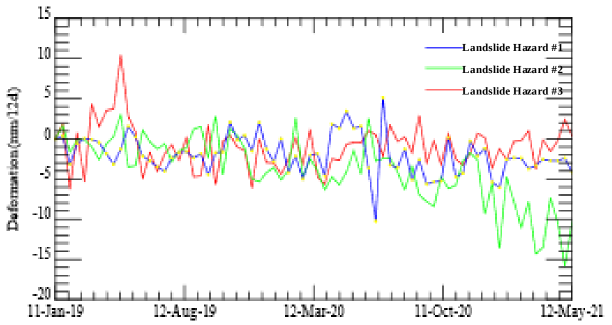

(a)

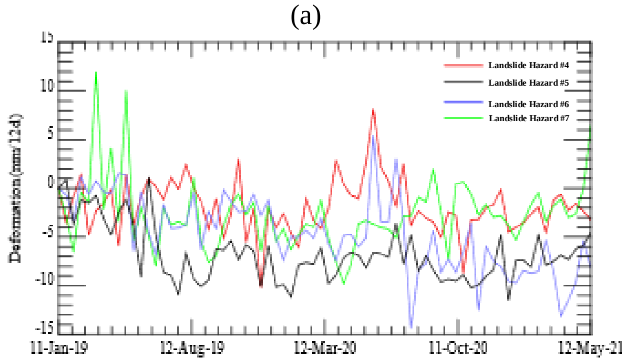

(b)

Figure 3-6　Temporal deformation curves in the western part of Kwang Luen Village

VI　CONCLUSION AND FUTURE WORK

Fusing InSAR and deep learning methods, not only realized the accurate identification of landslide hazardous areas, but also used the deformation information of the study area to analyze the temporal deformation of landslide hazards, and the accuracy of landslide identification reached 96.81%, and the average accuracy of pixel segmentation reached 90.11%, which compared with the DeeplabV3+ and U-net methods in terms of mIoU and mPA has been improvement, proving the effectiveness of the attention fusion method in landslide identification. Firstly, combining the optical remote sensing images and DEM elevation data of the study area, the location information of landslide hazards in the study area is successfully extracted by using the remote sensing landslide recognition algorithm proposed in this paper; subsequently, two time-series InSAR techniques, PS-InSAR and SBAS-InSAR, are used to obtain the surface deformation information in the study area; finally, taking the northern part of Wenbao Village, the western and southern part of Guanglian Village as an example of the deformation area, the effectiveness of the The feasibility of the combination of deep learning landslide identification method and InSAR technique in landslide hazard identification and analysis.

References

[1] GUO Chen, XU Qiang, DONG Xiujun, et al. Landslide identification based on SVF terrain visualization method--A case study of typical landslide in Danba County, Sichuan Province[J]. Journal of Chengdu University of Technology (Natural Science Edition). 2021, 48(06): 705-713.

[2] Jian Xiaoting, Zhao Kang, Zuo Xiaoqing, et al. Landslide Hazard Recognition Based on Faster R-CNN Target Detection - A Case Study of Urban Area in Fugong County[J]. Chemical Minerals and Processing. 2022: 1-9.

[3] WANG Yu, ZHANG Peng, SUN Kaiyue et al. Remote sensing landslide target recognition based on attention fusion[J]. Liquid Crystal and Display,2022,37(11):1498-1506.

[4] HU Fangchi, FAN Yajing. Application research on landslide disaster identification by remote sensing images[J]. Agricultural Disaster Research. 2021, 11(04): 98-99.

[5] LU Huiyan, LI Weile, XU Qiang et al. Early identification of landslide hazards upstream and downstream of Jinshajiang Baige landslide by combining optical remote sensing and InSAR[J]. Journal of Wuhan University(Information ScienceEdition),2019,44(09):1342-1354.

[6] Xuan Wu. Research on object-oriented convolutional neural network

Landsat8 image classification method [D]. Wuhan: Wuhan University, 2019.

[7] WANG W H. Landslide hazard identification based on SBAS-InSAR and machine learning — Taking Lanzhou City as an example［D］.Lanzhou：Lanzhou Jiaotong University，2021.（in Chinese）

[8] ZHANG Y L，FU Y H，SUN Y，et al. Landslide detection from high-resolution remote sensing image using deep neural network［J］.Highway，2021，66（5）：188-194.（in Chinese）

[9] ZHANG P F. Research on automatic extraction of remote sensing images of co-seismic landslides［D］.Beijing：Institute of Geology，China Earthquake Administration，2021.（in Chinese）

[10] LIAO M S，DONG J，LI M H，et al. Radar remote sensing for potential landslides detection and deformation monitoring［J］.National Remote Sensing Bulletin，2021，25（1）：332-341.（in Chinese）

[11] XU B Z，ZHU Q，LI H F，et al.A landslide extraction method of remote sensing image based on multi-scale depth attention model［J］.Journal of Geomatics，2022，47（3）：108-112.（in Chinese）

About the authors

Tong Li was born in Ningxia and studied in the College of Electronic and Electrical Engineering of Ningxia University, with research interests in remote sensing image processing. (Email: 1187532325@qq.com)

Liping Liu was born in Ningxia, China. She received her master's degree from Xi'an Jiaotong University in 2001, and is mainly engaged in the research of graphic image processing and application, big data algorithm and artificial intelligence.(E-mail ：liuliping8186@126.com)

Wang Yu was born in Henan Province, received his master's degree from Ningxia University in 2021, focusing on remote sensing information processing and target recognition.(E-mail：18095117315@ 126.com)

Jin Yimin was born in Inner Mongolia and studied electrical and electronic engineering at Ningxia University, mainly from the research of behavioral recognition. (Email: 791264646@qq.com)

Liu Yu was born in Ningxia and studied electrical and electronic engineering at Ningxia University, mainly from the research of behavioral recognition. (Email: 1047636161@qq.com)

Qiao Feng was born in Shanxi Province and studied electrical and electronic engineering at Ningxia University, focusing on remote sensing image processing. (Email: 2604379477@qq.com)

面向卫星物联网的数据帧结构设计与应用

余忠洋，许蒙蒙，王园园，高继勋

河南工程学院计算机学院，河南郑州 451191

摘　要：针对卫星物联网传输中导频资源受限和物理层帧结构局限性的问题，在标准导频符号辅助调制（PSAM, pilot-symbol-assisted-modulation）帧结构的基础上设计了一种通用的 PSAM 帧结构并对其进行了优化。具体地，以联合数据辅助与非数据辅助的克拉美罗界（CRB, Cramer-Rao bound）为准则，利用经典的控制变量法对通用 PSAM 帧结构中的导频图样和数据图样进行了优化与组合，从而获得了一类实用的优化 PSAM 帧结构。仿真结果表明，与标准 PSAM 帧结构相比，优化 PSAM 帧结构在短包传输和长包传输下获得了 1~2 个数量级的 CRB 性能增益；基于优化 PSAM 帧结构的几种编码调制方案均获得了接近于理想情况的误码性能，且比基于标准 PSAM 帧结构的方案要好 0.6dB~2.3dB。

关键词：导频符号辅助调制；参数估计；克拉美罗界；卫星物联网

Data frame structure design and application for satellite Internet of Things

YU Zhong-yang, XU Meng-meng, WANG Yuan-yuan, GAO Ji-xun

School of Computer Science, Henan University of Engineering, Zhengzhou, Henan 451191, China

Abstract: Considering the limitations of pilot resource and physical layer frame in satellite Internet of Things (IoT) transmission, this paper designs a general pilot-symbol-assisted-modulation (PSAM) frame structure and optimizes it based on the standard PSAM frame. Taking the joint data-aided and non-data-aided Cramer-Rao bound (CRB) as a criterion, pilot and data patterns of the general PSAM frame are optimized and combined via the classical control variable method, thus obtaining a class of optimized PSAM frame with practical values. Simulation results show that compared to the standard PSAM frame, the optimized PSAM frame achieves the CRB performance gain of 1~2 orders of magnitude under both short-packet and long-packet transmissions; several coded modulation schemes based on the optimized PSAM frame obtain the error performance close to the ideal case, which are 0.6dB to 2.3dB better than those based on the standard PSAM frame.

Key words: pilot-symbol-assisted-modulation; parameter estimation; Cramer-Rao bound; satellite IoT

1　引言

对于卫星物联网传输，在资源限制（尤其是功率资源和导频资源）情况下探索更高的功率效率和更好的系统性能是非常有挑战性的[1, 2]。这一点激发了对一些优化问题的深入研究。其中，关于物理层帧结构的设计与优化问题就具有较高的研究意义。

对于物理层帧结构的设计，往往需要考虑实际通信场景的复杂程度(比如是否存在多普勒频移、传输时延和多径衰落等)和采用的同步模式（比如数据辅助、非数据辅助等）。以数据辅助的同步模式为例，其同

基金项目：国家自然科学基金青年项目（62201198），河南省科技攻关项目（232102210156，232102210068），河南省高等学校重点科研项目（23A510016，23A510018）

步性能不仅取决于所使用的导频长度，还取决于导频序列的分布图样（即在数据帧结构中的位置）。文献[3]利用 LoRa（long range）物理层帧结构实现了帧同步、定时同步和多普勒频移的估计。实际上，这种帧结构类似于一种导频前置（preamble）帧结构，即一段导频序列放置到一段数据序列的头部。文献[4]通过仿真发现了在平坦衰落信道下导频等间隔分布的帧结构要优于常用的导频前后置（PP，preamble-postamble）帧结构。这里所谓的 PP 帧结构是由两个长度相同的导频块和一个放置在它们之间的数据序列组成。此外，还有一种导频中置（midamble）帧结构。它是由一段导频序列放置到一段数据序列的中间位置构成的[5]。由于以上三种帧结构具有相对简单的结构，因而已经广泛地应用到地面移动通信中，比如目前比较流行的物联网（IoT，internet of things）通信、第五代移动（5G，fifth-generation）通信以及以前的全球移动通信（GSM，global system for mobile communications）等。然而，它们的固定结构也限制了各自的应用范围。

为了适应更广的通信场景，文献[6]提出了一种基于导频符号辅助调制（PSAM，pilot-symbol-assisted-modulation）的数据帧结构。该帧结构的构造原理是，先将一定长度的导频序列分成两部分，其中包含若干个连续符号的部分作为帧头，包含多个单一符号的部分分别插至数据序列的尾部和其他位置。基于 PSAM 帧结构，文献[7, 8]考虑将一个导频序列等分成若干份后再均匀地插入到一个数据序列的头部、尾部和其他位置中，从而形成了一种应用更广泛的标准 PSAM 帧结构。这种帧结构具有多个相同长度的数据块。文献[9]提出了一种用于第二代数字视频广播（DVB-S2，digital video broadcasting- satellite-second generation）系统的数据帧结构，称之为 DVB-S2 帧结构。它的构造原理是将 90 个导频符号（用于帧同步和设置编码调制方式）作为帧头，再紧跟着以 1440 个数据符号附加 36 个导频符号为周期的若干个单元。包括标准 PSAM 和 DVB-S2 在内的导频等间隔分布的帧结构都可以看作是一种 PSAM 类帧结构。虽然这类帧结构可以适应很多的通信场景，但它们的导频块长度和数据块长度也是固定不变的，这样就会导致对应的系统性能无法再进一步提升。所以这类数据帧结构仍不具备真正意义上的通用性。

另一方面，物理层帧结构的优化主要取决于所采用的优化准则和优化方法。常用的优化准则包括有最小均方误差（MMSE，minimum mean-square error）、克拉美罗界（CRB，Cramer-Rao bound）等。常用的优化方法也有很多，比如拉格朗日乘子（Lagrange multiplier）法、遗传算法（GA，genetic algorithm）等。文献[10]推导出数据辅助下的载波频偏估计和相偏估计的 CRB 性能界，同时分析发现了 PP 帧结构要比 Midamble 帧结构具有更好的频偏估计 CRB 性能。考虑 5G 车联网通信，文献[11]利用 CRB 准则最小化载波相位估计和时延估计的均方误差（MSE，mean-square error），从而对导频图样进行了优化。进一步地，文献[12]通过最小化载波频偏估计、相偏估计和时延估计得到了最优的导频序列，同时还给出了这样的结论：如果要求从一组离散的星座点中提取导频序列，那么交替序列就是最小化 CRB 序列；如果放松星座约束并采用总能量约束，那么就可以得到三个最小化 CRB 序列。针对突发模式通信，文献[13]利用 CRB 准则结合 GA 方法搜索出一种最优的导频序列，同时仿真发现了从参数估计的 MSE 性能角度看，基于最优导频序列的估计器可以获得显著的性能增益。不同于 CRB 准则，文献[14]针对 5G 车联网应用提出了一种基于马尔科夫决策过程（MDP，Markov decision process）的导频图样优化方法，同时仿真结果表明了该

导频优化策略能够改善快时变信道下的信道估计性能。然而，这些文献都只是考虑了导频图样的优化而忽略了数据图样的优化。换句话说，基于最佳导频图样的参数估计器在估计精度上始终是有限的，因而可能无法满足卫星物联网传输中极低信噪比环境下的性能指标。

为此，本文利用联合数据辅助与非数据辅助下参数估计 CRB 准则对通用化的 PSAM 帧结构中导频图样和数据图样进行优化，从而得到了一类实用的优化 PSAM 帧结构，并通过一系列的应用试验验证了所设计 PSAM 帧结构的优越性。

2 PSAM 帧结构的通用化设计

在标准 PSAM 帧结构的基础上，设计了一种通用的 PSAM 帧结构，如图 1 所示，其中灰色方块代表导频块，白色方块代表数据块。

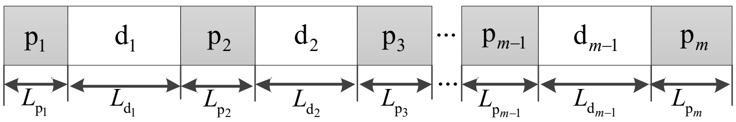

图1 通用PSAM帧结构

下面给出详细的设计步骤：

步骤 1）将长度为 L_{p} 的导频序列分割成 m 个导频块 $\{\mathrm{p}_1,\cdots,\mathrm{p}_m\}$，对应的长度为 $\{L_{\mathrm{p}_1},\cdots,L_{\mathrm{p}_m}\}$；

步骤 2）将长度为 L_{d} 的数据序列分割成 $m-1$ 个数据块 $\{\mathrm{d}_1,\cdots,\mathrm{d}_{m-1}\}$，对应的长度为 $\{L_{\mathrm{d}_1},\cdots,L_{\mathrm{d}_{m-1}}\}$；

步骤 3）将得到的所有导频块 $\{\mathrm{p}_1,\cdots,\mathrm{p}_m\}$ 和所有数据块 $\{\mathrm{d}_1,\cdots,\mathrm{d}_{m-1}\}$ 依次交替放置进行组帧。

这样就得到了图 1 所示的通用 PSAM 帧结构，其中帧长为 $L_{\mathrm{p}}+L_{\mathrm{d}}=\sum_{i=1}^{m-1}(L_{\mathrm{p}_i}+L_{\mathrm{d}_j})+L_{\mathrm{p}_m}$，导频开销为 $\varepsilon \triangleq L_{\mathrm{p}}/(L_{\mathrm{p}}+L_{\mathrm{d}}) \approx L_{\mathrm{p}}/L_{\mathrm{d}}$（因为在卫星物联网传输中总有且应有 $L_{\mathrm{d}} \gg L_{\mathrm{p}}$）。

另外，通过对通用 PSAM 帧结构进行波特采样可以分别得到对应于所有导频块的采样索引集合 $\kappa_{\mathrm{p}} \triangleq \{\kappa_{\mathrm{p}_1},\cdots,\kappa_{\mathrm{p}_m}\}$ 和对应于所有数据块的采样索引集合 $\kappa_{\mathrm{d}} \triangleq \{\kappa_{\mathrm{d}_1},\cdots,\kappa_{\mathrm{d}_{m-1}}\}$。根据图 1，第 i 个导频块所对应的采样索引集合 κ_{p_i} 和第 j 个数据块所对应的采样索引集合 κ_{d_j} 可以分别表示为：

$$\kappa_{\mathrm{p}_i}=\left\{k:0\le k\le L_{\mathrm{p}_1}-1,\ i=1\right\}\cup\left\{k:\sum_{l=1}^{i-1}\left(L_{\mathrm{p}_l}+L_{\mathrm{d}_l}\right)\le k\le\sum_{l=1}^{i-1}\left(L_{\mathrm{p}_l}+L_{\mathrm{d}_l}\right)+L_{\mathrm{p}_i}-1,\ i>1\right\} \quad (1)$$

$$\kappa_{\mathrm{d}_j}=\left\{k:L_{\mathrm{p}_1}\le k\le L_{\mathrm{p}_1}+L_{\mathrm{d}_1}-1,\ j=1\right\}\cup\left\{k:\sum_{l=1}^{j-1}\left(L_{\mathrm{p}_l}+L_{\mathrm{d}_l}\right)+L_{\mathrm{p}_j}\le k\le\sum_{l=1}^{j}\left(L_{\mathrm{p}_l}+L_{\mathrm{d}_l}\right)-1,\ j>1\right\} \quad (2)$$

3 通用 PSAM 帧结构的优化

3.1 联合数据辅助与非数据辅助 CRB 的推导

考虑卫星物联网的上行链路，其传输信道可以近似建模成加性高斯白噪声（AWGN，additive white Gaussian noise）信道[15]。基于此，对应的单载波传输系统下基于波特采样的接收信号可以表示为：

$$r(k)=s(k-\tau)\cdot e^{\mathrm{j}(2\pi f_d T_s k+\theta)}+n(k),\ k\in\kappa_{\mathrm{p}}\cup\kappa_{\mathrm{d}} \tag{3}$$

式中，T_s 为符号周期，f_d 表示载波频偏，θ 表示信道相偏，τ 表示传输时延，$s(k)$ 表示能量归一化的调制信号，$n(k)$ 表示均值为 0、方差为 σ_n^2 的复高斯随机变量。

接下来，分别用 $\boldsymbol{\lambda}=[f_d,\theta,\tau]^{\mathrm{T}}$ 和 $\hat{\boldsymbol{\lambda}}=[\hat{f}_d,\hat{\theta},\hat{\tau}]^{\mathrm{T}}$ 表示待估计参数矩阵和参数估计矩阵。不失一般性，假设所有数据信号的先验信息已知，这一点可以通过采用迭代同步策略实现。图 2 给出了编码 BPSK（binary phase shift keying）系统下的迭代同步实现框图，其中 $\Delta\hat{\boldsymbol{\lambda}}=[\Delta\hat{f}_d,\Delta\hat{\theta},\Delta\hat{\tau}]^{\mathrm{T}}$ 表示剩余参数估计矩阵，$\breve{s}(k)$ 和 $\hat{s}(k)$ 分别为导频调制信号和基于译码信息反馈的数据调制信号。

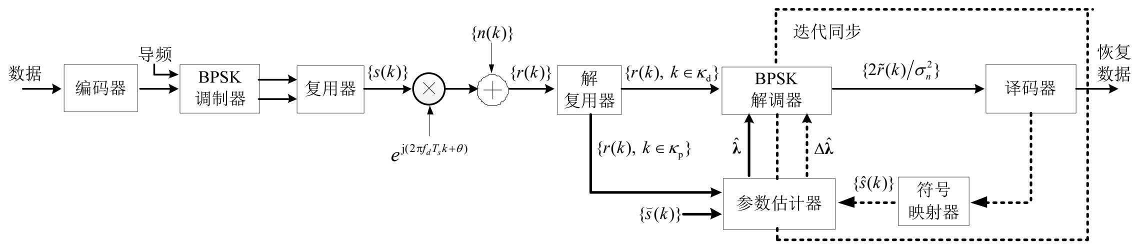

图 2 编码 BPSK 系统的迭代同步实现框图

对于一个无偏估计器，若想达到联合数据辅助与非数据辅助 CRB 性能，需要获得以下先验信息：

$$p(\mathbf{s})=\begin{cases}\prod_{k\in\kappa_{\mathrm{p}}}\delta\left(s(k)-\breve{s}(k)\right)\\ \prod_{k\in\kappa_{\mathrm{d}}}\delta\left(s(k)-\hat{s}(k)\right)\end{cases} \tag{4}$$

式中，$\mathbf{s}$ 为包含了所有导频信号和数据信号的调制序列，$\delta(\cdot)$ 为狄拉克函数。

在 $\boldsymbol{\lambda}=\hat{\boldsymbol{\lambda}}$ 的条件下可以推导出 AWGN 信道下接收信号 $r(k)$ 的对数似然概率，如式（5）所示：

$$\begin{aligned}\ln p\left(r(k)\,|\,\boldsymbol{\lambda}=\hat{\boldsymbol{\lambda}}\right)&=\ln\left\{\frac{1}{2\pi\sigma_n^2}e^{-\frac{\left|r(k)-s(k-\hat{\tau})e^{\mathrm{j}2\pi\hat{f}_d T_s k}e^{\mathrm{j}\hat{\theta}}\right|^2}{2\sigma_n^2}}\right\}\\&=\ln\left\{\frac{1}{2\pi\sigma_n^2}e^{-\frac{\left|r(k)\right|^2-2\mathrm{Re}\left\{r(k)s(k-\hat{\tau})^{*}e^{-\mathrm{j}2\pi\hat{f}_d T_s k}e^{-\mathrm{j}\hat{\theta}}\right\}+\left|s(k-\hat{\tau})e^{\mathrm{j}2\pi\hat{f}_d T_s k}e^{\mathrm{j}\hat{\theta}}\right|^2}{2\sigma_n^2}}\right\}\\&=\ln\left\{\frac{1}{2\pi\sigma_n^2}\right\}-\frac{\left|r(k)\right|^2+\left|s(k-\hat{\tau})\right|^2}{2\sigma_n^2}+\frac{\mathrm{Re}\left\{r(k)s(k-\hat{\tau})^{*}e^{-\mathrm{j}2\pi\hat{f}_d T_s k}e^{-\mathrm{j}\hat{\theta}}\right\}}{\sigma_n^2}\\&\simeq\frac{\mathrm{Re}\left\{r(k)s(k-\hat{\tau})^{*}e^{-\mathrm{j}2\pi\hat{f}_d T_s k}e^{-\mathrm{j}\hat{\theta}}\right\}}{\sigma_n^2}\end{aligned} \tag{5}$$

式中，$s(k)\in\mathbf{s}$ 来自于式（4），$(\cdot)^{*}$ 表示取共轭操作，$\mathrm{Re}\{\cdot\}$ 表示取实部操作。当忽略了与 $\hat{f}_d$、$\hat{\theta}$ 和 $\hat{\tau}$ 无关的项，式（5）中的约等式成立。进一步地，考虑所有的接收信号 $\mathbf{r}=\{r(k),\ k\in\kappa_{\mathrm{p}}\cup\kappa_{\mathrm{d}}\}$，则对应的联合对数似然概率可以表示为：

$$
\begin{aligned}
\ln p\left(\mathbf{r} \mid \hat{\boldsymbol{\lambda}}\right) &= \sum_{k \in \kappa_{\mathrm{p}} \cup \kappa_{\mathrm{d}}} \ln p\left(r(k) \mid \hat{\boldsymbol{\lambda}}\right) \\
&= \sum_{i=1}^{m} \sum_{k \in \kappa_{\mathrm{p}_i}} \ln p\left(r(k) \mid \hat{\boldsymbol{\lambda}}\right) + \sum_{j=1}^{m-1} \sum_{k \in \kappa_{\mathrm{d}_j}} \ln p\left(r(k) \mid \hat{\boldsymbol{\lambda}}\right) \\
&\approx \frac{1}{\sigma_n^2} \sum_{i=1}^{m} \sum_{k \in \kappa_{\mathrm{p}_i}} \mathrm{Re}\left\{ r(k) s(k-\hat{\tau})^* e^{-\mathrm{j}2\pi \hat{f}_d T_s k} e^{-\mathrm{j}\hat{\theta}} \right\} + \frac{1}{\sigma_n^2} \sum_{j=1}^{m-1} \sum_{k \in \kappa_{\mathrm{d}_j}} \mathrm{Re}\left\{ r(k) s(k-\hat{\tau})^* e^{-\mathrm{j}2\pi \hat{f}_d T_s k} e^{-\mathrm{j}\hat{\theta}} \right\}
\end{aligned} \tag{6}
$$

根据文献[17]中的费歇尔信息矩阵，利用式（6）的结果可以计算出对应于载波频偏估计、相偏估计和时延估计的联合数据辅助与非数据辅助 CRB。即，分别对费歇尔信息矩阵中的主对角元素取逆后便可以得到对应的联合数据辅助与非数据辅助 CRB，如式（7）、式（8）和式（9）所示：

$$
\begin{aligned}
\mathrm{CRB}\left(f_d\right)^{-1} &= \left(-\mathbb{E}\left[\frac{\partial^2 \ln p\left(\mathbf{r} \mid \hat{\boldsymbol{\lambda}}\right)}{\partial \hat{f}_d^2} \right] \right)^{-1} \\
&\approx \frac{4\pi^2 T_s^2}{\sigma_n^2} \cdot \left(\sum_{i=1}^{m} \sum_{k \in \kappa_{\mathrm{p}_i}} k^2 + \sum_{j=1}^{m-1} \sum_{k \in \kappa_{\mathrm{d}_j}} k^2 \right)
\end{aligned} \tag{7}
$$

$$
\begin{aligned}
\mathrm{CRB}(\theta)^{-1} &= \left(-\mathbb{E}\left[\frac{\partial^2 \ln p\left(\mathbf{r} \mid \hat{\boldsymbol{\lambda}}\right)}{\partial \hat{\theta}^2} \right] \right)^{-1} \\
&\approx \frac{1}{\sigma_n^2} \cdot \left(\sum_{i=1}^{m} \sum_{k \in \kappa_{\mathrm{p}_i}} 1 + \sum_{j=1}^{m-1} \sum_{k \in \kappa_{\mathrm{d}_j}} 1 \right) \\
&= \frac{1}{\sigma_n^2} \cdot \left(L_{\mathrm{p}_1} + \cdots + L_{\mathrm{p}_m} + L_{\mathrm{d}_1} + \cdots + L_{\mathrm{d}_{m-1}} \right) \\
&= \frac{1}{\sigma_n^2} \cdot \left(L_{\mathrm{p}} + L_{\mathrm{d}} \right)
\end{aligned} \tag{8}
$$

$$
\begin{aligned}
\mathrm{CRB}(\tau)^{-1} &= \left(-\mathbb{E}\left[\frac{\partial^2 \ln p\left(\mathbf{r} \mid \hat{\boldsymbol{\lambda}}\right)}{\partial \hat{\tau}^2} \right] \right)^{-1} \\
&\approx \frac{T_s^2}{\sigma_n^2} \cdot \left(\sum_{i=1}^{m} \sum_{k \in \kappa_{\mathrm{p}_i}} 1 + \sum_{j=1}^{m-1} \sum_{k \in \kappa_{\mathrm{d}_j}} 1 \right) \\
&= \frac{T_s^2}{\sigma_n^2} \cdot \left(L_{\mathrm{p}} + L_{\mathrm{d}} \right)
\end{aligned} \tag{9}
$$

由式（7）~式（9）的结果可以观察到，对于相偏估计和时延估计的联合数据辅助与非数据辅助 CRB，其大小只取决于通用 PSAM 帧结构中的导频序列长度 L_{p} 和数据序列长度 L_{d}；而对于频偏估计的联合数据辅助与非数据辅助 CRB，它的大小则由通用 PSAM 帧结构中的 m 个导频块长度 $\{L_{\mathrm{p}_1},\cdots,L_{\mathrm{p}_m}\}$ 和 $m-1$ 个数据块长度 $\{L_{\mathrm{d}_1},\cdots,L_{\mathrm{d}_{m-1}}\}$ 共同决定。

那么，再根据式（1）和式（2）可进一步推导出式（7）的近似结果：

$$
\mathrm{CRB}\left(f_d\right)^{-1} \approx C \cdot \left[\sum_{i=2}^{m} L_{\mathrm{p}_i} \left(\sum_{j=1}^{i-1} L_{\mathrm{d}_j} \right)^2 + \sum_{i=1}^{m-1} L_{\mathrm{d}_i} \left(\sum_{j=1}^{i} L_{\mathrm{d}_j} \right)^2 \right] \tag{10}
$$

式中，系数 $C \triangleq 4\pi^2 T_s^2 / \sigma_n^2$ 来自于式（7）。

由式（10）可知，通用 PSAM 帧结构的优化问题可以转化为最小化近似的联合数据辅助与非数据辅助的频偏估计 CRB，亦或转化为最大化式（10）。

下面给出式（10）的具体推导过程。由式（7）可以发现，对其中的 $\sum_{i=1}^{m}\sum_{k\in\kappa_{\mathrm{p}_i}}k^2$ 和 $\sum_{j=1}^{m-1}\sum_{k\in\kappa_{\mathrm{d}_j}}k^2$ 这两个求和项进行展开与近似便可以获得式（10）的结果。这里需要引入两个常用的代数求和公式：$\sum_{i=0}^{n-1}i=n(n-1)/2$ 和 $\sum_{i=0}^{n-1}i^2=n(n-1)(2n-1)/6$。另外，对于卫星物联网传输，应有且总有 $L_{\mathrm{p}}\ll L_{\mathrm{d}}$（即导频开销 $\varepsilon\ll 1$）。基于上述条件，这两个求和项可以分别进行展开与近似，如式（11）和式（12）所示：

$$\begin{aligned}\sum_{i=1}^{m}\sum_{k\in\kappa_{\mathrm{p}_i}}k^2&=\sum_{k=0}^{L_{\mathrm{p}_1}-1}k^2+\sum_{k=L_{\mathrm{p}_1}+L_{\mathrm{d}_1}}^{L_{\mathrm{p}_1}+L_{\mathrm{d}_1}+L_{\mathrm{p}_2}-1}k^2+\cdots+\sum_{k=\sum_{i=1}^{m-1}\left(L_{\mathrm{p}_i}+L_{\mathrm{d}_i}\right)}^{\sum_{i=1}^{m-1}\left(L_{\mathrm{p}_i}+L_{\mathrm{d}_i}\right)+L_{\mathrm{p}_m}-1}k^2\\&=\frac{1}{6}\sum_{i=1}^{m}L_{\mathrm{p}_i}\left(L_{\mathrm{p}_i}-1\right)\left(2L_{\mathrm{p}_i}-1\right)+\sum_{i=1}^{m}L_{\mathrm{p}_i}\left[\sum_{j=1}^{i-1}\left(L_{\mathrm{p}_j}+L_{\mathrm{d}_j}\right)\right]\left[\sum_{j=1}^{i-1}\left(L_{\mathrm{p}_j}+L_{\mathrm{d}_j}\right)-1\right]\\&\approx\sum_{i=1}^{m}L_{\mathrm{p}_i}\left[\sum_{j=1}^{i-1}\left(L_{\mathrm{p}_j}+L_{\mathrm{d}_j}\right)\right]^2\approx\sum_{i=1}^{m}L_{\mathrm{p}_i}\left[\sum_{j=1}^{i-1}L_{\mathrm{d}_j}\right]^2\end{aligned}\tag{11}$$

$$\begin{aligned}\sum_{j=1}^{m-1}\sum_{k\in\kappa_{\mathrm{d}_j}}k^2&=\sum_{k=L_{\mathrm{p}_1}}^{L_{\mathrm{p}_1}+L_{\mathrm{d}_1}-1}k^2+\sum_{k=L_{\mathrm{p}_1}+L_{\mathrm{d}_1}+L_{\mathrm{p}_2}}^{L_{\mathrm{p}_1}+L_{\mathrm{d}_1}+L_{\mathrm{p}_2}+L_{\mathrm{d}_2}-1}k^2+\cdots+\sum_{k=\sum_{i=1}^{m-2}\left(L_{\mathrm{p}_i}+L_{\mathrm{d}_i}\right)}^{\sum_{i=1}^{m-2}\left(L_{\mathrm{p}_i}+L_{\mathrm{d}_i}\right)+L_{\mathrm{d}_{m-1}}-1}k^2\\&=\frac{1}{6}\sum_{i=1}^{m}L_{\mathrm{d}_i}\left(L_{\mathrm{d}_i}-1\right)\left(2L_{\mathrm{d}_i}-1\right)+\sum_{i=1}^{m}L_{\mathrm{d}_i}\left[\sum_{j=1}^{i}\left(L_{\mathrm{p}_j}+L_{\mathrm{d}_j}\right)\right]\left[\sum_{j=1}^{i}\left(L_{\mathrm{p}_j}+L_{\mathrm{d}_j}\right)-1\right]\\&\approx\sum_{i=1}^{m}L_{\mathrm{d}_i}\left[\sum_{j=1}^{i}\left(L_{\mathrm{p}_j}+L_{\mathrm{d}_j}\right)\right]^2\approx\sum_{i=1}^{m}L_{\mathrm{d}_i}\left[\sum_{j=1}^{i}L_{\mathrm{d}_j}\right]^2\end{aligned}\tag{12}$$

再将这两个式子的结果代入到式（7）中即可推导出式（10）。

3.2 基于联合数据辅助与非数据辅助 CRB 的通用 PSAM 帧结构的优化

根据上一小节的讨论，首先可以将通用 PSAM 帧结构的优化问题建模成如下形式：

$$\left(\left\{\hat{L}_{\mathrm{p}_i}\right\},\left\{\hat{L}_{\mathrm{d}_j}\right\}\right)=\underset{\left(\left\{L_{\mathrm{p}_i}\right\},\left\{L_{\mathrm{d}_j}\right\}\right)}{\operatorname{argmax}}\left\{\mathrm{CRB}\left(f_d\right)^{-1}\right\}\tag{13}$$

并且其约束条件为：

$$\begin{cases}\sum_{i=1}^{m}L_{\mathrm{p}_i}=L_{\mathrm{p}}\\\sum_{j=1}^{m-1}L_{\mathrm{d}_j}=L_{\mathrm{d}}\end{cases}$$

对于有约束的优化问题，现有的优化策略包括有拉格朗日乘子法、遗传算法（GA，genetic algorithm）等。这里以拉格朗日乘子法为例来简述其优化过程。该优化方法需要同时联立关于通用 PSAM 帧结构中的 m 个导频块长度 $\{L_{\mathrm{p}_1},\cdots,L_{\mathrm{p}_m}\}$ 和 $m-1$ 个数据块长度 $\{L_{\mathrm{d}_1},\cdots,L_{\mathrm{d}_{m-1}}\}$ 的 $2m-1$ 个方程组，再对这些方程组求解关于每个导频块长度 L_{p_i} 和每个数据块长度 L_{d_j} 的偏导数，之后再推导出每个 L_{p_i} 和每个 L_{d_j} 与 L_{p} 和 L_{d} 之间的关系。这样虽然可以获得通用 PSAM 帧结构的最优解，但其求解过程过于复杂。鉴于此，将式（10）代入到式（13）中得到式（14）。

$$\begin{aligned}\left(\left\{\hat{L}_{\mathrm{p}_i}\right\},\left\{\hat{L}_{\mathrm{d}_j}\right\}\right) &\approx \underset{\left(\left\{L_{\mathrm{p}_i}\right\},\left\{L_{\mathrm{d}_j}\right\}\right)}{\operatorname{argmax}}\left\{C\sum_{i=2}^{m} L_{\mathrm{p}_i}\left(\sum_{j=1}^{i-1} L_{\mathrm{d}_j}\right)^2 + C\sum_{i=1}^{m-1} L_{\mathrm{d}_j}\left(\sum_{j=1}^{i} L_{\mathrm{d}_j}\right)^2\right\} \\ &= C\cdot \underset{\left(\left\{L_{\mathrm{p}_i}\right\},\left\{L_{\mathrm{d}_j}\right\}\right)}{\operatorname{argmax}}\left\{L_{\mathrm{p}_2}L_{\mathrm{d}_1}^2+\cdots+L_{\mathrm{p}_m}\left(L_{\mathrm{d}_1}+\cdots+L_{\mathrm{d}_{m-1}}\right)^2+L_{\mathrm{d}_1}L_{\mathrm{d}_1}^2+\cdots+L_{\mathrm{d}_{m-1}}\left(L_{\mathrm{d}_1}+\cdots+L_{\mathrm{d}_{m-1}}\right)^2\right\}\end{aligned} \quad (14)$$

由式（14）的特点（即导频长度之间的线性关系以及与数据长度之间解耦合）可以知道，经典的控制变量法要比现有的优化策略会更加合适些。

根据控制变量法，首先考虑所有的导频块长度$\{L_{\mathrm{p}_1},\cdots,L_{\mathrm{p}_m}\}$，则式（14）可以变成式（15）。

$$\begin{aligned}\left(\left\{\hat{L}_{\mathrm{p}_i}\right\},-\right) &\approx C\cdot \underset{\left(\left\{L_{\mathrm{p}_i}\right\},-\right)}{\operatorname{argmax}}\left\{0\cdot L_{\mathrm{p}_1}+\left(L_{\mathrm{d}}-\sum_{j=2}^{m-1}L_{\mathrm{d}_j}\right)^2 L_{\mathrm{p}_2}+\cdots+L_{\mathrm{d}}^2L_{\mathrm{p}_m}+\left(L_{\mathrm{d}}-\sum_{j=2}^{m-1}L_{\mathrm{d}_j}\right)^2 L_{\mathrm{d}_1}+\cdots+L_{\mathrm{d}}^2L_{\mathrm{d}_{m-1}}\right\} \\ &\triangleq C\cdot \underset{\left(\left\{L_{\mathrm{p}_i}\right\},-\right)}{\operatorname{argmax}}\left\{\omega_1^{\mathrm{d}}L_{\mathrm{p}_1}+\omega_2^{\mathrm{d}}L_{\mathrm{p}_2}+\cdots+\omega_m^{\mathrm{d}}L_{\mathrm{p}_m}+R\left(L_{\mathrm{d}_1},L_{\mathrm{d}_2},\ldots,L_{\mathrm{d}_{m-1}}\right)\right\}\end{aligned} \quad (15)$$

式中，$\omega_i^{\mathrm{d}} \triangleq (L_{\mathrm{d}}-\sum_{j=i}^{m-1}L_{\mathrm{d}_j})^2$为附加在第$i$导频块长度$L_{\mathrm{p}_i}$上的加权系数（$i=1,\ldots,m$）且满足$\omega_m^{\mathrm{d}}>\omega_{m-1}^{\mathrm{d}}>\cdots>\omega_2^{\mathrm{d}}>\omega_1^{\mathrm{d}}\equiv 0$，$R(L_{\mathrm{d}_1},L_{\mathrm{d}_2},\ldots,L_{\mathrm{d}_{m-1}})\triangleq\omega_2^{\mathrm{d}}L_{\mathrm{d}_1}+\cdots+\omega_m^{\mathrm{d}}L_{\mathrm{d}_{m-1}}$是一个与导频块长度无关的求和项，因此它不会影响到导频图样的优化。

对于具有单调加权系数且取值有限的若干个正变量的线性组合的求和项（比如式（15）），根据加权法的思想可以引入如下的渐近最大化准则：

对于上述的求和项，若给其具有最大加权系数的元素分配最大的试验值，再给其具有递减加权系数的其他元素按照非增顺序分配其他的试验值，那么该求和项就可以渐近地获得最大值。

下面将该准则使用到式（15）中便可以得到一个渐近最优（即次优）的导频图样：$\hat{L}_{\mathrm{p}_2}<\hat{L}_{\mathrm{p}_3}<\cdots<\hat{L}_{\mathrm{p}_{m-1}}<\hat{L}_{\mathrm{p}_m}\to L_{\mathrm{p}}-\hat{L}_{\mathrm{p}_1}$（$\to$表示趋向于）。由于$\omega_1^{\mathrm{d}}\equiv 0$，故$\hat{L}_{\mathrm{p}_1}$的取值不确定，但应当将其设置为尽可能大的值以保证较好的载波参数（粗）估计。此外，在式（15）中由于$L_{\mathrm{p}_i}\ll\omega_i^{\mathrm{d}}$（任意$i\neq 1$），一种等分且均匀分布的导频图样可供选择，即$\hat{L}_{\mathrm{p}_1}=\hat{L}_{\mathrm{p}_2}=\cdots=\hat{L}_{\mathrm{p}_m}=L_{\mathrm{p}}/m$[7, 8]。

再控制变量法，在次优导频图样的基础上，考虑所有的数据块长度$\{L_{\mathrm{d}_1},\cdots,L_{\mathrm{d}_{m-1}}\}$，则式（14）可以变成式（16）：

$$\begin{aligned}\left(\left\{\hat{L}_{\mathrm{p}_i}\right\},\left\{\hat{L}_{\mathrm{d}_j}\right\}\right) &\approx C\cdot \underset{\left(\left\{\hat{L}_{\mathrm{p}_i}\right\},\left\{L_{\mathrm{d}_j}\right\}\right)}{\operatorname{argmax}}\left\{\hat{L}_{\mathrm{p}_2}L_{\mathrm{d}_1}^2+\cdots+\hat{L}_{\mathrm{p}_m}\left(L_{\mathrm{d}_1}^2+\cdots+L_{\mathrm{d}_{m-1}}^2\right)^2+L_{\mathrm{d}_1}L_{\mathrm{d}_1}^2+\cdots+L_{\mathrm{d}_{m-1}}\left(L_{\mathrm{d}_1}+\cdots+L_{\mathrm{d}_{m-1}}\right)^2\right\} \\ &\triangleq C\cdot \underset{\left(\left\{\hat{L}_{\mathrm{p}_i}\right\},\left\{L_{\mathrm{d}_j}\right\}\right)}{\operatorname{argmax}}\left\{\left(\omega_1^{\mathrm{p\&d}}+\omega_1^{\mathrm{d\&d}}\right)L_{\mathrm{d}_1}+\left(\omega_2^{\mathrm{p\&d}}+\omega_2^{\mathrm{d\&d}}\right)L_{\mathrm{d}_2}+\cdots+\left(\omega_{m-1}^{\mathrm{p\&d}}+\omega_{m-1}^{\mathrm{d\&d}}\right)L_{\mathrm{d}_{m-1}}\right\}\end{aligned} \quad (16)$$

式中，$\omega_j^{\mathrm{p\&d}}\triangleq(L_{\mathrm{p}}-\sum_{i=1}^{j}\hat{L}_{\mathrm{p}_i})\cdot(2\sum_{i=1}^{j-1}L_{\mathrm{d}_i}+L_{\mathrm{d}_j})\approx\hat{L}_{\mathrm{p}_m}\cdot(2\sum_{i=1}^{j-1}L_{\mathrm{d}_i}+L_{\mathrm{d}_j})$和$\omega_j^{\mathrm{d\&d}}\triangleq(L_{\mathrm{d}}-\sum_{i=1}^{j-1}L_{\mathrm{d}_i})\cdot(L_{\mathrm{d}_j}+2\sum_{i=1}^{j-1}L_{\mathrm{d}_i})$为附加到第$j$数据块$L_{\mathrm{d}_j}$上的加权系数（$j=1,\ldots,m-1$）。另外，对于任意$L_{\mathrm{d}_j}$总有$\omega_{m-1}^{\mathrm{p\&d}}+\omega_{m-1}^{\mathrm{d\&d}}>\cdots>\omega_2^{\mathrm{p\&d}}+\omega_2^{\mathrm{d\&d}}>\omega_1^{\mathrm{p\&d}}+\omega_1^{\mathrm{d\&d}}$。因此，上述的渐近最大化准则也可以使用到式（16）中，从而

得到一个次优的数据图样：$\hat{L}_{\mathrm{d}_1} \le \hat{L}_{\mathrm{d}_2} \le \cdots < \hat{L}_{\mathrm{d}_{m-2}} < \hat{L}_{\mathrm{d}_{m-1}} \to L_{\mathrm{d}}$。显然，这种数据图样完全不同于一种等分且均匀分布的数据图样：$\hat{L}_{\mathrm{d}_1} = \hat{L}_{\mathrm{d}_2} = \cdots = \hat{L}_{\mathrm{d}_{m-2}} = \hat{L}_{\mathrm{d}_{m-1}} = L_{\mathrm{d}}/(m-1)$[7, 8]。最后，再将优化的导频图样和数据图样组合起来便可以得到一类实用的优化 PSAM 帧结构。

优化 PSAM 帧结构：具有非等分且非均匀分布的导频图样和数据图样，即 $\hat{L}_{\mathrm{p}_1} \ge \hat{L}_{\mathrm{p}_i}$（$i > 2$）且 $\hat{L}_{\mathrm{p}_2} < \hat{L}_{\mathrm{p}_3} < \cdots < \hat{L}_{\mathrm{p}_m}$，$\hat{L}_{\mathrm{d}_1} \le \hat{L}_{\mathrm{d}_2} \le \cdots < \hat{L}_{\mathrm{d}_{m-2}} < \hat{L}_{\mathrm{d}_{m-1}}$。

需要指出的是，上述的优化 PSAM 帧结构只是给出了在设定的导频长度和数据长度下每个导频块长度之间和每个数据块长度之间的关系。若想确定它们的具体取值，还需要根据所使用的载波频偏估计算法的特性（比如估计范围和估计精度等）。

为了后续的仿真比较，这里也给出标准 PSAM 帧结构的导频图样和数据图样，即

标准 PSAM 帧结构：具有等分且均匀分布的导频图样和数据图样，即 $\hat{L}_{\mathrm{p}_1} = \hat{L}_{\mathrm{p}_2} = \cdots = \hat{L}_{\mathrm{p}_m} = L_{\mathrm{p}}/m$，$\hat{L}_{\mathrm{d}_1} = \hat{L}_{\mathrm{d}_2} = \cdots = \hat{L}_{\mathrm{d}_{m-1}} = L_{\mathrm{d}}/(m-1)$。

4 应用试验与分析

本节将要评估短包传输和长包传输下基于优化PSAM帧结构和标准PSAM帧结构的CRB性能，并将这两种帧结构应用到LDPC（low-density parity-check）码编码的传输系统中，包括多元LDPC码编码的短包传输系统和二元LDPC码编码的长包传输系统，并比较了它们的误比特率（BER，bit error rate）性能。

4.1 基于两种帧结构的载波频偏估计 CRB 性能比较

不失一般性，考虑一个AWGN信道下的未编码BPSK系统。下面将评估短包传输和长包传输下不同导频块数所对应的优化PSAM与标准PSAM两种帧结构的载波频偏估计CRB性能（对数形式即 $\log_{10}\mathrm{CRB}$），包括数据辅助CRB性能对应于式（7）的第一个求和项或式（10）等式右边的第一项和联合数据辅助与非数据辅助CRB性能对应于式（7）或式（10），如图3（a）和（b）所示。在仿真中，对于短包传输，$L_{\mathrm{p}} = 45$ 和 $L_{\mathrm{d}} = 225$（可知导频开销 $\varepsilon \approx 0.2$）；对于长包传输，$L_{\mathrm{p}} = 300$ 和 $L_{\mathrm{d}} = 6144$（可知导频开销 $\varepsilon \approx 0.05$）。

从图3（a）和（b）的试验结果可以观察到，对于任意给定的导频块数，所提出的优化PSAM帧结构的CRB性能都要优于标准PSAM帧结构，且不管是在短包传输和长包传输下使用数据辅助模式还是联合数据辅助与非数据辅助模式。具体地，在短包传输下，联合数据辅助与非数据辅助CRB性能要比数据辅助CRB性能提升一个数量级，而在长包传输下这个性能提升可以达到两个数量级，这都表明了研究联合数据辅助与非数据辅助模式的载波频偏估计的重要性。此外，与优化PSAM帧结构相比，标准PSAM帧结构的联合数据辅助与非数据辅助CRB性能对较大的导频块数更为敏感。

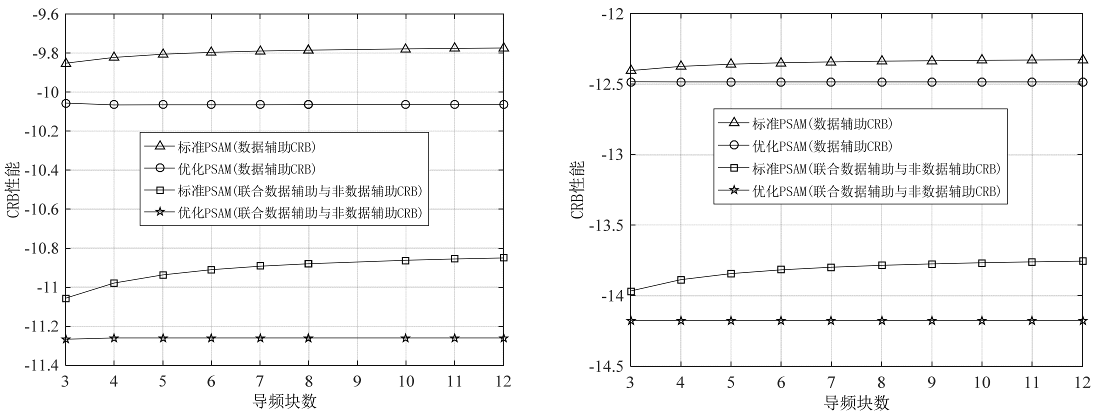

（a）短包传输　　　　　　　　　　（b）长包传输

图3 优化PSAM帧结构和标准PSAM帧结构的CRB性能

4.2 基于两种帧结构的编码系统性能比较

1）短包传输系统

假设一个在AWGN信道下多元LDPC码编码的QAM（quadrature amplitude modulation）系统，其中采用的编码为16元域（225, 173）LDPC码，QAM的调制进制数为16。再假设优化PSAM帧结构和标准PSAM帧结构都有三个导频块和两个数据块，总长度分别为$L_{\mathrm{p}}=45$和$L_{\mathrm{d}}=225$（可知导频开销$\varepsilon\approx0.2$）。图4给出了多元LDPC码级联QAM系统的BER性能，其中理想性能对应于没有载波频偏的情况。

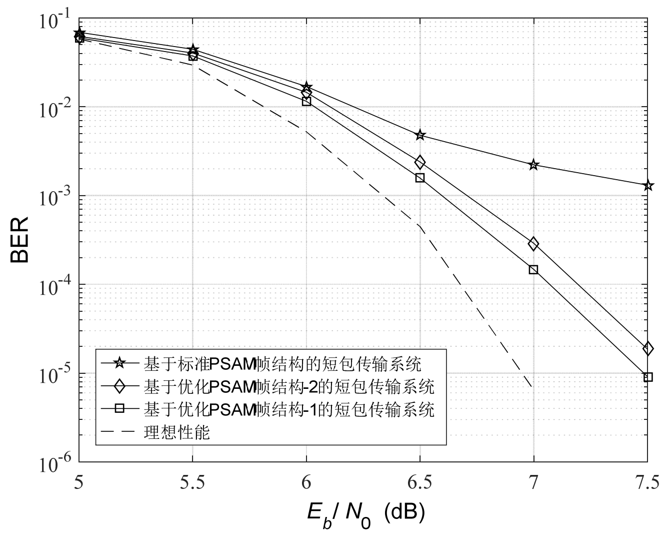

图4 多元LDPC码级联QAM系统的BER性能

从图4的试验结果可以发现，基于优化PSAM帧结构-1&2的短包传输系统可以提供明显优于基于标准PSAM帧结构的BER性能。具体地，相对于理想性能，在BER=10^{-3}下，这两种优化PSAM帧结构的性能损失约0.3~0.5dB，而标准PSAM帧结构的性能损失达到了1.2dB。

再假设一个在AWGN信道下二元LDPC编码的SCMA（sparse code multiple access）系统，其中采用的编码为IEEE 802.16e标准推荐的（576, 288）LDPC码，SCMA码本采用文献[18]所提的4点码本。这里仍假

设优化PSAM帧结构和标准PSAM帧结构都有三个导频块和两个数据块，总长度分别为 $L_p = 24$ 和 $L_d = 144$（可知导频开销 $\varepsilon \approx 0.16$）。图5给出了二元LDPC码级联SCMA系统的BER性能，其中理想性能也是没有载波频偏的情况。

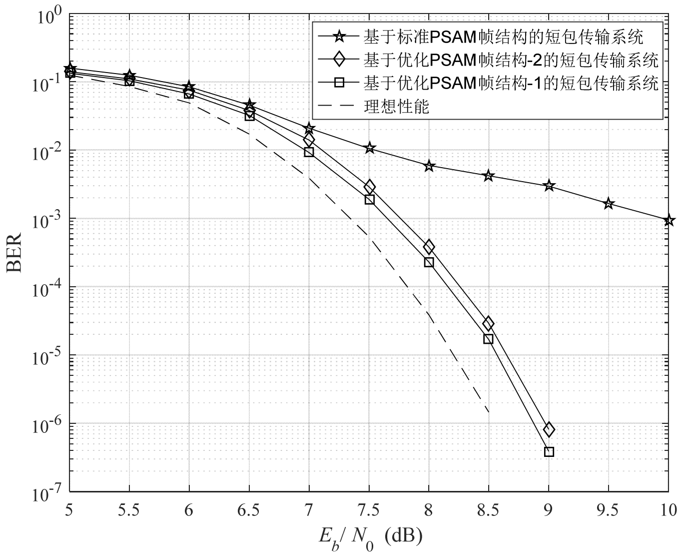

图5 二元LDPC码级联SCMA系统的BER性能

从上图的试验结果可以发现，有类似于图4中的仿真结果。考虑BER=10^{-3}，基于优化PSAM帧结构1&2的短包传输系统能够获得与理想性能仅差0.4~0.6dB左右的优异性能，而此时基于标准PSAM帧结构的短包传输系统与理想性能却存在着超过2.5dB的信噪比差距。

2）长包传输系统

考虑一个在AWGN信道下二元LDPC码编码的GMSK（Gaussian minimum shift keying）系统。其中，采用的编码是根据5G标准发展而来的（6144, 1024）LDPC码；GMSK调制参数是调制指数为0.5、记忆长度为2且归一化3dB带宽为0.5。该调制技术已经应用到美国及欧洲的深空通信系统、蜂窝数字分组数据系统、GSM系统以及Weightless-P物联网标准中。同样假设优化PSAM帧结构和标准PSAM帧结构都有三个导频块和两个数据块，且总长度分别为 $L_p = 300$ 和 $L_d = 6144$（导频开销 $\varepsilon \approx 0.05$）。图6展示了二元LDPC码级联GMSK系统的BER性能，其中理想性能也是没有载波频偏的情况。

从图6的试验结果可以看出，使用优化PSAM帧结构1&2的长包传输系统提供了优于使用标准PSAM帧结构的系统性能。具体而言，相对于理想性能，在BER=10^{-4}下，这两种优化PSAM帧结构仅带来了约0.2~0.4dB的性能损失，而标准PSAM帧结构却有超过0.8dB的性能损失。

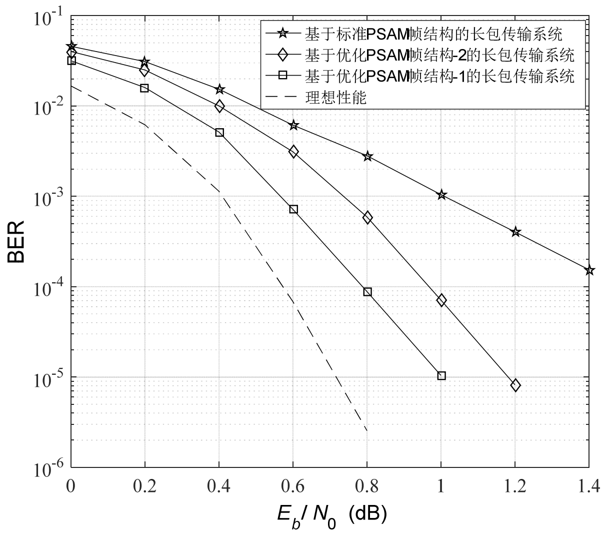

图6 二元LDPC码级联GMSK系统的BER性能

5 结束语

根据标准PSAM帧结构，本文设计了一种通用的PSAM帧结构并解决了其优化问题以期达到更高的导频利用率和更好的系统性能。根据费歇尔信息矩阵推导出载波频偏估计、相偏估计和时延估计的联合数据辅助与非数据辅助CRB，并进一步推导出对应于载波频偏估计CRB的近似结果。基于近似的CRB和经典的控制变量法，最后给出了一类实用的优化PSAM帧结构。通过应用试验结果可知，在短包传输和长包传输下，所提出的优化PSAM帧结构均获得了优于标准PSAM帧结构的CRB性能；同时在短包传输和长包传输的编码调制系统中，所提的优化PSAM帧结构要比标准PSAM帧结构表现出更出色的误码性能，因而更加适用于卫星物联网传输。

参考文献：

[1] IKPEHAI A, ADEBISI B, RABIE K M, et al. Low-power wide area network technologies for Internet-of-Things: A comparative review[J]. IEEE Internet of Things Journal, 2019, 6(2): 2225-2240.

[2] AYOUB W, SAMHAT A E, NOUVEL F, et al. Internet of mobile Things: Overview of LoRaWAN, DASH7, and NB-IoT in LPWANs standards and supported mobility[J]. IEEE Communications Survey & Tutorials, 2019, 21(2): 1561-1581.

[3] TAPPARE J, AFISIADIS O, MAYORAZ P, et al. An open-source LoRa physical layer prototype on GNU radio[C]// SPAWC 2020, Atlanta: IEEE Press, 2020.

[4] CAI X, CHEN Q, FAN P, et al. Enhanced frequency offset estimation based on pilot signal design over flat-fading channel[C]// CCWMC 2009, Shanghai: IET Press, 2009: 468-471.

[5] KRUEGER M, DENK R, YANG B. The training sequence code dependence of EDGE receivers using zero IF sampling[J]. IEEE Transactions on Wireless Communications, 2006, 5(2): 274-279.

[6] MOHER M L, LODGE J H. TCMP-a modulation and coding strategy for Rician fading channels[J]. IEEE Journal on Selected Areas in Communications, 1989, 7: 1347-1355.

[7] NESHAASTEGARAN P, BANIHASHEMI A H. Log-likelihood ratio calculation for pilot symbol assisted coded modulation schemes with residual phase noise[J]. IEEE Transactions on Communications, 2019, 67(5): 3782-3790.

[8] KAMIYA N, SASAKI E. Pilot-symbol-assisted phase noise compensation with forward-backward Wiener smoothing filters[J]. IEEE Transactions on Signal Processing, 2017, 65(17): 4443-4453.

[9] IX-ETSI. ESTI EN 302.307, V1.2.1 Digital Video Broadcasting (DVB); Second generation framing structure, channel coding and modulation systems for Broadcasting, Interactive Service, News Gathering and other broadband satellite applications (DVB-S2)[S]. 2009.

[10] RICE F. Carrier-phase and frequency-estimation bounds for transmissions with embedded reference symbols[J]. IEEE Transactions on Communications, 2006, 54(2): 221-225.

[11] PERAL-ROSADO J A, BARRETO-ARBOLEDA M A, ZANIER F, et al. Pilot placement for power-efficient uplink positioning in 5G vehicular networks[C]// SPAWC 2017, Sapporo: IEEE Press, 2017.

[12] SHAW C, RICE M. Optimum pilot sequences for data-aided synchronization[J]. IEEE Transactions on Communications, 2013, 61(6): 2546-2556.

[13] HOSSEINI E, PERRINS E. The Cramer-Rao bound for training sequence design for burst-mode CPM[J]. IEEE Transactions on Communications, 2013, 61(6): 2396-2407.

[14] YANG Y, DANG S, HE Y, et al. Markov decision-based pilot optimization for 5G V2X vehicular communications[J]. IEEE Internet of Things Journal, 2019, 6(1): 1090-1103.

[15] LOPEZ-SALAMANCA J J, SEMAN L O, BEREJUCK M D, et al. Finite-state Markov chains channel model for cubesats communication uplink[J]. IEEE Transactions on Aerospace and Electronic Systems, 2020, 56(1): 142-154.

[16] HERZET C, NOEL N, LOTTICI V, et al. Code-aided turbo synchronization[J]. Proceedings of the IEEE, 2007, 95(6): 1255-1271.

[17] TREES H L V, BELL K L. Bayesian Bounds for Parameter Estimation and Nonlinear Filtering/Tracking[M]. Hoboken, NJ, USA: Wiley, 2007.

[18] TAHERZADEH M, NIKOPOUR H, BAYESTEH A, et al. SCMA codebook design[C]//VTC2014-Fall, Vancouver: IEEE Press, 2014: 1-5.

[作者简介]

余忠洋（1989—），男，博士，讲师，主要研究方向：移动通信、卫星通信和物联网通信相关信号处理技术。

通信作者 E-mail：xd_yzy2013@sina.com

许蒙蒙（1987—），男，博士，讲师，主要研究方向：传感器网络、资源优化、路由技术。

王园园（1991—），男，博士，讲师，主要研究方向：人工智能、智能制造、工业图像智能检测。

高继勋（1980—），男，硕士，教授，主要研究方向：人工智能、图像识别、无线车联网络等。

基于改进 IDW 算法的未知环境多无人机协同频谱感知

施杰①种竞争①黄泽疆①杨志华①②
①(哈尔滨工业大学（深圳）深圳 518055)
②(鹏城实验室深圳 518055)

摘　要：针对传统的单无人机频谱感知精度低、效率低的问题，本文提出了一种基于改进 IDW 算法的未知环境多无人机协同频谱感知方法。该方法在多无人机频谱感知问题模型的基础上，通过对无人机路径规划代价函数中加入频谱强度代价因子，使得无人机更高效地在电磁环境中进行探索并采集频谱数据，通过将 IDW 算法与传播模型结合，提出改进 IDW 算法来对频谱数据补全形成最终的频谱地图。仿真结果表明，环境探索任务完成时间相比于当前先进的路径规划方法有所减少，补全算法精度相比于 IDW、张量补全法都有所提高，具有较高的实用价值。

关键词：多无人机；频谱感知；路径规划；反距离加权法
中图分类号：TN92 文献标识码：A 文章编号：
DOI：10.11999/JEIT××××××

A Multi-UAVs Cooperative Spectrum Sensing Method based on Improved IDW Algorithm

SHI Jie① CHONG Jing-zheng① Huang Ze-jiang① Yang Zhi-hua①②
① (Harbin Institute of Technology(Shenzhen), Shenzhen518055, China)
② (PengCheng Laboratory, Shenzhen518055, China)

Abstract: To solve the problems of low accuracy and efficiency in traditional single UAV spectrum sensing, a multi-UAVs collaborative spectrum sensing method based on improved IDW algorithm is proposed in this paper. Firstly, a spectrum sensing model for collaborative exploration of multiple UAVs was constructed; Secondly, a spectral intensity cost factor is added to the cost function of UAV path planning, enabling UAVs to explore electromagnetic environment more efficiently; Finally, the accuracy of spectrum data completion is improved by combining IDW algorithm with propagation model. The simulation results show that the task completion time is reduced compared to current advanced path planning methods, and the accuracy of the completion algorithm is improved compared to IDW and tensor completion methods, which has high practical value.

Key words: Unmanned Aerial Vehicle; Spectrum Sensing; Path Planning; Inverse Distance Weighting Method

1　引言

随着通信技术的发展和电磁设备数量的激增，频谱环境日益复杂，导致了电磁频谱资源的稀缺和严重的频谱安全状况，为频谱管理带来了新的挑战。如何有效利用有限的频谱资源和打击防范非法电磁设备的问题受到了相当大的关注。

频谱态势感知为解决以上问题提供了途径，其以频谱数据为基础，获知特定区域的电磁环境现况，并预测未来趋势。电磁频谱地图是一种多角度精确反映特定空间中电磁频谱分布情况的可视化方法[1]。其一般通过映射特定空间中无线电参数如接收信号强度(received signal strength ,RSS)的分布以达到获得频谱态势的目的。频谱地图的构建，对于频谱资源的分配和电磁环境的综合管治都具有重要意义。

构建频谱地图，首先需要使用频谱测量设备对原始数据进行采集。大部分现存方法中，原始数据采集方式为在特定区域内部署大量的频谱感应器。该类测量方法感应器部署量大，且感应器不具备移动性，仅能在固定范围内进行频谱数据的采集，若

采集区域发生变更，需要重新收集和部署感应器。无人机凭借其机动性高的优势可以应用于数据的采集及测量。随着待测区域的增大，不同场景下的多无人机协同路径规划算法被提出，文献[2]和[3]提出了一种基于人工势场的无人机路径规划方法，文献[4]和[5]提出了一种基于体素地图的无人机路径规划方法，使无人机平均分配探索区域并且避免无人机之间发生碰撞，文献[6]提出了一种基于遗传算法的路径规划方法，使得无人机尽可能地减少飞行能耗。但目前为了更好地进行频谱感知而设计的路径规划方法很少。

由于无人机所采集的原始数据在空间上具有离散性，需要在原始数据的基础上，对空缺值进行估计，以补全整个频谱地图。频谱地图补全方法通常分为两大类，即直接方法和间接方法。直接方法基于原始数据进行地图补全，其中最常见方法为逆距离加权法(Inverse Distance Weight，IDW)[7]。在文献[8,9]中，Melvasalo, M 和 Mao, D.等人使用克里金空间插值法实现缺失数据的预测。在文献[10]中，Tang, M.等人提出了一种结合先验模型的张量补全方法，据此可以获得测量区域的完整谱图。在文献[11]中，Huang, X.等人提出了一种新的大规模认知无线电网络（Cognitive Radio Nets, CRNs）的频谱映射方案，其中使用了历史频谱决策结果。与直接方法由原始数据获得缺失数据不同，间接方法由信道模型驱动的。在文献[12,13]中，作者分别采用了基于位置估计（Location Estimate, LE）的方法和信噪比辅助的方法，他们利用无线电传播模型等关于电磁环境的先验信息来提高数据恢复的性能。在文献[14]中，Sato, K.等人使用克里金空间插值法来估计基于实时方法的阴影衰落。在文献[15]中，Isselmou, Y.O.等人首先根据测量区域的先验信息获得原始频谱地图，然后根据实际测量数据对原始频谱地图进行校正。除以上提到的两类方法外，部分学者将神经网络运用于电磁频谱态势的构建，宋文佳等人利用长短期记忆(Long Short-Term Memory，LSTM)神经网络对无人机通信频谱进行感知判断[16]。张晗等人通过建立和训练残差自编码器(Residual Autoencoder, RA)，完成了特定电磁环境频谱地图的构建[17]。

大部分直接方法都基于某种空间插值算法，受限于算法特性，其未知元素的估计值往往介于所测量数据的最大值与最小值之间，不会超越此范围。因此，当所采集的频谱数据均匀分布在实际数据区域内时，直接方法可以在频谱地图构建中获得较好的性能；然而，当已知的数据集中分布在实际区域的某一部分时，估计值必然也全部处于该部分范围以内，算法性能无疑会下降。此外，上述 CRNs 等间接方法一般比直接方法具有更好的性能，且收集到的频谱数据是否在测量区域均匀分布，不会对算法性能产生影响；然而，间接方法对于电磁环境的先验信息依赖性较大，在对缺乏先验信息的未知区域进行频谱地图构建时，无法取得令人满意的效果，且现有大多数文献所介绍的间接方法中，都建立在整个测量区域仅有一个辐射源的假设上，这是不切实际的。利用神经网络构建频谱地图无需对电磁传播环境建模，也不需要使用空间插值算法，网络模型在得到充分训练后可以得到较好的结果。但神经网络系统如 RA 等需要足够现有的数据以进行训练，这要求提供大量在实际场景中不同电磁传播环境下的完整频谱数据，可行性不高，仍待进一步优化。另外，目前绝大多数关于频谱地图构建的文献都着眼于获得测量数据后的频谱地图补全阶段，往往未考虑数据采集阶段的工作，未根据所采用的数据处理算法的特性进行测量方法的调整与优化，如考虑到直接方法对于数据分布均匀性要求较高的特性，测量阶段需采用特定方法，使测量数据涵盖尽可能大的范围。

针对上述问题，本文提出了一种基于改进 IDW 算法的未知环境多无人机协同频谱感知方法，通过无人机编队获取区域内关键位点的测量数据，利用改进 IDW 算法对缺失数据进行估计，构建出高精确度的完整频谱地图。本文主要贡献如下：

（1）提出一种多无人机协同频谱感知方案。利用多无人机路径规划进行高效获取频谱数据，通过测量数据实时调整无人机行进轨迹，以获得辐射源附近位点信号强度的准确值，与插值算法的特性相契合，便于更精确地构建频谱地图。

（2）提出了改进的 IDW 算法用于频谱数据的补全。基于测量数据、信道模型和角度因子对经典 IDW 算法进行改进，以较高精度估计未知频谱数据，所构建的频谱地图相较于传统方法有明显的性能提升。

2　多无人机协同频谱感知问题

本文提出的多无人机协同频谱测绘系统如图 1 所示。在辐射源未知的前提下，多架无人机位于待

测区域的上方固定高度，进行完全自主的环境探索与路径规划，通过无人机上搭载频谱仪不断收集当前位置的 RSS 值，无人机在该高度的二维坐标记为 (x_i, y_i)，其中 $i \in [1, 2, \cdots, K]$ 为无人机编号，x_i、y_i 分别为无人机在二维空间中的横轴、纵轴坐标。

为了使多无人机高效、安全地完成探索任务，本文将无人机飞行时间以及飞行距离作为优化指标。首先考虑无人机飞行时间的优化。无人机路径规划的一个重点问题就是需要保证无人机在限定的时间内完成探索任务，因此从无人机开始探索到最后一个无人机结束探索所经历的时间应尽可能短；为了减少无人机的能耗，需要使得无人机的飞行距离尽可能短。具体表示为：

$$\begin{cases} J_T = \min[\max(t_i)] \\ J_D = \min \sum_{i=1}^{K} d_i \end{cases} \tag{1}$$

其中，t_i 为第 i 个无人机完成探索的时间，d_i 为第 i 个无人机的飞行距离。

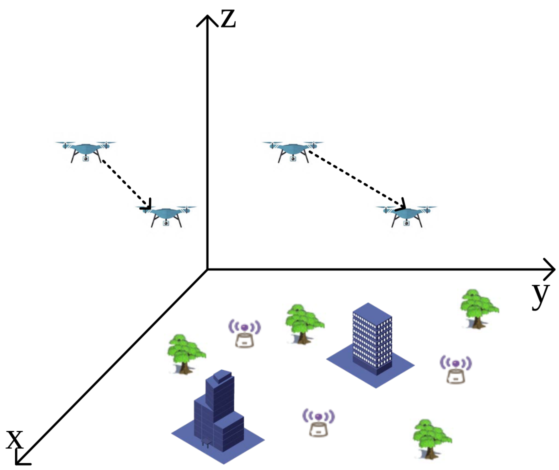

图 1　多无人机协同频谱测绘系统图

本文中的电磁频谱地图采用热力图的形式来展示接收到的 RSS 分布，不同的颜色代表不同的 RSS 值。为了更方便地进行数据的采集与处理，本文根据待测区域的起点与终点构建立体直角坐标系。该坐标系将待测区域分为 $N_1 \times N_2 \times N_3$ 个立方体，那么序号为 (n_1, n_2, n_3) 的立方体的坐标即可表示为 $((n_1 - 0.5) \times d_1, (n_2 - 0.5) \times d_2, (n_3 - 0.5) \times d_3)$，其中 d_1，d_2 和 d_3 分别为所设定的立方体的长、宽、高，每个立方体中存储该位置的 RSS 值。

RSS 取决于传播信道模型以及测量区域内所有辐射源的发射功率。某一立方体的理想接收频谱强度 P^{rx} 可以表示为：

$$\begin{cases} P_{\mathrm{i}}^{\mathrm{rx}}[\mathrm{dBm}] = P_{\mathrm{i}}^{\mathrm{tx}}[\mathrm{dBm}] - L_i[\mathrm{dB}] \\ P_{\mathrm{i}}^{\mathrm{rx}}[\mathrm{mW}] = 10^{P_{\mathrm{i}}^{\mathrm{rx}}[\mathrm{dBm}]/10} \\ P^{\mathrm{rx}}[\mathrm{mW}] = \sum_{i=1}^{N_{\mathrm{tx}}} P_{\mathrm{i}}^{\mathrm{rx}}[\mathrm{mW}] \end{cases} \tag{2}$$

式中，P^{tx} 代表第 i 个辐射源的发射功率，L_i 代表立方体与第个辐射源的路径损耗。

本文所采用的路径损耗模型(path loss, PL)在自由空间路径损耗模型(free space path loss)的基础上，考虑了正态阴影环境所产生的衰落信道的影响，并增加了无人机高度因素。PL 可以表示为：

$$PL[\mathrm{dB}] = 32.4 + 20\log_{10}(f_c) + 10(A + {h_{\mathrm{UAV}}}^{B}) \cdot \log_{10}(d) + \chi_\sigma \tag{3}$$

式中，d，f_c 和 h_{UAV} 分别为距离、载波频率和无人机所处高度；A 和 B 为环境所决定的参数。

考虑到存在多无人机对同一个立方体进行重复测量的可能，取多次测量结果的均值作为最终的测量值是合理的。因此，立方体的最终 RSS 测量值可表示为：

$$P^{\mathrm{mea}} = \frac{1}{N_{\mathrm{mea}}} \sum_{k=1}^{N_{\mathrm{mea}}} P^{\mathrm{meak}} \tag{4}$$

式中，P^{mea} 和 P^{meak} 分别代表立方体 RSS 的最终测量值和第 k 次测量值，N_{mea} 代表该立方体的测量次数。

利用插值算法对未知立方体 RSS 值进行估计，估计值取决于已知立方体的测量值及其所对应的权重值。未知立方体 RSS 估计值 $\hat{P}$ 可表示为：

$$\hat{P} = \sum_{j=1}^{N} \omega_j {P^{\mathrm{mea}}}_j \tag{5}$$

式中，ω_i 代表第 j 个测量值对于该估计值的权重，${P^{mea}}_j$ 代表第 j 个 RSS 测量值，N 表示测量值数目。

通过估计计算可得所有未知立方体的 RSS 值，构建完整频谱强度矩阵，为反映所构建频谱地图的精确度，可利用均方根误差（RSE）对其进行表示。RSE 表示频谱地图估计值与真实值之间的误差，其可表示为：

$$RSE(\mathrm{dB}) = 10\log_{10}\frac{\|\tilde{\chi} - \chi\|_2}{\|\chi\|_2} \tag{6}$$

其中，χ 为理论的频谱强度矩阵，$\tilde{\chi}$ 为恢复的频谱强度矩阵。

本文的电磁频谱地图构建整体流程图如图 2 所示。首先，多架无人机在设定的未知区域范围内自主探索并实时互通信息，根据规划的路径均匀地收集频谱强度数据；接着根据收集到的频谱强度数据通过频谱补全算法进行数据补全；最终生成补全后的电磁频谱地图。

3　基于频谱强度的多无人机协同路径规划方法

为了提高系统的探索效率，本文提出了一种基于频谱强度的多无人机协同路径规划方法。首先，我们基于无人机的状态和传感器数据进行地图边界的更新；其次，综合考虑飞行层面，边界层面，以及频谱强度的变化趋势来进行全局路径规划；最终，根据全局路径规划结果生成每个无人机高质量的局部路径结果。路径规划的结果会提交飞控来执行，并且上述过程将根据重规划策略来持续进行。

本文采用基于边界的方法来进行路径规划，而边界选择顺序的合理性直接影响到整个探索过程的效率。许多方法使用旅行商问题（Traveling Salesman Problem，TSP）来确定边界选择顺序。然而，大多数方法仅将边界之间的欧几里得距离作为 TSP 的代价，这种方法简单但不足。并且，传统的 TSP 方法规定多个无人机应从同一起点出发，该方法具有局限性。在本文的应用场景中，使用另一种非对称 TSP 的方法使无人机可从不同起点出发，并且为了更高效地获取频谱强度，无人机应往频谱强度变大的方向进行探索来缩小探索的范围以致于更好地恢复频谱地图并确定辐射源的大致位置。因此，本文在无人机路径规划的边界代价函数中加入频谱强度代价因子，通过求解非对称 TSP 问题生成更好的全局探索路径。

如图 3 所示，无人机从上一个位置 p_{-1} 飞行到当前位置 p_0，上一个位置收集到的频谱强度为 RSS_{-1}，当前收集到的频谱强度为 RSS_0，由此可以计算出当前位置与上一个位置的频谱强度差 ΔRSS：

$$\Delta RSS = RSS_0 - RSS_{-1} \tag{7}$$

若 ΔRSS 为正，则无人机上一时刻的飞行方向为频谱强度增大的方向；反之，则为频谱强度减小的方向。V_i 为下一时刻无人机的目标视点，为了使无人机往频谱强度变大的方向探索，本文计算了每个边界视点对应的频谱强度代价因子 $c_b(k)$：

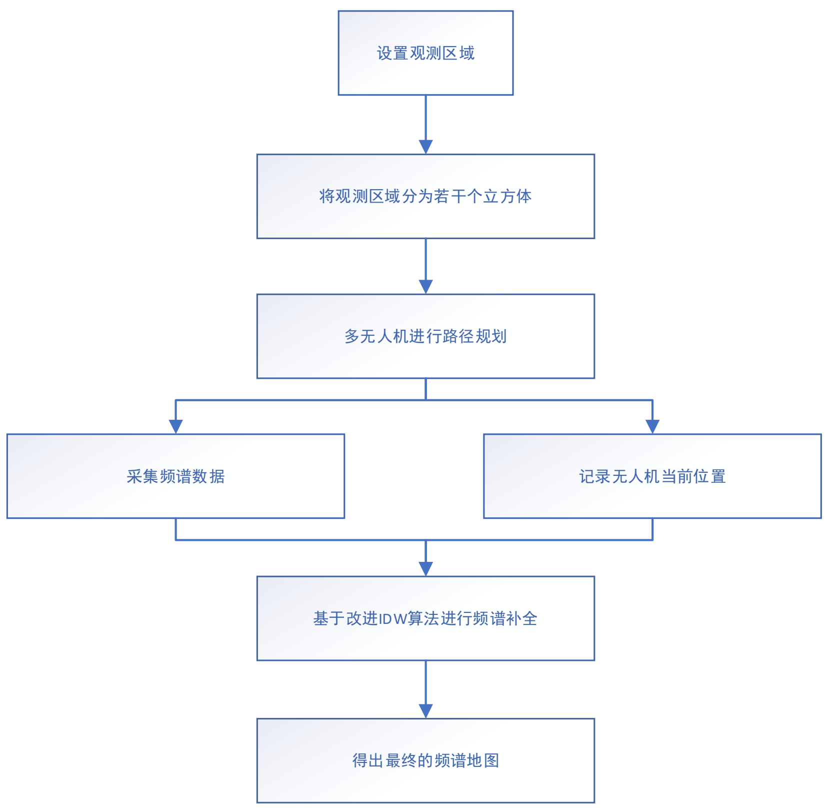

图 2　电磁频谱地图构建流程图

$$c_b(k)=\begin{cases}-1 & \Delta RSS\cdot\cos\theta_{0k}<0\\ 1 & \Delta RSS\cdot\cos\theta_{0k}>0\end{cases}\tag{8}$$

其中，θ_{0k} 为 p_{-1}、p_{-1}、V_k 三点连线的夹角。

最终，本文将 $c_b(k)$ 与文献[11]中使用的飞行层面因素整合到 ATSP 问题的代价矩阵 M_{TSP} 中：

$$M_{\mathrm{tsp}}(0,k)=t_{\mathrm{lb}}(V_0,V_k)+\omega_c\cdot c_b(k)\tag{9}$$

其中，$t_{\mathrm{lb}}(V_0,V_k)$ 为两视点之间的飞行时间因素，ω_c 为分配给 $c_b(k)$ 的权重。

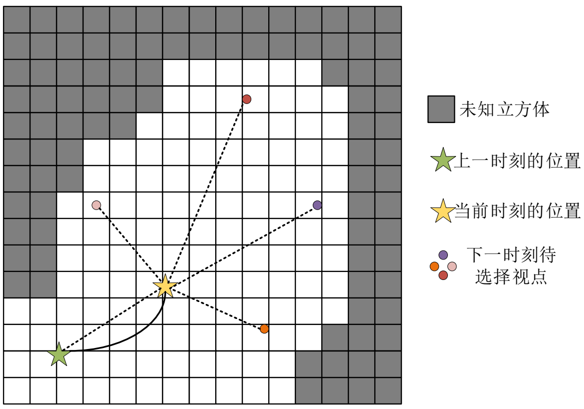

图 3　视点选择示意图

4　基于改进 IDW 算法的电磁频谱地图构建

利用无人机采集特定区域内部分采样点的RSS值，根据已知数据，利用加权插值方法对未知点的RSS 值进行估计。估计的 RSS 值可表示为：

$$\hat{P}_{S_0}=\sum_{i=1}^{N}\omega_i P_{S_i}\tag{10}$$

式中，S_i 代表编号为 i 的已知测量点，S_0 代表需要估计的点，代表估计的 RSS 值，ω_i 代表 S_i 的 RSS 值对于该估计值的权重，代表 S_i 的 RSS 值。

传统 IDW 算法的权重值可表示为：

$$\omega_i=\frac{\dfrac{1}{d_i^{\,p}}}{\sum\limits_{i=1}^{N}\dfrac{1}{d_i^{\,p}}}\tag{11}$$

式中，d_i 表示 S_i 与 S_0 的距离，p 为方次参数。

传统的 IDW 方法是建立在未知点接近已知测量点这一假设上的，而构建频谱地图的现实情况并不总满足该条件。同时，该方法只考虑了距离的影响，忽略了天线角度和路径损耗等在真实电磁传播环境中影响 RSS 的其他因素。由于存在这些缺陷，利用传统的 IDW 算法进行频谱地图的补全往往效果不佳。针对以上问题，本文从以下几个方面对IDW 算法的权重计算方法进行改进：

首先，采用基于修正的谢泼德方法（modified Shepard's method, MSM）的距离因子，这是一种基于数学函数的优化逆距离加权插值方法[7]。距离系数可表示如下：

$$p_i=\begin{cases}\dfrac{1}{d_i} & ,0<d_i\le\dfrac{r}{3}\\ \dfrac{27}{4r}(\dfrac{d_i}{r}-1)^2 & ,\dfrac{r}{3}<d_i\le r\end{cases}\tag{12}$$

式中，r 代表所测量区域的半径。

其次，考虑文献[18]所提出方法中的角度因素，该方法计算每个已知点位置和每个估计点位置的角度，并将角度因素作为控制测量值对估计值影响力大小的参数之一。角度系数可以表示如下：

$$a_i=\frac{\sum\limits_{j=1,j\ne i}^{N}p_i\cdot(1-\cos\varphi_{ij})}{\sum\limits_{j=1,j\ne i}^{N}p_i}\tag{13}$$

S_i 与 S_0 的位置角度：

$$\begin{aligned}\cos\varphi_{ij}&=\frac{v_iv_j}{|v_i|\cdot|v_j|},\\ v_i&=(x_i,y_i,z_i),\\ v_j&=(x_j,y_j,z_j)\end{aligned}\tag{14}$$

最后，考虑所测量区域的传播环境特征，将信道传播模型因素纳入计算权重值的要素之一，其可以表示如下：

$$l_i=\frac{L_i^{-1}}{\sum\limits_{j=1}^{N}L_j^{-1}}\tag{15}$$

式中，l_i 为 S_i 与 S_0 的之间的路径损耗。L_i 由所使用的信道传播模型所决定，如考虑无人机高度与阴影效应的自由空间传播模型，其传播损耗公式为：

$$L(f_c,d,h_{\mathrm{UAV}})[\mathrm{dB}]=32.4+20\lg(f_c)+10(A+h_{\mathrm{UAV}}{}^{B})\cdot\\ \cdot\lg(d)+\chi_\sigma\tag{16}$$

式中，d，f_c 和 h_{UAV} 分别为距离、载波频率和无人机所处高度；A 和 B 为环境所决定的参数。

考虑以上所有因素，的 RSS 值对于预测值的权重为：

$$\omega_i = \frac{p_i^{t_1} \cdot (1+a_i)^{t_2} \cdot (1+l_i)^{t_3}}{\sum_{j=1}^{N} p_i^{t_1} \cdot (1+a_i)^{t_2} \cdot (1+l_i)^{t_3}} \tag{17}$$

式中，t_1，t_2 和 t_3 分别为控制距离因子、角度因子和路径损耗因子对权重影响程度的参数。

将权重值 ω_i 代入式(9)，便可计算得到未测量点的估计值。

5　仿真结果与分析

一般来说，无人机现场进行频谱采集的费用昂贵并且在实际场景存在较高误差，因此一种基于光线追踪（RT）模拟的建模方法被当作一种替代方案。针对本文提出的频谱补全算法，使用 Matlab 平台进行仿真验证，场景设置如下：选取哈工大深圳校园为实验场景，在场景中随机设置多个辐射源。重建频谱地图的区域设为 100m×100m 的正方形，将其划分成 100×100 个网格，每个网格为边长为 1m 的正方形，信号源的频谱设为 20MHz，辐射源的功率为 0dB，通过理论分析出的该场景下的频谱地图如图 4 所示。无人机数量设置为 3，无人机飞行的安全距离设置为 10m，各个无人机飞行参数相同，其中直线飞行时无人机为匀速飞行，速度设置为 5m/s，飞行高度始终为 50m。

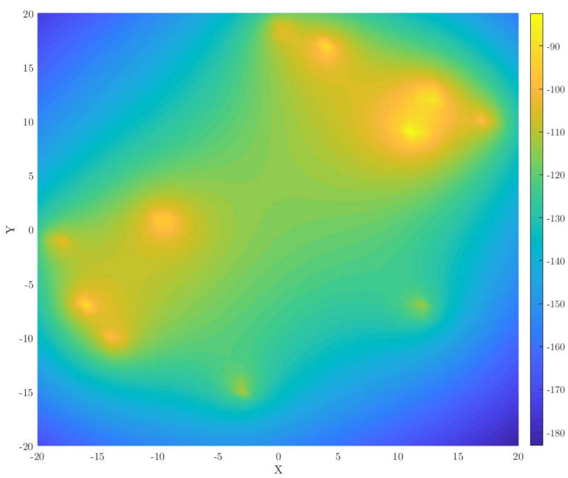

图 4　理论频谱地图

根据本文提出的路径规划算法，无人机根据频谱强度的变化来自主规划路径，我们将本文提出的算法与三种目前最先进的路径规划算法进行比较，包括 FUEL、Aeplanner、NBVP。本文采用这三种算法的开源程序及默认参数设定放在我们设定的场景中进行仿真，仿真的结果如表 1 所示。

表 1　　路径规划仿真结果

路径规划算法	探索时间（s）				飞行距离（m）			
	Avg	Std	Max	Min	Avg	Std	Max	Min
Aeplanner	418	49	422	203	202	26	255	142
NVBP	680	143	941	426	305	62	422	205
FUEL	154	11	188	148	209	16	246	203
Proposed	125	9	157	103	156	11	180	135

由表 2 可以看出，本文提出的算法在探索时间和飞行距离上有了明显的缩短，主要原因在于本文提出的算法根据频谱强度使无人机往频谱强度更大的区域探索，并且实时缩小了所需要探索的范围，由此证明本文提出的无人机路径规划算法适用于频谱测绘的应用场景。

收集到的频谱数据如图 5(a)所示，为了验证本文提出的频谱补全算法的有效性，根据无人机采集到的频谱数据，经过频谱补全算法，得出最终的补全结果如图 5(b)所示，为了衡量频谱地图重建的性能，计算其 RSE。

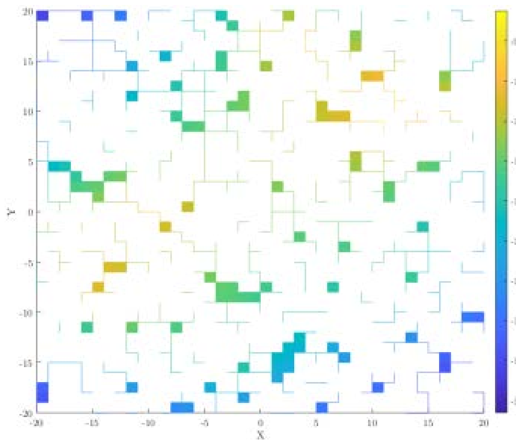

(a)频谱数据采集

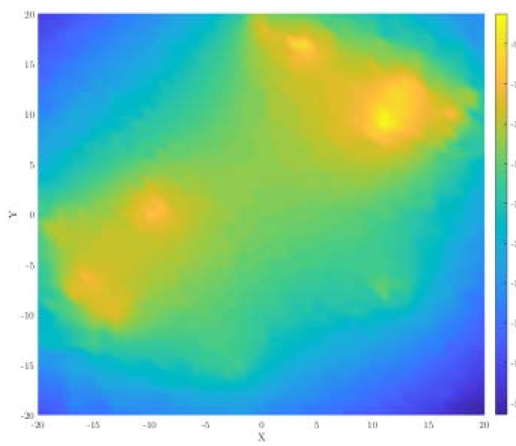

(b)频谱数据补全结果

图 5　收集到的频谱数据

在比较频谱数据处理方法的性能时，我们对数据进行随机采样，使得频谱地图中只保留了部分采样点，该采样率表示在频谱中观察到的 RSS 百分比。仿真中，本文将改进的 IDW 算法与经典的 IDW 算法与张量补全算法（HaLRTC）在不同采样率下的 RSE 进行比较，仿真结果如图 6 所示。

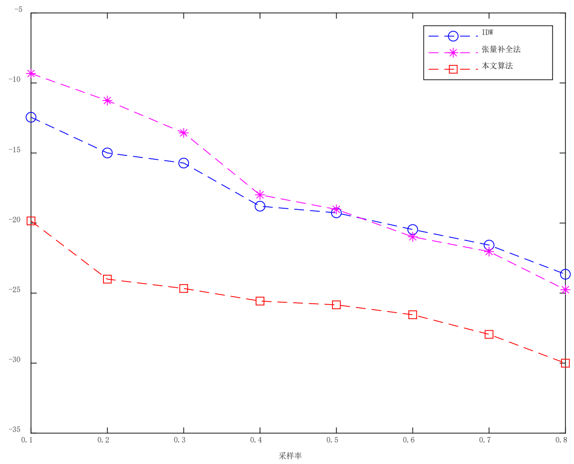

图 6　三种算法的 RSE 对比图

经过对比可以发现，频谱重建的误差随着采样率的增大而减小。在不同的采样率下，本文提出的方法相对 IDW 和张量补全法都更加准确和稳定。由此可以证明本文提出的改进 IDW 算法在频谱重建精度上有显著地提升。

6　结束语

针对单无人机进行频谱感知存在精度低、效率低的问题，提出了一种基于改进 IDW 算法的多无人机协同频谱感知方法，携带频谱仪的无人机在同一高度从不同起点根据代价函数对未知区域进行探索，采集频谱数据，使用结合传播模型的改进 IDW 算法对频谱数据进行补全，最终恢复出未知区域的频谱地图。通过仿真可以发现，本文提出的多无人机路径规划算法可以有效地提高无人机探索效率，并且改进 IDW 算法相比于传统的 IDW 以及张量补全算法都有大幅提升。本文中只考虑了单一频率下的频谱强度，后续研究将对频谱环境更复杂的情景进行进一步研究，并且进一步优化无人机路径规划算法。

参考文献

[1] GUO L,WANG M,LIN Y. Electromagnetic Environment Portrait Based on Big Data Mining[J]. Wireless Communications and Mobile Computing,2021(3):1-13.

[2] JAYAWEERA H M,HANOUN S. A dynamic artificial potential field （D-APF） UAV path planning technique for following ground moving targets[J]. IEEE Access,2020,8:192760-192776.

[3] SULIEMAN M H, GURSOY M C, KONG Fanxin. Antenna pattern aware UAV trajectory planning using artificial potential field[C]. 2021 IEEE/AIAA 40th Digital Avionics Systems Conference(DASC). San Antonio,TX,USA,2021:1-7.

[4] Y. Zhao, L. Yan, H. Xie, J, P. Wei. Autonomous Exploration Method for Fast Unknown Environment Mapping by Using UAV Equipped with Limited FOV Sensor[J]. IEEE Transactions on Industrial Electronics, 2023, doi: 10.1109.

[5] B. Zhou, H. Xu and S. Shen. RACER: Rapid Collaborative Exploration With a Decentralized Multi-UAV System. IEEE Transactions on Robotics, 2023, 39(3):1816-1835.

[6] ASIM M, MASHWANI W K, BELHAOUARI S B, et al. A novel genetic trajectory planning algorithm with variable population size for multi-UAV-assisted mobile edge computing system[J]. IEEE Access,2021,9:125569-125579.

[7] Denkovski, D., Atanasovski, V., Gavrilovska, L., Riihijärvi, J., and Mähönen, P. Reliability of a radio environment Map: Case of spatial interpolation techniques[C]. In Proceedings of the 7th International ICST Conference on Cognitive Radio Oriented Wireless Networks and Communications (CROWNCOM 2012), Stockholm, Sweden, 18–20 June 2012; pp. 248–253.

[8] Melvasalo, M., Koivunen,V., and Lundn, J. Spectrum maps for cognition and coexistence of communication and radar systems[C]. In Proceedings of the 50th Asilomar Conference on Signals, Systems and Computers (ACSSC 2016), Pacific Grove, CA, USA, 6–9 November 2016; pp. 58–63.

[9] Mao, D., Shao, W., Qian, Z., Xue, H., Lu, X., and Wu, H. Constructing accurate Radio Environment Maps with Kriging Interpolation in Cognitive Radio Networks[C]. In Proceedings of the 2018 Cross Strait Quad-Regional Radio Science and Wireless Technology Conference (CSQRWC 2018), Xuzhou, China, 21–24 July 2018; pp. 1–3.

[10] Tang, M., Ding, G., Wu, Q., Xue, Z., and Tsiftsis, T.A. A Joint Tensor Completion and Inference Scheme for Multi-Dimensional Spectrum Map Construction[J]. IEEE Access 2016, 4, 8044–8052.

[11] Huang, X., Gao, Y., Tang, X., and Wang, S. Spectrum Mapping in Large-Scale Cognitive Radio Networks with Historical Spectrum Decision Results Learning[J]. IEEE Access 2018, 6, 21350–21358.

[12] Yilmaz, H.B. and Tugcu, T. Location estimation-based radio environment map construction in fading channels[J]. Wirel. Commun. Mob.Comput. 2015, 15, 561–570.

[13] Sun, G. andBeek, J. Simple distributed interference source localization for radio environment mapping[C]. In Proceedings of the 2010 IFIP Wireless Days (WD 2010), Venice, Italy, 20–22 October 2010; pp. 1–5.

[14] Sato, K.,　Inage, K., and Fujii, T. Radio Environment Map Construction with Joint Space-Frequency Interpolation[C]. In Proceedings of the 2020 International Conference on Artificial Intelligence in Information and Communication (ICAIIC 2020), Fukuoka, Japan, 19–21 February 2020; pp. 051–054.

[15] Isselmou, Y.O., Wackernagel, H., Tabbara, W., and Wiart, J. Geosta-

tistical interpolation for mapping radio-electric exposure levels[C]. In Proceedings of the First European Conference on Antennas and Propagation (EUCAP 2006), Nice, France, 6–10 December 2006; pp. 1–6.

[16] 宋文佳,何昊轩,钟天宇等.基于 LSTM 神经网络的无人机通信频谱感知算法[J].科技风, 2023(14): 1-3. DOI: 10.19392/j.cnki.1671-7341.202314001.
Song Wenjia, He Haoxuan, and Zhong Tianyu. Spectrum Sensing Algorithm for UAV Communication Based on LSTM Neural Network[J]. Science and Technology Wind, 2023 (14): 1-3. DOI: 10.19392/ j.cnki.1671-7341. 202314001

[17] 张晗,韩宇,姜航等.基于残差自编码器的电磁频谱地图构建方法[J].无线电通信技术,2023,49(02):255-261.
Zhang Han, Han Yu, and Jiang Hang. Construction method of electromagnetic spectrum map based on residual Autoencoder [J]. Radio Communication Technology, 2023,49 (02): 255-261

[18] Debroy, S., Bhattacharjee, S., and Chatterjee, M. Spectrum Map and Its Application in Resource Management in Cognitive Radio Networks[J]. IEEE Trans. Cogn. Commun. 2015, 1, 406–419.

[19] B. Zhou, Y . Zhang, X. Chen, and S. Shen. Fuel: Fast uav exploration using incremental frontier structure and hierarchical planning[J]. IEEE Robotics and Automation Letters, 2021, 6(2), 779–786.

[作者简介]

施杰：男，哈尔滨工业大学（深圳）在读研究生，研究方向为无人机路径规划.

种竟争：男，哈尔滨工业大学（深圳）在读博士生，研究方向为无人机集群技术

黄泽疆：男，哈尔滨工业大学（深圳）本科毕业生，研究方向为电磁频谱感知

杨志华：男，哈尔滨工业大学（深圳）副教授，博士生导师，研究方向为空间通信、DTN 网络、无人机集群技术.